Advanced Structured Materials

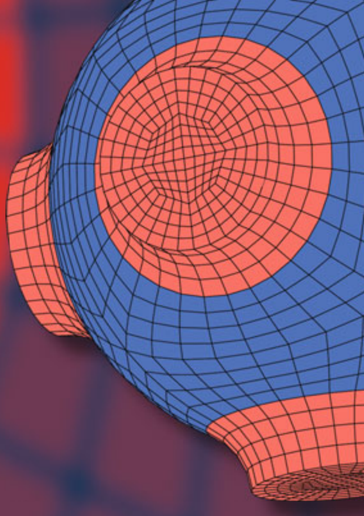

Holm Altenbach
Alexander Belyaev
Victor A. Eremeyev
Anton Krivtsov
Alexey V. Porubov *Editors*

# Dynamical Processes in Generalized Continua and Structures

Springer

# Advanced Structured Materials

## Volume 103

Common engineering materials reach in many applications their limits and new developments are required to fulfil increasing demands on engineering materials. The performance of materials can be increased by combining different materials to achieve better properties than a single constituent or by shaping the material or constituents in a specific structure. The interaction between material and structure may arise on different length scales, such as micro-, meso- or macroscale, and offers possible applications in quite diverse fields.

This book series addresses the fundamental relationship between materials and their structure on the overall properties (e.g. mechanical, thermal, chemical or magnetic etc) and applications.

The topics of *Advanced Structured Materials* include but are not limited to

- classical fibre-reinforced composites (e.g. glass, carbon or Aramid reinforced plastics)
- metal matrix composites (MMCs)
- micro porous composites
- micro channel materials
- multilayered materials
- cellular materials (e.g., metallic or polymer foams, sponges, hollow sphere structures)
- porous materials
- truss structures
- nanocomposite materials
- biomaterials
- nanoporous metals
- concrete
- coated materials
- smart materials

Advanced Structured Materials is indexed in Google Scholar and Scopus.

More information about this series at http://www.springer.com/series/8611

Holm Altenbach · Alexander Belyaev ·
Victor A. Eremeyev · Anton Krivtsov ·
Alexey V. Porubov
Editors

# Dynamical Processes in Generalized Continua and Structures

Springer

*Editors*
Holm Altenbach
Lehrstuhl Technische Mechanik
Otto-von-Guericke-Universität Magdeburg
Magdeburg, Sachsen-Anhalt, Germany

Victor A. Eremeyev
Faculty of Civil and Environmental Engineering
Gdańsk University of Technology
Gdańsk, Poland

Alexey V. Porubov
Institute of Problems of Mechanical Engineering
Russian Academy of Sciences
St. Petersburg, Russia

Alexander Belyaev
Institute of Problems of Mechanical Engineering
Russian Academy of Sciences
St. Petersburg, Russia

Anton Krivtsov
Department of Theoretical Mechanics
Peter the Great St. Petersburg Polytechnic University
St. Petersburg, Russia

ISSN 1869-8433 ISSN 1869-8441 (electronic)
Advanced Structured Materials
ISBN 978-3-030-11664-4 ISBN 978-3-030-11665-1 (eBook)
https://doi.org/10.1007/978-3-030-11665-1

Library of Congress Control Number: 2018967738

© Springer Nature Switzerland AG 2019
This work is subject to copyright. All rights are reserved by the Publisher, whether the whole or part of the material is concerned, specifically the rights of translation, reprinting, reuse of illustrations, recitation, broadcasting, reproduction on microfilms or in any other physical way, and transmission or information storage and retrieval, electronic adaptation, computer software, or by similar or dissimilar methodology now known or hereafter developed.
The use of general descriptive names, registered names, trademarks, service marks, etc. in this publication does not imply, even in the absence of a specific statement, that such names are exempt from the relevant protective laws and regulations and therefore free for general use.
The publisher, the authors and the editors are safe to assume that the advice and information in this book are believed to be true and accurate at the date of publication. Neither the publisher nor the authors or the editors give a warranty, express or implied, with respect to the material contained herein or for any errors or omissions that may have been made. The publisher remains neutral with regard to jurisdictional claims in published maps and institutional affiliations.

This Springer imprint is published by the registered company Springer Nature Switzerland AG
The registered company address is: Gewerbestrasse 11, 6330 Cham, Switzerland

# Preface

Professor Dmitry Anatol'evich Indeitsev is one of the leading Russian scientists in the field of solid mechanics, who won recognition from the world scientific community. A wide range of his scientific interests includes wave dynamics, dynamic problems of coupled processes in continuum mechanics, wave and diffusion processes in multi-component media, contact interaction of bodies with varying boundary. It should be especially emphasized that Dmitry Indeitsev is one of the pioneers initiating investigation of the trapped mode phenomenon in solids. He found out a complete class of mechanical models admitting closed form solutions. Study of this class allowed him to formulate a number of fundamental results and identify the basic conditions for existence of localized solutions. These results were later confirmed by a large number of examples for more complex waveguide models of different physical nature (fluid–structures interaction problems, film structures, meta-materials, etc.). His results stimulated many scientists to carry out research in this particular field.

Another direction of research by Prof. Indeitsev is the development of new approaches to description of dynamic processes in materials with a complex internal structure on the basis of first principles of continuum mechanics. He developed a mathematical model of influence of the dynamic stresses on the diffusion processes in materials. The model is based upon the equations of a two-component medium and takes into account the internal interaction forces, as well as the effect of the spherical part of stress tensor of the crystal lattice on the magnitude of these forces. In recent years, Prof. Indeitsev was successfully engaged in the development of new models of heat transfer in dielectrics and metals under laser excitation.

Dmitry Indeitsev was born on December 2, 1948, in Gorky, now Nizhny Novgorod. In 1972, he graduated from the Leningrad Polytechnic Institute (now Peter the Great St. Petersburg Polytechnic University), Faculty of Physics and Mechanics with a degree in Dynamics and Strength of Machines. In 1972–1987, he was a member of the research laboratory of Leningrad Higher Naval Engineering School named after F. E. Dzerzhinsky.

An important stage of scientific and organizational activities of Prof. Indeitsev is associated with work at the Institute for Problems in Mechanical Engineering of the Russian Academy of Sciences (IPME RAS) which he joined in March 1987. First he worked as a senior researcher, in February 1989 he was appointed the head of laboratory “Hydroelasticity” and in 1993 the deputy director for scientific work. In 1994, he defended his dissertation for the degree of Doctor of Sciences in Physics and Mathematics (habilitation) and in 1999 he was awarded the title of Professor in “Mechanics of Solids”. In July 2002, he was appointed the Acting Director, in May 2004 Director of IPME RAS, since June 2015 he is the Scientific Head of IPME RAS. In May 2006, he was elected a Corresponding Member of the Russian Academy of Sciences in the field of solid mechanics.

Under his supervision, the Institute for Problems in Mechanical Engineering of the Russian Academy of Sciences has passed a difficult period of formation and grown into an authoritative research center in Russia and abroad; nowadays it keeps leading positions in many scientific fields of engineering, mechanics, and automatic control. Many members of the Institute have achieved significant success in research and teaching due to the great support and invaluable help by Prof. Indeitsev. The most important role in the development of the Institute, as well as all the Russian science, is played by regular scientific events organized by IPME RAS. Since 1994, Prof. Indeitsev is the main organizer and supervisor of the Annual International Summer School for mechanical scientists “Analysis and Synthesis of Nonlinear Oscillatory Mechanical Systems. Actual Problems of Mechanics”, which developed into a celebrated Annual International Conference “Advanced Problems in Mechanics”, where numerous famous scientists from different countries have reported their results. Regular participation of this conference helped young researchers, not only the Institute members, went from being Ph.D. students to candidates and doctors of science.

Professor Indeitsev is the Head of Department “Mechanics and Control Processes” of the Institute of Applied Mathematics and Mechanics at Peter the Great St. Petersburg Polytechnic University, he is also Professor of the Department “Theory of Elasticity” of the Faculty of Mathematics and Mechanics at the St. Petersburg State University.

He is a member of many scientific societies: Russian National Committee on Theoretical and Applied Mechanics (RNCTAM), European Mechanics Society (EUROMECH), Society of Applied Mathematics and Mechanics, Germany (GAMM), etc.

Professor Indeitsev is a member of the editorial boards of eight scientific journals, among them “Physics and Mechanics of Materials”, “Acta Mechanica”, “Advances in Mechanics”, “Reviews on Advanced Materials”.

Professor Indeitsev is author of more than 200 scientific papers. He is not only a brilliant scientist and organizer, but also a splendid scientific adviser who is able to create an atmosphere of scientific creativity by generating bright and productive scientific ideas. He belongs to those people who are able to unite the team, support and cultivate young talents. His enthusiasm, true passion, and uncompromising attitude toward science are transferred to all who have the good fortune to communicate with him. We are amazed by his human and scientific generosity which he shares his time, forces, and ideas with us.

This volume of the Advanced Structured Materials Series is dedicated to the seventieth birthday of Prof. Dmitry Indeitsev and contains a selection of scientific papers prepared by his friends and colleagues from different countries. Some of these works are devoted to research related to the scientific interest by Prof. Indeitsev, while the others to some extent are inspired by fruitful scientific discussions with him. Finally, the collection presents works devoted to those modern directions in mechanics that may become the subject of his scientific interest in the future.

| | |
|---|---|
| Magdeburg, Germany | Holm Altenbach |
| St. Petersburg, Russia | Alexander Belyaev |
| Gdańsk, Poland | Victor A. Eremeyev |
| St. Petersburg, Russia | Anton Krivtsov |
| St. Petersburg, Russia | Alexey V. Porubov |
| December 2018 | |

# Contents

# New Nonlinear Model for Ice Induced Vibrations

**A. K. Abramian and S. A. Vakulenko**

**Abstract** In this paper a new simple oscillator model is considered describing ice induced vibrations of upstanding, water surrounded, and bottom-founded offshore structures. Existing models are extended by taking into account deformations of an ice floe, and a moving contact interaction between an ice rod, which is cut out from the floe, and the oscillator which represents the offshore structure. Special attention is paid to a type of ice-induced vibrations (IIV) of structures, known as frequency lock-in, and characterized by having the dominant frequency of the ice forces near a natural frequency of the structure. We propose a new asymptotical method that allows us to exclude ice floe deformations and obtain a nonlinear equation for structure vibrations. We investigate instability onset, and resonance effects for these vibrations.

## 1 Introduction

In this paper, we investigate ice induced vibrations (IIV) of structures such as offshore drilling platforms, lighthouses, and bridge pierces. This problem has important applications for engineering in Arctic region. In fact, as a result of an ice sheet impact, such structures can exhibit large amplitude vibrations, which break their functioning and even destroying them. The IIV are generated by a complicated process involving ice failure, nonlinear dynamics of structures and an interaction between ice and structures. This problem was considered in many papers, and we, do not pretending on an overview, concern here with some works, which were corner-stones for our model. The first model of IIV was proposed in [1], where the ice failure was considered as a sequence of discrete events. Actually, for small ice velocities interaction between a structure and an ice sheet leads to a crack formation in the ice sheet. Then the ice sheet crunches in the structure-ice contact area. This model was extended by Sodhi

---

A. K. Abramian (✉) · S. A. Vakulenko
Institute for Problems in Mechanical Engineering, Saint Petersburg, Russia
e-mail: andabr55@gmail.com

S. A. Vakulenko
e-mail: vakulenfr@mail.ru

H. Altenbach et al. (eds.), *Dynamical Processes in Generalized Continua and Structures*, Advanced Structured Materials 103,
https://doi.org/10.1007/978-3-030-11665-1_1

[2] and more recently [3], where randomness of the ice failure is taken into account. Mathematically, these models describe oscillators under an external time depending force, which simulates an action of the discrete events. These models exhibit a resonance effect as a possible source of large IIV's. Other IIV's models treat the ice failure as a continuous process (see, for example, [4]) and can be applied for large ice velocities. In this case the crushing ice force has a relatively low magnitude and structure oscillations have low magnitudes and high frequencies. As it was mentioned in [3] these situations are less important for safety applications since dangerous vibrations start with smaller velocities. In this paper, we propose a model extending the previous ones, in particular, suggested in [1–3]. Following [1–3] we consider structures as oscillators, however, we suppose that these oscillators can involve a number of interaction modes. A novelty with respect to previous investigations is that we study the ice sheets and ice-structure interactions in more detail. We describe deformations of the ice sheets taking into account a contact between structures and ice. For oscillator-ice interactions, we take into account extrusion effects. This consideration leads to a difficult problem, which involves partial differential equations (PDE's) for the ice sheets and ordinary differential equations (ODE's) for structures. The main difficulty is that these PDE and ODE are coupled via boundary conditions for the ice sheet deformations on a contact line between the ice sheet and the structure. This contact line is unknown. Such contact problems are difficult, nonetheless, we are capable to resolve our problem using a new asymptotic approach. This approach exploits mechanical properties of the ice sheet model, namely, we assume that the ice sheet internal friction is small whereas the sound velocity of the ice is large. This asymptotic approach based on such assumptions allows us to find an ODE for the structure, where ice deformations are excluded. This equation describes (for a single mode approximation) a linear oscillators perturbed different nonlinear terms. These terms admit transparent physical interpretations and describe the following effects:

**i** The effect of water mass extrusion under the ice sheet action that leads to a friction, nonlinear effects and a time periodic forcing;
**ii** The effect of a contact interaction between ice-sheet and structure that leads to nonlinearities, a oscillator frequency shift, an "added" mass and a friction, which depend on ice velocity $V$;

Note that in **i** and **ii** we take into account randomness of the ice failure process. The resulting equation for the IIV terms involve many parameters, but a crucial parameter is the ice velocity $V$. The dynamics of this oscillator model can be studied by well known methods (for example, [5]). The following main results were obtained by this asymptotic investigation and numerical simulations.

A resonance is possible for some $V$ that can lead to large vibrations amplitude $A$. We obtain a plot of $V - A$ dependence, which, for some parameters choice, shows a peak. This means that for small speeds $V$ we have no amplitude increase, as well as for large $V$. The height and width of the peak depend on the system parameters. The randomness decreases the height and increases the width and a larger randomness can produce many smaller peaks. Other parameters also affect the peak properties. Note that simulations by Matlock and extended Matlock models [1, 3] show a few of peaks, and relatively small vibration amplitude increase (see Fig. 3 in [3]). Some simulations by our models show similar pictures, but under an appropriate parameters choice our model exhibits an essentially larger amplitude growth and a single peak. Effect **ii** essentially depends on the ice velocity $V$. For $V$ this effect reinforces the resonance. Moreover, we obtained that increase of $V$ can decrease the friction, which can become even negative, and it also decreases the effective structure mass (effect of negative “added mass”). These results are consistent with experimental data [6]. The numerical simulations show an exponentially growth of amplitude vibrations when a negative friction contribution is large enough. We find thus the second mechanism of structure destruction alternative to the resonance.

For multi oscillator models peaks corresponding to the resonances becomes higher and the peak width increases. Moreover, the peak form may be complicated as a result of many resonances and a nonlinear interaction between modes. Note that the vibrations for small $V$, resonance $V$ and large $V$ have quite different form. A Fourier analysis of the structure response was made to understand oscillation form. For large $V$ the response is essentially more stochastic and noisy than for resonance and small $V$.

## 2 Statement of the Problem

Our model is defined by a system of two equations. Following [1–3], we consider the structure as a rigid body having a contact with the ice sheet. The first equation describes a nonlinear oscillator and has the form

$$Mq_{tt} + Gq + g(q, q_t, t) = \mu(t), \tag{1}$$

where $q = q(t)$ is a unknown function of time $t$, which defines the structure vibration amplitude, $M$ and $G$ are positive coefficients describing the mass and the stiffness of the structure. The term $g(q, q_t, t)$ defines nonlinear effects caused by the interaction of the structure with the water, which can depend on $t$. We assume that

$$g(q, q_t, t) = -a_0 \frac{q_t - s_t}{q - s}, \quad a_0 > 0. \tag{2}$$

The term $\mu$ defines an influence of the ice on the structure and has the form

$$\mu(t) = \rho_0 c_0^2 u_x(x, t)|_{x=q(t)}, \tag{3}$$

where $u(x, t)$ is a displacement of the ice, $\rho_0$ and $c_0$ are positive parameters, where $\rho_0$ is the ice density and $c_0$ stands for the ice sound velocity. The oscillator frequency is defined by $\omega^2 = G/M$.

The second equation describes the displacement $u(x, t)$ of the ice sheet, which occupies the domain $I_q = \{x : q < x < L\}$. This equation is a PDE, which reads

$$u_{xx} - c_0^{-2} u_{tt} - \beta u_t - k_0 u = -\beta s_t + k_0 s, \tag{4}$$

where $u(x, t)$ is a unknown ice displacement, and $\beta$ and $k_0$ are positive parameters, which determine the internal ice sheet friction and the ice sheet compression, respectively. The function $s(t)$ is a shift of the structure center and we suppose that $s(t)$ is defined by

$$s(t) = s_0 - Vt + \rho(t), \quad V > 0, \tag{5}$$

where

$$\rho(t) = \sum_{k=1}^{M(t)} d_k H(t - t_k). \tag{6}$$

Here $t_k$ are time moments when the ice sheet breaks, $d_k$ are lengths of ice blocks (tooths) that split off and $H(z)$ stands for the Heaviside step function. The time moments $t_k$ are defined by the condition

$$p(t_k) = p_c, \tag{7}$$

which means the pressure $p$ attains a critical level $p_c$. The pressure $p$ can be computed by the relation

$$p(t) = p_0 \frac{v(t - t_k)}{s(t)}, \tag{8}$$

where $t_k$ is the moment of the previous break. Therefore, the breaks are determined by the relation

$$p(t_{k+1}) = p_0 \frac{v(t_{k+1} - t_k)}{s(t_{k+1})} = p_c. \tag{9}$$

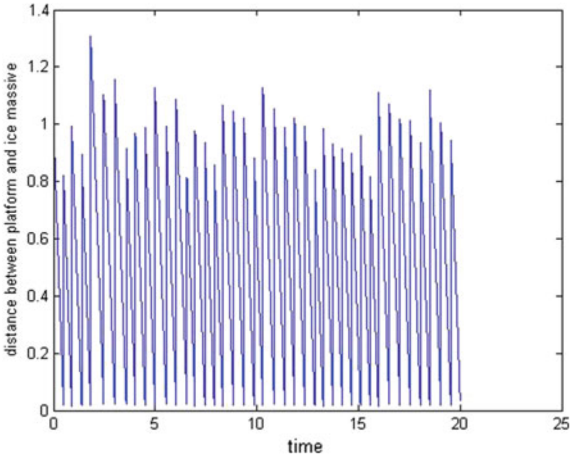

**Fig. 1** This plot shows a dependence $s(t)$ on the time. Parameters are $V = 2$ and $p_c = 50$, the time step $dt = 0.001$. The quantities $d_k$ are random numbers distributed according to the normal law $\mathbf{N}(d, \sigma)$, where $d = 1$ and $\sigma = 0.1$

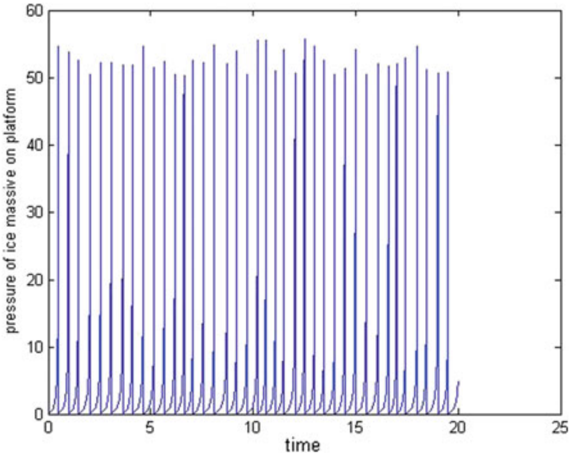

**Fig. 2** The pressure $p$ for $V = 2$ and $p_c = 50$, the time step $dt = 0.001$

The pressure and $s(t)$ can be computed numerically and the corresponding plots are represented by Figs. 1 and 2.

Note that for $d_k = const$ the pressure $p(t)$ and the distance $s(t)$ are periodic time functions and the corresponding period $T$ equals

$$T = \frac{p_c d}{V(p_0 + p_c)}. \tag{10}$$

However, really the process of ice failure is random, thus, the intervals between the breaks $t_k$ are random. We assume that the quantities $d_k$ are random numbers distributed according to the normal law $\mathbf{N}(d, \sigma)$ therefore the averaged period is $d$. We set the following boundary conditions

$$u(q, t) = q(t), \quad u(L, t) = 0 \tag{11}$$

(the first one is a contact relation between the ice sheet and the structure) and the initial conditions

$$u(x, 0) = 0, \quad u_t(x, 0) = 0. \tag{12}$$

## 3 Simplified Nonlinear Equation for Structure Vibrations

### *3.1 Equation for q*

The aim of this subsection is to express the displacement $u(x, t)$ via $q$ and obtain an equation involving $q$ only. We assume that parameters $\beta$ and $c_0^{-2}$ are small:

$$0 < \beta, c_0^{-2} \ll 1, \tag{13}$$

however, $\beta s_t$ may be large. We suppose that the size $L$ of the ice sheet is large: $L \gg 1$. The following assumption is important: $L^{-1/2}$ is much less than all the rest small parameters, i.e., we suppose $L^{-1/2} \ll \beta, c_0^{-2}$. Note that the contact problems are very complicated. Here, however, we can find an asymptotic solution. The main mathematical idea of this asymptotic construction can be described as follows. First we represent $u^{(0)}$ in the form

$$u^{(0)} = q \exp(-\alpha(x-q)) + \tilde{u}(x,t),$$

where $\tilde{u}$ is a new unknown function and $L^{-1/2} \gg \alpha \gg L^{-1}$. Then the $\tilde{u}$ satisfies the following equation:

$$\tilde{u}_{xx} - c_0^{-2}\tilde{u}_{tt} - \beta\tilde{u}_t - k_0\tilde{u} = h, \tag{14}$$

where

$$h = -\beta s_t + k_0 s + (c_0^{-2} q_{tt} + \beta q_t + k_0 q + \alpha^2) \exp(-\alpha(x-q)), \tag{15}$$

and the boundary conditions

$$\tilde{u}(q,t) = 0, \quad \tilde{u}(L,t) = O(\exp(-\alpha L)). \tag{16}$$

We see that the boundary condition at $x = L$ is satisfied, up to exponentially small terms.

Given a function $h(x,t)$, under assumption (5) we can solve the initial boundary value problem (22), (16) by iterations setting

$$u = \tilde{u}^{(0)} + \tilde{u}^{(1)} + \cdots$$

For the main term $\tilde{u}^{(0)}$ one obtains

$$\tilde{u}^{(0)}_{xx} - k_0\tilde{u}^{(0)} = h, \tag{17}$$

and for $= \tilde{u}^{(1)}$

$$\tilde{u}^{(1)}_{xx} - k_0\tilde{u}^{(1)} = c_0^{-2}\tilde{u}^{(0)}_{tt} + \beta\tilde{u}^{(0)}_t = g. \tag{18}$$

The boundary conditions take the form

$$u^{(i)}(q,t) = 0, \quad u^{(i)}(L,t) = 0, \quad i = 0, 1. \tag{19}$$

Using assumptions (5) one obtains

$$\tilde{u}^{(0)} \approx -k_0^{-1} f(t)(1 - \exp(-\kappa(x-q))) \exp(-\alpha(x-q)), \tag{20}$$

where $\kappa^2 = k_0$ and

$$f(t) = -\beta s_t - k_0 s + c_0^{-2} q_{tt} + \beta q_t + k_0 q. \tag{21}$$

Substituting this result into Eq. (18) and taking into account assumptions (5) we have

$$\tilde{u}^{(1)}_{xx} - k_0 \tilde{u}^{(1)} = \gamma, \tag{22}$$

where

$$\tilde{u}^0_t = k_0^{-1}(-f_t + \exp(-\kappa(x-q))(f_t + \kappa f q_t)),$$

$$\tilde{u}^0_{tt} = k_0^{-1}(-f_{tt} + \exp(-\kappa(x-q))(f_{tt} + 2\kappa f_t q_t + f\kappa^2 q_t^2 - \kappa q_{tt} f)).$$

Finally,

$$\gamma = k_0^{-1}(G_0 + G_1 \exp(-\kappa(x-q))), \tag{23}$$

where

$$G_0(t) = -c_0^{-2} f_{tt} - \beta f_t, \tag{24}$$

$$G_1(t) = c_0^{-2}(f_{tt} + 2\kappa f_t q_t + f\kappa^2 q_t^2 - \kappa\omega^2 q f) + \beta(f_t + \kappa f q_t). \tag{25}$$

We solve Eq. (18) and obtain

$$\tilde{u}^{(1)} \approx U_1 + U_2, \tag{26}$$

where

$$U_1 = -k_0^{-2} G_0(t)(1 - \exp(-\kappa(x-q)))\exp(-\alpha(x-q)), \tag{27}$$

$$U_2 = -(2k_0\kappa)^{-1} G_1(t)(x-q)\exp(-\kappa(x-q))\exp(-\alpha(x-q)). \tag{28}$$

These relations give

$$u_x(q) = -\kappa^{-3}(\kappa^2 f + G_0 + G_1/2). \tag{29}$$

To simplify the expression for $f$, $f_t$ and $f_{tt}$ we take into account that for small $\mu$ we can use the approximation $q_{tt} \approx -\omega^2 q$. Then by (5) we obtain

$$f = \beta s_t + k_0 s + k_0 q + \beta q_t + c_0^{-2} q_{tt}, \tag{30}$$

$$f_t = \beta s_{tt} + k_0 s_t + (k_0 - \omega^2 c_0^{-2}) q_t + \beta q_{tt}, \tag{31}$$

$$f_{tt} = \beta s_{ttt} + k_0 s_{tt} - \omega^2 \beta q_t + (k_0 - \omega^2 c_0^{-2}) q_{tt}, \tag{32}$$

Finally, using relations obtained above, one obtains an equation for $q$:

$$q_{tt} + \omega^2 q = \xi(q, q_t), \tag{33}$$

where $\xi$ is defined by

$$\xi = \xi_0 - M^{-1} g(q, q_t), \tag{34}$$

and

$$\xi_0 = \rho_0 c_0^2 M^{-1} u_x(q). \tag{35}$$

In this equation the ice sheet deformation is excluded due to our asymptotic approach. This main equation for structure vibrations describes a weakly perturbed linear oscillator with the frequency $\omega^2$.

### 3.2 Simplification of Vibration Structure Equation

Before solving Eq. (33) we simplify the right hand side $\xi$ of this equation and find a physical meaning of different terms involving in $\xi$. To proceed we take into account that $\beta$ and $c_0^{-2}$ are small parameters, and removing terms of the order $O(\beta^2)$ and $O(\beta c_0^{-2})$ in $\xi$, however, we conserve terms that involve $\beta^2 V$. Moreover, we assume that the amplitude of oscillations $q$ is small, therefore, we also remove nonlinear terms in $\xi$ proportional to $\beta$ or $c_0^{-2}$. In the term $g$ we conserve contributions $O(q_t)$ and $O(q)$. Moreover, we suppose $\rho_0 M^{-1} c_0^{-2} = O(1)$ and conserve some terms proportional $\beta s_t$ since they can be large at the break time moments $t_k$.

After straight forward computations, we obtain the following relation:

$$\xi_0 = h(t) + \mu_0 q + \mu_1 q_t + \mu_2 q_{tt} + O(\beta^2 + c_0^{-4}), \tag{36}$$

where

$$h(t) = -\rho_0 c_0^2 M^{-1} \kappa^{-3} (\frac{1}{2} k_0 \beta s_t + k_0^2 s + \frac{1}{2} \beta s_{ttt}), \tag{37}$$

$$\mu_0(t) = -\rho_0 c_0^2 M^{-1} \kappa, \tag{38}$$

$$\mu_1(t) = -\rho_0 c_0^2 M^{-1} \kappa^{-3} (\frac{\beta k_0}{2} + c_0^{-2} \kappa k_0 s_t), \tag{39}$$

and

$$\mu_2(t) = -\rho_0 c_0^2 M^{-1} \kappa^{-3} (c_0^{-2} k_0 + \frac{k_0 s}{2} + \frac{\beta s_t}{2}). \tag{40}$$

The term $\mu_0 q$ defines a perturbation of the oscillator vibration frequency, The term $\mu_1 q_t$ gives a contribution in the friction, and the term $\mu_2 q_{tt}$ determines the effect of the added mass. All these terms appear as a result of the ice sheet-structure interaction.

Note that the friction perturbation $-\mu_1 q_t$ involves two terms. The first term is positive and it does not depend on $V$, the second one is negative and proportional to $V$ (when $t \neq t_k$, i.e., between breaks). The first term diminishes and the second one increases the friction. The frequency shift does not depend on $V$ and it is positive. The dependence of the added mass term $-\mu_2 q_{tt}$ on $V$ is similar to the friction perturbation: we have a positive contribution independent on $V$ and a negative one, which is proportional to $V$. Finally, our main equation for $q$ takes the following form:

$$q_{tt} + \omega^2 q = R(q, q_t), \tag{41}$$

where

$$R(q, q_t) = -g(q, q_t, t) + h(t) + \mu_0(t)q + \mu_1(t)q_t + \mu_2(t)q_{tt}, \tag{42}$$

Below we discuss two possible mechanisms of the structure instability.

## 4 A New Mechanism of Structure Instability

A mechanism of the structure instability may be connected with a dependence of the friction on the speed $V$. We can therefore call this mechanism as "negative friction" one. Let us linearize the Eq. (41) at $q = 0$ assuming that oscillations are small before the bifurcation point. We consider the case when the friction is defined by physically realistic term (2). Removing external load terms we obtain then the following equations for free vibrations

$$(1 + \tilde{M})q_{tt} + (\omega + \tilde{\omega})^2 q + \theta(t)q_t = 0, \tag{43}$$

where $\tilde{M}(t)$ and $\tilde{\omega}$ are small perturbations of the mass and the frequency, respectively. These perturbations can be computed by relations of the previous section, but in this section the main role plays the friction term defined by

$$\theta(t) = a_0/s(t) - \mu_1(t). \tag{44}$$

Let us compute $\theta(t)$ between the two subsequent break moments $t_k$ and $t_{k+1}$. We obtain then by (39) that $s(t) = d_k - v(t - t_k)$ and $\mu_1(t) = -\rho_0 c_0^2 M^{-1}\kappa^{-3}(\frac{\beta k_0}{2} - c_0^{-2}\kappa k_0 V)$. Therefore,

$$\theta(t) = M^{-1}a_0(d_k - v(t - t_k))^{-1} + \rho_0 c_0^2 M^{-1}\kappa^{-3}(\frac{\beta k_0}{2} - c_0^{-2}\kappa k_0 V) \quad t \in (t_k, t_{k+1}). \tag{45}$$

Assuming that $\theta(t)$ is small, we represent solutions of (43) as $A(t)\sin(\omega t + \phi(t))$, where $dA/dt \ll 1$. A computation shows that the amplitude $A(t)$ increases between the two break moments if

$$\bar{\theta} = (\Delta_k)^{-1} \int_{t_k}^{t_k+\Delta_k} \theta(s)ds > 0, \tag{46}$$

where $\Delta_k = t_{k+1} - t_k$ is the time interval between the breaks. We can find $\Delta_k$ by condition (9) that gives

$$V\Delta_k = \frac{p_c d}{p_0 + p_c}. \tag{47}$$

Finally,

$$\bar{\theta}(V) = M^{-1}(V(d^{-1}(p_0 + p_c)p_c^{-1} \log(1 + p_c/p_0) - \rho_0\kappa^{-1}) + \rho_0 c_0^2 \kappa^{-1}\frac{\beta}{2}). \tag{48}$$

Let us make a simple assumption that all $d_k$ are equal, $d_k = d$ and $d$ does not depend on $V$. Then we observe a bifurcation point and instability at $V = V_{crit}$ such that

$$\bar{\theta}(V_{crit}) = 0. \tag{49}$$

Such bifurcation is possible if

$$(p_0 + p_c)p_c^{-1} \log(1 + p_c/p_0) < d\rho_0\kappa^{-1}. \tag{50}$$

Under this condition, the critical velocity is defined by

$$V_{crit} = \frac{\rho_0 c_0^2 \kappa^{-1}\beta}{2(\rho_0\kappa^{-1} - d^{-1}(p_0 + p_c)p_c^{-1} \log(1 + p_c/p_0))}. \tag{51}$$

In this case the instability exists for all $V > V_{crit}$.

Interesting effect can appear if we suppose that the average $d$ of $d_k$ over $k$ depends on $V$ and that $d(V) \to 0$ as $V \to +\infty$. Then if for some $V$ condition (49) holds, the function $\bar{\theta}(V)$ has two roots $V = V_1$ and $V = V_2$. The first root corresponds to the instability onset, and the second one corresponds to the instability fall.

## 5 Asymptotic Analysis of Nonlinear Equation

Under some assumptions we can consider (33) as an equation that describes a weakly nonlinear oscillator with a weak damping. By this equation, we can describe both mechanisms of instability: resonance and friction ones and also obtain resonance conditions. We introduce a formal small parameter $\varepsilon$ assuming that $R = O(\varepsilon)$. The asymptotic approach to study such equations is well known, see [5]. Let $\tau = \varepsilon t$ is a slow time. We seek solutions in the form

$$q = A(\tau)\sin(\omega t + \phi(\tau)) + \varepsilon q_1(t, \tau) + \cdots, \tag{52}$$

where $A$ and $\phi$ are unknown slowly evolving in time the amplitude and the phase, respectively. We have

$$q_{tt} = -\omega^2 q + 2\varepsilon\omega(A_\tau \cos(\omega t + \phi(\tau)) - A\phi_\tau \sin(\omega t + \phi(\tau)) + O(\varepsilon^2).$$

For any smooth function $H(q, q_t)$

$$H(q, q_t) = H_0 + O(\varepsilon), \quad H_0 = g(A\omega \cos(\omega t + \phi(\tau)), A \sin(\omega t + \phi(\tau))).$$

Using these relations, for $q_1$ one has

$$q_{1tt} + \omega^2 q_1 = S(t, \tau, \varepsilon), \tag{53}$$

where

$$S(t, \tau) = 2\omega(-A_\tau \cos(\omega t + \phi(\tau)) + A\phi_\tau \sin(\omega t + \phi(\tau)) + R_0(A, \phi), \tag{54}$$

and

$$R_0(A, \phi, t) = R(A \sin(\omega t + \phi(\tau)), A\omega \cos(\omega t + \phi), t). \tag{55}$$

For large times $t = O(\varepsilon^{-1})$ Eq. (53) has a bounded solution if and only if

$$\lim_{T\to+\infty} T^{-1} \int_0^T S(t, \tau) \cos(\omega t + \phi) dt = 0, \tag{56}$$

and

$$\lim_{T\to+\infty} T^{-1} \int_0^T S(t, \tau) \sin(\omega t + \phi) dt = 0. \tag{57}$$

Finally, by (54) and (55) these relations lead to the following system of equations for the amplitude $A$ and the phase $\phi$:

$$\omega A_\tau = \lim_{T\to+\infty} T^{-1} \int_0^T R_0(A, \phi, t) \cos(\omega t + \phi) dt, \tag{58}$$

and

$$\omega A\phi_\tau = -\lim_{T\to+\infty} T^{-1} \int_0^T R_0(A, \phi, t) \sin(\omega t + \phi) dt = 0. \tag{59}$$

We investigate this system in the next section.

## 6 Amplitude Evolution, Instability and Resonances

Let us focus our attention on the equation for amplitude $A$. Assuming that $A \ll 1$, and therefore $|q| \ll 1$, we can represent the term $g$ from (2) by the Taylor series

$$-(q_t - s_t)(q-s)^{-1} = s_t s^{-1} + s_t s^{-2} q - s^{-1} q_t + s_t s^{-3} q^2 - s^{-2} q_t q + O(|q^3| + |q_t|^3). \tag{60}$$

We obtain then that (58) reduces to

$$\omega \frac{dA}{d\tau} = D_0 A - D_1 A^2 + \bar{a}, \tag{61}$$

where $D_0, \bar{a}$ and $D_1$ are coefficients depending on the system parameters. Equation (61) describes a simple dissipative system, where for $\bar{a} = 0$ we are dealing with a transcritical bifurcation. If $D_0 < 0$ and $D_1 > 0$, we have the stable equilibria $A_{eq} = 0$, which is a local attractor corresponding to small amplitude vibrations and the saddle solution $A_s = D_0/D_1$. For $D_0 > 0$ and $D_1 > 0$, we observe an inverse picture: dynamics defined by (61) has the local attractor $A_{eq} = D_0/D_1$ and the saddle solution $A = 0$. Therefore, then the structure exhibits oscillations with relatively larger amplitudes.The bifurcation point is defined by condition $D_0 = 0$.

We compute the coefficients $D_i$ and $\bar{a}$ using relations (38), (39), (40) and (60). One has

$$D_0 = d_1 + d_2, \tag{62}$$

where

$$d_1 = \int_0^{2\pi\omega^{-1}} (\sin(\omega t + \phi)\cos(\omega t + \phi)(-a_0 M^{-1} s_t s^{-2} + \mu_0(t) - \omega^2 \mu_2(t))dt,$$

and

$$d_2 = \omega \int_0^{2\pi\omega^{-1}} \cos^2(\omega t + \phi)(\mu_1(t) + a_0 M^{-1} s(t)^{-1})dt,$$

$$D_1 = a_0 M^{-1} \int_0^{2\pi\omega^{-1}} (s(t)^{-2}\omega \cos^2(\omega t + \phi)\sin(\omega t + \phi) \\ - s_t s(t)^{-3} \sin^2(\omega t + \phi)\cos(\omega t + \phi))dt. \tag{63}$$

and

$$\bar{a} = 2 \int_0^{2\pi\omega^{-1}} h(t)\cos(\omega t + \phi)dt. \tag{64}$$

To calculate these coefficients, first let us consider the simplest case when the lengths $d_k$ of the ice blocks equal a constant: $d_k = \bar{d}$. Then $s(t)$ and $\mu_i$ are time periodic functions, having a period $T(V)$ defined by (10). By relations (65), (63) and (62) one can show that the resonances occur on the frequencies $\omega$ and $2\omega$ (terms with the frequency $3\omega$ vanish that can be shown by an integration by parts).

As a result, we obtain the following resonance conditions:

$$2\pi\omega^{-1} = T(V), \quad \pi\omega^{-1} = T(V), \tag{65}$$

where $T(V)$ is defined by (10). Assume $d_k$ are random numbers distributed according to the normal law $\mathbf{N}(\bar{d}, \sigma)$. Clearly, for large $\sigma$ these resonance effects vanish but for small $\sigma$ they are possible that is checked by numerical simulations.

## 7 Multioscillator Model

In the previous section we have shown that in the ice sheet-structure system resonances appear, which can lead to an oscillation amplitude growth. Consider the averaged amplitude $A_{eq}$ as a function of speed $V$. The resonance effect leads to a narrow peak in the plot of $A_{eq}(V)$. Therefore, this resonance mechanism is not quite consistent with experiments since experiments show existence of a sufficiently large plato on the plot $A_{eq}(V)$, i.e., amplitudes $A$ are sufficiently large for an interval of values $V$.

In this section, to explain experimental data, we consider a multioscillator model. The main idea of this model is simple. It is clear that real structures have a broad spectrum of eigenfrequencies. Therefore, they can be represented as systems of many connected oscillators with frequencies close to $\omega_1, \dots, \omega_n$. Then the resonance effect appears if $\omega_{ice}(v_0) \approx \omega_j$ for some $j$. If we assume that there is a set of close frequencies, located in an interval, then the peak extends. A model for multimode situation has the form

$$\frac{d^2 q_i}{dt^2} + \omega_i^2 q_i = R_i(q, \frac{dq}{dt}), \tag{66}$$

where $q_i(t)$ is an amplitude of $i$-th oscillator, $R_i$ are friction and nonlinearity terms given by

$$R_i = M^{-1} a_0 \frac{\bar{p} - s_t}{\bar{q} - s} + h(t) + \mu_0(t) q_i + \mu_1(t) \frac{dq_i}{dt} + \mu_2(t) \frac{d^2 q_i}{dt^2}, \tag{67}$$

where $\bar{q} = \sum_i c_i q_i$, $\bar{p} = \sum_i c_i \frac{dq_i}{dt}$, $c_i$ are some weights that determines relative contributions of the modes, $\mu_j$ are defined by (38), (39) and (40). The asymptotic analysis of (66) follows Sect. 5 and it leads to a system of equations for slowly time evolving amplitudes $A_i(t)$. Note that although the terms $R_i$ are small and thus the oscillator interaction is weak, nonetheless, the observed effects may be essential. The peak corresponding to resonance extends and can take a more complicated form (Fig. 3).

## 8 Numerical Simulations

Numerical simulations confirm analytical results and ideas of the previous sections. For models with a single oscillator ($n = 1$) we have that the resonances exist even for random tooth lengths $d_k$ but the vibration magnitude fall as randomness increases; there are possible two resonances or a single one depending on parameters that is consistent with resonance conditions; and the effects connected with the added mass and negative friction essentially affect resonances. For example, the negative friction reinforce the resonances and if this term is large enough, we obtain a "blow up", an exponential growth of the vibration amplitudes. The case of $n = 2$ oscillators is investigated numerically. We took the matrix $\mathbf{G}$ with entries $G_{11} = 100$, $G_{12} = G_{21} = 20$, $G_{22} = 100$ and compare two models: one oscillator model for $\omega = 10$ and two oscillator model. The results are represented by Fig. 4. For $n = 1$ we observe a peak for a speed $v_0 \approx v_c$. We have observed a resonance effect for two frequencies that leads to the peak extension (Fig. 4), and a beginning of a plato formation for the case of three oscillators (see Fig. 5).

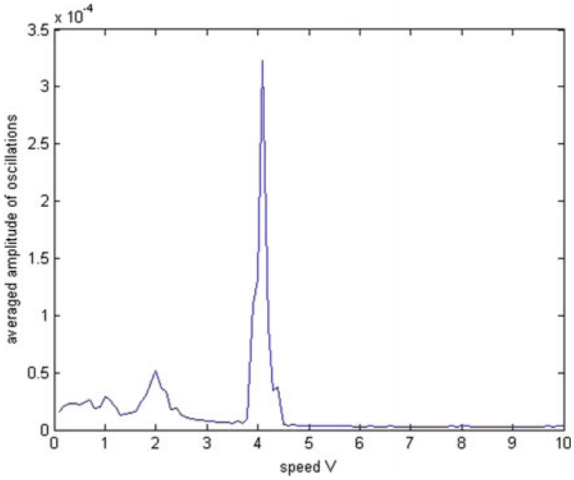

**Fig. 3** This plot shows a dependence of stationary averaged vibration amplitudes on $V$ for the case of a single oscillator $n = 1$

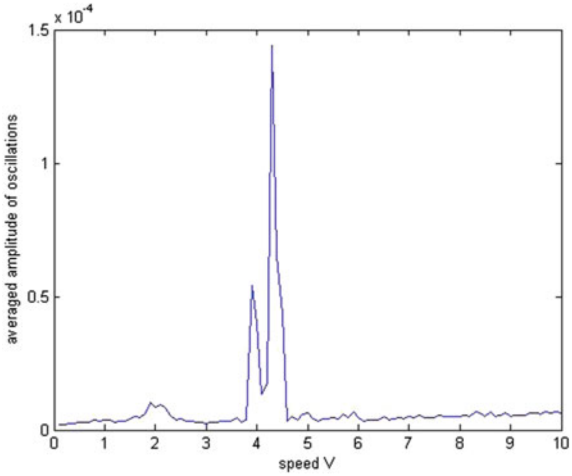

**Fig. 4** This plot shows a dependence of stationary averaged oscillation amplitudes on the speed *V* for the case of two oscillator

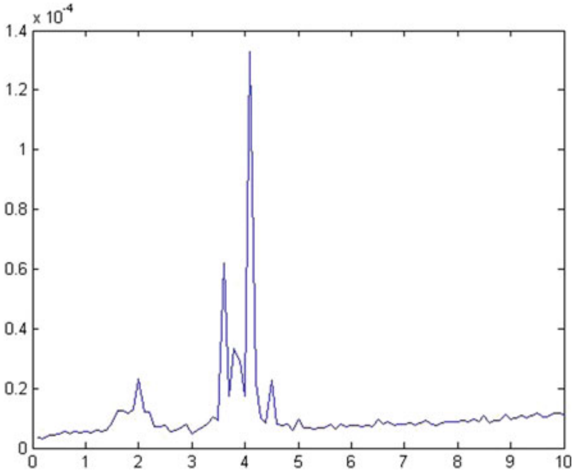

**Fig. 5** This plot shows a dependence of stationary averaged oscillation amplitudes on the speed *V* for the case of three connected oscillators. We see that the peak extends and takes a complicated form with comparison to a single mode case

## 9 Conclusion

A new model of IIV is presented. This model extends the previous ones (see [1, 3]) and allows to describe new effects in IIV. Mathematically the model leads to a complicated system of PDE and ODE, nonetheless an asymptotic approach to resolve this system is developed. The main new effect is that a ices-structure contact produces a negative contribution into the friction, which can reinforce resonance an thus vibration amplitude, and destroy structure. Moreover, one can assume as a hypothesis that there is possible a new mechanism of structure instability without resonance effects and based on negative friction only.

## References

1. Matlock, H., Dawkins, W.P., Panak, J.J.: Analytical model for ice structure interaction. ASCE J. Eng. Mech. Div. **4**, 1083–1092 (1971)
2. Sodhi, D.S.: A theoretical model for ice-structure interaction. In: Proceedings of the OMAE-94 conference, ASME, Vol. IV, pp. 29–34. New York
3. Huang, G., Liu, P.: A dynamic model for ice-induced vibrations of structures. J. Offshore Mech. Arct. Eng. **13**(1), 011501–011506 (2009)
4. Blenkarn, K.: A Measurement and analysis of ice forces on cook inlet structures. In: Offshore Technology Conference, Houston, TX (1970)
5. Bogoliubov, N., Mitropolsky, Y.A.: Asymptotic Methods in the Theory of Non-Linear Oscillations (1961)
6. Gagnon, R.: An explanation for the Molikpaq May 12, 1986 Event. Cold Reg. Sci. Technol. **82**, 75–93 (2012)
7. Abramian, A., Vakulenko, S.: Oscillations of a beam with a time varying mass. Nonlinear Dyn. **63**, 135–147 (2011)
8. Irschik, H., Holl, H.J.: Mechanics of variable-mass systems–Part 1: Balance of mass and linear momentum. Appl. Mech. Rev. **57**(1–6), 145–160
9. De Bruijn, N.: Asymptotic Methods in Analysis. North-Holland, Amsterdam (1961)
10. Suweken, G., van Horssen, W.T.: On the weakly nonlinear, transversal vibrations of a conveyor belt with a low and time-varying velocity. Nonlinear Dyn. **31**, 197–233 (2003)
11. Peyton, H.R.: Ice and Marine structures, Part II, Sea Ice Properties, Ocean Industr. **3**, 59–65

# On the Deformation of a Hyperelastic Tube Due to Steady Viscous Flow Within

**Vishal Anand and Ivan C. Christov**

**Abstract** In this chapter, we analyze the steady-state microscale fluid–structure interaction (FSI) between a generalized Newtonian fluid and a hyperelastic tube. Physiological flows, especially in hemodynamics, serve as primary examples of such FSI phenomena. The small scale of the physical system renders the flow field, under the power-law rheological model, amenable to a closed-form solution using the lubrication approximation. On the other hand, negligible shear stresses on the walls of a long vessel allow the structure to be treated as a pressure vessel. The constitutive equation for the microtube is prescribed via the strain energy functional for an incompressible, isotropic Mooney–Rivlin material. We employ both the thin- and thick-walled formulations of the pressure vessel theory, and derive the static relation between the pressure load and the deformation of the structure. We harness the latter to determine the flow rate–pressure drop relationship for non-Newtonian flow in thin- and thick-walled soft hyperelastic microtubes. Through illustrative examples, we discuss how a hyperelastic tube supports the same pressure load as a linearly elastic tube with smaller deformation, thus requiring a higher pressure drop across itself to maintain a fixed flow rate.

## 1 Introduction

Traditionally, physiological flows in soft and deformable tubes form a large class of literature on *collapsible tubes* [19, 20, 39]. These phenomena related to air flow in the lungs or blood flow in large blood vessels (such as arteries) are inherently a moderate-to-large-Reynolds number phenomenon. At the extreme of very large Reynolds number (inviscid) flow lies *hydroelasticity* (to use the term of the group led by D. I. Indeitsev at the Institute of Problems of Mechanical Engineering Rus-

---

V. Anand · I. C. Christov (✉)
School of Mechanical Engineering, Purdue University, West Lafayette, IN 47907, USA
e-mail: anand32@purdue.edu

I. C. Christov
e-mail: christov@purdue.edu

H. Altenbach et al. (eds.), *Dynamical Processes in Generalized Continua and Structures*, Advanced Structured Materials 103,
https://doi.org/10.1007/978-3-030-11665-1_2

sian Academy of Sciences in St. Petersburg). Nowadays, there is a vast literature on hydroelasticity, covering both stable and unstable internal and external flows [18, 35] that are capable of supporting nonlinear wave phenomena [22], including wave localization [1]. A common example of such high-Reynolds-number hydroelastic interactions is aerodynamic flutter [7], which can lead to potentially disastrous instabilities such as failure of airplane wings and suspension bridges. A variety of nonlinear wave phenomena also arise when embedding a linearly elastic solid body (e.g., a rod) into an ambient viscoelastic medium and studying the coupled structure–structure interactions [37]. More recently, *however*, there has been significant interest in "viscous–elastic" fluid–structure interactions (FSIs) between internal fluid flows at low Reynolds numbers and soft tubes and annuli [10, 14, 15], including the effect of non-Newtonian rheology [3, 9, 38]. This renewed interest comes from the need for understanding these systems in order to design microfluidic [38] and soft robotic [14] devices. At these smaller scales (or, for such "creeping" viscous flows), fluid inertia is negligible.

Here, we present a first foray into the mathematical analysis of low-Reynolds-number FSI, at steady state, due to the flow of a non-Newtonian fluid in a microtube composed of a *hyperelastic* material. Hyperelastic materials have the "advantage" of being completely specified by a strain energy functional from which the constitutive equation between stress and strain follows. The structural response of complex soft solids, such as biological tissue and blood vessels, can be appropriately described by a hyperelastic solid with a *pseudo* strain energy function (see, e.g., [17, Chaps. 8 and 9]). Similarly, due to its complex constituents, blood is a non-Newtonian fluid and an appropriate rheological model (beyond the simple Newtonian viscous fluid) should be used (see, e.g., [17, Chap. 3]).

This chapter is thus organized as follows: in Sect. 2, we address the fluid mechanics problem, including the velocity profile of a generalized Newtonian (specifically, power-law) fluid in a tube of slowly varying cross-section. In Sect. 3, we discuss the deformation of the soft hyperelastic microtube due to uniform loading from within. Then, in Sect. 4, we specifically choose the load to be the hydrodynamic pressure and obtain the appropriate pressure–deformation relations describing such fluid–structure interactions. In Sect. 5, the results are discussed and compared to limiting cases, such as a linearly elastic microtube, in order to highlight the effects of hyperelasticity. Conclusions and avenues for future work are stated in Sect. 6. An appendix is included for completeness, in which the pressure–deformation and flow rate–pressure drop relations for FSI in a thick-walled linearly elastic tube are also derived.

## 2 Summary of the Fluid Mechanics Problem

Consider a fluid flow $\mathbf{v} = v_r\hat{\mathbf{r}} + v_\theta\hat{\boldsymbol{\theta}} + v_z\hat{\mathbf{z}}$ in cylindrical coordinates. A diagram of the deformed microtube geometry is shown in Fig. 1, specifically the tube has uniform thickness $t$, undeformed inner radius $a$, and length $\ell$. Now, following [3], let us assume that

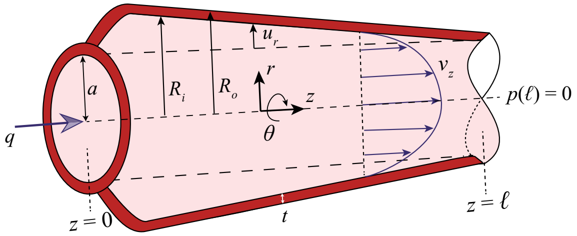

**Fig. 1** Schematic of the microtube geometry, including notation used

1. The flow is steady: $\frac{\partial}{\partial t}(\,\cdot\,) = 0$.
2. The flow is axisymmetric: $\frac{\partial}{\partial \theta}(\,\cdot\,) = 0$ and $v_\theta = 0$.
3. The geometry of the flow vessel is a slender tube: $\ell \gg a \;\Leftrightarrow\; a/\ell = \epsilon \ll 1$.

Assumption 3 is key to the mathematical analysis below. Specifically, this assumption leads us to the appeal to the *lubrication approximation* of fluid mechanics (see, e.g., [27, 36]), which will allow us to solve for the flow profile analytically.

As shown with due diligence in our previous work [3], to the leading order in $a/\ell$, the velocity field is *unidirectional* [27]: $\bar{\mathbf{v}} = \bar{v}_{\bar{z}}\,\hat{\mathbf{z}}$ but weakly varying with the (long) flow-wise direction i.e., $\bar{v}_{\bar{z}} = \bar{v}_{\bar{z}}(\bar{r}, \bar{z})$. Here, and henceforth, bars over quantities denote dimensionless variables according to the following scheme:

$$\bar{r} = r/a, \qquad \bar{p} = p/\mathcal{P}_c, \qquad \bar{z} = z/\ell, \qquad \bar{v}_{\bar{z}} = v_z/\mathcal{V}_z, \qquad \bar{v}_{\bar{r}} = v_r/\mathcal{V}_r, \tag{1}$$

where the characteristic radial velocity scale is $\mathcal{V}_r \equiv \epsilon\mathcal{V}_z$, the characteristic axial velocity scale is $\mathcal{V}_z$, and $\mathcal{P}_c$ is the characteristic pressure scale. Upon specifying the rheology of the fluid (see below), $\mathcal{P}_c$ and $\mathcal{V}_z$ will be related to each other.

Next, we specify the fluid's rheological behavior. We are interested in biofluid mechanics applications such as blood flow through a deformable artery or vein. Blood is known to have a shear-dependent viscosity due to the fact that red blood cells deform. Haemorheology is a complex topic [17, Chap. 3], nevertheless experiments suggest [21] that blood flow can be accurately fit to a power-law fluid model (a generalized Newtonian rheology often going by the name Ostwald–de Waele [6]) at steady state. Now, the dominant shear stress component is $\tau_{rz}$; likewise the corresponding rate-of-strain tensor component is just $\dot{\gamma}_{rz} = \partial v_z/\partial r$ to the leading order in $a/\ell$ (i.e., under the slenderness assumption). Thus the fluid's rheological model takes the "simple shear" form:

$$\tau_{rz} = \underbrace{m\left|\frac{\partial v_z}{\partial r}\right|^{n-1}}_{=\eta}\frac{\partial v_z}{\partial r}, \tag{2}$$

where $\eta$ is the *apparent viscosity*, $m(>0)$ is the *consistency factor*, and $n(>0)$ is the *power-law index*. On making Eq. (2) dimensionless using the variables from Eq. (1), we obtain the relationship between the axial velocity $\mathcal{V}_z$ scale and the pressure scale $\mathcal{P}_c$: $\mathcal{V}_z = \left[a^{n+1}\mathcal{P}_c/(m\ell)\right]^{1/n}$.

The power-law rheological model captures the flow behavior of fluids that are shear thinning ($\eta$ decreases with $\dot{\gamma}_{rz}$), such as blood [11, 21] as mentioned above, for $n < 1$. It also captures the flow behavior of shear-thickening fluids ($\eta$ increases with $\dot{\gamma}_{rz}$) such as as woven Kevlar fabrics impregnated with a colloidal suspension of silica particles [41] used for ballistic armors, for $n > 1$. The viscous Newtonian fluid is obtained as the special case of $n = 1$ in Eq. (2). Our motivation is mainly fluid mechanics of blood vessels, so our examples consider $n < 1$, but the theory applies to both cases.

Finally, considering the dynamics of the flow under the constitutive relationship in Eq. (2), we found that the dimensionless axial velocity profile is [3]:

$$\bar{v}_{\bar{z}} = \left(-\frac{1}{2}\frac{\mathrm{d}\bar{p}}{\mathrm{d}\bar{z}}\right)^{1/n}\left(\frac{\bar{R}_i^{1+1/n} - \bar{r}^{1+1/n}}{1+1/n}\right), \tag{3}$$

where $\bar{R}_i = R_i/a$ is the dimensionless *inner* radius of the deformed microtube. More importantly, $\bar{R}_i$ is not necessarily equal to unity because we allow the microtube to deform due to FSI, as discussed in the next section. Likewise, the pressure gradient $\mathrm{d}\bar{p}/\mathrm{d}\bar{z}$ is *not* constant but, rather, varies with $\bar{z}$. As a result, while $\bar{p}$ is at most a function of $\bar{z}$ (but not a linear function), $\bar{v}_{\bar{z}}$ can depend upon both $\bar{r}$ and $\bar{z}$.

## 3 Structural Mechanics Problem: Solving for the Deformation

In this section, we address the structural mechanics aspect of the coupled FSI problem posed above. To this end, we treat the structure as a *pressure vessel*, wherein the only load acting on the structure is the hydrodynamic pressure from the fluid, and the load due to viscous and shear stresses is neglected. This assumption stems from the lubrication approximation for the fluid flow, wherein the viscous shear stress scale is $\approx \epsilon$ times the hydrodynamic pressure scale [36, Chap. 22]. We begin our discussion by first analyzing a *thin-walled* pressure vessel, then we move onto its *thick-walled* counterpart.

### *3.1 Thin-Walled Cylinder*

Let us consider the case of a thin-walled initially cylindrical microtube with thickness $t \ll a$. This assumption allows us to consider the cylinder in a state of plane stress and plane strain, thus simplifying the analysis of the structural mechanics problem. As a consequence, the walls of the cylinder act like a membrane, which does not sustain any bending or twisting moments. There is no variation of stress and deformation throughout the thickness of the cylinder.

### 3.1.1 Deformation

In the undeformed material coordinate system, the coordinates of a material point are given by $r = a, \theta \in [0, 2\pi]$, and $z \in [0, \ell]$. Upon *axisymmetric* deformation, the coordinates of the same material point become

$$R = R(r), \qquad \Theta = \theta, \qquad Z = \alpha z. \tag{4}$$

We further assume that the deformation is homogeneous along the axial direction, thus $\alpha = L/\ell$, with $L$ being the deformed cylinder's length and $\ell$ being the undeformed cylinder's length (as in Fig. 1). Now, since the cylinder is clamped at both its ends, its length does not change and $L = \ell$. Hence, $\alpha = 1$. The foregoing discussion reduces the coordinates of the point in the spatial coordinate system to:

$$R = R(r), \qquad \Theta = \theta, \qquad Z = z. \tag{5}$$

As the shell is considered (infinitesimally) thin in this theory, we denote the inner radius $R_i$ by $R$ (in this section) without fear of confusion.

For the case of a deformation defined by Eq. (5), the deformation gradient tensor $\underline{\underline{\mathcal{F}}}$ can be easily computed:

$$\underline{\underline{\mathcal{F}}} = \begin{pmatrix} \partial R/\partial r & 0 & 0 \\ 0 & R/r & 0 \\ 0 & 0 & 1 \end{pmatrix}. \tag{6}$$

Since $\underline{\underline{\mathcal{F}}}$ is a diagonal tensor, then its principal axes are just the $r$, $\theta$, and $z$ axes of the cylindrical coordinate system. Indeed, we deduce from the deformation field introduced in Eq. (5) that a line segment oriented along either the $r$, $\theta$ or $z$ coordinate directions will, at most, only *stretch* and cannot rotate.

Consequently, for this type of deformation, the rotation tensor $\underline{\underline{\mathcal{R}}} = \underline{\underline{\mathcal{I}}}$ (the identity tensor) and the stretch tensor is simply

$$\underline{\underline{\mathcal{U}}} = \underline{\underline{\mathcal{F}}} = \begin{pmatrix} \lambda_1 & 0 & 0 \\ 0 & \lambda_2 & 0 \\ 0 & 0 & \lambda_3 \end{pmatrix}. \tag{7}$$

Here, $\lambda_1, \lambda_2, \lambda_3$ are the principal stretches, which one can immediately write down by comparison of Eqs. (6) and (7). Now, since the material is incompressible, $\det \underline{\underline{\mathcal{F}}} = \lambda_1 \lambda_2 \lambda_3 = 1$, we can determine $\lambda_1$, and thus

$$\lambda_1 = r/R, \qquad \lambda_2 = R/r, \qquad \lambda_3 = 1. \tag{8}$$

### 3.1.2 Constitutive Equation

We consider the material from which the cylindrical tube is composed to be an isotropic, incompressible, *hyperelastic* material. For such a material, the constitutive equation is specified through a strain energy functional $W$ [5, 8], which depends upon the principal stretches $\lambda_i$, i.e., $W = W(\lambda_1, \lambda_2, \lambda_3)$. Specifically, we assume that the hyperelastic material is defined by the *incompressible* Mooney–Rivlin constitutive equation [5, 8, 29] with strain energy given by

$$W = \mathbb{C}_1 \left(\lambda_1^2 + \lambda_2^2 + \lambda_3^2\right) + \mathbb{C}_2 \left(\lambda_1^2\lambda_2^2 + \lambda_2^2\lambda_3^2 + \lambda_3^2\lambda_1^2\right) \qquad (\lambda_1\lambda_2\lambda_3 = 1). \tag{9}$$

Here, $\mathbb{C}_1$ and $\mathbb{C}_2$ are two material constants characterizing the structural response of the hyperelasic material; they are determined empirically by comparison to experiments [34]. Equation (9) is traditionally invoked to describe the response of highly elastic, i.e., “rubber-like,” materials under isothermal conditions [34]. In particular, setting $\mathbb{C}_2 = 0$ reduces the Mooney–Rivlin model to the neo-Hookean solid. For most “rubber-like” materials, $\mathbb{C}_1 > 0$ and $\mathbb{C}_2 \leq 0$ [28, 31, 32]. For compatibility with linear (i.e., small-strain) elasticity theory (see [5, Eq. (6.11.29)]), we must have

$$G = 2(\mathbb{C}_2 + \mathbb{C}_1) \tag{10}$$

as the shear modulus of elasticity. We also recall that, for a linearly elastic material,

$$2G(1 + \nu) = E, \tag{11}$$

where $\nu$ is the Poisson ratio, and $E$ is Young’s modulus.

Now, for isotropic materials, the principal Cauchy stresses are coaxial with the principal stretches and are given by

$$\sigma_1 - \sigma_3 = \lambda_1 \frac{\partial W}{\partial \lambda_1} - \lambda_3 \frac{\partial W}{\partial \lambda_3}, \tag{12a}$$

$$\sigma_2 - \sigma_3 = \lambda_2 \frac{\partial W}{\partial \lambda_2} - \lambda_3 \frac{\partial W}{\partial \lambda_3}. \tag{12b}$$

Substituting Eq. (9) into Eq. (12), we obtain

$$\sigma_1 - \sigma_3 = 2\mathbb{C}_1 \left(\lambda_1^2 - \lambda_3^2\right) - 2\mathbb{C}_2 \left(\lambda_1^{-2} - \lambda_3^2\right), \tag{13a}$$

$$\sigma_2 - \sigma_3 = 2\mathbb{C}_1 \left(\lambda_2^2 - \lambda_3^2\right) - 2\mathbb{C}_2 \left(\lambda_2^{-2} - \lambda_3^2\right). \tag{13b}$$

### 3.1.3 Static Equilibrium

As mentioned above, our exemplar thin-walled cylinder acts as a pressure vessel, i.e., a structure that sustains only stretching and tension but no bending or twisting. For such a structure, the equations of static equilibrium take the form:

$$\sigma_1 = \sigma_{rr} = -p, \tag{14a}$$

$$\sigma_2 = \sigma_{\theta\theta} = \frac{pR}{t}, \tag{14b}$$

$$\sigma_3 = \sigma_{zz} = \frac{pR}{2t}. \tag{14c}$$

Since the tube is thin, i.e., $t \ll a$ and $R = \mathcal{O}(a)$, then $\sigma_1 \ll \sigma_2 \approx \sigma_3$. Substituting Eqs. (14) (stress balance) into Eqs. (13) (constitutive) and employing Eqs. (8) (deformation), we obtain

$$-\frac{pR}{2t} = 2\mathbb{C}_1\left(\frac{a^2}{R^2} - 1\right) - 2\mathbb{C}_2\left(\frac{R^2}{a^2} - 1\right), \tag{15a}$$

$$\frac{pR}{2t} = 2\mathbb{C}_1\left(\frac{R^2}{a^2} - 1\right) - 2\mathbb{C}_2\left(\frac{a^2}{R^2} - 1\right). \tag{15b}$$

Combining the last two equations, we arrive at the pressure–radius relation

$$\frac{pa}{2t(\mathbb{C}_1 + \mathbb{C}_2)} = \frac{R}{a} - \frac{a^3}{R^3}, \tag{16}$$

where $R = a + u_r$ is the deformed tube radius, and $u_r$ is the radial deformation (recall Fig. 1).

Notice that the cross-sectional area of the tube at some fixed axial location, $z$, is $A = \pi R^2$ [here, $R = R(z)$ due to FSI]. Then, Eq. (16) can be rewritten as a *pressure–area* relationship:

$$p(\bar{A}) = 2(\mathbb{C}_1 + \mathbb{C}_2)\frac{\bar{t}}{\sqrt{\bar{A}}}\left(\bar{A} - \frac{1}{\bar{A}}\right), \tag{17}$$

where $\bar{t} = t/a$ is the dimensionless (reduced) thickness of the tube, and $\bar{A} = A/(\pi a^2)$ is the dimensionless (reduced) area of the deformed tube under axisymmetric conditions (initial circular cross-section remains circular under deformation). Equation (17) represent a *tube law* [42] for microscale FSI in a hyperelastic pressure vessel. This "law" is often used as a "constitutive" equation (closure) in unsteady FSI problems in which the flow is cross-sectionally averaged [39]. Of interest is to note that $p(\bar{A})$ in Eq. (17) is *nonlinear*.

Finally, let us make Eq. (16) dimensionless using the following dimensionless variables

$$\bar{u}_{\bar{r}} = u_r/a, \qquad \bar{p} = p/\mathcal{P}_c, \tag{18}$$

to yield

$$\gamma\bar{p} = (1 + \bar{u}_{\bar{r}}) - \frac{1}{(1 + \bar{u}_{\bar{r}})^3}, \qquad \gamma := \frac{\mathcal{P}_c}{2(\mathbb{C}_1 + \mathbb{C}_2)\bar{t}}, \tag{19}$$

where $\bar{t} = t/a$ as above, and we have defined $\gamma$ as a dimensionless parameter that captures the "strength" of fluid–structure coupling, i.e., the so-called *FSI parameter*. In our previous work on linearly elastic incompressible microtubes [3], the FSI parameter was defined as $\beta = \mathcal{P}_c/(E\bar{t})$. To connect the hyperelastic theory to the linearly elastic theory, we can use Eqs. (10) and (11), taking $\nu = 1/2$ for an incompressible material, to find that

$$\gamma = \beta/3. \tag{20}$$

A few remarks are in order. Equation (19) represents the final dimensionless form of the pressure–deformation relation for a thin-walled incompressible hyperelastic cylinder. Second, note that, being a quartic (polynomial) equation in $(1 + \bar{u}_{\bar{r}})$, Eq. (19) can be solved explicitly for $\bar{u}_{\bar{r}}$ as a function of $\bar{p}$ using, e.g., MATHEMATICA. However, the resulting expression is too lengthy to be worth including here. Third, observe that both $\bar{p}$ and $\bar{u}_{\bar{r}}$ can (and do) depend on the dimensionless flow-wise coordinate $\bar{z}$, but $\bar{z}$ does not feature explicitly in the pressure–deformation relationship in Eq. (19).

## 3.2 Thick-Walled Cylinder

In this section, we account for the non-negligible thickness of a cylinder, i.e., the case of thick-walled pressure vessel, also known as *Lamé's first problem* (see, e.g., [33]).

Unlike the case of a thin-walled cylinder, the inner and outer radii of the thick-walled cylinder differ. They are, thus, denoted by $r_i$ and $r_o$ before deformation, and by $R_i$ and $R_o$ after deformation. Specifically,

$$r_i = a, \tag{21a}$$

$$r_o = a + t, \tag{21b}$$

$$R_i = a + u_r, \tag{21c}$$

where $u_r$ is the radial displacement of the inner surface of the cylinder. For the problem that we have posed, the displacement of the outer surface is of no consequence to the flow within the cylinder, hence we do not discuss it; then, denoting the displacement of the inner surface by $u_r$ is unambiguous. Since the cylinder's wall is assumed to be composed of an incompressible material (constant volume), and it is clamped at both its ends (constant length), its cross sectional area remains constant. Therefore,

$$R_o^2 - R_i^2 = r_o^2 - r_i^2. \tag{22}$$

The cylinder kinematics (Sect. 3.1.1) and the hyperelastic constitutive equations (Sect. 3.1.2) developed for the thin-walled cylinder also apply to the thick-walled one.

However, unlike the previously discussed case, the stress and deformation fields are not constant for a thick-walled cylinder. Specifically, the stress and deformation vary across the thickness of the cylinder. Consequently, the equations for static equilibrium of a thick-walled tube are differential equations. Neglecting body forces (due to the small scale of the posed FSI problem) and shear stresses, the equations for static equilibrium [13, 16, 24, 29] are thus:

$$\frac{\partial \sigma_{rr}}{\partial R} + \frac{1}{R}(\sigma_{rr} - \sigma_{\theta\theta}) = 0, \tag{23a}$$

$$\frac{\partial \sigma_{zz}}{\partial Z} = 0. \tag{23b}$$

The latter equations, when written in terms of material coordinates in association with the deformation field described in Eq. (5), reduce to

$$\frac{\partial (R\sigma_{rr})}{\partial r} + \frac{r}{R}\sigma_{\theta\theta} = 0, \tag{24a}$$

$$\frac{\partial \sigma_{zz}}{\partial z} = 0. \tag{24b}$$

Note that Eq. (24b) is satisfied identically.

As above, $\sigma_{rr} (= \sigma_1)$ and $\sigma_{\theta\theta} (= \sigma_2)$ are also related by Eq. (13), i.e., the principal stress relations for an isotropic, hyperelastic Mooney–Rivlin material. Thus, we can eliminate $\sigma_{\theta\theta}$ from the constitutive Eq. (13) and the static equilibrium equations (24). Then, employing the expressions for the principal stretches $\lambda_1$ and $\lambda_2$ from Eq. (8), we obtain the following differential equation governing $\sigma_{rr}$:

$$\frac{\partial (R\sigma_{rr})}{\partial r} + \frac{r}{R}\left\{\sigma_{rr} + 2(\mathbb{C}_1 + \mathbb{C}_2)\left[\left(\frac{R}{r}\right)^2 - \left(\frac{r}{R}\right)^2\right]\right\} = 0. \tag{25}$$

We solve Eq. (25) for $\sigma_{rr}$ subject to the loading boundary conditions

$$\sigma_{rr}|_{r=r_o} = 0, \tag{26a}$$

$$\sigma_{rr}|_{r=r_i} = -p, \tag{26b}$$

to obtain the pressure–radius relation

$$p = \left[f\left(\frac{r_1^2}{R_1^2}\right) - f\left(\frac{r_i^2}{R_i^2}\right)\right](\mathbb{C}_1 + \mathbb{C}_2), \tag{27}$$

where, for convenience, the function $f$ is defined (see also [29]) as

$$f(\xi) := \xi + \ln \xi. \tag{28}$$

Note that Eq. (27) is equivalent to Eq. (3.4.3) in [29, Chap. 9]. It is relevant to remind the reader that $p \neq p(r)$, so the integration of Eq. (25) is straightforward.

Finally, substituting the geometric relationships from Eqs. (21) and (22) into Eq. (27), we obtain

$$\frac{p}{\mathbb{C}_1+\mathbb{C}_2}=\left[f\left(\frac{(1+t/a)^2}{(1+t/a)^2-1+(1+u_r/a)^2}\right)-f\left(\frac{1}{(1+u_r/a)^2}\right)\right]. \tag{29}$$

The last equation can be re-written in dimensionless form using the variables from Eq. (18) as

$$2\bar{t}\gamma\bar{p}=\left[f\left(\frac{(1+\bar{t})^2}{(1+\bar{t})^2-1+(1+\bar{u}_{\bar{r}})^2}\right)-f\left(\frac{1}{(1+\bar{u}_{\bar{r}})^2}\right)\right], \tag{30}$$

where $\gamma$ is the FSI parameter as defined in Eq. (19) above. Equation (30) represents the final dimensionless form of the pressure–deformation relation for a thick-walled incompressible hyperelastic cylinder.

## 4 Coupling of the Fluid and Structural Mechanics Problems

We now turn to the main task, which is coupling the flow and deformation. As shown in our previous work [3], this task is accomplished by computing the flow rate $q$ explicitly using its definition for an axisymmetric cylindrical tube:

$$q=\int_0^{2\pi}\int_0^{R_i}v_z\,r\,\mathrm{d}r\,\mathrm{d}\theta=\mathcal{V}_z2\pi a^2\int_0^{\bar{R}_i}\bar{v}_{\bar{z}}\,\bar{r}\,\mathrm{d}\bar{r}, \tag{31}$$

where we have also introduced the dimensionless variables from Eq. (1). Now, substituting the expression for $\bar{v}_{\bar{z}}$ from Eq. (3) into Eq. (31), we obtain the *dimensionless* flow rate

$$\bar{q}\equiv\frac{q}{\mathcal{V}_z\pi a^2}=\left(-\frac{1}{2}\frac{\mathrm{d}\bar{p}}{\mathrm{d}\bar{z}}\right)^{1/n}\frac{\bar{R}_i^{3+1/n}}{3+1/n}, \tag{32}$$

where $\bar{R}_i=1+\bar{u}_{\bar{r}}$ is the dimensionless *inner* radius of the deformed tube.

Thus, since $\bar{q}=const.$ by conservation of mass in a steady flow [36], Eq. (32) becomes an ordinary differential equation (ODE) for $\bar{p}(\bar{z})$:

$$\frac{\mathrm{d}\bar{p}}{\mathrm{d}\bar{z}}=-2[(3+1/n)\bar{q}]^n[1+\bar{u}_{\bar{r}}(\bar{z})]^{-(1+3n)}. \tag{33}$$

Now, we must specify the deformation profile $\bar{u}_{\bar{r}}$ to complete the calculation. Even in the special case of a Newtonian fluid ($n=1$), Eq. (33) represents a strongly nonlinear pressure gradient–deformation coupling.

### 4.1 Thin-Walled Cylinder

To finish the derivation of the coupled FSI theory for a thin-walled cylinder, we differentiate the pressure–deformation relation from Eq. (19) with respect to $\bar{z}$ to obtain

$$\gamma \frac{\mathrm{d}\bar{p}}{\mathrm{d}\bar{z}} = \left[1 + \frac{3}{(1+\bar{u}_{\bar{r}})^4}\right] \frac{\mathrm{d}\bar{u}_{\bar{r}}}{\mathrm{d}\bar{z}}. \tag{34}$$

Then, we eliminate $\mathrm{d}\bar{p}/\mathrm{d}\bar{z}$ between Eqs. (33) and (34) to obtain an ODE for $\bar{u}_{\bar{r}}$:

$$-2\gamma[(3+1/n)\bar{q}]^n = \left[(1+\bar{u}_{\bar{r}})^{3n+1} + (1+\bar{u}_{\bar{r}})^{3n-3}\right] \frac{\mathrm{d}\bar{u}_{\bar{r}}}{\mathrm{d}\bar{z}}. \tag{35}$$

Since conservation of mass dictates that $\bar{q} = \mathit{const}.$, and $\gamma$ and $n$ are known constants, the ODE (35) can be separated and directly integrated, subject to the boundary condition (BC) $\bar{u}_{\bar{r}}(\bar{z}=1)=0$,[1] to yield:

$$2\gamma[(3+1/n)\bar{q}]^n(1-\bar{z}) = \frac{[1+\bar{u}_{\bar{r}}(\bar{z})]^{3n+2}}{(3n+2)} + \frac{[1+\bar{u}_{\bar{r}}(\bar{z})]^{3n-2}}{(3n-2)} - \frac{6n}{(3n+2)(3n-2)}. \tag{36}$$

Equations (19) and (36) fully specify (albeit implicitly) the static response of a thin hyperelastic cylinder due to internal flow of a generalized Newtonian fluid within it. For example, the displacement at $\bar{z}=0$ found from Eq. (36) can be used in Eq. (19) to determine $\bar{p}(0)$ from which the full dimensionless pressure drop follows: $\Delta\bar{p} := \bar{p}(0) - \bar{p}(1)$, where $\bar{p}(1)=0$ is our chosen pressure gauge for the pressure at the outlet and also in the surrounding medium exterior to the cylinder. Thus, the flow rate–pressure drop relationship ($\bar{q}$ as a function of $\Delta\bar{p}$, or vice versa), i.e., a generalized Hagen–Poiseuille law, in the presence of FSI can be obtained analytically.

### 4.2 Thick-Walled Cylinder

For a thick-walled cylinder, we differentiate Eq. (30) with respect to $\bar{z}$ to obtain

$$\begin{aligned}\gamma \frac{\mathrm{d}\bar{p}}{\mathrm{d}\bar{z}} = -\Bigg\{ &\frac{2(1+\bar{t})^2(1+\bar{u}_{\bar{r}})}{[(1+\bar{t})^2 + (\bar{u}_{\bar{r}})^2 + 2\bar{u}_{\bar{r}}]^2} + \frac{2(1+\bar{u}_{\bar{r}})}{(1+\bar{t})^2 + (\bar{u}_{\bar{r}})^2 + 2\bar{u}_{\bar{r}}} \\ &- \frac{2}{(1+\bar{u}_{\bar{r}})} - \frac{2}{(1+\bar{u}_{\bar{r}})^3} \Bigg\} \frac{\mathrm{d}\bar{u}_{\bar{r}}}{\mathrm{d}\bar{z}}.\end{aligned} \tag{37}$$

---

[1] Note, more importantly, that although in general we cannot expect to satisfy *clamping* BCs, i.e., $\bar{u}_{\bar{r}} = \mathrm{d}\bar{u}_{\bar{r}}/\mathrm{d}\bar{z} = 0$ at $\bar{z}=0$ and $\bar{z}=1$ in this leading-order analysis of deformation, we *must* respect the pressure outlet BC, i.e., $\bar{p}(\bar{z}=1)=0$. From Eq. (19), it is then clear that the pressure BC requires that $\bar{u}_{\bar{r}}(\bar{z}=1)=0$ as assumed.

Then, we eliminate $\mathrm{d}\bar{p}/\mathrm{d}\bar{z}$ between Eqs. (33) and (37) to obtain an ODE for the dimensionless transverse deflection $\bar{u}_{\bar{r}}$:

$$\left\{\frac{2(1+\bar{t})^2(1+\bar{u}_{\bar{r}})}{[(1+\bar{t})^2+(\bar{u}_{\bar{r}})^2+2\bar{u}_{\bar{r}}]^2}+\frac{2(1+\bar{u}_{\bar{r}})}{(1+\bar{t})^2+(\bar{u}_{\bar{r}})^2+2\bar{u}_{\bar{r}}}-\frac{2}{(1+\bar{u}_{\bar{r}})}\right.$$
$$\left.-\frac{2}{(1+\bar{u}_{\bar{r}})^3}\right\}\frac{\mathrm{d}\bar{u}_{\bar{r}}}{\mathrm{d}\bar{z}}=\bar{t}\gamma[(3+1/n)\bar{q}]^n(1+\bar{u}_{\bar{r}})^{-(1+3n)}, \tag{38}$$

subject to the BC that $\bar{u}_{\bar{r}}(1)=0$, as before. Unlike, Eq. (35), Eq. (38) cannot be integrated directly, thus it must be solved numerically. We employ the `odeint` subroutine of the Python package SciPy [23], with default error tolerances, for this integration.

Equations (30) and (38) fully specify the static FSI response of the thick-walled hyperelastic cylinder due to the flow of the generalized Newtonian fluid within. Together these two equations can be used to develop the flow rate–pressure relationship for a thick-walled hyperelastic tube, however the calculation must be done via numerical quadratures, unlike the case of the thin-walled cylinder (Sect. 4.1).

## 5 Results and Discussion

Let us now illustrate the deformation–pressure and flow rate–pressure drop relationships predicted by our FSI theory for the interaction between the steady flow of a power-law fluid within a soft hyperelastic cylindrical vessel containing it. Specifically, in this section, we wish to highlight the effect of hyperelasticity on the structural response of the microtube.

In Fig. 2, we plot the dimensionless pressure drop $\Delta\bar{p}$ across a thin-walled microtube as a function of the dimensionless inlet flow rate $\bar{q}$ for different values of the FSI parameter $\beta(=3\gamma)$. The curves (solid) for the thin-walled hyperelastic tube are obtained from the present theory, namely Eqs. (19) and (36), while the curves (dashed) pertaining to the thin-walled linearly elastic tube are calculated based on the results from our previous study [3], namely:

$$\Delta\bar{p}=\frac{1}{(1-\nu/2)\beta}\left(\left\{1+2(2+3n)(1-\nu/2)\beta[(3+1/n)\bar{q}]^n\right\}^{1/(2+3n)}-1\right), \tag{39}$$

We note that, for both linearly elastic and hyperelastic tubes, the pressure drop decreases with $\beta(=3\gamma)$. This observation is attributed to the very definition of $\beta$ as the parameter symbolizing the strength of the FSI coupling. For large $\beta$ values, there is "stronger" FSI coupling than at small $\beta$ values and, hence, there is larger deformation of the tube. Consequently, the cross-sectional area increases, lowers the resistance to the flow, and culminates in a smaller pressure drop for large $\beta$ compared to small $\beta$.

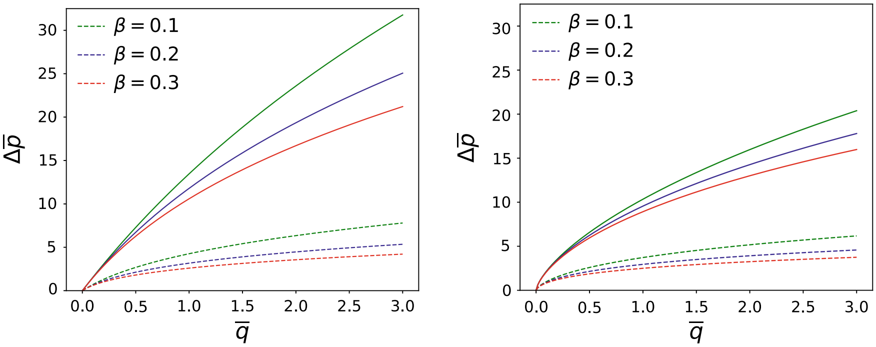

**(a)** $n$ = 1 (Newtonian) **(b)** $n$ = 0.7 (pseudoplastic)

**Fig. 2** The dimensionless (full) pressure drop across a thin-walled microtube as a function of the dimensionless inlet flow rate $\bar{q}$ for different values of FSI parameter $\beta = 3\gamma$. Hyperelastic thin-walled tubes correspond to solid curves, while linearly elastic thin-walled tubes correspond to dashed curves for **a** a Newtonian fluid with $n = 1.0$ (e.g., blood plasma), and **b** a shear-thinning fluid with $n = 0.7$ (e.g., whole blood). For the hyperelastic tube, the corresponding theory has been presented in Sect. 4.1, while for linearly elastic tubes the predicted pressure drop is given by Eq. (39) derived in [3]

Perhaps more attuned to the thesis of this chapter is the difference in the response of a hyperelastic and the theory of a linearly elastic tube for the *same* FSI coupling strength. Thus, comparing the solid and dashed curves, respectively, in Fig. 2 at fixed $\gamma$ (i.e., same color), we observe that a hyperelastic tube supports a higher pressure drop than a linearly elastic tube. We explain this trend by noting that a hyperelastic tube, in general, is stiffer and has a higher tendency to preserve its original configuration compared to a linearly elastic tube. In other words, a hyperelastic material requires higher pressure than a linearly elastic material to sustain the same deformations (see also [25, 26]).

Next, we move on to the case of thick-walled tubes and compare, in Fig. 3, the flow rate–pressure drop relation in a thick-walled hyperelastic tube obtained from the present theory, namely Eqs. (30) and (38), with the corresponding relationship for a thick-walled linearly elastic tube calculated based on

$$\Delta\bar{p} = \frac{1}{\mathfrak{K}\beta}\left(\left\{1 + 2(2+3n)\mathfrak{K}\beta[(3+1/n)\bar{q}]^n\right\}^{1/(2+3n)} - 1\right), \tag{40}$$

which was derived from Eq. (52) in the appendix; $\mathfrak{K} = [(1+\bar{t})^2(1+\nu) + (1-2\nu)]/(2+\bar{t})$ and $\bar{t} = t/a$. For the same reason as above, an increase in $\beta(= 3\gamma)$ causes $\Delta\bar{p}$ to decrease.

Things become more interesting, however, when the curves corresponding to same value of the FSI parameter $\beta$ are compared (solid vs. dashed) in Fig. 3. For small $\bar{q}$ and small $\beta$, the linearly elastic tube deforms less and sustains a larger $\Delta\bar{p}$ compared to the hyperelastic one. However, this trend is reversed for large $\bar{q}$ and large

$\beta$, for which the hyperelastic tube sustains a higher $\Delta\bar{p}$ than the linearly elastic one. This interesting observation can be explained by the very nature of hyperelasticity. It is more difficult to deform a hyperelastic material as the deformation increases, i.e., hyperelastic materials exhibit *strain-stiffening* [28, 31, 32]. Mathematically, this resistance to deformation can be measured through the rate of change of the stress with respect to the strain (or deformation). To this end, when we differentiate the constitutive equation for a hyperelastic material, namely Eq. (13), with respect to the principal deformation along the "1" direction, whilst keeping the deformations in the other directions constant for simplicity, to obtain:

$$\frac{\partial \sigma_1}{\partial \lambda_1} = 4\mathbb{C}_1\lambda_1 + 4\mathbb{C}_2/\lambda_1^3. \tag{41}$$

From the latter equation it follows that the resistance to deformation increases with deformation (keeping in mind that $\mathbb{C}_2 < 0$). On the other hand, for a linearly elastic material, the resistance to deformation is given by Young's modulus $E$ (at least for a uniaxial load), which is a constant!

One could also interpret the much larger $\Delta\bar{p}$ in hyperelastic (over linearly elastic) thin-wall cylinders in Fig. 2 as a consequence of strain-hardening. However, in that case, due to significant resistance to deformation of the thin-walled hyperelastic vessel (there is almost one order of magnitude difference in the vertical scales between Figs. 2 and 3), the interplay between $\bar{q}$ and $\beta$ values just described is not present.

Finally, we also note that an increase in the cylinder thickness will lead to a corresponding decrease in the pressure drop, although this is not shown in Fig. 3,

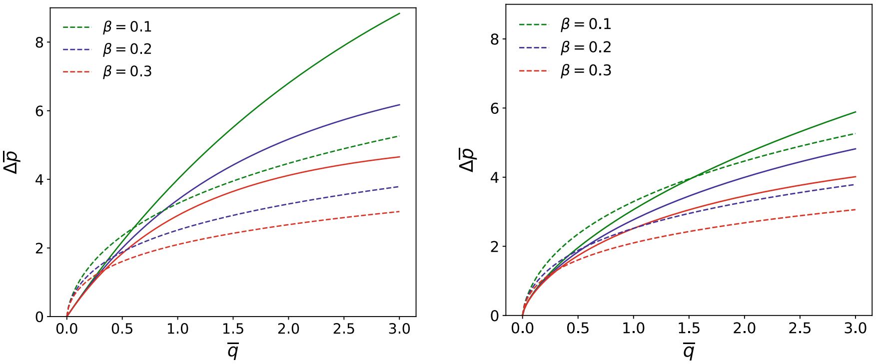

**(a)** $n$ = 1 (Newtonian) **(b)** $n$ = 0.7 (pseudoplastic)

**Fig. 3** The dimensionless (full) pressure drop across a thick-walled microtube as a function of the dimensionless inlet flow rate $\bar{q}$ for different values of FSI parameter $\beta = 3\gamma$ and $\bar{t} = t/a = 0.3$. Hyperelastic thick-walled tubes correspond to solid curves, while linearly elastic thick-walled tubes correspond to dashed curves, for **a** a Newtonian fluid with $n = 1.0$ (e.g., blood plasma), and **b** a shear-thinning fluid with $n = 0.7$ (e.g., whole blood). For a thick-walled hyperelastic tube, the corresponding theory was presented in Sect. 4.2, while for thick-walled linearly elastic tubes the predicted pressure drop is given by Eq. (40) derived from the appendix in which all the curves have been plotted for a constant ratio $\bar{t} = t/a = 0.3$. This result is similar to the one for thick linearly elastic plates, which was discussed in our previous work [4], and it can be attributed to an increase in the normal stress throughout the structure's thickness as $\bar{t}$ increases.

## 6 Conclusion

In this chapter, we have solved the problem of steady-state low Reynolds number fluid–structure interaction (FSI) between a generalized Newtonian fluid and a hyperelastic cylindrical tube. The hydrodynamic pressure, which is needed to maintain a unidirectional flow in a deformed cylindrical pipe, was transferred as a load onto the elastic structure, the mechanics of which were analyzed using the *thin* and *thick* pressure vessels theories for isotropic, incompressible Mooney–Rivlin materials. The fluid and solid mechanics were brought together to yield a coupled equation relating the constant inlet flow rate $q$ to the tube's radial deformation $u_r(z)$. For a thin-walled pressure vessel, the latter relation takes the *implicit* dimensional form

$$\frac{m[(3+1/n)q]^n}{(\mathbb{C}_1+\mathbb{C}_2)t}(\ell - z) = \frac{[a+u_r(z)]^{(3n+2)}}{a^2(3n+2)} + \frac{a^2[a+u_r(z)]^{(3n-2)}}{(3n-2)} - \frac{6na^{3n}}{(3n+2)(3n-2)}. \tag{42}$$

As a special case, we have also found the flow rate–deformation relation for a Newtonian fluid ($n = 1$, and $m = \mu$ is the shear viscosity):

$$\frac{4\mu q}{(\mathbb{C}_1+\mathbb{C}_2)t}(\ell - z) = \frac{[a+u_r(z)]^5}{5a^2} + a^2[a+u_r(z)] - \frac{6a^3}{5}, \tag{43}$$

which is an implicit relation for $u_r(z)$ given $q$. Whence, the equation relating the pressure $p(z)$ at an axial location $z$ with the deformation $u_r(z)$ is

$$p(z) = 2(\mathbb{C}_1+\mathbb{C}_2)\left(\frac{t}{a}\right)\left\{[1+u_r(z)/a] - \frac{1}{[1+u_r(z)/a]^3}\right\}. \tag{44}$$

Consonant with our previous FSI results [3, 4], the pressure–deformation relationship is set by the structural mechanics alone, hence it *does not explicitly depend* upon the fluid's rheology.

Equations (42) [or (43)] and (44) fully specify the FSI problem for a thin-walled hyperelastic cylinder. In deriving these equations, we arrived at the dimensionless *FSI parameter* $\gamma$, which determines the "strength" of the coupling between flow and deformation fields:

$$\gamma := \frac{\mathcal{P}_c}{2(\mathbb{C}_1+\mathbb{C}_2)}\left(\frac{a}{t}\right) \tag{45}$$

for a hyperelastic cylinder with material constants $\mathbb{C}_1$ and $\mathbb{C}_2$. Here, the pressure scale $\mathcal{P}_c$ depends on the nature of the physical scenario at hand. For a flow-rate-controlled experiment and/or simulation, as considered in this chapter for example, we set $\mathcal{P}_c = [q/(\pi a^3)]^n m\ell/a$, as dictated by the fluid's momentum balance. On the other hand, for a pressure-drop-controlled experiment or simulation, we can directly set $\mathcal{P}_c = \Delta p$, which means the fluids velocity scale $\mathcal{V}_z$ discussed above becomes a function of the dimensional pressure drop $\Delta p$.

We compared the predicted $q - \Delta\, p$ relation due to the hyperelastic FSI theory developed in this chapter with the corresponding relation due to linearly elastic FSI theory form previous work [3]. In particular, we concluded that a hyperelastic microtube supports smaller deformations than a linearly elastic microtube for the same hydrodynamic pressure, or conversely a hyperelastic microtube can sustain a higher pressure drop than a linearly elastic one, for the same deformation. Finally, our observation in Sect. 5 that the pressure drop across a soft microtube *decreases* with the wall thickness is in agreement with the case of rectangular microchannels with a plate for a top wall, which we considered in our previous work [4].

In future work, we will report benchmarks of this chapter's purely theoretical considerations against full-fledged three-dimensional FSI simulations and/or experiments (as in [3, 4]). Future work could also include extending our approach to FSI between internal viscous flows and composite structures governed by *generalized* continua continua [2], such as Cosserat continua [30] or microstructured materials [12].

**Acknowledgements** This research was supported by the U.S. National Science Foundation under grant No. CBET-1705637. We dedicate this work to the 70th anniversary of the director of the Institute of Problems in Mechanical Engineering of the Russian Academy of Sciences: Prof. Dr. Sc. D. I. Indeitsev. We also thank Prof. Alexey Porubov for his kind invitation to contribute to this volume, and for his efforts in organizing it.

## Appendix

In this appendix, we consider the flow rate–pressure drop relationship for steady flow of a power-law fluid within a linearly elastic, thick-walled pressure vessel of thickness $t$, and inner radius $r_i = a$. The pressure vessel is subject only to an internal distributed pressure load $p$, with zero external pressure. Then, the state of stress evaluated at the inner radius (see [40]) is:

$$\sigma_{\theta\theta} = \left(\frac{r_o^2 + r_i^2}{r_o^2 - r_i^2}\right) p, \tag{46a}$$

$$\sigma_{rr} = -p, \tag{46b}$$

$$\sigma_{zz} = \left(\frac{r_i^2}{r_o^2 - r_i^2}\right) p. \tag{46c}$$

The hoop strain is given by the constitutive equations of linear elasticity as:

$$\varepsilon_{\theta\theta} = \frac{u_r}{r_i} = \frac{1}{E}\big[\sigma_{\theta\theta} - \nu(\sigma_{zz} + \sigma_{rr})\big]. \tag{47}$$

Using Eqs. (46) and (47) yields

$$\frac{u_r}{r_i} = \frac{1}{E}\left[\left(\frac{r_o^2 + r_i^2}{r_o^2 - r_i^2}\right) p - \nu\left(\frac{r_i^2}{r_o^2 - r_i^2} - 1\right) p\right], \tag{48}$$

which, upon using Eqs. (18) and (21), becomes

$$\frac{u_r}{r_i} = \bar{t}\left[\frac{(1+\bar{t})^2(1+\nu) + (1-2\nu)}{(1+\bar{t})^2 - 1}\right]\beta\bar{p}; \qquad \beta = \frac{\mathcal{P}_c}{E\bar{t}}. \tag{49}$$

After deformation, the inner radius is $R_i = r_i + u_r$ (where, initially, $r_i = a$). Thus, the dimensionless inner radius is

$$\bar{R}_i = \frac{r_i + u_r}{r_i} = 1 + \frac{u_r}{r_i} = 1 + \left[\frac{(1+\bar{t})^2(1+\nu) + (1-2\nu)}{2+\bar{t}}\right]\beta\bar{p}. \tag{50}$$

Substituting the expression for $\bar{R}_i$ from Eq. (50) into Eq. (33), we obtain an ODE for the dimensionless pressure $\bar{p}$:

$$\frac{\mathrm{d}\bar{p}}{\mathrm{d}\bar{z}} = -2[(3+1/n)\bar{q}]^n\,(1 + \mathfrak{K}\beta\bar{p})^{-(1+3n)}, \tag{51}$$

where we have defined $\mathfrak{K} := [(1+\bar{t})^2(1+\nu) + (1-2\nu)]/(2+\bar{t})$ for convenience. As usual, the ODE (51) is separable and subject to a pressure outlet BC [i.e., $\bar{p}(1) = 0$], thus we obtain:

$$\bar{p}(\bar{z}) = \frac{1}{\mathfrak{K}\beta}\left(\left\{1 + 2(2+3n)\mathfrak{K}\beta[(3+1/n)\bar{q}]^n(1-\bar{z})\right\}^{1/(2+3n)} - 1\right). \tag{52}$$

Then, the full pressure drop is simply $\Delta\bar{p} = \bar{p}(\bar{z} = 0)$. Note that $\mathfrak{K} = (1 - \nu/2) + \mathcal{O}(\bar{t})$, thus the expression for $\Delta\bar{p}$ based on Eq. (52) [i.e., Eq. (40) above] reduces to Eq. (39) (based on [3]) identically for thin shells ($\bar{t} \ll 1$).

## References

1. Abramian, A.K., Indejtsev, D.A., Vakulenko, S.A.: Wave localization in hydroelastic systems. Flow Turbul. Combust. **61**, 1–20 (1998). https://doi.org/10.1023/A:1026484701275
2. Altenbach, H., Maugin, G.A., Erofeev, V. (eds.): Mechanics of generalized continua. In: Advanced Structured Materials, vol 7. Springer, Berlin, Heidelberg. https://doi.org/10.1007/978-3-642-19219-7 (2011)

3. Anand, V., Christov, I.C.: Steady low Reynolds number flow of a generalized Newtonian fluid through a slender elastic tube. arXiv:1810.05155 (2018)
4. Anand, V., David JR, J., Christov, I.C.: Non-Newtonian fluid–structure interactions: static response of a microchannel due to internal flow of a power-law fluid. J Non-Newtonian Fluid Mech **264**, 62–72 (2018). https://doi.org/10.1016/j.jnnfm.2018.12.008
5. Başar, Y., Weichert, D.: Nonlinear Continuum Mechanics of Solids. Springer, Berlin, Heidelberg. https://doi.org/10.1007/978-3-662-04299-1 (2000)
6. Bird, R.B.: Useful non-Newtonian models. Annu. Rev. Fluid. Mech. **8**, 13–34 (1976). https://doi.org/10.1146/annurev.fl.08.010176.000305
7. Bisplinghoff, R.L., Ashley, H., Halfman, R.L.: Aeroelasticity. Dover Publications, Mineola, NY (1996)
8. Bonet, J., Wood, R.J.: Nonlinear Continuum Mechanics for Finite Element Analysis, 2nd edn. Cambridge University Press, New York, NY (2008)
9. Boyko, E., Bercovici, M., Gat, A.D.: Viscous-elastic dynamics of power-law fluids within an elastic cylinder. Phys. Rev. Fluids **2**, 073301. https://doi.org/10.1103/PhysRevFluids.2.073301 (2017)
10. Čanić, S., Mikelić, A.: Effective equations modeling the flow of a viscous incompressible fluid through a long elastic tube arising in the study of blood flow through small arteries. SIAM J. Appl. Dyn. Syst. **2**, 431–463 (2003). https://doi.org/10.1137/S1111111102411286
11. Chien, S., Usami, S., Taylor, H.M., Lundberg, J.L., Gregersen, M.I.: Effects of hematocrit and plasma proteins on human blood rheology at low shear rates. J. Appl. Physiol. **21**, 81–87 (1966). https://doi.org/10.1152/jappl.1966.21.1.81
12. Dell'Isola, F., Eremeyev, V.A., Porubov, A. (eds.): Advances in mechanics of microstructured media and structures. In: Advanced Structured Materials, vol. 87. Springer International Publishing, Cham, Switzerland. https://doi.org/10.1007/978-3-319-73694-5 (2018)
13. Dym, C.L.: Intoduction to the Theory of Shells. Hemisphere Publishing Corporation, New York, NY (1990)
14. Elbaz, S.B., Gat, A.D.: Dynamics of viscous liquid within a closed elastic cylinder subject to external forces with application to soft robotics. J. Fluid Mech. **758**, 221–237 (2014). https://doi.org/10.1017/jfm.2014.527
15. Elbaz, S.B., Gat, A.D.: Axial creeping flow in the gap between a rigid cylinder and a concentric elastic tube. J. Fluid Mech. **806**, 580–602 (2016). https://doi.org/10.1017/jfm.2016.587
16. Flügge, W.: Stresses in Shells. Springer, Berlin, Heidelberg. https://doi.org/10.1007/978-3-662-01028-0 (1960)
17. Fung, Y.C.: Biomechanics: Mechanical Properties of Living Tissues. Springer, New York, NY. https://doi.org/10.1007/978-1-4757-2257-4 (1993)
18. Gay-Balmaz, F., Georgievskii, D., Putkaradze, V.: Stability of helical tubes conveying fluid. J. Fluids Struct. **78**, 146–174 (2018). https://doi.org/10.1016/j.jfluidstructs.2017.12.020
19. Grotberg, J.B., Jensen, O.E.: Biofluid mechanics in flexible tubes. Annu. Rev. Fluid Mech. **36**, 121–147 (2004). https://doi.org/10.1146/annurev.fluid.36.050802.121918
20. Heil, M., Hazel, A.L.: Fluid-structure interaction in internal physiological flows. Annu. Rev. Fluid Mech. **43**, 141–162 (2011). https://doi.org/10.1146/annurev-fluid-122109-160703
21. Hussain, M.A., Kar, S., Puniyani, R.R.: Relationship between power law coefficients and major blood constituents affecting the whole blood viscosity. J. Biosci. **24**, 329–337 (1999). https://doi.org/10.1007/BF02941247
22. Indeitsev, D.A., Osipova, E.V.: Nonlinear effects in trapped modes of standing waves on the surface of shallow water. Tech. Phys. **45**, 1513–1517 (2000). https://doi.org/10.1134/1.1333186
23. Jones, E., Oliphant, T., Peterson, P., et al.: SciPy: Open source scientific tools for Python. GitHub. http://www.scipy.org/ (2001)
24. Kraus, H.: Thin Elastic Shells. Wiley, New York, NY (1967)
25. Lazopoulos, A., Tsangaris, S.: Flow of incompressible viscous fluid through a tube with non-linear elastic membrane insertion: applications. Eng. Appl. Comput. Fluid Mech. **2**, 222–233 (2008a). https://doi.org/10.1080/19942060.2008.11015223

26. Lazopoulos, A., Tsangaris, S.: Fluid flow of incompressible viscous fluid through a non-linear elastic tube. Arch. Appl. Mech. **78**(11), 895–907 (2008b). https://doi.org/10.1007/s00419-008-0205-x
27. Leal, L.G.: Advanced Transport Phenomena: Fluid Mechanics and Convective Transport Processes. Cambridge University Press, New York, NY. https://doi.org/10.2277/0521849101 (2007)
28. Liu, I.S.: A note on the Mooney-Rivlin material model. Continuum Mech. Thermodyn. **24**(4–6), 583–590 (2012). https://doi.org/10.1007/s00161-011-0197-6
29. Lurie, A.I.: Theory of Elasticity. Foundations of Engineering Mechanics, Springer, Berlin, Heidelberg. https://doi.org/10.1007/978-3-540-26455-2 (2005)
30. Maugin, G.A., Metrikine, A.V. (eds): Mechanics of Generalized Continua: One Hundred Years After the Cosserats, Advances in Mechanics and Mathematics, vol. 21. Springer Science+Business Media, LLC, New York, NY. https://doi.org/10.1007/978-1-4419-5695-8 (2010)
31. Mihai, L.A., Goriely, A.: Positive or negative Poynting effect? The role of adscititious inequalities in hyperelastic materials. Proc. R. Soc. A **467**, 3633–3646 (2011). https://doi.org/10.1098/rspa.2011.0281
32. Moon, H., Truesdell, C.: Interpretation of adscititious inequalities through the effects pure shear stress produces upon an isotropie elastic solid. Arch. Rational Mech. Anal. **55**, 1–17 (1974). https://doi.org/10.1007/BF00282431
33. Muskhelishvili, N.I.: Some Basic Problems of the Mathematical Theory of Elasticity: Fundamental Equations, Plane Theory of Elasticity, Torsion and Bending, 2nd edn. Springer Science+Business Media, Dordrecht. https://doi.org/10.1007/978-94-017-3034-1 (1977)
34. Ogden, R.W.: Large deformation isotropic elasticity—on the correlation of theory and experiment for incompressible rubberlike solids. Proc. R. Soc. Lond. A **326**, 565–584 (1972). https://doi.org/10.1098/rspa.1972.0026
35. Païdoussis, M.P.: Fluid-Structure Interactions: Slender Structures and Axial Flow. Academic Press, an imprint of Elsevier Inc., San Diego, CA (1998)
36. Panton, R.L.: Incompressible Flow, 4th edn. Wiley, Hoboken, NJ. https://doi.org/10.1002/9781118713075 (2013)
37. Porubov, A.V., Velarde, M.G.: Strain kinks in an elastic rod embedded in a viscoelastic medium. Wave Motion **35**, 189–204 (2002). https://doi.org/10.1016/S0165-2125(01)00101-9
38. Raj, M.K., Chakraborty, J., DasGupta, S., Chakraborty, S.: Flow-induced deformation in a microchannel with a non-Newtonian fluid. Biomicrofluidics **12**, 034116 (2018). https://doi.org/10.1063/1.5036632
39. Shapiro, A.H.: Steady flow in collapsible tubes. ASME J. Biomech. Eng. **99**, 126–147 (1977). https://doi.org/10.1115/1.3426281
40. Vable, M.: Mechanics of Materials, 2nd edn. Expanding Educational Horizons, LLC, http://madhuvable.org/ (2009)
41. Wagner, N.J., Brady, J.F.: Shear thickening in colloidal dispersions. Phys. Today **62**(10), 27–32 (2009). https://doi.org/10.1063/1.3248476
42. Whittaker, R.J., Heil, M., Jensen, O.E., Waters, S.L.: A rational derivation of a tube law from shell theory. Q. J. Mech. Appl. Math. **63**, 465–496 (2010). https://doi.org/10.1093/qjmam/hbq020

# Benchmark Study of Measurements of Hydrogen Diffusion in Metals

**D. G. Arseniev, Alexander Belyaev, A. M. Polyanskiy, V. A. Polyanskiy and Yu. A. Yakovlev**

**Abstract** The chapter is concerned with the model of multichannel diffusion of hydrogen in a solid. The model is developed for analysis of diffusion of small, so-called natural, hydrogen concentrations, describes experiments for the model verification, and presents data on the hydrogen binding energies in a solid obtained by identifying the model parameters by means of the experimental data. A critical analysis of some disadvantages of the widely known method of thermo-desorption spectra is provided. The energy spectra of hydrogen obtained by the latter method and the multichannel diffusion model are compared and discussed. 15 years ago we first introduced Dmitry Indeitsev to the idea of applying the model of multichannel diffusion to determine the hydrogen binding energy in a solid. He enthusiastically supported our activity, both by discussing the results and participating in projects by Russian Foundation for Basic Research. Our experimental results served as a basis for the two-continuum model proposed by him. The authors express deep gratitude to him for the extremely useful and friendly participation in the development of our ideas.

---

D. G. Arseniev
Saint-Petersburg University, St.Petersburg, Russia
e-mail: vicerector.int@spbstu.ru

A. Belyaev · V. A. Polyanskiy (✉)
Institute for Problems in Mechanical Engineering RAS, St.Petersburg, Russia
e-mail: vapol@mail.ru

A. Belyaev
e-mail: vice.ipme@gmail.com

A. M. Polyanskiy
RDC Electron and Beam Technology, Ltd., St.Petersburg, Russia
e-mail: ampol@electronbeamtech.com

Yu. A. Yakovlev
Peter the Great Saint-Petersburg Polytechnic University, St.Petersburg, Russia
e-mail: yura.yakovlev@gmail.com

H. Altenbach et al. (eds.), *Dynamical Processes in Generalized Continua and Structures*, Advanced Structured Materials 103,
https://doi.org/10.1007/978-3-030-11665-1_3

# 1 Introduction

The study of hydrogen diffusion in solids has a great practical importance. Its adequate description is necessary for prediction of the working resource of constructions, development of the storage systems and safe technologies aa well as for reliable measurement of hydrogen concentration.

It was Gorsky [19, 20] who found out that, apart from temperature and concentration gradient, the mechanical stresses in crystal matrix affect the diffusion of atoms in solids. This allows one to explain the mechanism of gradual evolution of hydrogen embrittlement in metallic parts, elements and formation of cold cracks in welds. The hydrogen diffusion plays an important role in the processes of corrosion, cracking and brittle failure [12, 23, 27, 37, 44, 62]. The influence of hydrogen on electric properties of semiconductors is also essential, see [39].

The systems for storage and transport of gas are designed to withstand high pressure. Hydrogen diffuses into metal walls and other parts of these systems cf. [66]. The gradual accumulation of hydrogen in metal leads to the hydrogen embrittlement and destruction.

There are some hydrogen storage systems in which the hydrogen is accumulated in metals, composites and nanostructures. The hydrogen diffusion is the main working process in charging and discharging, cf. [51].

In the thermonuclear reactors the diffusion of hydrogen and its isotopes leads to the hydrogen saturation in the inner parts of reactor, cf. [2]. Increasing the temperature of the inner walls leads to the hydrogen extraction from the walls to plasma, cf. [10]. This process destroys the plasma's stability during energy pumping. Hydrogen accumulation results in cracking on the inner parts of reactor due to the hydrogen embrittlement and temperature shocks. The tritium diffusion through the reactor walls leads to reducing the level of radiation safety of the thermonuclear synthesis technology.

In all these cases, the hydrogen concentrations are close to the upper limit for structural materials.

However, hydrogen is always present in metals and semiconductors. For majority of metals, the "natural" values of hydrogen concentration are in the range from 0.2 ppm (for aluminum alloys and high strength steels) up to 80 ppm (for titanium alloys). Even the double excess of the "natural" hydrogen concentration leads to loss of plasticity of structural materials, see [30, 32].

The hydrogen in solids was established to occupy several energy levels. It was found that hydrogen with binding energy in the range of 0.2–0.4 eV considerably influences on plasticity and strength of steels.

The method of thermo-desorption spectra (TDS) is usually utilised for determination of binding energy. This method is proposed in Ref. [28]. Extraction of hydrogen from a sample is considered as a chemical reaction of the first order with the activation energy equal to the binding energy. Thus the effect of the hydrogen diffusion inside the studied sample is considered to be negligible. The TDS method is widely used in material science. In practice, all studies of the effect of hydrogen on the structure and properties of metals and non-metals utilise this method, see e.g. [11, 25, 34, 36, 38, 47, 57, 60]. An important feature of TDS is an independent determination of the binding energy. Under identical conditions (size and shape of the samples, the hydrogen charging conditions etc.) TDS method allows one to trace the influence of sample structure and the concentration of individual alloy components on the binding energy value, cf. [57]. However, significant differences appear when we compare data from various researchers.

The influence of various factors on the result of research carried out by TDS method is addressed in a number of papers. For instance, Ref. [26] reports the influence of the sample thickness and the holding time after hydrogen charging on the shape and position of the TDS peak by means of the mathematical modeling. A detailed description and benchmark of the hydrogen charging methods are provided in [61]. The individual TDS peaks are shown to merge into one peak because of high hydrogen concentrations under charging and it yields only an average value of the energy of hydrogen bonds.

The use of additional assumptions allows one to interpret TDS even in the case in which the test yields a single peak rather than several ones. A Finite-Element Modeling of the hydrogen diffusion reported in [33] shows that a single peak of TDS can be accurately and adequately approximated as the hydrogen desorption from two energy levels by adjusting the prescribed diffusion constants and the binding energy values. However, this approach deprives the main advantage of the TDS method which is the possibility of independent determination of value of the hydrogen binding energy from the test results.

The diffusion process is not taken into account in the TDS equations for binding energies. Regretfully, this fact does not always take into consideration by researchers. For example, Ref. [17] suggests the existence of several channels of hydrogen diffusion in the martensitic steels. The authors of present paper have substantiated the existence of such channels earlier in their paper [48, 49]. However, all measurements in Ref. [17] were carried out by TDS method.

On the one hand, this contradicts to the experimental data since the account for diffusion introduces essential corrections to the values of binding energy even for relatively small sample sizes [42]. On the other hand, the experimental measurements evidences for low accuracy of the TDS approach [56]. As a rule, the hydrogen's binding energies of about 0.2 eV should yield notable hydrogen fluxes at normal conditions which is not observed experimentally.

Regardless of the specific values of the hydrogen binding energy it is important to know what happens to the hydrogen during annealing and how it changes the energy spectrum since this change demonstrates the predominance of a particular structure creating the hydrogen traps. This information allows one to simulate the behavior of both materials and loaded structures [5, 7, 8] and predict the crack growth, cf. [55, 65].

It is possible to estimate the binding energy using some other methods, e.g. the spectral one [39]; however this method is adequate only for thin samples such as films and membranes.

Due to the strong influence of hydrogen with different binding energies on the structure and strength of materials it becomes necessary to develop approaches which take to account the diffusion as a main process the hydrogen redistribution inside a solid body.

## 2 Measurement of Hydrogen Concentration by Vacuum Hot Extraction Method

The vacuum heating method is used both in experiments and in industrial control of hydrogen concentration in a solid probe [1, 29, 39, 46, 52] (Hydrogen Analysis by Vacuum Hot Extraction, VHE). In our experiments we used industrial hydrogen analyzer AV-1 with mass-spectrometric registration of dependence of hydrogen flux from the sample on time, in the process of the sample heating in vacuum. The apparatus exterior is shown in Fig. 1.

A schematic drawing of the AV-1 is presented in Fig. 2.

The system of probe preparation composed of the glass extractor made of the fused silica (see Fig. 2) and the radiation furnace whose temperature maintained constant during the analysis. The samples are placed in the cold appendix of extractor. In

**Fig. 1** Hydrogen analyzer AV-1

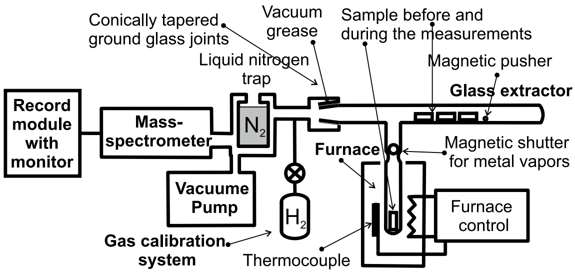

**Fig. 2** Scheme of the hydrogen measurement in AV-1

performing analysis, the sample is thrown off to the analytical appendix without spoiling of vacuum. The analytical appendix is maintained at a constant temperature of extraction, which is provided by the furnace put on the appendix.

For majority of alloys the extraction temperature is in the range 400–800 °C. The extractor volume is pumped continuously with the analyzer pump down to the working pressure of 100 μPa. The investigated sample is heated slowly up to the extractor temperature. The hydrogen flux from the sample is measured by mass-spectrometric analyzer preliminarily calibrated on the standard hydrogen containing samples or on the gas calibration. As a result, dependence of hydrogen flux from the extractor system on time (the extraction curve) is obtained. An integral of the extraction curve over time is proportional to the amount of hydrogen extracted from the sample. The shape of curve is typical for the aluminum, magnesium, titanium alloys and the different marks of steels. In determining the diffusion parameters, we compare the experimental extraction curve to the calculated one obtained by mathematical modeling of the time dependent hydrogen diffusion in the sample under consideration.

## 3 Modeling of Diffusion Process in Sample

For example, we consider the process of the sample heating in vacuum using the titanium samples studied experimentally. The prismatic sample sizes are as follows: $a; l; b$.

The extractor walls are made of fused silica. In the process of analysis, their temperature is maintained at a constant value $T_0$. The fused silica has practically zeroth thermal conductivity, the area of the sample contact with the walls is small, so the heat transfer occurs only due to radiation.

The fused silica does not transmit infrared radiation of the radiation furnace, that is, the sample is heated due to the heat radiation of the extractor walls. The amount of heat absorbed by the sample during the time interval $dt$ is:

$$dQ = \varepsilon_n \sigma S (T_0^4 - T^4) dt, \tag{1}$$

where $\sigma = 5,6687 \cdot 10^{-8}$ W/m$^2$K$^4$ is the Stefan–Boltzmann constant, $T$ is the sample temperature, $T_0$ is the wall temperature of the analytical appendix of extractor (see Fig. 1) and $\varepsilon_n$ is the sample absorption coefficient.

$$\varepsilon_n = \frac{1}{\frac{1}{\varepsilon_t} + \frac{S}{S_2}\left(\frac{1}{\varepsilon_2} - 1\right)},$$

where $\varepsilon_t$ is the absorption coefficient of titanium, $\varepsilon_2$ is the absorption coefficient of fused silica walls of analytical appendix of extractor (equal to 1 for infrared radiation), $S$ is the sample area, $S_2$ is the area of wall of analytical appendix of extractor involved in the heat transfer.

If $\varepsilon_2 = 1$ or $\varepsilon_2 >> \varepsilon_t$ then the approximate relation $\varepsilon_n \approx \varepsilon_t$ can be used. For titanium in the temperature range 200–900 °C we have

$$\varepsilon_t = 0.2. \tag{2}$$

In this condition, the heat capacity of titanium weakly depends on temperature and equals $c = 0.6$ kJ/kg·K. The heat $dQ$ (1) absorbed by the sample gives rise to the increase in the temperature by $dT$:

$$dQ = c\rho V dT, \tag{3}$$

where $\rho$ is mass density and $V$ is volume of the sample.

From Eqs. (1)–(3) one obtains the following equation for the sample heating:

$$\frac{dT}{dt} = \frac{\sigma S}{c\rho V} \cdot 0.2 \cdot (T_0^4 - T^4). \tag{4}$$

Dependence of hydrogen concentration on coordinates and time is obtained from solution of the time-dependent diffusion equation

$$\begin{array}{l} \Delta C = \frac{1}{D}\frac{\partial C}{\partial t} \\ C|_S = 0 \\ C|_{t=0} = C_0 \end{array}, \tag{5}$$

where $C$ is the hydrogen concentration, $D = D_0 \cdot \exp(-\frac{u}{kT})$ is the hydrogen diffusion coefficient, $u$ is the hydrogen activation energy, $D_0$ is the diffusion constant and $k$ is the Boltzmann constant.

In the given boundary conditions, the first term of the Fourier expansion for the hydrogen concentration $C$ of the solution of Eq. (5) can be written as

$$C(x, y, z, t) = \frac{C_0\pi^3}{8} \sin\frac{\pi x}{a} \cdot \sin\frac{\pi y}{b} \cdot \sin\frac{\pi z}{l} \cdot f_1(t, u, D_0) \tag{6}$$

where $l, a, b$ are the height and transversal sizes of the sample, respectively. Function $f_1(t, u, D_0)$ is solution of the following equation

$$\begin{array}{l} \dot{f}_1 + D_0 \cdot \exp(-\frac{u}{kT})(\frac{\pi^2}{a^2} + \frac{\pi^2}{b^2} + \frac{\pi^2}{l^2}) f_1 = 0, \\ f_1(0, u, D_0) = 1. \end{array} \tag{7}$$

In tests, the apparatus registers the overall hydrogen flux $q(t)$ thought the sample surface as a time function. According to Fick's law of diffusion we have:

$$q(t) = -\int_S D\frac{dC}{dn} dS, \tag{8}$$

where $S$ is the sample surface.

Inserting Eq. (6) for the hydrogen concentration $C$ in (8) and performing integration yields:

$$q(t) = \pi^2 C_0 abl \cdot \left[\frac{1}{a^2} + \frac{1}{b^2} + \frac{1}{l^2}\right] \cdot D_0 \cdot \exp(-\frac{u}{kT}) \cdot f_1(t, u, D_0). \tag{9}$$

When assuming that hydrogen in the sample is contained in the reversible traps with different binding energies $u_i$, the corresponding diffusion constants $D_{0i}$ and initial hydrogen concentrations $C_{0i}$ we use the superposition principle because of linearity of the diffusion equation (5).

The time dependence of the hydrogen flux $q(t)$ from the sample is defined by the following sum:

$$q(t) = \pi^2 abl \cdot \left[\frac{1}{a^2} + \frac{1}{b^2} + \frac{1}{l^2}\right] \cdot \sum_i C_{0i} \cdot D_{0i} \cdot \exp(-\frac{u_i}{kT}) \cdot f_1(t, u_i, D_{0i}), \tag{10}$$

where $f_1(t, u_i, D_{0i})$ is solution of Eq. (7) for the given values of constants $u_i$, $D_{0i}$, $C_{0i}$ and the sample dimensions $(l, a, b)$.

Comparison of the experimental extraction curve and the calculated curve Eq. 10 for initial concentrations $C_{0i}$ and diffusion constants $u_i$ and $D_{0i}$ yields the activation energy and diffusion constants of hydrogen.

Figure 3 shows the plots of extraction curves measured experimentally and obtained by means of Eq. (10).

Therefore, the extraction curve measured by the hydrogen analyzer AV-1 by means of the vacuum heating method allows one to determine fundamental parameters characterizing the hydrogen state in the solid, namely (i) the energy levels of hydrogen $u_i$, (ii) the hydrogen concentration $C_{0_i}$ in different energy states (populations of energy levels), and (iii) the diffusion constant $D_{0i}$ for hydrogen with binding energy $u_i$.

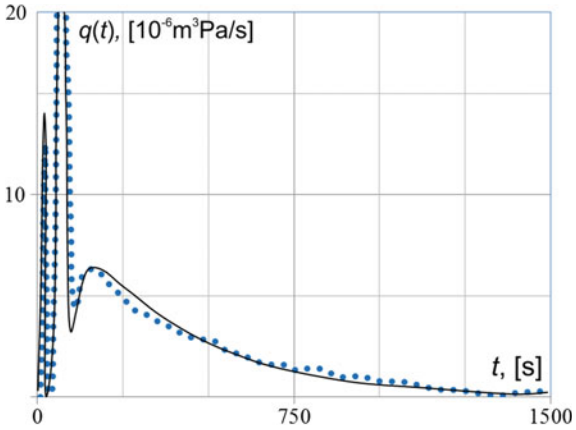

**Fig. 3** Experimental (points) and calculated (solid line) extraction curves with three maxima for the titanium alloy PT7M

## 4 Verification of Main Approximations of Method for Determination of Binding Energies

For experimental testing of reliability of the accepted assumption, the samples of titanium alloy PT7M were prepared. which had shape of parallelepiped with the sizes 2*2*2.5 mm. The samples were parallelepipeds of dimension 2*2*2.5 mm and were cut from a tube of outer diameter of 28 mm.

Six samples were loaded in the extraction system of the hydrogen analyzer AV-1. Testing of each sample was performed at the fixed extraction temperature, beginning with 550 °C and ending by 800 °C. The analytical appendix of extraction system was heated up to the extraction temperature without sample, then the sample was placed into the heated analytical appendix, and the extraction curve was recorded. Each sample was tested only once, i.e. only a part of hydrogen was extracted from the sample at low temperature. The test results are shown in Fig. 4.

Analysis of the extraction curves shows that the hydrogen diffusion from titanium alloy has an activation character. The hydrogen with higher binding energy remains in the sample when the extraction temperatures is under 700 °C.

Provided that the assumption about existence of states with different binding energies $u_i$ and corresponding diffusion constants $D_{0i}$ is valid then the measured extraction curves for other temperatures can be properly described.

Modeling of the process of high-temperature vacuum extraction was performed six times at different extraction temperatures with calculation of the extracted hydrogen flux by means of (10).

The modeling result is shown in Fig. 5. All the calculated extraction curves, obtained at the analysis temperatures of 530 °C, 600 °C, 700 °C, 750 °C, 775 °C, 800 °C, are given in one plot by analogy with the experimental curves presented in Fig. 4.

The obtained modeling results show good agreement with experiment. The modeling assumed diffusion parameters determined by analysis of the experimental

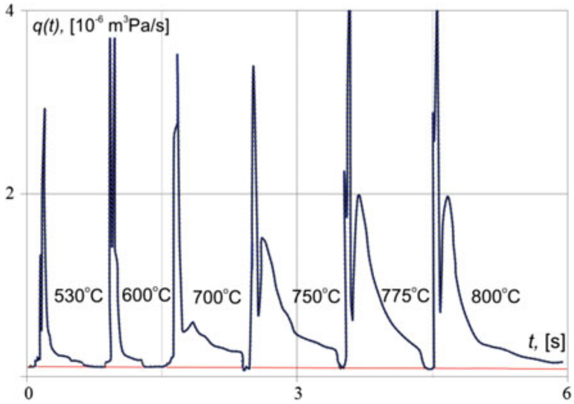

**Fig. 4** Experimental extraction curves for samples of the titanium alloy PT7M obtained at different extraction temperatures

**Fig. 5** Results of modeling of extraction curves for the titanium sample PT7M at different extraction temperatures

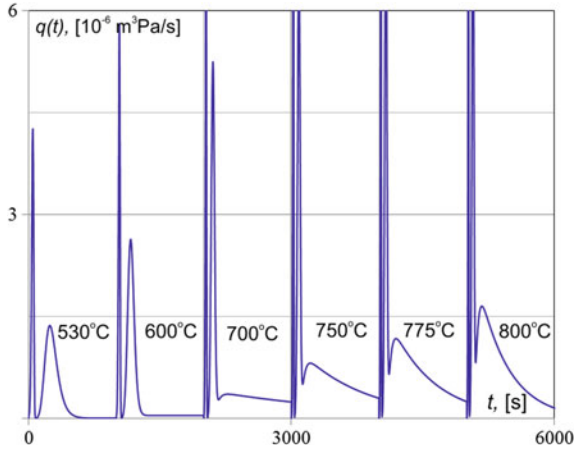

extraction curve obtained at the temperature of 800 °C. It enables us to make extrapolation to lower temperatures without using adjustable parameters and obtain result coinciding with the corresponding experiment.

Thus the proposed model is adequate to the real physical process occurring in realization of the method of high-temperature vacuum extraction of hydrogen from analyzed sample of solid probe.

In the model describing the process of sample heating, only transfer of heat due to radiation was taken into account. Possible sources of uncertainly in determination of activation energy of diffusion are as follows:

(i) non-zeroth thermal conductivity of fused silica,
(ii) uncertainty in used value of the absorption coefficient of heat radiation.

The following experiment was performed to test the proposed model of the sample heating.

Two identical samples of diameter $2a = 8\,\mathrm{mm}$ and length $l = 15\,\mathrm{mm}$ were machined from the same rod of the aluminum alloy AMg6. Before loading in the extractor the first sample was covered by soot obtained in incomplete combustion of acetylene.

The sample heating was minimal due to small time of contact between the sample and the flame of burner containing soot.

The working temperature of the extraction system was 530 °C. The blackened sample was placed in the analytical appendix by a magnetic pusher without spoiling vacuum.

The extractor wall temperature was maintained equal to the working temperature. The cold sample (at room temperature) was heated up to the extraction temperature and then heated at this temperature up to the end of analysis.

A standard sample had small absorption ability which was typical for the aluminum alloy whereas the sample covered by soot had the absorption ability that was practically equal to 1.

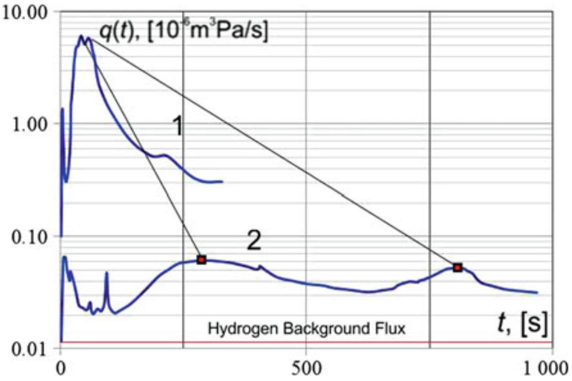

**Fig. 6** Initial part of the extraction curve obtained for the sample of aluminum alloy AMg6 covered with soot (curve 1) and initial part of the extraction curve obtained for the sample of aluminum alloy AMg6 (curve 2). The same peaks are connected by straight lines

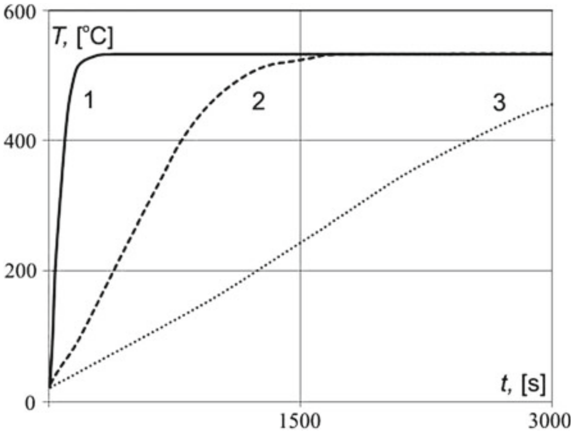

**Fig. 7** Dependence of temperature of analyzed sample on time. Modeling is performed at different values of absorption coefficient: **curve 1 corresponds to the sample is covered with soot** $\varepsilon_t = 1$; **curve 2 corresponds to the sample is prepared according to** [1] $\varepsilon_t = 2 \cdot 10^{-4} \cdot (T + 64, 3)$; **curve 3 is obtained for pure polished aluminum** $\varepsilon_t = 7 \cdot 10^{-5} \cdot (T + 64, 3)$

The extraction curves for blackened and standard samples were measured. They are shown in Fig. 6. It is established that the sample covered by soot was heated about 20 times faster. If one suppose that the hydrogen diffusion has activating character then the extractor curve can provide information on the rate of sample heating.

The first peak on the extraction curve is associated with absorption of the "surface" hydrogen from the sample. The maximum position corresponds to the sample temperature 100–150 °C.

Equation (4) was used for modeling dynamics of sample heating. The absorption coefficient was taken to be 1 for the sample covered by soot. Figure 7 shows results of modeling dependence of the sample temperature on time.

Curve 1 corresponds to the sample covered by soot. Curve 3 is obtained for pure polished aluminum, and curve 2 corresponds to the sample of aluminum alloy AMg6 prepared according to the requirements of [1]. The absorption coefficient of the sample corresponds to the experimental curve presented in Fig. 6.

Analysis of the presented results of modeling dynamics of the sample heating allows us to make conclusion that the real absorption coefficient for aluminum alloys is higher than that for pure polished aluminum presented in literature. Probably this is caused by existence of alloying and quality of treatment of the sample surface. The performed experiments show that the real absorption coefficient can be determined for each alloy.

The above technology of comparative analysis of the hydrogen amount in the samples with regulated absorption coefficient allows more precise determination of temporal dependence of the sample temperature during the process of analysis.

Other methods for determination of sample temperature in vacuum either distort considerably results of the analysis or have low accuracy.

Fastening of a thermocouple on the sample in vacuum makes experiment and extraction system very cumbersome. At $T = 500$–$600\,^{\circ}\mathrm{C}$ it is necessary to isolate the thermocouple conductors by special materials: the insulators themselves and thermocouple materials can contain hydrogen, that will give rise to essential distortion of the analysis result of, especially in determination of small hydrogen concentrations. Fastening the thermocouple is possible only by its pressing in a cavity or in the sample orifice, that results in considerable plastic deformation of material, even at the sample masses of about 2–5 g.

Mounting of the thermocouple on a special pedestal or melting pot leads to the fact that material of the pedestal itself or melting pot can distort considerably the analysis results. The use of pyrometers for determination of the sample temperature does not provide the necessary accuracy in conditions of large hitch created by heat radiation of the furnace. Moreover, at $T < 500\,^{\circ}\mathrm{C}$ the pyrometry has uncertainty higher than $\pm 50\,^{\circ}\mathrm{C}$.

Therefore the proposed experimental procedure for determining time dependence of the sample temperature in realization of the method of high temperature vacuum-extraction of hydrogen allows one to obtain reliable data on the value of absorption ability of the sample surface and to get adequate results in approximation of the extraction curves for determination of binding energies $u_i$ and the diffusion constants $D_{0i}$ for hydrogen in various materials.

## 5 Multichannel Diffusion Versus TDS Model

The study of the binding energy of hydrogen carried out by TDS method in Ref. [31] has a significant drawback. The hydrogen activation energy is changed twofold when the tempering temperature changes in 100 °C only. It is difficult to assume that the physical nature of dislocations or the lattice structure is changing so drastically that the binding energy changes twofold. In addition to this, only one peak is observed in TDS, cf. [31]. Hence, the structure of the material changes completely, so that there no longer exist the old type traps for hydrogen in the metal tempered at higher temperatures. Similar discrepancies are observed in other publications where the study was carried out by using the TDS method. For example, in Ref. [50] the binding energy of hydrogen dislocations was specified as 24.1–29.9 kJ/mol and the binding energy of the grain boundaries was shown to lie in the range from 26 kJ/mol to

**Fig. 8** Extraction curves for samples M400 and M520 at the extraction temperature of 900 °C

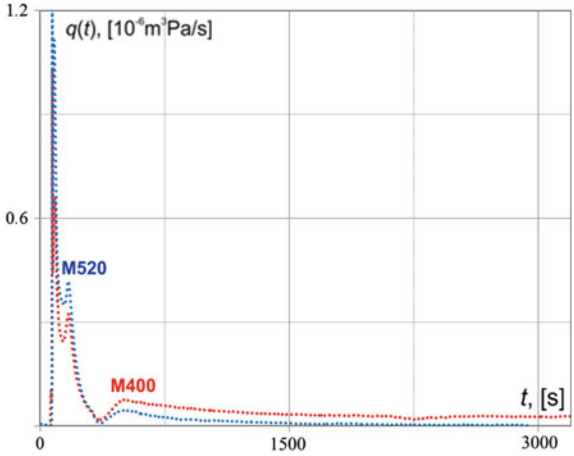

**Fig. 9** Extraction curves for samples M400 and M520 at the extraction temperature of 400 °C

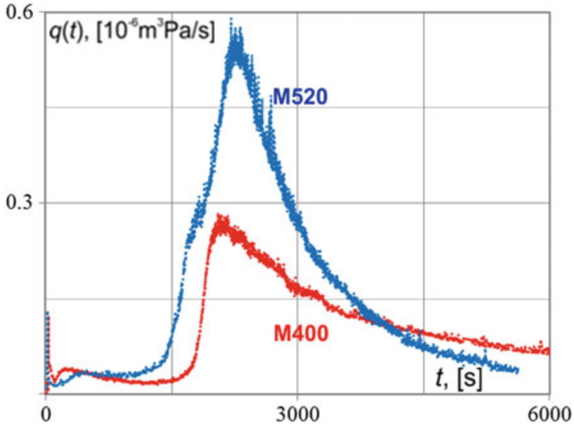

53.1–58.9 kJ/mol. The ranges of the binding energy of hydrogen traps of different nature are overlapping and it greatly reduces the practical value of the TDS method.

We took the samples M400 (tempered at 400 °C) studied in [31] as well as M520 (tempered at 520 °C) and applied different types of hydrogen analysis in order to critically discuss and develop the results of Ref. [31].

The samples M400 and M520 were tested at extraction temperatures of 400–900 °C with steps of 100 °C and cooled after complete degassing at each temperature step. A set of extraction curves at different extraction temperatures was obtained and shown in Figs. 8 and 9 for 900 and 400 °C.

These extraction curves demonstrate the same energy spectrum of bound hydrogen in samples M400 and M520. This fact has a physical reason. At temperature 400 °C the main peak of extraction curve is well approximated by the multichannel diffusion model.

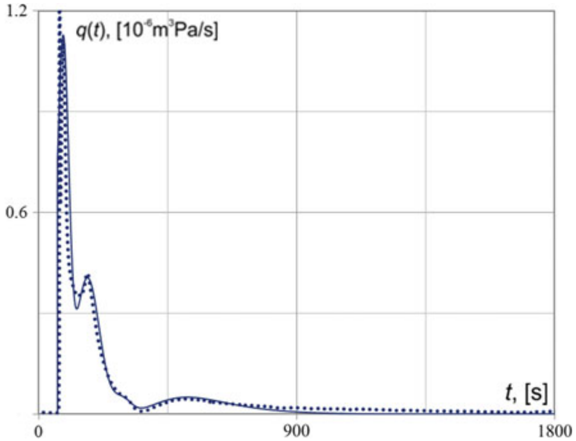

**Fig. 10** Extraction curves for sample M520 for the extraction temperature 900 °C. solid line - multichannel model, points - experiment

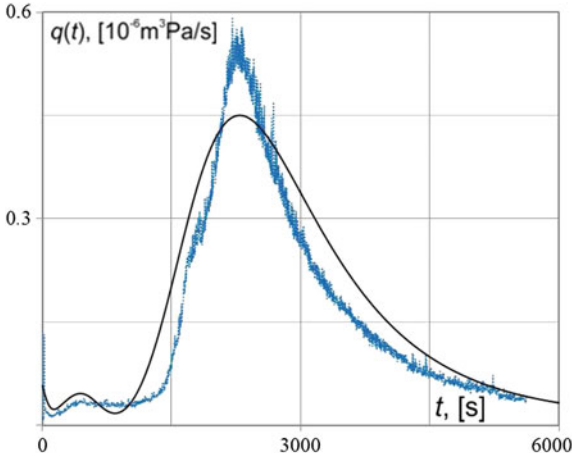

**Fig. 11** Extraction curves for sample M520 for the extraction temperature 400 °C. solid line - multichannel model, points - experiment

The results of this approximation are shown in Fig. 10 for the extraction temperature 900 °C and in Fig. 11 for the extraction temperature 400 °C.

The presence of small pulses indicates the great influence of the surface hydrogen which is associated with microdefects on the sample surface after lathe treatment (it will be discussed in what follows). The difference in extraction curves in Fig. 11 is most likely due to the different properties of the sample surface and presents a shortcoming of the method. At low temperatures of about 400 °C the effect of surface processes can be considerable for the hydrogen extraction. These processes are not described by the diffusion mechanism. It should be mentioned that TDS method is principally not appropriate for correct interpretation of the surface processes since it aggregates them with the processes of internal desorption and hydrogen diffusion.

The total hydrogen content in sample M400 is 0.22 ppm and in sample M520 is 0.27 ppm. The overall spectra of the hydrogen binding energy are given in Table 1.

**Table 1** Values of the hydrogen binding energy in 34CrNiMo6

| # Hydrogen binding energy | |
|---|---|
| | kJ/mol |
| 1 | 14.5 |
| 2 | 27.3 |
| 3 | 77.6 |
| 4 | 102 |

Practically the entire difference in the initial concentration corresponds to the hydrogen binding energy with the levels lower than 80 kJ/mol.

The binding energies with level 14.5 kJ/mol and 27.3 kJ/mol agree very well with the known data on the binding energies of hydrogen in steels [3, 63].

The initial hydrogen concentrations in both samples is small, however it was determined experimentally that the higher level of initial concentration leads to lower susceptibility to hydrogen embrittlement [31]. This fact is very well known and is related to irreversible traps with activation energies higher than 60 kJ/mol [41], which make the difference between the initial hydrogen concentrations in the samples M400 and M520. The initial volume of the irreversible traps in M520 is higher than in M400 and these traps lead to a greater resistance to hydrogen embrittlement.

Thus, it appears that the smaller initial volume of the traps with a binding energy of about 80 kJ/mol leads to greater sensitivity of mechanical properties of steels to hydrogen. It should be noted that this result is difficult to obtain when the samples are saturated by hydrogen because it occurs at the expense of other types of traps; in this case we would obtain the opposite effect, namely the more hydrogen with low binding energy (10–40 kJ/mol) the higher degradation of mechanical properties. Thus, the proposed approach allows us to obtain unique information about the initial state of the material and predict its interaction with hydrogen at saturation.

The role of hydrogen embrittlement is correlated with the high-energy traps. The energy range of 100 kJ/mol is too high to see a significant change in the state of these traps in a short time. Therefore, the outside saturation of the samples which is carried out at TDS measurements is not appropriate for filling these traps uniformly. This level of binding energy of hydrogen was not found out during the investigation by TDS [31]. This is explained by the fact that hydrogen absorption for 30 min is not sufficient to saturate this type of traps and the natural concentrations turn out to be too low (0.04 ppm). As a result, hydrogen saturation results in non-uniform volume distribution of the hydrogen, namely the low energy hydrogen is distributed more uniformly (at high concentrations) in the sample whereas the hydrogen with high binding energy saturates only a thin surface layer.

In the classical TDS analysis the hydrogen diffusion and the volume distribution of hydrogen are not considered at all. Therefore, the traps with high binding energy which are close to the sample surface do not exhibit any separate peak however these traps significantly displace the hydrogen peaks with low binding energy towards those with higher energies.

These traps may have a strong covalent bond to hydrogen atoms which could be addressed to sulfur and its compounds [18, 24]. Such covalent bonds accompanied by complex chemical compounds of sulfur and hydrogen have minor influence on the mechanical properties of the metal, however the chemical resistance to corrosion is reduced due to the presence of sulfur.

The difference between the TDS and VHE methods is primarily concerned with the hydrogen saturation which is necessary for TDS. This saturation does not allow detecting traps with a small capacity limit which can play a role in other types of exposure. The application of VHE however allows gaining additional information about the hydrogen trapping.

It is justified in Refs. [21, 23] for iron that it is dislocations which are the main traps with low energy in the annealed state. However, as pointed out in [21] this is true for iron with a purity higher than 99.99%.

This issue requires further study for several reasons:

1. The model of hydrogen extraction from samples under the TDS process was first reported in [28] however the diffusion of hydrogen in samples was ignored there. Adequate results can only be obtained for thin films. In all other cases a slow heating is used to reduce the influence of the hydrogen diffusion. The increase in the temperature rate causes increasing error. To determine the binding energy it is necessary to use at least three rates of warm-up. The diffusion shifts the spectrum peaks toward greater binding energy under a faster heating.
2. Account for diffusion for TDS method carried out in [42, 43] did not allow one to avoid saturation of samples with hydrogen. This account was performed for only one type of steel and cannot be considered as a well established approach.
3. Slow heating at TDS can take dozens of hours, and one must have measured the hydrogen flux from the sample during this time interval. As a result, the TDS method does not work without special hydrogen saturation. In fact, one measures the distribution of hydrogen traps that can be filled relatively quickly when exposed to the electrolyte or gaseous hydrogen rather than the hydrogen distribution over the binding energies in the sample. Saturation of hydrogen leads not only to a structural change in the spectra of natural hydrogen but also to a substantial change in the mechanical properties of metal itself. Reference [54] reports the cases of twinning and hence the increase in the traps' volume at hydrogen saturation. Saturating carbon steels with external hydrogen leads to appearance of methane which not only causes the formation of microvoids and cracking (changes in the steel structure) but also absorbs the dissolved hydrogen and changes its energy spectrum, cf. [53].
4. Physical methods of investigation of dislocations and other mechanical imperfections of the crystal structure does not always give a clear quantitative result. For example, Ref. [59] reports that the dislocation density of the specimens was measured by X-ray diffractometry after tensile testing in a hydrogen atmosphere. It was found that all the hydrogen absorbed by high-strength low-alloy steel samples is accumulated in dislocations. This conclusion is based on the method of Ref. [64] which measures the amount of dislocations. However, X-ray diffrac-

tometry is known to measure the strains. Reference [64] suggests a formula for determining the dislocation density according to X-ray diffractometry on the basis of unsubstantiated assumption that the overall deformation of the sample is caused by dislocations only.

5. All these factors lead to the fact that the levels of binding energies of hydrogen traps of the same nature deviate considerably. E.g., for steels the binding energy of hydrogen dislocations lies in the range of 26–35 kJ/mol [45], 20–30 kJ/mol [13], 20–60 kJ/mol [22].

Thus, applying the technique of [48] and VHE on the same samples, we were able to determine more energy levels for bound hydrogen than by using TDS [31]. We estimated filling of each energy level or each type of traps by natural hydrogen which was inside the metal when it was processed. The absence of procedure of the hydrogen charging allowed us to keep the original natural structure of samples. The results show that change in the trap volume with binding energy 77.6 kJ/mol occurs at different annealing temperatures. The physical nature of these traps requires additional investigation, however we can use the mechanical models [6, 9, 58] for predicting material properties.

## 6 Discussion of Results

No assumption about parameters of samples was made while determining the binding energy by the method of thermo-desorption spectra. The algorithm for determining the binding energies seems independent and objective. Such independence is not always confirmed by experiments. In Ref. [42] the shape and sizes of samples were taken into account and it changed essentially the data on binding energies. Study [3] of a special sort of steels showed large spread of values of diffusion parameters. Additionally the values of activation energy $u_i$ and diffusion constant $D_{0i}$ were strongly dependent of the sample sizes (also observed in Ref. [42]).

The TDS method is based on the hypothesis which states that there exists only one channel for hydrogen diffusion in a solid and traps are uniformly distributed in the sample. Hydrogen is accumulated in these traps. Physical considerations that diffusion is only model for the process of statistically equilibrium variation of states of atoms and molecules are not taken into account. The equations for hydrogen diffusion and amount of hydrogen in traps are different. Let us study contradictions of the approach on example of a thin sample.

Let us consider the case in which the hydrogen is contained in traps of several types (with different binding energies or activation energies). After escaping from the traps hydrogen passes to the diffusion-mobile state with binding energy $u_0$. In this state the hydrogen diffusion is possible in a thin layer of thickness $l$ in direction of $Ox$ axis.

The equation for deallocation of hydrogen from traps with binding energy $u_i$ has the standard form:

$$\begin{array}{l} \frac{dw_i}{dt} = -D_i w_i \\ w_i(0) = w_{i0} \end{array} \tag{11}$$

where $w_i(t)$ is the hydrogen concentration in the trap, $D_i = D_{0i}e^{-\frac{u_i}{kT(t)}}$ is the rate of trap deallocation, $D_{0i}$ is the trap deallocation constant analogous to the diffusion constant, $k$ is Boltzmann's constant, $T(t)$ is the layer's temperature which is time dependent. Let us assume that the distribution of traps over the layer's volume is not uniform, that is, $w_i\ (t, x) = w_i\ (t) \sin(\frac{\pi x}{l})$.

The solution of Eq. (11):

$$w_i(t) = w_{i0} \exp(-\int_0^t D_i(\theta)\, d\theta).$$

The diffusion equation is written as

$$\begin{array}{l} \frac{\partial w}{\partial t} = D\frac{d^2 w}{dx^2} - \sum_i \frac{dw_i}{dt}, \\ w(t, 0) = w(t, l) = 0 \\ w(0, x) = w_0 \sin(\frac{\pi x}{l}) \end{array} \tag{12}$$

Here $D = D_0 e^{-\frac{u_0}{kT(t)}}$ is the diffusion coefficient, $w$ is the mass concentration of hydrogen in the layer, the source terms describing the flux of hydrogen from traps inside the layer. Using (11) we can rewrite the diffusion equation in the form:

$$\frac{\partial w}{\partial t} = D\frac{d^2 w}{dx^2} + \sum_i D_i w_i, \tag{13}$$

The substitution $\tau = \int D(t)dt$ yields

$$\begin{array}{l} \frac{\partial w}{\partial \tau} = \frac{d^2 w}{dx^2} + \sum_i \frac{D_i}{D} w_i, \\ w(\tau, 0) = w(\tau, l) = 0 \\ w(0, x) = w_0 \sin(\frac{\pi x}{l}) \end{array} \tag{14}$$

General solution of the homogeneous differential equation is written as

$$w(\tau, x) = w_0 \sin(\frac{\pi x}{l}) \exp(-\frac{\pi^2}{l^2}\tau), \tag{15}$$

Solution to the homogeneous differential equation is given by

$$\begin{aligned} w(t, x) = w_0 \exp\left(-\frac{\pi^2}{l^2}\tau(t)\right) \cdot \sin(\frac{\pi x}{l}) + \\ + \int_0^{\tau(t)} \exp\left(-\frac{\pi^2(\tau(t) - \theta)}{l^2}\right) \sum_j \frac{D_j(\theta)}{D(\theta)} w_j(\theta) d\theta \cdot \sin(\frac{\pi x}{l}) \end{aligned} \tag{16}$$

The first important conclusion is that the ratios $\frac{D_j(\theta)}{D(\theta)} = \frac{D_{0j}}{D_0} \exp\left(-\frac{u_j - u_0}{kT(\theta)}\right)$ are involved in the convolution integral in (16). It is possible to consider hydrogen tending to diffusion of molecules located in a trap with binding energy $u_0$, and liberation of hydrogen from traps as a transition from the energy level $u_j$ to the energy level $u_0$ accompanied by the energy loss $(u_j - u_0)$.

Let us now rewrite the time-dependent factor in (16) after inserting the solution for mass concentrations $w_j$:

$$\begin{aligned} w_t(t) = w_0 \exp\left(-\frac{\pi^2}{l^2}\int_0^t D(\theta)d\theta\right) + \\ + \int_0^{\int_0^t D(\theta)d\theta} \exp\left(-\frac{\pi^2(\int_0^t D(\theta)d\theta - \theta)}{l^2}\right) \times \\ \times \sum_j \left[\frac{D_j(\theta)}{D(\theta)} w_{j0} \exp\left(-\int_0^\theta D_i(\sigma)\,d\sigma\right)\right] d\theta \end{aligned} \tag{17}$$

and consider the case of very thin layer. Then Eq. (11) can be written as:

$$\begin{aligned} w_t(t) \approx w_0 \exp\left(-\frac{\pi^2}{l^2}\int_0^t D(\theta)d\theta\right) + \\ + \frac{l^2}{\pi^2}\sum_j \left[\frac{D_j(\int_0^t D(\theta)d\theta)}{D(\int_0^t D(\theta)d\theta)} w_{j0} \exp\left(-\int_0^{\int_0^t D(\theta)d\theta} D_i(\sigma)\,d\sigma)\right)\right] \end{aligned} \tag{18}$$

There is a principal difference between exponents of the first and second components of the sum (18). In the first term, the exponent is multiplied by the scaling factor $\frac{\pi^2}{l^2}$, and this is not the case in the second term. Consequently, the diffusion from traps practically does not depend on the layer thickness which contradicts the experimental data.

In experiments with films of 7–10 μm thick, the duration of hydrogen peaks on the extraction curve is 7–10 min.

Attempts for modeling fluxes of "natural" hydrogen from samples with thickness of 10 μm using the model of "one-channel" diffusion lead to the fact that the activation energy of the diffusion channel itself has reasonable values, 0.2–0.4 eV, and binding energies in traps yield additional several hundredths eV. Thus the thermal motion energy at room temperature is sufficient for effective emptying of traps.

On the contrary, the multichannel model yields the difference between activation energies of different channels in the range 0.4–1.0 eV.

Therefore the experimental data, physical arguments and relevant mathematical modeling show that the multichannel model of hydrogen diffusion gives more accurate description of experimental results.

There is an additional source of errors of the TDS method. It consists in existence of background fluxes of hydrogen from the extraction system, which depends on the

**Table 2** The activation energies of the hydrogen determined for titanium alloys using different models: a multi-channel diffusion (PT7M alloy) and the classical method TDS [28]

| # | PT7M ($\alpha$+$\beta$ alloy) | Ti–6Al–4V ($\alpha$+$\beta$ alloy) [14] | $\beta$ -21S ($\beta$ alloy) [15] | $\beta$ -21S ($\beta$ alloy) [16] | Ti–6.8Mo–4.5Fe–1.5Al ($\beta$ alloy) [4] |
|---|---|---|---|---|---|
| | eV | eV | eV | eV | eV |
| 1 | 0.4 | $(1.04 - 1.29)^{a,b}$ | 0.12 | $1.15^{a,c}$ | $(0.49 - 0.66)^{a,d}$ |
| 2 | 0.8 | | 0.280 | | |
| 3 | 1.4 | | 1.06 | | |

[a] only one peak TDS was observed

[b] depends on the method of the hydrogen introducing into the alloy

[c] after hydrogen introduced by GTAW welding in a mixed Ar + 5% $H_2$ shield

[d] depends on the hydrogen saturation time

sample's temperature. The temperature of surrounding parts of the extraction system increases with the sample heating. In some cases the background flux of hydrogen increases by several hundred times in the course of TDS measurement, Ref. [39].

Table 2 shows the comparison the activation energies for the different channels of hydrogen diffusion in the titanium alloy PT7M and the hydrogen desorption activation energies obtained by the TDS.

Preliminary saturation of samples with hydrogen widely used in the TDS method allows one to reduce the influence of background fluxes. To estimate their influence in measuring natural concentrations of hydrogen, an experiment was performed on stepwise changing temperature of the extraction system of hydrogen analyzer AV-1. Figure 12 shows the extraction curve for the aluminum alloy sample with mass of 2g and hydrogen concentration of 0.2 ppm arising in the stepwise heating of the

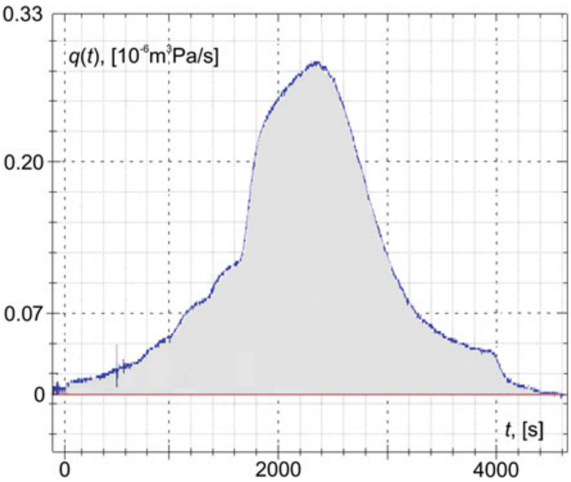

**Fig. 12** The extraction curve for the background fluxes arising in the stepwise heating of the extraction system with the aluminum alloy sample with mass of 2g and hydrogen concentration of 0.2 ppm up to 700 °C

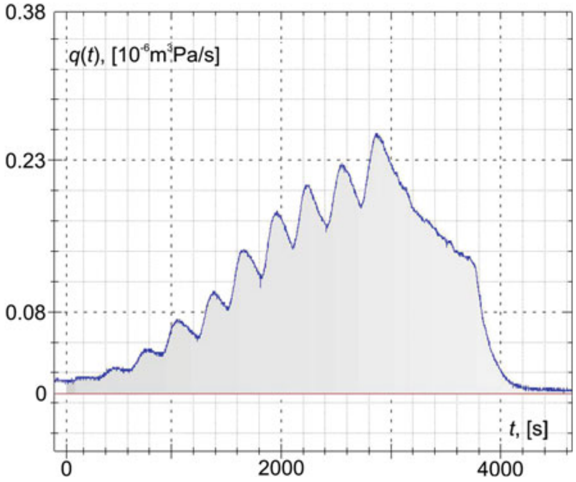

**Fig. 13** The extraction curve for the background fluxes arising in the stepwise heating of the void extraction system up to 700 °C

extraction system up to 700 °C. Figure 13 shows background fluxes arising in the stepwise heating of the void extraction system up to 700 °C.

The hydrogen flux from the wall of extraction system coincides with the flux from sample, as seen from Figs. 12 and 13. Thus, the heating of the extraction system during TDS can cause error in determining the hydrogen binding energy.

Prehydrogenated samples are typically applied for TDS method. During preliminary saturation, we obtain a new hydrogen-material system whose properties can differ from those of the original material (see Tables 1, 2). Increasing of hydrogen concentration is known to lead to changing the material properties. For example, casting of aluminum alloys is cracked in the process of crystallization for double hydrogen concentration compared with the natural one. As shown in Ref. [40] for steels, the saturation of material with hydrogen gives rise to decreasing tensile strength up to 3–5 times. The strong side of our approach is the possibility of measuring the hydrogen binding energy without special hydrogenation of samples.

The mass-spectrometric hydrogen analyzer AV-1 measures the instantaneous hydrogen flux from the sample. As shown in Fig. 9, the extraction curves exhibit a plurality of small peaks which are not observed under the higher temperature extraction, Fig. 8. The volume of molecular hydrogen that corresponds to these peaks is approximately $10^{-8}$–$10^{-9}$ mm$^3$. The average grain size in the samples is 50 μm. Thus, each small peak can correspond to a single microcrack or dislocation at the sample surface. According to [35] the grain size affects the hydrogen content. Assuming that the surface dislocations and micro-cracks are of the order of grain size, the volume of small hydrogen peaks corresponds to the volume of single dislocation.

This hypothesis has been verified. Experiments on the distribution of hydrogen diffusion over some specially created lattice defects in silicon monocrystal were carried out by authors of the present paper. The idea was to create some monocrystal internal defects of the size of about 30 μm and compare the results of high-temperature vacuum extraction of hydrogen of the original monocrystal and the monocrystal with the artificially produced defects. An infrared pulse laser with a wavelength of 1024 nanometers was used for creating defects. The duration of the laser pulse was 12 nanoseconds and the energy of one pulse was 2 mJ. Such a laser is usually used for creating chips in optical glass. The coherent infrared radiation of a pulse is focused on a certain point in the glass. The size of focused spot is about 30μm. The energy density in the focus is ca. $2 \cdot 10^{15}$ W/m$^2$. Such energy density can heat up the substance to ca. 1500 °K depending on the coefficient of radiation absorption. In the heat affected zone one can observe a visible chip. The monocrystal silicon plates of the thickness of 0.3 mm were tested. The plates were placed in a parallelepiped made of optical glass. Some other plates (not radiated by the laser) and the plate with the chips on the surface were cut in prismatic samples of the size 8 mm × 15 mm × 0.3 mm. They were placed in vacuum for carrying out experiments on the hydrogen diffusion. After extraction of the hydrogen with lower binding energy the gas accumulated in the surface defects starts moving and this effect is recorded as a noise which in turn results in the noise in the form of a number of small peaks. These peaks are due to the emission of hydrogen from silicon. For the regular holes these peaks become regularised and increase their sizes, that is, the volume of the extracted hydrogen increases as well. The observed effect can be interpreted as a regularisation of the diffusion caused by a uniform grid of chips on the surface of the sample. So the hypothesis verification gives us an opportunity to determine the approximate number of surface microdefects and their average size with the help of the hydrogen analyzer.

Summarizing, the extraction curve shows a lot of noise during constant hydrogen charging and discharging of surface dislocations and micro-cracks. This may indicate that in the investigated steel the main traps are released at a temperature of 400 °C.

## 7 Conclusions

This study shows that by using the experimental technique of high temperature vacuum extraction the model of multichannel diffusion gives a more precise description of the real hydrogen diffusion in solids than other approaches.

Application of the method of high temperature vacuum extraction with mass-spectrometric measuring of instant values of the hydrogen flux allows recording small natural hydrogen concentrations and the concentration distribution over the activation energy.

There is no need of preliminary saturation of samples by hydrogen in tests. High sensitivity of analysis using AV-1 makes it possible to trace evolution of natural hydrogen in samples under different thermo-mechanical and physical-chemical effects.

Application of the vacuum hot extraction analysis enbles detecting new energy levels, namely at 77.6 kJ/mol and 102 kJ/mol, related to strong covalent bonds.

The increased hydrogen embrittlement resistance at 520 °C tempering condition can be explained by its higher capacity of irreversible hydrogen.

In contrast to TDS our study does not require pre-saturation of samples by hydrogen. This does keep the original structure of samples and ensures that all types of traps are present in both M400 and M520 samples. Their binding energy does not change, however the total amount of traps depends on the annealing temperature. It was not possible to draw this obvious conclusion from TDS data since TDS provides the researcher with a single binding energy.

The proposed method based on Vacuum Hot Extraction allows one to obtain adequate data on the binding energies and hydrogen concentration. Additional research is required to determine the nature of these traps.

**Acknowledgements** The research is carried out under the financial support by Russian Science Foundation, grant 18-19-00160.

## References

1. Aluminum and aluminum alloys. Methods for determination of hydrogen in solid metal by vacuum heating (in Russian). GOST (State Standard) 21132.198. Izdatelstvo Standartov, Moscow (2000)
2. Anderl, R., Causey, R., Davis, J., Doerner, R., Federici, G., Haasz, A., Longhurst, G., Wampler, W., Wilson, K.: Hydrogen isotope retention in beryllium for tokamak plasma-facing applications. J. Nucl. Mater. **273**(1), 1–26 (1999)
3. Asahi, H., Hirakami, D., Yamasaki, S.: Hydrogen trapping behavior in vanadium-added steel. ISIJ Int. **43**(4), 527–533 (2003)
4. Barel, E., Hamu, G.B., Eliezer, D., Wagner, L.: The effect of heat treatment and HCF performance on hydrogen trapping mechanism in timetal LCB alloy. J. Alloy. Compd. **468**(12), 77–86 (2009)
5. Belyaev, A., Polyanskiy, A., Polyanskiy, V., Yakovlev, Y.: Parametric instability in cyclic loading as the cause of fracture of hydrogenous materials. Mech. Solids **47**(5), 533–537 (2012)
6. Belyaev, A.K., Kudinova, N.R., Polyanskiy, V.A., Yakovlev, Y.A.: The description of deformation and destruction of materials containing hydrogen by means of rheological model. St. Petersburg Polytech. Univ. J. Phys. Math. **1**(3), 305–314 (2015)
7. Belyaev, A.K., Polyanskiy, V.A., Yakovlev, Y.A.: Stresses in a pipeline affected by hydrogen. Acta Mech. **223**(8), 1611–1619 (2012)
8. Belyaev, A.K., Polyanskiy, V.A., Yakovlev, Y.A.: Hydrogen as an indicator of high-cycle fatigue. Procedia IUTAM **13**, 138–143 (2015). Dynamical Analysis of multibody systems with design uncertainties
9. Belyaev, A.K., Polyanskiy, V.A., Yakovlev, Y.A.: Rheological model of materials with defects containing hydrogen. Key Eng. Mater. **651–653**, 604–609 (2015)
10. Causey, R.A.: Hydrogen isotope retention and recycling in fusion reactor plasma-facing components. J. Nucl. Mater. **300**(23), 91–117 (2002)
11. Depover, T., Monbaliu, O., Wallaert, E., Verbeken, K.: Effect of Ti, Mo and Cr based precipitates on the hydrogen trapping and embrittlement of Fe–C–X Q&T alloys. Int. J. Hydrog. Energy **40**(47), 16977–16984 (2015). Special issue on 1st international conference on hydrogen storage, embrittlement and applications (Hy-SEA 2014), Rio de Janeiro, Brazil, 26–30 October 2014
12. Dmytrakh, I., Smiyan, O., Syrotyuk, A., Bilyy, O.: Relationship between fatigue crack growth behaviour and local hydrogen concentration near crack tip in pipeline steel. Int. J. Fatigue **50**(0), 26–32 (2013). Recent progress in the understanding of fatigue crack propagation

13. Doshida, T., Takai, K.: Dependence of hydrogen-induced lattice defects and hydrogen embrittlement of cold-drawn pearlitic steels on hydrogen trap state, temperature, strain rate and hydrogen content. Acta Mater. **79**, 93–107 (2014)
14. Eliezer, D., Tal-Gutelmacher, E., Cross, C., Boellinghaus, T.: Hydrogen absorption and desorption in a duplex-annealed TI6AL4V alloy during exposure to different hydrogen-containing environments. Mater. Sci. Eng. A **433**(12), 298–304 (2006)
15. Eliezer, D., Tal-Gutelmacher, E., Cross, C., Boellinghaus, T.: Hydrogen trapping in $\beta$-21s titanium alloy. Mater. Sci. Eng. A **421**(12), 200–207 (2006). Internal stress and thermo-mechanical behavior in multi-component materials systems, TMS Annual Meeting (2004)
16. Eliezer, D., Tal-Gutelmacher, E., Cross, C., Boellinghaus, T.: Irreversible hydrogen trapping in welded beta-21s titanium alloy. In: Gdoutos, E. (ed.) Fracture of Nano and Engineering Materials and Structures, pp. 985–986. Springer, Netherlands (2006)
17. Garcia, D.C.S., Carvalho, R.N., Lins, V.F.C., Rezende, D.M., Santos, D.S.D.: Influence of microstructure in the hydrogen permeation in martensitic-ferritic stainless steel. Int. J. Hydrog. Energy **40**(47), 17102–17109 (2015). Special issue on 1st international conference on hydrogen storage, embrittlement and applications (Hy-SEA 2014), Rio de Janeiro, Brazil, 26–30 October 2014
18. Garet, M., Brass, A.M., Haut, C., Guttierez-Solana, F.: Hydrogen trapping on non metallic inclusions in Cr-Mo low alloy steels. Corros. Sci. **40**(7), 1073–1086 (1998)
19. Gorsky, W.: Theorie der elastischen nachwirkung in ungeordneten mischkristallen (elastische nachwirkung zweiter art.). Physikalische Zeitschrift der Sowjetunion **8**, 457–471 (1935)
20. Gorsky, W.: Theorie der elastischen nachwirkung in ungeordneten mischkristallen von cuau. Physikalische Zeitschrift der Sowjetunion **8**, 443–456 (1935)
21. Hagi, H.: Diffusion coefficient of hydrogen in iron without trapping by dislocations and impurities. Mater. Trans. JIM **35**(2), 112–117 (1994)
22. Hagi, H., Hayashi, Y.: Effect of dislocation trapping on hydrogen and deuterium diffusion in iron. Trans. Jpn. Inst. Metals **28**(5), 368–374 (1987)
23. Hirth, J.: Effects of hydrogen on the properties of iron and steel. Metall. Trans. A **11**(6), 861–890 (1980)
24. Hno, M.: Influence of sulfur content on the hydrogen-induced fracture in linepipe steels. Metall. Trans. A **10**(11), 1691–1698 (1979)
25. Hodille, E.A., Begrambekov, L.B., Pascal, J.Y., Saidi, O., Layet, J.M., Pegourie, B., Grisolia, C.: Hydrogen trapping in carbon film: from laboratories studies to tokamak applications. Int. J. Hydrog. Energy **39**(35), 20054–20061 (2014)
26. Hultquist, G., Graham, M.J., Smialek, J.L., Jonsson, B.: Hydrogen in metals studied by thermal desorption spectroscopy (TDS). Corros. Sci. **93**, 324–326 (2015)
27. Kimura, Y., Sakai, Y., Hara, T., Belyakov, A., Tsuzaki, K.: Hydrogen induced delayed fracture of ultrafine grained 0.6 with dispersed oxide particles. Scr. Mater. **49**(11), 1111–1116 (2003)
28. Kissinger, H.E.: Reaction kinetics in differential thermal analysis. Anal. Chem. **29**(11), 1702–1706 (1957)
29. Konar, J., Banerjee, N.: Vacuum heating hydrogen determination in aluminium and aluminium alloys. NML Tech. J. **16**(1–2), 18–19 (1974)
30. Konopel'ko, L.A., Polyanskii, A.M., Polyanskii, V.A., Yakovlev, Y.A.: New metrological support for measurements of the concentration of hydrogen in solid samples. Meas. Tech. **60**(12), 1222–1227 (2018)
31. Kuduzovic, A., Poletti, M.C., Sommitsch, C., Domankova, M., Mitsche, S., Kienreich, R.: Investigations into the delayed fracture susceptibility of 34crnimo6 steel, and the opportunities for its application in ultra-high-strength bolts and fasteners. Mater. Sci. Eng. A **590**, 66–73 (2014)
32. Leeuwen, H.V.: The kinetics of hydrogen embrittlement: a quantitative diffusion model. Eng. Fract. Mech. **6**(1), 141–161 (1974)
33. Legrand, E., Oudriss, A., Savall, C., Bouhattate, J., Feaugas, X.: Towards a better understanding of hydrogen measurements obtained by thermal desorption spectroscopy using FEM modeling. Int. J. Hydrog. Energy **40**(6), 2871–2881 (2015)

34. Liu, Y., Wang, M., Liu, G.: Hydrogen trapping in high strength martensitic steel after austenitized at different temperatures. Int. J. Hydrog. Energy **38**(33), 14364–14368 (2013)
35. Martinez-Madrid, M., Chan, S.L.I., Charles, J.A., Lopez, J.A., Castano, V.: Effect of grain size and second phase particles on the hydrogen occlusivity of iron and steels. Mater. Res. Innov. **3**(5), 263–270 (2000)
36. Matsuo, T., Yamabe, J., Matsuoka, S.: Effects of hydrogen on tensile properties and fracture surface morphologies of type 316L stainless steel. Int. J. Hydrog. Energy **39**(7), 3542–3551 (2014)
37. Mohtadi-Bonab, M., Szpunar, J., Razavi-Tousi, S.: A comparative study of hydrogen induced cracking behavior in API 5l X60 and X70 pipeline steels. Eng. Fail. Anal. **33**, 163–175 (2013)
38. Neklyudov, I.M., Morozov, O.M., Kulish, V.G., Zhurba, V.I., Khaimovich, P.A., Galitskiy, A.G.: Hydrogen diagnostics of structural states 18Cr10NiTi steel. Int. J. Hydrog. Energy **36**(1), 1192–1195 (2011). 11th International conference: hydrogen materials science and chemistry of carbon nanomaterials
39. Nickel, N.H., Brendel, K., Saleh, R.: Laser crystallization of hydrogenated amorphous silicon. Phys. Status Solidi (c) **1**(5), 1154–1168 (2004)
40. Nie, Y., Kimura, Y., Inoue, T., Yin, F., Akiyama, E., Tsuzaki, K.: Hydrogen embrittlement of a 1500-mpa tensile strength level steel with an ultrafine elongated grain structure. Metall. Mater. Trans. A **43**(5), 1670–1687 (2012)
41. Olson, D.L., Maroef, I., Lensing, C., Smith, R.D., Wang, W.W., Liu, S., Wildeman, T., Eberhart, M.: Hydrogen management in high strength steel weldments. In: Davidson, J.L., Olson, D.L. (eds.) Proceedings of the Joint Seminar, Melbourne, $23^{th}$ October 1996, Organising Committee of the Joint Seminar on behalf of Defence Science and Technology Organisation and Welding Technology Institute of Australia, pp. 1–19 (1996)
42. Padhy, G., Ramasubbu, V., Murugesan, N., Ramesh, C., Parvathavarthini, N., Albert, S.: Determination of apparent diffusivity of hydrogen in 9cr-1movnbn steel using hot extraction-pemhs technique. Int. J. Hydrog. Energy **38**(25), 10683–10693 (2013)
43. Padhy, G.K., Ramasubbu, V., Parvathavarthini, N., Wu, C.S., Albert, S.K.: Influence of temperature and alloying on the apparent diffusivity of hydrogen in high strength steel. Int. J. Hydrog. Energy **40**(20), 6714–6725 (2015)
44. Park, G.T., Koh, S.U., Jung, H.G., Kim, K.Y.: Effect of microstructure on the hydrogen trapping efficiency and hydrogen induced cracking of linepipe steel. Corros. Sci. **50**(7), 1865–1871 (2008)
45. Park, I.-J., Jo, S.Y., Kang, M., Lee, S.-M., Lee, Y.-K.: The effect of Ti precipitates on hydrogen embrittlement of Fe-18Mn-0.6C-2Al-xTi twinning-induced plasticity steel. Corros. Sci. **89**(0), 38–45 (2014)
46. Petushkov, E., Tserfas, A., Maksumov, T.: Determination of hydrogen in molybdenum by a diffusion-manometric method. In: Arifov, U. (ed.) Secondary Emission and Structural Properties of Solids, pp. 107–109. Springer, US (1971)
47. Phaniraj, M.P., Kim, H.-J., Suh, J.-Y., Shim, J.-H., Park, S.-J., Lee, T.-H.: Hydrogen embrittlement in high interstitial alloyed 18Cr10Mn austenitic stainless steels. Int. J. Hydrog. Energy **40**(39), 13635–13642 (2015)
48. Polyanskiy, A., Polyanskiy, V., Yakovlev, Y.A.: Experimental determination of parameters of multichannel hydrogen diffusion in solid probe. Int. J. Hydrog. Energy **39**(30), 17381–17390 (2014)
49. Polyanskiy, A.M., Popov-Diumin, D.B., Polyanskiy, V.A.: Determination of hydrogen binding energy in various materials by means of absolute measurements of its concentration in solid probe. In: Veziroglu, T., Zaginaichenko, S., Schur, D., Baranowski, B., Shpak, A., Skorokhod, V., Kale, A. (eds.) Hydrogen Materials Science and Chemistry of Carbon Nanomaterials. NATO Security through Science Series A: Chemistry and Biology, pp. 681–692. Springer, Netherlands (2007)
50. Pressouyre, G.M.: A classification of hydrogen traps in steel. Metall. Trans. A **10**(10), 1571–1573 (1979)

51. Ross, D.: Hydrogen storage: the major technological barrier to the development of hydrogen fuel cell cars. Vacuum **80**(10), 1084–1089 (2006). The world energy crisis: some vacuum-based solutions
52. Sayi, Y., Ramakumar, K., Prasad, R., Yadav, C., Shankaran, P., Chhapru, G., Jain, H.: Determination of H2 and D2 content in metals and alloys using hot vacuum extraction. J. Radioanal. Nucl. Chem. **230**(1–2), 5–9 (1998)
53. Shewmon, P.G.: Hydrogen attack of carbon steel. Metall. Trans. A **7**(2), 279–286 (1976)
54. So, K.H., Kim, J.S., Chun, Y.S., Park, K.-T., Lee, Y.-K., Lee, C.S.: Hydrogen delayed fracture properties and internal hydrogen behavior of a Fe18Mn1.5Al0.6C TWIP steel. ISIJ Int. **49**(12), 1952–1959 (2009)
55. Sofronis, P., Liang, Y., Aravas, N.: Hydrogen induced shear localization of the plastic flow in metals and alloys. Eur. J. Mech.-A/Solids **20**(6), 857–872 (2001)
56. Song, E.J., Suh, D.-W., Bhadeshia, H.: Theory for hydrogen desorption in ferritic steel. Comput. Mater. Sci. **79**, 36–44 (2013)
57. Suwarno, S., Solberg, J.K., Maehlen, J.P., Denys, R.V., Krogh, B., Ochoa-Fernandez, E., Borresen, B.T., Rytter, E., Gabis, I.E., Yartys, V.A.: Non-isothermal kinetics and in situ SR XRD studies of hydrogen desorption from dihydrides of binary Ti-V alloys. Int. J. Hydrog. Energy **38**(34), 14704–14714 (2013)
58. Taha, A., Sofronis, P.: A micromechanics approach to the study of hydrogen transport and embrittlement. Eng. Fract. Mech. **68**(6), 803–837 (2001)
59. Takasawa, K., Ishigaki, R., Wada, Y., Kayano, R.: Absorption of hydrogen in high-strength low-alloy steel during tensile deformation in gaseous hydrogen. ISIJ Int. **50**(10), 1496–1502 (2010)
60. Tarzimoghadam, Z., Rohwerder, M., Merzlikin, S.V., Bashir, A., Yedra, L., Eswara, S., Ponge, D., Raabe, D.: Multi-scale and spatially resolved hydrogen mapping in a ninb model alloy reveals the role of the $\delta$ phase in hydrogen embrittlement of alloy 718. Acta Mater. **109**, 69–81 (2016)
61. Verbeken, K.: 2 - Analysing hydrogen in metals: bulk thermal desorption spectroscopy (TDS) methods. In: Gangloff, R.P., Somerday, B.P. (eds.) Gaseous Hydrogen Embrittlement of Materials in Energy Technologies. Woodhead Publishing Series in Metals and Surface Engineering, vol. 1, pp. 27–55. Woodhead Publishing, Elsevier (2012)
62. Wang, M., Akiyama, E., Tsuzaki, K.: Determination of the critical hydrogen concentration for delayed fracture of high strength steel by constant load test and numerical calculation. Corros. Sci. **48**(8), 2189–2202 (2006)
63. Wei, F.G., Tsuzaki, K.: Quantitative analysis on hydrogen trapping of TiC particles in steel. Metall. Mater. Trans. A **37**(2), 331–353 (2006)
64. Williamson, G.K., Smallman, R.E.: III. Dislocation densities in some annealed and cold-worked metals from measurements on the X–ray debye-scherrer spectrum. Philos. Mag. **1**(1), 34–46 (1956)
65. Zan, N., Ding, H., Guo, X., Tang, Z., Bleck, W.: Effects of grain size on hydrogen embrittlement in a Fe–22Mn–0.6C TWIP steel. Int. J. Hydrog. Energy **40**(33), 10687–10696 (2015)
66. Zheng, J., Liu, X., Xu, P., Liu, P., Zhao, Y., Yang, J.: Development of high pressure gaseous hydrogen storage technologies. Int. J. Hydrog. Energy **37**(1), 1048–1057 (2012). 11th China hydrogen energy conference

# An Approach to Modeling Structural Materials with Low Hydrogen Concentration

**Alexander Belyaev, A. M. Polyanskiy, V. A. Polyanskiy and Yu. A. Yakovlev**

**Abstract** A general approach to modeling the effect of hydrogen on stress-strain diagram of materials is addressed. A bicontinua model is constructed which allows one to describe the kinetics of hydrogen in metals. The suggested rheological model is appropriate for estimation of the hydrogen transition from mobile to bounded state depending on the stress-state relation and description of localization of the bonded hydrogen that results in the material fracture. A novel approach to modeling the solids with account for the influence of hydrogen on properties of free surface on monocrystals at various scales is suggested. The idea of representing two continua as a single solid and describing the hydrogen effect on the material properties belongs to D. A. Indeitsev. It was first consistently presented in his work Indeitsev and Semenov (Acta Mechanica, 195:295–304, 2008, [32]). We see our task in generalization and application of his idea to specific problems and classes of problems in solid mechanics. We generalized the bicontinua model by Indeitsev to the multidimensional case. For the first time, we considered the dissolved hydrogen as the second medium and performed its simulation as an ideal gas. This made it possible to account for the temperature dependence of hydrogen. In the general, the present chapter is based upon the general approach by D. A. Indeitsev, whom the authors express their deep gratitude to.

---

A. Belyaev (✉)
Peter the Great St. Petersburg Polytechnic University (SPbPU), St. Petersburg, Russia
e-mail: vice.ipme@gmail.com

A. M. Polyanskiy
RDC Electron & Beam Technology, Ltd., St. Petersburg, Russia
e-mail: ampol@electronbeamtech.com

V. A. Polyanskiy · Yu. A. Yakovlev
Institute for Problems in Mechanical Engineering RAS, St. Petersburg, Russia
e-mail: vapol@mail.ru

Yu. A. Yakovlev
e-mail: yura.yakovlev@gmail.com

H. Altenbach et al. (eds.), *Dynamical Processes in Generalized Continua and Structures*, Advanced Structured Materials 103,
https://doi.org/10.1007/978-3-030-11665-1_4

# 1 Introduction

One of the most challenging problems of the material science is the influence of hydrogen on the mechanical properties of materials. This influence itself is a good example of crucial importance of small parameter in mechanics since the mean mass concentration of 0.4–0.8 ppm causes hydrogen embrittlement in aluminum alloys.

The hydrogen embrittlement is a source of many technical catastrophes and for this reason its nature is carefully investigated, cf. [15, 16, 29, 53]. Nowadays the structural design is not possible without precise strength computation. However the hydrogen considerably affects the strength of metals, that is why modeling of the hydrogen influence is a subject of many papers.

It is worth mentioning several approaches which are: (i) account of the influence of hydrogen on origination and motion of dislocations, (ii) account of the influence of hydrogen on the crack development, (iii) account of the internal pressure of hydrogen in metals and (iv) some physical approaches.

Origination and motion of dislocations as well as the hydrogen-enhanced localized plasticity (HELP) in the vicinity of the crack tips leads to the local plasticity because of the high concentration of dislocations. The very concept HELP was first developed in [14]. Later, based upon the physical reasoning about the potential of interaction of hydrogen with dislocations the constitutive laws modeling the local rheological changes in the crack mouth were suggested in [19, 20, 66]. However the calculations in [66] demonstrated that some considerable changes in the strain-stress diagram take place only under the concentration about 9000 ppm which is extremely high concentration for the majority of metals. The above constitutive law contains an implicit dependence on the local hydrogen concentration which cannot be exactly measured. In other words, the parameters of the law (the exponent included) can be estimated only indirectly and this can lead to considerable errors. E.g. in [68] a calculation of the local plasticity for a crack with special tip was carried out for verification of the model. The local hydrogen concentrations reached at the modeling are approximately 100 times higher than the initial mean values however the latter are about 1 ppm, i.e. the increase even by the factor of 100 does not result in the concentration of the order of 9000 ppm (for steels). A second source of possible errors is the modified law by Fikh [41] which contains a temperature dependence of the influence coefficients of the stress fields however it does not contain the exponential dependence of the diffusion coefficient on temperature. The authors of the above model discussed a plenty of uncertainties. In particular, they mentioned a nonlinear dependence of the internal potential on the stresses and hydrogen concentration. Since one deals with extremely high local concentrations these uncertain nonlinear functional dependences will play more and more important part.

Another model which is analogous to the HELP is the De-cohesion model (hydrogen enhanced decohesion model, or HEDE for short), cf. [71]. The difference between them is that the HEDE model takes into account that the energy of appearance of the free surfaces of fracture reduces with increase of the local hydrogen concentration. As mentioned in [30] the HELP approach requires a great computational costs for solving any practical problems. For this reason the only solution is utilizing a continual model of dislocation growth however this substitution turns out to be not adequate and the authors suggest to make use of the criterion of growth of submicrocrack, i.e. they reduce all the hydrogen problems to the modeling of the crack developing and reduction of the crack resistance.

It should be noted that the HELP and HEDE models have become universally recognized in modern material science. Some inconsistencies, among them contradition to the above experimental data, are ignored, and the latest scientific discussions are reduced to applying these models to describe the same material. This is very difficult to manage due to large computational complexity; therefore, only quasistatic problems of uniaxial stretching of cylindrical specimens are solved and analysed.

The development of the cracks induced by hydrogen is modeled in [69]. It is assumed ab initio that a crack has already been formed along the tube wall and due to the diffusion into the crack the hydrogen takes the form of molecular gaseous state and causes excessive pressure which leads to the crack growth. The gradient of the chemical potential is stress-dependent and is considered as a main cause of the hydrogen diffusion. In addition to this, reduction of the crack resistance is taken into account by changing parameters in the failure criterion for determining the conditions of the crack growth. As a result, one succeeds only in estimation of the rate of the crack growth which is compared with the test results, see [17]. However in this case even the character of the crack model appears to be of crucial importance. The difference between two-dimensional and three-dimensional model of developing of the hydrogen crack is discussed in [2]. There established some essential differences in the following parameters: higher cohesive strength and threshold stress intensity which should be prescribed for approximation the same test results in two-dimensional and three-dimensional statements of the problem. These parameters are selected only from three-dimensional model in [3]. Paper [57] reported results of calculation of changing in the shear modulus and parameters of the crystal lattice of the alloy platinum-zirconium carried out by means of plane-wave pseudopotential applied for the relationship: one hydrogen atom versus 3–4 atoms of the matrix (4000 ppm) which is absolutely not feasible to achieve in the conventional structural materials.

Some materials have a leading mechanism of destruction based on the formation and development of micro voids and nano voids cf. [22, 23, 27, 45, 48, 65, 72, 75]. The formation and propagation of voids is associated with the accumulation and redistribution of internal hydrogen in the material [8, 13, 37, 38, 62, 63, 74].

Modeling the development of voids is done by homogenization. Only there are parameters involved in the homogenization of the representative volume [76]. This reduces the possibility of strongly uneven concentrations of hydrogen in the presence of voids.

Summarising, we can state that for adequate modeling the behaviour of structures containing hydrogen one needs a special approach which is capable for account for influence of small concentration of hydrogen on the mechanical characteristics of materials.

## 2 Bicomponent Continuum for Modelling the Hydrogen Effects

An important role is played by the binding energy of hydrogen in material. It is known that, inside the materials, hydrogen is found in traps with different binding energies. In steels the total hydrogen content is 0.1–6 (n.sm$^3$/100 g) (eq. 0.1–0.55 ppm), while it is only hydrogen with a low binding energy that affects the strength, i.e. diffusively mobile hydrogen. In aluminum alloys the entire hydrogen diluted in the metal has a low binding energy—about 0.2–0.8 eV. The concentrations that are critical for the mechanical strength of weakly bound hydrogen in steels and aluminum alloys are similar—they are decimal ppm fractions. In aluminium alloys it includes the entire diluted hydrogen, while in steels it amounts to 5–10% of the total amount of diluted hydrogen.

Quite the contrary, the hydrogen with low binding energy tends to zones of tensile stresses (Gorsky's effect [24, 25]). Accumulation of hydrogen in the destruction zone occurs both by the input from outside and by redistribution of natural hydrogen inside the material. The hydrogen with low binding energy is diffuse however its interaction with material is very weak. The hydrogen with high binding energy interacts with material very intensively resulting in degradation of the mechanical material properties because of this interaction.

The mass equation for diffuse hydrogen inside volume $V$ is given by

$$m_H^- = \int\limits_V \rho_H^- dV$$

Here $m_H^-$ and $\rho_H^-$ are the mass and volume density of the diffuse hydrogen respectively. The differential form of the equation of mass balance is as follows

$$\frac{\partial \rho_H^-}{\partial t} + \nabla \cdot (\mathbf{v}_H^- \rho_H^-) = j_H^-$$

where $j_H^-$ denotes the mobile hydrogen source and $\mathbf{v}_H^-$ is the velocity of hydrogen particles. In terms of the concentration $N_H^- = \rho_H^- / m_H$ this mass balance equation takes the form

$$\frac{\partial N_H^-}{\partial t} + \nabla \cdot (\mathbf{v}_H^- N_H^-) = \frac{j_H^-}{m_H}$$

The bound hydrogen obeys the similar equation of the mass balance:

$$\frac{\partial N_H^+}{\partial t} + \nabla \cdot (\mathbf{v}_H^+ N_H^+) = \frac{j_H^+}{m_H}$$

Here $N_H^+$ and $\mathbf{v}_H^+$ are the concentration and the particle velocity for bound hydrogen (and material particles bounded with them) and $-j_H^- = j_H^+ = j$ denotes the redistribution hydrogen source inside the material. Since the concentrations are low we can assume a linear dependence for this source on the concentrations

$$j = \alpha(\varepsilon, T)N_H^- - \beta(\varepsilon, T)N_H^+ \tag{1}$$

This equation describes the hydrogen redistribution over the different binding energy levels. Here $\alpha(\varepsilon, T)$ and $\beta(\varepsilon, T)$ are positive factors describing the sorption and desorption of mobile hydrogen into the lattice from the diffusion channels.

In contrast to the classical approach to derivation of the hydrogen diffusion equations by Oriani [56], we use the denotation $j$ only for a part of the distributed hydrogen flux in the material volume. This flux is associated with changes in the binding energy of hydrogen. The diffusion flux associated with the hydrogen concentration gradient is described by the mass balance equation.

This approach does not contradict the model by Oriani [56].

First, Oriani discusses the equilibrium concentrations of hydrogen in various types of traps, which are related by chemical equilibrium constant. The excessive hydrogen that does not fit in the traps should be distributed due to diffusion, therefore, the variations of hydrogen concentrations in different types of traps do not result in vanishing overall value. The above relations are valid for the instantaneous concentration values, whereas their variations are related by the mass balance and yields the zero mean value.

Secondly, we consider the hydrogen concentrations to be very small quantities. Modern high-strength materials are very sensitive to hydrogen, and this effect was not observed 40 years ago. The overall hydrogen concentration in steels, as Oriani reported, is about 15 ppm, while the concentration of diffuse mobile phase is about 14.6 ppm. Modern high-strength steels begin to “feel” hydrogen at concentrations of diffuse mobile hydrogen of about 0.1 ppm [54], which is a hundred times less than the above value. Under these conditions, the possibility of overflowing traps can be neglected and dependence $j(N_H^-, N_H^+)$ can be considered in the linear approximation.

If we considered the interaction of external gaseous hydrogen with a solid, it would be necessary to take into account the capacity of traps and their activity associated with the Sieverts law [36]. Then the dependence of $j$ on concentrations (1) would be non-linear, however we consider the dissolved hydrogen with different binding energies, therefore, there is no dissociation of molecules obeying Sieverts’s law.

The adequacy of our model will be discussed in what follows. The coefficients $\alpha(\varepsilon, T)$ and $\beta(\varepsilon, T)$ expose exponential dependence on temperature. The effect of strains is determined by increasing the volume of traps due to development of microcracks and formation of a large number of dislocations. These processes proceed intensively at the upper boundary in the region of elastic deformations and plastic flow in most metals. However the dependence is weak under small and moderate elastic deformation.

Similar results are given by models describing accumulation of hydrogen damage and destruction as a second-order phase structural transition, see [31].

Now we proceed to the equation of dynamics. The rheological model of material containing hydrogen assume bi-continuum. The first continuum is a solid and plays a part of a carrying structure. The dynamic equation for the first continuum is

$$\nabla \cdot \boldsymbol{\tau} = (\rho_0 + \rho_H^+)\dot{\mathbf{v}}_H^+ + j\dot{\mathbf{v}}_H^+ + \mathbf{R}$$

Here $\boldsymbol{\tau}$ is the stress tensor and $\mathbf{R}$ is the force of interaction between the continua.

The second continuum models the behavior of hydrogen which behaves as a gas. The gas is characterized by pressure $p$ which is assumed to be positive for compression. Hence we can put the dynamic equation in the form

$$-\nabla p = \rho_H^- \dot{\mathbf{v}}_H^- - j\mathbf{v}_H^- - \mathbf{R}$$

The velocity $\mathbf{v}_H^-$ of hydrogen particles is very low because is describes the hydrogen diffusion in materials.

The strain energy of elastic solids is known to have two parts, namely the dilatation energy and shear energy. So we introduce the spherical part and deviator of the stress tensor by the equation

$$\boldsymbol{\tau} = \sigma \mathbf{I} + \mathbf{s}$$

where $\sigma$ denotes the mean stress, $\mathbf{s}$ stands for the deviator and $\mathbf{I}$ is the unit tensor. The Gorsky effect means that the dilatation energy determines the hydrogen diffusion and its interaction with material. For this reason only spherical part of the stress tensor is considered in what follows. The dynamic equations take now the form

$$\nabla \sigma = (\rho_0 + \rho_H^+)\frac{\partial \mathbf{v}_H^+}{\partial t} + j\mathbf{v}_H^+ + \mathbf{R} - \nabla \cdot \mathbf{s}\,,$$

$$-\nabla p = \rho_H^- \frac{\partial \mathbf{v}_H^-}{\partial t} - j\mathbf{v}_H^- - \mathbf{R}\,.$$

For the sake of simplicity the further analysis is limited to the one-dimensional case since it allows the reader to catch the main idea of construction of the rheological model for material with low hydrogen concentration.

Let us consider a virgin lattice. In one-dimensional case it can be schematically depicted as a 1D spring. The weakening of the internuclear bonds caused by "landing" of the hydrogen particles can produce the chain formations of new internuclear bonds, see Fig. 1, as the serial connections of elastic bonds of the basic lattice and the introduced elastic bonds of new elements which are the hydrogen particles.

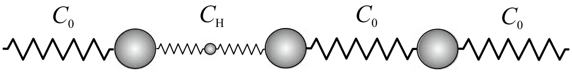

**Fig. 1** One-dimensional model of the lattice with "landed" hydrogen particles

Obviously, such chain is possible under the assumption that the mass of particles of a mobile structure is small, i.e. $m_0 \gg m_H$.

The overall rigidity of the spring of with $N_0$ volumetric concentration of particles is obtained from the equation

$$\frac{N_0}{C_\Xi} = \frac{N_0 - N_H^+}{C_0} + \frac{N_H^+}{C_H}$$

The constitutive equation for the equivalent 1D solid is obtained by analogy with the above equation

$$\sigma = E_\Xi \varepsilon, \quad E_\Xi = \frac{E_0 E_H N_0}{N_0 E_H + N_H^+ (E_0 - E_H)}$$

Here $N_0$ denotes the total volumetric concentration of the lattice particles in the elementary volume, $N_H^+$ is the volumetric concentration of lattice particles that attached to the hydrogen with the bonds of rigidity $C_H$. On the other hand $N_H^+$ is the volumetric concentration of the bound hydrogen particles.

The overall elastic modulus $E_\Xi$ of the lattice with hydrogen can be much lower than the elastic modulus of the virgin material since $E_H \ll E_0$

$$E_\Xi = E_H \frac{E_0 N_0}{N_0 E_H + N_H^+ E_0} \approx E_H \frac{1}{(N_H^+ / N_0)} \ll E_0 \tag{2}$$

A strong influence of the concentration of the attached particles $N_H^+$ on the overall elastic property is also seen from the above equation, namely, the higher fraction $N_H^+$ of the attached hydrogen, the lower the elastic modulus of the material.

The number of the lattice settled by the hydrogen particles depends on the stress state of the lattice at every point and, in general, on time. The unknown functional dependence of $E_\Xi$ on $N_H^+(\varepsilon, x, t)$ should be determined with the help of the model of bi-component continuum.

Taking into account Eq. (2) the state equation $\sigma = \sigma(\varepsilon, N_H^+(\varepsilon, x, t))$ can be presented in the standard form of 1D elastic solid

$$\sigma = E_\Xi \varepsilon = E_0 \varepsilon \left[ 1 - \frac{N_H^+}{N_H^+ + N_0 E_H / (E_0 - E_H)} \right] \approx E_0 \varepsilon \left[ 1 - \frac{N_H^+}{N_H^+ + N_0 E_H / E_0} \right],$$

confirming an essential dependence of the stress on concentration of the bounded hydrogen.

By analogy with ideal gas occupying the clear space (voids) in porous medium the state equation describing the relation between pressure $p$ and density $\rho_H^-$ is given by

$$p = \frac{3}{2} N_H^- k T$$

Here $N_H^-$ is the volumetric concentration of particles of mobile hydrogen, $k$ is Boltzmann's constant, $T$ is the absolute temperature of the moving medium.

We suggest that the flux of the non-attached hydrogen particles through the lattice of the carrying structure can be described within the approach used for the flow of ideal gas. This us equivalent the following representation for $R$

$$R = F(\varepsilon)\rho_H^-[v_H^- - v_H^+] \tag{3}$$

The interaction force can be taken as a linear function of the difference in the continuum particles velocities. Parameter $F(\varepsilon)$ (dependent on strain $\varepsilon$) is proportional to the passage cross-sectional area and is determined in terms of the material properties such as crystal grain surface area, crystal grain volume etc.

The source term $J$ is taken in the form of [32], i.e. in the form (1).

Let us prove the adequacy of dynamic mechanism of hydrogen trapping by means of bi-continuum model are relation (1).

Assume a uniform volume distribution of the concentration of bound and mobile hydrogen and constant temperature and equal strain in the whole solid, then we can fix the factors of sorption and desorption $\alpha = \alpha(\varepsilon_{\mathbf{0}}, T_0)$ and $\beta = \beta(\varepsilon_{\mathbf{0}}, T_0)$. The gradients vanish, i.e. the mass balance equation yields

$$\begin{aligned} \tfrac{dN_H^+}{dt} &= \alpha N_H^- - \beta N_H^+ \\ \tfrac{dN_H^-}{dt} &= -\alpha N_H^- + \beta N_H^+ \end{aligned} \tag{4}$$

Assuming the following initial conditions

$$N_H^+(0) = 0, \qquad N_H^-(0) = \Psi^-,$$

we obtain the solution of system (4)

$$N_H^+ = \frac{\alpha}{\alpha+\beta}\Psi^-(1 - e^{-(\alpha+\beta)t}),$$

$$N_H^- = \Psi^-[1 - \frac{\alpha}{\alpha+\beta}(1 - e^{-(\alpha+\beta)t})].$$

This time-dependences are shown in Fig. 2. They demonstrate the process of hydrogen saturation in the carrying medium and decrease of the mobile hydrogen. Parameters $\alpha$ and $\beta$ should be determined experimentally because they describe the rate of the above processes.

The relation between these coefficients determines the filling level of different traps resulting in dynamic equilibrium while the overall value determines the rate of hydrogen redistribution between levels with different binding energies.

It should be noted that Eq. (4) describes the interchange of hydrogen particles (bounded and mobile) under the condition that the mobile hydrogen particles have zero velocity. As follows from Eq. (3), this is realized under the condition $F(\varepsilon) = 0$,

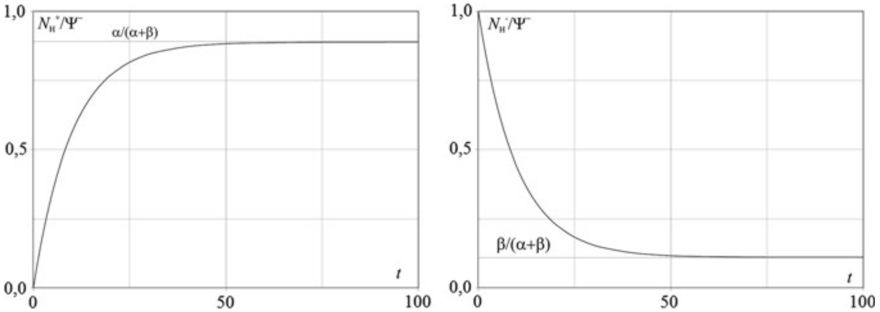

**Fig. 2** The diffuse and bound hydrogen concentrations versus time

i.e. easy access of free hydrogen particles is excluded. Obviously, in this case the whole free hydrogen satisfies this condition; hence $\alpha \gg \beta$.

After apparent replacement $\rho_H^+ = m_H N_H^+$, $\rho_H^- = m_H N_H^-$ and $n^+ = \frac{N_H^+}{N_0}$ we can now write down the complete system of equations in one-dimensional case

$$\begin{aligned}
&\tfrac{\partial \sigma}{\partial x} = (\rho_0 + \rho_H^+)\tfrac{\partial v_H^+}{\partial t} + J v_H^+ + R,\\
&-\tfrac{\partial p}{\partial x} = \rho_H^- \tfrac{\partial v_H^-}{\partial t} + J v_H^- - R,\\
&\tfrac{\partial \rho_0}{\partial t} + \tfrac{\partial(\rho_0 v_H^+)}{\partial x} = 0\\
&\tfrac{\partial N_H^+}{\partial t} + \tfrac{\partial(N_H^+ v_H^+)}{\partial x} = J/m_H\\
&\tfrac{\partial N_H^-}{\partial t} + \tfrac{\partial(N_H^- v_H^-)}{\partial x} = -J/m_H
\end{aligned} \tag{5}$$

where

$$\sigma = \frac{E_0 E_H}{E_H + n^+(E_0 - E_H)}\varepsilon,$$

$$R = F(\varepsilon)\rho_H^-[v_H^+ - v_H^-],$$

$$j = \alpha(\varepsilon, T)N_H^- - \beta(\varepsilon, T)N_H^+.$$

The derived system of Eq. (5) is complete however it is strongly nonlinear, for this reason we limit our consideration by the simple static case of the uniaxial tension-compression.

It is necessary to note here that the concept of a static stress state is rather conditional since it is necessary to attribute the carrying component of medium with regard for Eq. (5) stating that movement of the second component is determined pure kinematically. In other words, the reorganization of the material structure with time is a sort of dynamics. Therefore, it is natural to search for the solution of the problem in the following form

$$\varepsilon = \varepsilon_{st} + \tilde{\varepsilon}(x,t), \qquad v_H^+ = 0 + \tilde{v}_H^+, \qquad v_H^- = 0 + \tilde{v}_H^-$$

Here $\varepsilon_{st}$ is a homogeneous static strain field. It is obvious that $N_H^+ = N_H^+(x, \varepsilon, t)$ can be submitted as

$$N_H^+(x, \varepsilon_{st} + \tilde{\varepsilon}, t) = N_H^+(x, \varepsilon_{st}, t) + \left.\frac{\partial N_H^+}{\partial \varepsilon}\right|_{\varepsilon=\varepsilon_{st}} \tilde{\varepsilon}(x,t)$$

It is naturally to present stresses $\sigma$ as

$$\sigma = \sigma_{st} + \tilde{\sigma} = E_0\left[1 - \frac{n^+}{E_H/E_0 + n^+}\right]\varepsilon_{st} + E_0\left[1 - \frac{n^+}{E_H/E_0 + n^+}\right]\tilde{\varepsilon} + O(\tilde{\varepsilon})$$

Note that $\sigma$ here is related to $\tilde{\varepsilon}$, emphasizing that there is an induced strains due to reorganization of internal structure and this strain generates stress $\tilde{\sigma}$. A complex dependence $\sigma = \sigma(\varepsilon, N_H^+(\varepsilon, x, t)) = \sigma(\varepsilon, N_0 \cdot n^+(\varepsilon, x, t))$ on deformation converts the first equation of system (5) into:

$$\frac{\partial \sigma}{\partial \varepsilon}\frac{\partial \varepsilon}{\partial x} + \frac{\partial \sigma}{\partial n^+}\left[\frac{\partial n^+}{\partial \varepsilon}\frac{\partial \varepsilon}{\partial x} + \frac{\partial n^+}{\partial x}\right] = (\rho_0 + \rho_H^+)\frac{\partial v_H^+}{\partial t} + J v_H^+ + R.$$

Staying in the framework of the first approach, one can write down Eq. (5) in the following form

$$\frac{\partial \sigma_{st}}{\partial \varepsilon}\frac{\partial \varepsilon_{st}}{\partial x} = 0 \tag{6}$$

$$\frac{\partial \tilde{\sigma}}{\partial x} = (\rho_0 + \rho_H^+)\frac{\partial \tilde{v}_H^+}{\partial t} + J|_{\varepsilon=\varepsilon_{st}}\tilde{v}_H^+ + R|_{\varepsilon=\varepsilon_{st}} - \left.\frac{\partial \sigma}{\partial n^+}\right|_{\varepsilon=\varepsilon_{st}}\left.\frac{\partial n^+}{\partial x}\right|_{\varepsilon=\varepsilon_{st}}$$

Here

$$\begin{aligned} \sigma &= E_0\varepsilon_{st}\left\{1 - \left.\left[\tfrac{n^+}{n^+ + E_H/E_0}\right]\right|_{\varepsilon=\varepsilon_{st}}\right\}, \\ \tilde{\sigma} &= E_0\tilde{\varepsilon}\left\{1 - \left.\left[\tfrac{n^+}{n^+ + E_H/E_0}\right]\right|_{\varepsilon=\varepsilon_{st}}\right\}, \\ R|_{\varepsilon=\varepsilon_{st}} &= -F\left(\varepsilon_{st}\right)\rho_H^- v_H^- \end{aligned} \tag{7}$$

The second equation in (6) serves for definition of the induced field of strain $\tilde{\varepsilon}$ when the main term $\frac{\partial \sigma}{\partial n^+} \cdot \left.\frac{\partial n^+}{\partial x}\right|_{\varepsilon=\varepsilon_{st}}$ is known.

For the second component we can state that

$$-\frac{\partial p}{\partial x} = F(\varepsilon_{st}) m_H N_H^- v_H^-, \quad p = \frac{3}{2}N_H^- kT. \tag{8}$$

Here $\rho_H^- = m_H \cdot N_H^-$ is the mobile hydrogen density.

Equation (8) can be transformed into:

$$\frac{3}{2}kT\frac{\partial N_H^-}{\partial x} = -F(\varepsilon_{st})m_H N_H^- v_H^-$$

The latter equation is similar to the Darcy formula but it has the generalized factor of diffusion dependent on the strain field $\varepsilon_{st}$.

Thus, we have

$$v_H^- = -\frac{3kT}{2F(\varepsilon_{st})m_H}\frac{1}{N_H^-}\frac{\partial N_H^-}{\partial x}. \tag{9}$$

As mentioned above, the dependence $\alpha(\varepsilon, T)$ and $\beta(\varepsilon, T)$ on strain is weak in elastic regions, that is, it can be neglected. Let us introduce the denotation $\alpha(T) = \alpha(\varepsilon, T)$ and $\beta(T) = \beta(\varepsilon, T)$. The above equations should be added by the balance equation for the number of bounded and free hydrogen particles:

$$\begin{aligned} N_0\tfrac{\partial n^+}{\partial t} &= \alpha(T)N_H^- - \beta(T)N_0 n^+ \\ \tfrac{\partial N_H^-}{\partial t} + \tfrac{\partial N_H^- v_H^-}{\partial x} &= -(\alpha(T)N_H^- - \beta(T)N_0 n^+) \end{aligned}$$

Inserting Eq. (9) we obtain

$$\frac{\partial^2 n^+}{\partial t^2} + (\alpha(T)+\beta(T))\frac{\partial n^+}{\partial t} - \frac{3kT}{2m_H F\,(\varepsilon_{st})}\left[\beta(T)\frac{\partial^2 n^+}{\partial x^2} + \frac{\partial^3 n^+}{\partial t\partial x^2}\right] = 0 \tag{10}$$

Equation (10) is the equation of mixed type since it contains terms inherent in the hyperbolic equation, i.e. $\partial^2 n^+/\partial t^2$, $\partial^2 n^+/\partial x^2$, and also terms typical for the parabolic equations $\partial n^+/\partial t$, $\partial^3 n^+/\partial t\partial x^2$. This means that the detailed analysis of a non-stationary problem subjected to a finite initial perturbation should demonstrate a characteristic moving front of increasing (or decreasing) bounded hydrogen concentration, i.e. an exposed strong dispersion.

In order to carry out analysis of this equation let us apply the Fourier method of separation of variables. To this end we assume

$$n^+(t, x) = T_+(t)\cdot X_+(x).$$

Then

$$\frac{\ddot{T}_+(t) + (\alpha(T)+\beta(T))\dot{T}_+(t)}{\frac{3kT}{2m_H F(\varepsilon_{st})}(\beta(T)T_+(t) + \dot{T}_+(t))} = \frac{X_+''(x)}{X_+(x)} = -\gamma_x^2.$$

This yields the ordinary differential equation for $X_+(x)$:

$$X_+''(x) + \gamma_x^2 X_+(x) = 0.$$

and the ordinary differential equation for $T_+(t)$:

$$\ddot{T}_+(t) + (\alpha(T) + \beta(T) + \gamma_x^2 \frac{3kT}{2m_H F(\varepsilon_{st})})\dot{T}_+(t) + \gamma_x^2 \frac{3kT}{2m_H F(\varepsilon_{st})}\beta(T)T_+(t) = 0.$$

Let us solve the problem under the following initial condition

$$\begin{aligned} &n^+(0, x) = 0, \\ &N_H^-(0, x) = \Psi^- \left(1 + \cos \tfrac{2\pi x}{\lambda}\right), \\ &\dot{n}^+(0, x) = \tfrac{\alpha\Psi^-}{N_0} \left(1 + \cos \tfrac{2\pi x}{\lambda}\right) \end{aligned} \tag{11}$$

where parameter $\lambda$ is determined by parameters of the particular microstructure of the material under consideration.

To begin with, we obtain the solution for the constant term in Eq. (11). In this case $\gamma_x^2 = 0$ and the equation for the time-dependent function $T_+(t)$ takes the form

$$\ddot{T}_+(t) + (\alpha(T) + \beta(T))\dot{T}_+(t) = 0.$$

The solution is as follows

$$T_+(t) = T_0 + T_1 e^{-(\alpha(T)+\beta(T))t},$$

where the integration constants $T_0$ and $T_1$ are determined by the initial conditions.

For the second term in Eq. (11) $\gamma_x^2 = \frac{4\pi^2}{\lambda^2}$ and the equation for $T_+(t)$ is given by

$$\ddot{T}_+(t) + \left(\alpha(T) + \beta(T) + \frac{4\pi^2}{\lambda^2}\frac{3kT}{2m_H F(\varepsilon_{st})}\right)\dot{T}_+(t) + \frac{4\pi^2}{\lambda^2}\frac{3kT}{2m_H F(\varepsilon_{st})}\beta T_+(t) = 0. \tag{12}$$

Introducing

$$G(\varepsilon_{st}) = \frac{3kT}{2m_H F(\varepsilon_{st})}\left(\frac{2\pi}{\lambda}\right)^2, \alpha = \alpha(T), \beta = \beta(T),$$

We can rewrite Eq. (12) in the form

$$\ddot{T}_+(t) + (\alpha + \beta + G(\varepsilon_{st}))\dot{T}_+(t) + G(\varepsilon_{st})\beta T_+(t) = 0. \tag{13}$$

The solution is

$$T_+(t) = T_3 e^{-\xi_1 t} + T_4 e^{-\xi_2 t},$$

where

$$\xi_1 = \frac{1}{2}\left[\alpha + \beta + G(\varepsilon_{st}) - \sqrt{(\alpha + \beta + G(\varepsilon_{st}))^2 - 4\beta G(\varepsilon_{st})}\right]$$

$$\xi_2 = \frac{1}{2}\left[\alpha + \beta + G(\varepsilon_{st}) + \sqrt{(\alpha + \beta + G(\varepsilon_{st}))^2 - 4\beta G(\varepsilon_{st})}\right]$$

Satisfying the above initial condition yields

$$\begin{aligned} T_0 &= -T_1 = \tfrac{\alpha\Psi^-}{N_0(\alpha+\beta)} \\ T_3 &= -T_4 = \tfrac{\alpha\Psi^-}{N_0\sqrt{(\alpha+\beta-G(\varepsilon_{st}))^2+4\beta G(\varepsilon_{st})}} \end{aligned}.$$

It allows one to write down the final expression for the concentration of the mobile hydrogen

$$n^+(t,x) = \frac{\alpha\Psi^-}{N_0}\left(\frac{(1-e^{-(\alpha+\beta)t})}{\alpha+\beta} + \frac{(e^{-\xi_1 t}-e^{-\xi_2 t})\cos\frac{2\pi x}{\lambda}}{\sqrt{(\alpha+\beta+G(\varepsilon_{st}))^2-4\beta G(\varepsilon_{st})}}\right). \quad (14)$$

As might be expected, the uniformly distributed mobile hydrogen increases the binding energy regardless of the diffusion whereas the rate of diffusion of the non-uniformly distributed hydrogen is determined by $F(\varepsilon_{st})$ that characterizes the "flow cross section" of the diffusion channel and depends on strain $\varepsilon_{st}$.

Decrease in $F(\varepsilon_{st})$ leads increase in $G(\varepsilon_{st})$. If $F(\varepsilon_{st}) \to 0$ $\xi_1$ tends to zero and the factor $(e^{-\xi_1 t} - e^{-\xi_2 t})$ in formula (14) tends to $e^{-\beta t}$. This factor determines the nonuniformity of the concentration of hydrogen along 1D solid. Therefore, the alignment of the hydrogen concentration due to diffusion is slowed down to the pure desorption process. In limiting case we obtain

$$n^+(t,x) = \frac{\alpha\Psi^-}{N_0}\left(\frac{1}{\alpha+\beta} + \frac{e^{-\beta t}}{G(\varepsilon_{st})}\cos\frac{2\pi x}{\lambda}\right).$$

Equation (7) is used for modelling the hydrogen influence on $\sigma(\varepsilon)$. It is necessary to mention that the effects related to the temperature change as well as the nonlinear effects caused by the change in the content of bound hydrogen due to the material deformation can be described in terms of dependences of $\alpha$, $\beta$ on temperature and strain. The experimental data [43] data indicate that the yield strength is particularly strongly dependent upon the hydrogen concentration.

It is logically substantiated that for the elastic material the area of free surfaces is proportional to the strain itself under small deformation. Therefore, the factors of sorption $\alpha$ and desorption $\beta$ of hydrogen are a linear function of strain. It allows one to assume a linear relationship between these factors

$$\frac{\beta(\varepsilon, T)}{\alpha(\varepsilon, T)} = k_0(T) + k_1(T)\varepsilon \quad (15)$$

The latter dependence describes the material properties modification during the hydrogen redistribution within the material. The simple dependence (15) allows us to make a good approximation of the experimental data. Figure 3 demonstrates the dependence of the maximal tensile stress on the initial concentration of the diffuse mobile hydrogen calculated by formulae (15) for steels. This experimental data [54]

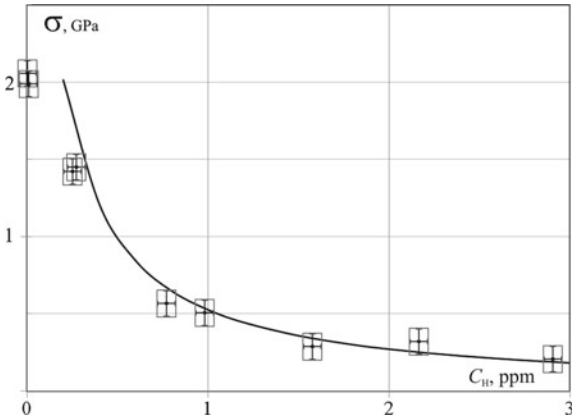

**Fig. 3** Variations in notch AISI 4135 steel samples as a function of diffuse hydrogen content: the present approach (solid line) and test values [54]

of the maximal tensile stress versus the concentration of the diffuse mobile hydrogen in AISI 4135 steel are also displayed in the figure beneath.

The suggested approach is equally applicable for studying of the effect of hydrogen on fatigue and destruction, cf. Refs. [6, 12].

## 3 Bicomponent Model of Fatigue

Fatigue of metals is a subject of great practical importance because most of the material failures in engineering components and structures are fatigue failures cf. [21]. The most striking characteristic of fatigue failures is the lack of deformation in the region of the fractures, even in materials like mild steel, which are quite ductile when broken by a static load. This is one of the dangers of fatigue, for there is generally no prior indication of impending failure.

Among all the factors influencing fatigue, the hydrogen is the most dangerous and unpredictable, cf. [52]. Numerous experimental studies have shown that the presence of hydrogen in metal or environment accelerate the process of fatigue failure by tens or even hundreds of times, cf. [35, 46, 50, 51, 55, 67, 70]. An important feature of the hydrogen effect on fatigue is the dependence of failure acceleration on frequency of external fatigue loading [46, 52, 73].

Modeling of the hydrogen effect on fatigue is usually attributed to consideration of a single fatigue crack. As mentioned in [52], most research on hydrogen embrittlement over the past 40 years have only examined the influence of hydrogen on tensile properties. To calculate the growth rate, the models of static stretching are used as. As a rule, the HEDE model and its various modifications are applied, cf. [2, 49].

As noted above, this approach is limited by the need to know the parameters of crack initiation. Use of the bi-component model enables analysis of the destruction causes without these additional assumptions.

Consider the one-dimensional case of periodic uniaxial fatigue loading of the rod. We assume that the frequency of loading is low, relative to rate of the other processes.

This will allow us to ignore the solid dynamics. In this case Eq. 10 describes the bound hydrogen concentration. After the standard procedure of separation of variables, we obtain Eq. 13 for the time concentration factor similar to the quasistatic version.

We consider a cyclic loading with small strain amplitude of frequency $\omega$, i.e. $\varepsilon = \varepsilon_1 \cdot \cos(\omega t)\,,\ 0 < \varepsilon_1 \ll 1$. It allows us to linearise the dependence $G(\varepsilon)$, to have $G(\varepsilon) = G_0 + G_1 \cdot \varepsilon$. Substituting the latter into the second equation in Eq. 13 enables us to put it in the form of the generalized Mathieu equation

$$\ddot{T} + 2\Gamma(1 + \gamma + 2\mu\cos\omega t)\dot{T} + \Omega^2(1 + 2\mu\cos\omega t)T = 0 \qquad (16)$$

where the new parameters are $\Omega = \sqrt{G_0\beta},\ \mu = G_1/2G_0,\ \Gamma = G_0/2,\ \gamma = (\alpha + \beta)/G_0$, $\Omega$ having the dimension of frequency. The dimensionless parameter $\mu$ can be understood as the intensity of the external mechanical loading expressed in terms of the hydrogen concentration. The first approximation of the boundary of the principal region of instability of this equations allows one to obtain the functional dependence $\mu = \mu(\omega)$. According [?], the boundaries of the principle instability region of Eq. 16 are given by

$$\mu^2 = \frac{\left[\Omega^2 - \left(\frac{\omega}{2}\right)^2\right]^2 + \left[\Gamma\omega(1 + \gamma)\right]^2}{\Omega^4 + \Gamma^2\omega^2} \qquad (17)$$

are shown in Fig. 4. From this figure one can conclude that the boundary of the instability region in the plane of parameters $(\mu, \xi)$ with the frequency ratio $\xi = \omega/\Omega$ has a minimum which can be understood as a safe level of load under which the fatigue fracture does not occur at all. The exact expression for the boundary of the

**Fig. 4** Stability chart of the system under consideration

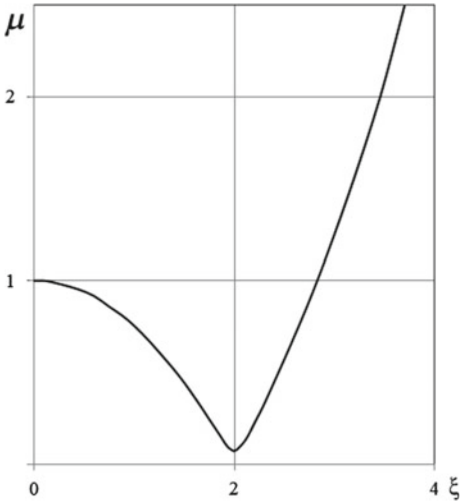

instability region at the “resonance frequency” is rather cumbersome however it can be approximated by

$$\mu^2 = \left(\frac{\Omega^2}{\beta^2} + \frac{\alpha + \beta}{\beta}\right)\left(\frac{\Omega^2}{\beta^2} + 1\right)^{-1} \tag{18}$$

## 4 Wave Approach for Modelling of Destruction

The majority of structural metals suffer from plastic deformation prior to failure. The plastic deformations are observed even in the case of multicyclic fatigue. Therefore, the process of plastic flow is critical for the strength of materials and the stability of structures made of these materials.

The Portevin-Le Chatelier effect and the associated mechanism of formation of plastic deformation localization bands (the Lüders bands) are important aspects of plastic deformation. Different explanations of mechanisms of such localization are proposed in the literature.

The main part of the authors are of the opinion that this phenomenon is due to the non-monotonic dependence of stress on strain, cf. [40, 60].

The actual instability of the deformation process is also described by introducing either nonlinearities [33, 47] or random variables [42] into the continuous medium equations. The source of nonlinear dependences is the diffusion of vacancies and associated dislocations, as well as the non-linear constitutive equations for the material under consideration. The source of randomness is the process of dislocations appearance.

In fact, the main feature of these approaches is that the one-dimensional approaches are utilised. All equations are written down either for a homogeneous material, or for composites consisting of inclusions of one material in the matrix of other material. Meanwhile, it has been established that surface tension or surface forces of crystallites play an important role in the plastic deformation of polycrystalline materials, cf. [39]. Thus, it is necessary to take into account the presence of a surface layer with special properties.

We conducted a study of samples with large plastic deformations and samples after failure, see [5, 7, 9–11, 26, 63] for detail. Preloading of samples was carried out in tensile machines as well as by various processing (pin-machining, thermo-mechanical loads, grinding, etc.). The process of plastic deformation is accompanied by a sharp change in acoustoelasticity of the sample material, cf. [9, 28, 34, 58, 59]. It is generally accepted that this is a consequence of turns of the metal grains and residual stresses, see [58, 59]. Our study of samples after standard HIC test steels allowed us to establish that this effect could be associated with microcracking [1]. Consequently, the surface microcracking can be one of the leading mechanisms for the structure modification under plastic deformation.

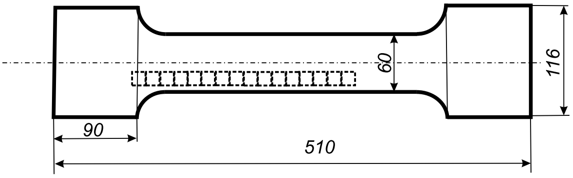

**Fig. 5** Samples for mechanical test. The dashed line shows the scheme of cutting samples for measuring the hydrogen distribution

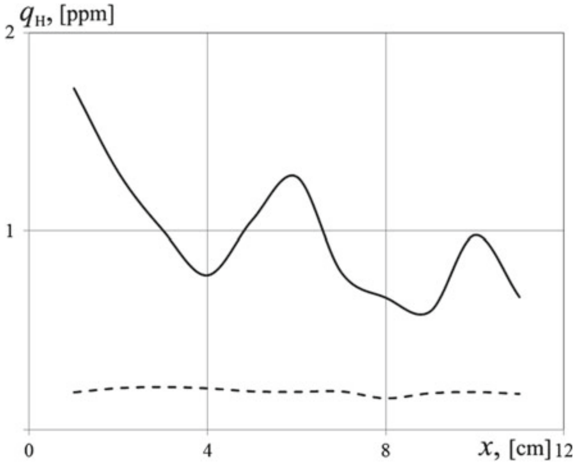

**Fig. 6** Hydrogen concentration versus distance from the central part of the initial donor specimen. Solid line stands for samples with a surface layer while the dashed line marks the hydrogen concentration with removed 500 μm layer from surface of the original sample

In order to prove this effect we measured the spatial distribution of hydrogen in samples of the aluminum alloys obtained after cyclic and static loading in a tensile machine. Samples were cut from plates of 16 to 20 mm thick. They had a standard dumbbell shape and their sketch is depicted in Fig. 5. The dashed line shows the pattern of cutting samples for measuring the hydrogen distribution. The characteristic size of the samples was 6 mm.

Cutting samples for measuring the hydrogen distribution was done by manual saw to prevent their heating and the associated redistribution of hydrogen. A layer with a thickness of about 500 μm was removed from surface of some samples of the large donor specimen. The results of measurement are shown in Fig. 6 as function of the distance (in centimeters) from the central part of the initial donor specimen.

The measurement techniques are described in Refs. [4, 61]. The aluminum alloys are actually a saturated solution of hydrogen. A significant increase in the initial hydrogen concentration is possible only in the case of appearance of the additional pores and microcracks [4].

Our experimental studies of a large number of samples have shown that all these pores and microcracks are concentrated in a thin surface layer of the metal. The new regularity that we established allows us to model the material as a three-dimensional medium containing a thin surface layer with some special properties.

We found out that the surface layer contains significant amounts of hydrogen and this fact allows us to model it as a solid that consists of bicontinuous media.

An important role is played by the binding energy of hydrogen in material. It is known that, inside the materials, hydrogen is found in traps with different binding energies. In steels the total hydrogen content is 0.1–6 ppm, while it is only hydrogen with a low binding energy that affects the strength, i.e. diffusively mobile hydrogen. In aluminum alloys the entire hydrogen diluted in the metal has a low binding energy—about 0.2–0.8 eV. The concentrations that are critical for the mechanical strength of weakly bound hydrogen in steels and aluminum alloys are similar—they are decimal ppm fractions. In aluminium alloys it includes the entire diluted hydrogen, while in steels it amounts to 5–10% of the total amount of diluted hydrogen.

Accumulation of hydrogen in the destruction zone occurs both by the input from outside and by redistribution of natural hydrogen inside the material. The hydrogen with low binding energy is diffuse however its interaction with material is very weak. The hydrogen with high binding energy interacts with material very intensively resulting in degradation of the mechanical material properties because of this interaction.

We assume that the thin surface layer is attached to the base material which is slowly stretched by law $\varepsilon_{st} = \varepsilon_{st}(t)$. The strains are assumed to be small and

$$F\left(\varepsilon_{st}\right) = F_0 - k_0 \varepsilon_{st}^2$$

is a decreasing function of strain value. From Eq. 10 we can put approximately

$$\frac{\partial^2 n^+}{\partial t^2} + (\alpha + \beta)\frac{\partial n^+}{\partial t} - \frac{3kT}{2m_H F_0}(1 + \frac{k_0}{F_0}\varepsilon_{st}^2)\left[\beta\frac{\partial^2 n^+}{\partial x^2} + \frac{\partial^3 n^+}{\partial t \partial x^2}\right] = 0 \tag{19}$$

In this equation, we can single out a small parameter that allows us to apply the method of successive approximations. The generating solution is obtained from the equation

$$\frac{\partial^2 n^+}{\partial t^2} + (\alpha + \beta)\frac{\partial n^+}{\partial t} - \frac{3kT}{2m_H F_0}\left[\beta\frac{\partial^2 n^+}{\partial x^2} + \frac{\partial^3 n^+}{\partial t \partial x^2}\right] = 0$$

Then subtracting the generating solution from Eq. 19 we can obtain the following approximation which has the order of $O(\varepsilon_{st}^2)$. The generating solution can be considered as a wave solution. This is facilitated by the oscillatory nature of the distribution of hydrogen concentrations observed experimentally, see Fig. 6.

We seek solutions in the following form

$$n^+ = n^+(\theta), \;\; \theta = \kappa x - \lambda t + \varphi,$$

where $\kappa$, $\lambda$ are the wave numbers and $\varphi$ denotes the phase, then

$$\lambda^2\frac{d^2 n^+}{d\theta^2} - (\alpha + \beta)\lambda\frac{dn^+}{d\theta} - \frac{3kT}{2m_H F_0}\left[\beta\kappa^2\frac{d^2 n^+}{d\theta^2} - \kappa^2\lambda\frac{d^3 n^+}{d\theta^3}\right] = 0$$

Denoting $\gamma = \frac{3kT}{2m_H F_0}$ we obtain

$$\gamma\kappa^2\lambda\frac{d^3n^+}{d\theta^3} + (\lambda^2 - \gamma\kappa^2\beta)\frac{d^2n^+}{d\theta^2} - (\alpha+\beta)\lambda\frac{dn^+}{d\theta} = 0$$

This equation has constant coefficients and the eigenvalues are determined by the equation

$$\begin{gathered}
\gamma\kappa^2\lambda p^3 + (\lambda^2 - \gamma\kappa^2\beta)p^2 - (\alpha+\beta)\lambda p = 0 \\
p_1 = 0, \;\; p_{2,3} = \frac{-(\lambda^2 - \gamma\kappa^2\beta) \pm \sqrt{D}}{2\gamma\kappa^2\lambda}, \\
D = \lambda^4 + \gamma^2\kappa^4\beta^2 + 2\lambda^2\gamma\kappa^2\beta + 4\lambda^2\gamma\kappa^2\alpha
\end{gathered}$$

The dispersion relationship is given by

$$-i\gamma k^2\omega - \omega^2 + \gamma k^2\beta - i(\alpha+\beta)\omega = 0,$$

therefore

$$k^2 = \frac{\omega^2 + i(\alpha+\beta)\omega}{\gamma\beta - i\gamma\omega} = \frac{1}{\gamma}\frac{-\alpha\omega^2 + i((\alpha+\beta)\omega\beta + \omega^3)}{\beta^2 + \omega^2}$$

Thus, the time-decay is combined with the positive real-valued part of the exponential with respect to the coordinate and vice versa.

On the other hand, in the case $\kappa = ik,\ \lambda = i\omega$ we obtain one zero and two purely imaginary roots of different signs

$$\begin{gathered}
p_{2,3} = \frac{(\omega^2 - \gamma k^2\beta) \pm \sqrt{D}}{2\gamma k^2\omega}i \\
D = \omega^4 + \gamma^2k^4\beta^2 + 2\omega^2\gamma k^2\beta + 4\omega^2\gamma k^2\alpha
\end{gathered}$$

It enables putting the solution in the following form

$$n^+ = n^+(\theta) = A_1 + A_2\exp(p_2\theta) + A_3\exp(p_3\theta),$$

Here the second term describes a wave that attenuates in space but increases exponentially to infinity. On the contrary the third term describes a solitary wave decaying in time with an increase in amplitude over space.

In order to satisfy arbitrary boundary conditions one needs all three functions, so in a linear formulation one cannot avoid the amplitude growth to infinity. On the other hand, there is a stable solution

$$n^+ = n^+(\theta) = A_1\,.$$

If the concentration is uniform, then this uniform concentration can remain forever. Once distortions in the boundary conditions and/or any inhomogeneities occured, all three solutions appear and the concentration magnitude increases exponentially. This explains the critical effect of small inhomogeneities (hydrogen traps) and non-uniform boundary conditions on stability of the entire system.

## 5 Discussion

The discrepancy between the theoretical and experimental data in Fig. 3 observed for small initial diffuse hydrogen content can be explained by the nonhydrogen effect. The remaining points demonstrate a good coincidence which can be viewed as confirmation that the present model is adequate.

This model describes the material fracture without any preliminary assumptions about existence of microcracks or a certain concentration of dislocation and their orientation [14]. This approach is also differs from the way of modeling the hydrogen embrittlement by introducing the parameter of crack resistance [69].

According to a large array of experimental studies that were carried out for decades [44, 64] the extraordinary strong influence of hydrogen can be explained only by the micro-localization of its accumulation in traps like cracks and dislocations. The attempts to describe the mechanism by means of HELP or HEDE models lead to a need to describe the processes at different scales simultaneously and even under the condition that the process at the micro level is localized in the material and unstable it time. As a result, one needs to prescribe some averaged characteristics (i.e. smearing of singularities) which is actually deprives these models the initial physical transparency.

To justify the constitutive law HELP model [66] has to use the models of the hydrogen influence, which give a visible effect in terms of changes in the local characteristics of the metal only at the local hydrogen concentrations of the order of 1:1 with the atoms of metal. It is difficult to imagine from a physical perspective since the lattice of the solid hydrogen has the constant which is one and half times larger than the constant of the most metals.

The main advantage of the constitutive law and equations of the bi-component model is that they are applicable at the macro-level. Micro-mechanisms of the influence of hydrogen have been included in the rheological model. Parameters $\alpha$, $\beta$, $E_H$, $k_0$ and $k_1$ should be determined in terms of the macro-quantities such as the experimental strain—stress diagrams.

Despite the seeming simplicity of this approach and the large number of published data, not all of them can be used for the approximation. Almost all experimental data were obtained as a result of the saturation of specimens either in the electrolyte solution or in gaseous hydrogen.

In spite of the established conception of the rapid redistribution of hydrogen inside the metal under the concentration gradient, a simple calculation shows that such a redistribution can last from tens of hours to several years depending upon the binding energy of the traps with hydrogen from the surface layer of the environment. Our own experiments show that in the case of hydrogenation with the electroplating of zinc the hydrogen concentrations are not aligned within one year of exposure of the specimens at the room temperature.

Thus, when determining the characteristics of rheological model one should perform a correct determination of the hydrogen concentration and its volume distribution. This presents problems and the most researchers determine this parameter indirectly in terms of the cathode current and charging time. As a result, the data obtained are not suitable for approximation since the hydrogen is localized on the surface. For example, there exists no dependence of tensile strength on the hydrogen charging time, cf. [18].

The presence of the descending part on $\sigma(\varepsilon)$ diagram of the material with hydrogen implies instability of the material under load. Under real loading the failure will take place when the maximum point of the curve $\sigma(\varepsilon)$ is achieved and this fact can be interpreted as the tensile strength due to the hydrogen saturation.

The governing equation for 1-D diffusion is shown to be reduced to a generalized Mathieu equation. A closed form expression for the principle instability regions is obtained and a safe level of harmonic load is determined under which the fatigue fracture does not occur. Using the bicontinual model, we were able to describe the experimentally observed "resonant effect" which is observed experimentally [46, 52, 73]. This effect is described without additional assumptions about presence and parameters of the fatigue crack.

The generating solution of the equations for concentration of the bound hydrogen in a thin surface layer is of the wave nature for any non-uniform distribution of hydrogen concentration over the surface.

This solution always has a complex frequency of oscillations which describes the magnitude of the concentration wave that exponentially increases in time. Due to the equations of bicontinua solid it leads to degradation of the mechanical characteristics of the material in regions of maximum hydrogen concentration. Such non-uniform characteristics can easily explain the occurrence of bands of localization of plastic deformation especially since often they have a characteristic wavelength. In other words, they are spaced approximately at the same distance from each other on the sample surface.

This novel approach is of great practical importance since it makes it possible to relate the hydrogen concentration to the plastic deformation of material. Thus measurements of the concentration of dissolved hydrogen can be used to estimate the residual life of materials and structures.

## 6 Conclusions

A model is constructed which allows one to describe the kinetics of hydrogen in metals, and in particular to estimate the hydrogen transition from mobile into bounded state depending on the stress-state relation and to describe the localization of the connected hydrogen resulting in the material fracture.

We suggest a novel approach to modeling the solids with account for the influence of hydrogen on the properties of free surface on monocrystals at various scales.

Application of the bi-component model to describing the multiscale materials allows obtaining the adequate results which describe the hydrogen influence on properties of these structures.

**Acknowledgements** The research is carried out under the financial support by Russian Science Foundation, project 18-19-00413.

## References

1. Alekseeva, E., Alhimenko, A., Belyaev, A., Lobachev, A., Polyanskiy, V., Rostovykh G., Tretyakov, D., Shtukin, L., Yakovlev, Y.: Evaluation of stress-strain state and cracking of weatherproof structural steel by acoustoelasticity. Stroitel'stvo Unikal'nyh Zdanij i Sooruzenij (12), 33 (2016)
2. Alvaro, A., Olden, V., Akselsen, O.M.: 3d cohesive modelling of hydrogen embrittlement in the heat affected zone of an X70 pipeline steel. Int. J. Hydrog. Energy **38**(18), 7539–7549 (2013)
3. Alvaro, A., Olden, V., Akselsen, O.M.: 3d cohesive modelling of hydrogen embrittlement in the heat affected zone of an X70 pipeline steel part II. Int. J. Hydrog. Energy **39**(7), 3528–3541 (2014)
4. Andronov, D., Arseniev, D., Polyanskiy, A., Polyanskiy, V., Yakovlev, Y.: Application of multichannel diffusion model to analysis of hydrogen measurements in solid. Int. J. Hydrog. Energy **42**(1), 699–710 (2017)
5. Belyaev, A., Polyanskiy, A., Polyanskiy, V., Sommitsch, C., Yakovlev, Y.A.: Multichannel diffusion vs tds model on example of energy spectra of bound hydrogen in 34crnimo6 steel after a typical heat treatment. Int. J. Hydrog. Energy **41**(20), 8627–8634 (2016)
6. Belyaev, A., Polyanskiy, A., Polyanskiy, V., Yakovlev, Y.: Parametric instability in cyclic loading as the cause of fracture of hydrogenous materials. Mech. Solids **47**(5), 533–537 (2012)
7. Belyaev, A.K., Blekhman, I.I., Polyanskiy, V.A.: Equation for the evolution of trapped hydrogen in an elastic rod subjected to high-frequency harmonic excitation. Acta Mech. **227**(5), 1515–1518 (2016)
8. Belyaev, A.K., Grishchenko, A.I., Polyanskiy, V.A., Semenov, A.S., Tretyakov, D.A., Shtukin, L.V., Arseniev, D.G., Yakovlev, Y.A.: Acoustic anisotropy and dissolved hydrogen as an indicator of waves of plastic deformation. In: 2017 Days on Diffraction (DD), pp. 39–44, June 2017
9. Belyaev, A.K., Lobachev, A.M., Modestov, V.S., Pivkov, A.V., Polyanskii, V.A., Semenov, A.S., Tret'yakov, D.A., Shtukin, L.V.: Estimating the plastic strain with the use of acoustic anisotropy. Mech. Solids **51**(5), 606–611 (2016)
10. Belyaev, A.K., Polyanskiy, V.A., Grishchenko, A.I., Lobachev, A.M., Mansyrev, D.I., Modestov, V.S., Pivkov, A.V., Semenov, A.S., Shtukin, L.V., Tretyakov, D.A., Yakovlev, Y.A.: Application of the acoustic anisotropy approach for technical diagnostics of structures with large plastic deformations. AIP Conf. Proc. **1785**(1), 030004 (2016)
11. Belyaev, A.K., Polyanskiy, V.A., Lobachev, A.M., Modestov, V.S., Semenov, A.S., Grishchenko, A.I., Yakovlev, Y.A., Shtukin, L.V., Tretyakov, D.A.: Propagation of sound waves in stressed elasto-plastic material. In: 2016 Days on Diffraction (DD), pp. 56–61, June 2016
12. Belyaev, A.K., Polyanskiy, V.A., Yakovlev, Y.A:. Hydrogen as an indicator of high-cycle fatigue. In: Procedia IUTAM, Dynamical Analysis of Multibody Systems with Design Uncertainties, vol. 13, pp. 138–143 (2015)

13. Belyaev, A.K., Polyanskiy, V.A., Yakovlev, Y.A., Mansyrev, D.E., Polyanskiy, A.M.: Surface effect of the waves of plastic deformation and hydrogen distribution in metals. In: 2017 Days on Diffraction (DD), pp. 45–50, June 2017
14. Birnbaum, H., Sofronis, P.: Hydrogen-enhanced localized plasticitya mechanism for hydrogen-related fracture. Mater. Sci. Eng.: A **176**(12), 191–202 (1994)
15. Bond, G., Robertson, I., Birnbaum, H.: The influence of hydrogen on deformation and fracture processes in high-strength aluminum alloys. Acta Metall. **35**(9), 2289–2296 (1987)
16. Bourcier, R., Koss, D.: Hydrogen embrittlement of titanium sheet under multiaxial states of stress. Acta Metall. **32**(11), 2091–2099 (1984)
17. Brouwer, R.D., De Jong, E.C.J.N., De Mul, L.M., Handel, G.: Modelling Hydrogen Induced Crack Growth: Validation by Comparison with Experiment. NACE International, Houston, TX, US, Oct 1995
18. Bueno, A., Moreira, E., Gomes, J.: Evaluation of stress corrosion cracking and hydrogen embrittlement in an API grade steel. Eng. Fail. Anal. **36**, 423–431 (2014)
19. Delafosse, D., Magnin, T.: Interfaces in stress corrosion cracking: a case study in duplex stainless steels. In: Solid State Phenomena, vol. 59, pp. 221–250. Trans Tech Publ (1998)
20. Delafosse, D., Magnin, T.: Hydrogen induced plasticity in stress corrosion cracking of engineering systems. Eng. Fract. Mech. **68**(6), 693–729 (2001)
21. Forrest, P.G.: Fatigue of Metals. Elsevier (2013)
22. Ghadbeigi, H., Pinna, C., Celotto, S., Yates, J.: Local plastic strain evolution in a high strength dual-phase steel. Mater. Sci. Eng.: A **527**(18), 5026–5032 (2010)
23. Gludovatz, B., Hohenwarter, A., Catoor, D., Chang, E.H., George, E.P., Ritchie, R.O.: A fracture-resistant high-entropy alloy for cryogenic applications. Sci. **345**(6201), 1153–1158 (2014)
24. Gorsky, W.: Theorie der elastischen nachwirkung in ungeordneten mischkristallen (elastische nachwirkung zweiter art.). Physikalische Zeitschrift der Sowjetunion **8**, 457–471 (1935)
25. Gorsky, W.: Theorie der elastischen nachwirkung in ungeordneten mischkristallen von cuau. Phys. Z. Sowjetunion **8**, 443–456 (1935)
26. Grishchenko, A.I., Modestov, V.S., Polyanskiy, V.A., Tretyakov, D.A., Shtukin, L.V.: Experimental investigation of the acoustic anisotropy field in the sample with a stress concentrator. St. Petersburg Polytech. Univ. J.: Phys. Math. **3**(1), 77–82 (2017)
27. Hasegawa, K., Kawamura, K., Urabe, T., Hosoya, Y.: Effects of microstructure on stretch-flange-formability of 980 mpa grade cold-rolled ultra high strength steel sheets. ISIJ Int. **44**(3), 603–609 (2004)
28. Hirao, M., Pao, Y.: Dependence of acoustoelastic birefringence on plastic strains in a beam. J. Acoust. Soc. Am. **77**(5), 1659–1664 (1985)
29. Hirth, J.: Effects of hydrogen on the properties of iron and steel. Metall. Trans. A **11**(6), 861–890 (1980)
30. Ignatenko, A., Pokhodnya, I., Paltsevich, A., Sinyuk, V.: Dislocation model of hydrogen-enhanced localizing of plasticity in metals with bcc latttice. Paton Weld. J. **3**, 15–19 (2012)
31. Indeitsev, D., Osipova, E., Polyanskiy, V.: A statistical model of hydrogen-induced fracture of metals. Dokl. Phys. **59**(11), 534–538 (2014)
32. Indeitsev, D., Semenov, B.: About a model of structural-phase transformations under hydrogen influence. Acta Mech. **195**(1–4), 295–304 (2008)
33. Kalk, A., Nortmann, A., Schwink, C.: Dynamic strain ageing and the boundaries of stable plastic deformation in cu-mn single crystals. Philos. Mag. A **72**(5), 1239–1259 (1995)
34. Kamyshev, A.V., Makarov, S.V., Pasmanik, L.A., Smirnov, V.A., Modestov, V.S., Pivkov, A.V.: Generalized coefficients for measuring mechanical stresses in carbon and low-alloyed steels by the acoustoelasticity method. Russ. J. Nondestruct. Test. **53**(1), 1–8 (2017)
35. Kanezaki, T., Narazaki, C., Mine, Y., Matsuoka, S., Murakami, Y.: Effects of hydrogen on fatigue crack growth behavior of austenitic stainless steels. Int. J. Hydrog. Energy **33**(10), 2604–2619 (2008)
36. Kirchheim, R.: Hydrogen solubility and diffusivity in defective and amorphous metals. Prog. Mater. Sci. **32**(4), 261–325 (1988)

37. Koyama, M., Akiyama, E., Lee, Y.-K., Raabe, D., Tsuzaki, K.: Overview of hydrogen embrittlement in high-mn steels. Int. J. Hydrog. Energy **42**(17), 12706–12723 (2017)
38. Koyama, M., Springer, H., Merzlikin, S.V., Tsuzaki, K., Akiyama, E., Raabe, D.: Hydrogen embrittlement associated with strain localization in a precipitation-hardened femnalc light weight austenitic steel. Int. J. Hydrog. Energy **39**(9), 4634–4646 (2014)
39. Kudinova, N.R., Polyanskiy, V.A., Polyanskiy, A.M., Yakovlev, Y.A.: Contribution of surface tension energy during plastic deformation of nanomaterials. Dokl. Phys. **61**(10), 514–516 (2016)
40. Lebyodkin, M., Brechet, Y., Estrin, Y., Kubin, L.: Statistical behaviour and strain localization patterns in the portevin-le chatelier effect. Acta Mater. **44**(11), 4531–4541 (1996)
41. Leeuwen, H.V.: The kinetics of hydrogen embrittlement: a quantitative diffusion model. Eng. Fract. Mech. **6**(1), 141–161 (1974)
42. Leoni, F., Zapperi, S.: Dislocation mutual interactions mediated by mobile impurities and the conditions for plastic instabilities. Phys. Rev. E **89**, 022403 (2014)
43. Lunarska, E., Wokulski, Z.: Effect of hydrogen charging on stress-strain curves for iron whiskers. Acta Metall. **30**(12), 2173–2179 (1982)
44. Lynch, S.: Hydrogen embrittlement phenomena and mechanisms. Corros. Rev. **30**(3–4), 105–123 (2012)
45. Mackenzie, A., Hancock, J., Brown, D.: On the influence of state of stress on ductile failure initiation in high strength steels. Eng. Fract. Mech. **9**(1), 167–188 (1977)
46. Matsuoka, S., Tanaka, H., Homma, N., Murakami, Y.: Influence of hydrogen and frequency on fatigue crack growth behavior of cr-mo steel. Int. J. Fract. **168**(1), 101–112 (2011)
47. McCormigk, P.: A model for the portevin-le chatelier effect in substitutional alloys. Acta Metall. **20**(3), 351–354 (1972)
48. McVeigh, C., Vernerey, F., Liu, W.K., Moran, B., Olson, G.: An interactive micro-void shear localization mechanism in high strength steels. J. Mech. Phys. Solids **55**(2), 225–244 (2007)
49. Moriconi, C., Hnaff, G., Halm, D.: Cohesive zone modeling of fatigue crack propagation assisted by gaseous hydrogen in metals. Int. J. Fatigue **68**, 56–66 (2014)
50. Murakami, Y., Kanezaki, T., Mine, Y., Matsuoka, S.: Hydrogen embrittlement mechanism in fatigue of austenitic stainless steels. Metall. Mater. Trans. A **39**(6), 1327 (2008)
51. Murakami, Y., Matsunaga, H.: The effect of hydrogen on fatigue properties of steels used for fuel cell system. Int. J. Fatigue **28**(11), 1509–1520 (2006). Third International Conference on Very High Cycle Fatigue (VHCF-3)
52. Murakami, Y., Matsuoka, S.: Effect of hydrogen on fatigue crack growth of metals. Eng. Fract. Mech. **77**(11), 1926–1940 (2010). International Conference on Crack Paths, 2009
53. Nagumo, M.: Function of hydrogen in embrittlement of high-strength steels. ISIJ Int. **41**(6), 590–598 (2001)
54. Nie, Y., Kimura, Y., Inoue, T., Yin, F., Akiyama, E., Tsuzaki, K.: Hydrogen embrittlement of a 1500-mpa tensile strength level steel with an ultrafine elongated grain structure. Metall. Mater. Trans. A **43**(5), 1670–1687 (2012)
55. Oda, Y., Noguchi, H.: Observation of hydrogen effects on fatigue crack growth behaviour in an 18cr-8ni austenitic stainless steel. Int. J. Fract. **132**(2), 99–113 (2005)
56. Oriani, R.: The diffusion and trapping of hydrogen in steel. Acta Metall. **18**(1), 147–157 (1970)
57. Pan, Y., Guan, W., Wen, M., Zhang, J., Wang, C., Tan, Z.: Hydrogen embrittlement of pt3zr compound from first-principles. J. Alloy. Compd. **585**, 549–554 (2014)
58. Pao, Y.-H.: Theory of acoustoelasticity and acoustoplasticity. In: Achenbach, J.D., Rajapakse, Y. (eds.) Solid Mechanics Research for Quantitative Non-destructive Evaluation, pp. 257–273. Springer Netherlands, Dordrecht (1987)
59. Pao, Y.-H., Wu, T.-T., Gamer, U.: Acoustoelastic birefringences in plastically deformed solids: part itheory. J. Appl. Mech. **58**(1), 11–17 (1991)
60. Penning, P.: Mathematics of the portevin-le chatelier effect. Acta Metall. **20**(10), 1169–1175 (1972)
61. Polyanskiy, A., Polyanskiy, V., Yakovlev, Y.A.: Experimental determination of parameters of multichannel hydrogen diffusion in solid probe. Int. J. Hydrog. Energy **39**(30), 17381–17390 (2014)

62. Polyanskiy, A., Popov-Diumin, D., Polyanskiy, V.: Determination of hydrogen binding energy in various materials by means of absolute measurements of its concentration in solid probe. In: Veziroglu, T.N., Zaginaichenko, S.Y., Schur, D.V., Baranowski, B., Shpak, A.P., Skorokhod, V.V., Kale, A. (eds.) Hydrogen Materials Science and Chemistry of Carbon Nanomaterials, pp. 681–692. Springer Netherlands, Dordrecht (2007)
63. Polyanskiy, V.A., Belyaev, A.K., Arseniev, D.G., Yakovlev, Y.A., Polyanskiy, A.M., Stoschka, M.: Measurement of dissolved hydrogen distributions after ultrasonic peening of heat-affected zone of welded joint. AIP Conf. Proc. **1785**(1), 030022 (2016)
64. Robertson, I., Sofronis, P., Nagao, A., Martin, M., Wang, S., Gross, D., Nygren, K.: Hydrogen embrittlement understood. Metall. Mater. Trans. B **46**(3), 1085–1103 (2015)
65. Senkov, O., Wilks, G., Scott, J., Miracle, D.: Mechanical properties of nb25mo25ta25w25 and v20nb20mo20ta20w20 refractory high entropy alloys. Intermet. **19**(5), 698–706 (2011)
66. Sofronis, P., Liang, Y., Aravas, N.: Hydrogen induced shear localization of the plastic flow in metals and alloys. Eur. J. Mech.—A/Solids **20**(6), 857–872 (2001)
67. Spitzig, W., Talda, P., Wei, R.: Fatigue-crack propagation and fractographic analysis of 18ni(250) maraging steel tested in argon and hydrogen environments. Eng. Fract. Mech. **1**(1), 155–166 (1968)
68. Taha, A., Sofronis, P.: A micromechanics approach to the study of hydrogen transport and embrittlement. Eng. Fract. Mech. **68**(6), 803–837 (2001)
69. Traidia, A., Alfano, M., Lubineau, G., Duval, S., Sherik, A.: An effective finite element model for the prediction of hydrogen induced cracking in steel pipelines. Int. J. Hydrog. Energy **37**(21), 16214 – 16230 (2012). Advances in Hydrogen Production (Selected papers from ICH2P-2011)
70. Ulmer, D., Altstetter, C.: Hydrogen-induced strain localization and failure of austenitic stainless steels at high hydrogen concentrations. Acta Metall. Mater. **39**(6), 1237–1248 (1991)
71. Varias, A., Massih, A.: Simulation of hydrogen embrittlement in zirconium alloys under stress and temperature gradients. J. Nucl. Mater. **279**(23), 273–285 (2000)
72. Wang, F., Zhang, Y., Chen, G., Davies, H.A.: Tensile and compressive mechanical behavior of a cocrcufenial0.5 high entropy alloy. Int. J. Mod. Phys. B **23**(06n07), 1254–1259 (2009)
73. Yamabe, J., Yoshikawa, M., Matsunaga, H., Matsuoka, S.: Effects of hydrogen pressure, test frequency and test temperature on fatigue crack growth properties of low-carbon steel in gaseous hydrogen. Procedia Struct. Integr. **2**, 525–532. 21st European Conference on Fracture, ECF21, 20–24 June 2016. Catania, Italy (2016)
74. Yu, H., Olsen, J.S., He, J., Zhang, Z.: Hydrogen-microvoid interactions at continuum scale. Int. J. Hydrog. Energy **43**(21), 10104–10128 (2018)
75. Zhang, Z., Mao, M.M., Wang, J., Gludovatz, B., Zhang, Z., Mao, S.X., George, E.P., Yu, Q., Ritchie, R.O.: Nanoscale origins of the damage tolerance of the high-entropy alloy crmnfeconi. Nat. Commun. **6**, 10143 (2015)
76. Zybell, L., Mühlich, U., Kuna, M.: Constitutive equations for porous plane-strain gradient elasticity obtained by homogenization. Arch. Appl. Mech. **79**(4), 359 (2008)

# Modeling of Elastic-Plastic Deformation Based on Updated Initial Configuration of Solid Body

**Nikolay M. Bessonov**

**Abstract** In this paper we discuss some modifications of the classical two-step algorithm (elastic-predictor, inelastic-corrector) usually called the radial return-map method. The neo-Hooke rheological model is employed in the analysis of elastic behavior instead of the Hooke model. The von Mises yield criterion $-J_2(\mathbf{S}) \leq \sigma_s^2/3$ is used in the equivalent form $-J_2(\mathbf{B}_D) \leq \sigma_s^2/(3\mu^2)$. The main difference of the proposed algorithm in comparison with the traditional one is that in the simulations of plastic deformations we switch the emphasis from corrections of the stress tensor to irreversible corrections of the initial configuration of the solid body. The stress tensor is automatically corrected by this procedure. The implicit integration method is suggested for the correction of the initial configuration in the case of plastic flows. While changing the initial configuration, we automatically get plastic (irreversible) deformation at any time step. This algorithm allows us to calculate residual stresses in the elastic-plastic solid after removing the external load as a result of unloading after non-uniform plastic deformation. It is also used for an accurate simulation of deformations of both perfectly plastic and elastic-plastic solids with workhardening including the Bauschinger effect. Numerical examples show some advantages of the algorithm developed in this work for a springback problem.

**Keywords** Clastic-plastic flow · Computational plasticity · Return-map algorithm · Updated initial configuration · Bauschinger effect

**AMS subject classification:** 74C15 · 74M15 · 65M06

## 1 Introduction

A radial return-map two-step algorithm (elastic-predictor, plastic-corrector) was developed in order to correct the stress tensor components. It is widely used for time-discrete elastic-plastic models. At the first step, a purely elastic trial state is

---

N. M. Bessonov (✉)
Institute of the Problems of Mechanical Engineering, 199178 St. Petersburg, Russia
e-mail: nickbessonov1@gmail.com; nickbessonov@yahoo.com

H. Altenbach et al. (eds.), *Dynamical Processes in Generalized Continua and Structures*, Advanced Structured Materials 103,
https://doi.org/10.1007/978-3-030-11665-1_5

computed. If the constitutive model it violated, an inelastic correction is computed at the second step using the trial state as an initial condition.

Wilkins [33, 34] was among the first who tried this algorithm, splitting the total deformation between the elastic and plastic components. This approach is still being used with few modifications ([1–4, 7–12, 17, 19, 20, 22, 23, 25, 26, 28–32, 35–37] and more).

In the literature cited above, the return-map algorithm is used both directly and with some additional development. In this paper we will discuss some possible modifications of the Wilkins (or classical) method whose efficacy we have verified in practice. We use a more general formulation of the problem for simulation of the elastic part of the deformation, neo-Hooke's law instead of Hooke's law. Moreover, this formulation also allows us to avoid unnecessary differentiation with respect to time and to avoid corrections of the stress rotation (Eqs. 6 and 7). Thus, we consider a more general formulation of the problem and simplify its practical realization. Let us emphasize that the introduction of neo-Hooke's law in the algorithm changes our point of view on the plastic part of the deformation and brings us to the idea to describe it as a process of continuous modification of the initial configuration of the solid.

## 2 Short Description of the Classical Time-Stepping Return-Map Algorithm

Let us analyze schematically the classical time-stepping return-map algorithm with the minimum level of detail needed for the explanation of our modifications (see [33, 34] for further details).

Initially, the Lagrangian mesh is introduced; a fragment of the 2D mesh is shown in Fig. 1a. The computational domain is divided into cells. Each cell consists of two triangles in the 2D case (or six tetrahedra in the 3D case) called elements as illustrated in Fig. 1b and 1c, respectively. A control volume $V$ with mass $M$ (gray in Fig. 1a) corresponds to every node of the mesh.

For calculation of the new values of the velocity at each node, the explicit approximation is used. The conservation of momentum law may be represented by the equality:

$$M\frac{\vec{\mathbf{v}}^{n+1}-\vec{\mathbf{v}}^{n}}{\Delta t}=\oint_{S}\boldsymbol{\sigma}\cdot d\vec{\mathbf{s}} \tag{1}$$

where $\vec{\mathbf{v}}^{n+1}$ and $\vec{\mathbf{v}}^{n}$ are velocities at the "new" and "old" time steps, respectively, $\Delta t$ is the time step, $\boldsymbol{\sigma}$ is the stress tensor, $S$ is the surface of $V$, $d\vec{\mathbf{s}}=\vec{\mathbf{n}}dS$, and $\vec{\mathbf{n}}$ is an outward normal vector to $S$. In the explicit algorithm, all quantities included in the right-hand sides of the equations (in particular, in Eq. (1)) are taken from the old time step unless they are already calculated at the new time step. In order to simplify

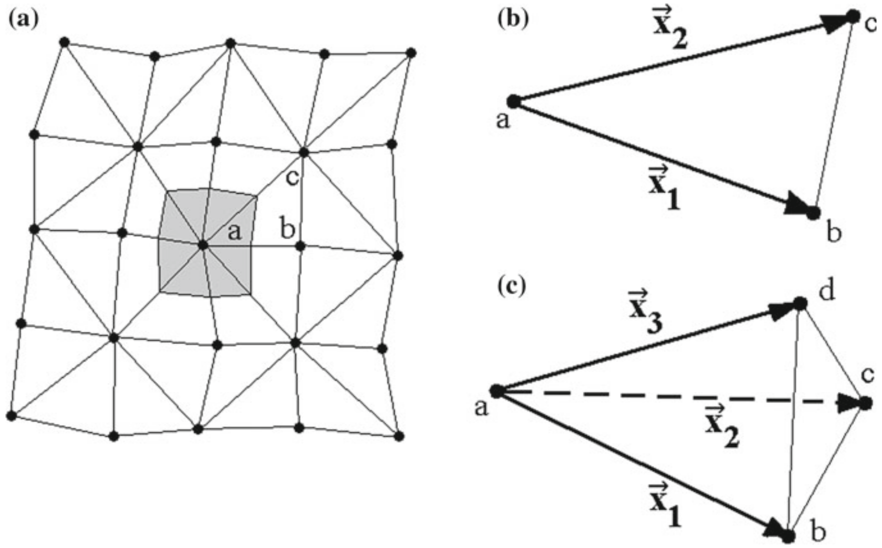

**Fig. 1** **a** Fragment of 2D Lagrangian mesh (• are nodes); **b** 2D element; **c** 3D element

the notation, we omit the superscript showing the number of the time step in the right-hand sides of the equations.

For every node of the mesh we have

$$\frac{\vec{\mathbf{x}}^{n+1} - \vec{\mathbf{x}}^{n}}{\Delta t} = \vec{\mathbf{v}}, \tag{2}$$

where $\vec{\mathbf{x}}$ is the radius-vector of the node. The stress tensor $\boldsymbol{\sigma}$ is defined at the elements of the mesh and decomposed as the sum of spherical and deviatoric parts:

$$\boldsymbol{\sigma} = \mathbf{I}p + \mathbf{S}, \tag{3}$$

where $\mathbf{I}$ is the unit tensor. A perfectly elastic material is characterized by a linear relationship between the stress and the strain in the form of the Hooke model:

$$p = K\nabla_{\vec{\mathbf{x}}} \cdot \vec{\mathbf{u}}, \tag{4}$$

$$\mathbf{S} = \mu \left( \nabla_{\vec{\mathbf{x}}}\vec{\mathbf{u}} + \vec{\mathbf{u}}\nabla_{\vec{\mathbf{x}}} - \mathbf{I}\frac{2}{3}\nabla_{\vec{\mathbf{x}}} \cdot \vec{\mathbf{u}} \right), \tag{5}$$

where $K$ and $\mu$ are the bulk and the shear elastic modulus, respectively, $\vec{\mathbf{u}}$ is the displacement of the node, $\nabla_{\vec{\mathbf{x}}}\vec{\mathbf{u}} = \partial u_k/\partial x_m \vec{\mathbf{e}}_m \vec{\mathbf{e}}_k$, $\vec{\mathbf{u}}\nabla_{\vec{\mathbf{x}}} = \partial u_k/\partial x_m \vec{\mathbf{e}}_k \vec{\mathbf{e}}_m$, $\vec{\mathbf{e}}_k$ are base unit vectors of a fixed rectangular cartesian coordinate system ($k = 1, 2, 3$). The summation convention over the repeated indices is assumed.

Equations (4) and (5) are differentiated by time and are written, respectively, as

$$\frac{p^{n+1}-p^{n}}{\Delta t}=K\nabla_{\vec{\mathbf{x}}}\cdot\vec{\mathbf{v}}, \tag{6}$$

$$\frac{\mathbf{S}'-\mathbf{S}^{n}}{\Delta t}=\mu\left(\nabla_{\vec{\mathbf{x}}}\vec{\mathbf{v}}+\vec{\mathbf{v}}\nabla_{\vec{\mathbf{x}}}-\mathbf{I}\frac{2}{3}\nabla_{\vec{\mathbf{x}}}\cdot\vec{\mathbf{v}}\right)+\boldsymbol{\gamma}, \tag{7}$$

where $\boldsymbol{\gamma}=\mathbf{S}\cdot\boldsymbol{\Omega}-\boldsymbol{\Omega}\cdot\mathbf{S}$ corresponds to the correction resulting from the rigid body rotation, $\boldsymbol{\Omega}$ is the spin tensor. More detailed explanation why in left hand side of Eq. (7) $\mathbf{S}'$ is used instead of $\mathbf{S}^{n+1}$ will be provided below.

According to the theory of plastic flows, all possible stress states corresponding to the plastic yield constitute a closed hyper-surface in the stress space [21, 24]. The yield function can be written in the general form as

$$F(\mathbf{S})\leq K, \tag{8}$$

where $K$ is the material constant. Condition (8) determines the restrictions on the stress field. The von Mises yield criterion is a particular case of condition (8) and is conventionally used to describe the elastic limit:

$$-J_2(\mathbf{S})\leq\frac{\sigma_s^2}{3}\ , \tag{9}$$

where $\sigma_s$ is the limit of elastic stress. When the new values of the deviatoric part of the stress tensor $\mathbf{S}'$ are found from Eq. (7), condition (9) is verified (predictor step). If (9) is satisfied, then $\mathbf{S}^{n+1}=\mathbf{S}'$; otherwise, the values of the deviatoric stress tensor are corrected according to the formula (corrector step)

$$\mathbf{S}^{n+1}=m\mathbf{S}', \tag{10}$$

where

$$m=\frac{\sigma_s}{\sqrt{-3J_2(\mathbf{S}')}}\ . \tag{11}$$

This approach allows the correction of the deviatoric stress tensor, so that the following equation is valid:

$$-J_2(\mathbf{S}^{n+1})=\frac{\sigma_s^2}{3}\ . \tag{12}$$

Finally, we find the new value of the stress tensor:

$$\boldsymbol{\sigma}^{n+1}=\mathbf{I}p^{n+1}+\mathbf{S}^{n+1}\ , \tag{13}$$

and we can proceed to the next time step.

# 3 Formulation of a New Time-Stepping Return-Map Algorithm

## 3.1 1D Example

We start with a simple example. Let us consider an elastic-plastic spring with the initial length $X$ (at $t = 0$) and the actual length $x$ (at time $t$). We can represent the spring as a single 1D elastic-plastic element of the mesh. Assume that the stress $\sigma$ depends on $x$:

$$\sigma = E\left(\frac{x}{X} - 1\right) \tag{14}$$

and the plasticity condition is

$$\sigma^2 \le \sigma_s^2, \tag{15}$$

where $\sigma_s$ is the limit of elastic stress and $E$ is the material coefficient. Using Eqs. (14) and (15), we obtain an equivalent expression for the plasticity condition:

$$\left(\frac{x}{X} - 1\right)^2 \le \frac{\sigma_s^2}{E^2} = \varepsilon_s^2, \tag{16}$$

where $\varepsilon_s$ is the limit of elastic strain.

Let us solve the problem "numerically", step by step in time. Suppose that the length $x$ changes at each time step and that we calculate the new value of the actual length $x^{n+1}$ instead the old one $x^n$ (predictor step). After that we must check condition (16). If this condition holds true, then the deformation remains elastic. This means that once the force is removed, the spring returns to its initial length, i.e. $x \to X$.

Suppose that at some time step, condition (16) is no longer satisfied. Therefore, plastic deformation begins, and the change of the material is irreversible, i.e., it will not return to the initial length $X$ when we remove the external force. From this analysis we can naturally conclude that if condition (16) is not satisfied, then we must change the initial configuration $X$, which should also depend on $n$. We denote it by $X^n$. In particular, if condition (16) remains true, then $X^{n+1} = X^n$.

Thus, if we calculate the value $J_2 = -\left(x^{n+1}/X^n - 1\right)^2$ and find that $-J_2 > k^2$, then we make a corrector step and define the new, updated value of the initial configuration $X^{n+1}$ which satisfies the following equation:

$$\left(\frac{x^{n+1}}{X^{n+1}} - 1\right)^2 = \varepsilon_s^2. \tag{17}$$

All information about the initial configuration is contained in the multiplier $1/X$ in condition (16). In order to have the presentation similar to the 3D case, which will be considered below, we define here the initial configuration as $1/X$, and not as $X$. This modification is not essential for what follows.

If $1/X = 1/X^n$, then condition (16) is violated while for $1/X = 1/x^{n+1}$ it is satisfied and the left-hand side of (16) becomes equal to zero. For this reason, we choose $1/X^{n+1}$ in the interval between $1/X^n$ and $1/x^{n+1}$, i.e.,

$$\frac{1}{X^{n+1}} = a\frac{1}{X^n} + (1-a)\frac{1}{x^{n+1}}\ , \tag{18}$$

where $a$ is a parameter, $0 < a < 1$. Let us substitute (18) into Eq. (17) and choose $a$ such that the following equality is satisfied:

$$\left[x^{n+1}\left(a\frac{1}{X^n} + (1-a)\frac{1}{x^{n+1}}\right) - 1\right]^2 = \varepsilon_s^2 \tag{19}$$

As a result we obtain

$$a = \pm\frac{\varepsilon_s}{\sqrt{-J_2}} \tag{20}$$

and keep only the positive solution. We calculate the new initial configuration $1/X^{n+1}$ substituting the value of $a$ in (18). Note that in this example we can find $1/X^{n+1}$ from Eq. (17) in a single step. We do it by intermediate of Eqs. (18)–(20) in order to show how it will work in the 3D case.

The new value of the initial configuration satisfies the plastic yield condition exactly, so that we can move to the next time step.

Obviously, if we remove the external force at this time step, then the spring returns back to the last updated value of the initial length, i.e., $x \to X^{n+1}$. After the correction of the initial configuration, the value of $\sigma^{n+1}$ calculated from Eq. (14) satisfies the equality in condition (15).

Let us summarize the above discussion. At each time step, if condition (16) is not satisfied, then we adjust the initial configuration and calculate the new one. The old one is "forgotten" by the material. If at this moment of time we remove the external force, then the spring returns to its new initial length $X^{n+1}$.

At the elastic stage the initial length does not change, $X^{n+1} = X^n$. At each time step, the difference $X^{n+1} - X^n$ is equal to the plastic (irreversible) deformation.

We emphasize that the meaning of the expression "initial configuration" is changed here. It is no longer the length at the initial moment of time but the length to which the spring returns when we remove the external force. Hence, the initial length defined in this way depends on time.

## *3.2 Return-Map Algorithm for 3D Case*

We can now try to generalize the approach discussed above to the 3D unsteady elastic-plastic problem. Let us critically review the basic system of equations employed in

Wilkins' method (Eqs. 1–5) in order to define the components responsible for the initial configuration of the solid.

Equation (1) represents conservation of momentum expressed in the general integral form; Eq. (2) represents velocity as derivative of the displacement; Eq. (3) represents the stress tensor consisting of spherical and deviatoric parts. Equations (1)–(3) are expressed in appropriate general form. More attention should be paid to Eqs. (4) and (5) where Eqs. (6) and (7) follow from. The classical return map algorithm does not include any evidence of the initial configuration of the solid. In order to bring it back into the rheological model, we will use the neo-Hooke model with constitutive equation for the Cauchy stress tensor [1, 27] instead of Eqs. (4) and (5):

$$p = K\left(\frac{V}{V_0} - 1\right), \tag{21}$$

$$\mathbf{S} = \mu\left[\mathbf{B} - \frac{1}{3}\mathbf{I}J_1(\mathbf{B})\right] = \mu\mathbf{B}_D, \tag{22}$$

where

$$\mathbf{B} = \mathbf{F}\cdot\mathbf{F}^T \tag{23}$$

is the left Cauchy-Green deformation tensor,

$$\mathbf{F} = \frac{d\vec{\mathbf{x}}}{d\vec{\mathbf{X}}} = \vec{\mathbf{x}}\nabla_{\vec{\mathbf{X}}} = \frac{\partial x_i}{\partial X_m}\vec{\mathbf{e}}_i\vec{\mathbf{e}}_m = \begin{vmatrix} \frac{\partial x_1}{\partial X_1} & \frac{\partial x_1}{\partial X_2} & \frac{\partial x_1}{\partial X_3} \\ \frac{\partial x_2}{\partial X_1} & \frac{\partial x_2}{\partial X_2} & \frac{\partial x_2}{\partial X_3} \\ \frac{\partial x_3}{\partial X_1} & \frac{\partial x_3}{\partial X_2} & \frac{\partial x_3}{\partial X_3} \end{vmatrix} \tag{24}$$

is the deformation gradient, $\vec{\mathbf{x}}$ is the actual position vector, $\vec{\mathbf{X}}$ is the initial position vector, $V$ is the actual volume, and $V_0$ is the initial volume.

Let us analyze how Eqs. (4) and (5) are obtained from Eqs. (21) and (22). Let $\vec{\mathbf{x}} = \vec{\mathbf{X}} + \vec{\mathbf{u}}$. Then

$$\mathbf{B} = \vec{\mathbf{x}}\nabla_{\vec{\mathbf{X}}}\cdot\nabla_{\vec{\mathbf{X}}}\vec{\mathbf{x}} = \left(\vec{\mathbf{u}}\nabla_{\vec{\mathbf{X}}} + \mathbf{I}\right)\cdot\left(\nabla_{\vec{\mathbf{X}}}\vec{\mathbf{u}} + \mathbf{I}\right)$$

Next $\nabla_{\vec{\mathbf{X}}} \approx \nabla_{\vec{\mathbf{x}}}$ is assumed. At this point all the information about the initial configuration is lost. Further,

$$\approx (\vec{\mathbf{u}}\nabla_{\vec{\mathbf{x}}} + \mathbf{I})\cdot(\nabla_{\vec{\mathbf{x}}}\vec{\mathbf{u}} + \mathbf{I}) = \mathbf{I} + \vec{\mathbf{u}}\nabla_{\vec{\mathbf{x}}} + \nabla_{\vec{\mathbf{x}}}\vec{\mathbf{u}} + \vec{\mathbf{u}}\nabla_{\vec{\mathbf{x}}}\cdot\nabla_{\vec{\mathbf{x}}}\vec{\mathbf{u}}$$

Assuming that $\vec{\mathbf{u}}$ is small and the second order terms can be neglected, then

$$\approx \mathbf{I} + \vec{\mathbf{u}}\nabla_{\vec{\mathbf{x}}} + \nabla_{\vec{\mathbf{x}}}\vec{\mathbf{u}} \tag{25}$$

Using the same assumptions, it is possible to obtain

$$J_1(\mathbf{B}) \approx 2\nabla_{\vec{\mathbf{x}}} \cdot \vec{\mathbf{u}} + 3 \quad \text{and} \quad p \approx K\nabla_{\vec{\mathbf{x}}} \cdot \vec{\mathbf{u}} \tag{26}$$

Thus, relations (4) and (5) provide an approximation of relations (21) and (22). In order to retain the information about the initial configuration in the rheological model of the solid, we will use the neo-Hooke model (Eqs. 21 and 22) instead of the Hooke model Eqs. (4) and (5).

Taking into account Eq. (22), we can write condition (8) in the alternative form

$$f(\mathbf{B}_D) \leq k, \tag{27}$$

where $k$ is a material constant. Condition (27) will determine the restrictions on the deformation field. For simplicity, we will limit our analysis to the von Mises yield criterion (9). We can rewrite (9) in the following form:

$$-J_2(\mathbf{B}_D) \leq \frac{4\varepsilon_s^2(1+\nu)^2}{3} \equiv k^2, \tag{28}$$

where $\varepsilon_s = \sigma_s/E$ is the limit of elastic strain, $\nu$ is Poisson's ratio, and $E = 2\mu(1+\nu)$ is Young's modulus.

We will illustrate the specific features of the new return-map algorithm considering only one tetrahedral element of the mesh $abcd$, (Fig. 1c). We denote the initial position of the tetrahedron vertices at the initial time by position-vectors $\vec{\mathbf{X}}_a$, $\vec{\mathbf{X}}_b$, $\vec{\mathbf{X}}_c$ and $\vec{\mathbf{X}}_d$. Due to deformation, the vertices move from their initial positions. We denote the actual position of the vertices at time $t$ by $\vec{\mathbf{x}}_a$, $\vec{\mathbf{x}}_b$, $\vec{\mathbf{x}}_c$ and $\vec{\mathbf{x}}_d$. Let $\vec{\mathbf{x}}_i$ and $\vec{\mathbf{X}}_i$ $(i = 1, 2, 3)$ be the right-hand set of vectors directed along any three different ribs of the tetrahedron:

$$\vec{\mathbf{x}}_1 = \vec{\mathbf{x}}_b - \vec{\mathbf{x}}_a, \quad \vec{\mathbf{x}}_2 = \vec{\mathbf{x}}_c - \vec{\mathbf{x}}_a, \quad \vec{\mathbf{x}}_3 = \vec{\mathbf{x}}_d - \vec{\mathbf{x}}_a \tag{29}$$

and

$$\vec{\mathbf{X}}_1 = \vec{\mathbf{X}}_b - \vec{\mathbf{X}}_a, \quad \vec{\mathbf{X}}_2 = \vec{\mathbf{X}}_c - \vec{\mathbf{X}}_a, \quad \vec{\mathbf{X}}_3 = \vec{\mathbf{X}}_d - \vec{\mathbf{X}}_a \tag{30}$$

We will use the following quantities:

$$V = \frac{1}{6}\vec{\mathbf{x}}_1 \cdot (\vec{\mathbf{x}}_2 \times \vec{\mathbf{x}}_1) \tag{31}$$

is the actual volume of the tetrahedral element,

$$\vec{\mathbf{x}}^1 = \frac{\vec{\mathbf{x}}_2 \times \vec{\mathbf{x}}_3}{6V}, \quad \vec{\mathbf{x}}^2 = \frac{\vec{\mathbf{x}}_3 \times \vec{\mathbf{x}}_1}{6V}, \quad \vec{\mathbf{x}}^3 = \frac{\vec{\mathbf{x}}_1 \times \vec{\mathbf{x}}_2}{6V} \tag{32}$$

is a set of vectors reciprocal with $\vec{\mathbf{x}}_i$, with the properties

$$\vec{\mathbf{x}}_k \cdot \vec{\mathbf{x}}^m = \delta_{km}, \quad \vec{\mathbf{x}}_i \vec{\mathbf{x}}^i = \vec{\mathbf{x}}^i \vec{\mathbf{x}}_i = \mathbf{I} \tag{33}$$

and the second-order tensors:

$$\mathbf{R}^{\vec{\mathbf{x}}} = \vec{\mathbf{e}}_i \vec{\mathbf{x}}^i, \quad \mathbf{R}_{\vec{\mathbf{x}}} = \vec{\mathbf{e}}_i \vec{\mathbf{x}}_i, \quad (\mathbf{R}^{\vec{\mathbf{x}}})^T = \vec{\mathbf{x}}^i \vec{\mathbf{e}}_i, \quad \mathbf{R}_{\vec{\mathbf{x}}}^T = \vec{\mathbf{x}}_i \vec{\mathbf{e}}_i, \tag{34}$$

$$\mathbf{G}^{\vec{\mathbf{x}}} = \mathbf{R}^{\vec{\mathbf{x}}} \cdot (\mathbf{R}^{\vec{\mathbf{x}}})^T, \quad \mathbf{G}_{\vec{\mathbf{x}}} = \mathbf{R}_{\vec{\mathbf{x}}} \cdot \mathbf{R}_{\vec{\mathbf{x}}}^T \tag{35}$$

with the properties which follow from Eq. (33):

$$\mathbf{R}_{\vec{\mathbf{x}}} \cdot (\mathbf{R}^{\vec{\mathbf{x}}})^T = \mathbf{R}^{\vec{\mathbf{x}}} \cdot \mathbf{R}_{\vec{\mathbf{x}}}^T = \mathbf{R}_{\vec{\mathbf{x}}}^T \cdot \mathbf{R}^{\vec{\mathbf{x}}} = (\mathbf{R}^{\vec{\mathbf{x}}})^T \cdot \mathbf{R}_{\vec{\mathbf{x}}} = \mathbf{I}, \tag{36}$$

$$\mathbf{G}_{\vec{\mathbf{x}}} = \mathbf{G}_{\vec{\mathbf{x}}}^T, \quad \mathbf{G}^{\vec{\mathbf{x}}} = (\mathbf{G}^{\vec{\mathbf{x}}})^T, \quad \mathbf{G}^{\vec{\mathbf{x}}} \cdot \mathbf{G}_{\vec{\mathbf{x}}} = \mathbf{G}_{\vec{\mathbf{x}}} \cdot \mathbf{G}^{\vec{\mathbf{x}}} = \mathbf{I}, \quad \mathbf{G}^{\vec{\mathbf{x}}} \cdot\cdot \mathbf{G}_{\vec{\mathbf{x}}} = 3 \tag{37}$$

(see also Appendix A). Similar to formulas (31)–(37), we introduce $V_0$, $\vec{\mathbf{X}}^i$, $\mathbf{R}^{\vec{\mathbf{X}}}$, $\mathbf{R}_{\vec{\mathbf{X}}}$, $\mathbf{G}^{\vec{\mathbf{X}}}$, and $\mathbf{G}_{\vec{\mathbf{X}}}$ based on the set of vectors $\vec{\mathbf{X}}_i$.

Having defined these values, we can return to the tetrahedral element under consideration. Substituting $V$ and $V_0$ into Eq. (21), we can find the pressure p in the element. The next step is to define the approximation of the tensor **B** given by (23). Let us introduce the linear transformation of the element from its initial to its actual position [6]:

$$\vec{\mathbf{x}} = \mathbf{A} \cdot \vec{\mathbf{X}} + \vec{\mathbf{b}}, \tag{38}$$

where **A**, and $\vec{\mathbf{b}}$ are parameters of the transformation. Substituting (38) into (24), we can find the tensor **F** in the element:

$$\mathbf{F} = \frac{\partial (A_{ik} X_k + b_i)}{\partial X_m} \vec{\mathbf{e}}_i \vec{\mathbf{e}}_m = A_{ik} \delta_{km} \vec{\mathbf{e}}_i \vec{\mathbf{e}}_m = \mathbf{A}. \tag{39}$$

Using Eq. (38), we can write for vertices of the element as

$$\begin{cases} \vec{\mathbf{x}}_a = \mathbf{A} \cdot \vec{\mathbf{X}}_a + \vec{\mathbf{b}} \\ \vec{\mathbf{x}}_b = \mathbf{A} \cdot \vec{\mathbf{X}}_b + \vec{\mathbf{b}} \\ \vec{\mathbf{x}}_c = \mathbf{A} \cdot \vec{\mathbf{X}}_c + \vec{\mathbf{b}} \\ \vec{\mathbf{x}}_d = \mathbf{A} \cdot \vec{\mathbf{X}}_d + \vec{\mathbf{b}} \end{cases} \tag{40}$$

In order to determine **F** (and then **B**) in the element, we should find the value of **A** from system (40). Let us rewrite (40) in the following form:

$$\begin{cases} \vec{\mathbf{x}}_1 = \mathbf{A} \cdot \vec{\mathbf{X}}_1 \\ \vec{\mathbf{x}}_2 = \mathbf{A} \cdot \vec{\mathbf{X}}_2 \\ \vec{\mathbf{x}}_3 = \mathbf{A} \cdot \vec{\mathbf{X}}_3 \end{cases} \tag{41}$$

Each equation of system (41) is multiplied from the right by a corresponding vector $\vec{\mathbf{e}}_i$. Taking their sum, we obtain

$$\vec{\mathbf{x}}_i\vec{\mathbf{e}}_i = \mathbf{A} \cdot \vec{\mathbf{X}}_m\vec{\mathbf{e}}_m. \tag{42}$$

Using Eqs. (34) and (36), we find the tensor $\mathbf{A}$

$$\mathbf{A} = \vec{\mathbf{x}}_i\vec{\mathbf{e}}_i \cdot (\vec{\mathbf{X}}_m\vec{\mathbf{e}}_m)^{-1} = \mathbf{R}_{\vec{\mathbf{x}}}^T \cdot \mathbf{R}^{\vec{\mathbf{X}}}. \tag{43}$$

Finally, combining Eqs. (23), (35), (39), and (43), we obtain the finite difference approximation of $\mathbf{B}$ for the element:

$$\mathbf{B} = \mathbf{R}_{\vec{\mathbf{x}}}^T \cdot \mathbf{G}^{\vec{\mathbf{X}}} \cdot \mathbf{R}_{\vec{\mathbf{x}}}. \tag{44}$$

The tensor $\mathbf{G}^{\vec{\mathbf{X}}}$ can be expressed as

$$\mathbf{G}^{\vec{\mathbf{X}}} = \mathbf{R}^{\vec{\mathbf{X}}} \cdot (\mathbf{R}^{\vec{\mathbf{X}}})^T = \vec{\mathbf{e}}_k\vec{\mathbf{X}}^k \cdot \vec{\mathbf{X}}^m\vec{\mathbf{e}}_m = \begin{vmatrix} \vec{\mathbf{X}}^1 \cdot \vec{\mathbf{X}}^1 & \vec{\mathbf{X}}^1 \cdot \vec{\mathbf{X}}^2 & \vec{\mathbf{X}}^1 \cdot \vec{\mathbf{X}}^3 \\ \vec{\mathbf{X}}^2 \cdot \vec{\mathbf{X}}^1 & \vec{\mathbf{X}}^2 \cdot \vec{\mathbf{X}}^2 & \vec{\mathbf{X}}^2 \cdot \vec{\mathbf{X}}^3 \\ \vec{\mathbf{X}}^3 \cdot \vec{\mathbf{X}}^1 & \vec{\mathbf{X}}^3 \cdot \vec{\mathbf{X}}^2 & \vec{\mathbf{X}}^3 \cdot \vec{\mathbf{X}}^3 \end{vmatrix} \tag{45}$$

As follows from Eq. (45), the components of the tensor $\mathbf{G}^{\vec{\mathbf{X}}}$ are scalar products between the vectors $\vec{\mathbf{X}}^1$, $\vec{\mathbf{X}}^2$, and $\vec{\mathbf{X}}^3$, which determine the initial element. Obviously, the translation and rotation of the initial element as a rigid body does not affect the value of the tensor $\mathbf{G}^{\vec{\mathbf{X}}}$ and of the tensor $\mathbf{B}$. Specifically, if the initial and actual configurations of an element coincide up to translation and rotation, then $\mathbf{B} \equiv \mathbf{I}$.

It is important to stress that all information about the initial configuration of the element contains in the tensor $\mathbf{G}^{\vec{\mathbf{X}}}$ and in the initial volume $V_0$. If the external force is removed, then $\mathbf{G}^{\vec{\mathbf{x}}} \to \mathbf{G}^{\vec{\mathbf{X}}}$ and $V \to V_0$. We can assert that $\mathbf{G}^{\vec{\mathbf{X}}}$ and $V_0$ play the role of the memory of the element and keep the information about its initial configuration. We recall that neither $\mathbf{G}^{\vec{\mathbf{X}}}$ nor $V_0$ depend on translations and rotations.

By virtue of equality (44), among two values $\mathbf{G}^{\vec{\mathbf{X}}}$ and $V_0$, the condition (27) contains only $\mathbf{G}^{\vec{\mathbf{X}}}$. More general plasticity conditions including both $\mathbf{G}^{\vec{\mathbf{X}}}$ and $V_0$ can be also analyzed. The tensor $\mathbf{G}^{\vec{\mathbf{X}}}$ will play a crucial role in the subsequent considerations. We call it the tensor of initial configuration. (In Sect. 3.1, the value $1/X$ served as an analogue of $\mathbf{G}^{\vec{\mathbf{X}}}$ for 1D problem.)

Here for simplicity we consider only the von Mises criterion in the form (28). In the elastic regime, condition (28) holds and $\mathbf{G}^{\vec{\mathbf{X}}}$ does not change. If the deformation of the element exceeds the critical value, then condition (28) is not satisfied any more, and the internal structure of the solid body is irreversibly changed. In other words, the initial configuration of the element, and, consequently, the tensor $\mathbf{G}^{\vec{\mathbf{X}}}$ should be changed in such a way that the equation

$$-J_2(\mathbf{B}_D) = k^2 \tag{46}$$

is satisfied.

We proceed step by step in time. At the initial time step, in addition to all other values, we have to calculate the values of $\mathbf{G}^{\vec{\mathbf{X}}}$ and $V_0$ for every element of the mesh. Assume that we have already found the new positions of the element vertices from Eqs. (1) and (2). After that we calculate the set of vectors $\vec{\mathbf{x}}_s^{n+1}$ from Eq. (29). We carry out the predictor step and put

$$\mathbf{B}' = \mathbf{R}^T_{\vec{\mathbf{x}}^{\mathrm{n+1}}} \cdot \mathbf{G}^{\vec{\mathbf{X}}^{\mathrm{n}}} \cdot \mathbf{R}_{\vec{\mathbf{x}}^{\mathrm{n+1}}}, \tag{47}$$

where $\mathbf{R}_{\vec{\mathbf{x}}^{\mathrm{n+1}}} = \vec{\mathbf{e}}_k \vec{\mathbf{x}}_k^{n+1}$, and $\mathbf{G}^{\vec{\mathbf{X}}^{\mathrm{n}}}$ is known from the previous time increment. If the condition

$$-J_2(\mathbf{B}'_D) \le k^2 \tag{48}$$

is satisfied, then the tensor $\mathbf{G}^{\vec{\mathbf{X}}^{\mathrm{n}}}$ does not change, that is $\mathbf{G}^{\vec{\mathbf{X}}^{\mathrm{n+1}}} = \mathbf{G}^{\vec{\mathbf{X}}^{\mathrm{n}}}$.

Suppose that condition (48) does not hold. Then we should find the new tensor $\mathbf{G}^{\vec{\mathbf{X}}^{\mathrm{n+1}}}$ for the element, such that $\mathbf{B}^{n+1} = \mathbf{R}^T_{\vec{\mathbf{x}}^{\mathrm{n+1}}} \cdot \mathbf{G}^{\vec{\mathbf{X}}^{\mathrm{n+1}}} \cdot \mathbf{R}_{\vec{\mathbf{x}}^{\mathrm{n+1}}}$ satisfies the following equation:

$$-J_2(\mathbf{B}_D^{n+1}) = k^2. \tag{49}$$

The value of $\mathbf{G}^{\vec{\mathbf{X}}^{\mathrm{n+1}}}$ satisfying this condition should be in the range between $\mathbf{G}^{\vec{\mathbf{X}}^{\mathrm{n}}}$ and $\mathbf{G}^{\vec{\mathbf{x}}^{\mathrm{n+1}}}$. Similar to the example above (see Eq. 18) we introduce the parameter $a$ and put

$$\mathbf{G}^{\vec{\mathbf{X}}^{\mathrm{n+1}}} = a\mathbf{G}^{\vec{\mathbf{X}}^{\mathrm{n}}} + (1-a)\mathbf{G}^{\vec{\mathbf{x}}^{\mathrm{n+1}}}. \tag{50}$$

Using Eq. (50) we can write

$$\mathbf{B}^{n+1} = \mathbf{R}^T_{\vec{\mathbf{x}}^{\mathrm{n+1}}} \cdot \left[a\mathbf{G}^{\vec{\mathbf{X}}^{\mathrm{n}}} + (1-a)\mathbf{G}^{\vec{\mathbf{x}}^{\mathrm{n+1}}}\right] \cdot \mathbf{R}_{\vec{\mathbf{x}}^{\mathrm{n+1}}} = a\mathbf{B}' + (1-a)\mathbf{I} \tag{51}$$

and therefore

$$\mathbf{B}_D^{n+1} = a\mathbf{B}' + (1-a)\mathbf{I} - \frac{1}{3}\left[aJ_1(\mathbf{B}') + 3(1-a)\right]\mathbf{I} = a\mathbf{B}'_D. \tag{52}$$

Then from Eq. (52)

$$J_2(\mathbf{B}_D^{n+1}) = a^2 J_2(\mathbf{B}'_D). \tag{53}$$

We would like to satisfy Eq. (49). Substituting Eq. (53) into Eq. (49), we obtain the equality

$$a = \pm \frac{k}{\sqrt{-J_2(\mathbf{B}'_D)}}\,. \tag{54}$$

We will keep here only the positive solution.

Note that the value of $a$ in (54) coincides exactly, up to notation, with $m$ from (11). This is related to the fact that $\mathbf{S}^{n+1}$, given by (10), can be written in the form $\mathbf{S}^{n+1} = m\mathbf{S}' + (1-m)\mathbf{0}$, where $0 < m < 1$.

Substitution of $a$ from (54) into (50) gives the new value of the tensor $\mathbf{G}^{\vec{\mathbf{X}}^{n+1}}$, which satisfies (49). Obviously, condition (9) is also satisfied. We can now proceed to the next time step.

Note that it is assumed in the theory of plastic flows that the plastic strain is proportional to the stress deviator $\mathbf{S}$ at any time. From (52) and (22) we get the following relation:

$$d\mathbf{B}_p^{n+1} = \mathbf{B}_D^{n+1} - \mathbf{B}'_D = (a-1)\mathbf{B}'_D = \frac{a-1}{a}\mathbf{B}_D^{n+1} = \frac{a-1}{\mu a}\mathbf{S}^{n+1} \tag{55}$$

Let us make some preliminary conclusions. According to the discussion above, at each time step we deal with three configurations of the element (Fig. 2): the configuration, which is based on the set of vectors $\vec{\mathbf{x}}_s^{n+1}$, and related to the tensor $\mathbf{G}^{\vec{\mathbf{x}}^{n+1}}$ (Fig. 2c); old initial configuration determined by the tensor $\mathbf{G}^{\vec{\mathbf{X}}^{n}}$ (Fig. 2a); new initial configuration determined by the tensor $\mathbf{G}^{\vec{\mathbf{X}}^{n+1}}$ (Fig. 2b).

Note that using the tensors $\mathbf{G}^{\vec{\mathbf{X}}^{n}}$ and $\mathbf{G}^{\vec{\mathbf{X}}^{n+1}}$ we can reconstruct the shapes of both old and new initial tetrahedron elements up to translation and rotation. However, this is not required.

The tensors $\mathbf{G}^{\vec{\mathbf{x}}^{n+1}}$ and $\mathbf{G}^{\vec{\mathbf{X}}^{n+1}}$ determine the critical elastic deformation of the element allowed by condition (49), while the tensors $\mathbf{G}^{\vec{\mathbf{X}}^{n+1}}$ and $\mathbf{G}^{\vec{\mathbf{X}}^{n}}$ determine the plastic (irreversible) deformation.

Having introduced the new independent value $\mathbf{G}^{\vec{\mathbf{X}}}$ into the algorithm, we obtain the following system of equations:

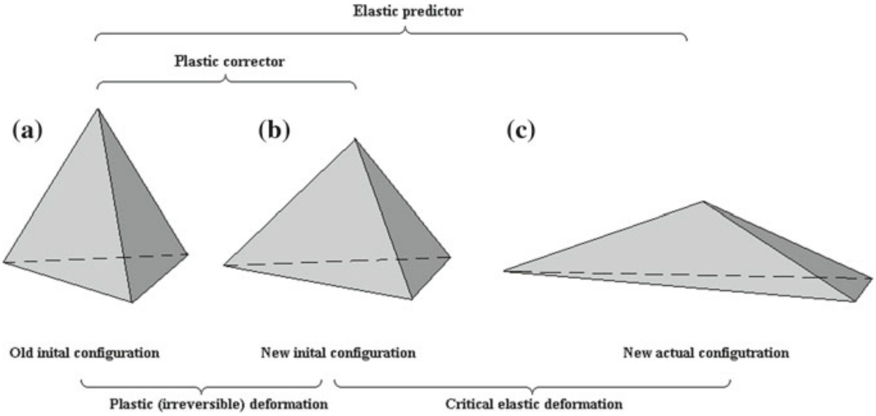

**Fig. 2** Diagram of elastic-predictor/plastic-corrector. The old (**a**) and new (**b**) initial configurations coincide up to translation and rotation. New actual configuration (**c**) is completely defined

$$\begin{cases} \vec{\mathbf{v}}^{n+1} = \vec{\mathbf{v}}^{n} + \dfrac{\Delta t}{M} \displaystyle\int_S \boldsymbol{\sigma}^n \cdot d\vec{\mathbf{s}} \\ \vec{\mathbf{x}}^{n+1} = \vec{\mathbf{x}}^{n} + \Delta t \vec{\mathbf{v}}^{n+1} \\ p^{n+1} = K\left(\dfrac{V^{n+1}}{V_0} - 1\right) \\ \mathbf{G}^{\vec{\mathbf{X}}^{\mathrm{n+1}}} = \begin{cases} \mathbf{G}^{\vec{\mathbf{X}}^{\mathrm{n}}}, & \text{at} \quad -J_2(\mathbf{B}'_D) \le k^2 \\ a\mathbf{G}^{\vec{\mathbf{X}}^{\mathrm{n}}} + (1-a)\mathbf{G}^{\vec{\mathbf{x}}^{\mathrm{n+1}}}, & \text{at} \quad -J_2(\mathbf{B}'_D) > k^2 \end{cases} \\ \mathbf{B}^{n+1} = \mathbf{R}^T_{\vec{\mathbf{x}}^{\mathrm{n+1}}} \cdot \mathbf{G}^{\vec{\mathbf{X}}^{\mathrm{n+1}}} \cdot \mathbf{R}_{\vec{\mathbf{x}}^{\mathrm{n+1}}} \\ \mathbf{S}^{n+1} = \mu \mathbf{B}^{n+1}_D \\ \boldsymbol{\sigma}^{n+1} = \mathbf{I}p^{n+1} + \mathbf{S}^{n+1} \end{cases} \tag{56}$$

It is written for the simplest explicit integration scheme. It is possible to develop more accurate explicit and implicit schemes but this is beyond the scope of this paper.

## 4 Simulations

In this section we will illustrate the discussion above with some examples.

### *4.1 A Perfectly Elastic-Plastic Model*

Let us consider a cylinder with typical material properties of $\rho = 3000, \mathrm{kg/m^3}$, $\nu = 0.45$ and $E = 100$, GPa subjected to an uniaxial cyclic loading. We assume that sliding is possible at the edges of the cylinder. Even though this problem is assumed to be 1D, we will use a 3D code for the analysis.

The classical explicit numerical scheme by [33, 34] is employed. For the new algorithm, a similar explicit procedure (with the exception of some minor changes of low importance) was used during the code development.

Elements of the 3D mesh (top-right corner of Fig. 3) have tensile strain in longitudinal direction and compression strain—in transverse direction. One cycle for the perfectly elastic-plastic model with no hardening of the material was simulated. The limit of elastic strain was set to be $\varepsilon_s = 0.01$ (which corresponds to $\sigma_s = 1$, GPa (28)).

The results of the modelling based upon classical and new algorithms with the same time integration step $dt$ are shown in Fig. 3. The curves obtained with two different methods coincide rather accurately. Some high frequency vibrations taking

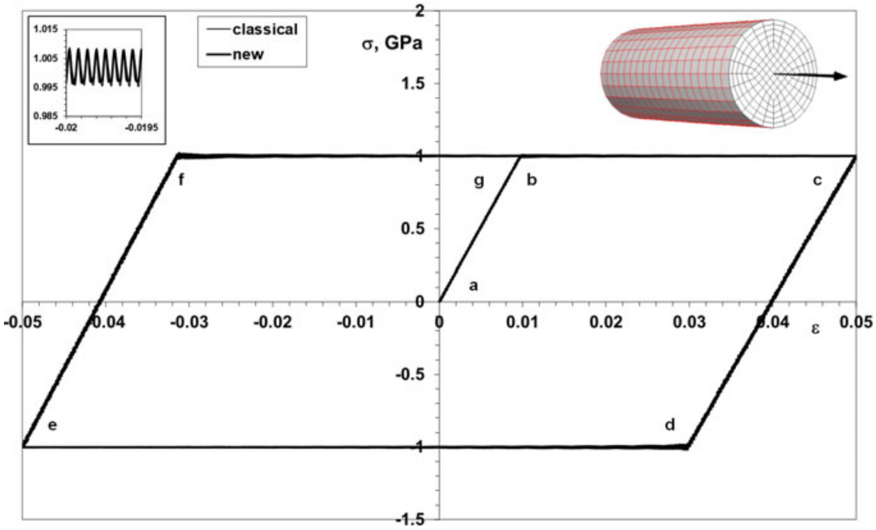

**Fig. 3** One cycle of calculations using perfectly elastic-plastic model for $\varepsilon_s = 0.01$

place during the slow quasi stationary process of deformation are related to the fact that we use full dynamic formulation with rather small time integration step.

Some aspects of validation of the explicit integration procedure for a given quasi stationary problem are not included in this paper. Employment of the same explicit integration procedure for both methods is convenient for the comparison of the results. The amplitude and the frequency of vibrations in both methods are identical (top-left corner of Fig. 3).

We can see from Fig. 3 that $ab$ is the elastic part of the curve. When the elastic strain $\varepsilon$ is greater than $\varepsilon_s$, plastic flow occurs along $bc$, where $\sigma = \sigma_s$. The unloading $cd$ and loading $ef$ parts are the same. This corresponds to the physics of the process.

The CPU time of both simulations was approximately the same with some minor advantage of the new algorithm. Most probably, it is related to a more detailed development of the code for the new algorithm.

## 4.2 A Model with Hardening

Let us consider a similar problem as in Sect. 4.1 taking into account workhardening of the material. In this case $\varepsilon_s$ depends on plastic strain $\varepsilon_p$.

As it was described in Sect. 3.2, at each time step, we calculate two tensors $\mathbf{G}^{\vec{\mathbf{X}}^{n}}$ and $\mathbf{G}^{\vec{\mathbf{X}}^{n+1}}$ corresponding to the old and new initial configurations of the element. The deformation of the initial configuration corresponds to the plastic strain of the element. We can define the effective plastic strain rate at any time step $d\varepsilon_p^{n+1}$. Let us introduce a deformation tensor for the new initial configuration relative to the old one:

$$\mathbf{B}_p = \mathbf{R}^T_{\vec{\mathbf{X}}^{\mathrm{n+1}}} \cdot \mathbf{G}^{\vec{\mathbf{X}}^{\mathrm{n}}} \cdot \mathbf{R}_{\vec{\mathbf{X}}^{\mathrm{n+1}}} \tag{57}$$

and define $d\varepsilon_p^{n+1}$ like

$$d\varepsilon_p^{n+1} = \frac{1}{\sqrt{3}}\sqrt{-J_2\left(\mathbf{B}_{pD}\right)} = \frac{1}{\sqrt{18}}\sqrt{3J_1\left(\mathbf{B}_p^2\right) - J_1^2\left(\mathbf{B}_p\right)} \tag{58}$$

Using Eqs. (34)–(37), we can transform Eq. (58) to the following form:

$$d\varepsilon_p^{n+1} = \frac{1}{\sqrt{18}}\sqrt{3\left(\mathbf{G}_{\vec{\mathbf{X}}^{\mathrm{n+1}}} \cdot \mathbf{G}^{\vec{\mathbf{X}}^{\mathrm{n}}}\right) \cdot\cdot \left(\mathbf{G}_{\vec{\mathbf{X}}^{\mathrm{n+1}}} \cdot \mathbf{G}^{\vec{\mathbf{X}}^{\mathrm{n}}}\right) - \left(\mathbf{G}_{\vec{\mathbf{X}}^{\mathrm{n+1}}} \cdot\cdot \mathbf{G}^{\vec{\mathbf{X}}^{\mathrm{n}}}\right)^2} \tag{59}$$

Then total plastic strain accumulated in the element can be expressed as

$$\varepsilon_p^{n+1} = \sum_{i=1}^{i=n} d\varepsilon_p^{i+1} \tag{60}$$

Let us assume for simplicity, that $\varepsilon_s$ depends linearly on $\varepsilon_p$, i.e.,

$$\varepsilon_s^{n+1} = \varepsilon_s' + \varepsilon_s'' \varepsilon_p^{n+1} \tag{61}$$

Results of simulation for the elastic-plastic material with hardening Eq. (61) for $\varepsilon_s' = 0.01$ and $\varepsilon_s'' = 0.1$ are shown in Fig. 4. The stress-strain function is piece-wise linear. The part of the curve between $b$ and $c$ corresponds to the plastic deformation with hardening, which is more representative for the behavior of a real material than the perfectly elastic-plastic model. As in the previous example in Sect. 4.1, Fig. 4 shows almost exact correspondence of the curves obtained with both methods.

### *4.3 Springback Problem*

The problem of springback of parts stamped from sheet metal is a very well known practical problem: as a result of an external load, a solid (sheet metal blank) is undergoing plastic deformation, then the load is removed, and the deformed solid unloads and takes a new shape (because of the elastic recovery of the material) which needs to be defined.

In order to compare the results of modelling obtained with both methods, let us consider the following simple problem. We take a 2D Cartesian mesh, which consists of a single square cell with surface $S_0$ and which includes four triangular elements (Fig. 5a).

The material properties in this example are the same as in the previous example in Sect. 4.2.

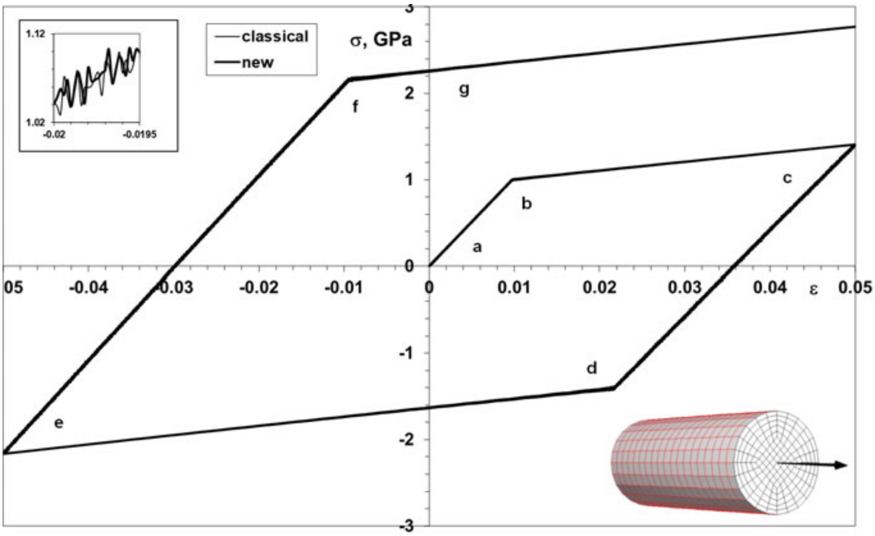

**Fig. 4** One cycle of calculations using elastic-plastic model with a simple model with hardening

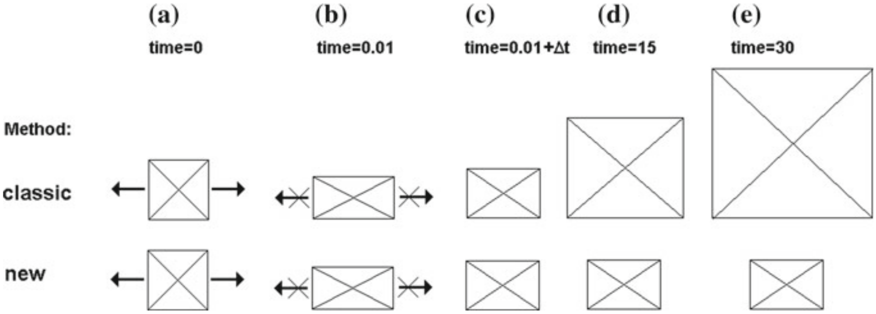

**Fig. 5** Shape of the solid versus time under tension parallel to the $x$ axis

The stretching load is applied to the solid in the horizontal direction and then removed at the time moment of 0.01 s (Fig. 5b).

Obviously, the solid body starts free vibrations, and the actual area of the solid $S$ will periodically change around its initial value $S_0$. A rapid change of compression and tension will take place correspondingly, and at the moment when $S$ becomes equal to $S_0$, the value of $p$ should be equal to zero. The shear stresses should be equal to zero at any time. The shape of the solid should stay rectangular. This is the expectation of how the solid body should behave in this example.

Now, let us review the results of the simulation. As it was expected, the calculated values of the pressure in the solid, after the load was removed, changed periodically around zero with the same amplitude: the values of pressure $p$ obtained by two

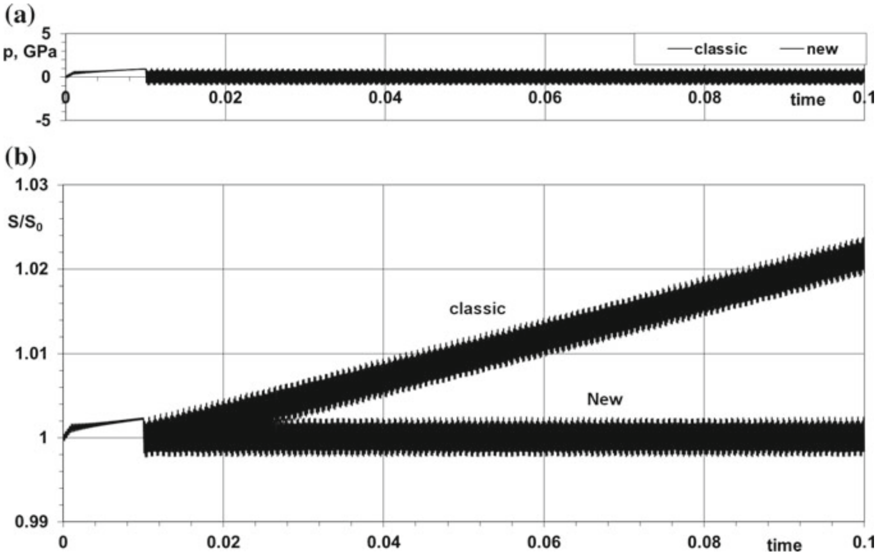

**Fig. 6** Simple tension. Variation of **a** pressure $p$ and **b** $S/S_0$

different methods are practically identical (Fig. 6a). The value of $\sigma_{xy}$ was equal to zero, as it was expected.

We now compare the ability of the two methods to predict the evolution of the shape of the solid during a substantial period of time. After relieving the external load, the solid took the shape of a rectangle slightly elongated in the horizontal direction. Then the shape stayed rectangular, and the solid rapidly vibrated around some average position.

During relatively short period of time after the load removal, the condition $S = S_0$ is satisfied for both methods (Fig. 5). However, for a longer period of time, the difference between the two methods becomes more and more visible. In the case of the new method, the value of $S/S_0$ oscillates around 1, while in case of the classical method, $S/S_0$ oscillates with the same amplitude but around the growing value (Fig. 6b). The shapes of the solid obtained with both methods at the moments of 15 and 30 s are shown in Fig. 5d, e.

The results obtained with the classical method show that the average area of the solid is growing with a constant velocity, and the effect of “swelling” of the mesh was observed. This effect can be suppressed by reducing the time integration step but can not be eliminated completely. The process of relaxation of the solid after the external load is removed can be sufficiently long. Therefore, the decrease of the time step is strongly undesirable. The new method is stable with respect to the “swelling” of the mesh.

This effect is determined by the fundamental difference between the classical and the new methods: the calculation of the pressure at the new time step $p^{n+1}$ in the classical method is conducted according to formula (6), while in the new method

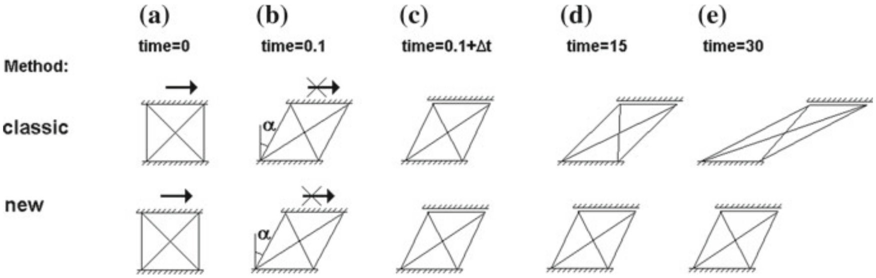

**Fig. 7** Shape of the solid versus time with simple shear

according to formula (21) where the initial volume $V_0$ of the cell (or the initial area $S_0$ in the 2D example) is included. As a result, according to formula (21), if the equation $V = V_0$ (or $S = S_0$) is violated, the counter pressure is generated. It tends to change the shape of the solid in such a way that the equation $V = V_0$ (or $S = S_0$) is restored.

When we calculate the pressure with the classical method according to formula (6), $p^{n+1}$ is found as a result of adding the pressure increment $\Delta t K \nabla_{\vec{x}} \cdot \vec{\mathbf{v}}$ to its value from the previous integration step $p^n$. Therefore, after a large number of integration steps, due to the accumulation of integration error, the information about the initial volume (area) of the cell is gradually "forgotten" and, as a result, the observed non-physical and unlimited "swelling" of the mesh takes place.

Let us carry out a similar comparison for the same mesh and for the same properties and configuration in the case of a simple shear. The initial shape and loading conditions are shown in Fig. 7a, where $\alpha$ is the angle of the side deviation from the $y$ axis.

We can expect that when the load is removed, the angle $\alpha$ will gradually decrease, and its value will oscillate around some fixed average value $\alpha_0$. The pressure $p$ should remain zero, and the stress tensor component $\sigma_{xy}$ should vary around its average value equal to zero. The shape of the solid should be a parallelogram.

The results of the calculations of the value $\sigma_{xy}$, obtained with the help of both methods, are practically identical. The value of $\sigma_{xy}$ varies periodically with consistent amplitude (Fig. 8a). The value of pressure at any moment of time is equal to zero.

As in the previous example, let us follow the evolution of the shape of the solid after a substantial interval of time. The value of the angle of inclination of the parallelogram $\alpha$, obtained with the new method varies around its steady average value $\alpha_0 \approx 27^0$.

The value of $\alpha_0$, obtained with the help of the classic method is gradually increasing, as shown in Fig. 8b. Additional calculations show that the growth of $\alpha_0$ in the classical method can be decreased by decreasing the time step.

The difference between the two methods is related to the fact that the calculation of the components of the tensor $\mathbf{S}$ according to the new method employs Eq. (22), which take into account the tensor of the initial configuration $\mathbf{G}^{\vec{\mathbf{X}}}$. In this example, the area $S$ of the solid is constant according to the formulation of the problem, and behavior of the solid is determined by the shear strains. In this case, any deviation of the actual

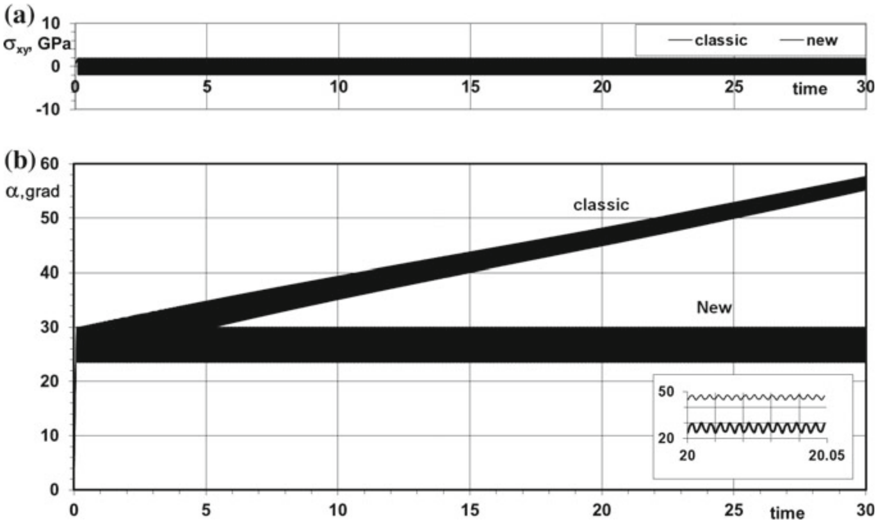

**Fig. 8** Simple shear. **a** Variation of $\sigma_{xy}$ and **b** angle of inclination $\alpha$

configuration of the cell from its initial configuration immediately generates opposite stresses which tend to return the actual shape of the cell to its original shape. The information about the initial configuration is kept in the tensor $\mathbf{G}^{\vec{\mathbf{X}}}$.

In the case of the classical method, calculation of the tensor **S** at the new time step is conducted according to formula (7) which does not include directly the information about the initial and actual configurations, unlike the new method. This leads to gradual error accumulation for large number of integration steps. In this example, it results in a non-physical unbounded growth of the angle $\alpha_0$ after removing the load.

Introduction of the artificial viscosity can suppress the high frequency oscillations in both methods but the problem of slow drift of $S_0$ or $\alpha_0$ when using the classical method can still appear.

Stability of the new method with respect to "swelling" of the mesh is a useful property. This method was used to solve a number of practical problems in [5, 15, 16]. In particular, we have simulated a multi-steps flanging process based on the idea of redistributing plastic strains around a larger area at each step, delivering additional metal into the bending zone and creating an additional axial compression.

The results of numerical simulations of a three-step flanging process is shown in Fig. 9. More details are given in the works cited above. Let us emphasize that we need to model here not only the stages $a \rightarrow b$, $c \rightarrow d$ and $e \rightarrow f$ but also the stages $b \rightarrow c$ and $d \rightarrow e$ when the load is removed and the deformed solid takes a new shape (Fig. 9).

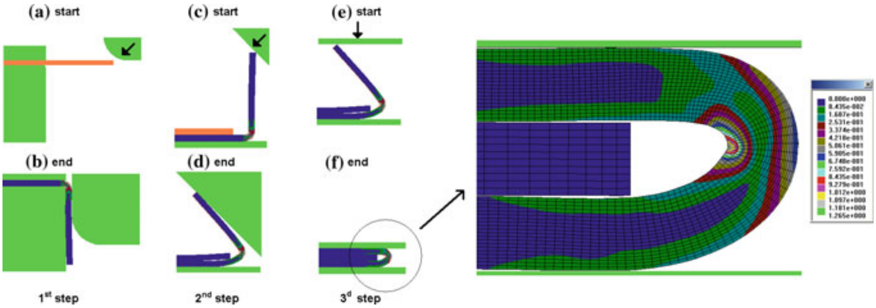

**Fig. 9** Distribution of plastic strains in a three-step flanging process

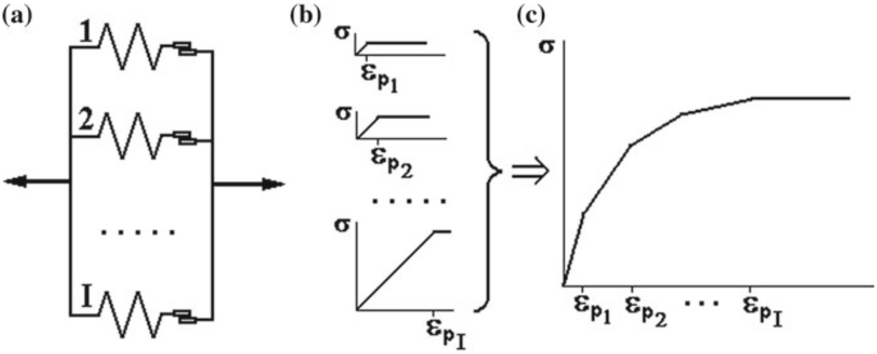

**Fig. 10** Schematic representation of the multi-yield surfaces model

## 4.4 A Multi-yield Surfaces Model

The multi-yield surfaces generalization of the model (8) can be presented in the following form

$$F_i(\mathbf{S} - \boldsymbol{\alpha}_i) \leq K_i, \quad i = 1, \ldots, I, \tag{62}$$

where $\boldsymbol{\alpha}_i$ are the back stress tensors [21, 24]. A multi-yield surface model is used in particular for simulation of cyclic plasticity. Many aspects of cyclic plasticity can be obtained using the evolutive Masing model [13].

In our case, we have to deal with a variable initial configuration. We can assume that the real structure of the solid body is not uniform. For example, we can consider a polycrystal structure with different sizes and properties of individual crystals. Suppose that each component behaves according to the perfectly elastic-plastic model, however, plastic (irreversible) deformation of different components of the structure can start at different levels of the strain $\varepsilon_{si}$.

Let us first discuss the following generalization of the model example described in a Sect. 3.1. The structure consists of $I$ perfectly elastic-plastic sub-springs (Fig. 10b) loaded in parallel (Fig. 10a) and having individual values of $\varepsilon_{si}$. This is so called Masing model [13]. Assume that $\varepsilon_{s1} < \varepsilon_{s2} < \cdots < \varepsilon_{sI}$.

Let us apply an external tensile load to this structure. If the total deformation of the system $\varepsilon$ is less than $\varepsilon_{s1}$, then it behaves as a single spring. The sub-springs are loaded in parallel. If we remove the external load, the system will return back to its initial configuration. If $\varepsilon$ exceeded $\varepsilon_{s1}$, then the first sub-spring turns to the plastic flow, while the others are still in the elastic stage. The stress-strain dependence becomes different. After that the next sub-spring turns to the plastic flow, and so on until all the sub-springs will switch to the plastic regime and the external load will become constant.

As a result, we obtain the stress-strain curve schematically presented in Fig. 10c. At this stage, if we relieve the external load, the system will not return to the initial length of any sub-spring $X_i$, but will stay somewhere in between. The residual stresses will stay inside the sub-springs with no external load applied. These residual stresses can be defined as a superposition of those for the sub-springs. Such process can be simulated in the framework of the described model using specifically the initial configuration of the solid body.

Thus, we can replace (14) by the following relation:

$$\sigma = \sum_{i=1}^{I} \gamma_i \sigma_i = E \sum_{i=1}^{I} \gamma_i \left( \frac{x}{X_i} - 1 \right). \tag{63}$$

Here the total stress $\sigma$ is the sum of the stresses $\sigma_i$ of $i$ sub-springs, $\gamma_i$ is the input of the given sub-spring, $\sum_{i=1}^{I} \gamma_i = 1$. We assume, for simplicity, that all sub-springs have the same elastic modulus $E$.

We note that all $X_i$ are the same at $t = 0$. Gradually they become different from each other when they are involved in plastic flow. Instead of the single condition (16), we have the system of conditions:

$$\left( \frac{x}{X_i} - 1 \right)^2 \leq \varepsilon_{si}^2, \quad i = 1, 2, \ldots, I. \tag{64}$$

The algorithm in this case is a direct generalization of the algorithm described above. At each time step we use Eqs. (18)–(20) for all the sub-springs.

Let us use a similar approach for a continuous model. We can now rewrite Eqs. (56) for the one-yield surface case as

$$\begin{cases} \vec{\mathbf{v}}^{n+1} = \vec{\mathbf{v}}^{n} + \dfrac{\Delta t}{M}\displaystyle\int_S \boldsymbol{\sigma}^n \cdot d\vec{\mathbf{s}} \\ \vec{\mathbf{x}}^{n+1} = \vec{\mathbf{x}}^{n} + \Delta t \vec{\mathbf{v}}^{n+1} \\ p^{n+1} = K\left(\dfrac{V^{n+1}}{V_0} - 1\right) \\ \mathbf{G}_i^{\vec{\mathbf{X}}^{\mathrm{n+1}}} = \begin{cases} \mathbf{G}_i^{\vec{\mathbf{X}}^{\mathrm{n}}}, & \text{at} \quad -J_2(\mathbf{B}'_{iD}) \le k_i^2 \\ a\mathbf{G}_i^{\vec{\mathbf{X}}^{\mathrm{n}}} + (1-a)\mathbf{G}^{\vec{\mathbf{x}}^{\mathrm{n+1}}}, & \text{at} \quad -J_2(\mathbf{B}'_{iD}) > k_i^2 \end{cases} \\ \mathbf{B}_i^{n+1} = \mathbf{R}^T_{\vec{\mathbf{x}}^{\mathrm{n+1}}} \cdot \mathbf{G}_i^{\vec{\mathbf{X}}^{\mathrm{n+1}}} \cdot \mathbf{R}_{\vec{\mathbf{x}}^{\mathrm{n+1}}} \\ \mathbf{S}^{n+1} = \mu \displaystyle\sum_{i=1}^{I} \gamma_i \mathbf{B}_{iD}^{n+1} \\ \boldsymbol{\sigma}^{n+1} = \mathbf{I}p^{n+1} + \mathbf{S}^{n+1} \end{cases} \tag{65}$$

where $\mathbf{B}_i = \mathbf{R}^T_{\vec{\mathbf{x}}} \cdot \mathbf{G}_i^{\vec{\mathbf{X}}} \cdot \mathbf{R}_{\vec{\mathbf{x}}}$. At the initial moment of time, we have to calculate the set of tensors $\mathbf{G}_i^{\vec{\mathbf{X}}}$ $(i = 1, \dots, I)$ for each mesh element. Then at any time step, we have to check the $i$-th yield condition and, if necessary, to correct the corresponding tensor $\mathbf{G}_i^{\vec{\mathbf{X}}}$.

A test simulation for the same cylinder under the axial load for the 2-yield surfaces model is shown in Fig. 11. Here $\varepsilon_{s1} = 0.01$, $\varepsilon_{s2} = 0.02$, and $\gamma_1 = \gamma_2 = 1/2$. The $ab$

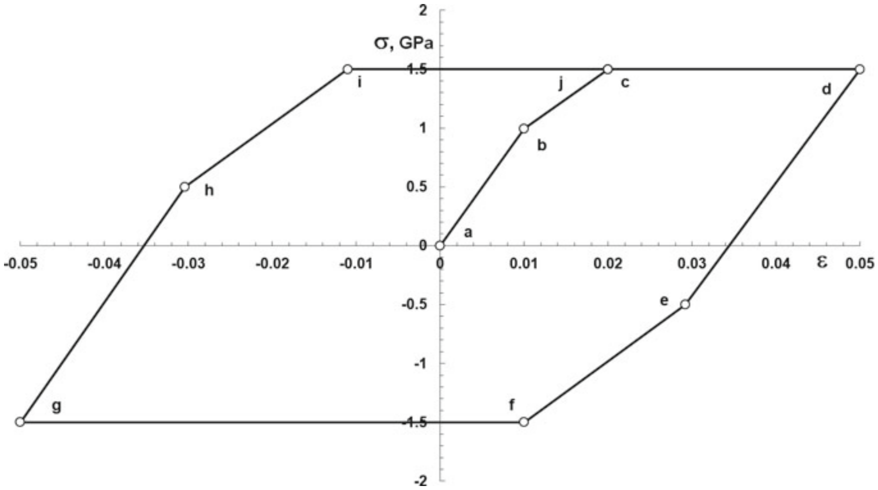

**Fig. 11** One cycle for 2-yield surfaces model

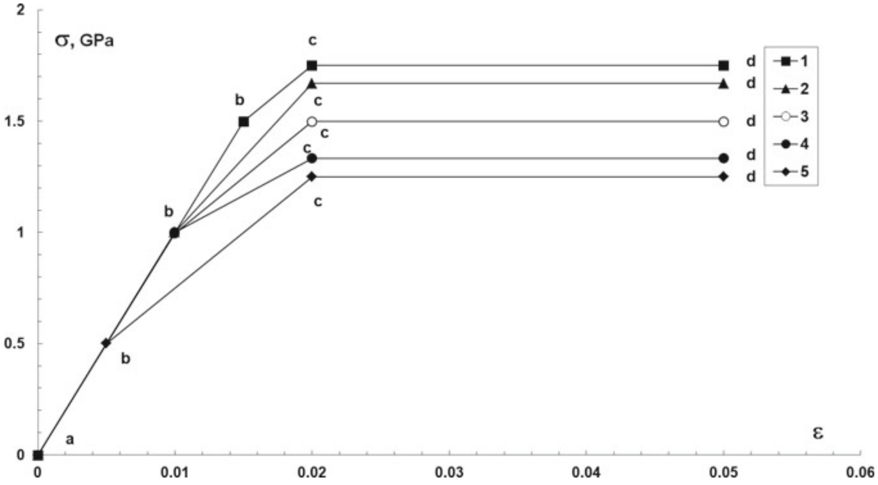

**Fig. 12** 2-yield surfaces model with various parameters: 1—$\varepsilon_{s1} = 0.015$, $\varepsilon_{s2} = 0.02$, $\gamma_1 = \gamma_2 = 1/2$; 2—$\varepsilon_{s1} = 0.01$, $\varepsilon_{s2} = 0.02$, $\gamma_1 = E/3$, $\gamma_2 = 2/3$; 3—$\varepsilon_{s1} = 0.01$, $\varepsilon_{s2} = 0.02$, $\gamma_1 = \gamma_2 = 1/2$; 4—$\varepsilon_{s1} = 0.01$, $\varepsilon_{s2} = 0.02$, $\gamma_1 = 1/3$, $\gamma_2 = 2/3$; 5—$\varepsilon_{s1} = 0.005$, $\varepsilon_{s2} = 0.02$, $\gamma_1 = \gamma_2 = 1/2$

part of the curve corresponds to the elastic region, where both components are elastic. For this region $\varepsilon_b = \varepsilon_{s1}$. In the interval $bc$ the first component is in the plastic regime, the second one is in elastic regime and we obtain the hardening of the material. For this range $\varepsilon_c = \varepsilon_{s2}$. In $cd$, both components are involved in the plastic flow. In $de$, both components are elastic and unloading of the material takes place. As follows from the Fig. 11, $|\sigma_d| > |\sigma_e|$, and $\varepsilon_d - \varepsilon_e = 2\varepsilon_b$ which represents the Bauschinger effect.

We vary the parameters for the 2-yield surfaces model (Fig. 12). The curve 3 here corresponds to the same parameters as in Fig. 11. All the other curves are obtained for different values of the parameters. The general trend of these curves is the same as in Fig. 11. We can see that it is possible to change the curves in a wide range varying the parameters of the model.

It is clear that the 2-yield surfaces model is rather rough and it does not give a smooth stress-strain graph. For practical cases, the simulation can be performed using a larger number of layers.

The results of the simulations for a 5-yield surface model with $\varepsilon_{s1} = 0.01$, $\varepsilon_{s2} = 0.02$, $\varepsilon_{s3} = 0.03$, $\varepsilon_{s4} = 0.04$, $\varepsilon_{s5} = 0.05$, and $\gamma_1 = \cdots = \gamma_5 = 1/5$ are shown in Fig. 13. The segment $ab$ is an elastic part for all the components. The segments $bc$, $cd$, $de$, $ef$, $fg$ correspond to the case where the components reach their critical conditions one after another and enter the regime of plastic flow. The hardening part of the curve $bcdef$ is more smooth than the same one in Fig. 11.

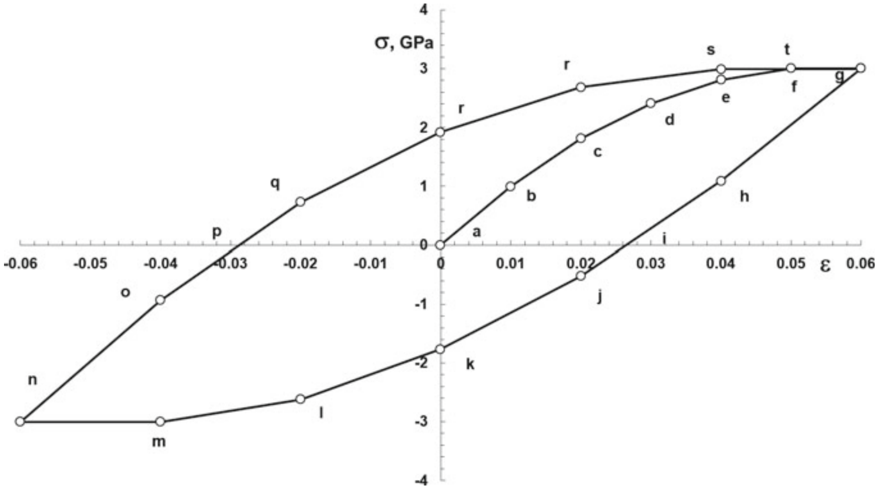

Fig. 13 One cycle for 5-yield surfaces model

## 4.5 Calculation of Residual Stresses

During the stamping operations of metal parts, non-uniform distributions of stresses and strains take place. As a result, the residual stresses are generated after the removal of external loads and relaxation of residual vibrations. The calculation of residual stresses and of final position of the solid body has very important practical applications, in particular, for prediction and correction of springback of sheet metal parts after stamping operations.

In order to solve this problem, it is necessary to simulate the whole process of deformation, the unloading process with decreasing residual vibrations. Residual stresses and the final positions of the nodes of the mesh will represent the solution of this important problem.

In general, both Wilkins method and the new algorithm described above allow us to determine the residual stresses. However, there is an important point of difference. We recall that while using the Wilkins method we calculate the increments of $p$ and $\mathbf{S}$ from Eqs. (6) and (7) at every integration step. Then we calculate the new values of $p^{n+1}$ and $\mathbf{S}^{n+1}$ as a sum of old values $p^n$ and $\mathbf{S}^n$ and their increments.

The accuracy of calculation of increments of $p$ and $\mathbf{S}$ is of the order $0(\Delta t)$. This means that the final error of calculations of $\boldsymbol{\sigma}$ accumulated in the elements of the mesh to the moment when the elastic vibrations and residual stresses relax depends both on $\Delta t$ and on the number of iterations.

In the new algorithm, the calculation of the stress tensor at any element of the mesh depends on the difference between the actual and the initial configurations. This is an essential difference of the suggested algorithm and the Wilkins method.

Let us consider the following example. We simulate the final stage of relaxation of elastic vibrations. The initial configuration of each element does not change any more. Each element taken independently would converge to it. However, taken all together they cannot do it because of the mutual interaction. Due to the fact that the initial configuration of every element is stabilized, the final error of calculations does not depend neither on $\Delta t$ nor on the number of iterations, no matter how large this number can be. On the contrary, in the Wilkins method we are accumulating the increments of the stress tensor and there is no "starting point". Hence the error grows even during elastic vibrations together with the number of integrations steps.

Earlier we discussed the calculation of residual stresses at different points of a solid subjected to non-uniform plastic deformation. Applying the new algorithm and using its multi-yield surface version, we can calculate the stresses in each structural component separately. They can differ from each other even if the body is deformed uniformly.

As was discussed in Sect. 4.2, total stress tensor consist of its components

$$\boldsymbol{\sigma} = \sum_{i=1}^{I} \gamma_i \boldsymbol{\sigma}_i, \tag{66}$$

where

$$\boldsymbol{\sigma}_i = \mathbf{I} p_i + \mathbf{S}_i. \tag{67}$$

Let us return back to the simulation of the loading of the cylinder using a multi-yield surfaces model. During its cyclic loading (Fig. 13), the total stress $\sigma_{xx}$ equals to zero at points $a$ and $p$. However, its components $\sigma_{xxi}$ are not equal to zero there because different components of the material experience different irreversible deformations and will have different initial configurations $\mathbf{G}_i^{\vec{\mathbf{X}}}$. We recall that $\gamma_1 = \cdots = \gamma_5 = 1/5$ here.

Figure 14 shows the part of the curve from Fig. 13 until the point where the total stress $\sigma_{xx}$ is equal to zero. This simulation is carried out assuming that all $p_i$ in Eq. (67) are equal to the total pressure $p$ (model 1). Because of this, the value of $\sigma_{xx1}$ continues to grow to a certain extent after the beginning of plastic flow in the 1st component. On the contrary, the values of $\sigma_{xx5}$ are less than in the case where the material 5 deforms independently.

In Fig. 15 similar results are shown for the case

$$p_i = K \frac{J_1(\mathbf{B}_i) - 3}{2} \tag{68}$$

(model 2). It can be obtained from (4) and (26) under a certain approximation. The components $\sigma_{xxi}$ correspond better here to the ideal elastic-plastic model than in Fig. 14 since the interconnection through $p_i$ is weaker than in model 1.

The results of calculations of $\sigma_{xxi}$ for both models are shown in the table below, where the stresses are given at the intersections of the cyclic curve with the axis $\varepsilon$.

| | Model 1 | Model 2 | Model 1 | Model 2 |
|---|---|---|---|---|
| $\varepsilon$ | 0.0267 | 0.0272 | −0.0292 | −0.028 |
| $\frac{1}{5}\sigma_{xx1}$ | −0.0997 | −0.17 | 0.096 | 0.233 |
| $\frac{1}{5}\sigma_{xx2}$ | −0.127 | −0.216 | 0.127 | 0.289 |
| $\frac{1}{5}\sigma_{xx3}$ | −0.0264 | −0.0456 | 0.0261 | 0.0715 |
| $\frac{1}{5}\sigma_{xx4}$ | 0.0749 | 0.13 | −0.0756 | −0.152 |
| $\frac{1}{5}\sigma_{xx5}$ | 0.176 | 0.301 | −0.178 | −0.447 |

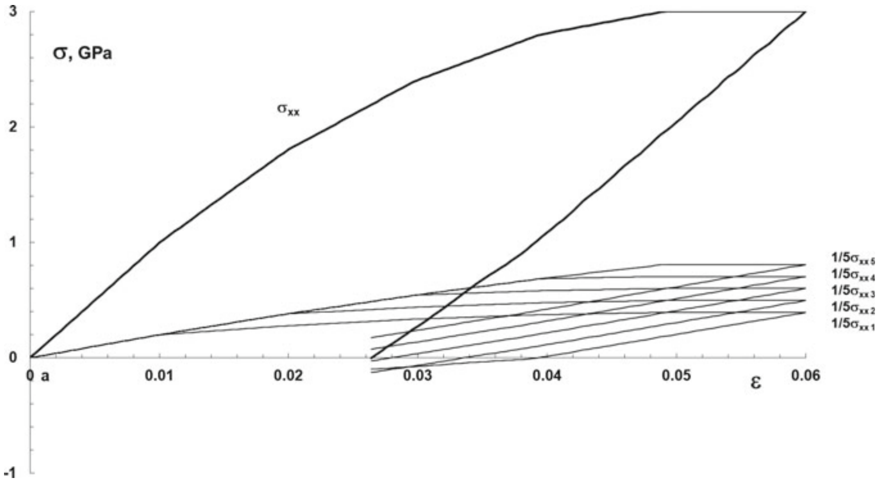

**Fig. 14** The values of the total stress $\sigma_{xx}$ and of its components $\sigma_{xxi}$ (model 1)

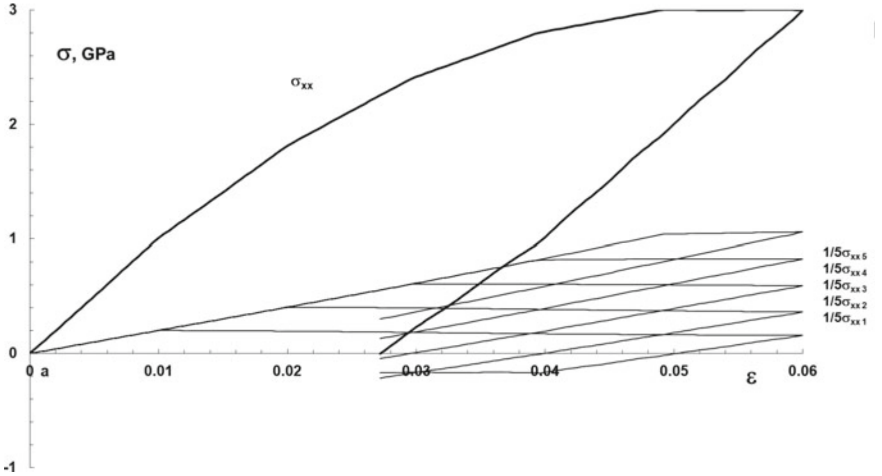

**Fig. 15** The values of the total stress $\sigma_{xx}$ and of its components $\sigma_{xxi}$ (model 2)

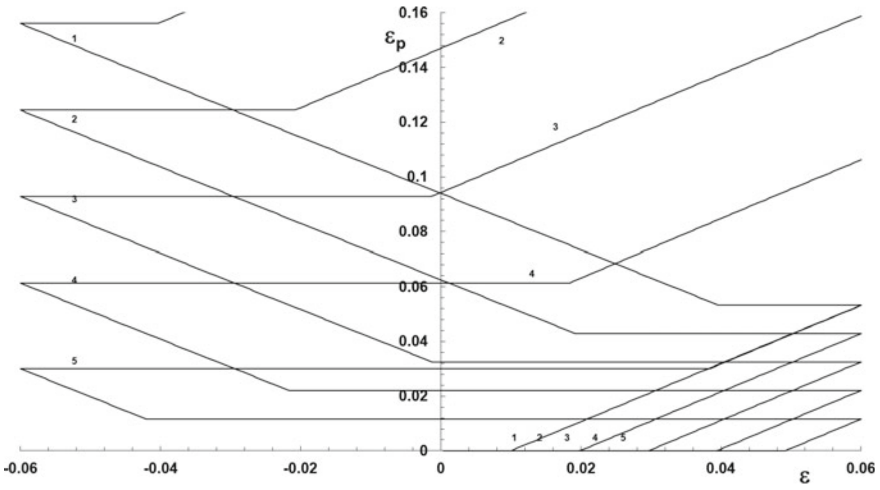

**Fig. 16** Variation of plastic deformations for selected components of $\varepsilon$

We can see for example from the first column that the components of the stress are different from zero while the total stress $\sigma_{xx}$ equals zero. While the first three components of the tensor pull the material in one direction, the the last two pull it in the other direction. This cannot be distinguished at the level of the whole structure. Even though the local values of the components of the stress tensor vary from one model to another, the total stress $\sigma_{xx}$ remains practically the same.

Figure 16 shows a plastic deformation of the same cylinder in the case of 5 level model. The components $\varepsilon_{pi}$ are computed by Eqs. (59) and (60). Obviously, the first component accumulates the largest value of plastic deformation while the last component accumulates the smallest value. Precise calculation of $\varepsilon_{pi}$ for each component can help to predict the fracture of the material in some manufacturing processes such as stamping.

## 5 Conclusions

In conclusion we can say that the difference of the approach developed in this work in comparison with the classic approach is that instead of changing the stress tensor we change the tensor $\mathbf{G}^{\vec{\mathbf{X}}}$ in the mesh elements. It corresponds to the change of the internal structure of the solid. The corresponding algorithm is illustrated for the von Mises yield criterion.

This algorithm allows us to adopt an alternative point of view on plastic flow simulations. We switch the emphasis from correction of the stress tensor to correction of the initial configuration of the solid body. In this case, the stress tensor is corrected automatically.

As far as it concerns the elastic part of deformation, we do not need to carry out the correction related to the stress rotation (see (7)).

The difference in the physical interpretation between the approach developed in this work and the classical algorithm is that the latter does not allow the stress tensor to exceed the yield condition. In the method introduced here, we irreversibly change the initial configuration of the solid body. As a result, the stress tensor is reduced to the required limit. Thus, we deal with the reason of plasticity and not with its consequences.

While changing the initial configuration, we can automatically get the plastic (irreversible) deformation at any time step.

A multi-yield surfaces model is developed as a natural generalization of the algorithm. It allows the simulation of multi-cycle loading with hardening and with Bauschinger effect.

The new algorithm allows us to calculate residual stresses in elastic-plastic solids after removing the external load as a result of unloading after a non-uniform plastic deformation.

Note that at the global level all steps are essentially elastic, since the preliminary predictor step adjusts the initial condition, and records the plastic strain, such that the current step ends on the yield surface. Due to this modification, the stiffness matrix does not need to be updated. Also, there is no need to calculate algorithmic or consistent tangent stiffness matrices. This is a one of computational benefit of this algorithm which allows the reduction of computational efforts.

As it is shown above, the "initial configuration" is always known as a byproduct of the algorithm so that the configuration after the removal of stamping loads is always available.

Introduction of the "initial configuration" in the algorithm reduces accumulation of error during stress integration in comparison with the classical Wilkins method. The results obtained with the classical method show the effect of unlimited "swelling" of the mesh. This effect can be suppressed by reducing the time integration step but can not be eliminated completely. The process of relaxation of the solid after the external load is removed can be sufficiently long. Therefore, the decrease of the time step is strongly undesirable. The new method is stable with respect to the "swelling" of the mesh, which is essential from the point of view of the CPU time.

**Acknowledgements** The authors would like to express their gratitude to Dr. Frode Maaseidvaag, former Director of Ford Research Laboratory (USA), for his financial and emotional support of our research efforts. The authors would like to acknowledge professor François Sidoroff from Ecole Centrale de Lyon (France) for his help and many useful discussions.

## A Notation

An orthogonal basis for the 3D vector space is a set of orthogonal unit vectors $\vec{\mathbf{e}}_i$ $(i = 1, 2, 3)$. We use here only fixed rectangular Cartesian coordinate system. The scalar product of any two of these vectors is

$$\vec{\mathbf{e}}_k \cdot \vec{\mathbf{e}}_s = \delta_{ks} = \begin{cases} 1, \text{ if } k = s, \\ 0, \text{ if } k \neq s, \end{cases}$$

where $\delta_{ks}$ is the Kronecker delta symbol. A vector (first-order tensor) $\vec{\mathbf{a}}$ can be decomposed in the introduced basis as

$$\vec{\mathbf{a}} = a_k \vec{\mathbf{e}}_k.$$

The usual summation convention is assumed over the repeated indices.

The dyadic product of the base vectors is the tensor $\vec{\mathbf{e}}_k\vec{\mathbf{e}}_s$. This tensor serves as a base tensor for the representation of a second-order tensor $\mathbf{A} = A_{ks}\vec{\mathbf{e}}_k\vec{\mathbf{e}}_s$. In particular, $\mathbf{A} \cdot \mathbf{B} = A_{ij}\vec{\mathbf{e}}_i\vec{\mathbf{e}}_j \cdot B_{ks}\vec{\mathbf{e}}_k\vec{\mathbf{e}}_s = A_{ij}B_{ks}\vec{\mathbf{e}}_i\delta_{jk}\vec{\mathbf{e}}_s = A_{ik}B_{ks}\vec{\mathbf{e}}_i\vec{\mathbf{e}}_s$ is the second-order tensor, $\mathbf{AB} = A_{ij}B_{ks}\vec{\mathbf{e}}_i\vec{\mathbf{e}}_j\vec{\mathbf{e}}_k\vec{\mathbf{e}}_s$ is the fourth-order tensor, $\vec{\mathbf{a}} \cdot \mathbf{A} = a_i\vec{\mathbf{e}}_i \cdot A_{ks}\vec{\mathbf{e}}_k\vec{\mathbf{e}}_s = a_iA_{ks}\delta_{ik}\vec{\mathbf{e}}_s = a_kA_{ks}\vec{\mathbf{e}}_s$ is the vector, $\mathbf{A} \cdot \cdot \mathbf{B} = A_{ij}\vec{\mathbf{e}}_i\vec{\mathbf{e}}_j \cdot \cdot B_{ks}\vec{\mathbf{e}}_k\vec{\mathbf{e}}_s = A_{ij}B_{ks}\delta_{jk}\delta_{is} = A_{sk}B_{ks}$ is the scalar.

## References

1. Alfano, G., Angelis, F., Rosati, L.: General solution procedures in elasto/viscoplasticity. Comput. Methods Appl. Mech. Eng. **190**, 5123–5147 (2001)
2. Auricchio, F.: A viscoplastic constitutive equation bounded between two generalized plasticity models. Int. J. Plast. **13**, 697–721 (1997)
3. Auricchio, F.: A robust integration-algorithm for a finite-strain shape-memory-alloy superelastic model. Int. J. Plast. **17**, 971–990 (2001)
4. Auricchio, F., Taylor, R.L.: Shape-memory alloys: modelling and numerical simulations of the finite-strain superelastic behavior. Comput. Methods Appl. Mech. Eng. **143**, 175–194 (1997)
5. Bessonov, N., Golovashchenko, S.: Numerical simulation of pulsed electromagnetic stamping processes. In: Proceedings of 1st International Conference on High Speed Forming, pp. 83–91. Dortmund, Germany (2004)
6. Bessonov, N.M., Song, D.J.: Application of vector calculus to numerical simulation of continuum mechanics problems. J. Comput. Phys. **167**(1), 22–38 (2001)
7. Brünig, M.: Nonlinear finite element analysis based on a large strain deformation theory of plasticity. Comput. & Struct. **69**, 117–128 (1998)
8. Christensen, P.W.: A nonsmooth Newton method for elastoplastic problems. Comput. Methods Appl. Mech. Eng. **191**, 1189–1219 (2002)
9. Düster, A., Rank, E.: A $p$-version finite element approach for two- and three-dimensional problems of the $J_2$ flow theory with non-linear isotropic hardening. Int. J. Numer. Methods Eng. **53**, 49–63 (2002)
10. Elgamal, A., Yang, Z., Parra, E., Ragheb, A.: Modeling of cyclic mobility in saturated cohesionless soils. Int. J. Plast. **19**, 883–905 (2003)
11. Engelen, R.A.B., Geers, M.G.D., Baaijens, F.P.T.: Nonlocal implicit gradient-enhanced elastoplasticity for the modelling of softening behaviour. Int. J. Plast. **19**, 403–433 (2003)
12. Fish, J., Shek, K.: Computational aspects of incrementally objective algorithms for large deformation plasticity. Int. J. Numer. Methods Eng. **44**, 839–851 (1999)
13. Fougeres, R., Sidoroff, F.: The evolutive masing model and its application to cyclic plasticity and ageing. Nucl. Eng. Des. **114**, 273–284 (1989)
14. Giarlet, P.G.: Mathematical elasticity, vol. 1. Three Dimensional Elasticity, Amsterdam, North-Holland (1993)

15. Golovashchenko, S., Bessonov, N.., Davies, R.: Analysis of blank-die contact interaction in pulsed forming processes. In: 3st International Conference on High Speed Forming, Germany (2008)
16. Golovashchenko, S., Bessonov, N.: Development of sharp flanging technology for aluminum panels. In: Proceedings of the 6th International Conference on Numerical Simulation of 3D Sheet Forming Processes, NUMISHEET 2005, Detroit, MI, pp. 687–690
17. Golovashchenko, S.F., Bessonov, N.M.: Numerical simulation of high-rate stamping of tubes and sheets. CRM Proc. Lect. Notes, Can. Math. Soc. **21**, 199–207 (1998)
18. Guo, J., Cox, J.V.: Implementation of a plasticity bond model for reinforced concrete. Comput. & Struct. **77**, 65–82 (2000)
19. Howell, B.P., Ball, G.J.: A free-Lagrange augmented Godunov method for the simulation of elastic-plastic solids. J. Comput. Phys. **175**(1), 128–167 (2002)
20. Kang, G., Ohno, N., Nebu, A.: Constitutive modeling of strain range dependent cyclic hardening. Int. J. Plast. **19**, 1801–1819 (2003)
21. Khan, A.S., Huang, S.: Continuum Theory of Plasticity. Wiley, New-York (1995)
22. Lin, R.C., Brocks, W.: On a finite strain viscoplastic theory based on a new internal dissipation inequality. Int. J. Plast. (2004). in print
23. Liu, C.S.: A consistent numerical scheme for the von Mises mixed-hardening constitutive equations. Int. J. Plast. (2004). in print
24. Lubarda, V.A.: Elastoplatcity Theory, p. 638. CRP Press, New York (2000)
25. Lubarda, V.A., Benson, D.J., Meyers, M.A.: Strain-rate effects in rheological models of inelastic response. Int. J. Plast. **19**, 1097–1118 (2003)
26. Mahnken, R.: Anisotropic creep modelling based on elastic projection operators with applications to CMSX-4 superalloy. Comput. Methods Appl. Mech. Eng. **191**, 1611–1637 (2002)
27. Marino, L., Saccomandi, G., Valente, C.: A note about three-dimentional exact dynamical solutions for new-Hookean materials. Int. J. Non-Linear Mech. **34**, 1–4 (1999)
28. Montáns, F.J.: Implicit algorithms for multilayer $J_2$ plasticity. Comput. Methods Appl. Mech. Eng. **189**, 673–700 (2000)
29. Papadopoulos, P., Lu, J.: On the formulation and numerical solution of problems in anisotropic finite plasticity. Comput. Methods Appl. Mech. Eng. **190**, 4889–4910 (2001)
30. Rubin, M.B., Bodner, S.R.: A three-dimensional nonlinear model for dissipative response of soft tissue. Int. J. Solids Struct. **39**(19), 5081–5099 (2002)
31. Simo, J.C., Hughes, T.J.R.: Computational Inelasticity. Springer, New York (1998)
32. Voyiadjis, G.Z., Abu Al-Rub, R.K.: Thermodynamic based model for the evolution equation of the backstress in cyclic plasticity. Int. J. Plast. **19**, 2121–2147 (2003)
33. Wilkins, M.L.: Calculation of elastic-plastic flow. In: Alder B., et al. (eds.) Methods in Computational Physics, vol. 3. Academic Press, New-York (1964)
34. Wilkins, M.L.: Computer Simulation of Dynamic Phenomena. Springer, Scientific Computation (1998)
35. Wu, H.C.: On finite plastic deformation of anisotropic metallic materials. Int. J. Plast. **19**, 91–119 (2003a)
36. Wu, H.C.: Effect of loading-path on the evolution of yield surface for anisotropic metals subjected to large pre-strain. Int. J. Plast. **19**, 1773–1800 (2003b)
37. Yoon, J.W., Barlat, F., Dick, R.E., Chung, K., Kang, T.J.: Plane stress yield function for aluminum alloy sheets-part II: FE formulation and its implementation. Int. J. Plast. **20**, 495–522 (2004)

# Modulation Instability of Flexural Waves in Cylindrical Shells: Modified Criterion

**Andrey V. Bochkarev, Vladimir I. Erofeev and Alexander I. Zemlyanukhin**

**Abstract** On the basis of asymptotic analysis of the Kirchhoff-Love cylindrical shell's element motion equations in displacements a nonintegrable fourth-order quasi-hyperbolic equation with cubic nonlinearity is derived. For the analysis of axisymmetric propagation of small-amplitude flexural-longitudinal waves along the shell, this equation is reduced to the generalized nonlinear Schrödinger equation. A criterion for the modulation instability of the waves is obtained, which clarifies the known Lighthill criterion.

## 1 Introduction

Nonlinear wave dynamics of thin-walled deformable systems is one of the rapidly developing areas of mechanics. The corresponding mathematical models are often based on the theory of thin shells [1, 2]. The greatest practical interest is the study of the process of development of modulation instability of propagating wave packets. The consequence of such instability is the possibility of formation and long-term propagation of stable stationary pulses in the form of envelope solitons, the parameters of which are used in the problems of acoustic diagnostics and non-destructive testing of materials.

The aim of this work is to study theoretically the possibility of the development of modulation instability of axisymmetric flexural waves propagating along the cylindrical shell.

The achievement of this goal is provided by the solution of the problem of modeling the propagation process of axisymmetric flexural waves packages along the cylindrical shell, the derivation and qualitative analysis of the nonintegrated quasi-hyperbolic equation.

---

A. V. Bochkarev · A. I. Zemlyanukhin
Yuri Gagarin State Technical University of Saratov, Saratov, Russia

V. I. Erofeev (✉)
Mechanical Engineering Research Institute of RAS, Nizhny Novgorod, Russia
e-mail: erof.vi@yandex.ru

H. Altenbach et al. (eds.), *Dynamical Processes in Generalized Continua and Structures*, Advanced Structured Materials 103,
https://doi.org/10.1007/978-3-030-11665-1_6

In the first section, on the basis of asymptotic analysis of the Kirchhoff—Love shell's element motion equations, the nonlinear quasi-hyperbolic equation is derived. In the second section, this equation, using the correct asymptotic procedure, is transformed into a generalized nonlinear Schrödinger equation (GNLSE) and the modulation instability of its solutions is analyzed. In the third section the results are discussed.

## 2 Asymptotic Analysis of the Shell's Element Motion Equations

Consider the thin-walled circular infinite cylindrical shell of the Kirchhoff-Love model, directing the $x$-axis along its centerline, the $y$-axis in the circumferential direction, and the $z$-axis in the radial direction from the center. The longitudinal, circumferential and radial displacement of the element of the shell's middle surface are designated as $u$, $v$ and $w$, respectively.

The motion equations of the shell interacting with an external nonlinear elastic medium in the axisymmetric case (under the condition that the circumferential displacement $v$, the derivatives with respect to circumferential coordinate $y$ and the parameter $k_x$ of the curvature in the longitudinal direction are equal to zero) have the form [1]:

$$\begin{gathered}
u_{xx} - \mu\, k_y w_x + \underline{\tfrac{h^2}{12} k_y w_{xx}} + w_x w_{xx} - \tfrac{\gamma}{g}\tfrac{1-\mu^2}{E} u_{tt} = 0, \\
\tfrac{h^2}{12}\left( w_{xxxx} - \underline{\underline{\tfrac{3}{2}(w_x^2 w_{xx})_{xx}}} \right) - \mu\, k_y u_x + \underline{\tfrac{h^2}{12} k_y u_{xxx}} + k_y^2 w - \tfrac{1}{2}\mu\, k_y w_x^2 - \\
-\left( w_x \left( u_x - \mu\, k_y w + \underline{\underline{\underline{\tfrac{1}{2} w_x^2}}} \right) \right)_x + \tfrac{\gamma}{g}\tfrac{1-\mu^2}{E} w_{tt} + \tfrac{k_1}{R^2} w - \tfrac{k_2}{h^2 R^2} w^3 = 0,
\end{gathered} \tag{1}$$

where $E$ is the Young's modulus, $\mu$ is the Poisson ratio, $k_y = 1/R$ is the curvature parameter in the circumferential direction, $R$ is the radius of curvature, $\gamma$ is the unit weight of shell material, $g$ is the acceleration of gravity, $h$ is the shell thickness, the subscripts $t$ and $x$ represent the partial derivatives with respect to the corresponding variables, $k_1$ и $k_2$ are the parameters of the nonlinear elastic medium surrounding the shell (Fig. 1). Note that we consider the case of "soft" nonlinearity of the environment (the last two terms of the second equation of the system (1) have opposite signs).

The Eqs. (1) contain several additional terms. The terms underlined by a single line arise when taking into account the variation of geometrical parameters on the thickness of the shell, [3], as well as in structurally inhomogeneous shells [4].

The twice-underlined summand appears due to the use of a refined expression for the curvature $K$, which holds the first two terms of the expansion in a series by $w_x$:

$$K = \frac{w_{xx}}{(1 + w_x^2)^{3/2}} \approx w_{xx}\left(1 - \frac{3}{2} w_x^2\right).$$

**Fig. 1** Geometry of the shell

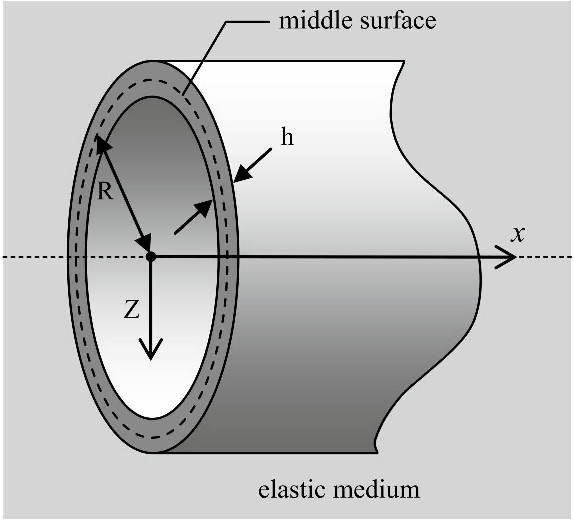

For geometrically nonlinear flexible shells, the squares of rotation angles associated with the shell's deflection have the same order as the linear deformations in the material array [5], so that the second equation of the system (1) holds the triple underlined summand which is usually discarded.

After transition to dimensionless variables $U, W, X, T$:

$$u = \frac{h^2}{l}U, \quad w = hW, \quad x = lX, \quad t = \frac{l^2}{h}\sqrt{\frac{\gamma}{g}\frac{1-\mu^2}{E}}\,T \tag{2}$$

and introduction of dimensionless small parameter $\varepsilon$ and scaling factor $q = O(1)$:

$$\varepsilon = \frac{h}{R}, \quad q\varepsilon = \frac{h^2}{l^2}, \tag{3}$$

Equation (1) will take the form

$$\begin{gathered} U_{XX} - q\,\varepsilon\,U_{TT} - \tfrac{\mu}{q}W_X + \tfrac{\varepsilon}{12}W_{XXX} + W_X W_{XX} = 0, \\ \tfrac{q}{12}W_{XXXX} + \tfrac{k_1+1}{q}W + q\,W_{TT} - \mu\,U_X + \tfrac{q\,\varepsilon}{12}U_{XXX} + \tfrac{\mu}{2}W_X^2 + \mu\,W W_{XX} - q(U_X W_X)_X - \\ -\tfrac{k_2}{q}W^3 - \tfrac{3q}{2}W_X^2 W_{XX} - \tfrac{q^2\varepsilon}{8}(W_X^2 W_{XX})_{XX} = 0. \end{gathered} \tag{4}$$

For further asymptotic simplification of the system (4) we will use the approach proposed in [6, 7]. Using the fact that the linear part of the system (4) has solutions in the form of plane harmonic waves

$$
\begin{aligned}
U &= U_0 \exp[i(\Omega T - kX)] + \overline{U_0} \exp[-i(\Omega T - kX)],\\
W &= W_0 \exp[i(\Omega T - kX)] + \overline{W_0} \exp[-i(\Omega T - kX)],
\end{aligned} \tag{5}
$$

where the upper dash denotes complex conjugation, to determine the amplitudes $U_0$, $W_0$ we have a homogeneous system of equations

$$
\begin{aligned}
&12q(q\varepsilon\,\Omega^2 - k^2)U_0 + ik(k^2q\varepsilon + 12\mu)W_0 = 0,\\
&ikq(k^2q\varepsilon + 12\mu)U_0 + [k^4q^2 - 12q^2\Omega^2 + 12(k_1 + 1)]W_0 = 0,
\end{aligned}
$$

a non-trivial solution of which

$$
U_0 = i\frac{k^4q^2 - 12q^2\Omega^2 + 12(k_1 + 1)}{kq(k^2q\varepsilon + 12\mu)}W_0, \tag{6}
$$

exists if the dispersion relation is satisfied:

$$
\begin{aligned}
&144q^3\varepsilon\,\Omega^4 - 12q[k^4q^2\varepsilon + 12k^2q + 12\varepsilon(k_1 + 1)]\Omega^2 +\\
&\quad + k^6q^2(12 - \varepsilon^2) + 144k^2(k_1 + 1 - \mu^2) - 24k^4q\mu\varepsilon = 0.
\end{aligned} \tag{7}
$$

The solution of Eq. (7) with respect to $\Omega^2$ has two branches, high-frequency and low-frequency ones. In this paper we will consider the low-frequency branch.

Asymptotic simplification of the function $\Omega^2(k)$ and expression (6) at $k = O(1)$, carried out under the assumption

$$
\frac{1}{5} < \mu < \frac{1}{3}, \quad \frac{1}{500} < \varepsilon < \frac{1}{100} \tag{8}
$$

leads to approximate equations:

$$
\Omega^2 \approx \frac{k_1 + 1 - \mu^2}{q^2} + \frac{1}{12}k^4, \quad U_0 \approx i\frac{\mu}{kq}W_0. \tag{9}
$$

The revealed relationship between the amplitudes of longitudinal and transverse displacements (9) allows us to record the relationship between the displacements themselves in the form

$$
W \approx \frac{q}{\mu}U_X. \tag{10}
$$

Under the condition $kq > \mu$ we have $|U_0| < |W_0|$, that corresponds to predominantly transverse (flexural-longitudinal) wave. Excluding with (10) the derivatives of the function $U$ included in Eq. (4) for the transverse displacement $W$, we obtain

$$
\frac{1}{12}W_{XXXX} + c_1W + W_{TT} - c_2W_X^2 - \frac{3}{2}W_X^2W_{XX} + c_3W_{XX} - c_4(W_X^2W_{XX})_{XX} - c_5W^3 = 0, \tag{11}
$$

where $T$ and $X$ are dimensionless time and axial coordinates and coefficients

$$c_1 = \frac{k_1 + 1 - \mu^2}{q^2}, \quad c_2 = \frac{\mu}{2q}, \quad c_3 = \frac{\varepsilon\mu}{12q}, \quad c_4 = \frac{q\varepsilon}{8}, \quad c_5 = \frac{k_2}{q^2}, \tag{12}$$

contain the physical and geometrical parameters of the shell, as well as the small parameter $\varepsilon = h/R$, the ratio of the shell thickness to its radius.

## 3 Modulational Instability of Axisymmetric Flexural Waves

The construction of exact solutions for Eq. (11) is difficult, so we carry out its further asymptotic simplification. It is known from the analysis of problems of nonlinear acoustics that in media with cubic nonlinearity the effect of self-action of a wave prevails over the effect of generation of higher harmonics. In this case, the solution is found in the form of a traveling modulated wave with a slowly varying small amplitude, resulting in the nonlinear Schrödinger equation (NLSE).

In the article [8] the Eq. (11) was transformed to the NLSE

$$iA_\tau + \rho A_{\zeta\zeta} + \lambda |A|^2 A = 0, \tag{13}$$

in which the complex amplitude $A$ is a function of slow time $\tau = \alpha T$ and slow coordinate $\zeta = \alpha(X - \nu_g T)$; $\alpha$ is the small parameter, $\nu_g$ is the group velocity. It is shown [8], that when the approximate inequality

$$k_2 > \frac{1}{2} k^4 q^2 \tag{14}$$

is fulfilled, the transverse axisymmetric wave is subject to modulation instability: small harmonic perturbations of its amplitude grow indefinitely over time [9].

The inequality (14) is obtained using the well-known Lighthill criterion, which for NLSE in the form (13) has the form

$$\rho\lambda > 0. \tag{15}$$

The analysis shows [8], that the inequality $\rho > 0$ is satisfied for any $k$, while the nonlinear term coefficient $\lambda$ is positive for small $k$ and negative for large $k$. Therefore, the upper limit $k_{\max}$ of the modulation instability zone is in the region of $\lambda$-values closing to zero. In this area, the correct description of the propagation of weakly modulated nonlinear waves requires the retention of higher order nonlinear terms, that is, requires the transition from NLSE to generalized NLSE (GNLSE).

We will use the method of many scales to derive the GNLSE [10]. Suppose that the function $W$ depends on three variables: fast phase $\theta = kX - \omega T$, slow coordinate

$\xi = \alpha X$ and slow time $\tau = \alpha T$, $\alpha \ << \ 1$, so that the Eq. (11) is transformed by substitutions of derivatives of the form

$$\begin{aligned} W_{TT} &\to \alpha^2 W_{\tau\tau} - 2\alpha\,\omega\, W_{\theta\tau} + \omega^2 W_{\theta\theta}, \\ W_X &\to k W_\theta + \alpha\, W_\xi, \\ W_{XX} &\to \alpha^2 W_{\xi\xi} + 2k\alpha\, W_{\theta\xi} + k^2 W_{\theta\theta}, \end{aligned} \tag{16}$$

and so on. Taking into account that the transformed Eq. (11) contains both quadratic and cubic nonlinearity, we will look for its solution in the form

$$W = \alpha[A(\xi,\tau)\mathrm{e}^{i\theta} + \bar{A}(\xi,\tau)\mathrm{e}^{-i\theta}] + \alpha^2[B(\xi,\tau)\mathrm{e}^{2i\theta} + \bar{B}(\xi,\tau)\mathrm{e}^{-2i\theta} + C(\xi,\tau)] + O(\alpha^3), \tag{17}$$

including the first and second harmonics, as well as the average displacement described by the summand $C(\xi, \tau)$.

We call the equation obtained from (11) after substitutions (16) and (17) as the equation for the amplitudes. In this equation, we collect the terms proportional to $e^{i\theta}$ and equating the multiplier at $\alpha^1$ to zero, obtain the dispersion relation

$$\omega = \pm\sqrt{\frac{1}{12}k^4 - c_3 k^2 + c_1}. \tag{18}$$

Limiting further to positive values of $\omega$ and $k$, for phase velocity $v_f$ and group velocity $v_g$ we have

$$v_f = \frac{\omega}{k}, \quad v_g = \frac{\partial\omega}{\partial k} = \frac{(k^2 - 6c_3)k}{6\omega}. \tag{19}$$

In the following orders of $\alpha$ we obtain

$$\begin{aligned} &\alpha^2[i(A_\tau + v_g A_\xi)] \\ &\quad + \alpha^3\left[\frac{1}{2\omega}\left(\left(\frac{k^2}{2} - c_3\right)A_{\xi\xi} - A_{\tau\tau} + \left(c_4 k^6 - \frac{3}{2}k^4 + 3c_5\right)A^2\bar{A} + 4c_2 k^2 \bar{A}B\right)\right] + \\ &\quad + \alpha^4\left[\frac{ik}{\omega}\left(-\frac{1}{6}A_{\xi\xi\xi} - c_4 k^4 A\left(4\bar{A}A_\xi + A\bar{A}_\xi\right) + 3k^2 A\bar{A}A_\xi + c_2(2B\bar{A}_\xi - \bar{A}B_\xi + AC_\xi)\right)\right] + \\ &\quad + O(\alpha^5) = 0. \end{aligned} \tag{20}$$

Expressing the second-order derivative with respect to time $A_{\tau\tau} = v_g^2 A_{\xi\xi} + O(\alpha)$ from the $\alpha^2-$order of (20), substitute it in $\alpha^3-$order. Then we express from the $\alpha^3-$order the value of

$$E \equiv (\bar{A}B)_\xi = -\frac{1}{4c_2k^2}\left[\omega\omega_{kk}A_{\xi\xi\xi} + \left(c_4k^6 - \frac{3}{2}k^4 + 3c_5\right)(A^2\bar{A})_\xi\right] + O(\alpha), \tag{21}$$

and find the parameter $\gamma$ in the identity

$$\bar{A}B_\xi \equiv \gamma E + (1-\gamma)(\bar{A}B)_\xi - B\bar{A}_\xi + O(\alpha), \tag{22}$$

in such a way that after substitution (22) in $\alpha^4$—order of the Eq. (20) the coefficient at $A_{\xi\xi\xi}$ would be equal to $-(1/6)i\,\omega_{kkk}$. Turning to superslow time $\tau_1$ and the running variable $\zeta$:

$$\tau_1 = \alpha\tau, \quad \zeta = \xi - v_g\tau, \tag{23}$$

for the Eq. (20) we have

$$\alpha^3\left[\left(iA_{\tau_1} + \frac{\omega_{kk}}{2}A_{\zeta\zeta} + \frac{1}{2\omega}\left(c_4k^6 - \frac{3}{2}k^4 + 3c_5\right)A^2\bar{A} + \frac{2}{\omega}c_2k^2\bar{A}B\right)\right] + \\ + \alpha^4\left[i\left(-\frac{\omega_{kkk}}{6}A_{\zeta\zeta\zeta} + d_1A\bar{A}A_\zeta + d_2A^2\bar{A}_\zeta + d_3B\bar{A}_\zeta + d_4\bar{A}B_\zeta + \frac{kc_2}{\omega}AC_\zeta\right)\right] + \\ + O(\alpha^5) = 0. \tag{24}$$

In the Eq. (24), we introduced short notations for derivatives $\omega_{kk} = \partial^2\omega/\partial k^2$, $\omega_{kkk} \equiv \partial^3\omega/\partial k^3$; the coefficients $d_1, \ldots, d_4$ depend on the wave number $k$ and the coefficients $c_1, \ldots, c_5$ are not given here because of the bulkiness.

To express in $A(\xi, \tau)$ the function $B(\xi, \tau)$, which is included in the $\alpha^4$—order of (24), we collect all the summands proportional to $e^{2i\theta}$ in the equation for the amplitudes. After switching to the variables (23), taking into account the equalities (18) and (19), we have

$$\alpha^2\left[c_2k^2A^2 + (k^4 - 3c_1)B\right] + \alpha^3\left[-2i(c_2kAA_\zeta + k^3B_\zeta)\right] + O(\alpha^4) = 0. \tag{25}$$

Higher orders in (25) are not needed because in (17) the function $A$ is multiplied by $\alpha$, while the functions $B$ и $C$ are multiplied by $\alpha^2$.

We will look for a solution of (25) in the form

$$B = B_0(\zeta, \tau_1) + i\,\alpha\,B_1(\zeta, \tau_1) + O(\alpha^2). \tag{26}$$

Substituting (26) in (25), neglecting the terms with the order above $\alpha^3$ and equating the real part to zero, we find

$$B_0 = -\frac{c_2k^2}{k^4 - 3c_1}A^2. \tag{27}$$

Substituting (27) in the equation for the imaginary part, we have

$$B_1 = -\frac{2kc_2(k^4 + 3c_1)}{(k^4 - 3c_1)^2}AA_\zeta. \tag{28}$$

To express in $A(\xi, \tau)$ the function $C(\xi, \tau)$, which is included in the в $\alpha^4$- order of (24), let us collect in the equation for the amplitudes all the terms that do not contain an exponential factor:

$$\alpha^2[-2c_2k^2A\bar{A} + c_1C] + \alpha^3[2ic_2k(\bar{A}A_\zeta + A\bar{A}_\zeta)] + O(\alpha^4) = 0, \tag{29}$$

from where we obtain

$$C = \frac{2c_2k}{c_1}[kA\bar{A} - \alpha\, i(\bar{A}A_\zeta - A\bar{A}_\zeta)] + O(\alpha^2). \tag{30}$$

Substituting (27) and (28) in (26), and then substituting (26) and (30) in (24), we obtain the GNLSE for the amplitude $A(\xi, \tau)$ of the first harmonic (17):

$$i\,A_{\tau_1} + \rho\,A_{\zeta\zeta} + \lambda\,A^2\bar{A} + i\,\rho_1A_{\zeta\zeta\zeta} + i\,\lambda_1A(A\bar{A})_\zeta + i\,\lambda_2A\bar{A}A_\zeta = 0, \tag{31}$$

where

$$\begin{aligned}
&\rho = \frac{\omega_{kk}}{2}, \quad \lambda = \frac{1}{2\omega}\left(c_4k^6 - \frac{3}{2}k^4 + 3c_5 - \frac{4k^4c_2^2}{k^4 - 3c_1}\right), \quad \rho_1 = -\frac{\alpha\omega_{kkk}}{6},\\
&\lambda_1 = 12\alpha\Big[-c_1c_4k^{17} + \Big(18c_1c_3c_4 + c_2^2\Big)k^{15} - \Big(18c_1^2c_4 + 12c_2^2c_3 + 9c_1c_3\Big)k^{13} -\\
&\quad - c_1\Big((108c_3c_4 - 18)c_1 - c_2^2 - 3c_5\Big)k^{11} - 9c_1\Big(15c_1^2c_4 + 6c_1c_3 + 2c_3(6c_2^2 - c_5)\Big)k^9 -\\
&\quad - c_1^2\Big((108 - 162c_3c_4)c_1 + 72c_2^2 + 18c_5\Big)k^7 - 9c_1^2\Big(24c_1^2c_4 + 9c_1c_3 + 4c_3(2c_2^2 - 3c_5)\Big)k^5 +\\
&\quad + 27c_1^3(6c_1^2 + c_5)k^3 - 162c_1^3c_3c_5k\Big]/Q,\\
&\lambda_2 = -\alpha\,kc_1[12c_4k^{16} - 9(1 + 20c_3c_4)k^{14} + 18(9c_3 + 8c_1c_4)k^{12} +\\
&\quad + 6\Big(4c_2^2 - 27c_1 - 3c_5 + 180c_1c_3c_4\Big)k^{10} - 3\Big(4c_1(99c_1c_4 + 81c_3) + 12c_3(4c_2^2 - 3c_5)\Big)k^8 +\\
&\quad + 9c_1\Big(45c_1(3 - 4c_3c_4) + 8c_2^2 + 12c_5\Big)k^6 + 162c_1\Big(12c_1^2c_4 + 9c_1c_3 - 4c_3(2c_2^2 + c_5)\Big)k^4 -\\
&\quad - 54c_1^2\Big(-32c_2^2 + 36c_1 + 3c_5\Big)k^2 + 81c_1^2c_2c_5]/Q,\\
&Q = \sqrt{3}(k^4 - 12c_3k^2 + 12c_1)^{3/2}c_1(k^4 - 3c_1)^2.
\end{aligned} \tag{32}$$

The Eq. (31) has various classes of exact solutions, in particular, a plane wave

$$A = A_0e^{i(K\zeta - \Omega\tau_1)} \tag{33}$$

with complex amplitude $A_0$ and frequency $\Omega$ that satisfies the nonlinear dispersion relation

$$\Omega = (\rho - \rho_1K)K^2 - (\lambda - \lambda_2K)A\bar{A}. \tag{34}$$

Let's investigate the stability of the solution (33) to small periodic perturbations. To do this, following [11], we will look for a solution to GNLSE (31) in the form

$$A = (1 + \delta \cdot E)A_0 e^{i(K\zeta - \Omega\tau_1)}, \tag{35}$$

where $\delta$ is the small real parameter and $E = E(\zeta, \tau_1)$ is the complex amplitude of the perturbation. Substituting (35) in (31) and linearizing with respect to $E$, we have

$$\begin{aligned} &iE_{\tau_1} + (\rho - 3\rho_1 K) + E_{\zeta\zeta} + i\rho_1 E_{\zeta\zeta\zeta} + (\lambda - \lambda_2 K)A_0\overline{A_0}(E + \bar{E}) + \\ &+ i\lambda_1 A_0\overline{A_0}(E + \bar{E})_\zeta + i(\lambda_2 A_0\overline{A_0} - 2\rho K + 3\rho_1 K^2)E_\zeta = 0. \end{aligned} \tag{36}$$

We will look for a solution to the Eq. (36) in the form

$$E = E_1 e^{i(\kappa\zeta - w\tau_1)} + E_2 e^{-i(\kappa\zeta - \bar{w}\tau_1)}, \tag{37}$$

where $E_1$, $E_2$ are complex constants, $\kappa$ is the real wave number, $w$ is the frequency of perturbation, which can be complex. The substitution (37) in (36) leads us to the system of homogeneous equations for $E_1$, $\overline{E_2}$:

$$\begin{aligned} &(a - b - c)\,E_1 + (d - c)\,\overline{E_2} = 0, \\ &(d + c)\,E_1 + (a + b + c)\,\overline{E_2} = 0, \end{aligned} \tag{38}$$

where

$$\begin{aligned} &a = \kappa^3\rho_1 + \kappa\left[3\rho_1 K^2 - 2\rho K - (\lambda_1 + \lambda_2)A_0\overline{A_0}\right] + w, \\ &b = \kappa^2(\rho - 3\rho_1 K), \quad c = (\lambda_2 K - \lambda)A_0\overline{A_0}, \quad d = -\kappa\lambda_1 A_0\overline{A_0}. \end{aligned} \tag{39}$$

Taking into account that $A_0\overline{A_0} = |A_0|^2$, all values contained in the right parts of (39) are real, with the exception, maybe, of frequency $w$. If the right part of the compatibility condition

$$a^2 = b^2 + 2bc + d^2 \tag{40}$$

of the system (38) is negative, then the frequency $w$ must be complex and the initial perturbations can grow with time. The condition for the right part of (40) to be negative after the substitution (39) takes the

$$2(\rho - 3\rho_1 K)(\lambda - \lambda_2 K) > \frac{\kappa^2}{|A_0|^2}(\rho - 3\rho_1 K)^2 + |A_0|^2\lambda_1^2. \tag{41}$$

When the inequality (41) is satisfied, GNLSE solution (33) is modulation unstable. In addition to the coefficients of the Eq. (31), this inequality contains the amplitude $A_0$ and the wave number $K$ of the equality (33) together with the wave number $\kappa$ of modulation perturbation (37). If we put $\rho_1 = \lambda_1 = \lambda_2 = 0$, then the GNLSE (31) is reduced to NLSE (13) and the inequality (41) under the additional condition $\kappa = 0$ turns into the Lighthill criterion (15).

## 4 Discussion of the Results

Let's take the following values of constant parameters as basic ones: $\alpha = 1/10$, $k_1 = k_2 = 1$, $\mu = 1/4$, $q = 1$, $\varepsilon = 1/100$. Figure 2 for the case $A_0 = 1$, $\kappa = 0$ shows the dependence of the difference between the left and right sides of the inequality (41) и (15) on the wave number $k$. Areas of positive ordinate values correspond to the modulation instability of the solution. Neglecting the narrow resonance region of the first and second harmonics of the solution (17) in the neighborhood $k_{rez} \approx 1.55$, it can be argued that the upper limit $k_{\max}$ of the instability zone depends significantly on $K$: for positive $K$ the zone is narrowed, for negative $K$ it is expanded.

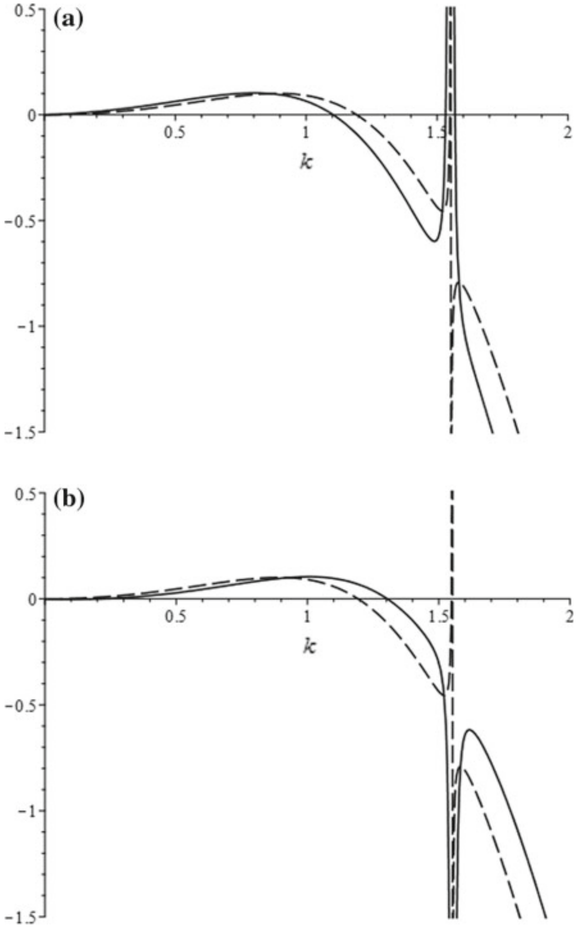

**Fig. 2** Differences between left and right sides of inequalities (41) (solid line) and (15) (dashed line) at **a** $K = 1$ and **b** $K = -1$

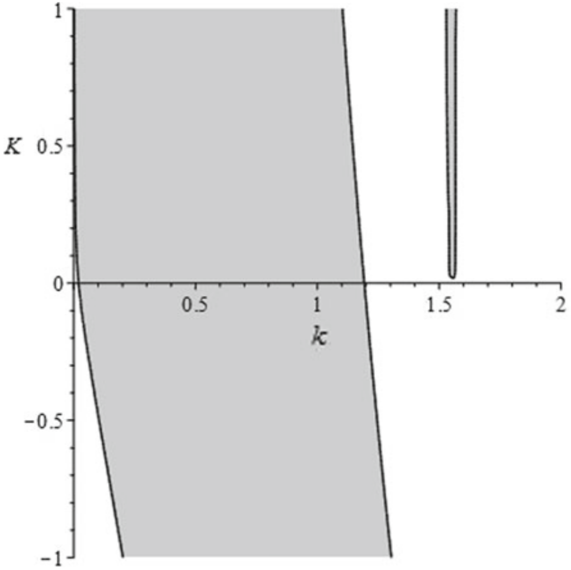

**Fig. 3** Instability zone in the coordinates $(k, K)$

On the contour plot (Fig. 3) of the instability zone in the coordinates $(k, K)$ it can be seen that at negative $K$ the lower limit $k_{\text{min}}$ also shifts and in general with an increase in $|K|$ the width of the zone decreases.

The size of the instability zone is very sensitive to the value of the parameter $k_2$ of the elastic medium surrounding the shell. In Fig. 4, you can see that with increasing in $k_2$ the upper boundary of zone $k_{\text{max}}$ tends to $k_{rez}$; with reduction in $k_2$ the zone is narrowed and when you reach $k_2 = 0$ the zone disappears. Thus, for a linear elastic medium ($k_2 = 0$) and for a nonlinear elastic one with a nonlinearity of the “rigid” type ($k_2 < 0$) modulation instability is not observed.

Figure 5 shows the dependence of the upper boundary $k_{\text{max}}$ of the instability zone on the amplitude $A_0$ of the first harmonic: the zone narrows with $A_0$ decreasing.

## 5 Conclusions

The system of element motion equations of the Kirchhoff–Love cylindrical shell interacting with a nonlinear elastic medium is reduced to single 4th-order nonlinear quasi-hyperbolic equation. For the slowly varying amplitude of small flexural-longitudinal axisymmetric waves, a generalized nonlinear Schrödinger equation is obtained. The modified criterion of the modulation instability of such waves allowed us to significantly clarify the size of the instability zone for different combinations of the shell’s geometric and physical parameters. It is shown that the modulation

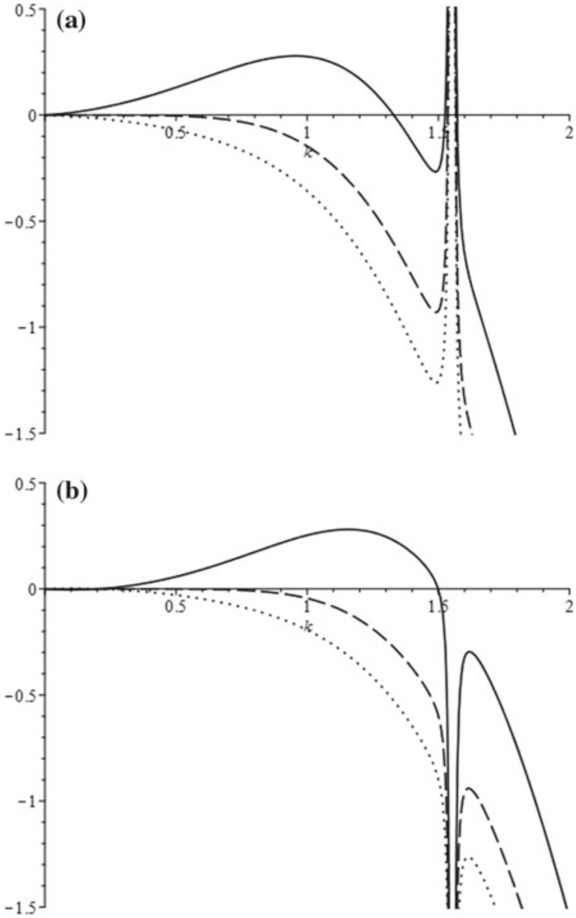

**Fig. 4** Difference between left and right sides of inequality (41) at $k_2 = 2$ (solid line), $k_2 = 0$ (dashed line) and $k_2 = -1$ (dotted line) when **a** $K = 1$ and **b** $K = -1$

instability is absent both in the case of linear and in the case of a rigid nonlinear elastic law of deformation of the medium surrounding the shell.

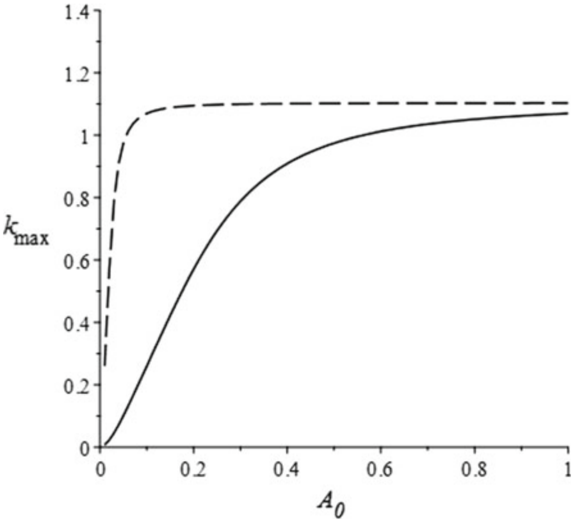

**Fig. 5** Dependence of $k_{\max}$ on $A_0$ at $K = 1, \kappa = 1$ (solid line) and at $K = 1, \kappa = 0.1$ (dashed line)

**Acknowledgements** The work was carried out within the Russian state task for conducting fundamental scientific research for 2013–2020 on the topic No. 0035-2014-0402, state registration number 01201458047 and the work was supported of the RFBR (project no. 16-01-00176-a, project no. 18-29-10073).

## References

1. Amabili, M.: Nonlinear Vibrations and Stability of Shells and Plates. Cambridge University Press (2008)
2. Zemlyanukhin, A.I., Bochkarev, A.V., Mogilevich, L.I., Tindova, E.G.: Axisymmetric longitudinal-bending waves in a cylindrical shell interacting with a nonlinear elastic medium. Model. Simul. Eng. Article ID 6596231 (2016)
3. Flugge, W.: Statik und Dynamik der Schalen. Springer, Berlin (1957)
4. Bochkarev, A.V., Zemlyanukhin, A.I., Mogilevich, L.I.: Solitary waves in an inhomogeneous cylindrical shell interacting with an elastic medium. Acoust. Phys. **63**(2), 148–153 (2017)
5. Donnell, L.H.: Beams, Plates and Shells. McGraw-Hill Companies (1976)
6. Smirnov, V.V., Manevitch, L.I., Strozzi, M., Pellicano, F.: The Radial Breathing Mode in CNT—The Nonlinear Theory of the Resonant Energy Exchange. (2015). arXiv:1502.07081
7. Smirnov, V., Manevitch, L., Strozzi, M., Pellicano, F.: Nonlinear optical vibrations of single-walled carbon nanotubes. 1. Energy exchange and localization of low-frequency oscillations. Phys. D Nonlinear Phenom. **325**, 113–125 (2016)
8. Zemlyanukhin, A.I., Bochkarev, A.V.: Axisymmetric nonlinear modulated waves in a cylindrical shell. Acoust. Phys. **64**(4), 408–414 (2018)
9. Grimshaw, R., Stepanyants, Yu., Alias, A.: Formation of wave packets in the Ostrovsky equation for both normal and anomalous dispersion. In: Proceedings of the Royal Society a Mathematical, Physical and Engineering Science, vol. 472, p. 20150416 (2016). https://doi.org/10.1098/rspa.2015.0416

10. Grimshaw, R., Malomed, B., Benilov, E.: Solitary waves with damped oscillatory tails: an analysis of the fifth-order Korteweg-de vries equation. Phys. D **77**, 473–485 (1994)
11. Parkes, E.J.: The modulation of weakly non-linear dispersive waves near the marginal state of instability. J. Phys. Math. Gen. **20**, 2025–2036 (1987)

# Dynamic Research of Shape Memory Alloys

**A. M. Bragov, L. A. Igumnov, A. Yu. Konstantinov, A. K. Lomunov and A. I. Razov**

The results of dynamic tests of the TiNi and CuAlNi shape memory alloys are given. Compressive and tensile tests of the TiNi alloy were carried out in the temperature range of 20–300 °C. A significant change was revealed in the elastic modulus before the dislocation plastic flow and the dislocation yield stress with a change in the test temperature in the range of the reverse martensitic transformation.

For the CuAlNi alloy, the effect of the strain rate on the phase yield stress and on the phase and dislocation moduli of elasticity was insignificant. In this case the value of the dislocation yield stress increases markedly with increase in the strain rate. Using the CuAlNi alloy as an example, the method for determining the duration of the reverse martensitic transformation was implemented and the shape recovery diagram during this transformation was constructed.

## 1 Introduction

Thanks to unique properties of shape memory alloys (SMA), namely high corrosion resistance and strength, good strain recovery parameters, high recovery stresses, excellent biocompatibility, high damping ability, they are successfully used in many areas of engineering [1, 2], medicine [3–5], space technology [2, 6, 7]. Nonlinear elastic properties of these alloys are used to create energy-absorbing devices for seismic protection of buildings and structures [8–11] as well as for various drives and converters [12, 13].

---

A. M. Bragov · L. A. Igumnov (✉) · A. Yu. Konstantinov · A. K. Lomunov
Research Institute for Mechanics, National Research Lobachevsky State University of Nizhny Novgorod, Nizhny Novgorod, Russia
e-mail: igumnov@mech.unn.ru

A. I. Razov
St. Petersburg State University, Saint Petersburg, Russia

H. Altenbach et al. (eds.), *Dynamical Processes in Generalized Continua and Structures*, Advanced Structured Materials 103,
https://doi.org/10.1007/978-3-030-11665-1_7

Shape memory alloys belong to a group of materials that, due to phase transformations, can recover their original shape when heated. Examples of such alloys are Ag-Cd, Au–Cd, Cu–Al–Ni, Cu–Sn, Cu–Zn–(X), In-Ti, Ni–Al, Ni–Ti, Fe–Pt, Mn–Cu, Fe–Mn–Si and others. The shape memory effect is due to their temperature-dependent crystal structure. When the SMA is below phase transition temperatures it has a crystallography with low yield stress. In this state the material may be deformed into other shapes by relatively small force. A new form is maintained, provided that the material remains below the temperature of reverse transformation. When heated above this temperature, the material returns to its parent structure and recovers its original shape.

Thus, in the typical operating temperature range SMAs have two phases with the different crystal structure each, and therefore have different properties. One of them is the high-temperature phase called austenite ($A$), and the other is the low-temperature phase called martensite ($M$). Austenite (usually cubic) has a crystal structure different from martensite (tetragonal, rhombic or monoclinic). Transformation from one structure to another is not a diffusion of atoms, but a distortion of the crystal lattice. Such a transformation is known as martensitic transformation. To initiate such transformations in the material either the mechanical stress or the temperature change can be used.

A set of martensitic variants can exist in two forms. The first is the twinned martensite ($M_t$) which is formed by a combination of "self-sufficient" martensitic variants. The second is the deterministic or reoriented martensite, in which the characteristic variant ($M_d$) prevails. The reversible phase transformation from austenite (parent phase) to martensite and vice versa is the basis of the unique behavior of SMA. This behavior is found at the temperature range of $M_f$–$A_f$ which are the temperatures of the ends of the direct and reverse martensitic transformations respectively.

The transformation temperatures increase with increasing of the load magnitude, regardless of loading type (tension or compression). When an uniaxial tensile load is applied with the corresponding stress σ, the new transformation temperatures are represented as $M^{\sigma f}$, $M^{\sigma s}$, $A^{\sigma s}$ and $A^{\sigma f}$ for the martensitic finish, martensitic start, austenitic start and austenitic finish temperatures, respectively.

If the material temperature is slightly higher than $A_f$ then, after loading the material, accompanied by direct martensitic transformation, the complete recovery of the shape occurs due to reverse martensitic transformation during unloading. This material behavior is called the superelastic effect. The associated change in macroscopic shape due to the applied load is reflected in the resulting stress-strain curve as shown schematically in Fig. 1. The stresses, at which the initiation and the completion of the direct martensitic transformation during loading occur, are marked as $\sigma^{Ms}$ and $\sigma^{Mf}$ respectively. Similarly, when the SMA is unloading, the stresses at which the reverse transformation into austenite is initiated and completed are marked, respectively, as $\sigma^{As}$ and $\sigma^{Af}$. If the material in the austenitic phase is tested above the $M_s$ temperature but below the $A_f$ temperature, only a partial recovery of the shape is observed.

Now there are the papers on study of structural features, martensitic transformations [14–16], mechanical properties [17–22] and behavior modeling of SMA [23–25]. However, as noted in [20], the description of the mechanical behavior of

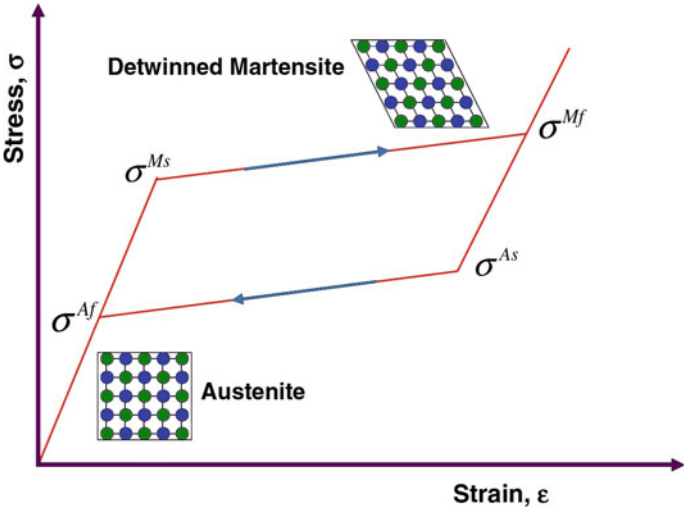

**Fig. 1** Schematic superelastic σ–ε diagram

SMA in a wide range of strain rates requires the knowledge of empirical dependencies of the deformation characteristics on loading parameters.

One of the most common alloys with shape memory is titanium nickelide (TiNi) which has wide application in various fields from medicine to space technology. However many applications require the characteristics titanium nickelide does not hase. For example, the narrow hysteresis which allows deformation under almost constant stress, or a perfect shape memory at high temperatures are required. In this regard, it is of interest to consider copper-based alloys which both have the above functional properties and also are less expensive.

An important feature of SMA is the possibility to generate the recovery stresses (the ability to develop stresses under constrained strain conditions, due to the shape memory effect during heating of predeformed specimens). This process is widely used in various mechanical couplings and control devices, so the study of its response time to high-strain-rate loading is very important.

In this paper the results of our study on the behavior of TiNi alloy during high-strain-rate deformation in the temperature range of the reversible martensitic transformation and the deformation diagrams of CuAlNi alloy at the strain rates of 2000 and 6000 $s^{-1}$ are represented. In addition, for the CuAlNi alloy the time of the reverse martensitic transformation is estimated and the shape recovery diagram is constructed.

## 2 Specimens for Testing

For compression tests of the TiNi alloy the specimens in the form of short cylinders with 8 mm in diameter and 4 mm in height were used. For high-strain-rate tension the cylindrical specimens were used with threaded heads with the diameter and the length of the working part of 5 mm and 10 mm respectively. All specimens were made of hot-rolled TiNi-alloy bars. To reduce residual stresses and create an equilibrium structure the specimens were annealed at 500 °C for 1 h and then cooled in a furnace.

The temperatures of the direct and reverse martensitic transformations of the alloy were determined in the Mettler Toledo 822e differential scanning calorimeter (DSC). The rate of cooling and heating of the samples in the calorimeter was 10 °/min. The results of determining the temperatures of martensitic transformations by the DSC method are presented in Fig. 2. As can be seen, after aging at 500 °C for 1 h and subsequent cooling in the furnace the alloy had the following temperatures of reversible martensitic transformation $M_s = 74$ °C, $M_f = 32$ °C, $A_s = 74$ °C, $A_f = 98$ °C.

These features of the structural-phase state of the alloy after aging should have affected its mechanical behavior under quasistatic and high-strain-rate tension. To separate the contributions of the structure and high strain rate into mechanical behavior of the alloy we conducted quasistatic tension of the specimens at the strain rate of $10^{-3}$ s$^{-1}$, which was most often used to study the mechanical behavior of quenched single-phase TiNi alloys under quasistatic tension.

Figure 3a shows the typical diagrams of quasistatic tension of the TiNi alloy specimens at the temperatures of 20 and 130 °C. The choice of these diagrams

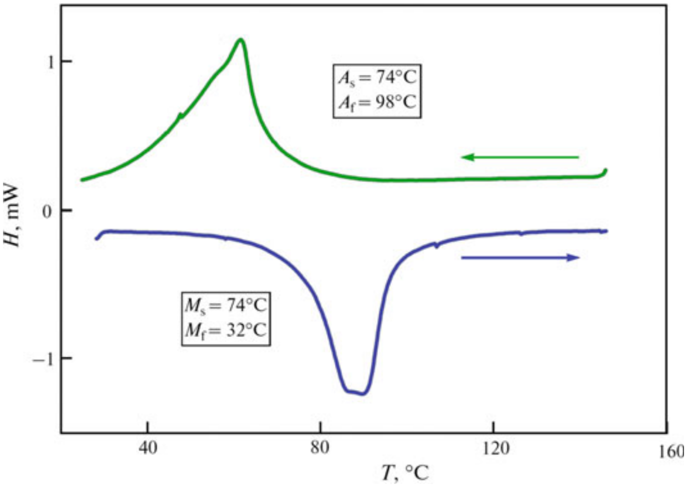

**Fig. 2** Temperature dependence of heat release and heat absorption of TiNi alloy after aging at 500 °C for 1 h and cooling in a furnace

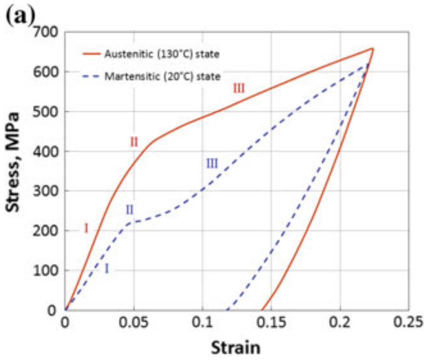

**Fig. 3** Typical diagrams of quasistatic **a** and dynamic **b** TiNi alloy loading in martensitic (at 20 °C) and in austenitic (at 130 °C) states

is due to the fact that, according to the characteristic temperatures of martensitic transformations, the specimens at these test temperatures were in the martensitic and austenitic states, respectively. A distinctive feature of these diagrams from the well-known TiNi binary alloys diagrams is the absence of the stress peak usually observed at the beginning of the second stage of quasistatic tension and associated with the formation, growth and fusion of localized deformation zones. If we turn to the deformation diagrams under high-strain-rate loading at the same temperatures, which are shown in Fig. 3b, in this case the stress peak is clearly visible. The diagrams highlight three stages of deformation (I, II, and III), the choice of which is also based on the different nature of the stress change.

In addition, the specimens of the CuAlNi alloy in the martensitic state ($\rho = 7.2$ g/cm$^3$, $E = 65$ GPa, $\sigma_t = 50$ MPa, $T_{pr} = 1500$ °C) in the form of tablets with 6 mm in diameter and 3 mm in height were made to study them under compression.

## 3 Methods of Testing

The dynamic tests of TiNi and CuAlNi alloys at the strain rate of (1–6) $\times$ $10^3$ s$^{-1}$ were carried out on the installations that implement the split Hopkinson pressure bar method [26] with measuring bars of 10 mm in diameter (compression) and 20 mm (compression and tension). The tensile tests were carried out according to the Nicholas scheme [27, 28].

To provide the required test temperature, the coaxial electric heater was used which was placed at the ends of the measuring bars and the specimen between them. The specimen temperature was measured by a miniature thermocouple. When testing the TiNi alloy, the test temperatures near the temperatures of martensitic transformations were achieved by two ways. In the first, the specimens were heated to the selected temperature from room temperature. In the second, the specimens were preheated

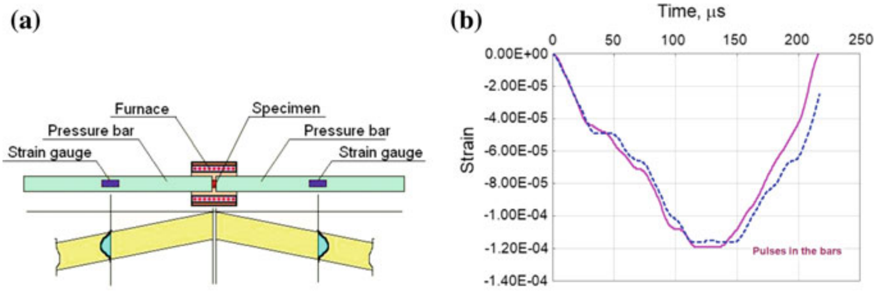

**Fig. 4** The scheme of the experiment to determine the time of the reverse martensitic transformation (**a**) and pulses recorded in the measuring bars (**b**)

to 180 °C to convert them into the austenitic state, and then they were cooled to the required test temperature. This made it possible to change the phase composition at the same temperature within the interval of reversible martensitic transformations and to compare the mechanical response of the alloy to high-strain-rate and quasistatic tension, depending on its phase state.

The quasistatic tension of TiNi specimens at the strain rate of $10^{-3}$ $s^{-1}$ under the same temperatures was carried out in the Lloyd 30 K Plus universal mechanical testing machine equipped with a heat chamber. The residual strain was 12–25%.

To determine the time of duration of the reverse martensitic transformation and to plot the σ-ε curve in the process of shape superelastic recovering, a preformed specimen of CuAlNi alloy was placed between the measuring bars and heated in the temperature range of the reverse martensitic transformation. During the heat-induced transformation, the specimen recovered its shape rapidly. This process was accompanied by pulsed loading of the measuring bars ends in contact with the specimen. As a result, the elastic deformation waves in the bars were recorded by strain gauges. The scheme of the specimen layout as well as pulses registration are shown in Fig. 4a. Figure 4b shows the recorded strain pulses in the measuring bars.

The proposed method allowed us to estimate the duration of the process of recovering the original (parent) shape during heating.

## 4 Results of TiNi Alloy Testing

Before testing the alloy was in the martensitic state.

Tests at elevated temperatures were carried out as follows. The specimen was placed between the end faces of measuring bars, then heated to a temperature of +180 °C and then cooled to the required test temperatures (+137, +117, +87 °C). After that the specimen was subjected to high-strain-rate deformation. In addition, the tests were performed when the specimen was heated to +300 °C. The selected test temperatures correspond to the dilatogram points of this alloy (Fig. 5).

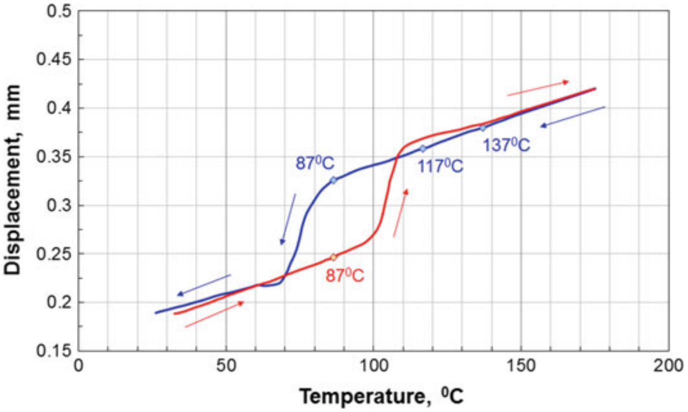

**Fig. 5** TiNi alloy dilatogram

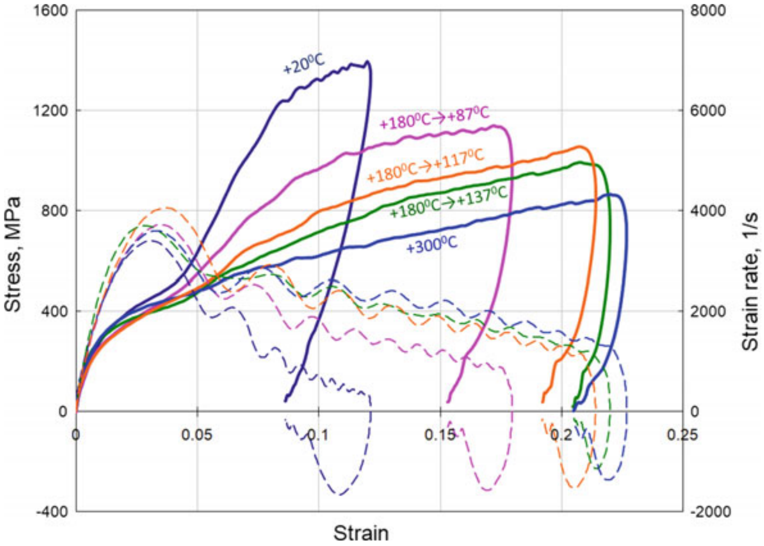

**Fig. 6** Dynamic deformation diagrams of TiNi alloy under compression

Figure 6 shows the deformation curves of the TiNi alloy under compression at a strain rate of 2000 $s^{-1}$, obtained under various temperature conditions. The effect of the test temperature and of the way of the test temperature achievement on the phase yield stress, phase modulus and phase hardening modulus is insignificant. An increase in the test temperature leads to significant decreases in the dislocation yield stress and in dislocation modulus of elasticity. At the temperature of +300 °C there is no phase transition.

Figure 7 shows the deformation curves of TiNi alloy under compression and tension at the strain rates of 2500 and 1000 $s^{-1}$ respectively.

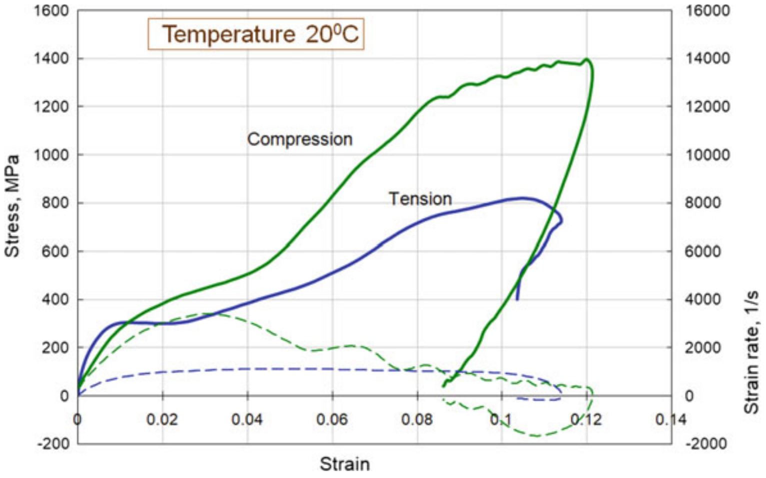

**Fig. 7** TiNi alloy deformation diagrams under compression and tension

To analyze the effect of the phase composition on the mechanical behavior of TiNi quasistatic and high-strain-rate tension of the alloy were carried out at the temperatures of 60, 77, 87 and 100 °C. To reach these test temperature two ways were used. In one case the specimens were heated from the room temperature (martensitic state) to the temperature at which the test deformation was performed. In the other case the material was heated to 180 °C to transform it completely into the austenitic state, and then the specimen was cooled to the specified temperatures at which the deformation was performed. This approach is due to the fact that at the same temperature the alloy could be in the martensitic, austenitic or in the mixed state with a different content of the martensitic and austenitic phases depending on how the test temperature was reached. The phase composition of the alloy at these temperatures can be estimated as follows. At 60 °C in the first case (when the specimen was heated from room temperature) the alloy was in a stable martensitic state, in the second case (preheating to 180 °C and then cooling) the alloy contained the austenitic and martensitic phases in approximately equal proportions. At 77 °C in the first case the alloy was in martensitic state with small amount of austenite, while in the second case it was in austenitic premartensitic state probably with small amount of martensite. At 87 °C in the first case the alloy contained martensitic and austenitic phases in approximately equal proportions, while in the second case it was in the austenitic premartensitic state. At 100 °C in the first case the alloy was in austenitic state with small proportion of martensite, while in the second case it was in austenitic premartensitic state.

Figure 8 shows the quasistatic and dynamic stress-strain diagrams of the alloy with different ways to achieve the temperature at which the loading was performed, namely the heating from the room temperature to the test temperature or the cooling from 180 °C to the test temperature. These diagrams show that the lengths of first

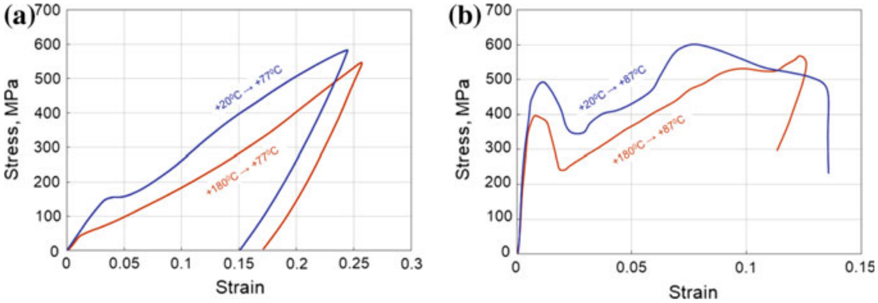

**Fig. 8** Quasistatic (**a**) and dynamic (**b**) deformation diagrams of the TiNi alloy under tension when two modes to achieve the required temperature were used

stages on the curves of quasi-static tension of martensite were determined by the transformations that took place under stress.

It is revealed that the phase and dislocation yield stresses behave differently when the test temperature increases, but they have approximately the same values at the room temperature. The phase yield stress continuously increases in the dynamic case, and in the quasi-static case it firstly decreases to a certain minimum and only then begins to increase. This means that the processes of twinning, detwinning and reorientation of the martensitic phase are very sensitive to the loading rate. And the value of the phase yield stress at high-strain-rate loading is always higher than that at quasistatic loading.

The high tensile rate has influence on the dependence of the phase yield stress on the test temperature, both for martensite and for austenite, and specifies at what temperature the dislocation mechanism of deformation begins to act.

## 5 Results of CuAlNi Alloy Testing

The tests of the CuAlNi alloy in the martensitic state under compression at room temperature were carried out using an installation with measuring bars of 10 mm in diameter. Because the phase transformation temperatures for this alloy were about +150 °C, the specimens during loading received the residual strain of 8% (at strain rate of $5 \times 10^3$ $s^{-1}$) to 10% (at strain rate of $9 \times 10^3$ $s^{-1}$). The phase transformation in this case occurred under the applied stress. The above-mentioned increased residual strain was associated with plastic deformation of the material after phase transformation. Repeated loading of such specimen did not reveal a noticeable residual strain after loading. Annealing at a temperature of +170 °C caused complete recovering of the original specimen shape. Double reloading of the annealed specimen showed a similar character of deformation. Figure 9 shows typical σ-ε curves (solid lines) and the corresponding dependences of the change in strain rate (dashed lines in the lower part of the figure), where 1 is the 1st cycle, initial state of the specimen; 2 is the 2nd

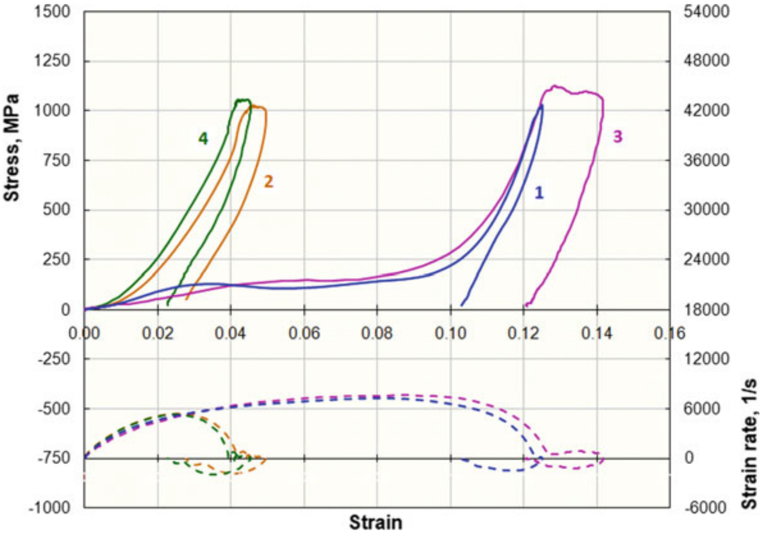

**Fig. 9** Dynamic diagrams of CuAlNi alloy before and after annealing at a strain rate of ~6000 $s^{-1}$

**Table 1** Mechanical characteristics of the CuAlNi alloy

| No | Striker velocity, m/s | Residual strain, % | Load branch module, MPa | Module of hardening site, MPa | Unloading branch module, MPa | Conventional yield stress, MPa |
|---|---|---|---|---|---|---|
| 1 | 24.6 | 8.4 | 5123 | 404 | 48,545 | 124.8 |
| 2 | 25.0 | 0.4 | 28,468 | 4842 | 55,221 | 1012.4 |
| 3 | 25.8 | 8.4 | 4436 | 311 | 49,225 | 122.6 |
| 4 | 25.8 | 0.4 | 29144 | 3497 | 43,560 | 1041.0 |

cycle, initial state; 3 is the 1st cycle, the specimen after annealing; 4 is the 2nd cycle, after annealing.

The residual strain of the specimens after testing was 8.4% for the specimens in the initial state and after annealing, as well as 0.4% for the specimens after their preliminary elastoplastic deformation in the initial state and after annealing.

On the basis of the obtained stress-strain curves the elastic moduli in the parts of active loading and unloading and the hardening modulus, as well as the conventional yield stress were determined (see Table 1).

Because there is practically no a section of ideal yield of 8–9% on the repeated loading diagrams (curves 2 and 4), unlike the first cycles (curves 1 and 3), the maximum achieved stress in the specimen is accepted as the conventional yield stress for curves 2 and 4.

Under other loading modes (according to the strain rate) the similar results were obtained. The obtained σ-ε curves and corresponding dependences of the change in

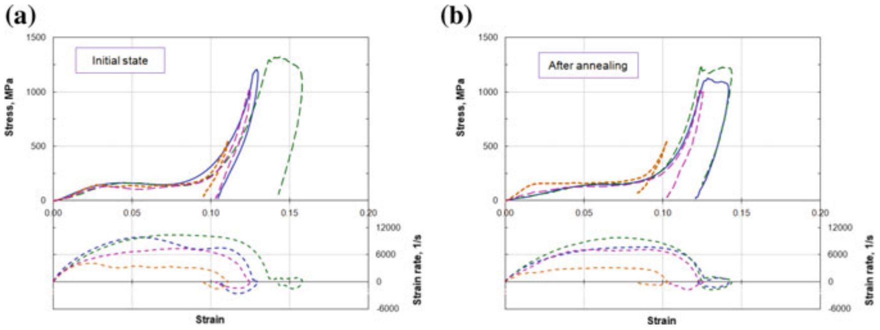

**Fig. 10** Mechanical behavior of CuAlNi alloy during compression in the initial state (**a**) and after annealing (**b**)

the strain rate of CuAlNi alloy in the initial (martensitic) state and after annealing of deformed specimens are shown in Fig. 10.

To determine the duration of the reverse martensitic transformation and to plot the diagram σ–ε in the process of unloading and shape recovering, a predeformed specimen of the CuAlNi alloy was placed between the measuring bars and then heated in the temperature range of reverse martensitic transformation (Fig. 4a). When constructing the recovery diagram (the lower curve in Fig. 11), displacements and forces on the two ends of the specimen were determined on the basis of the strain pulses $\varepsilon_i(t)$ $(i = 1, 2)$ in the measuring bars (Fig. 4b).

$$u_i(t) = c\int_0^t \varepsilon_i dt,$$

$$P_i(t) = EA\,\varepsilon_i(t),$$

where $c$, $E$ and $A$ are the sound speed, the modulus of elasticity and the cross-sectional area of the measuring bars, respectively. Then, using the Kolsky formulas [27], the engineering stress and strain of the specimen were calculated as shown below

$$\sigma_n(t) = \frac{P}{A_S^0} = \frac{P_1 + P_2}{2A_S^0}$$

$$\varepsilon_n(t) = \frac{u_2(t) - u_1(t)}{L_0},$$

where $A_S^0$ and $L_0$ are the initial area and the length of the specimen, respectively.

Figure 11 shows the change in stress and in strain of the specimen in time (Fig. 11a), and the diagram of the shape recovery when the specimen was heated (lower curve) after active loading (upper curve) (Fig. 11b). It is clearly seen that the deformation in martensitic state under applied dynamic stress takes about 20 μs

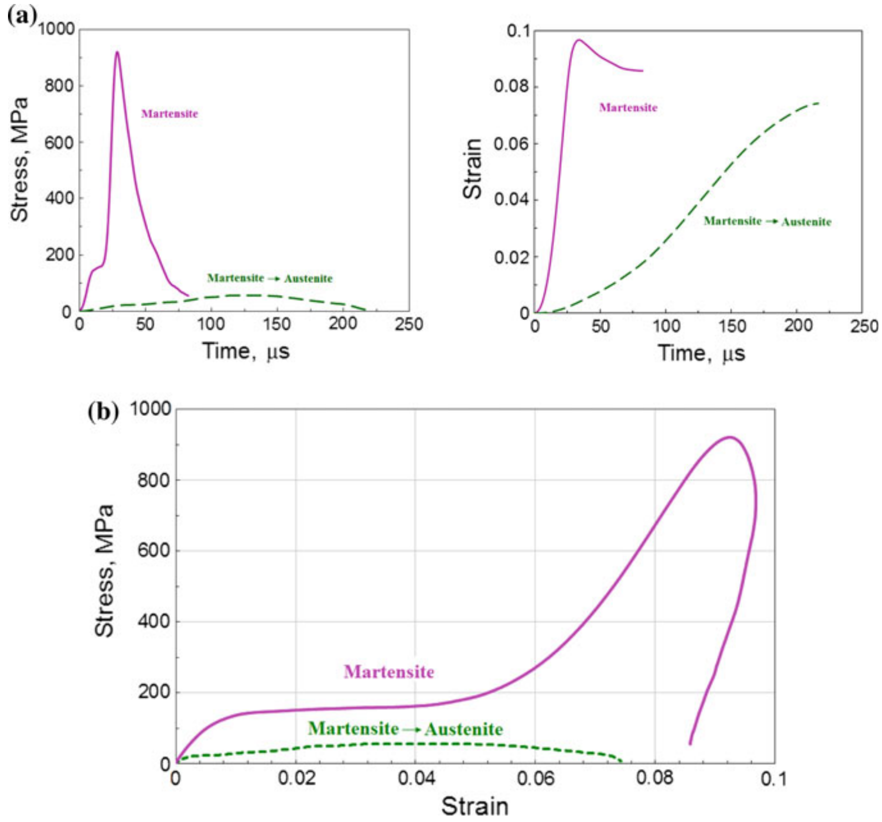

**Fig. 11** Parameters of the deformation and shape recovery

in a time, whereas the reverse martensitic transformation (martensite → austenite) (recovery of the shape) with slow heating of the specimen occurs quickly taking about 220 μs.

## 6 Conclusion

Using the Kolsky technique, we obtained the diagrams of deformation of TiNi alloys with the shape memory effect in the temperature range of the reverse martensitic transformation, as well as that of CuAlNi alloy at room temperature. Using the CuAlNi alloy as an example, we developed a method for determining the duration of the reverse martensitic transformation and constructed a diagram of the alloy shape recovery.

**Acknowledgements** The study was financially supported by the Federal Targeted Program for Research and Development in Priority Areas of Development of the Russian Scientific and Technological Complex for 2014–2020 under the contract No. 14.578.21.0246 (unique identifier RFMEFI57817X0246).

## References

1. Jani, J.M., Leary, M., Subic, A., Gibson, M.A.: A review of shape memory alloy research, applications and opportunities. Mater. Des. **56**(4), 1078–1113 (2014). https://doi.org/10.1016/j.matdes.2013.11.084
2. Razov, A. I.: Application of Titanium Nickelide-based alloys in engineering. Phys. Metals Metallogr. **97**(Suppl 1), 97–126 (2004)
3. Yahia, L. (ed.): Shape Memory Implants, p. 349. Springer-Verlag, Berlin-Heidelberg-New York (2000)
4. Petrini, L., Migliavacca, F.: Biomedical applications of shape memory alloys. J. Metall. **2011**, Art ID 501483 (2011)
5. Khmelevskaya, I., Ryklina, E., Korotitskiy, A.: Application of thermomechanically treated Ti-Ni SMA. In: Resnina, N., Rubanik, V. (eds.) Shape Memory Alloys: Properties, Technologies, Opportunities, pp. 603–637. Trans Tech Publications Ltd., Pfaffikon, Switzerland (2015)
6. Razov, A., Cherniavsky, A.: Application of SMAs in modern spacecraft and devices. J. de Physique IV **112**(10), 1173–1176 (2003)
7. Hartl, D.J., Lagoudas, D.C.: Aerospace applications of shape memory alloys. Proc. Inst. Mech. Eng. Part G: J. Aerosp. Eng. **221**(4), 35–552 (2007)
8. Tirelli, D., Mascelloni, S.: Characterisation and optimisation of shape memory alloys for seismic applications. J. Phys. IV **10**, 665–670 (2000)
9. Castellano, M.G., Indirli, M., Martelli, A.: Progress of application, research and development and design guidelines for shape memory alloy devices for cultural heritage structures in Italy. In: Proceedings of SPIE—The International Society for Optical Engineering, vol. 4330, pp. 250–261 (2001)
10. Wilson, J.C., Wesolowsky, M.J.: Shape memory alloys for seismic response modification: a state-of-the-art. Earthq. Spectra **21**(2), 569–601 (2005)
11. Torra, V., Isalgue, A., Lovey, F.C., Sade, M.: Shape memory alloys as an effective tool to damp oscillations: study of the fundamental parameters required to guarantee technological applications. J. Therm. Anal. Calorim. **119**(3), 1475–1533 (2015). https://doi.org/10.1007/s10973-015-4405-7
12. Leo, P.H., Shield, T.W., Bruno, O.P.: Transient heat transfer effects on the pseudoelastic behavior of shape-memory wires. Acta Metall. Mater. **41**, 2477–2485 (1993)
13. Millet, J.C., Bourne, N.K., Gray III, G.T.: Behavior of the shape memory alloy NiTi during One-dimensional shock loading. J. Appl. Phys. **92**, 3107–3110 (2002)
14. Thamburaja, P.: Constitutive equations for martensitic reorientation and detwinning in shape-memory alloys. J. Mech. Phys. Solids **53**, 825–856 (2005)
15. Melnik, R.V.N., Roberts, A.J., Thomas, K.A.: Coupled thermomechanical dynamics of phase transitions in shape memory alloys and related hysteresis phenomena. Mech. Res. Commun. **28**(6), 637–651 (2001)
16. Bragov, A.M., Danilov, A.N., Konstantinov, AYu., Lomunov, A.K., Motorin, A.S., Razov, A.I.: Mechanical and structural aspects of high-strain-rate deformation of NiTi alloy. Phys. Metals Metallogr. **116**(4), 385–392 (2015). https://doi.org/10.1134/S0031918X15040031)
17. Ogawa, K.: Characteristics of shape memory alloy at high strain rate. In: Proceedings of the International Conference on Mechanical and Physical Behaviour of Materials under Dynamic Loading (DYMAT-88), 19–23 Sept 1988, Ajaccio, France. J. Phys. IV. (1988). Coll. C3—Suppl. J. Phys. III **49**(11), 115–120

18. Liu, Y., Yulong, L., Ramesh, K.T., Van Humbeeck J.: High strain rate deformation of martensitic NiTi shape memory alloy. Scr. Mater. **41**(1), 89–95 (1999)
19. Liu, Y., Li, Y., Ramesh, K.T.: Rate dependence of deformation mechanisms in a shape memory alloy. Philos. Mag. Phys. Condens. Matter Struct. Defects Mech. Propert. **82**(12), 2461–2473 (2002)
20. Belyaev, S., Petrov, A., Razov, A., Volkov, A.: Mechanical properties of titanium nickelide at high strain rate loading. Mater. Sci. Eng. A **378**(1–2), 122–124 (2004). https://doi.org/10.1016/j.msea.2003.11.059
21. Jiang, F., Vecchio, K.S.: Fracture of Nitinol under quasistatic and dynamic loading. Metall. Mater. Trans. A. **38**(12), 2907–2915 (2007)
22. Qiu, Y., Young, M.L., Nie, X.: High strain rate compression of martensitic NiTi shape memory alloy at different temperatures. Metall. Mater. Trans. A **48**(2), 601–608 (2017). https://doi.org/10.1007/s11661-016-3857-0
23. Lexcellent, C., Rejzner, J.: Modelling of the strain rate effect, creep and relaxation of a Ni-Ti shape memory alloy under tension (compression)—torsional proportional loading in the pseudoelastic range. Smart Mater. Struct. **9**(5), 613–621 (2000)
24. Lagoudas, D.C., Ravi-Chandar, K., Sarh, K., Popov, P.: Dynamic loading of polycrystalline shape memory alloy rods. Mech. Mater. **35**, 689–716 (2003)
25. Evard, M., Motorin, A., Razov, A., Volkov, A.: Microstructural modeling of a TiNi alloy at high strain rate tension. Mater. Today Proc. **4**(3, Part B), 4637–4641 (2017). https://doi.org/10.1016/j.matpr.2017.04.043
26. Kolsky, H.: An investigation of the mechanical properties of material at very high rates of loading. Proc. Phys. Soc. **62B**, 676–700 (1949)
27. Bragov, A.M., Lomunov, A.K.: Methodological aspects of studying dynamic material properties using the Kolsky method. Int. J. Impact Eng. **16**(2), 321–330 (1995)
28. Nicholas, T.: Tensile testing of materials at high rates of strain. Exp. Mech. **21**(5), 177–195 (1981)

# Methods of Finding of Exact Analytical Solutions of Nonautonomous Nonlinear Klein-Fock-Gordon Equation

**A. N. Bulygin and Yu. V. Pavlov**

**Abstract** Methods of finding of exact analytical solutions of nonautonomous nonlinear Klein-Fock-Gordon (NKFG) equation are presented. They are based on the principles of construction of functionally invariant solutions of the wave equation. Solutions are sought as a composite function. The argument of the composite function (ansatz) is solution of the special equation. The choice of ansatz defines a type of the solution. Examples of exact analytical solutions of NKFG equation are given.

## 1 Introduction

The NKFG equation

$$U_{xx} + U_{yy} + U_{zz} - \frac{U_{tt}}{v^2} = F(U) \tag{1}$$

plays a fundamental role in the theoretical and applied physics, mechanics and biology. Here the lower index designates a partial derivative in respect to the corresponding variable, and $F(U)$ is an arbitrary function. The most extensively studied are cases with $F(U) = \exp \pm U, \sin U, \sinh U$ [1, 2]. These equations are used in the field theory and they are modeling various physical phenomena. However, usually it is supposed that media and external influences are uniform. More adequately physical processes are described by the nonautonomous NKFG equation

$$U_{xx} + U_{yy} + U_{zz} - \frac{U_{tt}}{v^2} = p(x, y, z, t)\, F(U). \tag{2}$$

Here $p(x, y, z, t)$ is some function characterizing properties of the medium or the external influences. Practically analytical methods of solution of the Eq. (2) are absent

---

A. N. Bulygin (✉) · Yu. V. Pavlov
Institute for Problems in Mechanical Engineering of Russian Academy of Sciences,
Saint Petersburg, Russia
e-mail: bulygin_an@mail.ru

Yu. V. Pavlov
e-mail: yuri.pavlov@mail.ru

H. Altenbach et al. (eds.), *Dynamical Processes in Generalized Continua and Structures*, Advanced Structured Materials 103,
https://doi.org/10.1007/978-3-030-11665-1_8

in the literature. The qualitative analysis of solutions of the Eq. (2) is made and its numerical solutions are provided [3–5]. In the theory of linear waves the function $p(x, y, z, t)$ can describe concentrated or distributed inhomogeneities of the continuous medium which cause localization of elastic waves [6–8]. Below are presented proposed methods of finding of nonautonomous NKFG equation exact analytical solutions based on the ideas and methods of finding of functionally invariant solutions of the wave equation.

The idea of the existence of functionally invariant solutions was suggested by Jacobi [9]. Forsyth [10] found functionally invariant solutions of the Laplace equation, wave equation, and of the Helmholtz equation. In studying of electromagnetic waves, Bateman [11] fundamentally and consistently developed the Jacobi idea as applied to the wave equation. Sobolev and Smirnov [12–15] successfully used the method to construct functionally invariant solutions to solve problems of diffraction and sound wave propagation in uniform and layered solid media. Erugin [16] made a significant contribution to developing the theory of this method. Functionally-invariant solutions of both autonomous and nonautonomous NKFG equation particularly sine-Gordon equation were obtained by authors in [17–21].

## 2 Methods of Obtaining of Analytical Solutions of Nonautonomous Klein-Fock-Gordon Equation

We will seek solutions of nonautonomous NKFG Eq. (2) in the form of composite function $U = f(W)$. Then Eq. (2) is as follows

$$f'' \left[ W_x^2 + W_y^2 + W_z^2 - \frac{W_t^2}{v^2} \right] + f' \left[ W_{xx} + W_{yy} + W_{zz} - \frac{W_{tt}}{v^2} \right] = p\, F[f(W)]. \tag{3}$$

Here and elsewhere prime denotes ordinary derivative with respect to the argument. Three obvious propositions could be made on the basis of (3).

**Proposition 1** *If function $W$ satisfies to equations*

$$W_x^2 + W_y^2 + W_z^2 - \frac{W_t^2}{v^2} = 0, \quad W_{xx} + W_{yy} + W_{zz} - \frac{W_{tt}}{v^2} = p(x, y, z, t), \tag{4}$$

*then solution of Eq. (2) is given by inversion of the integral*

$$\int \frac{df}{F(f)} = W(x, y, z, t). \tag{5}$$

**Proposition 2** *If function $W$ satisfies to equations*

$$W_x^2 + W_y^2 + W_z^2 - \frac{W_t^2}{v^2} = p(x, y, z, t), \quad W_{xx} + W_{yy} + W_{zz} - \frac{W_{tt}}{v^2} = 0, \tag{6}$$

*then solution of Eq. (2) is given by inversion of the integral*

$$\int \frac{df}{\sqrt{E+V}} = \pm\sqrt{2}W(x,y,z,t). \tag{7}$$

*Here $F(U) = V'(U)$ and $E$ is constant of integration.*

**Proposition 3** *If function $W$ satisfies to equations*

$$\begin{aligned} W_x^2 + W_y^2 + W_z^2 - \frac{W_t^2}{v^2} &= p(x,y,z,t)P(W), \\ W_{xx} + W_{yy} + W_{zz} - \frac{W_{tt}}{v^2} &= p(x,y,z,t)Q(W), \end{aligned} \tag{8}$$

*then $f(W)$ will be the solution of the second order ordinary nonlinear differential equation*

$$P(W)f'' + Q(W)f' = F(f). \tag{9}$$

*Here $P(W)$ and $Q(W)$ are arbitrary functions.*

In general case, i.e. for arbitrary functions $P(W)$, $Q(W)$ and $F(f)$, solutions of the Eq. (9) are not obtained. Its exact analytical solution can be found if functions of $P(W)$ and $Q(W)$ are connected by a condition

$$P'(W) = 2Q(W). \tag{10}$$

Taking into account (10) the Eq. (9) takes the form

$$\frac{d}{dW}\left[P(W)(f')^2 - 2V(f)\right] = 0, \quad \frac{dV}{df} = F(f). \tag{11}$$

Its solution is sought in quadratures

$$\int \frac{df}{\sqrt{V(f)+E}} = \pm\sqrt{2}\int \frac{dW}{\sqrt{P(W)}}. \tag{12}$$

Here $E$ is an integration constant. The solution can be found by the inversion of the first integral.

## 3 Exact Analytical Solutions of NKFG Equation

Suppose that anzatz

$$W = x\,L(\alpha) + y\,M(\alpha) + z\,N(\alpha) - tv^2D(\alpha) + G(\alpha). \tag{13}$$

Here $L(\alpha)$, $M(\alpha)$, $N(\alpha)$, $D(\alpha)$, $G(\alpha)$ are arbitrary functions of $\alpha$, and value $\alpha$ is a function of coordinates and time, which is implicitly set by the linear algebraic equation

$$x\, l(\alpha) + y\, m(\alpha) + z\, n(\alpha) - t v^2 d(\alpha) + g(\alpha) = 0. \tag{14}$$

Suppose that

$$l(\alpha) = L_\alpha, \quad m(\alpha) = M_\alpha, \quad n(\alpha) = N_\alpha, \quad d(\alpha) = D_\alpha, \quad g(\alpha) = G_\alpha. \tag{15}$$

Here the lower index designates a derivative with respect to an argument. The condition (15) allows in a simple form to write down partial derivatives of ansatz $W$ of the first and second order

$$\begin{aligned} &W_x = L, \quad W_y = M, \quad W_z = N, \quad W_t = -v^2 D, \\ &W_{xx} = -\frac{L_\alpha^2}{\beta}, \quad W_{yy} = -\frac{M_\alpha^2}{\beta}, \quad W_{zz} = -\frac{N_\alpha^2}{\beta}, \quad W_{tt} = -v^4 \frac{D_\alpha^2}{\beta}, \\ &\beta = x\, L_{\alpha\alpha} + y\, M_{\alpha\alpha} + z\, N_{\alpha\alpha} - t v^2 D_{\alpha\alpha} + G_{\alpha\alpha}. \end{aligned} \tag{16}$$

Taking into account (16) the Eq. (3) takes form

$$f'' R - f' \frac{S}{\beta} = pF(f), \tag{17}$$

$$R = L^2 + M^2 + N^2 - v^2 D^2, \quad S = L_\alpha^2 + M_\alpha^2 + N_\alpha^2 - v^2 D_\alpha^2. \tag{18}$$

The arbitrary functions $L, M, N, D, G$ can be chosen in such way that the conditions formulated in Propositions 1–3, will be satisfied and then it is possible to find the exact analytical solution of the NKFG equation on the basis of the corresponding assumption. Not focusing on finding of a general form of functions $L, M, N, D, G$ we will give examples of exact analytical solutions of the NKFG equation which are found on the basis of Proposition 1:

$$\begin{gathered} \mathbf{1}.\ L = \alpha, \quad M = \frac{1}{\alpha}, \quad N = -\sqrt{2}, \quad vD = \alpha + \frac{1}{\alpha}, \quad G = 0, \\ \alpha^2 = \frac{y - vt}{x - vt}, \quad W = 2\sqrt{(x - vt)(y - vt)} - \sqrt{2} z, \quad p = \frac{-1}{\sqrt{(x - vt)(y - vt)}}, \end{gathered} \tag{19}$$

$$\begin{gathered} \mathbf{2}.\ L = \frac{1}{\cosh \alpha}, \quad M = \tanh \alpha, \quad N = 0, \quad vD = 1, \quad G = 0, \\ \alpha = \log \frac{y + \sqrt{x^2 + y^2}}{x}, \quad W = \sqrt{x^2 + y^2} - vt, \quad p = \frac{1}{\sqrt{x^2 + y^2}}, \end{gathered} \tag{20}$$

$$\textbf{3}.\ L = \frac{\sqrt{2}\alpha}{1+\alpha^2}, \quad M = \frac{\sqrt{2}\alpha}{1+\alpha^2}, \quad N = \frac{1-\alpha^2}{1+\alpha^2}, \quad vD = 1, \quad G = 0,$$
$$\alpha^2 = \frac{\rho - z}{\rho + z}, \quad \rho = \sqrt{z^2 + \frac{(x+y)^2}{2}}, \quad W = \rho - vt, \quad p = \frac{1}{\rho}, \tag{21}$$

For the cases (19)–(21) the condition of applicability of the Proposition 1 is satisfied ($R = 0$). Therefore, accepting that

$$p(x, y, z, t) = -\frac{S}{\beta}, \tag{22}$$

the solution of Eq. (2) can be found by inversion of the integral (5).

As an example we will consider a case

$$F(f) = -b \sinh 2f, \quad b > 0. \tag{23}$$

Then

$$f = \frac{1}{2} \log \frac{\cosh(bW)}{\sinh(bW)}. \tag{24}$$

In the Fig. 1 and 2 graphs of the functions $p(x, y, z)$ and $U(x, y, z, t) = f(W)$ are given for the solutions (20), (21). For the case (20) function $W$ has the form of cylindrical perturbations, which diameter increases over time. For the case (21) function $W$ at $t = 0$ has form of a soliton which is divided into two soliton perturbation over time, the last extend along $XOY$ plane to the opposite sides.

We will give examples of exact analytical solutions which are constructed on the basis of the Proposition 2 ($S = 0$):

$$\textbf{4}.\ L = \sin\alpha, \quad M = -\cos\alpha, \quad N = 1, \quad vD = \alpha, \quad G = 0, \quad p = 2 - \alpha^2,$$
$$\tan\alpha = \frac{yvt + x\sqrt{x^2+y^2-v^2t^2}}{xvt - y\sqrt{x^2+y^2-v^2t^2}}, \quad W = \sqrt{x^2+y^2-v^2t^2} + z - vt\alpha, \tag{25}$$

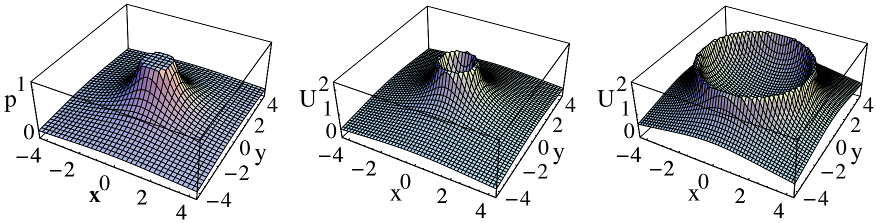

**Fig. 1** The function $p$ (at the left) and the solution **2** (see Eq. (20)) with $z = 0, t = 1$ (at the centre) and $t = 3$ (at the right)

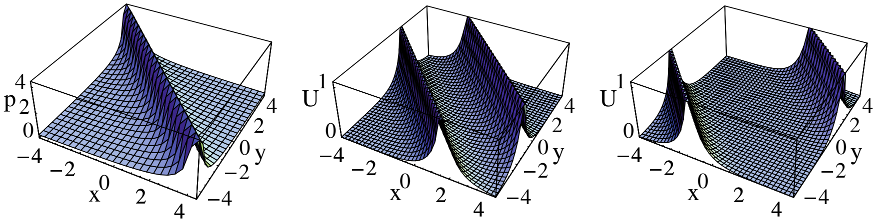

**Fig. 2** The function $p$ (at the left) and the solution **3** (see Eq. (21)) with $z = 0$, $t = 2$ (at the centre) and $t = 4$ (at the right)

$$\mathbf{5}.\ L = \cosh\alpha, \quad M = \alpha, \quad N = 0, \quad vD = \sinh\alpha, \quad G = 0, \quad p = 1 + \alpha^2,$$
$$\tanh\alpha = \frac{vt\sqrt{x^2 + y^2 - v^2t^2} - xy}{x\sqrt{x^2 + y^2 - v^2t^2} - yvt}, \quad W = \sqrt{x^2 + y^2 - v^2t^2} + y\alpha, \tag{26}$$

$$\mathbf{6}.\ L = \sin^{-1}\tanh\alpha, \quad M = \log\cosh\alpha, \quad N = 0, \quad vD = \alpha, \quad G = 0,$$
$$\tanh\alpha = \frac{vt\sqrt{x^2 + y^2 - v^2t^2} - xy}{y\sqrt{x^2 + y^2 - v^2t^2} - xvt}, \quad W = x\sin^{-1}\tanh\alpha + y\log\cosh\alpha - vt\alpha,$$
$$p = \left[\sin^{-1}\tanh\alpha\right]^2 + \log^2\cosh\alpha - \alpha^2. \tag{27}$$

The function $f$ can be found by the inversion of integral (7) for the solutions constructed on the basis of the Proposition 2. For the case (23) one has

$$f = \sinh^{-1}\left[\frac{k}{k'}\,\mathrm{cn}\left(\frac{\sqrt{2b}}{k'}W, k\right)\right], \quad k = \sqrt{\frac{E}{E+b}}, \quad k' = \sqrt{1-k^2}. \tag{28}$$

In Fig. 3 graphs of the functions $p(x, y, z, t)$ and $U(x, y, z, t)$ are given for the solution (25) with $E = 1, v = 1, b = 0.1, z = 0$. The solutions are real out of the domain $x^2 + y^2 < v^2t^2$. For $t = 0$ the solutions have the form (top view) of concentric rings which transform into spirals with growth $t$.

Further we consider the solution found on the basis of Proposition 3. The Eq. (17) is reduced to the form

$$f''W + \frac{f'}{2} = F(f), \tag{29}$$

taking into account that

$$P = \frac{R}{W}, \quad \frac{W}{\beta}\cdot\frac{S}{R} = \frac{xL + yM + zN - v^2tD + G}{xL_{\alpha\alpha} + yM_{\alpha\alpha} + zN_{\alpha\alpha} - v^2tD_{\alpha\alpha} + G_{\alpha\alpha}}\cdot\frac{S}{R} = -\frac{1}{2}. \tag{30}$$

The second condition (30) will be satisfied if functions $L, M, N, D, G$ satisfy to the following equations

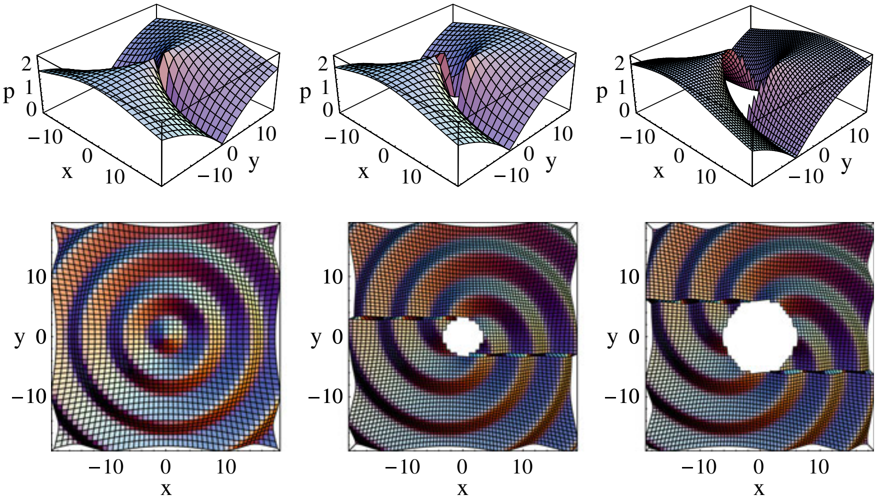

**Fig. 3** The function $p$ (at the top) and the solution **4** (see Eq. (25)) (at the bottom) with $z = 0$, $t = 0$ (at the left), $t = 3$ (at the centre), $t = 6$ (at the right)

$$L_{\alpha\alpha} = -2L\frac{S}{R},\ M_{\alpha\alpha} = -2M\frac{S}{R},\ N_{\alpha\alpha} = -2N\frac{S}{R},\ D_{\alpha\alpha} = -2D\frac{S}{R},\ G_{\alpha\alpha} = -2G\frac{S}{R}. \tag{31}$$

The system of Eq. (31) can be solved taking into account the following

$$L_\alpha L_{\alpha\alpha} + M_\alpha M_{\alpha\alpha} + N_\alpha N_{\alpha\alpha} - v^2 D_\alpha D_{\alpha\alpha} = \frac{S_\alpha}{2}, \tag{32}$$

$$LL_{\alpha\alpha} + MM_{\alpha\alpha} + NN_{\alpha\alpha} - v^2 DD_{\alpha\alpha} = \frac{R_{\alpha\alpha}}{2} - S. \tag{33}$$

Taking into account (32) and (33) the system of Eq. (31) takes the form

$$\frac{S_\alpha}{2} = -S\frac{R_\alpha}{R}, \quad \frac{R_{\alpha\alpha}}{2} = -S. \tag{34}$$

From the first equation (34) one obtains

$$SR^2 = C. \tag{35}$$

Here $C$ is an integration constant. The function $S$ can be expressed in terms of $R$ from second Eq. (34) with help of (35).

$$R_{\alpha\alpha} + \frac{2C}{R^2} = 0. \tag{36}$$

The Eq. (36) has partial solution

$$R = (9C)^{1/3}\alpha^{2/3}. \tag{37}$$

We will use it for finding the functions $L$, $M$, $N$, $D$, $G$. With help (37) one finds

$$S = \frac{1}{3}\left(\frac{C}{3}\right)^{1/3}\frac{1}{\alpha^{4/3}}, \quad \frac{S}{R} = \frac{1}{9\alpha^2}, \tag{38}$$

and system (31) takes the form

$$L_{\alpha\alpha} = -\frac{2}{9\alpha^2}L, \quad M_{\alpha\alpha} = -\frac{2}{9\alpha^2}M, \quad N_{\alpha\alpha} = -\frac{2}{9\alpha^2}N, \quad D_{\alpha\alpha} = -\frac{2}{9\alpha^2}D. \tag{39}$$

The system of Eq. (39) has the solution

$$\begin{aligned}
L &= a_1\alpha^{1/3} - a_2\alpha^{2/3}, \quad & l &= \frac{1}{3}\left(a_1\alpha^{-2/3} - 2a_2\alpha^{-1/3}\right),\\
M &= b_1\alpha^{1/3} - b_2\alpha^{2/3}, \quad & m &= \frac{1}{3}\left(b_1\alpha^{-2/3} - 2b_2\alpha^{-1/3}\right),\\
N &= c_1\alpha^{1/3} - c_2\alpha^{2/3}, \quad & n &= \frac{1}{3}\left(c_1\alpha^{-2/3} - 2c_2\alpha^{-1/3}\right),\\
D &= d_1\alpha^{1/3} - d_2\alpha^{2/3}, \quad & d &= \frac{1}{3}\left(d_1\alpha^{-2/3} - 2d_2\alpha^{-1/3}\right),
\end{aligned} \tag{40}$$

Here $a_1, a_2, b_1, b_2, c_1, c_2, d_1, d_2$ are arbitrary constants satisfying two equations

$$a_2^2 + b_2^2 + c_2^2 - v^2 d_2^2 = 0, \quad a_1a_2 + b_1b_2 + c_1c_2 - v^2 d_1 d_2 = 0. \tag{41}$$

On the basis (40) from the Eq. (13) we calculate ansatz $W$, from the Eq. (14) we calculate value $\alpha$ and from first Eq. (30) we calculate $p$

$$\alpha = \left(\frac{X_1}{2X_2}\right)^3, \quad W = \frac{X_1^3}{4X_2}, \quad p = \frac{A}{X_2}. \tag{42}$$

Here

$$\begin{gathered}
X_1 = xa_1 + yb_1 + zc_1 - v^2 t d_1 + e_1, \quad X_2 = xa_2 + yb_2 + zc_2 - v^2 t d_2 + e_2,\\
A = a_1^2 + b_1^2 + c_1^2 - v^2 d_1^2,
\end{gathered} \tag{43}$$

and also we assume that

$$g = \frac{1}{3}\left(e_1\alpha^{-2/3} - 2e_2\alpha^{-1/3}\right). \tag{44}$$

The solution of the Eq. (2), i.e. the function $f = f(W)$ is given by the inversion of first integral (12).

We will consider a special case. Let's

$$F(f) = b\sinh 2f, \quad V = b\sinh^2 f, \quad b = \text{const} > 0. \tag{45}$$

Then we will receive after calculation of integral (12) and its inversion

$$f(w) = \begin{cases} \dfrac{1}{2}\log\dfrac{1+\,\mathrm{sn}\,(\sqrt{E}\,q,k)}{1-\,\mathrm{sn}\,(\sqrt{E}\,q,k)}, & k^2 = 1-\dfrac{b}{E},\ \ 0<\dfrac{b}{E}<1, \\ \log\dfrac{1+\,\mathrm{cn}\,(\sqrt{b}\,q,k)}{\mathrm{sn}\,(\sqrt{b}\,q,k)}, & k^2 = 1-\dfrac{E}{b},\ \ 0<\dfrac{E}{b}<1, \\ \dfrac{1}{2}\log\dfrac{1+\sin(\sqrt{E}\,q)}{1-\sin(\sqrt{E}\,q)}, & E = b. \end{cases} \tag{46}$$

Here $q = 2\sqrt{2W} + C$, $C = \text{const}$.

Here we will note for $W(x, y, z, t)$ and of $p(x, y, z, t)$ received on the basis of Propositions 1–3 the solution of the Eq. (2) is found in quadratures for any functions $F(U)$ for which integrals (5) and (7) exist. The exact form of the solutions are given by its inversion.

Let ansatz $W$ be the root of the equation

$$x\,l(W) + y\,m(W) + z\,n(W) - tv^2 q(W) + g(W) = 0. \tag{47}$$

Here $l(W)$, $m(W)$, $n(W)$, $q(W)$ and $g(W)$ are arbitrary functions. Equation (47) implicitly defines dependency of ansatz $W$ from coordinates $x$, $y$, $z$ and time $t$. Following the rules of differentiation of implicit function we obtain from the Eq. (47)

$$W_x^2 + W_y^2 + W_z^2 - \frac{W_t^2}{v^2} = \frac{1}{v^2}\,P(W), \tag{48}$$

$$W_{xx} + W_{yy} + W_{zz} - \frac{W_{tt}}{v^2} = \frac{1}{v^2}\,Q(W). \tag{49}$$

Here

$$P(W) = l^2(W) + m^2(W) + n^2(W) - v^2 q^2(W), \tag{50}$$

$$Q(W) = P_W - P\frac{\nu_1}{\nu}, \tag{51}$$

$$\nu = x\,l_W + y\,m_W + z\,n_W - tv^2 q_W + g_W, \tag{52}$$

$$\nu_1 = x\,l_{WW} + y\,m_{WW} + z\,n_{WW} - tv^2 q_{WW} + g_{WW}. \tag{53}$$

Accepting that

$$p(x, y, z, t) = \frac{1}{\nu^2}, \tag{54}$$

according to the Proposition 3 functions $f(W)$ shall be the solutions of the equation

$$f_{WW} P(W) + f_W Q(W) = F[f[W)]. \tag{55}$$

As mentioned earlier Eq. (55) can be simply integrated if

$$P_W = 2Q(W). \tag{56}$$

It is seen from the relationship (51) that condition (56) will be satisfied if

$$\frac{\nu_1}{\nu} = \frac{P_W}{2P}. \tag{57}$$

Therefore functions $l(W)$, $m(W)$, $n(W)$, $q(W)$ and $g(W)$ should be selected so that condition (57) be fulfilled

$$\frac{x\, l_{WW} + y\, m_{WW} + z\, n_{WW} - t v^2 q_{WW} + g_{WW}}{x\, l_W + y\, m_W + z\, n_W - t v^2 q_W + g_W} = \frac{l\, l_W + m\, m_W + n\, n_W - v^2 q_W q}{l^2 + m^2 + n^2 - v^2 q^2}. \tag{58}$$

Observe that the right part of the Eq. (58) does not depend from coordinates and time. Therefore functions $l(W)$, $m(W)$, $n(W)$ and $q(W)$ should be selected so that left part of Eq. (58) also does not depend from coordinates and time. It should be done accepting that

$$\begin{aligned} l_{WW} &= l_W \frac{P_W}{2P} = l_W \frac{l\, l_W + m\, m_W + n\, n_W - v^2 q_W q}{l^2 + m^2 + n^2 - v^2 q^2}, \\ m_{WW} &= m_W \frac{P_W}{2P}, \quad n_{WW} = n_W \frac{P_W}{2P}, \\ q_{WW} &= q_W \frac{P_W}{2P}, \quad g_{WW} = g_W \frac{g_W}{2P}. \end{aligned} \tag{59}$$

System of Eq. (59) can be integrated taking into account the following relationships

$$l_W\, l_{WW} + m_W\, m_{WW} + n_W\, n_{WW} - v^2 q_W q_{WW} = \frac{1}{2} S_W, \tag{60}$$

$$l\, l_{WW} + m\, m_{WW} + n\, n_{WW} - v^2 q q_{WW} = \frac{P_{WW}}{2} - S, \quad S = l_W^2 + m_W^2 + n_W^2 - v^2 q_W^2. \tag{61}$$

Multiplying first equation of the system (59) by $l_W$, the second by $m_W$ and similarly transforming others then taking into account (61) we obtain

$$\frac{S_W}{2} = S\,\frac{P_W}{2P}. \tag{62}$$

Multiplying first equation of the system (59) by $l$, the second by $m$ and similarly transforming others then taking into account (61) we obtain

$$\frac{P_{WW}}{2} - S = \frac{P_W^2}{4P}. \tag{63}$$

From (62) it follows that

$$S = P, \tag{64}$$

and function $P(W)$ according to (63) shall satisfy the equation

$$P_{WW} = 2P + \frac{P_W^2}{2P}. \tag{65}$$

It can be integrated and finally we obtain

$$P(W) = A^2\cosh^2(W + C). \tag{66}$$

Here $A$ and $C$ are integration constants. Taking into account (66) we obtain from the system of Eq. (59)

$$\begin{aligned} &l = a_1 + a_2\sinh(W+C), \quad m = b_1 + b_2\sinh(W+C),\\ &n = c_1 + c_2\sinh(W+C), \quad q = d_1 + d_2\sinh(W+C),\\ &g = e_1 + e_2\sinh(W+C). \end{aligned} \tag{67}$$

Here $a_1, a_2, b_1, b_2, c_1, c_2, d_1, d_2, e_1, e_2$ are arbitrary constants. In order to satisfy relationships (66) they shall satisfy the following conditions

$$\begin{gathered} a_1^2 + b_1^2 + c_1^2 - v^2 d_1^2 = A^2, \quad a_2^2 + b_2^2 + c_2^2 - v^2 d_2^2 = A^2,\\ a_1 a_2 + b_1 b_2 + c_1 c_2 - v^2 d_1 d_2 = 0. \end{gathered} \tag{68}$$

We obtain from the system of algebraic Eq. (68)

$$\begin{aligned} \begin{pmatrix} a_1\\ a_2 \end{pmatrix} &= \frac{A}{\sqrt{2}}\left[\sqrt{1+\sigma^2}\cos\alpha\cos\beta \pm \cos\alpha\sin\beta\right],\\ \begin{pmatrix} b_1\\ b_2 \end{pmatrix} &= \frac{A}{\sqrt{2}}\left[\sqrt{1+\sigma^2}\sin\alpha\cos\beta \pm \sin\alpha\sin\beta\right],\\ \begin{pmatrix} c_1\\ c_2 \end{pmatrix} &= \frac{A}{\sqrt{2}}\left[\sqrt{1+\sigma^2}\sin\beta \mp \cos\beta\right]. \end{aligned} \tag{69}$$

Here $\alpha$, $\beta$ are arbitrary angles and

$$\sigma = 2v^2 d^2 / A^2, d_1 = d_2 = d. \tag{70}$$

From the Eq. (1) taking into account (66) we obtain the ansatz $W$

$$\sinh(W + C) = -\frac{X_1}{X_2}, \tag{71}$$

$$X_1 = x\,a_1 + y\,b_1 + z\,c_1 - t v^2 d_1 + e_1, \quad X_2 = x\,a_2 + y\,b_2 + z\,c_2 - t v^2 d_2 + e_2.$$

From the Eq. (52) taking into account (67) we get

$$\nu = X_2 \cosh(W + C) = \sqrt{X_1^2 + X_2^2}. \tag{72}$$

Because functions $P(W)$ and $Q(W)$ satisfy the conditions (56) $f(W)$ is found from the equation

$$f'' A^2 \cosh^2(W + C) \; + f' A^2 \cosh(W + C) \sinh(W + C) = \frac{dV}{dW}. \tag{73}$$

Its solution is reduced the calculation and inversion of the integral

$$\int \frac{df}{\sqrt{E + V}} = \frac{\sqrt{2}}{A} \tan^{-1}\left(\frac{X_1}{X_2}\right). \tag{74}$$

Here $E$ is the constant of integration.

Therefore if ansatz $W$ is found then on the basis of the Proposition 3 it is possible to find the solution of the Eq. (2) with any integrated function $F(U)$. Let us see the examples of solutions for the following cases.

$$F(U) = \left\{e^U,\ e^{-U},\ \sinh U,\ \sin U\right\}, \tag{75}$$

$$V(U) = \left\{E + e^U,\ E - e^{-U},\ E + \cosh U,\ E - \cos U\right\}.$$

Omitting algebraic calculations we state the final results:

$$U_{xx} + U_{yy} + U_{zz} - \frac{U_{tt}}{v^2} = \frac{F(U)}{X_1^2 + X_2^2},$$

$$\mathbf{1}.\quad F(U) = e^U, \quad U = \pi + \log\frac{E}{\sinh^2(q\sqrt{E}/2)}, \tag{76}$$

$$\mathbf{2}.\quad F(U) = e^{-U}, \quad U = \log\frac{\cosh^2(q\sqrt{E}/2)}{E}, \tag{77}$$

$$\textbf{3}.\quad F(U)=\sinh U,\quad U=\begin{cases}\log\left[\dfrac{1+\operatorname{sn}\left(\sqrt{E+1}\,q/2,r\right)}{1-\operatorname{sn}\left(\sqrt{E+1}\,q/2,r\right)}\right], & E\neq 1,\\[2ex] \log\left[\dfrac{1+\sin\left(q/\sqrt{2}\right)}{1+\sin\left(q/\sqrt{2}\right)}\right], & E=1,\end{cases}\tag{78}$$

$$\textbf{4}.\quad F(U)=\sin U,\quad U=\begin{cases}2\tan^{-1}\left[\sqrt{\dfrac{E-1}{E+1}}\dfrac{\operatorname{sn}\left(\sqrt{E+1}\,q/2,k\right)}{\operatorname{cn}\left(\sqrt{E+1}\,q/2,k\right)}\right], & E>1,\\[2ex] 2\pi-4\tan^{-1}\left[e^{q/\sqrt{2}}\right], & E=1,\\[2ex] 2\tan^{-1}\left[\dfrac{\operatorname{sn}\,(q,1/k)}{\operatorname{cn}\,(q,1/k)}\right], & o<E<1.\end{cases}\tag{79}$$

Here $\operatorname{sn}(q,k)$ is the elliptic sine, $\operatorname{cn}(q,k)$ is the elliptic cosine,

$$q(x,y,z,t)=\frac{\sqrt{2}}{A}\tan^{-1}\left(\frac{X_1}{X_2}\right),\quad r=\sqrt{\frac{E-1}{E+1}},\quad k=\sqrt{\frac{2}{E+1}}.\tag{80}$$

The solution (79) ($E>1$) can be written in another analytical form namely

$$U=\pi-2\,\mathrm{am}\,[\mathrm{K}\,(k)-\mathrm{F}\,(\psi,k),k],\quad \psi=\mathrm{am}\left[\sqrt{E+1}\,\frac{q}{2},k\right],\tag{81}$$

where $\mathrm{am}\,[\psi,k]$ is Jacobi amplitude, $\mathrm{K}\,(k)$ is complete elliptic integral, $\mathrm{F}\,(\psi,k)$ is incomplete elliptic integral. The first dependence (79) defines $U$ as periodic function and the second (81) continues $U$ out of the period $0<\sqrt{E+1}\,q/2<2\,\mathrm{K}\,(k)$ in the form of a "ladder". In the period value of $U$, calculated on (79) ($E>1$) and (81) coincide. On Fig. 4 graphs of the functions (79), (81) are represented with $E=1.2$.

In the Fig. 5 graph of the solution (79) is given with $E=1, v=1, e_1=1, e_2=0$, $a_1=0.38$, $a_1=0.33$, $b_1=0.66$, $b_2=0.57$, $c_1=0.66$, $c_2=0.76$, $z=0$, $t=0$ at the left and $t=2$ at the right. Solution has the form of soliton propagating in the plane $XOY$.

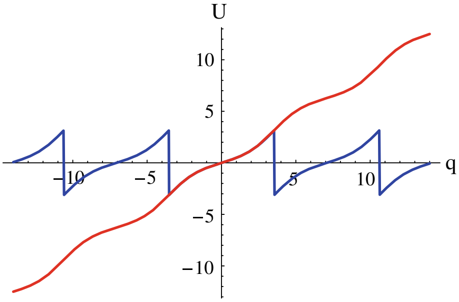

**Fig. 4** The solutions (79) (blue line) and (81) (red line) in the case $E=1.2$

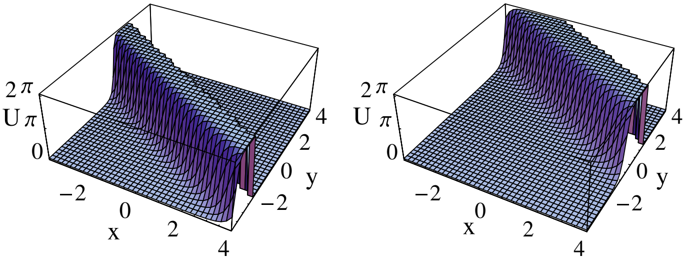

**Fig. 5** The solution (79) with $E = 1$, $z = 0$, $t = 0$ (at the left) and $t = 2$ (at the right)

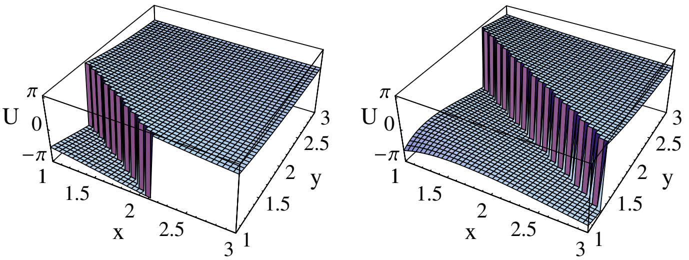

**Fig. 6** The solution (79) with $E = 0.2$, $z = 0$, $t = 0.4$ (at the left) and $t = 0.8$ (at the right)

With the same parameters in the Fig. 6 graph of the solution (79) is given with $E = 0.2$, $t = 0.4$ at the left and $t = 0.8$ at the right. Solution has a form of kink also propagating in the plane $XOY$.

## 4 Conclusion

Methods of obtaining of exact analytical solutions of the nonautonomous NKFG equation are proposed. The most important step in realization of the proposed methods is the calculation of ansatz. It could be obtained from the separate equations which can be algebraic, partial differential equations or equations of mixed type. It is obtained on the basis of the methods developed in the theory of construction of functionally invariant solutions of the wave equation. The choice of ansatz defines a type of the solution. Important feature of the offered methods is that ansatz determines also the function $p(x, y, z, t)$ which characterizes nonautonomous NKFG equation. It, undoubtedly, imposes restrictions for the Eq. (2) which can be solved by the proposed methods. However, methods proposed for obtaining of ansatz give the system of the equations which contains more arbitrary functions than number of required. The choice of these functions allows to receive rather broad set of analytical expressions for the function $p(x, y, z, t)$.

**Acknowledgements** This work was supported by the Russian Foundation for Basic Researches, Grant Nos. 16-01-00068-a and 17-01-00230-a.

## References

1. Bullough, R.K., Caudry, P.J. (eds.): Solitons. Springer, New York (1980)
2. Kudryashov, N.A.: Methods of Nonlinear Mathematical Physics. Intellekt Publishing, Moscow, Dolgoprudnyi (2010)
3. Sánchez, A., Scharf, R., Bishop, A.R., Vázquez, L.: Sine-Gordon breathers on spatially periodic potentials. Phys. Rev. A **45**, 6031–6037 (1992)
4. González, J.A., Cuenda, S., Sánchez, A.: Kink dynamics in spatially inhomogeneous media: the role of internal modes. Phys. Rev. E **75**, 036611 (2007)
5. Gumerov, A.M., Ekomasov, E.G., Zakir'yanov, F.K., Kudryavtsev, R.V.: Structure and properties of four-kink multisolitons of the sine-Gordon equation. Comput. Math. Math. Phys. **54**, 491–504 (2014)
6. Indeitsev, D.A., Kuznetsov, N.G., Motygin, O.V., Mochalova, Y.A.: Localization of Linear Waves. St. Petersburg University Publishing (2007)
7. Indeitsev, D.A., Meshcheryakov, Y., Kuchmin, A.Yu., Vavilov, D.S.: Multi-scale model of steady-wave shock in medium with relaxation. Dokl. Russ. Acad. Sci. **458**, 165–168 (2014)
8. Indeitsev, D.A., Naumov, V.N., Skubov, D.Y., Vavilov, D.S.: Problems of describing phase transitions in solids. In: Belyaev, A.K., Irschik, H., Krommer, M. (eds.) Mechanics and Model-Based Control of Advanced Engineering Systems, pp. 181–188. Springer, Wien (2014)
9. Jacobi, C.G.J.: Über eine particuläre Lösung der partiellen Differentialgleichung $\frac{\partial^2 V}{\partial x^2} + \frac{\partial^2 V}{\partial y^2} + \frac{\partial^2 V}{\partial z^2} = 0$. Crelle J. für die reine und angewandte Mathematik **36**(1848), 113–134. (Reprinted in C.G.J. Jacobi's Gesammelte Werke, Zweiter band, Herausgegeben K. von Weierstrass, Verlag von G. Reimer, Berlin, 1882, s. 191–216)
10. Forsyth, A.R.: New solutions of some of the partial differential equations of mathematical physics. Messenger Math. **27**, 99–118 (1898)
11. Bateman, H.: The Mathematical Analysis of Electrical and Optical Wave-Motion on the Basis of Maxwell's Equations. Cambridge University Press, Cambridge (1915)
12. Smirnov, V., Sobolev, S.: Sur une méthode nouvelle dans le problème plan des vibrations élastiques. Tr. Seism. Inst. **20**, 1–37 (1932). [English trans.: On a new method in the plane problem on elastic vibrations, in Selected Works of S.L. Sobolev, vol. I, pp. 45–80. Springer, New York (2006)]
13. Smirnoff, V., Soboleff, S.: Sur le problème plan des vibrations élastiques. C. R. Acad. Sci. Paris **194**, 1437–1439 (1932)
14. Sobolev, S.L.: Functionally invariant solutions of the wave equation. Tr. Fiz-Mat Inst Steklova **5**, 259–264 (1934). [English trans.: Selected Works of S.L. Sobolev, vol. I, pp. 195–199. Springer, New York (2006)]
15. Sobolev, S.L., Demidenko, G.V., Vaskevich, V.L. (eds.): Selected Works. Springer, New York (2006)
16. Erugin, N.P.: On functionally invariant solutions. Uchenye Zapiski Leningrad University Vyp. **15**(96), 101–134 (1948) (in Russian)
17. Aero, E.L., Bulygin, A.N., Pavlov, Yu.V.: Solutions of the three-dimensional sine-Gordon equation. Theor. Math. Phys. **158**, 313–319 (2009)
18. Aero, E.L., Bulygin, A.N., Pavlov, Yu.V.: Solutions of (3+1)-dimensional generalized sine-Gordon equation. Nelineinyi Mir **7**, 513–517 (2009) (in Russian)
19. Aero, E.L., Bulygin, A.N., Pavlov, Yu.V.: New approach to the solution of the classical sine-Gordon equation and its generalizations. Diff. Equat. **47**, 1442–1452 (2011)
20. Aero, E.L., Bulygin, A.N., Pavlov, Yu.V.: Functionally invariant solutions of nonlinear Klein-Fock-Gordon equation. Appl. Math. Comput. **223**, 160–166 (2013)
21. Aero, E.L., Bulygin, A.N., Pavlov, Yu.V.: Solutions of the sine-Gordon equation with a variable amplitude. Theor. Math. Phys. **184**, 961–972 (2015)

# Dynamic Fracture Analysis of Sandwich Composites with Face Sheet/Core Debond by the Finite Element Method

**Vyacheslav N. Burlayenko, Holm Altenbach and Tomasz Sadowski**

**Abstract** Numerical simulations using the finite element analyses within the code ABAQUS™ are used to study a dynamic fracture behaviour developing along the face sheet/core interface in sandwich panels. First, a virtual fracture test—the double cantilever sandwich beam subjected to uneven bending moments is simulated. In such analyses, the dynamic energy release rates and near-tip displacement and stress fields are extracted from finite element models developed within the two-dimensional elastodynamic theory and cohesive elements. These parameters are a basis for understanding the face sheet/core interface fracture in sandwich materials. Important computed results are that the inertia effects change the behaviour of fracture debonding parameters. Moreover, the analyses demonstrated the capability and the reliability of the finite element modelling technique for solving dynamic fracture mechanics problems. Also simulated and discussed is the dynamic interface crack progression in the sandwich specimen. In the second part of the work, the computational models are modified for analysing dynamic fracture of sandwich panels. For this, tree-dimensional models of sandwich plates with a penny-shaped debonded zone have been elaborated. In all simulations, computations of dynamic interface crack propagation are carried out in such a way when the crack history and inertial effects on cracking are direct outcomes of the analysis.

---

V. N. Burlayenko (✉) · T. Sadowski
Department of Solid Mechanics, Lublin University of Technology, 40 Nadbystrzycka str.,
20-618 Lublin, Poland
e-mail: burlayenko@yahoo.com

T. Sadowski
e-mail: t.sadowski@pollub.pl

V. N. Burlayenko
Department of Applied Mathematics, National Technical University KhPI,
2 Kyrpychova str., Kharkiv 61002, Ukraine

H. Altenbach
Institut für Mechanik, Otto-von-Guericke-Universität Magdeburg, Universitätsplatz 2,
39106 Magdeburg, Germany
e-mail: holm.altenbach@ovgu.de

H. Altenbach et al. (eds.), *Dynamical Processes in Generalized Continua and Structures*, Advanced Structured Materials 103,
https://doi.org/10.1007/978-3-030-11665-1_9

**Keywords** Sandwich panels · Face sheet/core debonding · Interface fracture · Finite element analysis

## 1 Introduction

The structural concept implying an assembly of two relatively stiff and strength layers (face sheets or skins) separated by a lightweight material (core) has opened up the possibility of creating constructions with new so-called sandwich materials. In these materials the top and bottom face sheets carry the in-plane and bending loads interacting through the core. In turn, the latter should be strong enough in order to keep the desired distance between the face sheets and to prevent their sliding with respect to each other [1]. As turned out, sandwich composites are competitive in comparison to conventional metallic materials due to their inherent high-performance features such as high specific stiffness and strength to weight ratios, acoustic and thermal insulation, protection against impacts, corrosion and wear resistance, etc. [2]. Due to these advantages, sandwich materials have found a wide engineering application, e.g. in aerospace, automotive, civil, medical, sports and other modern industries, e.g. [3–5].

The performance of such tri-material systems is highly dependent on the quality of the interface between face sheets and a core. Meanwhile, the interface is influenced by both initial bonding processes at a manufacturing stage (surface treatment, roughness, rheology, chemicals) and in-service effects (loading, temperature, time, moisture). Also, because of an inherent non-homogeneity of the sandwich structure, discontinuous stress fields exist at the material interface. All these factors make premises for an inevitable susceptibility of sandwich materials to the interface damage between the core and the face sheets called as debonding [6]. This damage affects significantly the behaviour of sandwich materials due to violating the transfer of mechanical responses between face sheets and a core. As a result, a substantial reduction in the compressive and bending strength occurs. This leads to decreasing overall load-carrying capability and increasing the risk of premature eventual failure of sandwich structures [7]. The presence of debond also alters the linear vibration characteristics of sandwich structures [8–10]. Moreover, it has also been shown that essential non-linear dynamic effects arise due to pre-existing debond, which cause quantitative and qualitative changes in the dynamics of sandwich structures in some regimes [11–15]. On the other hand, the knowledge about the influence of debonding on the dynamics is used as a means to identify and to quantify a dedonded site within sandwich panes as demonstrated, e.g. in [16–20].

Since the debonding poses a threat to the structural integrity of a whole sandwich construction, sandwich composites should be validated in terms of damage tolerance and possible failure [21]. In this respect, the engineering community has given considerable attention to fracture mechanics methods for sandwich composites subjected to static and dynamic loads. Herewith, the interface strength is quantified using the concept of interface fracture toughness [22]. Fracture specimens are used to supply necessary information regarding the fracture resistance of the material [23]. The fracture parameters such as stress intensity factors or strain energy release rates controlling the fracture process at the crack tip are inferred from the analysis of the fracture specimens by experimental, analytical or numerical methods. However, while testing methods for fracture research of composite laminates are at a high level of maturity, e.g. [24–26], the development of standard fracture tests for sandwich composites has not been completed yet [27]. This is related, from one hand, to the complexity of testing and analysing test data due to the bi-material nature of the face sheet/core interface and a non-symmetric geometry of sandwich specimens. On the other hand, the experimental data reported in the literature highlight a significant scatter in debonding toughness values for given sandwich systems because of various methods used in testing. Finally, a large variety of geometrical and material configurations of sandwich structures in service require an extensive campaign of experimental studies. Nevertheless, some progress has been achieved in the evaluation of interfacial fracture parameters under the assumption of static or quasi-static conditions [28].

Besides quasi-static fracture models, generally accepted for studying a majority of industrial applications of sandwich materials, there is a class of applications in which dynamic effects play a basic role in understanding the debonding resistance. This group includes the problems dealing with dynamic loading, in particular, impact-induced processes or static loading with a fast propagating crack running at a finite velocity. In these cases, to estimate accurately the face sheet/core interface strength, techniques based on a dynamic fracture framework are required. It implies to take into account inertia effects in the definition of the energy release rate and the crack growth behaviour [29]. Experimental measurements of dynamic crack growth in bi-material plate-like specimens [30, 31] revealed that cracks running along the weak plane can propagate, relatively to external energy supplied to the specimen, subsonically in predominantly Mode I or intersonically with the speed exceeding the shear wave speed of the more compliant material in Mode II dominated conditions. Discontinuous shock waves and a discernible contact zone were also observed for intersonic cracks. The findings of authors in [32] showed that dynamic interface cracks in laminated plates possess the similar features.

Despite these advances, dynamic face sheet/core interface fracture of sandwich composites still remains incomplete. Experimental data are very limited because of difficulties in obtaining accurate results when tracking a fast crack tip spped and a lack of reliable test configurations. Some existing dynamic testing methods adopt systems such as the split Hopkinson pressure bar, a one-point impact setup or the wedge cleavage test method as reviewed in [33]. However, they are not commonly accepted standards for dynamic fracture testing sandwich materials. Analytical solutions for bi-material stationary or dynamically propagated interface cracks, to which the face sheet/core debonding problem is attributed, exist mainly for infinite and semi-infinite continua are based on simple beam models, e.g. in [34–39] among many others. An attractive alternative is the use of numerical methods, among which the finite element method (FEM) is more popular because of its versatility and the existence of many commercially available FEM codes. Fracture mechanics-based tools implemented into commercial finite element analysis codes, for instance, ABAQUS™, ANSYS®, MSC Marc®, and others enable to make simulations of face sheet/core debonding in an effective and efficient way. The accuracy, however, of such predictions depends essentially on the reliability of both the fracture data such as fracture toughness and fracture criteria, which are used as inputs, and model-dependent parameters such as the stress intensity factors (SIFs) or the strain energy release rate (ERR), which are calculated during the analysis.

Within the context of FEM methodologies used for simulating dynamic fracture, the cohesive crack zone model has been widely applied to simulate crack initiation and propagation along an arbitrary, solution-dependent path in both homogeneous materials and composites, e.g. [40, 41] among the earliest works and [42–44] as more recent ones. In this modelling technique, discontinuities are easily incorporated into a finite element approximation through special either zero or finite thickness interface (cohesive) finite elements. A traction-separation law is embedded in the cohesive element (CE) to describe initiation and evolution of damage behaviour of the crack surface. This constitutive relationship defined in terms of strength and deformation of the interface is an additional material law relatively to other ones attributed to materials surrounding the cohesive interface. Local nonlinear assumptions near crack tip can be employed to simulate the crack initiation and propagation and can be used in appropriate fracture criteria of the cohesive crack model as well [45]. Also, CEs include a mixed-mode formulation that provides their generality for using in a broad variety of analyses. Nevertheless, the application of cohesive damage modelling in sandwich structures for the simulation of dynamic debonding failure is still limited, e.g. [46–48].

In light of the limited body of knowledge about dynamic fracture of sandwich materials, this work deals with modelling dynamic debonding to provide an insight into features of interfacial cracking of sandwich composites. The nonlinear dynamic fracture behaviour is modelled by means of ABAQUS package [49]. In simulations, the computations of dynamic interface crack propagation are carried out in such a way that the crack history and the influence of inertial effects on cracking are direct outcomes of the analyses with CEs. The present work is divided into two parts. The first one concerns the development of two-dimensional (2-D) FE models for detailed simulations of debonding in a double cantilever sandwich beam fracture specimen subjected to uneven bending moments (DCB-UBM). The results for quasi-static and dynamic loading are used as a basis for understanding the dynamic effects on fracture of sandwich materials. Fracture features observed in the analysed sandwich specimen have been discussed in detail. In the second part of the work, the results for the 2-D computational models are modified for analysing dynamic fracture of sandwich panels based on tree-dimensional (3-D) models. A rectangular sandwich plate with a penny-shaped debonded zone subjected to dynamic loading is considered.

## 2 Finite Element Methodology

A dynamic framework of the finite element method with cohesive finite elements is used in the present study. A brief review of the main steps of the finite element method strategy and some specific notes concerning the cohesive element model, time integration schemes applied to perform simulations and methods employed for extracting the fracture parameters are presented below.

### 2.1 Equation of Virtual Work with Cohesive Elements

We start from the principle of virtual work as a basis of the finite element method in the mechanics of solids. Let us consider a general case of a deformable body represented by a domain $V \subset \mathbb{R}^{\dim}$ for $1 \leq \dim \leq 3$ with a boundary $\partial V \subset \mathbb{R}^{\dim-1}$ oriented by a unit normal $\mathbf{n}$. Each a material point of the body is specified by $\mathbf{x}$ serving as a particle label in Lagrangian description. The body undergoes a motion described by a displacement field $\mathbf{u}$: $V \times [0, T] \rightarrow \mathbb{R}^{\dim}$ at time $t \in \times[0, T] \rightarrow \mathbb{R}_{+}$ under prescribed surface traction $\bar{\mathbf{t}}$ on the boundary $\partial V_t$ and prescribed displacements $\bar{\mathbf{u}}$ on the boundary $\partial V_u$. The boundaries comply with $\partial V_t \cup \partial V_u = \partial V$ and $\partial V_t \cap \partial V_u = \oslash$. Assume that the body is under the assumption on infinitesimal deformations, then, at an arbitrary time $t$, a strain can be measured by a tensor $\boldsymbol{\varepsilon}$: $V \rightarrow \mathbb{R}^{\dim\times\dim}$ defined as $\boldsymbol{\varepsilon} = \frac{1}{2}\left(\nabla\mathbf{u} + (\nabla\mathbf{u})^T\right)$, while a stress state induced by the deformations is defined by the Cauchy stress tensor $\boldsymbol{\sigma} : V \rightarrow \mathbb{R}^{\dim\times\dim}$. In addition, let the continuum contain a crack (or cracks), the locus of which is on an internal cohesive surface $\partial V_c = \partial V_c^{+} \cup \partial V_c^{-}$. The cohesive surface formulation provides the incorporation of the strong discontinuity in the displacement fields, caused by a localized fracture of the material in the form of cracks, by the accommodation of displacement jumps $\boldsymbol{\Delta}$ across the crack flanks on $\partial V_c^{+}$ and $\partial V_c^{-}$ and a cohesive driving traction $\mathbf{T} = \boldsymbol{\sigma} \cdot \mathbf{n}_c$ along the cohesive surface $\partial V_c$ with unit normal $\mathbf{n}_c$.

Under the conditions mentioned above, the weak form of the conservation of linear momentum or the principal of virtual work without body forces is stated in the form:

$$\int_{V\setminus\partial V_c} (\boldsymbol{\sigma} : \nabla\delta\mathbf{u} + \rho\ddot{\mathbf{u}} \cdot \delta\mathbf{u})\, dV + \int_{\partial V_c} \mathbf{T} \cdot \delta\boldsymbol{\Delta} dA - \int_{\partial V_t} \bar{\mathbf{t}} \cdot \delta\mathbf{u} dA = 0 \tag{1}$$

for all virtual (kinematically admissible) displacement fields $\delta\mathbf{u}$. Also, in (1) $\rho$ is the density of material, and the superscript dot means a time derivative, i.e. $\ddot{\mathbf{u}}$ stands for the acceleration filed.

Finally, to complete the formulation of the problem at hand, a set of constitutive relations for the bulk material and the cohesive layer should be specified. The constitutive relations between the cohesive traction and the displacement jump on $\partial V_c$ are independent on the material laws describing the bulk behaviour of the material surrounding the crack.

## 2.2 Constitutive Equations

As mentioned the continuum is featured by two sets of constitutive equations. The first one defines the behaviour of a bulk material in $V \times [0, T]$ and the second one is a traction-separation law (TSL) given on $\partial V_c \times [0, T]$.

### 2.2.1 Bulk Material Properties

Since an interfacial crack problem is considered, we assume that the crack modelled by a cohesive layer divides the continuum in two parts, i.e. $V = V_{\#1} \cup V_{\#2}$, which, in general, are different in geometrical configurations and material properties. Let the materials of each part ($k = \#1, \#2$) be orthotropic linear elastic obeying the general Hookes law in the form [50]:

$$\begin{Bmatrix} \varepsilon_{11} \\ \varepsilon_{22} \\ \varepsilon_{33} \\ 2\varepsilon_{23} \\ 2\varepsilon_{13} \\ 2\varepsilon_{12} \end{Bmatrix} = \begin{bmatrix} S_{11} & S_{12} & S_{13} & & & \\ S_{12} & S_{22} & S_{23} & & \mathbf{0} & \\ S_{13} & S_{23} & S_{33} & & & \\ & & & S_{44} & & \\ & \mathbf{0} & & & S_{55} & \\ & & & & & S_{66} \end{bmatrix} \cdot \begin{Bmatrix} \sigma_{11} \\ \sigma_{22} \\ \sigma_{33} \\ \sigma_{23} \\ \sigma_{13} \\ \sigma_{12} \end{Bmatrix}, \tag{2}$$

where $S_{11} = \frac{1}{E_1}$, $S_{22} = \frac{1}{E_2}$, $S_{33} = \frac{1}{E_3}$, $S_{12} = S_{21} = -\frac{\nu_{12}}{E_1} = -\frac{\nu_{21}}{E_2}$, $S_{13} = S_{31} = -\frac{\nu_{13}}{E_1} = -\frac{\nu_{31}}{E_3}$, $S_{23} = S_{32} = -\frac{\nu_{23}}{E_2} = -\frac{\nu_{32}}{E_3}$, $S_{44} = 1/G_{23}$, $S_{55} = \frac{1}{G_{13}}$ and $S_{66} = \frac{1}{G_{12}}$. In plane stress the compliance matrix reduces to a $3 \times 3$ matrix with components $S_{ij}$ for $i, j = 1, 2, 6$ and $S_{16} = S_{26} = 0$. In plane strain the coefficients of the reduced compliance matrix should be replaced by $\widetilde{S}_{ij} = S_{ij} - \frac{S_{i3} S_{j3}}{S_{33}}$ for $i, j = 1, 2, 6$.

### 2.2.2 Cohesive Elements and TSL

In the FEM context, the cohesive surface is represented by cohesive elements. The main idea of the cohesive element is a representation of crack initiation that reflects changes in the fracture process zone due to microscopic damage accumulation at the crack tip and a subsequent crack growth that is a creation of new free surfaces in the body. The element is idealized by a pair of separate top and bottom faces. In the finite element mesh, the element nodes have the same coordinates, but different node numbers as shown for 2-D and 3-D cohesive elements in Fig. 1a, b, respectively.

A TSL incorporating the ability of the cohesive element to simulate fracture is usually formulated in such a way that the onset of the softening process at the crack tip is a result of a strength-based analysis, whereas the crack propagation conditions are realized by satisfying fracture mechanics criteria. There have been proposed a number of TSLs in the literature. They can be subdivided into two groups: intrinsic and extrinsic relatively handling an initial elastic range within the cohesive element, in

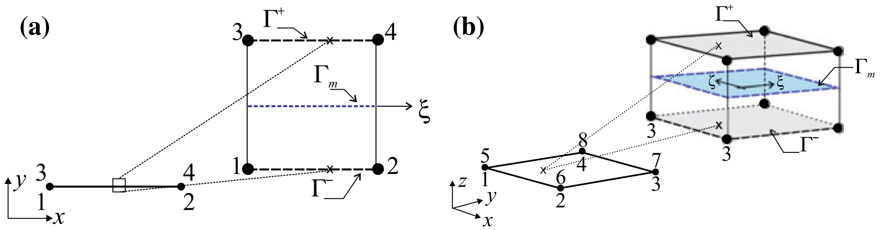

**Fig. 1** A sketch of cohesive elements after [49]: **a** 2-D line element; **b** 3-D surface element

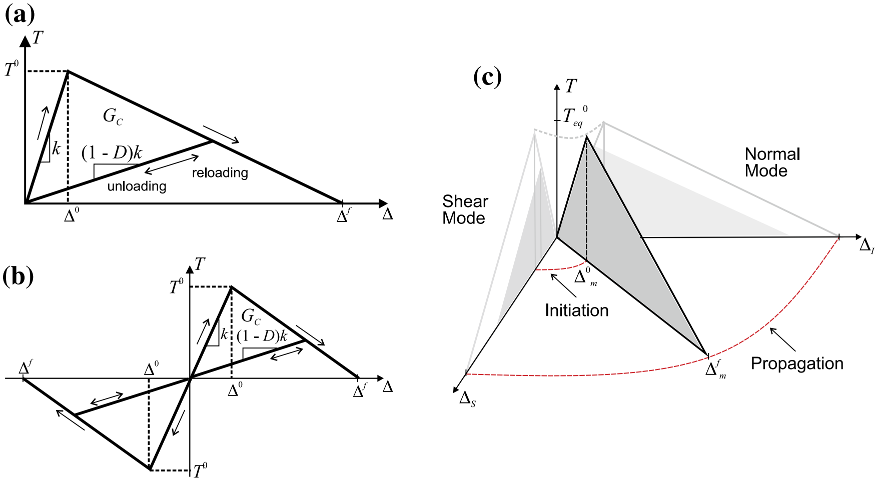

**Fig. 2** A cohesive bilinear TSL after [49] for: **a** normal mode; **b** shear mode; **c** mixed mode

turn, all they are distinguished from each other as potential-based and non-potential-based models depending on assumptions adopted for the fracture energy potential [51]. A typical bilinear cohesive law for single fracture modes is presented in Fig. 2a, b. The law contains an initial linear region defined by a penalty stiffness $k$ and the softening part starting from the value $\Delta^0$, where the traction reaches a maximum normal/shear cohesive value $T^0$ and, then, evolving linearly till $\Delta^f$, where complete failure occurs. The irreversibility conditions are assumed to be realized by unloading to the origin from the current state. The area under the lines being the work done per unit area for complete fracture defines the strain energy release rate. Analytically, for each fracture mode ($i = I, II, III$) the bilinear TSL can be presented as follows [52]:

$$T = \begin{cases} k_i \Delta_i & \Delta_i \le \Delta_i^0 \\ (1 - D_i) k_i \Delta_i & \Delta_i^0 \le \Delta_i \le \Delta_i^f \\ 0 & \Delta_i \ge \Delta_i^f \end{cases} \tag{3}$$

Here, a damage variable $D$ can be calculated as a function of current separation between the cohesive element faces, i.e. $D_i = \frac{\Delta_i^f(\Delta_i - \Delta_i^0)}{\Delta_i\left(\Delta_i^f - \Delta_i^0\right)}$.

In the case of mixed modes, an effective displacement jump $\Delta_m = \sqrt{\sum_{i=1}^{M} \Delta_i^2}$, where $M = I, II, III$ is the number of modes involved, is introduced and the damage initiation and evolution criteria are to be formulated in terms of interaction between the fracture parameters of each mode, Fig. 2c. In this regard, the equivalent mixed mode separations at damage onset $\Delta_m^0$ and failure $\Delta_m^f$ are to be defined. Following [52] the damage initiation based on the quadratic stress initiation criterion takes the form:

$$\Delta_m^0 = \Delta_I^0 \Delta_{II}^0 \sqrt{\frac{1+\gamma^2}{\left(\gamma \Delta_I^0\right)^2 + \left(\Delta_{II}^0\right)^2}}, \tag{4}$$

where $\gamma = \frac{\Delta_{II}}{\Delta_I}$ is a mixed mode ratio, whereas the damage propagation relying on the Benzeggagh-Kenane (B-K) fracture toughness criterion reads:

$$\Delta_m^f = \frac{1}{\Delta_I^0} \left\{ \Delta_I^0 \Delta_I^f + \left( \Delta_s^0 \Delta_s^f - \Delta_I^0 \Delta_I^f \right) \left[ \frac{G_{II} + G_{III}}{G_T} \right]^{\eta} \right\} \tag{5}$$

where $\Delta_s = \sqrt{\Delta_{II}^2 + \Delta_{III}^2}$, $G_T$ is the total ERR and $\eta$ is a parameter obtained by curve-fitting the fracture toughness of mixed mode tests. Once mixed mode separations are known the mixed mode damage parameter $D_m$ can be calculated identical to the expression for $D_i$ using $\Delta_m$, $\Delta_m^0$ and $\Delta_m^f$ instead the pure mode components there.

## 2.3 Contact and Friction Conditions

The crack flanks are assumed to be traction free. However, upon cracking the crack faces may come into contact as well as dynamic loading may cause interactions between them. Thus, contact and friction are to be determined as a part of the solution at a certain load level and an instant of time. In doing so, the cohesive interface model is included into the overall contact algorithm through nodal forces of the cohesive elements which are related to the cohesive traction vector. Thus, during the finite element analysis two possibilities for the calculation of nodal forces are handled. The first is the case of separation considered already in Sect. 2.2, and the second is the case of contact and friction, in which equivalent normal and tangential nodal forces are computed using a certain contact algorithm and a friction law. A brief description of the modelling of contact and friction constraints is given below.

From the modelling point of view, to impose contact and friction constraints within contact surfaces, the contact traction $\mathbf{t}_c$ acting between them is decomposed into normal $\mathbf{t}_N$ and tangential $\mathbf{t}_T$ components. Each the traction component is associated with an appropriate displacement jump. Using the master-slave contact definition, the displacement jumps can be expressed by the normal $g_N = (\mathbf{x}^- - \bar{\mathbf{x}}^+) \cdot \bar{\mathbf{n}}_c^+$ and tangential $\mathbf{g}_T = g_{T_\alpha} \bar{\mathbf{a}}^{+^\alpha}$ with $g_{T_\alpha} = (\mathbf{x}^- - \bar{\mathbf{x}}^+) \cdot \bar{\mathbf{a}}_{c_\alpha}^+$ gap functions. We denote that $\mathbf{x}^-$ is a point of the slave surface and $\bar{\mathbf{x}}^+ \left(\bar{\xi}^1, \bar{\xi}^2\right)$ is its orthogonal projection on the master surface parameterized by $\xi^\alpha$, $\alpha = 1, 2$; $\bar{\mathbf{n}}_c^+$ is the unit normal vector of the master surface and $\bar{\mathbf{a}}_{c_\alpha}^+$, $\alpha = 1, 2$ are the tangent base vectors at the point $\bar{\mathbf{x}}^+$ (see for more details in [53, 54] and the references there). The functions $g_N$ and $\mathbf{g}_T$ depend on a current displacement field induced by given loads at a time instant $t$. Then, the impenetrability and friction constraints are stated in the form of the Karush-Kuhn-Tucker conditions as follows:

$$t_N \leq 0,\ g_N \geq 0 \text{ and } t_N g_N = 0 \tag{6}$$

and

$$\|\mathbf{t}_T\| \leq \tau_{crit},\ \|\mathbf{g}_T\| \geq 0 \text{ and } \left(\|\mathbf{t}_T\| - \tau_{crit}\right) \|\mathbf{g}_T\| = 0, \tag{7}$$

respectively. Here, $t_N$ is the scalar quantity of the normal traction component, i.e. $\mathbf{t}_N = t_N \mathbf{n}_c$; $\tau_{crit}$ is a threshold of tangential contact traction due to the tangential slip. In the case of the Coulomb friction model, this value is expressed as $\tau_{crit} = \mu t_N$, where $\mu$ is the coefficient of friction.

Accounting for contact and friction leads to appearance of an additional term referred to as the work of contact forces in the variational equality (1). Therefore, this expression takes a new form:

$$\begin{gathered}\int_{V \setminus \partial V_c} (\boldsymbol{\sigma} : \nabla \delta \mathbf{u} + \rho \ddot{\mathbf{u}} \cdot \delta \mathbf{u})\, dV + \int_{\partial \underline{V}_c} \mathbf{T} \cdot \delta \boldsymbol{\Delta} dA + \\ \int_{\partial V_c} (t_N \delta g_N + \mathbf{t}_T \cdot \delta \mathbf{g}_T)\, dA - \int_{\partial V_t} \bar{\mathbf{t}} \cdot \delta \mathbf{u} dA = 0\end{gathered} \tag{8}$$

In general, contact problems are inherently nonlinear since the contact region is a priori unknown and nodal contact forces related to contact traction on this contact zone are a part of the solution. Also, the contact and friction laws are expressed by non-smooth multivalued force displacement relationships. In this respect, contact algorithms within the FEM context are subdivided into two major steps: contact detection and contact resolution [55]. The latter step depends also on a time-integration scheme used in the finite element discretization, [53, 54].

## *2.4 Finite Element Discretization*

Following the FEM framework, the actual continuous model is idealized as an assemblage of finite elements interconnected at nodal points. Consequently, (8) is transformed to the discrete system of equations of motion with respect to nodal degrees of freedom, e.g. displacements $\{U\}$, at time $t$ as follows:

$$[M]\{\ddot{U}\}_t + \{R_{int}\}_t + \{R_{coh}\}_t + \{R_{cont}\}_t = \{R_{ext}\}_t \tag{9}$$

where $\{R_{int}\}$, $\{R_{ext}\}$, $\{R_{coh}\}$ and $\{R_{cont}\}$ are the vectors attributed to the nodal internal, external, cohesive and contact forces, respectively, calculated using the corresponding integrals in (8); $[M]$ is the mass matrix associated with inertial properties; $\{\ddot{U}\}$ are the nodal accelerations. It should be noted that in the system (9) damping is not included and the nonlinearities other than contact and cracking with cohesive elements are not taking into account. The calculations of nodal equivalent forces require an approximation of the displacement field within the finite element in terms of shape functions and a set of the nodal displacements [56].

Besides the discretization in space, the finite element equations (9) still need to be discretized in time, i.e. $[0, T] = \bigcup_n \left[t_n, t_{n+1}\right]$. For this, either explicit or implicit time-stepping strategies are used. Two numerical methods implemented in ABAQUS [49] as main solution schemes are briefly presented below.

### 2.4.1 Explicit Integration Scheme

The explicit central difference time integrator is used in the dynamic explicit analysis. Accelerations and velocities at a particular time point $t_n$ are assumed to be constant during a time increment $\Delta t = t_{n+1} - t_n$ and are used to find a solution at the next point in time $t_{n+1}$. Then, the accelerations are computed at the start of the increment by solving (9) as follows:

$$\{\ddot{U}\}_t = [\widetilde{M}]^{-1} \left(\{R_{ext}\}_t - \{R_{int}\}_t - \{R_{coh}\}_t - \{R_{cont}\}_t\right) \tag{10}$$

To find velocities and displacements, ABAQUS/Explicit utilizes a forward Euler integration scheme, i.e. $\{\dot{U}\}_{t+\frac{1}{2}\Delta t} = \{\dot{U}\}_{t-\frac{1}{2}\Delta t} + \Delta t\{\ddot{U}\}_t$ and $\{U\}_{t+\Delta t} = \{U\}_t + \Delta t\{\dot{U}\}_{t+\frac{1}{2}\Delta t}$, respectively. In (10) $[\widetilde{M}]$ is a lumped mass matrix obtained by the transformation of the consistent mass matrix $[M]$ for the purpose of efficiency. The explicit scheme is stable if the time increment satisfies to the limit: $\Delta t \leq \frac{2}{\omega_{max}}$, where $\omega_{max}$ is the highest natural frequency in the finite element mesh of the discretized system [56].

### 2.4.2 Implicit Integration Scheme

The dynamic implicit analyses are carried out by using the implicit Hilber-Hughes-Taylor (HHT) temporal integrator in ABAQUS/Standard. In accordance with the HHT scheme, the equations of motion (9) at a particular time point $t_{n+1} = t + \Delta t$ can be rewritten in terms of displacements, velocities and accelerations at the point $t_n = t$ as follows:

$$\begin{gathered}[M]\{\ddot{U}\}_{t+\Delta t} + (1+\widetilde{\alpha})\left(\{R_{int}\}_{t+\Delta t} + \{R_{coh}\}_{t+\Delta t} + \{R_{cont}\}_{t+\Delta t}\right) = \\ \{R_{ext}\}_{t+(1+\widetilde{\alpha})\Delta t} + \widetilde{\alpha}\left(\{R_{int}\}_t + \{R_{coh}\}_t + \{R_{cont}\}_t\right),\end{gathered} \tag{11}$$

where displacements and velocities at the time point $t + \Delta t$ are approximated by the expressions: $\{U\}_{t+\Delta t} = \{U\}_t + \Delta t\{\dot{U}\}_t + \frac{\Delta t^2}{2}\left[\left(1 - 2\widetilde{\beta}\right)\left\{\ddot{U}\right\}_t + 2\widetilde{\beta}\{\ddot{U}\}_{t+\Delta t}\right]$ and $\{\dot{U}\}_{t+\Delta t} = \{\dot{U}\}_t + \Delta t\left[(1 - \widetilde{\gamma})\{\ddot{U}\}_t + \widetilde{\gamma}\{\ddot{U}\}_{t+\Delta t}\right]$, correspondingly. The scheme is second order accurate and unconditionally stable for $-\frac{1}{3} \leq \widetilde{\alpha} \leq 0$, $\widetilde{\gamma} = \frac{1}{2}(1 - 2\widetilde{\alpha})$ and $\widetilde{\beta} = \frac{1}{4}(1 - \widetilde{\alpha})^2$, [56]. The solution of the implicit analysis from $t$ to $t + \Delta t$ is updated incrementally within the well-known Newton-Raphson iterative scheme for finding the roots of (11).

## 2.5 *Near-Tip Fields at Bi-material Interface*

The analysis of bi-material interface cracks is more complicated than for cracks in homogeneous materials since bi-material cracks exhibit a coupling of tensile and shear effects even in the cases of pure either opening or shearing loading. Also, the oscillatory character of stress and displacement fields occurs. It leads to the variation of mode-mixity ratio with distance from the crack tip. To characterise the singular stress and displacement fields, a complex stress intensity factor (SIF), **K** together with the oscillation index, $\varepsilon$ relating to the elastic properties of the materials are used [35, 36]. Following these authors the structure of the asymptotic near-tip fields for either stationary or dynamically propagating interface crack results from the solution of the eigenvalue problem induced by the traction free boundary conditions on the crack flanks as

$$\bar{\mathbf{H}}\mathbf{w} = e^{2\pi\varepsilon}\mathbf{H}\mathbf{w}, \tag{12}$$

where $\mathbf{H}$ is a $3 \times 3$ positive defined compliance-like Hermitian matrix involving the bi-material elastic constants and $\bar{\mathbf{H}}$ is its complex conjugate matrix. Three eigenpairs such as $(\varepsilon, \mathbf{w})$, $(-\varepsilon, \bar{\mathbf{w}})$ and $(0, w_3)$, where $\mathbf{w}$, $\bar{\mathbf{w}}$ and $w_3$ are complex, complex conjugate and real eigenvectors, respectively, are the solutions of (12). Then, the stresses at the crack tip and the relative displacements at a distance $r$ behind the crack tip take the form [36, 57]:

$$\begin{gathered} {}_{(k)}\sigma_{mn}(r,\theta) = \frac{1}{\sqrt{2\pi r}}\left\{\mathfrak{R}e\left[\mathbf{K}r^{i\varepsilon}\right]{}_{(k)}\Sigma^{I}_{mn}(\theta,\varepsilon) + \right. \\ \left. \mathfrak{I}m\left[\mathbf{K}r^{i\varepsilon}\right]{}_{(k)}\Sigma^{II}_{mn}(\theta,\varepsilon) + K_{3(k)}\Sigma^{III}_{mn}(\theta)\right\} \end{gathered} \tag{13}$$

and

$$\boldsymbol{\Delta}(r,\theta) = \left(\mathbf{H} + \bar{\mathbf{H}}\right)\sqrt{\frac{r}{2\pi}}\left\{\frac{\mathbf{K}r^{i\varepsilon}\mathbf{w}}{(1 + 2i\varepsilon)\cosh\pi\varepsilon} + \frac{\bar{\mathbf{K}}r^{-i\varepsilon}\bar{\mathbf{w}}}{(1 - 2i\varepsilon)\cosh\pi\varepsilon} + K_3 w_3\right\}, \tag{14}$$

relatively, where $m, n = 1, 2$; $k = \#1, \#2$ denotes the materials of the interface, $\mathbf{K} = K_1 + iK_2 = |\mathbf{K}|\,e^{i\psi}$ with $K_1$ and $K_2$ used instead of $K_I$ and $K_{II}$ adopted for homogeneous materials and $K_3$ is the SIF associated with non-singular stress field in mode $III$, ${}_{(k)}\Sigma^{M}_{mn}$ with $M = I, II, III$ are universal angular functions in polar $(r, \theta)$ or Cartesian $(x_1, x_2)$ coordinate systems centred at the crack tip. The oscillation index $\varepsilon$ can be expressed in the form:

$$\varepsilon = \frac{1}{2\pi} \ln \left( \frac{1-\beta}{1+\beta} \right), \tag{15}$$

where $\beta$ is the second Dundurs parameter defined by

$$\beta = -\sqrt{-\frac{1}{2} \mathrm{tr} \left\{ \left( \frac{\Im m[\mathbf{H}]}{\Re e[\mathbf{H}]} \right)^2 \right\}} \tag{16}$$

An alternative description of the near-tip stress field involves the energy release rate (ERR), $\mathscr{G}$ together with the mode mixity parameter, $\psi$. To avoid oscillations in the mode mixity parameter, a characteristic length scale, $\hat{l}$ chosen in consistence with discussions in [22, 57] is introduced. Then, the non-oscillatory phase angle $\hat{\psi}$ is established as follows:

$$\hat{\psi} = \tan^{-1} \left( \frac{\sigma_{12}}{\sigma_{22}} \right) \Bigg|_{r=\hat{l}} = \tan^{-1} \frac{\Im m[\mathbf{K}\hat{l}^{i\varepsilon}]}{\Re e[\mathbf{K}\hat{l}^{i\varepsilon}]} \tag{17}$$

Here $\mathbf{K}\hat{l}^{i\varepsilon} = \hat{\mathbf{K}}$ is a normalized complex SIF with ordinary units of the SIF in homogeneous materials. The amplitudes of $\hat{\mathbf{K}}$ and $\mathbf{K}$ are the same, but their phase angles are different, i.e. $\hat{\psi} = \psi + \varepsilon \ln \hat{l}$. Following [36, 57] the expression of the ERR can be written in the form:

$$\mathscr{G} = \frac{\bar{\mathbf{w}}^T \left( \mathbf{H} + \bar{\mathbf{H}} \right) \mathbf{w}}{4 \cosh^2 \pi \varepsilon} |\mathbf{K}|^2 + \frac{1}{8} w_3^T \left( \mathbf{H} + \bar{\mathbf{H}} \right) w_3 K_3^2 \tag{18}$$

In the case of orthotropic materials surrounding the interface crack, the material symmetry axes of which are aligned along the face sheet-to-core interface (Fig. 3b), the matrix $\mathbf{H}$ takes the form [58]:

$$\begin{aligned} H_{11} &= \left[2n\lambda^{1/4}\sqrt{S_{11}S_{22}}\right]_{\#1} + \left[2n\lambda^{1/4}\sqrt{S_{11}S_{22}}\right]_{\#2}, \\ H_{22} &= \left[2n\lambda^{-1/4}\sqrt{S_{11}S_{22}}\right]_{\#1} + \left[2n\lambda^{-1/4}\sqrt{S_{11}S_{22}}\right]_{\#2}, \\ H_{12} &= \bar{H}_{21} = i\left[\sqrt{S_{11}S_{22}} + S_{12}\right]_{\#1} - \left[\sqrt{S_{11}S_{22}} + S_{12}\right]_{\#2}, \\ H_{33} &= \left[\sqrt{S_{44}S_{55}}\right]_{\#1} + \left[\sqrt{S_{44}S_{55}}\right]_{\#2}, \ H_{13} = H_{31} = H_{23} = H_{32} = 0, \end{aligned} \tag{19}$$

where $\lambda = S_{11}/S_{22} = E_2/E_1$ and $\varrho = \frac{(2S_{12}+S_{66})}{2\sqrt{S_{11}S_{22}}} = \frac{\sqrt{E_1E_2}}{2G_{12}} - \sqrt{\nu_{12}\nu_{21}}$ are parameters of anisotropy and $n = \sqrt{\frac{(1+\varrho)}{2}}$. Moreover, the eigenvectors take the form: $\mathbf{w} = \left\{-\frac{i}{2}, \frac{1}{2}\sqrt{\frac{H_{11}}{H_{22}}}, 0\right\}$ and $w_3 = \{0, 0, 1\}$.

The stresses $\sigma_{22}$ and $\sigma_{12}$ at a distance $r$ in front of the crack tip at $\theta = 0$ between two orthotropic materials can be inferred from (13) as follows [36, 57]:

$$\sqrt{\frac{H_{22}}{H_{11}}}\sigma_{22} + i\sigma_{12} = \frac{\mathbf{K}}{\sqrt{2\pi r}}\left(\frac{r}{\hat{l}}\right)^{i\varepsilon} \tag{20}$$

and the associated relative crack surface displacements (jumps) $\varDelta_1$ and $\varDelta_2$ at a distance $r$ behind the crack tip at $\theta = \pm\pi$, can be derived from (14) in the form [36, 57]:

$$\sqrt{\frac{H_{11}}{H_{22}}}\varDelta_2 + i\varDelta_1 = \frac{2H_{11}\mathbf{K}}{\sqrt{2\pi}(1+2i\varepsilon)\cosh\pi\varepsilon}\left(\frac{r}{\hat{l}}\right)^{\frac{1}{2}+i\varepsilon} \tag{21}$$

The relations (20) and (21) give a basis for numerical calculations of the interface crack fracture parameters within the framework of the FEM.

## *2.6 Evaluation of Interface Dynamic Fracture Parameters*

In LEFM the Rices $J$-integral is identical to the ERR. The generalization of this fundamental concept on an elastic solid with a crack advancing straightway along the $x_1$-axis direction under dynamic conditions can be expressed as [59]:

$$\mathscr{G}(t) = J' = \lim_{\varGamma\to 0}\int_{\varGamma}\left[(W+T)\,n_1 - \left(\boldsymbol{\sigma}\cdot\frac{\partial\mathbf{u}}{\partial x_1}\right)\cdot\mathbf{n}\right]d\varGamma\ , \tag{22}$$

where the path $\varGamma$ is an arbitrary contour surrounding a crack tip; $\mathbf{n}$ is an outward unit normal of $\varGamma$; $W$ is the strain energy density and $T$ is the kinetic energy density at a material point. Under a steady state crack growth condition, the dynamic integral (22) is path independent and corresponds to the instantaneous energy release rate for any crack configuration including the interface crack between two dissimilar orthotropic materials [59].

The domain integral formulation, which invokes the divergence theorem to convert a line integral to a domain one of the same filed, allows a simple FEM computation of the dynamic $J'$-integral (22). With using a weight function $q_1(\mathbf{x})$, the line integral (22) is transformed to a domain integral, i.e. the dynamic ERR can be evaluated by computing the expression [59]:

$$\mathscr{G}\,(t) = \int_A\left[\left(\boldsymbol{\sigma}\cdot\frac{\partial\mathbf{u}}{\partial x_1}\right)\frac{\partial q_1}{\partial\mathbf{x}} - (W+T)\,\frac{\partial q_1}{\partial x_1} + \rho\left(\frac{\partial^2\mathbf{u}}{\partial t^2}\frac{\partial\mathbf{u}}{\partial x_1} - \frac{\partial\mathbf{u}}{\partial t}\frac{\partial^2\mathbf{u}}{\partial x_1\partial t}\right)q_1\right]dA \tag{23}$$

where $A$ is the domain enclosed between the contour $\varGamma$, an arbitrary contour $\mathscr{C}$ with unit normal $\mathbf{m}$, which embraces $\varGamma$ and the surfaces of crack flanks, $\mathscr{C}_+$ and $\mathscr{C}_-$ between the two contours (Fig. 3a). The weighting parameter $q_1$ is chosen as a smooth function of $\mathbf{x}$ which takes the values from zero on the $\mathscr{C}$-contour to unity on $\varGamma$. A geometrical interpretation of $q_1(\mathbf{x})$ is a virtual displacement of the crack

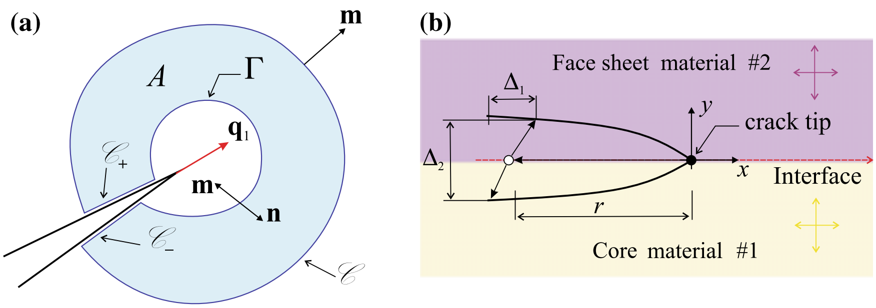

**Fig. 3** Sketches of: **a** a closed contour $\mathscr{C} + \mathscr{C}_+ + \Gamma + \mathscr{C}_-$ around the crack tip; **b** displacements of crack flanks at bi-material crack bounded by orthotropic materials

tip region, $\Delta l$. In the FEM model, $q_1$ is interpolated with the shape function of the element, $N_j(\boldsymbol{\xi})$, i.e. $q_1(\mathbf{x}) = \sum_j N_j(\boldsymbol{\xi})\bar{q}_1^j$, where $\bar{q}_1^j$ are nodal values.

If the crack faces are not traction free, for instance, due to forces arising in contact, an additional term $-\int_{\mathscr{C}_+ + \mathscr{C}_-} \mathbf{t}_c \cdot \frac{\partial \mathbf{u}}{\partial x_1} q_1 \, d\Gamma$ should be added to (23). Finally, the domain (2-D or 3-D) integral (23) is evaluated over a group of finite elements forming a ring around the crack tip, which are enclosed into the domain $A$, Fig. 3a. The numerical integration is achieved element by element with using the Gaussian quadrature. Then, the total result is a summation over all elements belonging $A$. A general form used for numerical computations of (23) can be presented by the expression:

$$\widetilde{\mathscr{G}}(t) = \sum_{n=1}^{El} \left( \sum_{p=1}^{G} [f]^{(p)} \, |\mathbf{j}|^{(p)} \, \widetilde{w}_p \right)_n /\Delta l, \tag{24}$$

where $n$ and $p$ indicate that all the entities are associated with the $n$-th finite element of the area $A$ and are determined at the $p$-th Gauss integration point; $[f]$ are the integrands in (23), $|\mathbf{j}|$ is the determinant of Jacobian matrix and $\widetilde{w}$ is the weight of the Gauss numerical quadrature. The domain integral is calculated by post-processing of results of the finite element analysis. The details of computational implementation of (24) in ABAQUS can be found in [49].

Although the $J$-integral approach allows calculating the dynamic ERR, the contribution of a separate fracture mode in its value remains unknown. Other methods are needed to evaluate the components of the mixed-mode ERR. Two of such methods suitable for bi-material interface cracks are described below. The methods are stated for a stationary crack, but they could be applied to a dynamically propagating crack by post-processing the displacement and stress fields in the vicinity of a moving crack tip at a certain instant of time.

### 2.6.1 Interaction Integral Method

The interaction integral method is based on the idea of superposition of actual and auxiliary fields ($aux$), where the latter are assumed to be known. An approximation is to take as the auxiliary fields the asymptotic Williams type solutions of corresponding material system regardless of the actual problem. Following Shih and Asaro [60] the interaction integral definition for a straight crack for any of fracture modes $M = I, II, III$ can be presented as

$$J_{int}^{M} = \lim_{\Gamma \to 0} \int_{\mathscr{C}+\mathscr{C}_{+}+\Gamma+\mathscr{C}_{-}} \mathbf{m} \cdot \mathbf{Q}^{M} \cdot \mathbf{q} d\Gamma, \tag{25}$$

with the integrand $\mathbf{Q}^M$ given as

$$\mathbf{Q}^{M} = \boldsymbol{\sigma} : (\boldsymbol{\varepsilon})_{aux}^{M} \mathbf{I} - \boldsymbol{\sigma} \cdot \left( \frac{\partial \mathbf{u}}{\partial x_1} \right)_{aux}^{M} - (\boldsymbol{\sigma})_{aux}^{M} \frac{\partial \mathbf{u}}{\partial x_1}, \tag{26}$$

On the other hand, the interaction integral can be expressed in terms of the stress intensity factors of both the actual and auxiliary fields in the form:

$$J_{int} = \tfrac{2}{H} \left( K_1 K_1^{aux} + K_2 K_2^{aux} \right), \text{ with } H = \tfrac{4 \cosh^2 \pi \varepsilon}{H_{11}} \tag{27}$$

Thereafter, making a judicious choice of the auxiliary stress intensity factors, which are assumed to be known, and taking the appropriate auxiliary displacement and stress fields from the known analytical solutions, e.g. [61], the separate stress intensity factors can be evaluated as follows:

$$K_M = \frac{H}{2 K_M^{aux}} J_{int}^{M} \tag{28}$$

In the FEM context, the interaction line integral (25) is computed similar to the domain formulation of the integral (23). The interaction integral method for the calculation of SIFs of a crack between two dissimilar isotropic materials is implemented into the ABAQUS code [49].

### 2.6.2 Crack Flank Displacements (CFD) Method

The CFD method is based on the approach proposed by Smelser [62], where SIFs have been determined from crack front displacements (Fig. 3b) by calculations of the absolute value of complex SIF and its phase angle. The method has an advantage of obtaining SIF components in terms FEM formulation since the displacement field is a direct outcome of the finite element analysis. In this respect, using (21) in conjunction with the expressions for the mode-mixity parameter (17) and the ERR (18) yields the following formulae:

$$\hat{\psi} = \tan^{-1}\left(\sqrt{\frac{H_{11}}{H_{22}}}\frac{\Delta_1}{\Delta_2}\right) - \varepsilon \ln\left(\frac{r}{\hat{l}}\right) + \tan^{-1} 2\varepsilon \tag{29}$$

and

$$\mathscr{G} = \frac{H_{11}\,|\mathbf{K}|^2}{4\cosh^2 \pi\varepsilon} = \frac{\pi(1+4\varepsilon^2)}{8H_{11}\left(r/\hat{l}\right)}\left(\frac{H_{11}}{H_{22}}\Delta_2^2 + \Delta_1^2\right), \tag{30}$$

where $\Delta_j = u_j\,(r, \pi) - u_j\,(r, -\pi)$ represents the relative crack flank displacements at distance $r$ behind the crack tip, $H_{11}$ and $H_{22}$ are components of the matrix $\mathbf{H}$ in (19). The nodal displacements are collected from opposing faces of the two crack flank elements that are approximately at a chosen specific distance $r = \frac{\hat{l}}{10}$ away from the crack tip [63].

## 3 Numerical Examples

In this section, the results of numerical simulations are presented. The simulations are carried out for both stationary interface crack problems and dynamic interface crack propagation tasks in sandwich panels idealized by beams and plates. The 2-D and 3-D models within the ABAQUS are developed for this purpose. Responses of static and dynamic fracture parameters are shown.

### *3.1 DCB UBM Specimen*

A sketch of the DCB UBM specimen of length $L = 270$ mm fixed at the ends of length $L_s = 27$ mm with a crack of length $a = 90$ mm, which consists of face sheets of thicknesses of $h_1 = h_2 = 2.4$ mm and a core of thickness of $h_c = 50$ mm is shown in Fig. 4a. The specimen is subjected to uneven bending moments, $M_1$ and $M_2$ (both being defined per unit specimen width, $B$) as illustrated in Fig. 4a. One of advantages of this test method is that the specimen allows loading the crack tip by a variety of

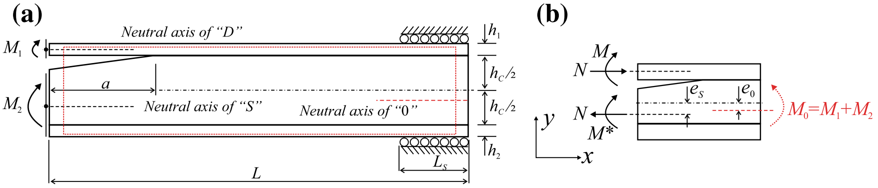

Fig. 4 DCB UBM specimen: **a** geometry and loading; **b** force and moment resultants

mode mixities by changing the moment ratio $M_R = M_1/M_2$ [64]. For this specimen, the steady state ERR can be determined analytically from the specimen geometry, elastic properties and applied external moments inducing a state of pure bending, then, the $J$-integral calculated along the outer boundaries of the specimen (Fig. 4b) leads to the expression [65]:

$$\mathscr{G}_s = \frac{1}{2B}\left\{\frac{N^2}{(EA)_D} + \frac{N^2}{(EA)_S} + \frac{M^2}{(EI)_D} + \frac{M^{*2}}{(EI)_S}\right\}, \tag{31}$$

where $N = \gamma_2 M_0$, $M = M_1 - \gamma_3 M_0$ and $M^* = N\left(e_s + \frac{h_c}{2} + \frac{h_1}{2}\right) - M$ are the equivalent axial load and bending moments, respectively, and $\gamma_2 = \frac{(EA)_D}{(EI)_0}\left(e_0 + \frac{h_c}{2} + \frac{h_1}{2}\right)$ and $\gamma_3 = \frac{(EI)_D}{(EI)_0}$; $e_0$ and $e_s$ are the locations of neutral axes of the whole specimen and the substrate, Fig. 4b; $(EA)_i$ and $(EI)_i$ are generalized axial and flexural rigidities of the debonded portion "$D$", substrate "$S$" and whole specimen "0", i.e. $i = D, S, 0$.

In the model, we assume that the principal axes of material orthotropy of both the debonded face sheet and the core are aligned with the co-ordinate axes of the specimen. The generalized Youngs moduli associated with the orthotropy directions of each the material along the $x$-axis of the beam define the generalized stiffness values mentioned in (31). The material properties of the sandwich specimen constituents related to the coordinated system in Fig. 4 are summarized in Table 1.

A 2-D finite element model of the DCB-UBM specimen is developed using eight-node reduced integration plane strain finite elements (`CPE8R`) available in ABAQUS,

**Table 1** Material properties of the DCB UBM sandwich specimen

| Constituents | Material constants |
|---|---|
| GFRP face sheet | $E_x = E_z = 16.5$ GPa; $E_y = 3.8$ GPa; $G_{xy} = G_{xz} = 1.3$ GPa;<br>$G_{yz} = 6.6$ GPa; $\nu_{xy} = 0.05$; $\nu_{xz} = \nu_{yz} = 0.25$; $\rho = 1650$ kgm$^{-3}$ |
| PVC H 100 foam core | $E_x = E_y = E_z = 105$ MPa; $G_{xy} = G_{xz} = G_{yz} = 78$ MPa;<br>$\nu_{xy} = \nu_{xz} = \nu_{yz} = 0.325$; $\rho = 100$ kgm$^{-3}$ |
| G-VE/H 100 interface | $k_I = k_{II} = k_{III} = 100$ GPa; $G_{Ic} = 400$ Jm$^{-2}$;<br>$G_{IIc} = G_{IIIc} = 500$ Jm$^{-2}$; $T_I = 10$ MPa; $T_{II} = T_{III} = 20$ MPa |

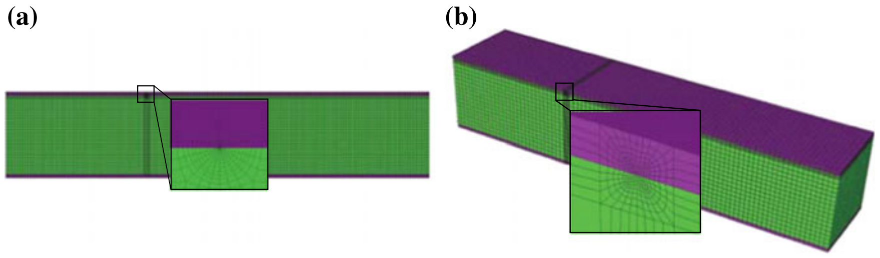

**Fig. 5** Finite element models of the DCB UBM specimen: **a** 2-D model; **b** 3-D model

Fig. 5a. The mesh contains a refinement near the crack-tip region as shown in Fig. 5a. A more complex 3-D finite element model of the specimen has also been elaborated. A layer-wise shell-solid approach for 3-D modelling of sandwich panels [14] is used. Eight-node reduced integration quadrilateral continuum shell elements (`CS8R`) obeying the assumptions of the FSDT theory and eight-node hexahedral (brick) elements (`C3D8R`) are utilized for the discretization of the face sheet and the core, respectively, as shown in Fig. 5b. In the calculations, bending moments are applied to the arms of DCB-UBM specimen at the points of the arms neutral axes, Fig. 5a. Coupling kinematic constraints between the nodes of the arm edge and the points of neutral axis are used to enforce equal rotation of the entire edge. The debonded region of the specimen is modelled by a real gap of $\frac{h_1}{100}$ along the damaged interface. The contact and friction conditions similar to (6) and (7) are introduced between the faces of finite elements along the pre-cracked interface. The contact behaviour under the assumptions of small displacement kinematics was assumed to be governed by the hard contact model with frictionless conditions [49]. In the case of the explicit dynamic analysis (10) the contact constraints were resolved using the kinematic predictor corrector method [49, 53], while the penalty contact algorithm was used for tracking contact in the case of the implicit dynamic analysis (11) as described in [49, 54].

### 3.1.1 A Stationary Crack Under Quasi-static Loading

To demonstrate the performance of the developed finite element models, steady state ERRs, $\mathscr{G}_s$ for a variety of moment ratios are computed by using both the $J$-integral option of ABAQUS [49] and the CFD method realized by post-processing the finite element results with an add-on subroutine in Matlab® environment. In the calculations, the bending moments were either rotated in opposite directions or co-rotated, but in all the cases they induced nearly the same ERRs. The results computed numerically were compared with those found using the analytical formula (31). A good agreement between the both solutions has been achieved as seen in Table 2, where, also, the phase angle $\hat{\psi}$ computed within the framework of the CFD method with the Matlab subroutine is presented.

**Table 2** Calculations of the ERR and the phase angle with respect to the moment ratio $M_R$

| | $M_1$ (Nmm) | 75.6 | 103.42 | 123.4 | 104.13 | 73.8 |
|---|---|---|---|---|---|---|
| | $M_2$ (Nmm) | −1512.2 | −1034.2 | −123.4 | 1041.3 | 1476 |
| | $M_R$ | −0.05 | −0.1 | −1.0 | 0.1 | 0.05 |
| ERR | $\mathscr{G}_s^{FEM}$ (N/mm) | 0.399 | 0.399 | 0.403 | 0.399 | 0.377 |
| | $\mathscr{G}_s^{Anl}$ (N/mm) | 0.351 | 0.363 | 0.376 | 0.365 | 0.332 |
| Phase angle | $\psi$ (°) | 30.26 | 11.31 | −17.16 | −51.87 | −70.71 |

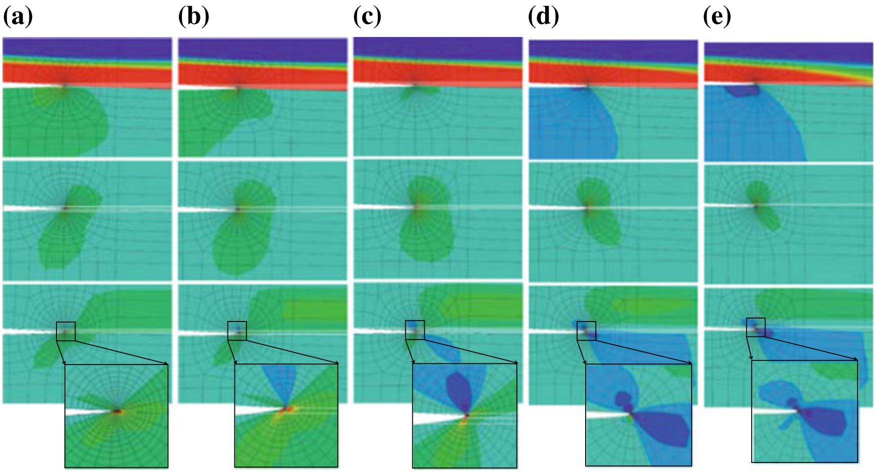

**Fig. 6** Contour plots of the stress components at the crack tip of the DCM-UBM specimen w.r.t. the moment ratio $M_R$ of: **a** −0.05; **b** −0.1; **c** −1; **d** 0.1; and **e** 0.05

The contour plots of the stress tensor components associated with the moment ratio $M_R$ listed in Table 2 are illustrated in Fig. 6, where the first row of the images corresponds to $\sigma_{11}$, the second and third ones show $\sigma_{22}$, and $\sigma_{12}$, respectively. A complicated nature of the near-tip stress field is clearly observed there. One can see that the shear stress exists in the vicinity of crack regardless of the loading case as seen in the third row of Fig. 6. This is an apparent evidence of the mode mixity condition being expected in sandwich type structures. The sign of the shear stress ahead crack may be used to define a favourable direction of interface crack propagation of the bi-material interface crack as mentioned in [27, 66]. The presence of the shear stress in the near tip region explains the differences in computations of the ERRs between the analytic formula and the FEM model. The former is not able to take into account the shear effect.

The 3-D model was adopted to study a distribution of the fracture parameters across the specimen width. For this purpose, a 3-D version of the $J$-integral available in ABAQUS and the CFD method have been used. Herewith, to apply the CFD method for the computations, the crack front of the specimen was cut in 12 sections through the width, and the Griffith energy and the mode mixity have been calculated in those locations using the formula (29) and (30). In Fig. 7 the width-wise variation of both the ERR and the phase angle and, also, the comparisons between the 2-D and 3-D models are illustrated. A large deviation between the 2-D and 3-D predictions is found for the phase angle values calculated in the middle part of the specimen width.

Also, the calculations showed that the displacement and stress fields computed using the 2-D and 3-D models are nearly identical as seen in Fig. 8, i.e. it has been proven that the 2-D model is valid for simulations of fracture. Thus, the 2-D

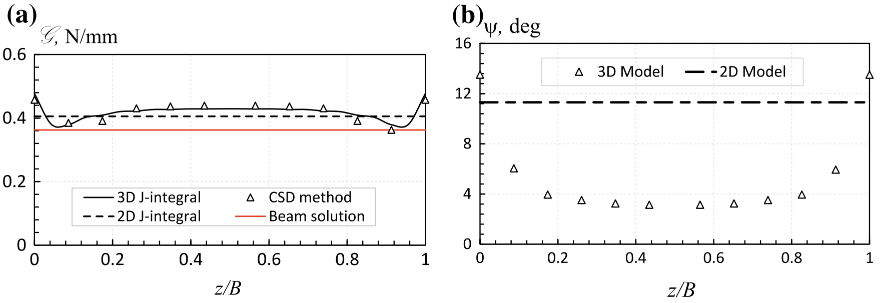

**Fig. 7** The width-wise variation of the fracture parameters: **a** the ERR; **b** the phase angle

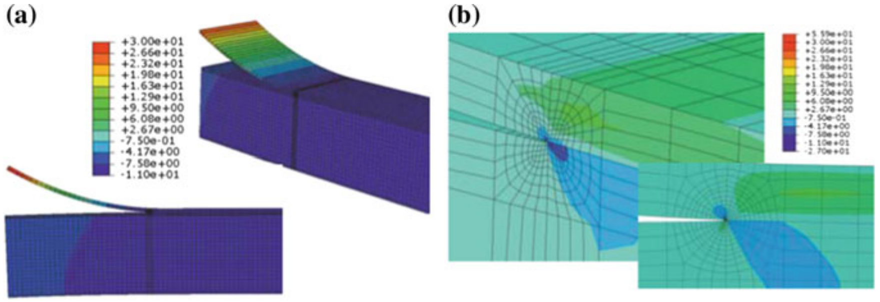

**Fig. 8** The comparison between 2-D and 3-D models: **a** transverse displacements; **b** $\sigma_{12}$ stresses

model is used in subsequent dynamic fracture analyses due to its substantially lower computational cost in comparison with the 3-D model.

### 3.1.2 A Stationary Crack Under Dynamic Loading

In the dynamic fracture analyses, the influence of inertia on the fracture parameters is considered as direct outcomes of the calculations. The dynamic ERR and dynamic SIFs are computed in the same way as for a static case, but dynamic mechanical fields calculated at each time increment are used instead. For the sake of simplicity, the materials of the sandwich specimen constitutive layers are reduced to linear isotropic, defined by elastic constants in the direction of $x$-axis, that is, $E_x$ and $\nu_{xz}$ characterize their mechanical properties. Then, the dynamic SIF components are computed using the interaction integral method implemented in ABAQUS.

First, the effects of impulse loading on the transient dynamic SIFs are examined. The bending moments are applied to the sandwich specimen arms as two impulses. Several types of the impulses of different forms such as a step function, a rectangular pulse and a triangular pulse and durations related to the values of $t_0$, which defines either a time of rising (a ramp time) of the step function or a time of the pulses duration, have been used in the calculations. The dynamic SIF components normalized by the corresponding static values of the SIFs versus time are presented in Fig. 9, where the

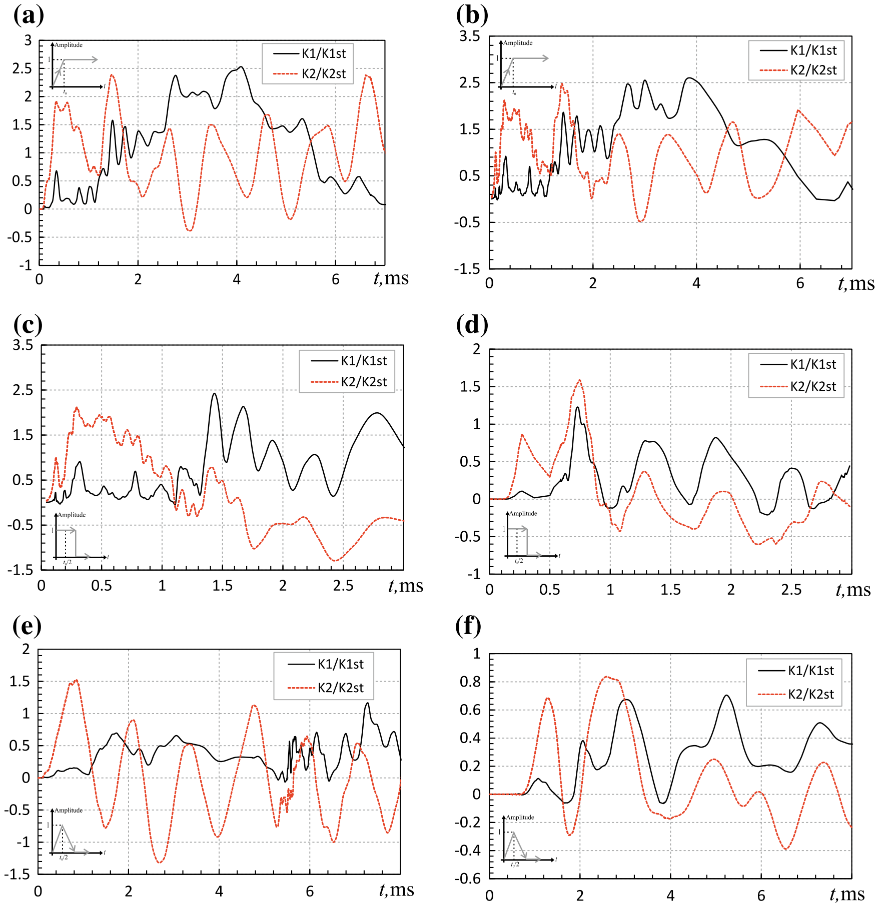

**Fig. 9** Transient dynamic SIFs: **a** step loading with $t_0 = 1$ ms; **b** step loading with $t_0 = 0.1$ ms; **c** rectangular pulse with $t_0 = 1$ ms; **d** rectangular pulse with $t_0 = 0.1$ ms; **e** triangular pulse with $t_0 = 1$ ms; **f** triangular pulse with $t_0 = 0.1$ ms

plots in the columns are related to different $t_0$ of 1 ms and 0.1 ms, respectively, and those in the rows correspond to the different forms of the pulses. One can see that the transient dynamic SIFs oscillate due to an evident effect of inertia. The latter is so remarkable that the dynamic SIFs exceed their static counterparts for all cases of impulse loading. Herewith, both the impulse duration and the impulse form strongly affect the dynamic SIFs. Moreover, it is obviously from the predictions that dynamic loading generates a significant mode II component, which is much larger than that in the static case.

Next, it is assumed that the specimen is subjected to the bending moments varying harmonically in time with driving frequencies, which could be either fraction or multiplier, $\xi = \Omega/\omega_1$ (1/2, 3/2, 3, 5) of the fundamental frequency of the same intact sandwich beam. The frequency $\omega_1$ was computed as 130.42 Hz. A long-term

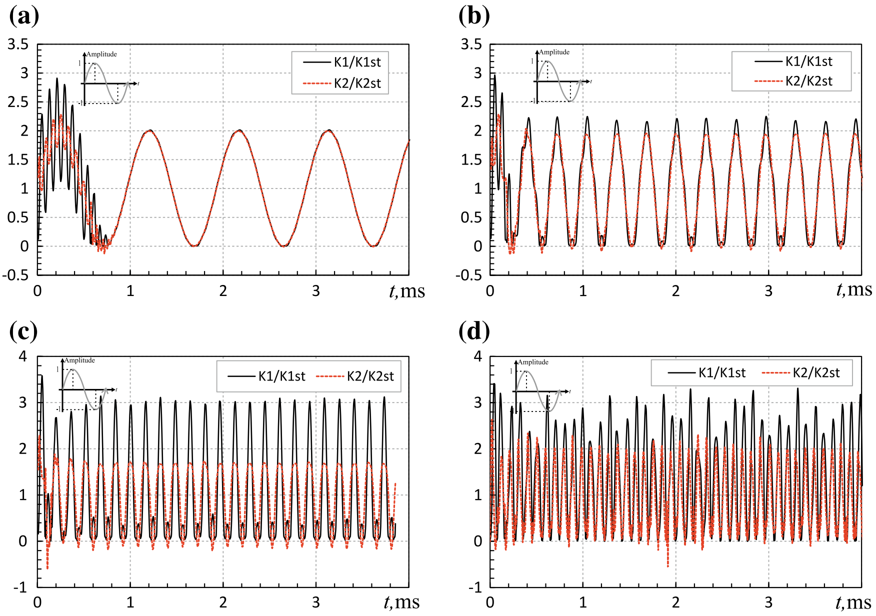

**Fig. 10** Long term dynamic SIFs: **a** $\xi = \frac{1}{2}$; **b** $\xi = \frac{3}{2}$; **c** $\xi = 3$; and **d** $\xi = 5$

behaviour of the dynamic complex SIF components is illustrated in Fig. 10, where the unsteady oscillations are included as well. The numerical results reveal that the long-term dynamic SIFs highly depends on the driving frequency value. The amplitude of the dynamic SIFs tends to increase with increasing the driving frequency. Also, the form of oscillations of the SIFs changes from a regular form at the low driving frequency in Fig. 10a to irregular ones at the higher driving frequencies as shown in Fig. 10b–d. Similar to the case of impulse loading, the intensity of shear stress is substantial in the harmonically loaded specimen as well, but it depends on the driving frequency.

### 3.1.3 Crack Propagation Analyses

In crack propagation analyses the cohesive elements, embodying the idea of the cohesive zone, in conjunction with appropriate contact algorithms are used to simulate the debonding behaviour in the sandwich DCB-UBM specimen. Four-node zero-thickness cohesive elements (`COH2D4`) available in ABAQUS for 2-D models were inserted into the finite element mesh between the `CPE8R` solid elements representing the face sheet and core of the specimen in Fig. 5a. The materials of the basic elements were assumed to be orthotropic linear elastic with parameters defined in Table 1. The CEs have been endowed with the properties of the face sheet/core interface listed in Table 1. The bi-linear TSL introduced in Sect. 2.2.2 was used for

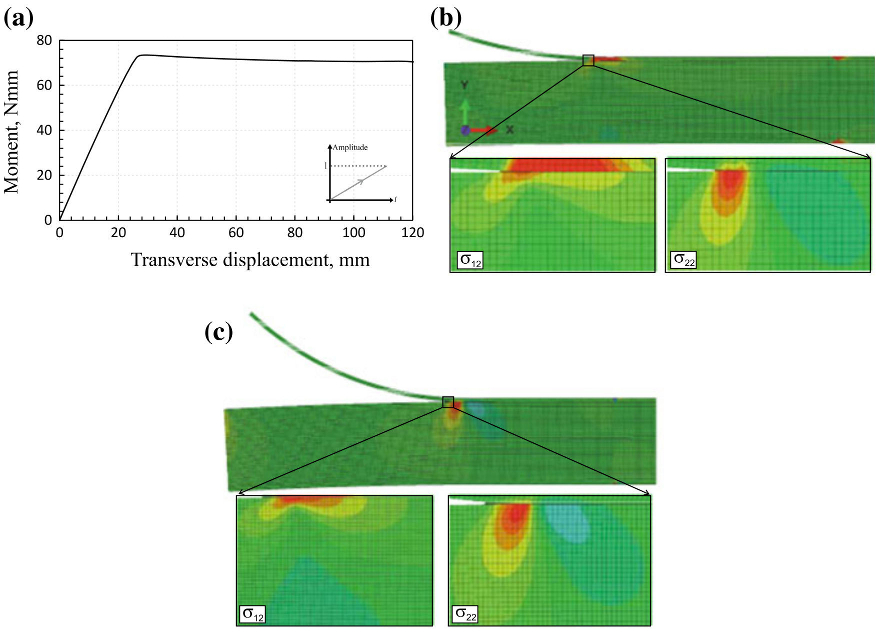

**Fig. 11** Quasi-static debonding propagation: **a** force-displacement curve; **b** deformation state and stress contour plots at the beginning of the debonding; and **c** deformation state and stress contour plots at the end of the debonding

modelling the debonding process. Tied constraints were applied to link the cohesive and solid elements together. In the case of contact, the hard contact model with no friction was exploited. This contact model defining the initial pre-cracked interface was then extended onto surfaces newly appeared along the interface due to cracking. It also was assumed that a presumed crack path is confined only the face sheet/core interface, i.e. no kinking is considered. The calculations have been performed under displacement-controlled loading, i.e. the specimen arms were subjected to prescribed rotations. Explicit time integration scheme with kinematic contact algorithm was used for the simulations of impact loading, while implicit time-stepping algorithm with penalty contact method was exploited for the simulations of quasi-static and long-term dynamic responses.

First, the case of quasi-static pure bending induced by prescribed rotations is simulated and force-displacement curve is extracted from the finite element solution as shown in Fig. 11. From this plot, one can see that the interface crack propagates between the face and the core in a stable manner as expected from this test method. Also, it is worth to note that the near crack tip stress field during the debonding growth involves both the normal and shear components as seen in Fig. 11c. This stress state is qualitatively similar to that in the linear phase of deformation of the specimen (Fig. 11b) except for a larger zone of negative shear stress beneath the crack tip which increases with increasing the crack length.

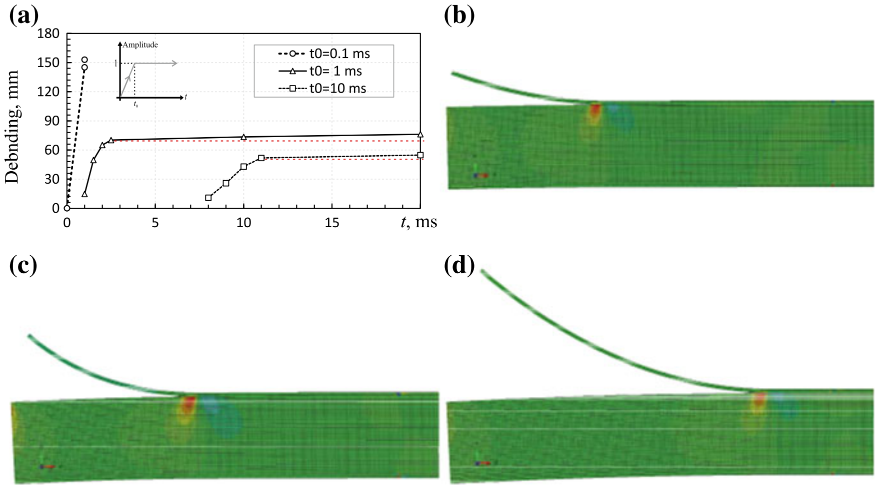

**Fig. 12** Debonding propagation under the impulse loads: **a** debonding extension vs. time curve; **b** deformation state for the case of $t_0 = 0.01$ s at an instant of $t = 3$ ms; **c** deformation state for the case of $t_0 = 0.01$ s at an instant of $t = 5$ ms; and **d** deformation state for the case of $t_0 = 0.01$ s at an instant of $t = 20$ ms

Next, the impulsive rotations of different durations, $t_0$, but the same step function like forms are applied to the DCB-UBM specimen. For all cases of loading, the same rotation magnitude is held. In Fig. 12a the simulations demonstrate that the total debonding extension increases with decreasing the impulse duration and for the shortest impulse load a complete disintegration of the specimen occurs. In the cases of loading without final failure, the debonding extends with a relatively constant speed after a short interval of fast growing. This time interval of fast crack speed becomes shorter with decreasing the pulse duration. The deformation and stress states of the specimen at different instants of time for the loading pulse with $t_0 = 1$ ms are presented in Fig. 12b–d.

Finally, the sandwich specimen is subjected to harmonic rotations with a given driving frequency accepted as high as 3/2 of $\omega_1$. The analysis was limited by 3000 increments and was lasting at least 100 increments after the steady state oscillation regime had been achieved. The results of simulation of the debonding behaviour under harmonic loading are shown in Fig. 13. It is seen that in this case the debonding propagates in a stick-slip manner, i.e. by jumping from one debonded state to another one. Moreover, the simulations revealed that the interface crack was intensively growing when the detached vibrating face sheet had the form of a concave downward curve, Fig. 13c. In doing so, the induced shear stress in the vicinity of the crack tip took values of different signs through the interface, Fig. 13c. This is associated with a mode II dominated regime. Unlike this situation, only small extensions of the debonding were observed in a mode I dominated state, shown in Fig. 13b.

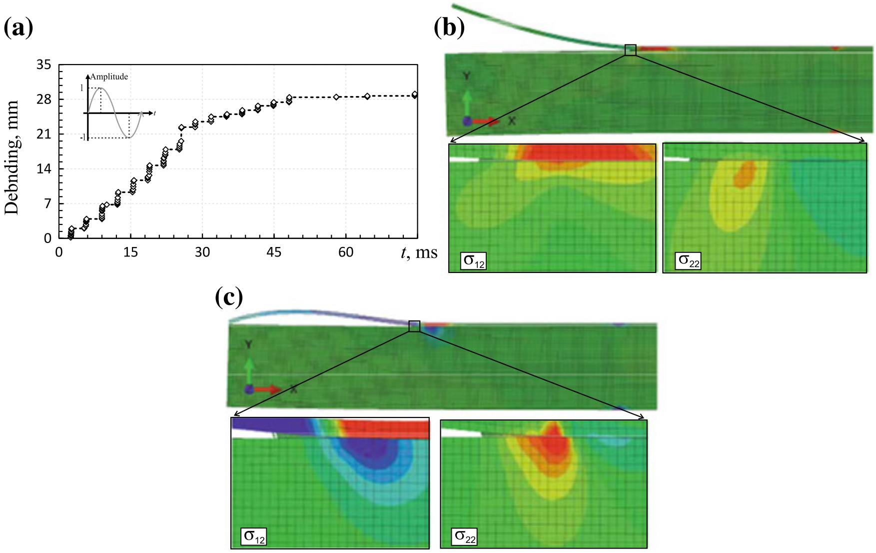

**Fig. 13** Debonding propagation under the harmonic load: **a** debonding extension versus time curve; **b** deformation state and stress contour plots at mode I dominated debonding; and **c** deformation state and stress contour plots at the mode II dominated debonding

## *3.2 Rectangular Panel with a Circular Debonded Zone*

To simulate debonding growth in a sandwich plate with a central penny-shaped debonded zone, the 2-D finite element model elaborated earlier was extended to a three-dimensional case. The finite element model of a tri-layer debonded plate was developed in ABAQUS using the layer-wise shell-solid approach [8] with an additional layer of eight-node 3-D cohesive elements (`COH3D8`) inserted into the interface between the shell continuum elements `SC8R` representing the face sheet and the solid continuum elements `C3D8R` discretizing the core. The TSL used in the previous 2-D cohesive zone model was generalized for the 3-D cohesive elements following the relations in Sect. 2.2.2. The surface-to-surface contact definition within the small-sliding displacement kinematics was used to model the hard pressure penetration law and the Coulomb friction law. The contact constraints were imposed on both the surfaces of the initially debonded region and the surfaces underlaying the cohesive elements along the face sheet/core interface.

One configuration of the sandwich plate is used throughout the current study. It is a simply supported rectangular sandwich plate of 180 by 270 mm × mm consisting of a 50 mm-thick WF51 foam core and of 2.4 mm-thick GFRP face sheets, which is weakened by a penny-shaped debonded zone of a radius of 39.3 mm at a plate centre. The constituent bulk materials of the plate are assumed to be orthotropic linear elastic with the material constants listed in Table 3. The cohesive layer obeying the 3-D bi-

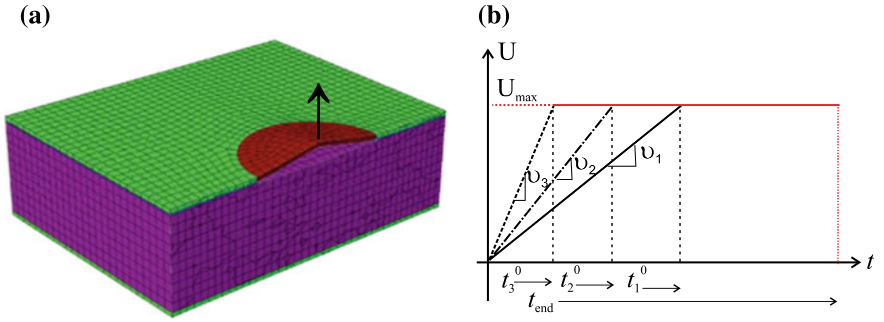

**Fig. 14** Sketches of: **a** a half of the finite element model of sandwich plate; and **b** graphs of prescribed displacements

linear constitutive law adopts the fracture parameters and the interfacial strength values associated with the resin-reach interface as defined in Table 3.

### 3.2.1 Impulse Loading

The debonded sandwich plate is assumed to be loaded by a prescribed impulsive displacement U at the centre of detached upper face sheet, Fig. 14a. The impulses had the form of a step function with various durations of the ramp time $t_0$ (a ramp time) defining the loading rate, $\upsilon_i$ ($i$ = 1, 2, 3) of the applied displacement (see Fig. 14b), i.e. the shorter is the ramp time, the larger is the loading rate. The total opening displacement is supposed to be the same for all cases of loading and when this displacement is achieved, it is held constant during the analysis. Also, the loading rates were estimated relatively to the Rayleigh wave speed of a more compliant foam material, which was found as $10^7$ mm/s. Although, the dynamic crack propagation is analysed, static critical ERRs have been used in the fracture criteria defined for the TSL of the cohesive elements due to deficiency of experimental data for this problem.

**Table 3** Material properties of the sandwich plate

| Constituents | Material constants |
|---|---|
| GFRP face sheet | $E_x = E_z = 19.3$ GPa; $E_y = 3.48$ GPa; $G_{xy} = G_{xz} = 1.65$ GPa;<br>$G_{yz} = 7.7$ GPa; $\nu_{xy} = 0.05$; $\nu_{xz} = \nu_{yz} = 0.25$; $\rho = 1468$ kgm$^{-3}$ |
| WF51 foam core | $E_x = E_y = E_z = 85$ MPa; $G_{xy} = G_{xz} = G_{yz} = 78$ MPa;<br>$\nu_{xy} = \nu_{xz} = \nu_{yz} = 0.325$; $\rho = 52$ kgm$^{-3}$ |
| Resin interface | $k_I = k_{II} = k_{III} = 100$ GPa; $G_{Ic} = 375$ Jm$^{-2}$;<br>$G_{IIc} = G_{IIIc} = 2125$ Jm$^{-2}$; $T_I = 3$ MPa; $T_{II} = T_{III} = 17.2$ MPa |

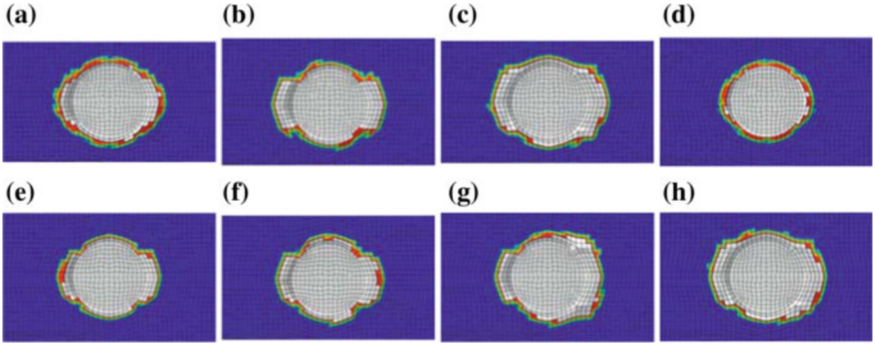

**Fig. 15** Debonding propagation under impulse loading: **a** static case $\upsilon = 0$; **b** $\upsilon_1 = 10^3$ mm/s; **c** $\upsilon_2 = 10^4$ mm/s; **d** $\upsilon_3 = 10^5$ mm/s at $t = 0.001$ ms; **f** $\upsilon_3 = 10^5$ mm/s at $t = 0.01$ ms; **g** $\upsilon_3 = 10^5$ mm/s at $t = 0.1$ ms; and **h** $\upsilon_3 = 10^5$ mm/s at $t = 1$ ms

Figure 15 shows the debonding area being grown under the impulsive displacements of the different rates. One can see that the debonded area increases with increasing the loading rate. Moreover, it was found that the inertia effect is minor for the first two rates of the loading, i.e. the quasi-static approach still remains valid for them. However, when the rate of the applied impulsive displacement increases to a value $U_3$ comparable with the Rayleigh wave speed, oscillations produced by incident and reflected stress waves become very strong inside the sandwich plate, i.e. inertia contributes much into its dynamic behaviour. As a result of the inertia effect, at the beginning of loading the debonding was postponed growing in comparison with the two previous cases, but after few a while the induced dynamic stresses promoted the debonding to advance up to the end of the analysis as shown in Fig. 15d–h.

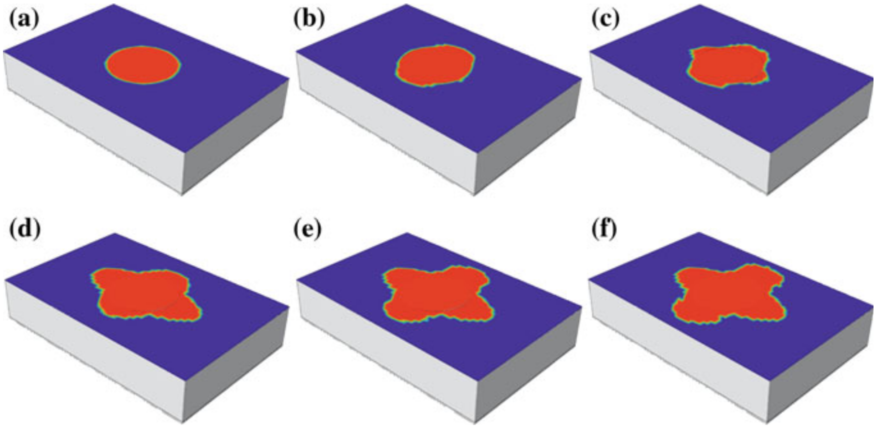

**Fig. 16** Debonding propagation under harmonic loading: **a** $t = 0$ ms; **b** $t = 1$ ms; **c** $t = 3$ ms; **d** $t = 5$ ms; **e** $t = 7$ ms; and **f** $t = 10$ ms

### 3.2.2 Harmonic Loading

Because a long-term cracking resistance is of concern rather than particular transient events, the debonded sandwich plate is considered to be subjected to harmonic loading. A concentrated force of the amplitude of 10 N oscillating with the frequency of 1000 Hz, which is less than the fundamental frequency of the same intact sandwich plate (about 1300 Hz), was applied to the centre of the bottom face sheet perfectly glued to the core. The results of the simulation of debonding growth are illustrated in Fig. 16, where the form and size of the debonded area are shown at different instants of time. As seen in the plots, the debonding grows with time. However, unlike the impulse loading, where the debonded area was increasing continuously with time and was spreading relatively uniformly in all directions, in this case the debonding advances in a stick-slip manner. The debonding becomes spontaneously growing and spreading in certain directions depending on the dynamic stress state at a current instant of time. In turn, the stress field in the debonded sandwich plate is very complicated because it combines incident and reflected stress waves which are generated by both the external harmonic load and due to intermittent contact between the detached face sheet and the core.

## 4 Conclusions

A finite element methodology to simulate the debonding of the face sheet from the core in sandwich panels under dynamic loading is presented. The main features of the problem are highlighted. A finite element implementation of the cohesive zone model accounting for contact and friction is used to model the dynamic fracture of sandwich panels. The interaction integral and crack flank displacement methods exploited for computing the fracture parameters of the face sheet/core interface crack such as complex SIFs, energy release rate and phase angle are reported. The applicability of the numerical schemes described in the present work is assessed by performing 2-D and 3-D finite element fracture analyses with ABAQUS for both the fracture specimen DCB-UBM and the sandwich plate with a central penny-shaped debonded zone.

A stationary debonding of a sandwich material consisting of orthotropic linear elastic constitutive layers within the DCB-UBM test is firstly considered. A two-dimensional finite element model has been used for predictions. The character of the stress field in the vicinity of the interface crack tip and the value of extracted fracture parameters have been examined over a wide range of bending moment ratios applied to the specimen. As revealed the stress profile shows a strong coupling between normal and shear stresses regardless the loading type, i.e. material-induced mode mixity of a bi-material interface crack has clearly been demonstrated. The dependence of ERR and phase angle on the mixed mode conditions has been shown as well. Moreover, the simulations with the 3-D model illustrated a width-wise variation of the mentioned fracture parameters. Secondly, the DCB-UBM sandwich specimen with stationary debonding has been studied under dynamic impulsive and harmonic loads. The 2-D dynamic virtual tests showed that significant mode II component is generated during dynamic loading. In addition, it was found that the dynamic SIFs are strongly dependent on both the form and duration of the impulses and the driving frequency.

The predictions of debonding propagation in the DCB-UBM specimen proved a stable character of the interface crack growth under quasi-static loading as expected from the analytic considerations. In contrast to this, the simulations of the specimen under dynamic loading have demonstrated an unstable debonding propagation, especially in the cases of the high rate impulse or harmonic loading at the high driving frequency. In all those cases, it was clearly observed that the debonding growth is associated with mode II dominated fracture.

The influence of dynamic loading on the debonding behaviour in sandwich plates has been examined using 3-D finite element models. The essential role of the loading rate on the debonding behaviour in the sandwich plate has been established by comparing the responses of the plates subjected to step function-like impulses of different intensities. The initial delay in the debonding growth and then its extensive advance due to inertia effects have been found in the cases of high rate impulse and harmonic load acting at high driving frequency. Also, a spontaneous debonding growth (a stick-slip behaviour) in the sandwich plate under harmonic loading has been observed. As found, this behaviour is governed by a complicated dynamic stress field at a current time instant, where the stresses evolve with time as a combination of incident and reflected stress waves generated by both the external harmonic load and intermittent contact between the detached face sheet and the core.

**Acknowledgements** The authors would like to mention that this research has been done within the POLONEZ 2 Project, Grant Agreement No. UMO-2016/21/P/ST8/00790, supported by the National Science Centre of Poland at the Lublin University of Technology within the European Unions Horizon 2020 research and innovation programme under the Marie Skodowska-Curie Grant Agreement No. 665778. The second author (H. Altenbach) also would like to acknowledge the financial support of the Foundation for Polish Science for his stay at the Lublin University of Technology.

## References

1. Altenbach, H., Altenbach, J., Kissing, W.: Mechanics of Composite Structural Elements, 2nd edn. Springer Nature, Singapore Pte Ltd. (2018)
2. Karlsson, K.F., Åström, B.T.: Manufacturing and applications of structural sandwich components. Compos. Part A **28A**, 97–111 (1997)
3. Shen, C., Xin, F.X., Lu, T.J.: Theoretical model for sound transmission through finite sandwich structures with corrugated core. Int. J. Non-Linear Mech. **47**(10), 1066–1072 (2012)
4. Amraei, M., Shahravi, M., Noori, Z., Lenjani, A.: Application of aluminium honeycomb sandwich panel as an energy absorber of high-speed train nose. J. Compos. Mater. **48**(9), 1027–1037 (2014)

5. Xie, S., Liang, X., Zhou, H.: Design and analysis of a composite energy-absorbing structure for use on railway vehicles. Proc. Inst. Mech. Eng. Part F: J. Rail Rapid Transit **230**(3), 825–839 (2016)
6. Funari, M.F., Greco, F., Lonetti, P.: Sandwich panels under interfacial debonding mechanisms. Compos. Struct. **203**, 310–320 (2018)
7. Vitale, J.P., Francucci, G., Xiong, J., Stocchi, A.: Failure mode maps of natural and synthetic fiber reinforced composite sandwich panels. Compos. Part A **94**, 217–225 (2017)
8. Burlayenko, V.N., Sadowski, T.: Dynamic analysis of debonded sandwich plates with flexible core—numerical aspects and simulation. In: Altenbach, H., Eremeyev, V.A. (eds.) Shell-like Structures, Advanced Structured Materials, vol. 15, pp. 415–440. Springer, Berlin, Heidelberg (2011)
9. Idriss, M., El Mahi, A.: Effects of debonding length on the fatigue and vibration behaviour of sandwich composite. J. Compos. Mater. **51**(13), 1839–1847 (2017)
10. Juhász, Z., Turcsán, T., Tóth, T.B., Szekrényes, A.: Sensitivity analysis for frequency based prediction of crack size in composite plates with through-the-width delamination. Int. J. Damage Mech. **27**(6), 859–876 (2018)
11. Elmalich, D., Rabinovitch, O.: On the effect of inter-laminar contact on the dynamics of locally delaminated FRP strengthened walls. Int. J. Non-Linear Mech. **77**, 141–157 (2015)
12. Pölöskei, T., Szekrényes, A.: Quasi-periodic excitation in a delaminated composite beam. Compos. Struct. **159**, 677–688 (2017)
13. Qu, Y., Meng, G.: Nonlinear vibro-acoustic analysis of composite sandwich plates with skin-core debondings. AIAA J. **55**(5), 1723–1733 (2017)
14. Burlayenko, V.N., Sadowski, T.: Linear and nonlinear dynamic analyses of sandwich panels with face sheet-to-core debonding. Shock Vib. **2018**(Article ID 5715863) (2018)
15. Saito, A.: Nonlinear resonances of chains of thin elastic beams with intermittent contact. ASME J. Comput. Nonlinear Dyn. **13**(8) (2018) (in press)
16. Burlayenko, V.N., Sadowski, T.: Numerical modeling of sandwich plates with partially dedonded skin-to-core interface for damage detection. In: De Roeck, G., Degrande, G., Lombaert, G., Muller, G. (eds.) Proceedings of the 8th International Conference on Structural Dynamics (EURODYN), pp. 2242–2249, Leuven, Belgium (2011)
17. Farhana, N.I.E., Abdul Majid, M.S., Paulraj, M.P., Fakhzan, M.N., Ahmadhilmi, E., Gibson, A.G.: A novel vibration based non-destructive testing for predicting glass fibre/matrix volume fraction in composites using a neural network model. Compos. Struct. **144**, 96–107 (2016)
18. Lu, L., Song, H., Yuan, W., Huang, C.: Baseline-free damage identification of metallic sandwich panels with truss core based on vibration characteristics. Struct. Health Monit. Int. J. **16**(1), 24–38 (2017)
19. Meruane, V., Lasen, M., Droguett, E.L., Ortiz-Bernardin, A.: Modal strain energy-based debonding assessment of sandwich panels using a linear approximation with maximum entropy. Entropy **19**(11), 22 (2017)
20. Seguel, F., Meruane, V.: Damage assessment in a sandwich panel based on full-field vibration measurements. J. Sound Vib. **417**(17), 1–18 (2018)
21. Rinker, M., Ratcliffe, J.G., Adams, D.O., Kruger, R.: Characterizing facesheet/core disbonding in honeycomb core sandwich structure. NASA/CR-2013-217959, Langley Research Center, Hampton, Virginia (2013)
22. Suo, Z., Hutchinson, J.W.: Sandwich test specimens for measuring interface crack toughness. Mater. Sci. Eng. A **107**, 135–143 (1989)
23. Krueger, R., Minguet, P.J., O'Brien, T.K.: Implementation of interlaminar fracture mechanics in design: an overview. In: Proceedings of ICCM14, San Diego (2003)
24. Szekrényes, A.: Crack stability of fracture specimens used to test unidirectional fiber reinforced material. Exp. Mech. **50**, 473–482 (2010)
25. Samborski, S.: Analysis of the end-notched flexure test configuration applicability for mechanically coupled fiber reinforced composite laminates. Compos. Struct. **163**, 342–349 (2017)
26. Valvo, P.S.: The effects of shear on Mode II delamination: a critical review. Frattura ed Integrita Strutturale **12**(44), 123–139 (2018)

27. Adams, D.O., Kessler, J.A., Kuramoto, B., Bluth, J., Weaver, C., Gill, A.: Development and evaluation of fracture mechanics test methods for sandwich composites. In: Proceedings of FAA JAMS Technical Review Meeting, Wichita, KS (2010)
28. Krueger, R., Shivakumar, K.N., Raju, I.S.: Fracture mechanics analyses for interface crack problems—a Review. In: 54th AIAA/ASME/ASCE/AHS/ASC Structures, Structural Dynamics and Materials Conference (2013)
29. Freund, L.B.: Dynamic Fracture Mechanics. Cambridge University Press, Cambridge, Massachusetts (1990)
30. Lambros, J., Rosakis, A.J.: Development of a dynamic decohesion criterion for subsonic fracture of the interface between two dissimilar materials. Proc. R. Soc. Lond. A **451**, 711–736 (1995)
31. Lambros, J., Rosakis, A.J.: Shear dominated transonic interface crack growth in a bimaterial I. Experimental observations. J. Mech. Phys. Solids **43**(2), 169–188 (1995)
32. Cocker, D., Rosakis, A.J.: Experimental observations of intersonic crack growth in asymmetrically loaded unidirectional composite plates. Philos. Mag. A **81**(3), 571–595 (2001)
33. Ravi-Chandar, K.: Experimental challenges in the investigation of dynamic fracture of brittle materials. In: Bouchaund, E. (ed.) Physical Aspects of Fracture, pp. 323–342. Springer, Netherlands (2001)
34. Willis, J.R.: Fracture mechanics of interfacial cracks. J. Mech. Phys. Solids **19**, 353–368 (1971)
35. Wu, K.-C.: Explicit crack tip fields of an extending interface crack in an anisotropic bimaterial. Int. J. Solid Struct. **27**(4), 455–466 (1991)
36. Yang, W., Suo, Z., Shih, C.F.: Mechanics of dynamic debonding. Proc. R. Soc. Lond. A **433**, 679–697 (1991)
37. Petrova, V., Schmauder, S.: Mathematical modelling and thermal stress intensity factors evaluation for an interface crack in the presence of a system of cracks in functionally graded/homogeneous bimaterials. Comput. Mater. Sci. **52**(1), 171–177 (2012)
38. Massabò, R., Cavicchi, A.: Interaction effects of multiple damage mechanisms in composite sandwich beams subject to time dependent loading. Int. J. Solids Struct. **49**, 720–738 (2012)
39. Szekrényes, A.: Analytical solution of some delamination scenarios in thick structural sandwich plates. J. Sandw. Struct. Mater. (2017) (In press)
40. Xu, X.P., Needlwman, A.: Numerical simulations of dynamic crack growth along an interface. Int. J. Fract. **74**, 289–324 (1996)
41. Dwivedi, S.K., Espinosa, H.D.: Modeling dynamic crack propagation in fiber reinforced composites including frictional effects. Mech. Mater. **35**, 481–509 (2003)
42. Caliskan, U., Apalak, M.K.: Bending impact behaviour of sandwich beams with expanded polystyrene foam core: analysis. J. Sandw. Struct. Mater. (2017) (in press)
43. Mariggiò, G., Reinoso, J., Paggi, M., Corrado, M.: Peeling of thick adhesive interfaces: the role of dynamics and geometrical nonlinearity. Mech. Res. Commun. **94**, 21–24 (2018)
44. Yan, Q., Xu, Y., Zhang, W., Geng, P., Yang, W.: Numerical analysis of the cracking and failure behaviors of segmental lining structure of an underwater shield tunnel subjected to a derailed high-speed train impact. Tunn. Undergr. Space Technol. **72**, 41–54 (2018)
45. Reinoso, J., Catalanotti, G., Blázquez, A., Areias, P., Camanhod, P.P., París, F.: A consistent anisotropic damage model for laminated fiber-reinforced composites using the 3D-version of the Puck failure criterion. Int. J. Solids Struct. **126–127**, 37–53 (2017)
46. Burlayenko, V.N., Sadowski, T.: Modeling of the dynamic debonding growth of sandwich plates. In: Mikhlin, Y.V., Perepelkin, N.V. (eds.) Proceedings of the 4th International Conference on Nonlinear Dynamics ND-KhPI2013, pp. 225–230. Tochka Publishing, Sevastopol, Ukraine (2013)
47. Burlayenko, V.N., Sadowski, T.: Simulations of post-impact skin/core debond growth in sandwich plates under impulsive loading. J. Appl. Nonlinear Dyn. **3**(4), 369–379 (2014)
48. Ji, W., Waas, A.M.: Dynamic failure of a sandwich structure subjected to an in-plane axial impact. Compos. Struct. **180**, 751–759 (2017)
49. ABAQUS Users manual, version 2016 (2016) Dassault Systémes Simulia Corporation, Providence, RI, USA

50. Lekhnitskii, S.: Theory of an Anisotropic Elastic Body. San Francisco, Holden-Day (1963)
51. Park, K.S., Paulino, G.H.: Cohesive zone models: a critical review of traction-separation relationships across fracture surfaces. Appl. Mech. Rev. **64** (2013)
52. Camanho, P.P., Dávila, C.G., de Moura, M.F.: Numerical simulation of mixed-mode progressive delamination in composite materials. J. Compos. Mater. **37**(16), 1415–1438 (2003)
53. Burlayenko, V.N., Sadowski, T.: Transient dynamic response of debonded sandwich plates predicted with finite element analysis. Meccanica **49**, 2617–2633 (2014)
54. Burlayenko, V.N., Sadowski, T.: Nonlinear dynamic analysis of harmonically excited debonded sandwich plates using finite element modelling. Compos. Struct. **108**, 354–366 (2014)
55. Aragón, A.M., Molinari, J.-F.: A hierarchical detection framework for computational contact mechanics. Comput. Methods Appl. Mech. Eng. **268**, 574588 (2014)
56. Bathe, K.J., Wilson, E.L.: Numerical Methods in Finite Element Analysis. Prentice-Hall, Englewood Cliffs, NJ, USA (1977)
57. Hutchinson, J.W., Suo, Z.: Mixed mode cracking in layered materials. In: Advances in Applied Mechanics, vol. 29, pp. 63–191. Academic Press Inc. (1992)
58. Wang, T.C., Shih, C.F., Suo, Z.: Crack extension and kinking in laminates and bicrystals. Int. J. Solids Struct. **29**, 327344 (1992)
59. Nakamura, T., Shih, C.F., Freund, L.B.: Computational methods based on an energy integral in dynamic fracture. Int. J. Fract. **27**, 229–243 (1985)
60. Shih, C.F., Asaro, R.J.: Elastic-plastic analysis of cracks on bimaterial interfaces: part I small scale yielding. J. Appl. Mech. **55**(2), 299316 (1988)
61. Deng, X.: Mechanics of debonding and delamination in composites: asymptotic studies. Compos. Eng. **5**(10–11), 1299–1315 (1995)
62. Smelser, R.E.: Evaluation of stress intensity factors for bi-materials bodies using numerical crack flank displacement data. Int. J. Fract. **15**, 135–315 (1979)
63. Marsavina, L., Sadowski, T.: Kinked crack at a bi-material ceramic interface—numerical determination of fracture parameters. Comput. Mater. Sci. **44**, 941–950 (2009)
64. Sørensen, B.F., Jørgensen, K., Jacobsen, T.K., Østregaard, R.C.: DCB-specimen loaded with uneven bending moments. Int. J. Fract. **141**, 163–176 (2006)
65. Burlayenko, V.N., Sadowski, T., Pietras, D.: Influence of dynamic loading on fracture behaviour of DCB sandwich specimen. In: Proceedings of the 1st International Conference on Computational Methods and Applications in Engineering (ICCMAE), 23–26 May 2018, UPT, Timisoara, Romania. ITM Web of Conferences (2018) (Submitted)
66. Burlayenko, V.N., Sadowski, T., Pietras, D.: A numerical analysis of near tip fields in a bending moment-loaded double cantilever sandwich beam fracture specimen. Bull. NTU “KhPI”. Ser. Math. Model. Eng. Technol. **3**(1279), 9–14 (2018)

# On Dynamic Boundary Conditions Within the Linear Steigmann-Ogden Model of Surface Elasticity and Strain Gradient Elasticity

**Victor A. Eremeyev**

**Abstract** Within the strain gradient elasticity we discuss the dynamic boundary conditions taking into account surface stresses described by the Steigmann–Ogden model. The variational approach is applied with the use of the least action functional. The functional is represented as a sum of surface and volume integrals. The surface strain and kinetic energy densities are introduced. The Toupin–Mindlin formulation of the strain gradient elasticity is considered. As a result, we derived the motion equations and the natural boundary conditions which include inertia terms.

## 1 Introduction

Nowadays the interest to modelling of surface phenomena is growing with respect to developments in manufacturing of micro- and nanostructured materials. Among the surface-related phenomena approaches the models of surface elasticity by Gurtin and Murdoch [18, 19] and by Steigmann and Ogden [34, 35] are often used for modelling of micro- and nanostructured materials, see, e.g., [9, 13, 20–22, 37, 38] and the reference therein. The presence of surface stresses changes essentially the natural boundary conditions and the properties of solutions of the corresponding boundary-value problems, see [3, 12, 24, 32].

Here we consider the dynamic boundary conditions which follow from the least action principle as natural ones. We use here the linear Steigmann–Ogden model of surface elasticity. The peculiarity of the model is the dependence of the surface strain energy on second derivatives of displacements. So for consistency with the material behaviour in the bulk we use the strain gradient elasticity introduced by Toupin [36]

---

V. A. Eremeyev (✉)
Faculty of Civil and Environmental Engineering, Gdańsk University of Technology,
ul. Gabriela Narutowicza 11/12, 80-233 Gdańsk, Poland
e-mail: eremeyev.victor@gmail.com; victor.eremeev@pg.edu.pl

V. A. Eremeyev
Institute of Mathematics, Mechanics and Computer Science, Southern Federal University,
Milchakova Street 8a, Rostov-on-Don 344090, Russia

H. Altenbach et al. (eds.), *Dynamical Processes in Generalized Continua and Structures*, Advanced Structured Materials 103,
https://doi.org/10.1007/978-3-030-11665-1_10

and Mindlin [28, 29], see also [30, 31] and more recent works by Eringen [16]; Aifantis [2]; Maugin [27]; Bertram [5]; Eremeyev et al. [14]. Let us also note that the strain gradient elasticity is also used for modelling of the material behavior at the nanoscale, see, e.g., [6, 23]. Unlike the classic linear elasticity the dynamic boundary conditions here include not only spatial derivatives of displacements but also their time derivatives. So inertia terms play a role also in boundary conditions.

## 2 Constitutive Relations

In what follows we consider the case of small deformations. As a result, the kinematics is described through the displacement vector

$$\mathbf{u} = \mathbf{u}(\mathbf{x}, t),$$

which is a differentiable vector-function of the position vector $\mathbf{x}$ and time $t$.

For a hyperelastic solid we introduce the surface and bulk strain energies as follows

$$\mathscr{U} = \mathscr{U}(\boldsymbol{\varepsilon}, \boldsymbol{\varkappa}), \quad \mathscr{W} = \mathscr{W}(\mathbf{e}, \mathbf{k}), \tag{1}$$

where the strain measures are given by

$$\begin{aligned}
\mathbf{e} = \mathbf{e}(\mathbf{u}) &= \tfrac{1}{2}(\nabla\mathbf{u} + \nabla\mathbf{u}^T), \quad \mathbf{k} = \nabla\nabla\mathbf{u},\\
\boldsymbol{\varepsilon} = \boldsymbol{\varepsilon}(\mathbf{u}) &= \tfrac{1}{2}(\nabla_s\mathbf{u}\cdot\mathbf{A} + \mathbf{A}\cdot\nabla_s\mathbf{u}^T),\\
\boldsymbol{\varkappa} = \boldsymbol{\varkappa}(\mathbf{u}) &= \tfrac{1}{2}(\nabla_s\boldsymbol{\vartheta}\cdot\mathbf{A} + \mathbf{A}\cdot\nabla_s\boldsymbol{\vartheta}^T), \quad \boldsymbol{\vartheta} = \nabla_s w + \mathbf{B}\cdot\mathbf{u}.
\end{aligned}$$

Here $w = \mathbf{u}\cdot\mathbf{n}$, "$\cdot$" denotes the scalar product, $\mathbf{B} = -\nabla_s\mathbf{n}$ is the tensor of curvature, $\mathbf{n}$ is the unit outward normal to the body boundary $\partial V$, and we introduce the spatial $\nabla$ and surface $\nabla_s$ nabla-operators, $\nabla_s = \mathbf{A}\cdot\nabla$, $\mathbf{A} = \mathbf{I} - \mathbf{n}\otimes\mathbf{n}$, $\mathbf{I}$ is the 3D unit tensor. Hereinafter we use the direct (coordinate-free) tensor calculus as in [14, 25, 26, 33]. Examples of $\mathscr{U}$ and $\mathscr{W}$ can be found in [5, 8, 12, 38]. A particular class of strain gradient media are Korteweg fluids, see [4, 11]. Here we will not specify the form of these functions.

We introduce the following stress measures

$$\boldsymbol{\sigma} = \frac{\partial\mathscr{W}}{\partial\mathbf{e}}, \quad \boldsymbol{\tau} = \frac{\partial\mathscr{W}}{\partial\mathbf{k}}, \quad \mathbf{T} = \frac{\partial\mathscr{U}}{\partial\boldsymbol{\varepsilon}}, \quad \mathbf{M} = \frac{\partial\mathscr{U}}{\partial\boldsymbol{\varkappa}}.$$

Here $\boldsymbol{\sigma}$, $\boldsymbol{\tau}$, $\mathbf{T}$ and $\mathbf{M}$ are the stress, hyper-stress, surface stress and surface couple stress tensors, respectively. Note that tensors $\boldsymbol{\sigma}$, $\mathbf{T}$ and $\mathbf{M}$ are symmetric second-order tensors, and $\mathbf{T}$ and $\mathbf{M}$ satisfy to relations

$$\mathbf{n}\cdot\mathbf{T} = \mathbf{0}, \quad \mathbf{n}\cdot\mathbf{M} = \mathbf{0}.$$

For dynamics we define the surface kinetic energy as a quadratic function of the velocity $\mathbf{v} = \dot{\mathbf{u}}$ and its surface gradient

$$\mathscr{K}_s = \tfrac{1}{2} m \mathbf{v} \cdot \mathbf{v} + \tfrac{1}{2} \nabla_s \mathbf{v} : \mathbf{J}_0 : \nabla_s \mathbf{v} + \nabla_s \mathbf{v} : \mathbf{J}_1 \cdot \mathbf{v},$$

where $m$ is the surface mass density, the overdot stands for the derivative with respect to $t$, $\mathbf{J}_0$ and $\mathbf{J}_1$ are forth- and third-order tensors of surface microinertia, respectively. Here for arbitrary second-order tensors $\mathbf{X}$ and $\mathbf{Y}$ we introduce the scalar product operation as follows

$$\mathbf{X} : \mathbf{Y} = \operatorname{tr}(\mathbf{X} \cdot \mathbf{Y}^T).$$

Note that $\mathbf{J}_0$ and $\mathbf{J}_0$ have the following properties

$$\mathbf{n} \cdot \mathbf{J}_0 = \mathbf{0}, \quad \mathbf{J}_0 : (\mathbf{n} \otimes \mathbf{a}) = \mathbf{0} \quad \forall \mathbf{a}, \quad \mathbf{n} \cdot \mathbf{J}_1 = \mathbf{0}. \tag{2}$$

The kinetic energy in the bulk takes the following form

$$\mathscr{K} = \tfrac{1}{2} \rho \mathbf{v} \cdot \mathbf{v} + \tfrac{1}{2} \nabla \mathbf{v} : \mathbf{K}_0 : \nabla \mathbf{v} + \nabla \mathbf{v} : \mathbf{K}_1 \cdot \mathbf{v},$$

where $\rho$ is the mass density, $\mathbf{K}_0$ and $\mathbf{K}_1$ are forth- and third-order tensors of microinertia, respectively.

## 3 Hamilton's Variational Principle

In order to obtain the natural boundary conditions we use the Hamilton variational principle (the least action principle). For the least action principle in strain gradient media we refer to [1, 4] and the reference therein. Here the functional is given by

$$\mathbb{H}[\mathbf{u}] = \int_{t_1}^{t_2} (\mathbb{K} - \mathbb{E})\, \mathrm{d}t, \tag{3}$$

where

$$\mathbb{K} = \mathbb{K}_S + \mathbb{K}_B, \quad \mathbb{E} = \mathbb{B} + \mathbb{S},$$

and

$$\mathbb{K}_S = \int_A \mathscr{K}_s \, \mathrm{d}S, \quad \mathbb{K}_B = \int_V \mathscr{K} \, \mathrm{d}V$$

$$\mathbb{B} = \int_V \mathscr{W}(\mathbf{e}(\mathbf{u}), \mathbf{k}(\mathbf{u}))\, \mathrm{d}V, \quad \mathbb{S} = \int_A \mathscr{U}(\boldsymbol{\varepsilon}(\mathbf{u}), \boldsymbol{\varkappa}(\mathbf{u}))\, \mathrm{d}S.$$

Here $A \subset \partial V$ is the part of the body surface where the surface stresses are defined, $t_1$ and $t_2$ are two time instants. Functionals $\mathbb{B}$ and $\mathbb{S}$ are the energy and surface energy functionals, respectively. For simplicity we omit here external loading. In other words, we consider a free surface with surface stresses.

Using standard calculus of variations from

$$\delta\mathbb{H} = 0$$

with constraints

$$\delta\mathbf{u}\big|_{t=t_1} = \mathbf{0}, \quad \delta\mathbf{u}\big|_{t=t_2} = \mathbf{0},$$

we intend to derive the natural boundary conditions at $A$ and its contour $\partial A$. Here $\delta\mathbf{u}$ is a vector of admissible virtual displacements.

In what follows we are restricted ourselves by smooth enough surface and contour, that is without edges and corner and end points.

### 3.1 First Variation of the Kinetic Energy Functional

Let us consider the calculations of the first variation of the kinetic energy. In order to find

$$\delta \int_{t_1}^{t_2} \mathbb{K}_B \,\mathrm{d}t$$

we successively consider all terms in $\mathscr{K}$. First, we get

$$\begin{aligned} \delta \int_{t_1}^{t_2} \int_V \tfrac{1}{2}\rho\mathbf{v}\cdot\mathbf{v}\,\mathrm{d}V\mathrm{d}t &= \int_{t_1}^{t_2} \int_V \rho\mathbf{v}\cdot\delta\dot{\mathbf{u}}\,\mathrm{d}V\mathrm{d}t \\ &= -\int_{t_1}^{t_2} \int_V (\rho\mathbf{v})^{\cdot}\cdot\delta\mathbf{u}\,\mathrm{d}V\mathrm{d}t. \end{aligned} \tag{4}$$

For the second term in $\mathscr{K}$ we have

$$\begin{aligned} \delta \int_{t_1}^{t_2} \int_V \tfrac{1}{2}\nabla\mathbf{v} : \mathbf{K}_0 : \nabla\mathbf{v}\,\mathrm{d}V\mathrm{d}t &= \int_{t_1}^{t_2} \int_V \nabla\mathbf{v} : \mathbf{K}_0 : \nabla\delta\dot{\mathbf{u}}\,\mathrm{d}V\mathrm{d}t \\ = -\int_{t_1}^{t_2} \int_V (\nabla\mathbf{v} : \mathbf{K}_0)^{\cdot} : \nabla\delta\mathbf{u}\,\mathrm{d}V\mathrm{d}t \end{aligned}$$

$$= \int\limits_{t_1}^{t_2} \int_V \nabla \cdot (\nabla \mathbf{v} : \mathbf{K}_0)^{\cdot} \cdot \delta \mathbf{u} \, \mathrm{d}V \mathrm{d}t - \int\limits_{t_1}^{t_2} \int_{\partial V} \mathbf{n} \cdot (\nabla \mathbf{v} : \mathbf{K}_0)^{\cdot} \cdot \delta \mathbf{u} \, \mathrm{d}S \mathrm{d}t. \tag{5}$$

Note that in (5) we used twice the integration by parts. Finally, we get the first variation of the third term

$$\begin{aligned} \delta \int\limits_{t_1}^{t_2} \int_V \nabla \mathbf{v} : \mathbf{K}_1 \cdot \mathbf{v} \, \mathrm{d}V \mathrm{d}t &= \int\limits_{t_1}^{t_2} \int_V [\nabla \mathbf{v} : \mathbf{K}_1 \cdot \delta \dot{\mathbf{u}} + \nabla \delta \dot{\mathbf{u}} : \mathbf{K}_1 \cdot \mathbf{v}] \, \mathrm{d}V \mathrm{d}t \\ &= - \int\limits_{t_1}^{t_2} \int_V \left[ (\nabla \mathbf{v} : \mathbf{K}_1)^{\cdot} \cdot \delta \mathbf{u} + \nabla \delta \mathbf{u} : (\mathbf{K}_1 \cdot \mathbf{v})^{\cdot} \right] \mathrm{d}V \mathrm{d}t \\ &= \int\limits_{t_1}^{t_2} \int_V \left[ \nabla \cdot (\mathbf{K}_1 \cdot \mathbf{v})^{\cdot} - (\nabla \mathbf{v} : \mathbf{K}_1)^{\cdot} \right] \cdot \delta \mathbf{u} \, \mathrm{d}V \mathrm{d}t - \int\limits_{t_1}^{t_2} \int_{\partial V} \mathbf{n} \cdot (\mathbf{K}_1 \cdot \mathbf{v})^{\cdot} \cdot \delta \mathbf{u} \, \mathrm{d}S \mathrm{d}t. \end{aligned} \tag{6}$$

As a result, we obtain

$$\begin{aligned} \delta \int\limits_{t_1}^{t_2} \mathbb{K}_B \, \mathrm{d}t = & \int\limits_{t_1}^{t_2} \int_V \left[ -(\rho \mathbf{v})^{\cdot} + \nabla \cdot (\nabla \mathbf{v} : \mathbf{K}_0)^{\cdot} + \nabla \cdot (\mathbf{K}_1 \cdot \mathbf{v})^{\cdot} - (\nabla \mathbf{v} : \mathbf{K}_1)^{\cdot} \right] \cdot \delta \mathbf{u} \, \mathrm{d}V \mathrm{d}t \\ & - \int\limits_{t_1}^{t_2} \int_{\partial V} \mathbf{n} \cdot \left[ (\nabla \mathbf{v} : \mathbf{K}_0)^{\cdot} + (\mathbf{K}_1 \cdot \mathbf{v})^{\cdot} \right] \cdot \delta \mathbf{u} \, \mathrm{d}S \mathrm{d}t. \end{aligned} \tag{7}$$

In a similar way we find the first variation of the surface kinetic energy

$$\begin{aligned} \delta \int\limits_{t_1}^{t_2} \mathbb{K}_S \, \mathrm{d}t = & \int\limits_{t_1}^{t_2} \int_A \left[ -(m \mathbf{v})^{\cdot} + \nabla_s \cdot (\nabla_s \mathbf{v} : \mathbf{J}_0)^{\cdot} + \nabla_s \cdot (\mathbf{J}_1 \cdot \mathbf{v})^{\cdot} - (\nabla_s \mathbf{v} : \mathbf{J}_1)^{\cdot} \right] \cdot \delta \mathbf{u} \, \mathrm{d}S \mathrm{d}t \\ & - \int\limits_{t_1}^{t_2} \int_{\partial A} \boldsymbol{\nu} \cdot \left[ (\nabla_s \mathbf{v} : \mathbf{J}_0)^{\cdot} + (\mathbf{J}_1 \cdot \mathbf{v})^{\cdot} \right] \cdot \delta \mathbf{u} \, \mathrm{d}s \mathrm{d}t. \end{aligned} \tag{8}$$

Here $\boldsymbol{\nu}$ is the unit normal to $\partial A$ such that $\boldsymbol{\nu} \cdot \mathbf{n} = 0$. Note that here we used (2) and formula (31) of the integration by parts.

### 3.2 First Variation of the Surface Energy Functional

We have

$$\begin{aligned}\delta\mathbb{S}[\mathbf{u}] = \int_A \delta\mathscr{U}(\boldsymbol{\varepsilon}(\mathbf{u}), \boldsymbol{\varkappa}(\mathbf{u}))\mathrm{d}S = \int_A \left(\frac{\partial\mathscr{U}}{\partial\boldsymbol{\varepsilon}} : \delta\boldsymbol{\varepsilon} + \frac{\partial\mathscr{U}}{\partial\boldsymbol{\varkappa}} : \delta\boldsymbol{\varkappa}\right)\mathrm{d}S \\ = \int_A (\mathbf{T} : \delta\boldsymbol{\varepsilon} + \mathbf{M} : \delta\boldsymbol{\varkappa})\,\mathrm{d}S. \end{aligned} \tag{9}$$

Here $\delta\boldsymbol{\varepsilon} = \boldsymbol{\varepsilon}(\delta\mathbf{u})$ and $\delta\boldsymbol{\varkappa} = \boldsymbol{\varkappa}(\delta\mathbf{u})$.

With identities

$$\begin{aligned}\mathbf{T} : \delta\boldsymbol{\varepsilon} =& \mathbf{T} : (\nabla_s\delta\mathbf{u}\cdot\mathbf{A}) = \mathrm{tr}\,[\mathbf{T}\cdot\mathbf{A}^T\cdot(\nabla_s\delta\mathbf{u})^T] = \mathrm{tr}\,[\mathbf{T}\cdot(\nabla_s\delta\mathbf{u})^T] \\ =& \mathbf{T} : (\nabla_s\delta\mathbf{u})\end{aligned}$$

and applying the surface divergence theorem (31) we integrate by part the first term in the line integral in (9) as follows

$$\int_A \mathbf{T} : \delta\boldsymbol{\varepsilon}\,\mathrm{d}S = -\int_A (\nabla_s\cdot\mathbf{T})\cdot\delta\mathbf{u}\,\mathrm{d}S + \int_{\partial A} \boldsymbol{\nu}\cdot\mathbf{T}\cdot\delta\mathbf{u}\,\mathrm{d}s. \tag{10}$$

In a similar way we get

$$\begin{aligned}\int_A \mathbf{M} : \delta\boldsymbol{\varepsilon}\,\mathrm{d}S =& \int_A \mathbf{M} : (\nabla_s\delta\boldsymbol{\vartheta})\,\mathrm{d}S \\ =& -\int_A (\nabla_s\cdot\mathbf{M})\cdot\delta\boldsymbol{\vartheta}\,\mathrm{d}S + \int_{\partial A} \boldsymbol{\nu}\cdot\mathbf{M}\cdot\delta\boldsymbol{\vartheta}\,\mathrm{d}s.\end{aligned} \tag{11}$$

Substituting into (11)

$$\delta\boldsymbol{\vartheta} = \nabla_s\delta w + \mathbf{B}\cdot\delta\mathbf{u} \tag{12}$$

we have

$$\begin{aligned}\int_A \mathbf{M} : \delta\boldsymbol{\varepsilon}\,\mathrm{d}S =& -\int_A (\nabla_s\cdot\mathbf{M})\cdot\mathbf{B}\cdot\delta\mathbf{u}\,\mathrm{d}S - \int_A (\nabla_s\cdot\mathbf{M})\cdot\nabla_s\delta w\,\mathrm{d}S \\ &+ \int_{\partial A} \boldsymbol{\nu}\cdot\mathbf{M}\cdot\delta\boldsymbol{\vartheta}\,\mathrm{d}s \\ =& -\int_A (\nabla_s\cdot\mathbf{M})\cdot\mathbf{B}\cdot\delta\mathbf{u}\,\mathrm{d}S \\ &+ \int_A [\nabla_s\cdot(\nabla_s\cdot\mathbf{M}) + 2H\mathbf{n}\cdot(\nabla_s\cdot\mathbf{M})]\,\delta w\,\mathrm{d}S \\ &- \int_{\partial A} \boldsymbol{\nu}\cdot(\nabla_s\cdot\mathbf{M})\delta w\,\mathrm{d}s\end{aligned}$$

$$+\int_{\partial A}\left[\boldsymbol{\nu}\cdot\mathbf{M}\cdot\mathbf{B}\cdot\delta\mathbf{u}+\boldsymbol{\nu}\cdot\mathbf{M}\cdot\boldsymbol{\nu}\frac{\partial\delta w}{\partial\nu}-\frac{\partial}{\partial s}\left(\boldsymbol{\nu}\cdot\mathbf{M}\cdot\boldsymbol{\tau}\right)\delta w\right]\mathrm{d}s. \tag{13}$$

As $\mathbf{n}\cdot(\nabla_s\cdot\mathbf{M})\neq 0$, for integration by parts we applied here Eq. (30). Here we also use the representation of $\nabla_s$

$$\nabla_s=\boldsymbol{\nu}\frac{\partial}{\partial\nu}+\boldsymbol{\tau}\frac{\partial}{\partial s},$$

where $\boldsymbol{\tau}$ is the unit vector tangent to $\partial A$, and $\frac{\partial}{\partial\nu}$ and $\frac{\partial}{\partial s}$ denotes the normal and tangent derivatives, respectively. Additionally, in (13) we performed the integration by parts along $\partial A$ to exclude $\frac{\partial}{\partial s}\delta w$.

Finally, the first variation of $\mathbb{S}$ takes the form

$$\begin{aligned}\delta\mathbb{S}=&\int_A\left[-\nabla_s\cdot\mathbf{T}-(\nabla_s\cdot\mathbf{M})\cdot\mathbf{B}+\nabla_s\cdot(\nabla_s\cdot\mathbf{M})\mathbf{n}+2H\mathbf{n}\cdot(\nabla_s\cdot\mathbf{M})\mathbf{n}\right]\cdot\delta\mathbf{u}\,\mathrm{d}S\\&+\int_{\partial A}\left[\boldsymbol{\nu}\cdot\mathbf{T}+\boldsymbol{\nu}\cdot\mathbf{M}\cdot\mathbf{B}-\boldsymbol{\nu}\cdot(\nabla_s\cdot\mathbf{M})\mathbf{n}-\frac{\partial}{\partial s}\left(\boldsymbol{\nu}\cdot\mathbf{M}\cdot\boldsymbol{\tau}\right)\mathbf{n}\right]\cdot\delta\mathbf{u}\,\mathrm{d}s\\&+\int_{\partial A}\boldsymbol{\nu}\cdot\mathbf{M}\cdot\boldsymbol{\nu}\frac{\partial\delta w}{\partial\nu}\,\mathrm{d}s.\end{aligned} \tag{14}$$

Using the identity

$$\nabla\cdot(\mathbf{a}\otimes\mathbf{b})=(\nabla\cdot\mathbf{a})\mathbf{b}+\mathbf{a}\cdot\nabla\mathbf{b}$$

we prove that

$$\begin{aligned}\nabla_s\cdot(\nabla_s\cdot\mathbf{M})\mathbf{n}=&\nabla_s\cdot[(\nabla_s\cdot\mathbf{M})\mathbf{n}]-(\nabla_s\cdot\mathbf{M})\cdot\nabla_s\mathbf{n}\\=&\nabla_s\cdot[(\nabla_s\cdot\mathbf{M})\mathbf{n}]+(\nabla_s\cdot\mathbf{M})\cdot\mathbf{B}.\end{aligned}$$

As a result, Eq. (14) transforms into a more compact form

$$\begin{aligned}\delta\mathbb{S}=&\int_A\left[-\nabla_s\cdot[\mathbf{T}-\ (\nabla_s\cdot\mathbf{M})\mathbf{n}]+2H\mathbf{n}\cdot(\nabla_s\cdot\mathbf{M})\mathbf{n}\right]\cdot\delta\mathbf{u}\,\mathrm{d}S\\&+\int_{\partial A}\left[\boldsymbol{\nu}\cdot\mathbf{T}+\boldsymbol{\nu}\cdot\mathbf{M}\cdot\mathbf{B}-\boldsymbol{\nu}\cdot(\nabla_s\cdot\mathbf{M})\mathbf{n}-\frac{\partial}{\partial s}\left(\boldsymbol{\nu}\cdot\mathbf{M}\cdot\boldsymbol{\tau}\right)\mathbf{n}\right]\cdot\delta\mathbf{u}\,\mathrm{d}s\\&+\int_{\partial A}\boldsymbol{\nu}\cdot\mathbf{M}\cdot\boldsymbol{\nu}\frac{\partial\delta w}{\partial\nu}\,\mathrm{d}s.\end{aligned} \tag{15}$$

Similar variational technique was used in the case of statics of simple elastic solids within the Steigmann–Ogden model in [38]. The static boundary conditions for strain gradient fluids with surface stresses as in Gurtin–Murdoch approach were derived by Eremeyev and Altenbach [11]; Eremeyev [10]. Let us also note that $\delta\mathbb{S}=0$ results in static equations which are similar to ones used in the Kirchhoff–Love shell theory, see Lebedev et al. [25].

### 3.3 First Variation of the Strain Energy in the Bulk

In the bulk we have

$$\delta\mathbb{B}[\mathbf{u}] = \int_V \delta\mathscr{W}(\mathbf{e}(\mathbf{u}), \mathbf{k}(\mathbf{u}))\,\mathrm{d}V = \int_V \left(\frac{\partial\mathscr{W}}{\partial\mathbf{e}} : \delta\mathbf{e} + \frac{\partial\mathscr{W}}{\partial\mathbf{k}} \mathbin{\therefore} \delta\mathbf{k}\right)\mathrm{d}V$$
$$= \int_V (\boldsymbol{\sigma} : \delta\mathbf{e} + \boldsymbol{\tau} \mathbin{\therefore} \delta\mathbf{k})\;\mathrm{d}V. \tag{16}$$

Here $\delta\mathbf{e} = \mathbf{e}(\delta\mathbf{u})$, $\delta\mathbf{k} = \nabla\nabla(\delta\mathbf{u})$, and "$\therefore$" stands for the inner product in the space of third-order tensors.

Using the identity $\boldsymbol{\sigma} : \delta\mathbf{e} = \boldsymbol{\sigma} : \nabla\delta\mathbf{u}$ and applying the divergence theorem we get

$$\int_V \boldsymbol{\sigma} : \delta\mathbf{e}\,\mathrm{d}V = \int_{\partial V} \mathbf{n}\cdot\boldsymbol{\sigma}\cdot\delta\mathbf{u}\,\mathrm{d}S - \int_V (\nabla\cdot\boldsymbol{\sigma})\cdot\delta\mathbf{u}\,\mathrm{d}V. \tag{17}$$

In a similar way we have

$$\int_V \boldsymbol{\tau} \mathbin{\therefore} \delta\mathbf{k}\,\mathrm{d}V = \int_{\partial V} \mathbf{n}\cdot\boldsymbol{\tau} : \nabla\delta\mathbf{u}\,\mathrm{d}S - \int_V (\nabla\cdot\boldsymbol{\tau}) : \nabla\delta\mathbf{u}\,\mathrm{d}V$$
$$= \int_V \nabla\cdot(\nabla\cdot\boldsymbol{\tau})\cdot\delta\mathbf{u}\,\mathrm{d}V - \int_{\partial V} \mathbf{n}\cdot(\nabla\cdot\boldsymbol{\tau})\cdot\delta\mathbf{u}\,\mathrm{d}S$$
$$+ \int_{\partial V} \mathbf{n}\cdot\boldsymbol{\tau} : \nabla\delta\mathbf{u}\,\mathrm{d}S. \tag{18}$$

With the surface divergence theorem the last integral can be transformed as follows:

$$\int_{\partial V} \mathbf{n}\cdot\boldsymbol{\tau} : \nabla\delta\mathbf{u}\,\mathrm{d}S = \int_{\partial V} \left[\mathbf{n}\cdot\boldsymbol{\tau} : \nabla_s\delta\mathbf{u} + \mathbf{n}\cdot\boldsymbol{\tau} : \left(\mathbf{n}\otimes\frac{\partial\delta\mathbf{u}}{\partial n}\right)\right]\mathrm{d}S$$
$$= \int_{\partial\partial V} \boldsymbol{\nu}\cdot(\mathbf{n}\cdot\boldsymbol{\tau})\cdot\delta\mathbf{u}\,\mathrm{d}s$$
$$- \int_{\partial V} \left[\nabla_s\cdot(\mathbf{n}\cdot\boldsymbol{\tau})\cdot\delta\mathbf{u} + 2H(\mathbf{n}\otimes\mathbf{n}) : \boldsymbol{\tau}\cdot\delta\mathbf{u}\right]\,\mathrm{d}S$$
$$+ \int_{\partial V} (\mathbf{n}\otimes\mathbf{n}) : \boldsymbol{\tau}\cdot\frac{\partial\delta\mathbf{u}}{\partial n}\,\mathrm{d}S.$$

Here $\frac{\partial}{\partial n}$ denotes the normal derivative whereas $\partial\partial V$ means a contour which bounds $\partial V$ if it exists or edges in the case of non-smooth surface. In what follows we assume that $\partial V = A$ and, therefore, $\partial\partial V = \partial A$.

As a result, Eq. (18) takes the following form

$$\begin{aligned}\int_V \boldsymbol{\tau} \therefore \delta\mathbf{k}\,\mathrm{d}V = \int_V &\nabla\cdot(\nabla\cdot\boldsymbol{\tau})\cdot\delta\mathbf{u}\,\mathrm{d}V\\ &+\int_{\partial\partial V}\boldsymbol{\nu}\cdot(\mathbf{n}\cdot\boldsymbol{\tau})\cdot\delta\mathbf{u}\,\mathrm{d}s\\ &+\int_{\partial V}(\mathbf{n}\otimes\mathbf{n}):\boldsymbol{\tau}\cdot\frac{\partial\delta\mathbf{u}}{\partial n}\,\mathrm{d}S\\ &-\int_{\partial V}\mathbf{n}\cdot(\nabla\cdot\boldsymbol{\tau})\cdot\delta\mathbf{u}\,\mathrm{d}S\\ &-\int_{\partial V}\left[\nabla_s\cdot(\mathbf{n}\cdot\boldsymbol{\tau})\cdot\delta\mathbf{u}+2H(\mathbf{n}\otimes\mathbf{n}):\boldsymbol{\tau}\cdot\delta\mathbf{u}\right]\mathrm{d}S.\end{aligned}$$

Thus, summarizing we have

$$\begin{aligned}\delta\mathbb{B}[\mathbf{u}] = &-\int_V[\nabla\cdot\boldsymbol{\sigma}-\nabla\cdot(\nabla\cdot\boldsymbol{\tau})]\cdot\delta\mathbf{u}\,\mathrm{d}V\\ &+\int_{\partial\partial V}\boldsymbol{\nu}\cdot(\mathbf{n}\cdot\boldsymbol{\tau})\cdot\delta\mathbf{u}\,\mathrm{d}s\\ &+\int_{\partial V}(\mathbf{n}\otimes\mathbf{n}):\boldsymbol{\tau}\cdot\frac{\partial\delta\mathbf{u}}{\partial n}\,\mathrm{d}S\\ &+\int_{\partial V}\{\mathbf{n}\cdot[\boldsymbol{\sigma}-\nabla\cdot\boldsymbol{\tau}]-\nabla_s\cdot(\mathbf{n}\cdot\boldsymbol{\tau})-2H(\mathbf{n}\otimes\mathbf{n}):\boldsymbol{\tau}\}\cdot\delta\mathbf{u}\,\mathrm{d}S\end{aligned}\qquad(19)$$

Let us note that the variational equation $\delta\mathbb{B}[\mathbf{u}]=0$ results in the homogeneous equilibrium equations and natural boundary conditions for linear strain gradient media, see, e.g., [5, 14] for more details.

## 3.4 Motion Equations and Natural Boundary Conditions

Summarizing (7), (8), (15) and (19) we obtain the following rather awkward expression of the first variation $\delta\mathbb{H}$:

$$\begin{aligned}\delta\mathbb{H} = &\int_{t_1}^{t_2}\int_V\Big[-(\rho\mathbf{v})^{\cdot}+\nabla\cdot(\nabla\mathbf{v}:\mathbf{K}_0)^{\cdot}+\nabla\cdot(\mathbf{K}_1\cdot\mathbf{v})^{\cdot}-(\nabla\mathbf{v}:\mathbf{K}_1)^{\cdot}\\ &\qquad+\nabla\cdot\boldsymbol{\sigma}-\nabla\cdot(\nabla\cdot\boldsymbol{\tau})\big]\cdot\delta\mathbf{u}\,\mathrm{d}V\mathrm{d}t\\ &+\int_{t_1}^{t_2}\int_A\Big[-(m\mathbf{v})^{\cdot}+\nabla_s\cdot(\nabla_s\mathbf{v}:\mathbf{J}_0)^{\cdot}+\nabla_s\cdot(\mathbf{J}_1\cdot\mathbf{v})^{\cdot}-(\nabla_s\mathbf{v}:\mathbf{J}_1)^{\cdot}\\ &\qquad-\mathbf{n}\cdot\Big[(\nabla\mathbf{v}:\mathbf{K}_0)^{\cdot}+(\mathbf{K}_1\cdot\mathbf{v})^{\cdot}\Big]\end{aligned}$$

$$
\begin{aligned}
&+ \nabla_s \cdot [\mathbf{T} - (\nabla_s \cdot \mathbf{M})\mathbf{n}] - 2H\mathbf{n} \cdot (\nabla_s \cdot \mathbf{M})\mathbf{n} \\
&-\mathbf{n} \cdot [\boldsymbol{\sigma} - \nabla \cdot \boldsymbol{\tau}] + \nabla_s \cdot (\mathbf{n} \cdot \boldsymbol{\tau}) + 2H(\mathbf{n} \otimes \mathbf{n}) : \boldsymbol{\tau}] \cdot \delta\mathbf{u}\,\mathrm{d}S\mathrm{d}t \\
-& \int\limits_{t_1}^{t_2} \int_A (\mathbf{n} \otimes \mathbf{n}) : \boldsymbol{\tau} \cdot \frac{\partial \delta\mathbf{u}}{\partial n}\,\mathrm{d}S\mathrm{d}t \\
+& \int\limits_{t_1}^{t_2} \int_{\partial A} \Big\{ -\boldsymbol{\nu} \cdot \left[ (\nabla_s \mathbf{v} : \mathbf{J}_0)^{\cdot} + (\mathbf{J}_1 \cdot \mathbf{v})^{\cdot} \right] - \boldsymbol{\nu} \cdot (\mathbf{n} \cdot \boldsymbol{\tau}) \\
-& \left[ \boldsymbol{\nu} \cdot \mathbf{T} + \boldsymbol{\nu} \cdot \mathbf{M} \cdot \mathbf{B} - \boldsymbol{\nu} \cdot (\nabla_s \cdot \mathbf{M})\mathbf{n} - \frac{\partial}{\partial s} (\boldsymbol{\nu} \cdot \mathbf{M} \cdot \boldsymbol{\tau})\,\mathbf{n} \right] \Big\} \cdot \delta\mathbf{u}\,\mathrm{d}s\mathrm{d}t \\
-& \int\limits_{t_1}^{t_2} \int_{\partial A} \boldsymbol{\nu} \cdot \mathbf{M} \cdot \boldsymbol{\nu} \frac{\partial \delta w}{\partial \nu}\,\mathrm{d}s\mathrm{d}t.
\end{aligned}
\tag{20}
$$

Following standard technique of the calculus of variations from $\delta\mathbb{H} = 0$ we get the motion equations in $V$

$$
\nabla \cdot \boldsymbol{\sigma} - \nabla \cdot (\nabla \cdot \boldsymbol{\tau}) = \rho\ddot{\mathbf{u}} - \nabla \cdot (\nabla\ddot{\mathbf{u}} : \mathbf{K}_0) - \nabla \cdot (\mathbf{K}_1 \cdot \ddot{\mathbf{u}}) + \nabla\ddot{\mathbf{u}} : \mathbf{K}_1. \tag{21}
$$

From $\delta\mathbb{H} = 0$ we also get the homogeneous boundary conditions on $A$

$$
\begin{aligned}
&m\ddot{\mathbf{u}} - \nabla_s \cdot (\nabla_s\ddot{\mathbf{u}} : \mathbf{J}_0) - \nabla_s \cdot (\mathbf{J}_1 \cdot \ddot{\mathbf{u}}) + \nabla_s\ddot{\mathbf{u}} : \mathbf{J}_1 + \mathbf{n} \cdot [\nabla\ddot{\mathbf{u}} : \mathbf{K}_0 + \mathbf{K}_1 \cdot \ddot{\mathbf{u}}] \\
&\;= \nabla_s \cdot [\mathbf{T} - (\nabla_s \cdot \mathbf{M})\mathbf{n}] - 2H\mathbf{n} \cdot (\nabla_s \cdot \mathbf{M})\mathbf{n} \\
&\quad - \mathbf{n} \cdot [\boldsymbol{\sigma} - \nabla \cdot \boldsymbol{\tau}] + \nabla_s \cdot (\mathbf{n} \cdot \boldsymbol{\tau}) + 2H(\mathbf{n} \otimes \mathbf{n}) : \boldsymbol{\tau},
\end{aligned}
\tag{22}
$$

$$
(\mathbf{n} \otimes \mathbf{n}) : \boldsymbol{\tau} = \mathbf{0}. \tag{23}
$$

Neglecting the microinertia terms that is when

$$
\mathbf{K}_0 = \mathbf{0}, \quad \mathbf{K}_1 = \mathbf{0}, \quad \mathbf{J}_0 = \mathbf{0}, \quad \mathbf{J}_1 = \mathbf{0},
$$

Eqs. (21) and (22) take more simple form

$$
\nabla \cdot \boldsymbol{\sigma} - \nabla \cdot (\nabla \cdot \boldsymbol{\tau}) = \rho\ddot{\mathbf{u}}, \tag{24}
$$

$$
\begin{aligned}
m\ddot{\mathbf{u}} = &\nabla_s \cdot [\mathbf{T} - \nabla_s \cdot \mathbf{M})\mathbf{n}] - 2H\mathbf{n} \cdot (\nabla_s \cdot \mathbf{M})\mathbf{n} \\
&- \mathbf{n} \cdot [\boldsymbol{\sigma} - \nabla \cdot \boldsymbol{\tau}] + \nabla_s \cdot (\mathbf{n} \cdot \boldsymbol{\tau}) + 2H(\mathbf{n} \otimes \mathbf{n}) : \boldsymbol{\tau},
\end{aligned}
\tag{25}
$$

In the case of statics and for simple materials that is if $\boldsymbol{\tau} = \mathbf{0}$, Eq. (25) coincides with the boundary conditions presented by Zemlyanova and Mogilevskaya [38]

$$
\nabla_s \cdot [\mathbf{T} - (\nabla_s \cdot \mathbf{M})\mathbf{n}] - 2H\mathbf{n} \cdot (\nabla_s \cdot \mathbf{M})\mathbf{n} = \mathbf{n} \cdot \boldsymbol{\sigma}. \tag{26}
$$

For the Gurtin–Murdoch model and for simple materials that is if $\mathbf{M} = \mathbf{0}$ and $\boldsymbol{\tau} = \mathbf{0}$, instead of (22) we have

$$\nabla_s \cdot \mathbf{T} = \mathbf{n} \cdot \boldsymbol{\sigma} + m\ddot{\mathbf{u}}. \tag{27}$$

As was shown by Eremeyev et al. [13] the presence in (27) the dynamic term $m\ddot{\mathbf{u}}$ results in new type of surface waves, which do not exists in the standard elasticity. These antiplane surface waves exist also within the Toupin–Mindlin strain gradient elasticity, see [17] and the comparison of these waves with ones in media with surface stresses given by Eremeyev et al. [15].

The analysis of the natural boundary conditions along $\partial A$ requires further assumptions on the kinematics at $\partial A$ and behaviour of admissible variations. So we will consider this analysis as well as analysis of dynamic boundary conditions along edges and at the corner point will be given in the forthcoming papers.

## 4 Conclusions

With the use of the least action principle we derived the motion equations and the natural boundary conditions on a free surface with surface stresses and discussed it along contours. Here we consider both strain gradient elasticity in the bulk and the Steigmann-Ogden model of surface elasticity. The natural boundary conditions include inertia terms which may change the wave propagation in such media. In particular, these inertia terms are responsible for new type of surface anti-plane waves, see [13, 15]. Here we have also the inertia terms in conditions along possible edges. The further analysis of the dynamic conditions along edges can be provided as was done by dell'Isola and Seppecher [7]; Eremeyev [10].

**Acknowledgements** Authors acknowledges financial support from the Russian Science Foundation under the grant "*Methods of microstructural nonlinear analysis, wave dynamics and mechanics of composites for research and design of modern metamaterials and elements of structures made on its base*" (No 15-19-10008-P).

## Appendix: Surface Divergence Theorems and Integration by Parts

For integration by parts we used the surface divergence theorem. Here we recall two statements, see, e.g., [14, 25] for details. Let $\mathbf{X}$ be a continuously differentiable tensor-valued field given on a smooth surface $A$ with the smooth contour $\partial A$. Then the following statement is valid

$$\int_A (\nabla_s \cdot \mathbf{X} + 2H\mathbf{n} \cdot \mathbf{X})\,\mathrm{d}S = \int_{\partial A} \boldsymbol{\nu} \cdot \mathbf{X}\,\mathrm{d}s, \tag{28}$$

where $2H = \operatorname{tr} \mathbf{B}$ is the mean curvature, $\mathbf{B} = -\nabla_s \mathbf{n}$, $\mathbf{n}$ is a unit normal to $A$, and $\boldsymbol{\nu}$ is outward normal to $\partial A$ such that $\boldsymbol{\nu} \cdot \mathbf{n} = 0$.

If $\mathbf{n} \cdot \mathbf{X} = \mathbf{0}$ or $H = 0$ then we get the following reduced form

$$\int_A \nabla_s \cdot \mathbf{X} \, \mathrm{d}S = \int_{\partial A} \boldsymbol{\nu} \cdot \mathbf{X} \, \mathrm{d}s. \tag{29}$$

Using (28) we get the following formula of integration by parts

$$\int_A \mathbf{X} : \nabla_s \mathbf{y} \, \mathrm{d}S = \int_{\partial A} \boldsymbol{\nu} \cdot \mathbf{X} \cdot \mathbf{y} \, \mathrm{d}s - \int_A \left[ (\nabla_s \cdot \mathbf{X}) \cdot \mathbf{y} + 2H \mathbf{n} \cdot \mathbf{X} \cdot \mathbf{y} \right] \mathrm{d}S \tag{30}$$

for ant fields $\mathbf{X}$ and $\mathbf{y}$. In particular, if $\mathbf{n} \cdot \mathbf{X} = \mathbf{0}$ or $H = 0$ we have more simple relation

$$\int_A \mathbf{X} : \nabla_s \mathbf{y} \, \mathrm{d}S = \int_{\partial A} \boldsymbol{\nu} \cdot \mathbf{X} \cdot \mathbf{y} \, \mathrm{d}s - \int_A (\nabla_s \cdot \mathbf{X}) \cdot \mathbf{y} \mathrm{d}S. \tag{31}$$

## References

1. Abali, B.E., Müller, W.H., dell'Isola, F.: Theory and computation of higher gradient elasticity theories based on action principles. Arch. Appl. Mech. **87**(9), 1495–1510 (2017)
2. Aifantis, E.C.: Gradient material mechanics: perspectives and prospects. Acta Mech. **225**(4–5), 999–1012 (2014)
3. Altenbach, H., Eremeyev, V.A., Lebedev, L.P.: On the spectrum and stiffness of an elastic body with surface stresses. ZAMM **91**(9), 699–710 (2011)
4. Auffray, N., dell'Isola, F., Eremeyev, V.A., Madeo, A., Rosi, G.: Analytical continuum mechanics à la Hamilton-Piola least action principle for second gradient continua and capillary fluids. Math. Mech. Solids **20**(4), 375–417 (2015)
5. Bertram, A.: Compendium on Gradient Materials. Otto von Guericke University, Magdeburg (2017)
6. Cordero, N.M., Forest, S., Busso, E.P.: Second strain gradient elasticity of nano-objects. J. Mech. Phys. Solids **97**, 92–124 (2016)
7. dell'Isola, F., Seppecher, P.: Edge contact forces and quasi-balanced power. Meccanica **32**(1), 33–52 (1997)
8. dell'Isola, F., Sciarra, G., Vidoli, S.: Generalized Hooke's law for isotropic second gradient materials. R. Soc. Lond. Proc. Ser. A **465**(2107), 2177–2196 (2009)
9. Duan, H.L., Wang, J., Karihaloo, B.L.: Theory of elasticity at the nanoscale. In: Advances in Applied Mechanics, vol. 42, pp. 1–68. Elsevier (2008)
10. Eremeyev, V.A.: On equilibrium of a second-gradient fluid near edges and corner points. In: Naumenko, K., Aßmus, M. (eds.) Advanced Methods of Continuum Mechanics for Materials and Structures, Advanced Structured Materials, vol. 60, pp. 547–556. Springer, Singapore (2016)
11. Eremeyev, V.A., Altenbach, H.: Equilibrium of a second-gradient fluid and an elastic solid with surface stresses. Meccanica **49**(11), 2635–2643 (2014)
12. Eremeyev, V.A., Lebedev, L.P.: Mathematical study of boundary-value problems within the framework of Steigmann-Ogden model of surface elasticity. Cont. Mech. Thermodyn. **28**(1–2), 407–422 (2016)
13. Eremeyev, V.A., Rosi, G., Naili, S.: Surface/interfacial anti-plane waves in solids with surface energy. Mech. Res. Commun. **74**, 8–13 (2016)

14. Eremeyev, V.A., Cloud, M.J., Lebedev, L.P.: Applications of Tensor Analysis in Continuum Mechanics. World Scientific, New Jersey (2018)
15. Eremeyev, V.A., Rosi, G., Naili, S.: Comparison of anti-plane surface waves in strain-gradient materials and materials with surface stresses. Math. Mech. Solids (2018). https://doi.org/10.1177/1081286518769960
16. Eringen, A.C.: Nonlocal Continuum Field Theories. Springer, New York (2002)
17. Gourgiotis, P., Georgiadis, H.: Torsional and SH surface waves in an isotropic and homogenous elastic half-space characterized by the Toupin-Mindlin gradient theory. Int. J. Solids Struct. **62**, 217–228 (2015)
18. Gurtin, M.E., Murdoch, A.I.: A continuum theory of elastic material surfaces. Arch. Ration. Mech. Anal. **57**(4), 291–323 (1975)
19. Gurtin, M.E., Murdoch, A.I.: Surface stress in solids. Int. J. Solids Struct. **14**(6), 431–440 (1978)
20. Han, Z., Mogilevskaya, S.G., Schillinger, D.: Local fields and overall transverse properties of unidirectional composite materials with multiple nanofibers and Steigmann-Ogden interfaces. Int. J. Solids Struct. **147**, 166–182 (2018)
21. Javili, A., dell'Isola, F., Steinmann, P.: Geometrically nonlinear higher-gradient elasticity with energetic boundaries. J. Mech. Phys. Solids **61**(12), 2381–2401 (2013a)
22. Javili, A., McBride, A., Steinmann, P.: (2013) Thermomechanics of solids with lower-dimensional energetics: on the importance of surface, interface, and curve structures at the nanoscale. A unifying review. Appl. Mech. Rev. **65**(1), 010802
23. Khakalo, S., Niiranen, J.: Form II of Mindlin's second strain gradient theory of elasticity with a simplification: for materials and structures from nano-to macro-scales. Eur. J. Mech. A/Solids **71**, 292–319 (2018)
24. Kim, C.I., Schiavone, P., Ru, C.Q.: The effects of surface elasticity on an elastic solid with mode-III crack: complete solution. Trans. ASME J. Appl. Mech. **77**(2), 021011 (2010)
25. Lebedev, L.P., Cloud, M.J., Eremeyev, V.A.: Tensor Analysis with Applications in Mechanics. World Scientific, New Jersey (2010)
26. Lurie, A.I.: Nonlinear Theory of Elasticity. North-Holland, Amsterdam (1990)
27. Maugin, G.A.: Non-Classical Continuum Mechanics: A Dictionary. Springer, Singapore (2017)
28. Mindlin, R.D.: Micro-structure in linear elasticity. Arch. Ration. Mech. Anal. **16**(1), 51–78 (1964)
29. Mindlin, R.D.: Second gradient of strain and surface-tension in linear elasticity. Int. J. Solids Struct. **1**(4), 417–438 (1965)
30. Mindlin, R.D., Eshel, N.N.: On first strain-gradient theories in linear elasticity. Int. J. Solids Struct. **4**(1), 109–124 (1968)
31. Mindlin, R.D., Tiersten, H.F.: Effects of couple-stresses in linear elasticity. Arch. Ration. Mech. Anal. **11**, 415–448 (1962)
32. Schiavone, P., Ru, C.Q.: Solvability of boundary value problems in a theory of plane-strain elasticity with boundary reinforcement. Int. J. Eng. Sci. **47**(11), 1331–1338 (2009)
33. Simmonds, J.G.: A Brief on Tensor Analysis, 2nd edn. Springer, New Yourk (1994)
34. Steigmann, D.J., Ogden, R.W.: Plane deformations of elastic solids with intrinsic boundary elasticity. Proc. R. Soc. A **453**(1959), 853–877 (1997)
35. Steigmann, D.J., Ogden, R.W.: Elastic surface-substrate interactions. Proc. R. Soc. A **455**(1982), 437–474 (1999)
36. Toupin, R.A.: Elastic materials with couple-stresses. Arch. Ration. Mech. Anal. **11**(1), 385–414 (1962)
37. Wang, J., Huang, Z., Duan, H., Yu, S., Feng, X., Wang, G., Zhang, W., Wang, T.: Surface stress effect in mechanics of nanostructured materials. Acta Mech. Solida Sinica **24**, 52–82 (2011)
38. Zemlyanova, A.Y., Mogilevskaya, S.G.: Circular inhomogeneity with Steigmann-Ogden interface: Local fields, neutrality, and Maxwell's type approximation formula. Int. J. Solids Struct. **135**, 85–98 (2018)

# Simple Energy Control in Frenkel–Kontorova Model

**Alexander L. Fradkov, Egor V. Usik and Boris Andrievsky**

**Abstract** In the paper the energy control problems for Frenkel–Kontorova Model are posed and their connection to the pendula chains control is discussed. Speed-gradient based energy control algorithm is proposed and analyzed. Simulation results illustrating the convergence of the proposed algorithm are presented.

## 1 Introduction

The celebrated *Frenkel–Kontorova (FM) model* since its first appearance in the paper by Ya. I. Frenkel and T. A. Kontorova in 1938 is getting more and more popular as a tool for description and analysis of nonlinear effects (solitons, kinks, breathers, etc.) in complex physical systems [1]. It has a variety of applications to study of dislocations in the crystalline structure of a solid body, study of friction mechanisms at nanoscale, to study of biological chains e.g. DNA), etc. In many cases, the elements of the FK model really correspond to real atoms, but they can also to simulate whole groups of atoms, as in the case of DNA type molecular chains, they can correspond magnetic circuit backs or even describe some complex objects such as point Josephson contacts in some lattice.

---

A. L. Fradkov · E. V. Usik · B. Andrievsky (✉)
Institute for Problems of Mechanical Engineering, The Russian Academy of Sciences,
61 Bolshoy prospekt, V.O., 199178 Saint Petersburg, Russia
e-mail: boris.andrievsky@gmail.com

E. V. Usik
e-mail: egor.usik@yandex.ru

A. L. Fradkov · B. Andrievsky
Saint Petersburg State University, 28 Universitetsky prospekt, 198504 Peterhof,
Saint Petersburg, Russia
e-mail: fradkov@mail.ru

A. L. Fradkov · B. Andrievsky
ITMO University, Saint Petersburg, Russia

H. Altenbach et al. (eds.), *Dynamical Processes in Generalized Continua and Structures*, Advanced Structured Materials 103,
https://doi.org/10.1007/978-3-030-11665-1_11

As a model of the motion of a dislocation in a crystal the FK model takes into account two chains of atoms, which are an approximation of two layers of atoms, with the bottom layer of atoms being replaced by a sequence of hills and hollows. In the hollows there are balls connected by elastic springs. Thus, the interaction of balls – "atoms" between themselves and with the bottom layer of "atoms" is taken into account [1].

The ultimate case of dislocation is the "hole" in the crystalline lattice. Such a hole can move through the crystal. To flip a nearby atom to an empty space, one needs to "swing it" so that it can break away from the surrounding atoms. A defect in which atoms around the "hole" are also shifted is easier to move.

One of the simplest macroscopic models describing the dynamics of the FK model was first proposed by Alvin Scott [2, 3]. This is an experimental mechanical transmission line, which is an effective pedagogical tool for observing kinks and study their remarkable properties. Then he showed [2] that such the mechanical system can be easily designed as a line of screws screwed into copper cylinders that are connected by steel springs and kept in horizontal position by the piano string. Changing the stiffness of the springs, one can get a chain, described either quasi-continual, or a strictly discrete FK model. Useful portable version of this mechanical transmission line can be constructed in a simpler way using rubber tape and dressmakers [4]. Thus, the FK system can be interpreted by a chain of pendulums, in which each pendulum is connected to its neighbors by elastic springs.

In the recent years the methods of cybernetics are penetrating a number of the physics areas and the whole new area in physics named "Cybernetical Physics" is getting more and more visible [5]. Since FK model has so many applications, it becomes of interest to investigate its *controlled* version. The first results of such kind related to control of friction were published both in physical journals [6] and in control related journals [7, 8]. However the problem of energy control was not addressed. The energy control problem for FK model was first posed in [5, 9] where the control of energy algorithm was also proposed. However neither analytical nor numerical study of energy control were performed previously up to the best authors' knowledge, though the related problem for sine-Gordon equation was studied more intensively [10–13].

Such an investigation is the mail aim of the present paper. In the next section the energy control problem for sine-Gordon system is recalled and the simple energy control problem for FK model is formulated. Then the control algorithm for FK model is described and the achievement of the control goal is examined.

In Sec. 3 some general nonlinear control framework useful in control of physical system is described. In Sec. 4 this framework will be applied to a more advanced problem when an integrator appears in the control loop. Section 4 is devoted to the problem of energy control in cascaded FK model. The simulation results are presented in Sec. 5. Concluding remarks in Sec. 6 finalize the paper.

## 2 Simple Energy Control for Sine-Gordon and Frenkel–Kontorova Models

Let us study possibilities of the speed-gradient method for control of energy in sin-Gordon-like systems [5]. Using the following notations: $x_t = \dfrac{\partial x}{\partial t}$, $x_{tt} = \dfrac{\partial^2 x}{\partial t^2}$, $x_{r_i} = \dfrac{\partial x}{\partial r_i}$, $x_{r_i t} = \dfrac{\partial^2 x}{\partial r_i \partial t}$ $x_{r_i r_i} = \dfrac{\partial^2 x}{\partial r_i^2}$, consider the system, described by sin-Gordon equation with dissipation

$$Jx_{tt} = k\Delta x - E\sin x - \rho x_t, \tag{1}$$

where $x = x(r,t)$ is the function of the system state; $r \in X \subset \mathbb{R}^n$ is the spatial variable, taking values from a set $X$; $\Delta$ is Laplace operator; $\Delta x = \sum_{i=1}^{n} x_{r_i r_i}$; $J$, $k$, $\rho$ are parameters of the system; $E = E(t)$ is the external action (e.g. external force or intensity of the external electrical field). Assume that $E = E_0 + u(t)$, where $E_0$ is the base level of the intensity of the force or field; $u(t)$ is the controlling variable. The system (1) can be considered as a model of diffusively coupled oscillators (e.g. pendulums, magnetic domains liquid crystals), each being positioned in the spatial point $r$. Then $x(r,t)$ is the deflection angle of $r$th oscillator at time $t$. Such a system belongs to a class of reaction-diffusion systems, but its study is of independent value.

Let us pose the problem of controlling the energy of the free system

$$H = \frac{1}{2}\int\limits_X \left( J\Big(\frac{\partial x}{\partial t}\Big)^2 + k\big|\nabla_r x\big|^2 + 2E_0\big(1-\cos x\big)\right) dr \tag{2}$$

to the prespecified level $H_*$. It means that we introduce the control goal as follows:

$$\lim_{t\to\infty} H(t) = H_*. \tag{3}$$

First let $\rho = 0$ and evaluate the rate of changing the energy along trajectories of the system (1) assuming that the controlling variable is frozen, $u(t) \equiv u$:

$$\begin{aligned} \frac{dH}{dt} &= \int\limits_X Jx_t \cdot x_{tt} - k\Delta x x_t + E_0 \sin x \cdot x_t \, dr = \\ &= \int\limits_X x_t\big(-E\sin x + E_0 \sin x\big)\, dr = -u(t)\int\limits_X x_t \sin x \, dr. \end{aligned} \tag{4}$$

It is easy to see that the choice of the control in the form

$$u(t) = -\gamma \int\limits_X x_t \sin x \, dr, \tag{5}$$

where $\gamma > 0$, guarantees that the energy $H(t)$ will not decrease in time.

Introducing the goal function $V(t) = \frac{1}{2}\big(H(t) - H_*\big)^2$, and evaluating the time derivative of $V(t)$, we obtain

$$\dot{V} = \frac{dV}{dt} = -u(t)\big(H(t) - H_*\big) \int\limits_X x_t \sin x \, dr, \tag{6}$$

and $\dot{V} \leq 0$ for

$$u(t) = \gamma\big(H(t) - H_*\big) \int\limits_X x_t \sin x \, dr. \tag{7}$$

Thus, if the system is affected by the action (7) it will have a tendency to approach the goal.

Consider in more detail the spatially one-dimensional, spatially discrete version of the problem, described by equations

$$J\ddot{x}_j = \frac{k}{h^2}\big(x_{j+1} - 2x_j + x_{j-1}\big) - \big(E_0 + u(t)\big)\sin x_j - \rho\dot{x}_j, \quad j = 1, 2, \ldots, N. \tag{8}$$

It corresponds to a continuous system

$$Jx_{tt} = kx_{rr} - \big(E_0 + u(t)\big)\sin x - \rho x_t \tag{9}$$

defined in the set $X = [a, b]$, if the correspondence is defined by the relations $x_j = x(a + j(b-a)/(N+1))$, $j = 0, 2, \ldots, N+1$.

The system (8) is suggested to be a controlled version of the classical *Frenkel–Kontorova chain*, proposed in 1939 and studied in numerous works, see, e.g. [14].

Before designing the control law, let us discuss the choice of boundary conditions. Usually when studying an uncontrolled system (9) two types of boundary conditions are used: either zero boundary conditions $x(a, t) = x(b, t) = 0$, corresponding in the discrete system (8) to the relations

$$x_0(t) \equiv x_{N+1}(t) \equiv 0, \tag{10}$$

or periodic (no flux across the boundary) conditions $x_r\big|_{r=a} = x_r\big|_{r=b} = 0$, corresponding to the relations

$$x_0 = x_1, \qquad x_N = x_{N+1}. \tag{11}$$

The speed-gradient energy control algorithm looks as follows:

$$u(t) = \gamma\big(H(t) - H_*\big)\sum_{j=1}^{N} \dot{x}_j \sin x_j, \tag{12}$$

where $\gamma > 0.$, $H(t)$ is a discrete analogue of (2), see (26) It follows from [5, Theorem 3.1] that the control goal (3) in the system (8), (12) for $\varrho = 0$ is achieved if the energy layer in the system phase space between the energy levels $H(0)$ and $H_*$ does not contain equilibria satisfying conditions $\sin x_j = 0$, $j = 1, \ldots, N$.

## 3 Nonlinear Control and Passivity

Consider the following non-affine time-invariant model of a nonlinear system:

$$\dot{x} = F(x, u), \quad y = h(x) \tag{13}$$

where $x(t) \in \mathbb{R}^n$ is the system state, $u(t) \in \mathbb{R}^m$ denotes the control input, $y(t) \in \mathbb{R}^m$ is the system output. System (13) behavior is considered on the temporary axis $[0, \infty)$ with initial condition $x(0) = x_0$. It is assumed that the set of admissible input functions consists of all piecewise-continuous, locally bounded functions. $u : \mathbb{R}_+ \to \mathbb{R}^m$, function $F : \mathbb{R}^n \times \mathbb{R}^m \times \mathbb{R}_+ \to \mathbb{R}^n$ is locally Lipshitz on $x$, $u$, and besides $F(0, 0) = 0$ and $h(0) = 0$.

**Definition 1** System (13) is called *passive* [15] if there is a non-negative $V : \mathbb{R}^n \to \mathbb{R}_+$ function, called the *storage function*, and all solutions satisfy the system integral dissipation inequality: $V(x(t)) - V(x(0)) \le \int_0^t y(\tau)^{\mathrm{T}} u(\tau) d\tau$. If, moreover, the storage function $V(x)$ is differentiable, then the dissipation inequality can be rewritten in differential form: $\dot{V} \le y^{\mathrm{T}} u$.

Passivity is closely related to stability: for $u \equiv 0$, a passive system with a positively defined storage function is Lyapunov stable.

**Definition 2** [15] System $\dot{x} = f(x) + g(x)u$, $y = h(x)$ possesses the *Yakubovich–Kalman–Popov property* (YKP-property) if there is a non-negative continuously differentiable function $V : \mathbb{R}^n \to \mathbb{R}_+$, $V(0) = 0$ such that

$$\big(\nabla_x V(x)\big)^{\mathrm{T}} f(x) \leqslant 0, \quad \big(\nabla V(x)\big)^{\mathrm{T}} g(x) = h(x)^{\mathrm{T}}.$$

**Lemma 1** [15] *System $\dot{x} = f(x) + g(x)u$, $y = h(x)$ is passive with a continuously differentiated storage function if and only if it possesses the property of YKP.*

The *backstepping method* [15] is based on the following statement
*Statement*. If system $\dot{x} = f(x, \xi)$, $\dot{\xi} = u$ is defined in $\mathbb{R}^n$ and is locally asymptotically stabilized at the point $x = x^*$ using control $\xi = U_\xi(x)$, then the control algorithm

$$u = \frac{\partial U_\xi}{\partial x} f(x, \xi) + k_0(\xi - U_\xi(x)),$$

where $k_0 < 0$, ensures (local) asymptotical stability of the initial system in the point $(x, \xi) = (x^*, 0)$. □

**Definition 3** The *Poisson bracket* of smooth functions $f(q, p)$ and $g(q, p)$ is defined as

$$\{f, g\} = \sum_{i=1}^{n} \Big( \frac{\partial f}{\partial q_i} \frac{\partial g}{\partial p_i} - \frac{\partial f}{\partial p_i} \frac{\partial g}{\partial q_i} \Big)$$

Consider the mathematical model of the system in the Hamiltonian form as follows:

$$\dot{q} = \nabla_p H(q, p, u), \tag{14}$$

$$\dot{p} = -\nabla_q H(q, p, u), \tag{15}$$

where $q \in \mathbb{R}^n$, $p \in \mathbb{R}^n$ are vectors of generalized coordinates and generalized momenta; $u(t) \in \mathbb{R}$ is the controlling input.

It is assumed that the Hamiltonian $H(q, p, u)$ is a continuously differentiable function on its arguments.

Consider the problem of approaching free (uncontrolled) system energy to a given energy level $H_*$, i.e. pose the following control aim:

$$\lim_{t\to\infty} H_0(q(t), p(t)) = H_*,$$

where $H_0(q, p) = H(q, p, 0)$ is the Hamiltonian of a free system, which is described by following equations:

$$\dot{q} = \nabla_p H_0(q, p),$$
$$\dot{p} = -\nabla_q H_0(q, p).$$

Introduce the following goal function

$$Q(x) = \frac{1}{2}(H_0(p, q) - H_*)^2,$$

where $x = \mathrm{col}(q, p)$. Then the control aim can be written as

$$\lim_{t\to\infty} Q(x(t)) = 0. \tag{16}$$

In what follows it is assumed that the Hamiltonian is linear in control:

$$H(q, p, u) = H_0(q, p) + H_1(q, p)^{\mathrm{T}} u,$$

where $H_0(q, p)$ denotes the free system Hamiltonian; $H_1(q, p)$ is the vector of the so-called *interaction Hamiltonians*.

Based on the Speed-gradient method [5, 15], the following control law is obtained:

$$u = -\gamma\psi\big((H_0 - H_*)\{H_0, H_1\}^{\mathrm{T}}\big), \quad \gamma > 0. \tag{17}$$

The following Theorem is known.

**Theorem 1** [15]. *Let the first and second partial derivatives of functions $H_0, H_1$ on the set $\Omega_0 = \{x : Q(x) < Q_0\}$ are bounded for some $Q_0 > O$, and function $\psi(x)$ is continuous and satisfies the following strict pseudo-gradient condition $\psi(z)^{\mathrm{T}} z > 0$ as $z \in \mathbb{R}^n$, $z \neq O$.*

*Then algorithm (17) in system (14) for initial condition $x(0) \in \Omega_0$ ensures $u(t) \to 0$ as $t \to \infty$ and, besides, the following alternative is valid: on the trajectory $x(t)$ either the aim (16) is achieved, or convergence of $\{H_0, H_1\}(x(t)) \to 0$ is ensured as $t \to \infty$.*

*Additionally, let the following conditions be fulfilled:*

1. *For any $c \neq H_*$ there exists $\varepsilon > 0$ such that any non-empty connected subset of a set*
$$D_{\varepsilon,c} = \{x : |\{H_0(x), H_1(x)\}| < \varepsilon, |H_0(x) - c| < \varepsilon\} \cap \Omega_0$$
*is bounded.*
2. *The largest invariant set $M \subset D_0$ of the free system (i.e., the set of whole trajectories of system (14), contained in $D_0$), where $D_0 = \big\{x : \{H_0(x), H_1(x)\} = 0\big\} \bigcap \Omega_0$ consists of no more than a countable number of isolated points without finite condensation points.*

*then any solution to (14), (17) either ensures aim (16), or tends to some point in $D_0$, which is the free system equilibrium. In addition, the set of initial conditions, for which the solution to system (14), (17) tends to an unstable equilibrium of a free system, has a zero measure.*

Consider a Hamiltonian system with an integrator:

$$\dot{q} = \nabla_p H(q, p, u), \tag{18}$$
$$\dot{p} = -\nabla_q H(q, p, u), \tag{19}$$
$$\dot{u} = \omega, \tag{20}$$

where $q \in \mathbb{R}^n$, $p \in \mathbb{R}^n$ are the vectors of generalized coordinates and generalized momenta; $u(t) \in \mathbb{R}$ denotes the virtual control (an integrator); $\omega(t) \in \mathbb{R}$ is a controlling input.

Moreover, function $H(q, p, u)$ is an invariant for a free system

$$\begin{aligned}\dot{q} &= \nabla_p H(q, p, u),\\ \dot{p} &= -\nabla_q H(q, p, u),\\ u &= \text{const}\,.\end{aligned}$$

Consider the problem of approaching the system energy to a given level $H_*$. To this end, let us introduce the objective function

$$Q(x) = \frac{1}{2}(H_0(p, q) - H_*)^2,$$

where $x = \text{col}(q, p)$, $H_0(p, q) = H(p, q, 0)$. Then the control aim has a form:

$$\lim_{t\to\infty} Q(x(t)) = 0. \tag{21}$$

The following Theorem is valid.

**Theorem 2** *Let $H(x, u) = H_0(x) + H_1(x)u$. Suppose that for system (18), (19) the following conditions are fulfilled:*

1. *For any $c \neq H_*$, there exists $\varepsilon > 0$ such that any non-empty connected subset of a set*
$$D_{\varepsilon,c} = \{x : |\{H_0(x), H_1(x)\}| < \varepsilon, |H_0(x) - c| < \varepsilon\} \bigcap \Omega_0$$
*is bounded.*
2. *The largest invariant set $M \subset D_0$ of the free system (i.e., the set of whole trajectories of system (18), (19), contained in $D_0$), where $D_0 = \big\{x : \{H_0(x), H_1(x)\} = 0\big\} \cap \Omega_0$ consists of no more than a countable number of isolated points without finite condensation points.*
3. *System (18), (19) is globally asymptotically stabilizable by means of feedback $\alpha(p, q)$.*

*Then control*

$$\omega = -\gamma_B(u - \alpha(p, q)) + \nabla\alpha(p, q)^{\mathrm{T}}\begin{pmatrix}\dot{q}\\ \dot{p}\end{pmatrix} + w, \tag{22}$$

*where $w$ is a new input of the system, passifies system (18)–(20) with a new output $y = 2\gamma_B^{-1}\big(u - \alpha(p, q)\big)$.*

*In addition, for $w = 0$, control (22) ensures the control aim fulfillment for system (18)–(20).*

*Proof of Theorem 2*

Define the storage function as:

$$W(x, u) = Q(x) + \gamma_B^{-1}\|u - \alpha(p, q)\|^2, \tag{23}$$

where $x = \text{col}(q, p)$.

By definition, a system is passive (see [15]) if the inequality

$$\dot{W}(x, u) \leqslant y^{\mathrm{T}} w$$

is fulfilled. Let us prove this.

$$\begin{aligned}\dot{W}(x, u) &= \dot{Q}(x) + 2\gamma_B^{-1}|u - \alpha(p, q)|\Big(\dot{u} - \nabla\alpha(p, q)^{\mathrm{T}}\begin{pmatrix}\dot{q}\\ \dot{p}\end{pmatrix}\Big) = \\ &= \dot{Q}(x) - 2|u - \alpha(p, q)|^2 + 2\gamma_B^{-1}(u - \alpha(p, q))w \leqslant y^{\mathrm{T}} w.\end{aligned}$$

To prove the fulfillment of the control goal in a closed-loop system, let us consider function (23) as a Lyapunov function.

Calculate the time derivative of (23) along the system trajectories, using Theorem 1 and control (22):

$$\begin{aligned}\dot{W}(x, u) &= \dot{Q}(x) + 2\gamma_B^{-1}|u - \alpha(p, q)|\Big(\dot{u} - \nabla\alpha(p, q)^{\mathrm{T}}\begin{pmatrix}\dot{q}\\ \dot{p}\end{pmatrix}\Big) = \\ &= \dot{Q}(x) - 2|u - \alpha(p, q)|^2 < 0.\end{aligned}$$

Applying the Barbalat lemma to the inequality obtained above, one obtains that $Q(x) \to 0$ as $t \to \infty$, i.e. the control goal is achieved.

Thus, the theorem is proven.

## 4 Control of Energy in Cascaded FK Model

Consider the following FK-model with an integrator [16]:

$$\ddot{x}_j = \frac{k}{h^2}(x_{j+1} - 2x_j + x_{j-1}) - \big(E_0 + u(t)\big)\sin(x_j) - \rho\dot{x}_j, \tag{24}$$

$$\dot{u} = \omega, \qquad j = 1, 2, \ldots, N, \tag{25}$$

where $k$, $\rho$ are the system parameters, $\omega(t)$ is the control action, $E_0$ is the base field level, $x_0(t) = x_1(t)$, $x_{N+1}(t) = x_N(t)$ (the so-called *zero flux conditions*).

The energy of (24) is determined by the equation:

$$H = \frac{1}{2}\sum_{j=1}^{N}\dot{x}_j^2 + \frac{k}{2}\sum_{j=1}^{N}(x_{j+1} - x_j)^2 + E_0\Big(N - \sum_{j=1}^{N}\cos(x_j)\Big). \tag{26}$$

Let us pose two following problems:

1. *Passification* of system (24), (25);
2. System (24), (25) *synchronization* with bringing the system energy to the specified level $H_*$:

$$\lim_{t\to\infty} H(t) = H_*.$$

To solve the problem in question, let us formulate Theorem 1 in a more general form.

Let us represent the state vector of system (24) as follows:

$$z = \begin{pmatrix} y_1 \\ x_1 \\ \dots \\ y_N \\ x_N \end{pmatrix},$$

where $y_i = \dot{x}_i$.

Then system (24), (25) can be represented as

$$\dot{z} = \begin{pmatrix} \frac{k}{h^2}(x_2 - 2x_1 + x_0) - (E_0 + u(t))\sin(x_1) - \rho y_1 \\ y_1 \\ \dots \\ \frac{k}{h^2}(x_{N+1} - 2x_N + x_{N-1}) - (E_0 + u(t))\sin(x_N) - \rho y_N \\ y_N \end{pmatrix}, \tag{27}$$

$$\dot{u} = \omega. \tag{28}$$

Let us introduce a new goal function:

$$Q(z) = Q_1(z) + Q_2(z) = \alpha\frac{1}{2}\sum_{i=1}^{N-1}(y_i + y_{i+1})^2 + (1-\alpha)\frac{1}{2}(H - H_*)^2, \tag{29}$$

where $\alpha$ $(0 \leqslant \alpha \leqslant 1)$ is a weight coefficient.

The first term, $Q_1(z)$, corresponds to the requirement that the oscillations are in antiphase. The second one, $Q_2(z)$, guarantees achievement of the required energy level.

System (24), (25) Hamiltonian is determined by the equation

$$H = \frac{1}{2}\sum_{j=1}^{N}\dot{x}_j^2 + \frac{k}{2}\sum_{j=1}^{N}(x_{j+1} - x_j)^2 + (E_0 + u)(N - \sum_{j=1}^{N}\cos(x_j)). \tag{30}$$

Let us show that for a free system

$$\begin{aligned}&\ddot{x}_j = \frac{k}{h^2}(x_{j+1} - 2x_j + x_{j-1}) - (E_0 + u(t))\sin(x_j) - \rho\dot{x}_j,\\ &u = \text{const}, \quad j = 1, 2, \dots, N,\end{aligned}$$

Hamiltonian (30) is an invariant.

$$\dot{H} = \sum_{j=1}^{N}\dot{x}_j\ddot{x}_j - k\sum_{j=1}^{N}(x_{j+1} - 2x_j + x_{j-1})\dot{x}_j + (u + E_0)\sum_{j=1}^{N}\sin(x_j)\dot{x}_j = 0$$

As follows from Theorem 2, control goal (29) in system (24), (25) with $\rho = 0$ and $\alpha = 0$ is achieved if the energy layer between levels $H(0)$ and $H_*$ does not contain equilibria of the system, satisfying conditions $\sin(x_j) = 0$, $j = 1, \dots, N$.

**Theorem 3** *Let the energy layer between the levels* $H(0)$ *and* $H_*$ *does not contain equilibria of the system, satisfying conditions* $\sin(x_j) = 0$, $j = 1, \dots, N$; $\rho = 0$, $\alpha = 0$, *then the control law*

$$\begin{aligned}&\omega(t) = -\gamma_B(u - \gamma_D(H - H_*)\sum_{j=1}^{N}y_j\sin(x_j)) +\\ &\gamma_D(H - H_*)\sum_{j=1}^{N}\Big(\sin(x_j)\Big(\frac{k}{h^2}(x_{j+1} - 2x_j + x_{j-1}) - (E_0 + u(t))\sin(x_j)\Big) + y_j^2\cos(x_j)\Big) + w,\end{aligned}$$

*obtained by applying the Speed-gradient method, and* $\dot{z}$ *is defined by (27), passifies system (24), (25) with respect to a new output* $y_{new} = u - \gamma_D(H - H_*)\sum_{j=1}^{N}y_j\sin(x_j)$. *The control goal is achieved when* $w = 0$.

*Remark 1* For $\alpha \neq 0$, an expression for $\alpha(z)$ has the following form:

$$\begin{aligned}&\alpha(z) = \gamma_D(1 - \alpha)(H - H_*)\sum_{j=1}^{N}y_j\sin(x_j) +\\ &\alpha\Big(\sum_{j=2}^{N-1}(y_{j-1} + 2y_j + y_{j+1})\sin(x_j) + (y_1 + y_2)\sin(x_1) + (y_{N-1} + y_N)\sin(x_N)\Big).\end{aligned}$$

## 5 Simulation Results

The simulations were done for the FK-chain (8) consisting of $N = 20$ elements and the following dimensionless parameters: $J = 1, k = 0.12, E_0 = 1, h = 0.0476$. The dissipation parameter $\rho$ was taken as $\rho = 0$ (non-dissipative case) and $\rho = 0.25$ (dissipative case) in different simulation runs. Desired energy level was set to $H_* = 50$. Initial conditions were taken as $x_j = 1 - \cos(2\pi r_j)$, where $r_j = jh$, $j = 1, \ldots, N$; initial values of $\dot{x}_j$ were set to zero. For simulations control algorithm (7) with $\gamma = 2$ was used.

The simulation results are depicted in Figs. 1, 2 and 3. As is seen from the plots, in the non-dissipative case the error in energy $H(t) - H_*$ may be neglected for

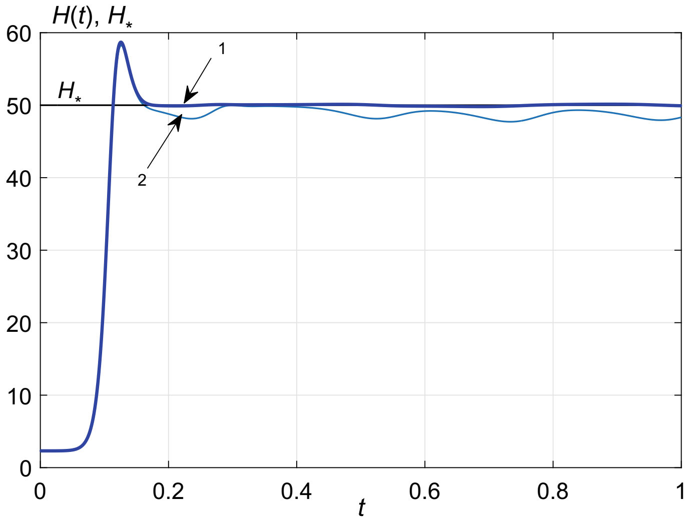

**Fig. 1** Energy $H(t)$, reference value $H_*$ time histories. 1 – $H(t)$ for non-dissipative case, $\rho = 0$; 2 – $H(t)$ for dissipative case, $\rho = 0.25$

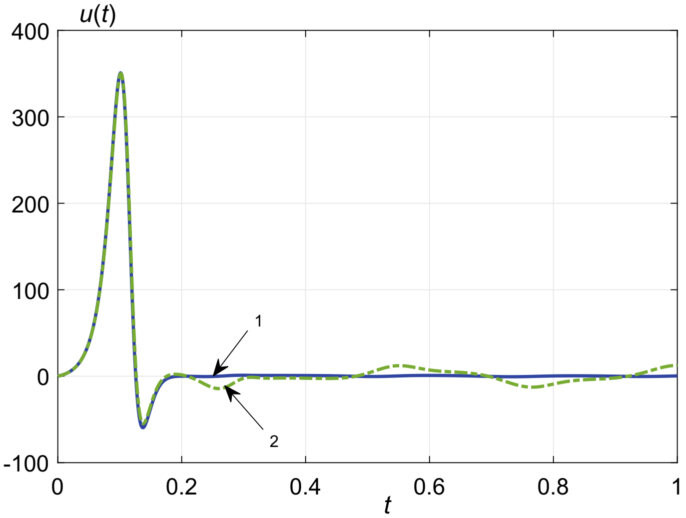

**Fig. 2** Control action $u(t)$ time history. 1 – non-dissipative case, $\rho = 0$; 2 – dissipative case, $\rho = 0.25$

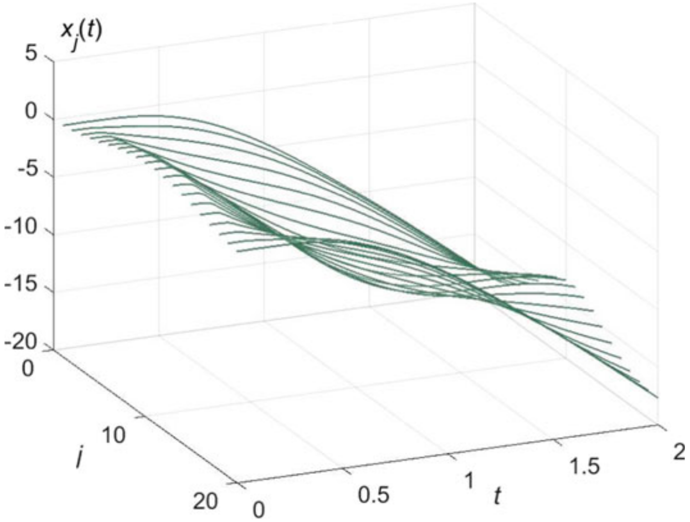

**Fig. 3** $x_j(t)$ time histories. $j = 1, \ldots, 20$, non-dissipative case, $\rho = 0$

sufficiently large $t$. In the presence of dissipation in the model, the visible control error arise.

## 6 Conclusions

The paper is dedicated to study of the energy control problem for celebrated Frenkel–Kontorova model describing numerous physical systems like dynamics of dislocations in the crystalline structure of a solid body, friction mechanisms at nanoscale, dynamics of biological chains e.g. DNA, etc. To this end modern nonlinear control methods like speed-gradient and passivity methods [5, 15] are employed. The analytical conditions of the achievement of the prespecified energy level in the control system are proposed and illustrated by computer simulation. It is seen from the simulation results that for sufficiently long chains the error in the limit energy is rather small and may be neglected. The proposed methods are also applied to a more advanced problem when an integrator appears in the control loop.

**Acknowledgements** The authors deeply appreciate the wisdom leadership of Professor Dmitry Indeitsev who was keeping and still is keeping a wonderful creativity atmosphere in the IPME institute for many years and made it possible to perform such researches like ours.

## References

1. Braun, O.M., Kivshar, Y.: The Frenkel-Kontorova Model. Concepts, Methods, and Applications. Theoretical and Mathematical Physics. Springer, Berlin (2004). https://doi.org/10.1007/978-3-662-10331-9
2. Scott, A.: Am. J. Phys. **37**, 52 (1969). https://doi.org/10.1119/1.1975404
3. Scott, A.: Nonlinear Science: Emergence and Dynamics of Coherent Structures. Oxford Texts in Applied and Engineering Mathematics (Book 8), 2nd edn. Oxford University Press, Oxford (2003)
4. Remoissenet, M.: Waves Called Solitons. Concepts and Experiments. Springer, Berlin (1999), pp. 116–137. https://doi.org/10.1007/978-3-662-03057-8
5. Fradkov, A.L.: Cybernetical Physics: From Control of Chaos to Quantum Control. Springer, Berlin (2007)
6. Braiman, Y., Barhen, J., Protopopescu, V.: Phys. Rev. Lett. **90**(9) (2003)
7. Guo, Y., Qu, Z.: Automatica **44**(10), 2560 (2008)
8. Hua, G., Dixon, W., Ding, H.: Automatica **48**, 442 (2012)
9. Fradkov, A.L.: Phys. Uspekhi **48**(2), 103 (2005)
10. Porubov, A., Fradkov, A., Andrievsky, B.: Appl. Math. Comput. **269**, 17 (2015)
11. Porubov, A., Fradkov, A., Andrievsky, B., Bondarenkov, R.: Wave Motion **65**, 147 (2016)
12. Orlov, Y., Fradkov, A., Andrievsky, B.: Int. J. Control **11**, 2554 (2017)
13. Porubov, A., Antonov, I., Indeitsev, D., Fradkov, A.: Mech. Res. Commun. **93**, 124 (2018)
14. Landa, P.S.: Nonlinear Oscillations and Waves in Dynamical Systems. Mathematics and Its Applications (MAIA, v. 360). Springer Nature Switzerland AG, Basel (1996). https://doi.org/10.1007/978-94-015-8763-1
15. Fradkov, A.L., Miroshnik, I.V., Nikiforov, V.O.: Nonlinear and Adaptive Control of Complex Systems. Kluwer, Dordrecht (1999)
16. Fradkov, A.L., Makarov, I.A., Shiriaev, A.S., Tomchina, O.P.: In: Proceedings of the 4th European Control Conference (ECC'97), Brussels (1997)

# On Kinetic Nature of Hysteresis Phenomena in Stress-Induced Phase Transformations

**A. B. Freidin and Victor A. Eremeyev**

**Abstract** A simplest model is developed which demonstrates that hysteresis phenomena in stress-induced phase transformations may have a kinetic nature and follow from the discrepancy between strain rate and characteristic rate of the new phase growth.

## 1 Introduction

Stress-induced phase transformations in shape memory alloys lead to pseudoelasticity with recovering relatively large strains (see, e.g., [1, 2]). Initially a material is in a austenite phase. At some stress martensite phase nucleates and then increases its volume fraction. Changing the geometry of a lattice, i.e. a transformation strain, produces a macroscopic deformation at practically constant stress, and a plateau appears at the stress-strain diagram. Unloading leads to a reverse transformation that takes

---

A. B. Freidin (✉)
Institute for Problems in Mechanical Engineering of Russian Academy of Sciences,
St. Petersburg, Russia
e-mail: alexander.freidin@gmail.com

A. B. Freidin
Peter the Great St. Petersburg Polytechnic University, St. Petersburg, Russia

A. B. Freidin
St. Petersburg University, St. Petersburg, Russia

A. B. Freidin
Beijing University of Civil Engineering and Architecture, Beijing, China

V. A. Eremeyev
Faculty of Civil and Environmental Engineering, Gdańsk University of Technology,
Gdańsk, Poland
e-mail: eremeyev.victor@gmail.com; victor.eremeev@pg.edu.pl

V. A. Eremeyev
Institute of Mathematics, Mechanics and Computer Science, Southern Federal University,
Rostov-on-Don, Russia

H. Altenbach et al. (eds.), *Dynamical Processes in Generalized Continua and Structures*, Advanced Structured Materials 103,
https://doi.org/10.1007/978-3-030-11665-1_12

place at lower stress that corresponds to another plateau at the diagram. As a result a flag-type stress-strain diagrams are formed with upper boundary corresponding to the direct transformation and lower boundary corresponding to the reverse transformation. The height and thickness of the flag depend on the temperature and loading rate. Kinetics of stress-induced phase transformations was studied by many researchers from various points of view, see, e.g., [3–5] and reference therein. In the present paper, we relate such a flag-type behavior with the discrepancy between strain rate and characteristic rate of the new phase growth with the kinetics considered within the frames of mechanics of configurational forces. We also discuss barrier effects of various nature. To demonstrate the role of various factors, for the simplicity sake, we consider 1D-case.

## 2 Phase Equilibrium and Kinetics in 1D-Model

Consider a rod $x \in [0, L]$ made of a material undergoing a phase transformation, $u(x)$ is the displacement of a material point $x$, $\varepsilon = \partial u/\partial x$ is the strain, $u(0) = 0$ and $u(L) = u_L$ are the displacements prescribed at the ends of the rod.

Assume that the Helmholtz free energy per unit length of the rod is represented as

$$f(\varepsilon) = \begin{cases} f_-(\varepsilon) = f_0^- + \dfrac{1}{2}\, C_-\varepsilon^2, & \varepsilon \le \widetilde{\varepsilon}, \\[2ex] f_+(\varepsilon) = f_0^+ + \dfrac{1}{2}\, C_+(\varepsilon - \varepsilon^{tr})^2, & \varepsilon > \widetilde{\varepsilon}, \end{cases} \tag{1}$$

where $C_\pm$ are Yong's modules of the phases "±", $\varepsilon^{tr}$ is the transformation strain, $f_0^\pm$ are the chemical energies of the phases (the temperature dependent Helmholtz free energies in stress-free states). The strain $\widetilde{\varepsilon}$ divides the domains of existence of the phases "+" and "−" and can be found from the equality of the energies, i.e. is defined by the equation

$$C_-\widetilde{\varepsilon}^2 = C_+(\widetilde{\varepsilon} - \varepsilon^{tr})^2 + 2\gamma.$$

where $\gamma = [\![ f_0 ]\!]$ is the energy parameter acting as a temperature in the model, square brackets denote the jump of a value due to the phase transformation, $[\![ \cdot ]\!] = (\cdot)_+ - (\cdot)_-$.

If $u_L$ increases then the part of the rod transforms into a new phase state. Let $pL$ ($p \in [0, 1]$) be the total length occupied by the phase "+", $\varepsilon_+$ and $\varepsilon_-$ be the strains in the phases "+" and "−" correspondingly. Then the average strain and average energy

$$\widehat{\varepsilon} = (1 - p)\varepsilon_- + p\,\varepsilon_+, \tag{2}$$

$$\widehat{f} = (1 - p) f_-(\varepsilon_-) + p f_+(\varepsilon_+) \tag{3}$$

The stress $\sigma$ in the rod is continuous and can be calculated as

$$\sigma = C_-\varepsilon_- = C_+(\varepsilon_+ - \varepsilon^{tr}) \tag{4}$$

Thermodynamic equilibrium corresponds to zero configurational force given by the formula

$$\chi = \frac{\partial \hat{f}}{\partial p} \quad \text{at} \quad \widehat{\varepsilon} = \text{const}$$

Simple calculations give [6] (see also [7])

$$\chi = [\![f]\!] - \sigma[\![\varepsilon]\!] \tag{5}$$

After simple derivation the expression (5) takes the form analogous to the expression for layered two-phase microstructure in the 3D-case where tensorial values have been presented [7]:

$$\chi = \gamma + \frac{1}{2}[\![B]\!]^{-1}(\varepsilon^{tr})^2 + \frac{1}{2}([\![C]\!]^{-1} + B_-)(Q_-e)^2 = 0, \tag{6}$$

where

$$Q_- = ([\![C]\!]^{-1} + (1-p)B_-)^{-1}, \quad e = \hat{\varepsilon} - [\![C]\!]^{-1}C_+\varepsilon^{tr}.$$

From the equation $\chi = 0$ and relationships (2), (4) it follows that the dependence of the equilibrium new phase fraction $p_{eq}$ on average strain and stresess $\sigma^*_{1,2}$ at which the equilibrium is possible are given by formulas

$$p_{eq} = \frac{\widehat{\varepsilon} - \sigma^*/C_-}{2\gamma/\sigma^* - \varepsilon^p} \tag{7}$$

$$\sigma^*_{1,2} = -\frac{\varepsilon^{tr}}{[\![B]\!]} \pm \sqrt{\frac{1}{[\![B]\!]}\left(2\gamma + \frac{(\varepsilon^{tr})^2}{[\![B]\!]}\right)} \tag{8}$$

where $B_\pm = C_\pm^{-1}$. The transformation takes place at strains $\widehat{\varepsilon} \in [\varepsilon^s, \varepsilon^f]$, where

$$\varepsilon^s = \frac{\sigma^*}{C_-} \quad (p = 0), \quad \varepsilon^f = \frac{2\gamma}{\sigma^*} + \frac{\sigma^*}{C_-} - \varepsilon^{tr} \quad (p = 1) \tag{9}$$

The dependence of the free energy and the stress-strain diagram for the case of equilibrium two phase states are shown in Fig. 1. Note that there is no hysteresis in this case.

If the thermodynamic equilibrium condition is not reached than $\chi \neq 0$ is a thermodynamic (configurational, driving) force. By linear thermodynamic approach, the new phase fraction is changing according to the kinetic equation

$$\dot{p} = -L\chi(p, \hat{\varepsilon}, \gamma), \quad p \in [0, 1], \tag{10}$$

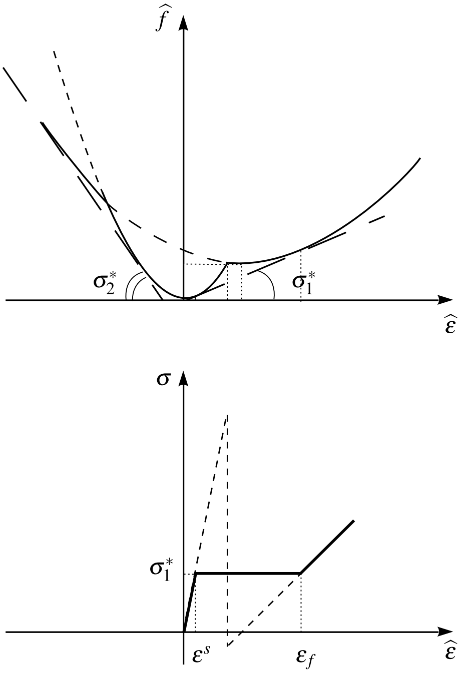

**Fig. 1** Average free energy and stress-strain diagram for equilibrium two phase states

where the dot denotes the derivative with respect to time $t$ and $L$ is a kinetic coefficient. The kinetic equation (10) is solved at initial conditions

$$t = t_0, \quad p = p_0, \quad \hat{\varepsilon} = \hat{\varepsilon}_0$$

and a given loading law $\hat{\varepsilon} = \hat{\varepsilon}(t)$ and/or temperature time dependence via $\gamma = \gamma(t)$. The choice of $p_0$ and $\hat{\varepsilon}_0$ depends on the nucleation assumptions.

## 3 Results

The dependencies of stresses on strains at stretching with a constant rate at various "temperatures" $\gamma$ for the case $C_+ > C_-$ are shown in Fig. 2. Horizontal dash lines correspond to equilibrium transformation. Upper and lower plateaus correspond to the direct and reverse transformations. The thickness of the flag decreases and the equilibrium stress increases if $\gamma$ increases.

The effect of strain rate is presented in Figs. 3, 4. If the loading rate decreases then upper and lower plateaus converge to the equilibrium dash line, as it is to be. The character of the influence of strain rate on stress-starin diagrams and the shape

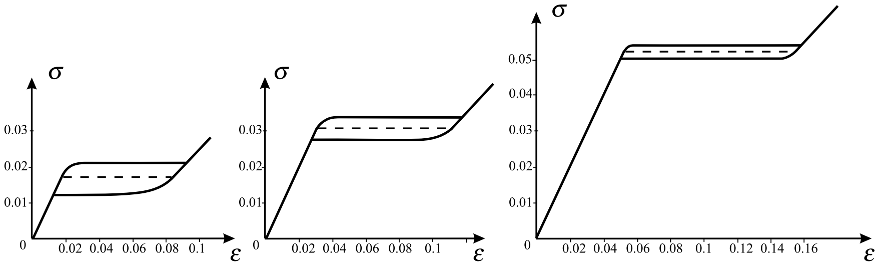

$\gamma_2$ $\gamma_3$ $\gamma_1$

**Fig. 2** Stress-strain diagrams at various energy parameters $\gamma$ (various "temperatures"): $\gamma_1 < \gamma_2 < \gamma_3$, $C_+ < C_-$

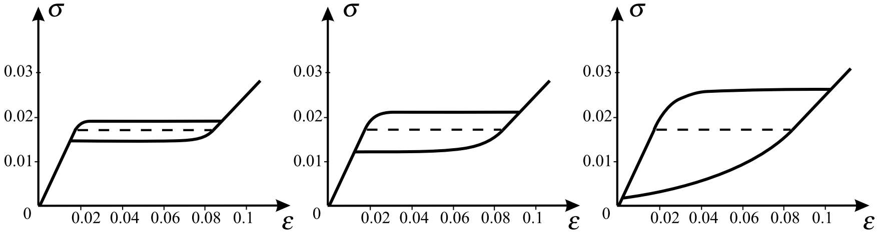

$v = 10^{-5}$ $v = 2 \cdot 10^{-5}$ $v = 5 \cdot 10^{-5}$

**Fig. 3** Stress-strain diagrams at various strain rates $v$, $C_+ < C_-$

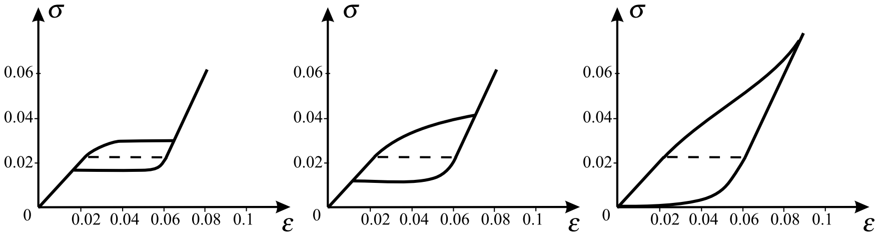

$v = 10^{-5}$ $v = 2 \cdot 10^{-5}$ $v = 5 \cdot 10^{-5}$

**Fig. 4** Stress-strain diagrams at various strain rates $v$, $C_+ > C_-$

of the diagram at higher rates depend on the relationship of Yong's modules $C_+$ and $C_-$.

Further modifications of the model can be considered in two directions: introducing a metastability barrier and a nucleation barrier. In the first case we assume that the direct reaction goes if the thermodynamic force is not just negative but is less than some negative number, and reverse transformation goes if the thermodynamic force is not just positive but is bigger than some positive number. This may be related with a hidden entropy production at the reaction front (as it was done recently for a chemical reaction front [8]). Such an assumption leads to the hysteresis even in

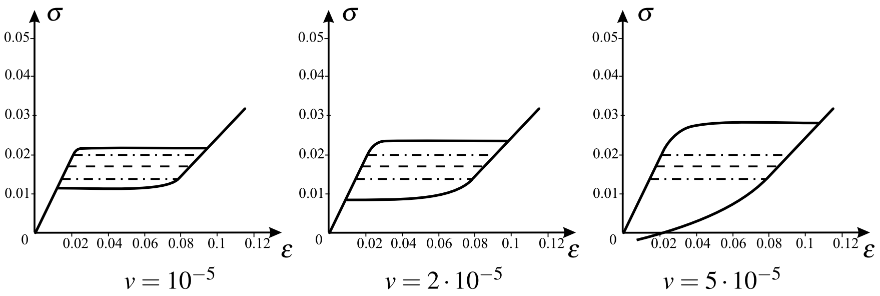

$v = 10^{-5}$ $v = 2 \cdot 10^{-5}$ $v = 5 \cdot 10^{-5}$

**Fig. 5** Stress-strain diagrams with a metastability barrier at various strain rates, $C_+ < C_-$

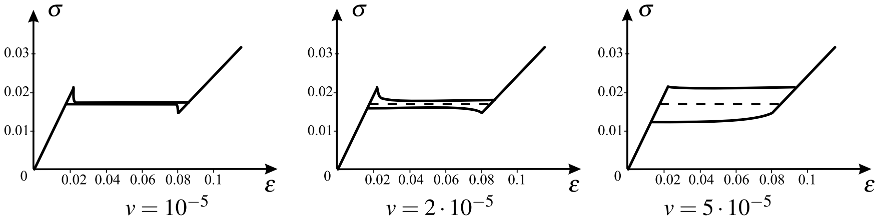

$v = 10^{-5}$ $v = 2 \cdot 10^{-5}$ $v = 5 \cdot 10^{-5}$

**Fig. 6** Stress-strain diagrams with a nucleation barrier at various strain rates, $C_+ < C_-$

quasi-equilibrium case and modifies the kinetic equation as follows:

$$\dot{p} = \begin{cases} 0, & |\chi| < \chi_*, \\ -k(\chi + \chi_*), & \chi < -\chi_* < 0 \\ -k(\chi - \chi_*), & \chi > \chi_* \end{cases}$$

(for simplicity sake we assume that the positive and negative barriers are of the same absolute values). Stress strain diagrams are shown in Fig. 5 for various strain rates. Dash lines correspond to equilibrium transformation without and with a barriers. The effects of the nucleation barrier at various strain rates are shown in Fig. 6.

## 4 Conclusions

The presented simplest model allowed us to give a qualitative description of hysteresis phenomena accompanying stress-induced phase transformations including systematic analysis of the kinetics itself as well as the role of various barriers. Further progress may be expected on the way of taking into account accompanying inelastic strains, microstresses and internal stresses produced by the transformation in 3D-case.

**Acknowledgements** A. B. Freidin greatly appreciates the financial support of the Russian Foundation for Basic Research (Grant No. 16-01-00815).

## References

1. Shaw, J.A., Kyriakides, S.: Thermomechanical aspects on NiTi. J. Mech. Phys. Solids **43**(8), 1243–1281 (1995)
2. Ma, J., Karaman, I., Noebe, R.D.: High temperature shape memory alloys. Int. Mater. Rev. **55**(5), 257–315 (2010)
3. Abeyaratne, R., Knowles, J.K.: Kinetic relations and the propagation of phase boundaries in solids. Arch. Rat. Mech. Anal. **114**, 119–154 (1991)
4. Abeyaratne, R., Knowles, J.K.: Evolution of Phase Transitions. A Continuum Theory. Cambridge, New York; Melbourne et al.: Cambridge University Press, Cambridge (2006)
5. Le, K.C.: On kinetics of hysteresis. Contin. Mech. Thermodyn. **18**, 335–342 (2007)
6. Ericksen, J.L.: Equilibrium of bars. J. Elast. **5**, 191–201 (1975)
7. Freidin, A.B., Sharipova, L.L.: On a model of heterogenous deformation of elastic bodies by the mechanism of multiple appearance of new phase layers. Meccanica **41**, 321–339 (2006)
8. Freidin, A.B.: On a chemical affinity tensor for chemical reactions in deformable solids. Mech. Solids **50**(3), 260–285 (2015)

# An Infinite-Length System Possessing a Unique Trapped Mode Versus a Single Degree of Freedom System: A Comparative Study in the Case of Time-Varying Parameters

**S. N. Gavrilov, E. V. Shishkina and Yu. A. Mochalova**

**Abstract** We compare large time behavior of an infinite system, with time-varying parameters, possessing a unique trapped mode (characterized by frequency $\Omega_0(\varepsilon\tau)$), with the behavior of a single degree of freedom system $\ddot{y} + \Omega_0^2(\varepsilon\tau)y = 0$ (a linear mass-spring oscillator with time-varying stiffness). The infinite length system is a string, lying on the Winkler foundation, and equipped with a discrete linear mass-spring oscillator of time-varying stiffness. We demonstrate that the classical formula $Y \propto \Omega_0^{-1/2}$ that relates the amplitude $Y(\varepsilon\tau)$ and the frequency $\Omega_0(\varepsilon\tau)$ for the single degree of freedom system is valid for amplitude of the localized string oscillation if and only if the oscillator mass, attached to the string, is big enough.

## 1 Introduction

In this paper we consider a mechanical system with mixed spectrum of natural oscillations. Namely, we deal with an infinite taut string, lying on the Winkler foundation, and equipped with a discrete linear mass-spring oscillator of time-varying stiffness (Fig. 1). In the case of a constant string tension the discrete part of the spectrum for such a system may contain unique (positive) eigenvalue, which is less than the lowest frequency for the string on the uniform foundation. This special natural frequency corresponds to a trapped mode of oscillation with eigenform localized

---

S. N. Gavrilov (✉) · E. V. Shishkina · Yu. A. Mochalova
Institute for Problems in Mechanical Engineering RAS, V.O., Bolshoy pr. 61,
St. Petersburg 199178, Russia
e-mail: serge@pdmi.ras.ru

E. V. Shishkina
e-mail: shishkina_k@mail.ru

Yu. A. Mochalova
e-mail: yumochalova@yandex.ru

S. N. Gavrilov
Peter the Great St. Petersburg Polytechnic University (SPbPU), Polytechnicheskaya str. 29,
St. Petersburg 195251, Russia

H. Altenbach et al. (eds.), *Dynamical Processes in Generalized Continua and Structures*, Advanced Structured Materials 103,
https://doi.org/10.1007/978-3-030-11665-1_13

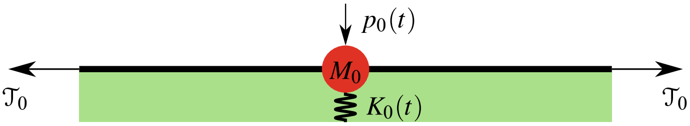

**Fig. 1** The schematic of the system

near the spring. The phenomenon of trapped modes was discovered in the theory of surface water waves [1]. The examples of various mechanical systems, where trapped modes can exist, can be found in studies [2–25].

It is known [5, 17, 22–27] that applying non-stationary external excitation to a system possessing trapped modes leads to the emergence of undamped oscillations localized near the inhomogeneity. If the system possesses a unique trapped mode and such an excitation is applied only during a finite interval of time, then, after sometime has passed, the system becomes to be similar, in some sense, to a single degree of freedom system (with natural frequency equal to the trapped mode frequency). The large time asymptotics for undamped oscillation can be found [5, 22, 23, 27] by means of the method of stationary phase [28, 29].

Gavrilov in [5, 8] suggested an asymptotic procedure based on successive application of two asymptotic methods, namely the method of stationary phase [28, 29] and the method of multiple scales [29, 30] that allows us to investigate non-stationary processes in perturbed systems, with slowly time-varying parameters, possessing trapped modes. In studies [5, 8] the problem concerning non-uniform motion of a point mass along a taut string on the Winkler foundation was considered and solved. Note that later the same problem was reconsidered in paper [31] by Gao et al. in very particular case of uniform motion at a given speed.

It is well known that for a single degree of freedom system with slowly time-varying stiffness $\ddot{y} + \Omega_0^2(\varepsilon\tau)y = 0$, formula $Y \propto \Omega_0^{-1/2}$ relates the amplitude $Y(\varepsilon\tau)$ and the frequency $\Omega_0(\varepsilon\tau)$ of free oscillation (the Liouville—Green approximation [30]).[1] The aim of this paper is to compare the law describing the evolution of the amplitude of undamped localized oscillation in the system possessing a unique trapped mode with this classical result for the single degree of freedom system. To do this in a correct way we need to consider (for first time in this context) a mechanical system with inhomogeneity of more complex structure (a discrete oscillator possessing both the inertia and the time-varying stiffness) than we considered in previous papers [5, 8, 22–25] where the evolution of the amplitude of a trapped mode was investigated in the cases of pure inertial [5, 8, 22] or pure elastic [23–25] inhomogeneity. We will demonstrate that for the system under consideration the classical formula for a single degree of freedom with time varying stiffness is valid if and only if the oscillator mass, attached to the string, is big enough.

We dedicate this paper to Prof. D. A. Indeitsev who initiated and stimulated our interest to linear wave localization. He is one of the pioneers in this field, who

---

[1] Here $\varepsilon$ is a formal small parameter, $\tau$ is the dimensionless time.

was the first suggested simple and physically clear models, which made possible the analytical investigation of trapped modes in solids. His kind attitude and wise advices are always very helpful to his colleagues in their work.

## 2 Mathematical Formulation

We consider transverse oscillation of an infinite taut string on the Winkler elastic foundation. The string is equipped with a discrete mass-spring oscillator of time-varying stiffness. The schematic of the system is shown in Fig. 1. Introduce the following notation: $u(x, t)$ is the displacement of a point of the string at the position $x$ and time $t$, $\mathscr{T}_0$ is the string tension, $\rho$ is the mass of the string per unit length, constant $M_0 \geq 0$ is the value of mass in the discrete oscillator, $K_0(t)$ is the spring stiffness for the discrete oscillator (a given function of time), $k_0$ is the stiffness for the Winkler foundation, $P_0(t)$ is the unknown force on the string from the spring, $p_0(t)$ is the given external force on the string. Quantities $\mathscr{T}_0$, $k_0$, $\rho$ are positive constants. We do not assume that $K_0 > 0$ (hence, the spring stiffness can be negative [15, 23–25] or zero).[2]

The governing equations are

$$\mathscr{T}_0\, u_{xx} - \rho u_{tt} - k_0 u = -P_0(t)\, \delta(x), \tag{1}$$

$$P_0(t) = -M_0 u_{tt}(0, t) - K_0(t) u(0, t) + p(t). \tag{2}$$

Here $\delta$ is the Dirac delta-function.

Now we introduce the dimensionless variables

$$\tau = t\sqrt{k_0/\rho}, \qquad \xi = x\sqrt{k_0/\mathscr{T}_0} \tag{3}$$

and rewrite governing equations (1), (2) in the following form

$$u'' - \ddot{u} - u = -P(\tau)\, \delta(\xi), \tag{4}$$

$$P(\tau) = -M\ddot{u}(0, \tau) - K(\tau) u(0, \tau) + p(\tau), \tag{5}$$

where

$$M = \frac{M_0}{\rho}\sqrt{\frac{k_0}{\mathscr{T}_0}}, \qquad K = \frac{K_0}{\sqrt{k_0 \mathscr{T}_0}}, \qquad p = \frac{p_0}{\sqrt{k_0 \mathscr{T}_0}}. \tag{6}$$

Here and in what follows, we denote by prime the derivative with respect to spatial coordinate $\xi$ and by overdot the derivative with respect to time $\tau$.

---

[2] It may be noted that springs with negative stiffness may be used in applications related to constructing dynamic metamaterials [32–39].

The initial conditions for Eq. (4) can be formulated in the following form, which is conventional for distributions (or generalized functions) [40]:

$$u\big|_{\tau<0} \equiv 0. \tag{7}$$

Note that according to Eqs. (4), (5), (7) we restrict ourselves to the important particular case of the general problem concerning non-stationary oscillation, where any external excitation (and, in particular, non-zero initial conditions) is applied only to the point of the string under the concentrated spring.

The problem under consideration (4), (5), (7) is symmetric with respect to $\xi = 0$. Integrating (4) over $\xi = 0$ results in the following condition

$$[u'] = -P(\tau) = M\ddot{u}(0, \tau) + Ku(0, \tau) - p(\tau). \tag{8}$$

Here, and in what follows, $[\mu] \equiv \mu(\xi + 0) - \mu(\xi - 0)$ for any arbitrary quantity $\mu$. Due to symmetry one has $[u'] = 2u'(\xi + 0)$. Thus, the problem for infinite string can be equivalently reformulated as the problem for homogeneous equation

$$u'' - \ddot{u} - u = 0 \tag{9}$$

for $\xi > 0$ with boundary condition at $\xi = 0$

$$u'(0, \tau) = \frac{M\ddot{u}(0, \tau) + Ku(0, \tau) - p(\tau)}{2}. \tag{10}$$

This equivalent formulation (9), (10), (7) is used for numerical calculations (Sect. 5).

## 3 The Mass-Spring Oscillator with a Constant Spring Stiffness

In this section we assume that the stiffness of discrete mass-spring oscillator is a constant: $K = \text{const}$.

### *3.1 Spectral Problem*

Put $p = 0$ and consider the steady-state problem concerning the natural oscillations of the system described by Eqs. (4), (5). Take

$$u = \hat{u}(\xi) \exp(-i\Omega\tau). \tag{11}$$

Let us show that such a system possesses a mixed spectrum of natural frequencies. There exists a continuous spectrum of frequencies, which lies higher than the cut-off (or boundary) frequency: $|\Omega| \geq \Omega_* \equiv 1$. The modes corresponding to the frequencies from the continuous spectrum are harmonic waves. Trapped modes correspond to the frequencies from the discrete part of the spectrum, which lies lower than the cut-off frequency:

$$0 < |\Omega| < 1. \tag{12}$$

We want to demonstrate that for the problem under consideration the only one trapped mode can exist. Trapped modes are modes with finite energy, therefore, we require

$$\int_{-\infty}^{+\infty} \hat{u}^2 \,\mathrm{d}\xi < \infty, \qquad \int_{-\infty}^{+\infty} \hat{u}'^2 \,\mathrm{d}\xi < \infty. \tag{13}$$

Now we substitute Eq. (11) into Eq. (4). This yields

$$\hat{u}'' - A^2(\Omega)\hat{u} = (K - M\Omega^2)\hat{u}(0)\,\delta(\xi), \tag{14}$$

where

$$A^2(\Omega) = 1 - \Omega^2. \tag{15}$$

Here, by definition, we assume that

$$A(\Omega) > 0 \tag{16}$$

for $0 < \Omega < 1$. The dispersion relation for the operator in the left-hand side of (14) is

$$\omega^2 + A^2(\Omega) = 0, \tag{17}$$

therefore, the wavenumber $\omega$ can be expressed as follows:

$$\omega = \pm \mathrm{i} A(\Omega). \tag{18}$$

The solution of Eq. (14), which satisfies (13), is

$$\hat{u} = -(K - M\Omega^2)\hat{u}(0)\frac{\exp\big(-A(\Omega)|\xi|\big)}{2A(\Omega)}. \tag{19}$$

Calculating the left-hand side of (19) at $\xi = 0$ yields the frequency equation

$$2\sqrt{1 - \Omega_0^2} = M\Omega_0^2 - K, \tag{20}$$

where $\Omega_0$ is the trapped mode frequency.

Consider the case $M > 0$ (the corresponding analysis for the special case $M = 0$ can be found in [23]). It follows from (20) that

$$\begin{aligned} \frac{K}{M} &< \Omega_0^2 < 1, \qquad K \geq 0; \\ 0 &< \Omega_0^2 < 1, \qquad K < 0; \end{aligned} \tag{21}$$

and

$$K < M. \tag{22}$$

Provided that restrictions (21) and (22) are true, we can square both sides of Eq. (20). This yields the biquadratic equation

$$M^2\Omega_0^4 - 2(MK - 2)\Omega_0^2 + K^2 - 4 = 0 \tag{23}$$

with its discriminant

$$\mathscr{D} = 16(M^2 - MK + 1). \tag{24}$$

The right-hand side if (24) is positive if and only if $K < M + 1/M$, which is true, according to (22). Thus,

$$\Omega_{0\,(\pm)}^2 = \frac{2}{M^2}\left(\pm\sqrt{M^2 - MK + 1} + \frac{MK}{2} - 1\right). \tag{25}$$

**Proposition 1** *Provided that* (22) *is true, the root* $\Omega_{0\,(-)}^2$ *does not satisfy restrictions* (21)*, whereas the root* $\Omega_{0\,(+)}^2$ *satisfy both restrictions simultaneously if and only if*

$$K > -2. \tag{26}$$

*Proof* At first, consider inequality $\Omega_{0\,(\pm)}^2 < 1$. It may be equivalently rewritten as

$$\begin{aligned} &\frac{2}{M^2}\left(\pm\sqrt{M^2 - MK + 1} + \frac{MK}{2} - 1\right) < 1 \\ &\qquad\iff \quad \pm\underbrace{\sqrt{M^2 - MK + 1}}_{Z} < \frac{1}{2}(M^2 - MK + 1) + \frac{1}{2} \\ &\qquad\qquad\iff \quad Z^2 \mp 2Z + 1 > 0 \quad \iff \quad (Z \mp 1)^2 > 0, \end{aligned} \tag{27}$$

which is true due to (22).

Consider inequality $\Omega_0^2 > K/M$ in the case $K \geq 0$. One has

$$\frac{2}{M^2}\left(\pm\sqrt{M^2 - MK + 1} + \frac{MK}{2} - 1\right) > \frac{K}{M} \quad \iff \quad \pm\sqrt{M^2 - MK + 1} > 1, \tag{28}$$

which is true if and only if $\Omega_{0\,(\pm)}^2 = \Omega_{0\,(+)}^2$.

Consider inequality $\Omega^2_{0\,(-)} > 0$ an the case $K < 0$. One has

$$\frac{2}{M^2}\left(-\sqrt{M^2 - MK + 1} + \frac{MK}{2} - 1\right) > 0 \quad \Longleftrightarrow \quad -\sqrt{M^2 - MK + 1} > 1 - \frac{MK}{2}, \tag{29}$$

which is false.

Finally, consider inequality $\Omega^2_{0\,(+)} > 0$ an the case $K < 0$. One has

$$\frac{2}{M^2}\left(+\sqrt{M^2 - MK + 1} + \frac{MK}{2} - 1\right) > 0 \quad \Longleftrightarrow \quad +\sqrt{M^2 - MK + 1} > 1 - \frac{MK}{2}$$

$$M^2 - MK + 1 > 1 - MK + \frac{M^2K^2}{4} \quad \Longleftrightarrow \quad K^2 < 4. \tag{30}$$

Thus, provided that restrictions (21) and

$$-2 < K < M \tag{31}$$

are true, there exists the unique trapped mode with frequency

$$\Omega^2_0 \equiv \Omega^2_{0\,(+)}. \tag{32}$$

The critical value $K = -2$ ($\Omega_0 = 0$) corresponds to the possibility of localized buckling of the string.

In the special case $M = 0$, one can obtain [23] formulas

$$-2 < K < 0, \tag{33}$$

$$\Omega^2_0 = 1 - \frac{K^2}{4}, \tag{34}$$

instead of formulas (31), (32), respectively.

Note that for the first time this spectral problem in the particular case of point inertial inclusion ($M > 0$, $K = 0$) was investigated in paper [2].

## 3.2 Inhomogeneous Non-stationary Problem

Put now $p \neq 0$. Applying to Eqs. (4) and (5) the Fourier transform in time $\tau$ results in

$$u''_F - A^2(\Omega)u_F = \big(Ku_F(0,\Omega) - M\Omega^2 u_F(0,\Omega) - p_F(\Omega)\big)\,\delta(\xi), \tag{35}$$

where $u_F(0,\Omega)$, $p_F(\Omega)$ are the Fourier transforms of $u(0,\tau)$ and $p(\tau)$, respectively. Resolving Eq. (35) with respect to $u_F(0,\Omega)$ and applying the inverse transform yields

$$u(0,\tau) = \frac{1}{2\pi}\int\limits_{-\infty}^{+\infty} \frac{p_F e^{-\mathrm{i}\Omega\tau}\,\mathrm{d}\Omega}{2\sqrt{1-\Omega^2} - (M\Omega^2 - K)} \tag{36}$$

Consider the case when $p(\tau)$ is a vanishing as $\tau \to \infty$ function such that its Fourier's transform $p_F(\Omega)$ does not have singular points on the real axis. Applying the residue theorem, Jordan's lemma, and the method of stationary phase to asymptotic evaluation of the integral in the right-hand side of (36) results in [28, 41]

$$u(0,\tau) = -\mathrm{i} \sum_{\bar\Omega=\pm\Omega_0-\mathrm{i}0} p_f(\bar\Omega)\,\mathrm{Res}\left(\frac{1}{2\sqrt{1-\Omega^2}-(M\Omega^2-K)}, \bar\Omega\right)\exp(-\mathrm{i}\bar\Omega\tau) + o(1), \qquad \tau \to \infty. \tag{37}$$

Here symbol $\mathrm{Res}\big(f(\Omega), \bar\Omega\big)$ means the residue of function $f(\Omega)$ at a pole $\Omega = \bar\Omega$. The terms $-\mathrm{i}0$ in the expression for the poles

$$\bar\Omega = \pm\Omega_0 - \mathrm{i}0 \tag{38}$$

are taken in accordance with the principle of limit absorption. One has

$$\mathrm{Res}\left(\frac{1}{2\sqrt{1-\Omega^2}-(M\Omega^2-K)}, \pm\Omega_0 - \mathrm{i}0\right) = \mp\frac{\sqrt{1-\Omega^2}}{2\Omega_0\big(1+M\sqrt{1-\Omega^2}\big)}, \tag{39}$$

thus

$$u(0,\tau) = \frac{\sqrt{1-\Omega_0^2}\,\big|p_F(\Omega_0)\big|}{\Omega_0\Big(1+M\sqrt{1-\Omega_0^2}\Big)}\sin\big(\Omega_0\tau - \arg p_F(\Omega_0)\big) + o(1), \quad \tau \to \infty. \tag{40}$$

Hence, for the large times, the non-stationary response of the system under consideration is undamped oscillations with the trapped mode frequency $\Omega_0$.[3]

## 4 The Mass-Spring Oscillator with Slowly Varying Spring Stiffness

Assume that the stiffness of the discrete mass-spring oscillator is a slowly varying piecewise monotone function of the dimensionless time $\tau$: $K = K(\varepsilon\tau)$. Here $\varepsilon$ is a formal small parameter. We use an approach [5, 8, 22] based on the modification of the method of multiple scales (see [30], Sect. 7.1.6) for equations with slowly varying coefficients. The corresponding rigorous proofs, which validate such asymptotic

---

[3] The asymptotic order of the reminder in formula (37) depends on the properties of $p_F$. In a common case when $p_F$ has no singular points on real axis, the main contribution is due to the cut-off frequency $\Omega_* = 1$ and has order $O(\tau^{-3/2})$ [26]. Therefore, in the case when $\Omega_0$ approaches $\Omega_* = 1$ asymptotical formula (40) needs to be refined (the case of merging singularities).

approach in the case of a one degree of freedom system, can be found in [42]. We look for the asymptotics for the solution under the following conditions:

- $\varepsilon = o(1)$,
- $\tau = O(\varepsilon^{-1})$,
- $K(\varepsilon\tau)$ satisfies restriction (31) for all $\tau$.

To construct the particular solution of (4) and (5), which describes the evolution of the trapped mode of oscillation in the case of slowly varying $K$, we require that in the perturbed system

- Frequency equation (20) for the trapped mode holds for all $\tau$;
- Dispersion relation (17) at $\xi = \pm 0$ holds for all $\tau$.

Accordingly, we use the following ansatz ($\tau > 0,\ \xi \lessgtr 0$):

$$u(\xi, \tau) = W(X, T)\ \exp \varphi(\xi, \tau), \tag{41}$$

$$T = \varepsilon\tau, \quad X = \varepsilon\xi, \tag{42}$$

$$\varphi' = \mathrm{i}\,\omega(X, T), \quad \dot{\varphi} = -\mathrm{i}\,\Omega(X, T), \tag{43}$$

$$W(X, T) = \sum_{j=0}^{\infty} \varepsilon^j W_j(X, T). \tag{44}$$

Here the amplitude $W(X, T)$, the wavenumber $\omega(X, T)$, and the frequency $\Omega(X, T)$ are the unknown functions to be defined in accordance with Eq. (4). The variables $X,\ T,\ \varphi$ are assumed to be independent. Accordingly, we use the following representations for the differential operators:

$$\begin{gathered}
\dot{(\cdot)} = -\mathrm{i}\,\Omega\,\partial_\varphi + \varepsilon\,\partial_T,\\
\ddot{(\cdot)} = -\Omega^2\,\partial^2_{\varphi\varphi} - 2\varepsilon\mathrm{i}\,\Omega\,\partial^2_{\varphi T} - \varepsilon\mathrm{i}\,\Omega'_T\,\partial_\varphi + O(\varepsilon^2),\\
(\cdot)' = \mathrm{i}\,\omega\,\partial_\varphi + \varepsilon\,\partial_X,\\
(\cdot)'' = -\omega^2\,\partial^2_{\varphi\varphi} + 2\varepsilon\mathrm{i}\,\omega\,\partial^2_{\varphi X} + \varepsilon\mathrm{i}\,\omega'_X\,\partial_\varphi + O(\varepsilon^2).
\end{gathered} \tag{45}$$

We require that $\omega(X, T)$ and $\Omega(X, T)$ satisfy dispersion relation (17) and equation

$$\Omega'_X + \omega'_T = 0 \tag{46}$$

that follows from (43). Since in the case of a mass-spring oscillator with a constant stiffness the undamped oscillation can be described by Eq. (40), we assume that

$$\Omega(\pm 0, T) = \Omega_0(T). \tag{47}$$

Additionally, we require that

$$[W] = 0, \qquad [\varphi] = 0. \tag{48}$$

In Eq. (47) the right-hand side is defined in accordance with the frequency equation (20), wherein $K = K(T)$. The phase $\varphi(\xi, \tau)$ should be defined by the formula

$$\varphi = \mathrm{i} \int (\omega \, \mathrm{d}\xi - \Omega \, \mathrm{d}\tau). \tag{49}$$

For large times, integrating formally Eq. (4) with respect to $\xi$ over the infinitesimal vicinity of $\xi = 0$ taking into account (5), one gets (8), wherein $p = 0$. Now we substitute ansatz (41)–(44) and representations (45) into Eq. (8) and equate coefficients of like powers $\varepsilon$. Taking into account frequency equation (20), and Eq. (47), one obtains that to the first approximation

$$M(2\Omega_0 {W_0}'_T + {\Omega_0}'_T W_0) = \mathrm{i}[{W_0}'_X]. \tag{50}$$

Note that in the special case $M = 0$ considered in [23], the corresponding equation has the form of

$$[{W_0}'_X] = 0, \tag{51}$$

i.e. it can be obtained as limiting case of (50) as $M \to +0$.

On the other hand, the quantity in the left-hand side of (50) can be defined by consideration of Eq. (4) at $\xi = \pm 0$. To do this, we substitute ansatz (41)–(44) and representations (45) into Eq. (4) and equate coefficients of like powers $\varepsilon$. Taking into account dispersion relation (20) and Eq. (47), one obtains that to the first approximation

$$2\omega \, {W_0}'_X + \omega'_X \, W_0 + 2\Omega_0 \, {W_0}'_T + {\Omega_0}'_T \, W_0 = 0 \tag{52}$$

at $\xi = \pm 0$. Due to (46) one has

$$\omega'_X = \omega'_\Omega \, \Omega'_X = -\omega'_\Omega \, \omega'_T, \tag{53}$$

where the right-hand side should be calculated in accordance with Eq. (18). Thus, Eqs. (52) and (53) result in

$${W_0}'_X = -\frac{2\Omega_0 \, {W_0}'_T + (-\omega'_\Omega \omega'_T + {\Omega_0}'_T) \, W_0}{2\mathrm{i}\gamma A(\Omega_0)}, \tag{54}$$

where $\gamma = \operatorname{sign} \xi$. Accordingly,

$$[{W_0}'_X] = -\frac{\Lambda_2 W_0 + \Lambda_1 {W_0}'_T}{\mathrm{i}A(\Omega_0)}, \tag{55}$$

$$\Lambda_1 \equiv 2\Omega_0, \tag{56}$$

$$\Lambda_2 \equiv A'_\Omega(\Omega_0) A'_T(\Omega_0) + {\Omega_0}'_T, \tag{57}$$

where the right-hand side of Eq. (55) is taken at $\xi = 0$. Using (15), one gets

$$A'_{\Omega} = -\frac{\Omega_0}{\sqrt{1-\Omega_0^2}}, \tag{58}$$

$$A'_{T} = -\frac{\Omega_0 {\Omega_0}'_T}{\sqrt{1-\Omega_0^2}}. \tag{59}$$

Substituting these expressions into (57) yields

$$\Lambda_2 = \frac{\Omega_0^2 {\Omega_0}'_T}{1-\Omega_0^2} + {\Omega_0}'_T. \tag{60}$$

Now, equating the right-hand sides of Eqs. (50) and (55) results in the first approximation equation for $\bar{W}_0(T) \equiv W_0(0, T)$:

$$M\left(2\Omega_0 \bar{W}_0{}'_T + {\Omega_0}'_T\, \bar{W}_0\right) = -\frac{\Lambda_2 \bar{W}_0 + \Lambda_1 \bar{W}_0{}'_T}{A(\Omega_0)}, \tag{61}$$

or, equivalently,

$$\bar{W}_0{}'_T + \left(\frac{{\Omega_0}'_T}{2\Omega_0} + \frac{\Omega_0 {\Omega_0}'_T}{2(1-\Omega_0^2)\left(1+M\sqrt{1-\Omega_0^2}\right)}\right)\bar{W}_0 = 0. \tag{62}$$

The general solution of the last equation is

$$\bar{W}_0 = \frac{C_0}{2}\exp\left(-\int \frac{\mathrm{d}\Omega_0}{2\Omega_0} - \int \frac{\Omega_0\,\mathrm{d}\Omega_0}{2(1-\Omega_0^2)\left(1+M\sqrt{1-\Omega_0^2}\right)}\right), \tag{63}$$

where $C_0$ is an arbitrary constant. Calculating the integrals yields the final result:

$$\bar{W}_0 = \frac{C_0}{2}\mathscr{A}(\Omega_0, M), \tag{64}$$

$$\mathscr{A}(\Omega_0, M) = \frac{\left(1-\Omega_0^2\right)^{1/4}}{\Omega_0^{1/2}\left(1+M\sqrt{1-\Omega_0^2}\right)^{1/2}}. \tag{65}$$

The plots of $\mathscr{A}(\Omega_0, M)$ against $\Omega_0$ for different values of $M$ are given in Fig. 2.

Combining the solution in the form of Eqs. (41)–(44) with its complex conjugate, we get the non-stationary solution as the following ansatz:

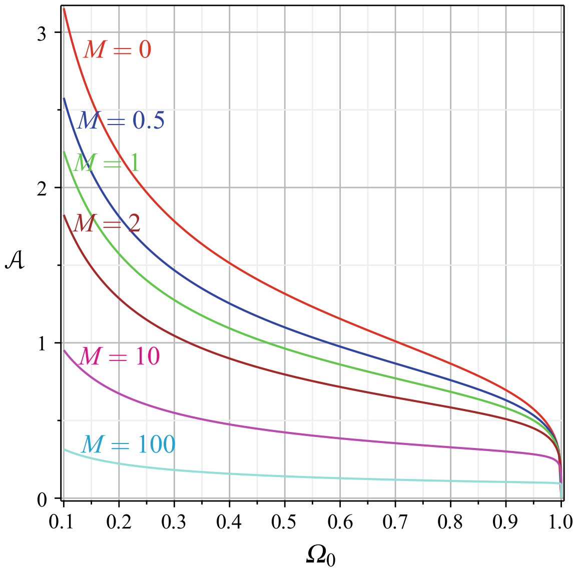

**Fig. 2** Plots of function $\mathscr{A}(\varOmega_0, M)$ defined by Eq. (65) against $\varOmega_0$ for different values of $M$

$$u(0,\tau) \sim C_0 \mathscr{A}\big(\varOmega_0(T), M\big) \sin\left(\int_0^\tau \varOmega_0(T)\,\mathrm{d}T - D_0\right), \tag{66}$$

where $\mathscr{A}$ is defined by (65). The unknown constants $C_0$ and $D_0$ should be defined by equating the right-hand sides of (40) and (66) taken at $\tau = 0$. This yields

$$C_0 = \frac{\big(1-\varOmega_0^2(0)\big)^{1/4}\,\big|p_F\big(\varOmega_0(0)\big|}{\varOmega_0^{1/2}(0)\Big(1+M\sqrt{1-\varOmega_0^2(0)}\Big)^{1/2}}, \tag{67}$$

$$D_0 = \arg p_F\big(\varOmega_0(0)\big). \tag{68}$$

In what follows, we restrict ourselves to the particular case $p(\tau) = \delta(\tau)$.[4] Thus,

$$C_0 = \frac{\big(1-\varOmega_0^2(0)\big)^{1/4}}{\varOmega_0^{1/2}(0)\Big(1+M\sqrt{1-\varOmega_0^2(0)}\Big)^{1/2}}, \tag{69}$$

$$D_0 = 0. \tag{70}$$

---

[4] Some examples of more complicated $p$ are considered in studies [8, 24, 25] for different, but similar problems.

## 5 Numerics

In previous studies [5, 8, 22–24] we dealt with several problems for linear PDE with constant coefficients. Numerical solutions were obtained by means of the reduction of the corresponding problem to an integral Volterra equation of the second kind with its kernel expressed in terms of the fundamental solution of corresponding PDE. This cannot be done for the problem under consideration in this paper, since for $M > 0$ we can obtain only integro-differential equation in such a way. Now we use alternative approach [25] based on finite difference schemes. The applicability of the approach was validated in the case $M = 0$ by comparison with the results obtained by numerical solution of the Volterra integral equation. To perform the numerical calculations we use SciPy software. To discretize PDE (9) we use the following implicit difference scheme:

$$\frac{u_{j+1}^i - 2u_j^i + u_{j-1}^i}{(\Delta\xi)^2} - \frac{u_j^{i+1} - 2u_j^i + u_j^{i-1}}{(\Delta\tau)^2} - \frac{u_j^{i+1} + u_j^{i-1}}{2} = 0, \tag{71}$$

where integers $i,\ j\ (0 \le j \le N,\ -1 \le i)$ are such that

$$u_j^i = u(j\Delta\xi, i\Delta\tau). \tag{72}$$

This scheme conserves [43, 44] the discrete energy for a nonlinear Klein-Gordon equation with constant coefficients. Numeric boundary conditions that correspond to (10) are taken in the form [45]

$$\frac{-3u_0^{i+1} + 4u_1^{i+1} - u_2^{i+1}}{2\Delta\xi} + \frac{-3u_0^{i-1} + 4u_1^{i-1} - u_2^{i-1}}{2\Delta\xi} - \frac{K^{i+1}u_0^{i+1} + K^{i-1}u_0^{i-1}}{2} - M\,\frac{u_0^{i+1} - 2u_0^i + u_0^{i-1}}{(\Delta\tau)^2} + \frac{p^{i+1} + p^{i-1}}{2} = 0. \tag{73}$$

where

$$K^i = K(i\Delta\tau). \tag{74}$$

At the right end we use the non-reflecting boundary condition [46]

$$u_N^i = u_{N-1}^i \tag{75}$$

that corresponds to the physical boundary condition $u' = 0$. Actually, the specific form of this boundary condition is not very important in our calculations, since we consider the discrete model of the string with big enough length such that the wave reflections at the right end do not occur.

Numerical initial conditions are

$$u_j^0 = u_j^{-1} = 0. \tag{76}$$

All numerical results below are obtained for the case

$$\Delta\xi = 0.008, \qquad \Delta\tau = 0.002. \tag{77}$$

When considering $p(\tau) = \delta(\tau)$ and calculating the corresponding numerical solutions, we approximate the Dirac delta-function as follows:

$$p = \tau_0^{-1}(H(\tau) - H(\tau - \tau_0)). \tag{78}$$

Now we want to compare the analytical and numerical solutions and demonstrate the difference in the behavior of the system under consideration and a single degree of freedom system with time-varying stiffness.

## 6 Comparison with a Single Degree of Freedom System

The result in the form of formulas (64), (65) is rather similar to the classical result for a single degree of freedom system with time-varying stiffness

$$\ddot{y} + \Omega_0^2(T)y = 0, \tag{79}$$

where the following formula

$$Y \propto \frac{1}{\Omega_0^{1/2}} \tag{80}$$

for the amplitude of free oscillations $Y$ is valid (the Liouville—Green approximation [30]). If $\Omega_0 \to +0$ (or, equivalently, $K \to -2 + 0$), then Eqs. (64), (65) result in

$$\bar{W}_0 = \frac{\bar{C}_0}{2\Omega_0^{1/2}} + o(1), \tag{81}$$

where $\bar{C}_0 = C_0/\sqrt{1 + M}$ is a constant. Hence, localized low-frequency oscillations with increasing amplitude precede the localized string buckling. On the other hand, unlike single degree of freedom system (79), for the system under consideration, formula (81) is valid only in the limiting case $\Omega_0 \to +0$. For finite $\Omega_0$ the dependence (65) is more complicated. Formulas (64), (65), coincide with formula (80) inside the whole interval $0 < \Omega_0 < 1$ of the admissible values for the trapped mode frequency $\Omega_0(T)$ only in the limiting case, where

$$M \gg 1, \tag{82}$$

and $K(T)$ is an uniformly bounded function: for all $T$ there exists a positive $\delta_0$ such that

$$-2 < K(T) < M - \delta_0. \tag{83}$$

Indeed, provided that conditions (82), (83) are true, using Eqs. (64), (65) and Eqs. (25), (32), respectively, one gets

$$\varOmega_0^2 = \frac{2}{M^2}\left(\sqrt{M^2 - MK + 1} + \frac{MK}{2} - 1\right) \sim \frac{K}{M}, \tag{84}$$

$$C_0\mathscr{A}(\varOmega_0) = \frac{C_0}{M^{1/2}} \frac{\left(1 - \varOmega_0^2\right)^{1/4}}{\varOmega_0^{1/2}\left(M^{-1} + \sqrt{1 - \varOmega_0^2}\right)^{1/2}} \sim \frac{\hat{C}_0}{\varOmega_0^{1/2}}, \tag{85}$$

where $\hat{C}_0 = C_0/\sqrt{M}$ is a constant. In terms of the original problem (1), (2) conditions (82), (83) are equivalent to the set of the following restrictions:

$$M_0 \gg \rho\sqrt{\frac{\mathscr{T}_0}{k_0}}, \qquad -2\sqrt{k_0\mathscr{T}_0} < K_0(T) < \left(\frac{M_0}{\rho}\sqrt{\frac{k_0}{\mathscr{T}_0}} - \delta_0\right)\sqrt{k_0\mathscr{T}_0}. \tag{86}$$

To compare the behavior of the system under consideration for various values of $M$ with the behavior of a single degree of freedom system it is very useful to consider the normalized amplitude function

$$\bar{\mathscr{A}}(\varOmega_0, \bar{\varOmega}_0, M) = \frac{\mathscr{A}(\varOmega_0, M)}{\mathscr{A}\left(\bar{\varOmega}_0, M\right)}. \tag{87}$$

Analogously, introduce the normalized amplitude function for a single degree of freedom system with time-varying stiffness

$$\bar{\mathscr{B}}(\varOmega_0, \bar{\varOmega}_0) = \frac{\bar{\varOmega}_0^{1/2}}{\varOmega_0^{1/2}}. \tag{88}$$

These curves describe the evolution of the normalized amplitude of the localized oscillations (with respect to initial value of the amplitude) for the corresponding systems wherein $\varOmega_0(0) = \bar{\varOmega}_0$. The plots of $\bar{\mathscr{A}}(\varOmega_0, \bar{\varOmega}_0, M)$ and $\bar{\mathscr{B}}(\varOmega_0, \bar{\varOmega}_0)$ against $\varOmega_0$ for different values of $M$ are given in Fig. 3, (a) $\bar{\varOmega}_0 = 0.1$, (b) $\bar{\varOmega}_0 = 0.9718$. One can see that in both cases the cyan lines corresponding to $\bar{\mathscr{A}}$ at $M = 100$ almost coincide (excepting a narrow left vicinity of the cut-off frequency $\varOmega_* = 1$) with the black dotted lines corresponding to $\bar{\mathscr{B}}$. This large enough value of $M$ corresponds to the limiting case (82). Decreasing of $M$ changes the behavior of the system under consideration to be farther from a single degree of freedom system with time-varying

**Fig. 3** Plots of functions $\bar{\mathscr{A}}(\Omega_0, \bar{\Omega}_0, M)$ (the color solid lines) and $\bar{\mathscr{B}}(\Omega_0, \bar{\Omega}_0)$ (the black dotted line), defined by Eqs. (87) and (88), respectively, against $\Omega_0$. (a) $\bar{\Omega}_0 = 0.1$, (b) $\bar{\Omega}_0 = 0.9718$

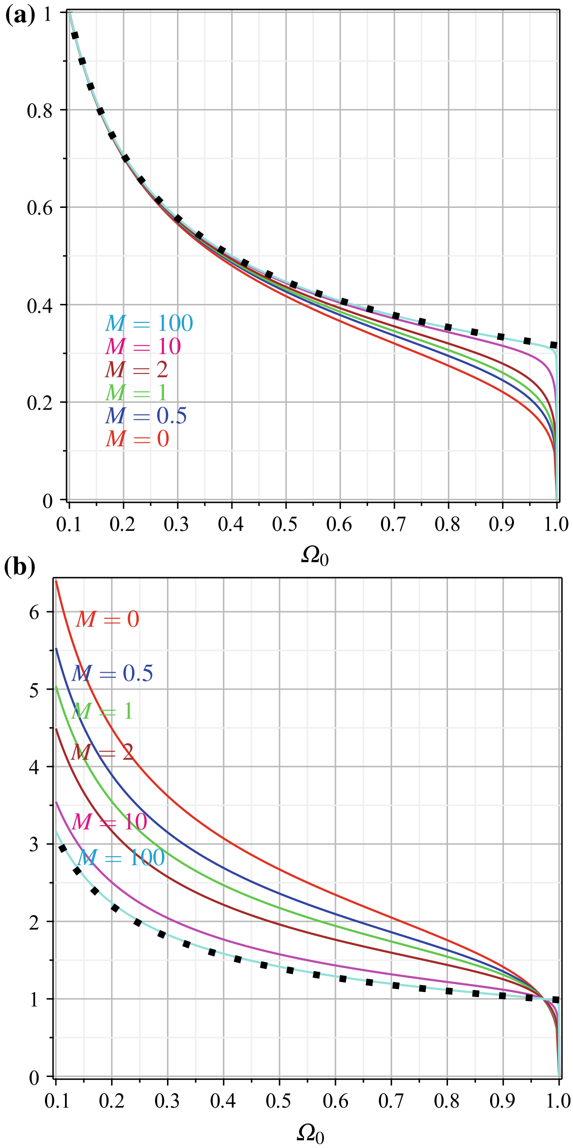

parameters. The special case $M = 0$ is the farthest one from a single degree of freedom system.

To demonstrate that numerics confirms our findings we take $M = 0.5$ and compare the analytical and numerical results obtained for the case of $p = \delta(\tau)$ and monotonically varying $K(\varepsilon\tau)$ (Figs. 4, 5).[5] Figure 4 corresponds to the case of increasing

---

[5] The case of oscillating properties is considered in [25] for a different, but similar problem.

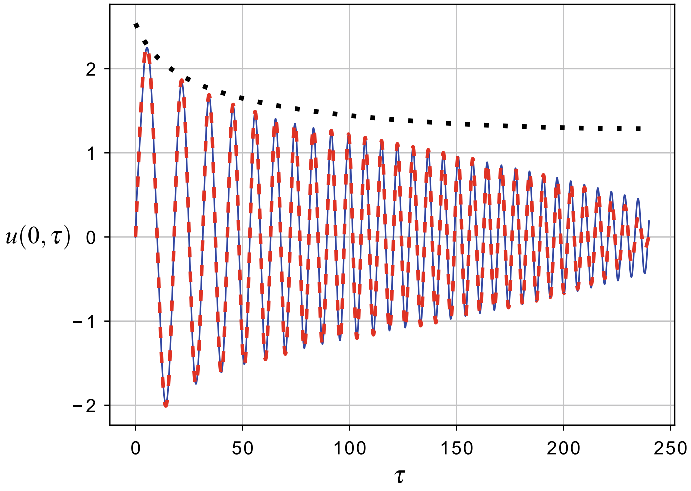

**Fig. 4** Comparing the analytical solution in the form of Eqs. (64), (65), (66), (69), (70) obtained for $p = \delta(\tau)$ (the red dashed line) and the numerical solution obtained for $p(\tau) = \tau_0^{-1}(H(\tau) - H(\tau - \tau_0))$ (the blue solid line) in the case $K(\varepsilon\tau) = -1.9 + \varepsilon\tau$. Here $M = 0.5$, $\varepsilon = 0.01$, $\tau_0 = 0.2$. At $\tau = 240$ the trapped mode frequency $\Omega_0(\varepsilon\tau)$ approaches the cut-off frequency $\Omega_* = 1$. The black dotted line corresponds to the evolution of the amplitude (80) in a single degree of freedom system with time-varying stiffness

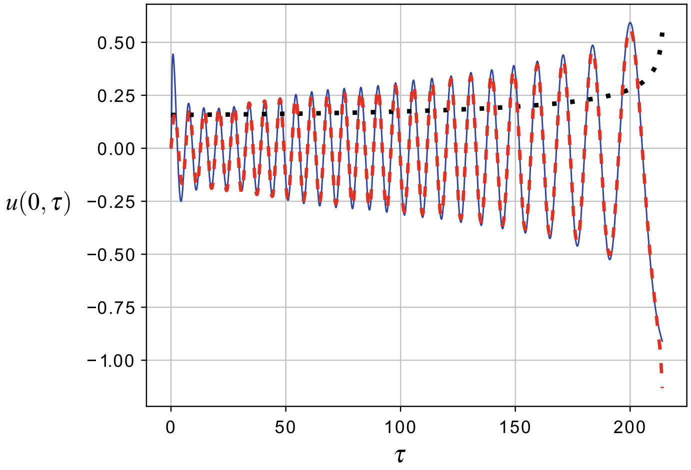

**Fig. 5** Comparing the analytical solution in the form of Eqs. (64), (65), (66), (69), (70) obtained for $p = \delta(\tau)$ (the red dashed line) and the numerical solution obtained for $p(\tau) = \tau_0^{-1}(H(\tau) - H(\tau - \tau_0))$ (the blue solid line) in the case $K(\varepsilon\tau) = 0.15 - \varepsilon\tau$. Here $M = 0.5$, $\varepsilon = 0.01$, $\tau_0 = 0.2$. The localized buckling occurs at $\tau = 215$. The black dotted line corresponds to the evolution of the amplitude (80) in a single degree of freedom system with time-varying stiffness

$K(\varepsilon\tau)$ and $\Omega_0(\varepsilon\tau)$, whereas Fig. 5 corresponds to the case of decreasing $K(\varepsilon\tau)$ and $\Omega_0(\varepsilon\tau)$. One can observe that the asymptotic solution (the red dashed line) approaches the numeric one (the blue solid line) very quickly (although the method of stationary phase yields reasonable results only after some time has passed). The black dotted line corresponds to the evolution of the amplitude (80) for a single degree of freedom system with time-varying stiffness.

In Fig. 4 one can observe that the asymptotic solution and the numerical one slightly diverge, when the trapped mode frequency $\Omega_0$ approaches the cut-off frequency $\Omega_* = 1$ (that corresponds to $K = 0.5$, $\tau = 240$). This is expectable, since the trapped mode exists only for $\Omega_0 < 1$. Moreover, for $\Omega_0 \to 1 - 0$ the finiteness of the string, assumed in the framework of numerics, becomes to be a very important factor. Thus, in our opinion, in the left vicinity of $\Omega_0 = 1$, where the asymptotic and numeric solutions diverge, we cannot trust in either of the solutions.

To consider the case of decreasing $K(\varepsilon\tau)$ and $\Omega_0(\varepsilon\tau)$ (Fig. 5) we take $K(0) = 0.15$ that corresponds to $\Omega_0(0) = 0.9718$ (this value is used in Fig. 3 (b)). One can observe that the asymptotic solution approaches the numeric one very quickly. The localized buckling occurs at $\tau = 215$ that corresponds to the critical value $K = -2$.

Finally, let us return to the beginning of Sect. 4 and formally

- put
$$W = W(T), \qquad W_j = W_j(T) \tag{89}$$
in Eqs. (41), (44);
- do not require that dispersion relation (17) at $\xi = \pm 0$ holds for all $\tau$.

Provided that $M > 0$, this simplified (and asymptotically inconsistent) procedure leads to the first approximation equation

$$2\Omega_0 \bar{W}_0{}'_T + \Omega_0{}'_T\, \bar{W}_0 = 0 \tag{90}$$

(instead of (61)) and formula (80) (instead of Eqs. (64), (65)) for a single degree of freedom system. In the special case $M = 0$ considered in [23], the first approximation equation has the form of Eq. (51) and cannot be obtained in such a way.

## 7 Conclusion

In the paper we have considered a localized oscillation of a string, lying on the Winkler foundation, and equipped with a discrete linear mass-spring oscillator of time-varying stiffness. The most important result is analytical formulas (64), (65), which allow us to describe the large time evolution of the amplitude of this oscillation. The obtained analytical results were verified by independent numerical calculations based on the finite difference method. The analysis shows us that the system under consideration behaves like a single degree of freedom system (79) with time-varying stiffness if and only if the oscillator mass is big enough (to be more precise, if and only if conditions (82), (83) are true). We also have demonstrated that simplified approach (see Eq. (89)) is asymptotically inconsistent and leads to formula (80) for a single degree of freedom system in all cases excepting the special case $M = 0$, wherein this approach becomes to be inapplicable.

## References

1. Ursell, F.: Trapping modes in the theory of surface waves. Math. Proc. Camb. Philos. Soc. **47**(2), 347–358 (1951)
2. Abramian, A., Andreyev, V., Indeitsev, D.: The characteristics of the oscillations of dynamical systems with a load-bearing structure of infinite extent. Modelirovaniye v mekhanike **6**(2), 3–12 (1992) (in Russian)
3. Kaplunov, J., Sorokin, S.: A simple example of a trapped mode in an unbounded waveguide. J. Acoust. Soc. Am. **97**, 3898–3899 (1995)
4. Abramyan, A., Indeitsev, D.: Trapping modes in a membrane with an inhomogeneity. Acoust. Phys. **44**, 371–376 (1998)
5. Gavrilov, S., Indeitsev, D.: The evolution of a trapped mode of oscillations in a "string on an elastic foundation—moving inertial inclusion" system. PMM J. Appl. Math. Mech. **66**(5), 825–833 (2002)
6. Alekseev, V., Indeitsev, D., Mochalova, Y.: Vibration of a flexible plate in contact with the free surface of a heavy liquid. Tech. Phys. **47**(5), 529–534 (2002)
7. Indeitsev, D., Osipova, E.: Localization of nonlinear waves in elastic bodies with inclusions. Acoust. Phys. **50**(4), 420–426 (2004)
8. Gavrilov, S.: The effective mass of a point mass moving along a string on a Winkler foundation. PMM J. Appl. Math. Mech. **70**(4), 582–589 (2006)
9. Porter, R.: Trapped waves in thin elastic plates. Wave Motion **45**(1–2), 3–15 (2007)
10. Kaplunov, J., Nolde, E.: An example of a quasi-trapped mode in a weakly non-linear elastic waveguide. Comptes Rendus Mécanique **336**(7), 553–558 (2008)
11. Motygin, O.: On trapping of surface water waves by cylindrical bodies in a channel. Wave Motion **45**(7–8), 940–951 (2008)
12. Nazarov, S.: Sufficient conditions on the existence of trapped modes in problems of the linear theory of surface waves. J. Math. Sci. **167**(5), 713–725 (2010)
13. Pagneux, V.: Trapped modes and edge resonances in acoustics and elasticity. In: Craster, R., Kaplunov, J. (eds.) Dynamic Localization Phenomena in Elasticity, Acoustics and Electromagnetism, pp. 181–223. Springer (2013)
14. Porter, R., Evans, D.: Trapped modes due to narrow cracks in thin simply-supported elastic plates. Wave Motion **51**(3), 533–546 (2014)
15. Gavrilov, S., Mochalova, Y., Shishkina, E.: Trapped modes of oscillation and localized buckling of a tectonic plate as a possible reason of an earthquake. In: 2016 IEEE Proceedings of the International Conferences Days on Diffraction (DD), pp. 161–165. IEEE (2016). https://doi.org/10.1109/DD.2016.7756834
16. Kaplunov, J., Rogerson, G., Tovstik, P.: Localized vibration in elastic structures with slowly varying thickness. Q. J. Mech. Appl. Math. **58**(4), 645–664 (2005)
17. Indeitsev, D., Kuznetsov, N., Motygin, O., Mochalova, Y.: Localization of Linear Waves. St. Petersburg University, Russian (2007)
18. Indeitsev, D., Sergeev, A., Litvin, S.: Resonance vibrations of elastic waveguides with inertial inclusions. Tech. Phys. **45**(8), 963–970 (2000)
19. Indeitsev, D., Abramyan, A., Bessonov, N., Mochalova, Y., Semenov, B.: Motion of the exfoliation boundary during localization of wave processes. Dokl. Phys. **57**(4), 179–182 (2012)
20. Wang, C.: Vibration of a membrane strip with a segment of higher density: analysis of trapped modes. Meccanica **49**(12), 2991–2996 (2014)

21. Indeitsev, D., Kuklin, T., Mochalova, Y.: Localization in a Bernoulli-Euler beam on an inhomogeneous elastic foundation. Vestn. St. Petersb. Univ. Math. **48**(1), 41–48 (2015)
22. Indeitsev, D., Gavrilov, S., Mochalova, Y., Shishkina, E.: Evolution of a trapped mode of oscillation in a continuous system with a concentrated inclusion of variable mass. Dokl. Phys. **61**(12), 620–624 (2016)
23. Gavrilov, S., Mochalova, Y., Shishkina, E.: Evolution of a trapped mode of oscillation in a string on the Winkler foundation with point inhomogeneity. In: 2017 IEEE Proceedings of the International Conferences Days on Diffraction (DD), pp. 128–133. IEEE (2017). https://doi.org/10.1109/DD.2017.8168010
24. Shishkina, E., Gavrilov, S., Mochalova, Y.: Non-stationary localized oscillations of an infinite bernoulli-euler beam lying on the winkler foundation with a point elastic inhomogeneity of time-varying stiffness. J. Sound Vib. **440C**, 174–185 (2019)
25. Gavrilov, S., Shishkina, E., Mochalova, Y.: Non-stationary localized oscillations of an infinite string, with time-varying tension, lying on the Winkler foundation with a point elastic inhomogeneity (2018). Nonlinear Dyn, 2019. https://doi.org/10.1007/s11071-018-04735-3
26. Kaplunov, J.: The torsional oscillations of a rod on a deformable foundation under the action of a moving inertial load. Izvestiya Akademii Nauk SSSR, MTT (Mechanics of solids) **6**, 174–177 (1986). (in Russian)
27. McIver, P., McIver, M., Zhang, J.: Excitation of trapped water waves by the forced motion of structures. J. Fluid Mech. **494**, 141–162 (2003)
28. Fedoruk, M.: The Saddle-Point Method. Nauka, Moscow (1977) (in Russian)
29. Nayfeh, A.: Introduction to Perturbation Techniques. Wiley (1993)
30. Nayfeh, A.: Perturbation Methods. Weily (1973)
31. Gao, Q., Zhang, J., Zhang, H., Zhong, W.: The exact solutions for a point mass moving along a stretched string on a Winkler foundation. Shock Vib. **2014**(136149) (2014)
32. Chronopoulos, D., Antoniadis, I., Collet, M., Ichchou, M.: Enhancement of wave damping within metamaterials having embedded negative stiffness inclusions. Wave Motion **58**, 165–179 (2015)
33. Pasternak, E., Dyskin, A., Sevel, G.: Chains of oscillators with negative stiffness elements. J. Sound Vib. **333**(24), 6676–6687 (2014)
34. Grekova, E.: Harmonic waves in the simplest reduced Kelvin's and gyrostatic media under an external body follower torque. In: 2018 IEEE Proceedings of the International Conferences Days on Diffraction (DD), pp. 142–148. IEEE (2018)
35. Oyelade, A., Wang, Z., Hu, G.: Dynamics of 1d mass-spring system with a negative stiffness spring realized by magnets: theoretical and experimental study. Theor. Appl. Mech. Lett. **7**(1), 17–21 (2017)
36. Huang, X., Liu, X., Sun, J., Zhang, Z., Hua, H.: Vibration isolation characteristics of a nonlinear isolator using euler buckled beam as negative stiffness corrector: a theoretical and experimental study. J. Sound Vib. **333**(4), 1132–1148 (2014)
37. Danh, L., Ahn, K.: Active pneumatic vibration isolation system using negative stiffness structures for a vehicle seat. J. Sound Vib. **333**(5), 1245–1268 (2014)
38. Li, Q., Zhu, Y., Xu, D., Hu, J., Min, W., Pang, L.: A negative stiffness vibration isolator using magnetic spring combined with rubber membrane. J. Mech. Sci. Technol. **27**(3), 813–824 (2013)
39. Wu, W., Chen, X., Shan, Y.: Analysis and experiment of a vibration isolator using a novel magnetic spring with negative stiffness. J. Sound Vib. **333**(13), 2958–2970 (2014)
40. Vladimirov, V.: Equations of Mathematical Physics. Marcel Dekker, New York (1971)
41. Gavrilov, S.: Non-stationary problems in dynamics of a string on an elastic foundation subjected to a moving load. J. Sound Vib. **222**(3), 345–361 (1999)
42. Feschenko, S., Shkil, N., Nikolenko, L.: Asymptotic Methods in Theory of Linear Differential Equations. North-Holland, NY (1967)
43. Donninger, R., Schlag, W.: Numerical study of the blowup/global existence dichotomy for the focusing cubic nonlinear Klein-Gordon equation. Nonlinearity **24**(9), 2547–2562 (2011)

44. Strauss, W., Vazquez, L.: Numerical solution of a nonlinear Klein-Gordon equation. J. Comput. Phys. **28**(2), 271–278 (1978)
45. Strikwerda, J.: Finite Difference Schemes and Partial Differential Equations, vol. 88. SIAM (2004)
46. Trangenstein, J.: Numerical Solution of Hyperbolic Partial Differential Equations. Cambridge University Press (2009)

# Reduced Enhanced Elastic Continua as Acoustic Metamaterials

**Elena F. Grekova**

**Abstract** We consider a linear complex elastic material whose body point motion is described by two vectorial generalised co-ordinates of any dimension. We suppose that the medium obeys Lagrange equations. Elastic energy depends on both of these vectorial generalised co-ordinates but does not depend on the gradient of one of them ("special" co-ordinate). Such a complex medium can be interpreted as a "bearing continuum" (corresponding to the non-special co-ordinate), whose body points are enhanced by body points of "continuum of dynamic absorbers" (corresponding to the special co-ordinate), the latter not connected directly between them. We obtain that under some restrictions for the strain energy bulk plane harmonic waves in this infinite medium have a band gap (or band gaps), the medium being thus a single negative acoustic metamaterial, and for some cases decreasing part(s) of dispersion curve, thus being a double negative acoustic metamaterial in this zone. We consider some examples of such continua with rotational degrees of freedom.

## 1 Introduction

Acoustic metamaterials are a popular direction of research nowadays [3–6, 16]. The medium is a single negative acoustic metamaterial in a certain frequency domain if harmonic waves with these frequencies do not propagate, and it is a double negative acoustic metamaterial if its dispersion curves have a decreasing part, i.e. if the frequency of harmonic wave decreases as the wave number increases. Acoustic metamaterials are a mechanical analogue of electromagnetic metamaterials, media with negative effective magnetic (electric) permettivity, whose existence was predicted by Veselago [21]. Acoustic metamaterials can be used, for instance, for noise reduction or for the control of wave beams, which can be important in applications. There are acoustic metamaterials of various kinds, among them those with rotational

---

E. F. Grekova (✉)
Institute of Problems of Mechanical Engineering, Russian Academy of Sciences,
Bolshoy pr. V.O., 61, 199178 St. Petersburg, Russia
e-mail: elgreco@pdmi.ras.ru

H. Altenbach et al. (eds.), *Dynamical Processes in Generalized Continua and Structures*, Advanced Structured Materials 103,
https://doi.org/10.1007/978-3-030-11665-1_14

degrees of freedom. Elastic and viscoelastic reduced Cosserat media, elastic reduced gyrocontinua, as well as other elastic **reduced continua**, whose strain energy depends on a certain generalised co-ordinate, but does not depend on its gradient, appear to be acoustic metamaterials, whose parameters in some cases can be controlled by means of external loading.

Among works on acoustic metamaterials one can mention [1, 2, 18]. Vasiliev and co-authors [20] have considered wave filters present in 2D Cosserat lattices. In work [15] it is shown that there exist a class of complex elastic media with band gaps, where these media act as single negative acoustic metamaterials. In this chapter we find another class of complex elastic media which appear to be acoustic metamaterials (single negative or double negative in different domains of frequencies). A body point of such a material may have many degrees of freedom.

In this chapter we generalise for $n$ dimensions work [9] for anisotropic continuum consisting of 3D "bearing" continuum enhanced by 3D "dynamic absorber" continuum, which appears to be an acoustic metamaterial. We also consider some examples of these media with rotational degrees of freedom.

The author is delighted to devote this work to Prof. Dmitri A. Indeitsev on the occasion of his 70th anniversary expressing her very best and warmest wishes. She is deeply grateful to Prof. Indeitsev for the fruitful discussions, for his interest to her work, for his scientific open-minded enthusiasm and care about his colleagues, which created and keeps the true scientific ambience in the IPME RAS.

## 2 Lagrange Equation for a Linear Reduced Elastic Continuum

Consider a linear continuum, whose body point's kinematics is described by scalar generalised co-ordinates $q_i$, $i = \overline{0, n}$. The body point may contain elements of various nature with elastic or rigid bonds: point masses, infinitesimal rigid bodies etc. All constraints are supposed to be holonomic and ideal. We suppose that this medium exists, i.e. the principle of material objectivity [17] is satisfied. We have to check it when we set a particular strain energy depending on certain generalised co-ordinates. The modified Lagrange equations of such a medium [14] can be written as follows

$$\frac{d}{dt}\frac{\partial L}{\partial \dot{q}_i} - \frac{\partial L}{\partial q_i} + \nabla \cdot \frac{\partial L}{\partial \nabla q_i} = 0 \tag{1}$$

Here $L = K - U$, $K$ is the mass density of the kinetic energy, $U$ is the mass density of the strain energy. In terms of vectorial generalised co-ordinates (of any dimension) we can write down the same equation as follows

$$\frac{d}{dt}\frac{\partial L}{\partial \dot{\mathbf{q}}} - \frac{\partial L}{\partial \mathbf{q}} + \nabla \cdot \frac{\partial L}{\partial \nabla \mathbf{q}} = \mathbf{0} \tag{2}$$

Here we have introduced a vector of generalised co-ordinates $\mathbf{q} = q_s \mathbf{i}^s$, where $\mathbf{i}^s$ is an orthonormal basis in the space of generalised co-ordinates, $s = 1, \ldots, n$. Let there exist a vectorial generalised co-ordinate $\mathbf{q}_0 = q_s^0 \mathbf{i}^s$, $s = 1, \ldots, n_0$, such that $U$ depends on it but does not depend on $\nabla \mathbf{q}_0$. Let us call such a generalised co-ordinate "special". For this generalised co-ordinate the last term in the left part of Eq. (2) is zero, and the form of Lagrange equations is the same as for the discrete system:

$$\frac{d}{dt}\frac{\partial L}{\partial \dot{\mathbf{q}}_0} - \frac{\partial L}{\partial \mathbf{q}_0} = \mathbf{0}, \tag{3}$$

where for the rest of generalised co-ordinates ("bearing" vectorial co-ordinate $\mathbf{q}_1$) it has its general form

$$\frac{d}{dt}\frac{\partial L}{\partial \dot{\mathbf{q}}_1} - \frac{\partial L}{\partial \mathbf{q}_1} + \nabla \cdot \frac{\partial L}{\partial \nabla \mathbf{q}_1} = \mathbf{0}. \tag{4}$$

Near its partial frequency the dynamics of the generalised co-ordinate $\mathbf{q}_0$ may start to prevail in the system. We can call this phenomenon "effect of the distributed dynamic absorber". Indeed, the medium can be considered now as the "bearing continuum", described by a generalised vectorial co-ordinate $\mathbf{q}_1 = q_s^1 \mathbf{i}^s$, $s = 1, \ldots, n_1$, on whose gradient $U$ depends, each body point of which is enhanced with another body point—complex dynamic absorber, whose kinematics is described by $\mathbf{q}_0$, but the dynamic absorbers are not connected between them (see Fig. 1). In this figure we show a simple example of the body point, but it may be very complex and have many degrees of freedom of different nature, depending on the concrete medium. Continuum, in which we have the special vectorial generalised co-ordinate—"dynamic absorber", we call the *reduced* continuum.

We will consider the linear case, i.e. we suppose $\mathbf{q}_0$, $\mathbf{q}_1$ and all their derivatives in space and time to be infinitesimal. Supposing this, we exclude from the consideration gyrocontinua [12], where the velocity of proper rotation is large, which results in the finite dynamic spin. We consider a particular case, when the mass densities of the elastic and kinetic energy of the linear reduced elastic material have the form

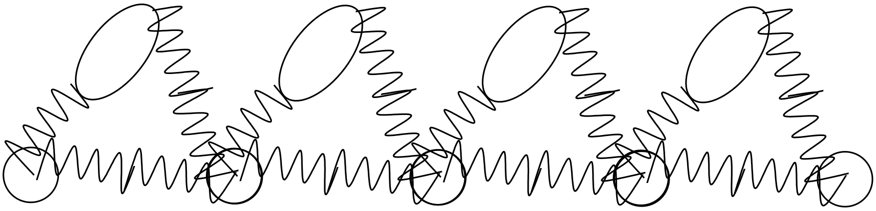

**Fig. 1** Reduced continuum. Continuum of mass centres of the spherical particles is the bearing continuum, rotations and translations of ellipsoidal particles form the special vectorial generalised co-ordinate—distributed dynamic absorber

$$\begin{aligned} U &= \nabla \mathbf{q}_1^\top \cdot\cdot {}^4\mathbf{K} \cdot\cdot \nabla \mathbf{q}_1/2 + C_{11}\mathbf{q}_1 \cdot \mathbf{q}_1/2 + \mathbf{q}_0 \cdot \mathbf{C}_{00} \cdot \mathbf{q}_0/2 + \\ &\qquad + \nabla \mathbf{q}_1^\top \cdot\cdot {}^3\mathbf{N}_{10} \cdot \mathbf{q}_0 + \mathbf{q}_1 \cdot \mathbf{C}_{10} \cdot \mathbf{q}_0, \\ K &= \dot{\mathbf{q}}_0 \cdot \mathbf{A}_{00} \cdot \dot{\mathbf{q}}_0/2 + A_{11}\dot{\mathbf{q}}_1 \cdot \dot{\mathbf{q}}_1/2. \end{aligned} \tag{5}$$

Here ${}^4\mathbf{K}, C_{11}, \mathbf{C}_{00}, \mathbf{N}_{10}, \mathbf{C}_{10}$ are elastic tensorial/scalar characteristics of the medium, $\mathbf{A}_{00}$, $A_{11}$ and $\mathbf{A}_{10}$ are inertial ones. We will require $\mathbf{C}_{00} = {\omega_0}^2\mathbf{A}_{00}$, i.e. the existence of the unique partial frequency $\omega_0$ of the special co-ordinate. Denote the partial frequency of the bearing co-ordinate $\omega_1 = \sqrt{C_{11}/A_{11}}$.

Dynamic equations (3), (4) for these densities of kinetic and strain energy $K, U$ look as follows:

$$\mathbf{A}_{00} \cdot (\ddot{\mathbf{q}}_0 + {\omega_0}^2\mathbf{q}_0) + \nabla \mathbf{q}_1^\top \cdot\cdot {}^3\mathbf{N}_{10} + \mathbf{q}_1 \cdot \mathbf{C}_{10} = \mathbf{0}, \tag{6}$$

$$A_{11}(\ddot{\mathbf{q}}_1 + \omega_1^2\mathbf{q}_1) + \mathbf{C}_{10} \cdot \mathbf{q}_0 - \nabla \cdot ({}^4\mathbf{K} \cdot\cdot \nabla \mathbf{q}_1 + {}^3\mathbf{N}_{10} \cdot \mathbf{q}_0) = \mathbf{0}. \tag{7}$$

We consider two cases:

(1) ${}^3\mathbf{N}_{10} \neq \mathbf{0}$, $\mathbf{C}_{10} = \mathbf{0}$;
(2) ${}^3\mathbf{N}_{10} = \mathbf{0}$, $\mathbf{C}_{10} \neq \mathbf{0}$.

The frequency $\omega_0$ is a characteristic frequency for the system in both these cases.

## 3 Motion at $\omega = \omega_0$. Regime of Independent Oscillators

(1) ${}^3\mathbf{N}_{10} \neq \mathbf{0}$, $\mathbf{C}_{10} = \mathbf{0}$. This case corresponds to the coupling in the elastic energy between two subcontinua which only couples the gradient of the bearing co-ordinate with the special (dynamic absorber) co-ordinate. Then at $\omega = \omega_0$ there exist a "regime of independent oscillators" $\mathbf{q}_1 \equiv \mathbf{0}$, $\mathbf{q}_0 = \mathbf{Q}_0 e^{i\omega t}$, if $\nabla \cdot ({}^3\mathbf{N}_{10} \cdot \mathbf{Q}_0) = \mathbf{0}$ (for instance, if $\mathbf{Q}_0$ does not depend on the point in space).

(2) ${}^3\mathbf{N}_{10} = \mathbf{0}$, $\mathbf{C}_{10} \neq \mathbf{0}$. In this case for non-degenerate $\mathbf{C}_{10}$ at $\omega = \omega_0$ there exist no $k$, even a complex one: equations of motion (6) and (7) give a trivial solution.

## 4 Dispersive Relations. Anisotropic Case

Let us look for the solution of (6), (7) in the form $\mathbf{q}_0 = \mathbf{Q}_0 e^{i(\mathbf{k}\cdot\mathbf{r}+\omega t)}$, $\mathbf{q}_1 = \mathbf{Q}_1 e^{i(\mathbf{k}\cdot\mathbf{r}+\omega t)}$. Here vectors $\mathbf{Q}_0, \mathbf{Q}_1$ have dimensions $n_0, n_1$, respectively. Then we have

$$(-\omega^2 + {\omega_0}^2)\mathbf{A}_{00} \cdot \mathbf{Q}_0 + \mathbf{Q}_1 \cdot (i\mathbf{k} \cdot {}^3\mathbf{N}_{10} + \mathbf{C}_{10}) = \mathbf{0}, \tag{8}$$

$$(\mathbf{k} \cdot {}^4\mathbf{K} \cdot \mathbf{k} + (-\omega^2 + \omega_1^2)A_{11}\mathbf{E}) \cdot \mathbf{Q}_1 + (\mathbf{C}_{10} - i\mathbf{k} \cdot {}^3\mathbf{N}_{10}) \cdot \mathbf{Q}_0 = \mathbf{0}. \tag{9}$$

Here $\mathbf{E}$ is the identity tensor. If $\omega \neq \omega_0$, and $\mathbf{A}_{00}$ is non-degenerate (i.e. all the generalised co-ordinates have inertia), we can express $\mathbf{Q}_0$ via $\mathbf{Q}_1$ from Eq. (8) and substitute this expression into (9):

$$\mathbf{Q}_0 = (\omega^2 - {\omega_0}^2)^{-1}\mathbf{A}_{00}^{-1} \cdot (\mathbf{C}_{10} + i\mathbf{k} \cdot {}^3\mathbf{N}_{10})^\top \cdot \mathbf{Q}_1, \tag{10}$$

$$\begin{aligned}(\mathbf{k} \cdot {}^4\mathbf{K} \cdot \mathbf{k} &+ (-\omega^2 + \omega_1^2)A_{11}\mathbf{E} + \\ &+ (\omega^2 - {\omega_0}^2)^{-1}(\mathbf{C}_{10} - i\mathbf{k} \cdot {}^3\mathbf{N}_{10}) \cdot \mathbf{A}_{00}^{-1} \cdot (\mathbf{C}_{10} + i\mathbf{k} \cdot {}^3\mathbf{N}_{10})^\top) \cdot \mathbf{Q}_1 = \mathbf{0}.\end{aligned} \tag{11}$$

Equation (11) is a reduced spectral problem for the "bearing" generalised co-ordinate $\mathbf{q}_1$.

### 4.1 Coupling Between the Gradient of the Bearing Co-ordinate and Special (Dynamic Absorber) Co-ordinate ($\mathbf{C}_{10} = \mathbf{0}$). Band Gaps and Decreasing Parts of Dispersion Curves for the Plane Waves

If $\mathbf{C}_{10} = \mathbf{0}$ and $\omega \neq \omega_0$, we can write the reduced spectral problem (7) as follows

$$(A_{11}(\omega_1^2 - \omega^2)\mathbf{E} + k^2(\boldsymbol{\kappa} + (\omega^2 - \omega_0^2)^{-1}\boldsymbol{\nu})) \cdot \mathbf{Q}_1 = \mathbf{0}, \tag{12}$$

where

$$\boldsymbol{\kappa} = \hat{\mathbf{k}} \cdot \mathbf{K} \cdot \hat{\mathbf{k}}, \qquad \boldsymbol{\nu} = \hat{\mathbf{k}} \cdot \mathbf{N}_{10} \cdot \mathbf{A}_{00}^{-1} \cdot (\hat{\mathbf{k}} \cdot \mathbf{N}_{10})^\top \overset{\text{def}}{=} \nu_i \mathbf{e}_i\, \mathbf{e}_i, \tag{13}$$

$\mathbf{e}_i$ being an orthonormal basis, formed by eigen vectors $\boldsymbol{\nu}$, $\nu_i \geqslant 0, i = 1, \ldots, n_1$ being the eigen values of the tensor $\boldsymbol{\nu}$, depending on the elastic and inertial characteristics and the direction of wave propagation.

Let us consider approximations for the dispersional relation near $\omega_0$ and near $\omega_1$. In the vicinity of $\omega_0$ at $\omega_0 \neq \omega_1$, $\nu_i > 0$, the dispersional curves look as

$$k_i^2 \approx (\omega - \omega_0)2A_{11}\omega_0(\omega_0^2 - \omega_1^2)/\nu_i. \tag{14}$$

Indeed, at $\omega \to \omega_0$ the eigen values of $\boldsymbol{\kappa}$ are much less than $\nu_i/(\omega^2 - {\omega_0}^2)$, and the spectral problem (12) can be written as

$$(A_{11}(\omega_1^2 - \omega^2)\mathbf{E} + k^2((\omega^2 - \omega_0^2)^{-1}\boldsymbol{\nu})) \cdot \mathbf{Q}_1 = \mathbf{0}, \tag{15}$$

which results in (14). If the direction of wave propagation is not a special direction for inertial and elastic tensors, i.e. if $\nu_i > 0$, then all the $n_1$ dispersion curves have a band gap, limited by $\omega_0$ (below $\omega_0$ if $\omega_0 > \omega_1$, and above it if $\omega_0 < \omega_1$). Tensor $\boldsymbol{\nu}$ will be non-degenerate if the elastic tensor $\mathbf{N}_{10}$ participating in the coupling will have a sufficiently low group of symmetry. (For the case $\omega_0 = \omega_1$ we obtain $k_i^2 \approx A_{11}(\omega^2 - \omega_0^2)2/\nu_i$ in the vicinity of this frequency, i.e. there is no band gap.)

In the vicinity of $\omega_1$, on the contrary, $A_{11}(\omega_1^2 - \omega^2)$ is much less then eigen values of the tensor $\boldsymbol{\kappa} + (\omega_1^2 - {\omega_0}^2)^{-1}\boldsymbol{\nu}$, if only the parameters are not chosen in such a way that this tensor is degenerate. For this reason in the vicinity of $\omega_1$ we have $k \approx 0$, more exactly,

$$\omega - \omega_1 \approx k^2 \frac{\xi_i}{2\omega_1}, \tag{16}$$

where $\xi_i$, $i = 1, \ldots, n_1$ are eigen vectors of the tensor $\boldsymbol{\kappa} + \boldsymbol{\nu}/(\omega_1^2 - {\omega_0}^2)$. Thus the sign of $k^2$ also changes when $\omega$ passes through $\omega_1$. Depending on the sign of $\xi_i$ the band gap is situated just below or just above $\omega_1$.

Performing a detailed asympthotical analysis, we obtain that at $\omega_0 < \omega_1$ band gaps (or band gap) are situated below $\omega_1$ and above $\omega_0$, where the medium is a single negative acoustic metamaterial, and that there is a decreasing part of the dispersion curve just below $\omega_0$, where the medium is a double negative acoustic metamaterial.

In the case $\omega_0 > \omega_1$, if both characteristic frequencies are sufficiently close to each other, or if the coupling between the bearing generalised co-ordinate and the dynamic absorber (special generalised co-ordinate) is strong enough, band gap(s) is (are) situated between these $\omega_1$ and $\omega_0$, and there is a decreasing part of dispersion curve just below $\omega_1$.

If partial frequencies are equal to each other ($\omega_0 = \omega_1$), then the band gap near $\omega_0$ is absent, but we have a decreasing part of dispersion curve just below $\omega_0$: the medium is a double negative metamaterial in this zone. In the opposite case there are two band gaps, just below of each of partial frequencies $\omega_0$, $\omega_1$.

## 4.2 *Coupling Between Bearing Generalised Co-ordinate and Special (Dynamic Absorber) Generalised Co-ordinates* ($\mathbf{N_{10} = 0}$). *Band Gaps and Decreasing Parts of Dispersion Curves for the Plane Waves*

The spectral problem (10), (11) in this case looks as follows:

$$(A_{11}(\omega_1^2 - \omega^2)\mathbf{E} - (\omega^2 - \omega_0^2)^{-1}\mathbf{C}_{10} \cdot \mathbf{A}_{00}^{-1} \cdot \mathbf{C}_{10}^{\top} + k^2\boldsymbol{\kappa}) \cdot \mathbf{Q}_1 = \mathbf{0}, \tag{17}$$

$$\mathbf{Q}_0 = -\mathbf{A}_{00}^{-1} \cdot \mathbf{C}_{10}^{\top} \cdot \mathbf{Q}_0/(\omega^2 - \omega_0^2). \tag{18}$$

Near $\omega_0$ we have $n_1$ dispersion curves with the band gap just above $\omega_0$:

$$k^2 = -\frac{\chi_i}{\omega^2 - {\omega_0}^2}. \tag{19}$$

Here $\chi_i$, $i = 1, \ldots, n_1$ are the eigenvalues of tensor $\boldsymbol{\kappa}^{-1/2} \cdot \mathbf{C}_{10} \cdot \mathbf{A}_{00} \cdot \mathbf{C}_{10}^{\top} \cdot \boldsymbol{\kappa}^{-1/2}$, they are non-negative if the strain energy is non-negatively defined. We consider the case when they are not zero. An isotropic material with 3D bearing and 3D special generalised co-ordinates has two band gaps [8].

# 5 Dispersional Relations for an Isotropic Material with 3D Vectorial Bearing and Special (Dynamic Absorber) Isotropic Generalised Co-ordinates

Several results of this section (concerning shear waves) can be found in [8], but we repeat them shortly here for the sake of completeness. For an isotropic material, whose body point is characterised by 3D vectorial special and bearing generalised co-ordinates, we have

$$\mathbf{A}_{00} = A_{00}\mathbf{E}, \quad \mathbf{C}_{10} = C_{10}\mathbf{E}, \quad \mathbf{N} = N\mathbf{E}\times\mathbf{E}, \tag{20}$$

$$\mathbf{K} = \lambda\mathbf{E}\mathbf{E} + 2\mu(\mathbf{i}^m\mathbf{i}^n)^S(\mathbf{i}_m\mathbf{i}_n)^S + 2\alpha(\mathbf{i}^m\mathbf{i}^n)^A(\mathbf{i}_m\mathbf{i}_n)^A, \tag{21}$$

where $\mathbf{i}_m$ is an orthonormal basis. The equations of motion for this medium are

$$A_{00}(\ddot{\mathbf{q}}_0 + \omega_0^2\mathbf{q}_0) - N\nabla\times\mathbf{q}_1 + C_{10}\mathbf{q}_1 = \mathbf{0}, \tag{22}$$

$$\begin{aligned} A_{11}\ddot{\mathbf{q}}_1 + C_{11}\mathbf{q}_1 + C_{10}\mathbf{q}_0 - (\lambda+2\mu)\nabla\nabla\cdot\mathbf{q}_1 + (\mu+\alpha)\nabla\times(\nabla\times\mathbf{q}_1)& \\ -N\nabla\times\mathbf{q}_0 = \mathbf{0}.& \end{aligned} \tag{23}$$

As in the general (anisotropic) case, discussed in the previous section, at $C_{10} = 0$, $N \neq 0$ there exists a regime $\mathbf{q}_1 \equiv \mathbf{0}$, $\mathbf{q}_0 = \mathbf{Q}_0 e^{i\omega_0 t}$, if $\nabla\times\mathbf{Q}_0 = \mathbf{0}$. If $N = 0$, $C_{10} \neq 0$, on the contrary, for $\omega = \omega_0$ there exists only a trivial solution.

The spectral problem (10), (11) can be written as follows:

$$\mathbf{Q}_0 = \frac{-iN\mathbf{k}\times\mathbf{Q}_1 + C_{10}\mathbf{Q}_1}{A_{00}(\omega^2 - {\omega_0}^2)}, \tag{24}$$

$$\begin{aligned} &(A_{11}(\omega_1^2 - \omega^2) + \frac{C_{10}^2}{A_{00}}\frac{1}{\omega^2 - {\omega_0}^2})\mathbf{Q}_1 + (\lambda+2\mu)\mathbf{k}\mathbf{k}\cdot\mathbf{Q}_1 + \\ &\quad -(\mu+\alpha+\frac{N^2}{A_{00}}\frac{1}{\omega^2-{\omega_0}^2})\mathbf{k}\times(\mathbf{k}\times\mathbf{Q}_1) - i\frac{NC_{10}}{A_{00}}\frac{1}{\omega^2-{\omega_0}^2}\mathbf{k}\times\mathbf{Q}_1 = \mathbf{0}. \end{aligned} \tag{25}$$

## 5.1 *Longitudinal Wave*

Note that the reduced spectral problem (25) allows us to obtain the dispersion relation for the longitudinal wave:

$$c_p^2k^2 = \omega^2 - \omega_1^2 - \frac{\hat{\omega}^4}{\omega^2 - {\omega_0}^2} = \frac{(\omega^2 - \omega_+^2)(\omega^2 - \omega_-^2)}{\omega^2 - {\omega_0}^2}. \tag{26}$$

Here

$$c_p^2 = \frac{\lambda + 2\mu}{A_{11}}, \quad \hat{\omega}^4 = \frac{C_{10}^2}{A_{00}A_{11}}, \tag{27}$$

expressions for $\omega_+$, $\omega_-$ are given by formulae (28), (29), and $\omega_- < \omega_0 < \omega_+$. In the case when all the inertial and elastic characteristics participating in this equation are not equal to zero, we have a band gap with the lower boundary $\omega_0$. The dispersion curve approaches from below the asymptote $\omega = \omega_0$. If the strain energy is positively defined with respect to $\mathbf{q}_0$, $\mathbf{q}_1$, we have $C_{10}^2 < C_{11}C_{00}$, and we obtain then ${\omega_0}^2\omega_1^2 > \hat{\omega}^4$. It means that $k^2 < 0$ at $\omega = 0$, thus there exist a cut-off frequency, and the plane wave has two band gaps, where the medium is a single negative acoustic metamaterial with respect to the longitudinal waves.

After calculations we obtain: $k^2 \geqslant 0$ either if

$$\omega \geqslant \omega_+ = \left(\frac{\omega_0^2 + \omega_1^2}{2} + \sqrt{D}\right)^{1/2}, \text{ or if} \tag{28}$$

$$\omega_- = \left(\frac{\omega_0^2 + \omega_1^2}{2} - \sqrt{D}\right)^{1/2} \leqslant \omega < \omega_0, \quad \text{where} \tag{29}$$

$$D = \left(\frac{\omega_0^2 - \omega_1^2}{2}\right)^2 + \hat{\omega}^4, \tag{30}$$

$$\omega_0 < \omega_+, \quad 0 < \omega_-. \tag{31}$$

The graph of dispersion relation is shown in Fig. 2. It looks in this way if $C_{10} \neq 0$. Otherwise $\hat{\omega} = 0$, $\omega_- = \omega_0$, $\omega_+ = \omega_1$, and we have only one branch with the cut-off frequency $\omega_0$. Note that this relation does not depend on modulus $N$ responsible for the coupling between $\nabla\mathbf{q}_1$ and $\mathbf{q}_0$.

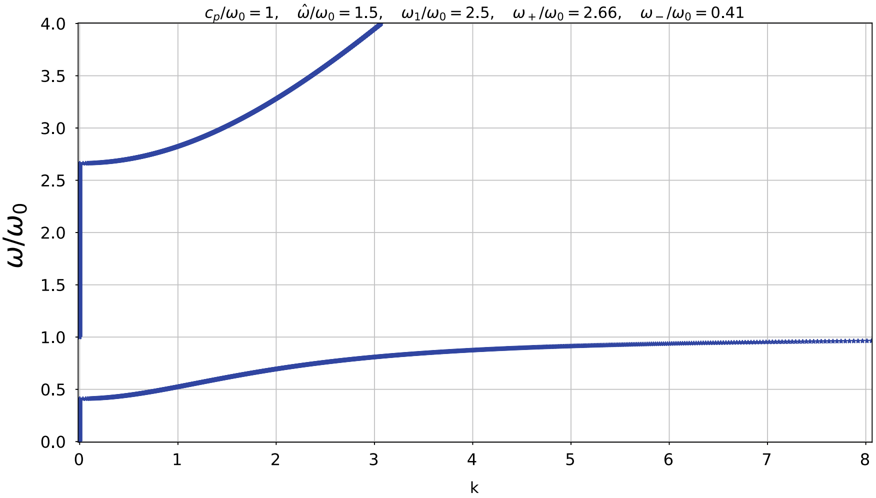

**Fig. 2** Dispersion relation for the longitudinal wave in the isotropic material with 3D bearing and 3D dynamic absorber generalised co-ordinates (with both coupling terms)

There exist two band gaps: $[0; \omega_-)$ and $[\omega_0; \omega_+)$. We have $k \to +\infty$ at $\omega \to \omega_0 - 0$, and $\omega \to c_p k$ at $k \to \infty$. We will discuss here shear waves in two particular cases.

## 5.2 Shear Plane Waves at $C_{10} = 0$

As it is easy to see from Eq. (26), the dispersion curve for the longitudinal wave in the isotropic material at $C_{10} = 0$, $C_{11} \neq 0$ is a parabola $\omega^2 = c_p^2 k^2 + \omega_1^2$. If we have $C_{11} = 0$, then the longitudinal wave is non-dispersive. The reduced spectral problem (25) for shear waves at $C_{10} = 0$ takes form

$$[A_{11}(\omega_1^2 - \omega^2) + k^2(\mu + \alpha + \frac{N^2}{A_{00}} \frac{1}{\omega^2 - {\omega_0}^2})](\mathbf{E} - \hat{\mathbf{k}}\hat{\mathbf{k}}) \cdot \mathbf{Q}_1 = \mathbf{0}. \tag{32}$$

Thus the dispersional relation for the shear wave is

$$k^2 = \frac{A_{11}}{\mu + \alpha} \frac{(\omega^2 - \omega_1^2)(\omega^2 - {\omega_0}^2)}{\omega^2 - \omega_*^2}, \tag{33}$$

where $\omega_*^2 = {\omega_0}^2 - N^2/((\mu + \alpha)A_{00})$. Graphs for shear dispersion relations are shown in Fig. 3. There are two band gaps, where the continuum is a single negative acoustic metamaterial with respect to the shear waves. It holds $\omega_* < \omega_0$. For sufficiently large value of $N$, responsible for the coupling of the bearing and special (dynamic absorber) generalised co-ordinates, when $\omega_* < \omega_1$, there appears a

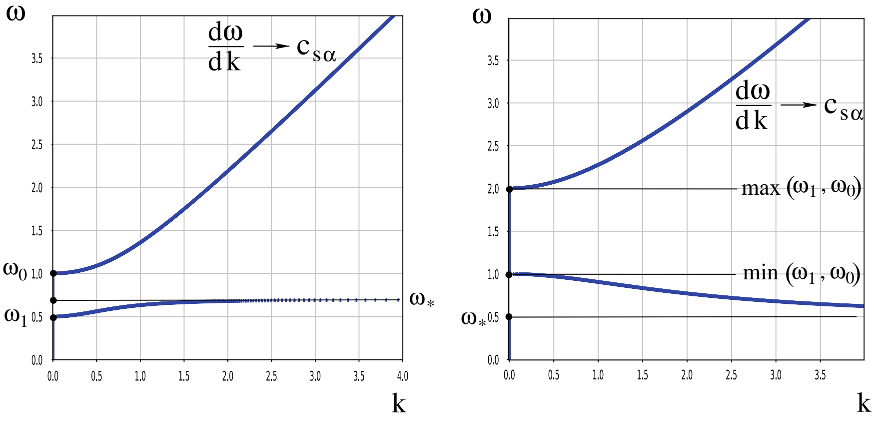

**Fig. 3** Dispersion curves for the shear wave in the isotropic material, $C_{10} = 0$. Frequency $\omega_* < \omega_0$ decreases when the coupling between bearing and dynamic absorber generalised co-ordinates increases. $c_{s\alpha}^2 = (\mu + \alpha)/A_{11}$. Numerical example for $c_{s\alpha} = 1$, $\omega_0 = 1$, left: $\omega_1 = 0.5$, $\omega_* = 0.7$, right: $\omega_1 = 2$, $\omega_* = 0.5$

decreasing part of dispersion curve, where the continuum is a double negative acoustic metamaterial for shear waves (right part of the figure).

## *5.3 Shear Plane Waves at $N = 0$*

Note that the longitudinal wave in the isotropic material does not depend on the elastic modulus $N$, determining the coupling term of the special (dynamic absorber) co-ordinate and the gradient of the bearing co-ordinate. The dispersion relation in this case coincides with the expression (26).

The reduced spectral problem for shear waves can be obtained from (25):

$$(\omega_1^2 - \omega^2 + \frac{\hat{\omega}^4}{\omega^2 - {\omega_0}^2})(\mathbf{E} - \hat{\mathbf{k}}\hat{\mathbf{k}}) \cdot \mathbf{Q}_1 - c_{s\alpha}^2 \mathbf{k} \times (\mathbf{k} \times \mathbf{Q}_1) = \mathbf{0}. \tag{34}$$

Thus we obtain the dispersion relation

$$c_{s\alpha}^2 k^2 = \omega^2 - \omega_1^2 + \frac{\hat{\omega}^4}{\omega^2 - {\omega_0}^2} = \frac{(\omega^2 - \omega_+^2)(\omega^2 - \omega_-^2)}{\omega^2 - {\omega_0}^2}. \tag{35}$$

It coincides with the dispersion relation for the longitudinal wave (26) with the only difference: characteristic speed $c_p$ (the velocity of the longitudinal wave at high frequencies) has to be changed for the velocity $c_{s\alpha}$ (the speed of the shear wave

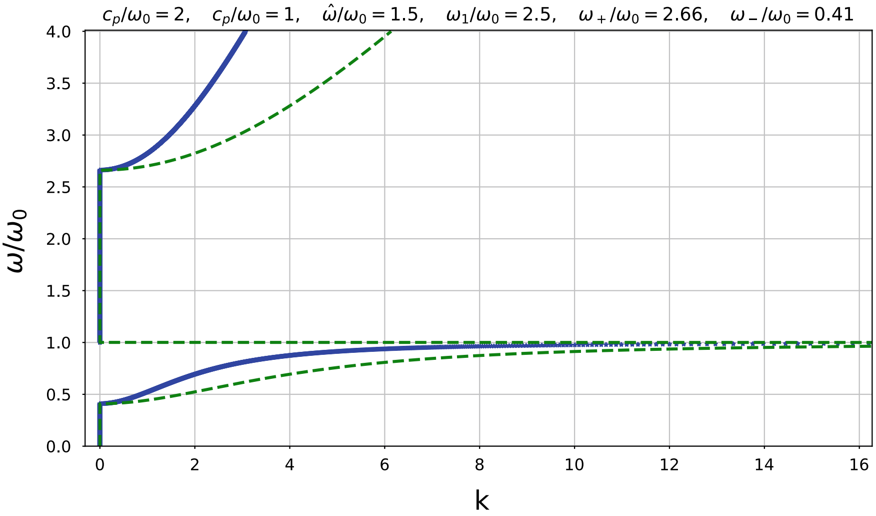

**Fig. 4** Dispersion curves for an isotropic material, $\mathbf{N}_{10} = \mathbf{0}$. Cut-off frequencies $\omega_-$ and $\omega_+$ are determined by medium parameters, $\omega_- - \omega_+$ increases as the coupling increases. Solid line corresponds to the longitudinal plane wave, dashed line to the transversal one (if $c_p > c_{s\alpha}$)

at high frequencies). Band gaps for both waves are the same. In these domains of frequencies the medium is a single negative acoustic metamaterial with respect to all waves. Their dispersion curves are shown in Fig. 4.

# 6 Reduced Continua with Rotational Degrees of Freedom

## 6.1 *Linear Reduced Cosserat Medium as an Example of a Single Negative Acoustic Metamaterial with $C_{10} = 0$*

Reduced linear elastic isotropic Cosserat medium is an example of a reduced continuum considered in previous sections. Its equations were suggested for the first time in [19]. Waves in this medium were investigated, in particular, in [13]. In this section we give only the results to illustrate the idea of the reduced continua as acoustic metamaterials.

Reduced Cosserat medium can serve as a model for soils and granular media in elastic domain. Each body point of this medium is an infinitesimal rigid body performing translational and rotational motions. Turns and translations are independent, however, this medium does not react to the gradient of turn. Let $\mathbf{u}, \boldsymbol{\theta}$ be vectors of infinitesimal translations and turns, respectively. In the elastic isotropic reduced linear Cosserat medium with spherical density of the inertia tensor $I\mathbf{E}$

$$K = \frac{1}{2}(\rho \dot{\mathbf{u}}^2 + I\dot{\boldsymbol{\theta}}^2), \tag{36}$$

$$U = \frac{1}{2}(\nabla \mathbf{u})^S \cdot\cdot (\lambda \mathbf{EE} + 2\mu(\mathbf{i}^m \mathbf{i}^n)^S (\mathbf{i}^m \mathbf{i}^n)^S) \cdot\cdot (\nabla \mathbf{u})^S + \frac{1}{2}\alpha(\boldsymbol{\theta} - \nabla \times \mathbf{u}/2)^2. \tag{37}$$

This medium is an example of the material considered in Sect. 5.2. In this medium $\omega_1 = 0$, so the first cut-off frequency is absent, and in this particular case the group velocity at $\omega = \omega_1 = 0$ is different from zero, contrary to the media with non-zero $\omega_1$. The longitudinal wave is the same as in the classical medium (again contrary to other media of this type with $\omega_1 \neq 0$), and the wave of shear–rotation obeys the dispersion relation

$$k^2 = \frac{\omega^2}{c_S^2} \frac{(1 - \omega^2/\omega_0^2)}{(1 - \omega^2/\omega_*^2)}, \tag{38}$$

whose graph is presented in Fig. 5. Here $c_s^2 = \mu/\rho$, $c_{s\alpha}^2 = (\mu + \alpha)/\rho$, $\omega_0^2 = 4\alpha/I$, $\omega_*^2 = \omega_0^2/(1 + \alpha/\mu)$.

The regime of “independent oscillators” exists at $\omega = \omega_0$, $\nabla \times \boldsymbol{\Theta}_0 = \mathbf{0}$.

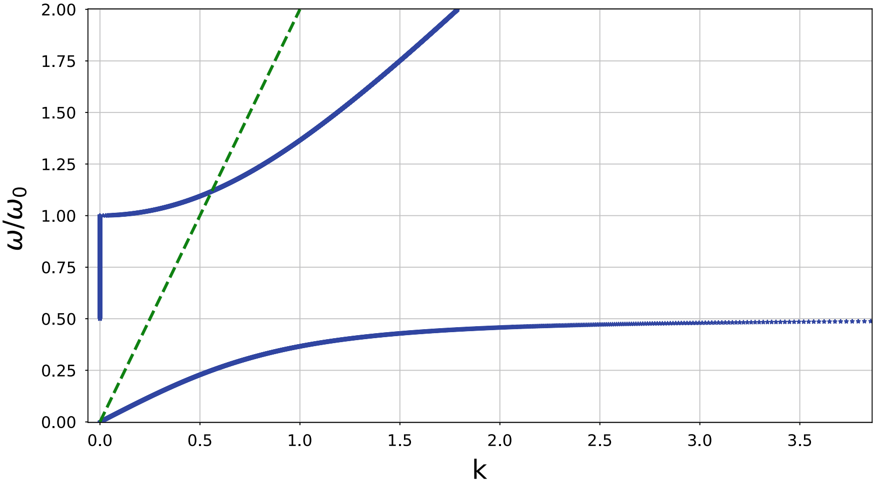

**Fig. 5** Dispersion curves of the elastic linear isotropic reduced Cosserat medium ($\omega_1 = 0, C_{10} = 0$). A numerical example for $\omega_* = 0.5\omega_0$, $c_p = 2$, $c_{s\alpha} = 1$. Shear wave: solid line, pressure wave: dashed line. The group velocity at $\omega = 0$ is not zero, contrary to the case $\omega_1 \neq 0$

## 6.2 *Birotational Material with an Anisotropic Coupling Between the Special Co-ordinate and the Gradient of the Bearing Co-ordinate*

Consider the medium whose body point contains two infinitesimal rigid bodies (two subparticles) with spherical tensors of inertia $I_0\mathbf{E}$, $I_1\mathbf{E}$, connected by elastic spiral springs with the rigid continuum of mass centres. Denote infinitesimal vectors of turn of subparticles $\boldsymbol{\theta}_0, \boldsymbol{\theta}_1$.

Let the densitites of the kinetic and elastic energy of the material be

$$K = \frac{1}{2}(I_0\dot{\boldsymbol{\theta}}_0^{\,2} + I_1\dot{\boldsymbol{\theta}}_1^{\,2}), \tag{39}$$

$$U = \frac{\kappa}{2}(\nabla \cdot \boldsymbol{\theta}_1)^2 + \frac{1}{2}(c_0\boldsymbol{\theta}_0^2 + c_1\boldsymbol{\theta}_1^2) + N\nabla \cdot \boldsymbol{\theta}_1\mathbf{n} \cdot \boldsymbol{\theta}_0. \tag{40}$$

Here $\mathbf{K} = \kappa\mathbf{EE}$, $\mathbf{N} = N\mathbf{En}$. Condition $U \geqslant 0$ is fulfilled if $\kappa c_0 \geqslant N^2$.

Dynamic equations of such a material look as follows:

$$I_0\ddot{\boldsymbol{\theta}}_0 + c_0\boldsymbol{\theta}_0 + N\nabla \cdot \boldsymbol{\theta}_1\mathbf{n} = \mathbf{0}, \tag{41}$$

$$I_1\ddot{\boldsymbol{\theta}}_1 + c_1\boldsymbol{\theta}_1 - \kappa\nabla\nabla \cdot \boldsymbol{\theta}_1 - N\nabla\boldsymbol{\theta}_0 \cdot \mathbf{n} = \mathbf{0}. \tag{42}$$

Looking for their solution in the form $\boldsymbol{\theta}_{1,2} = \boldsymbol{\Theta}_{1,2}e^{i(\omega t+\mathbf{k}\cdot\mathbf{r})}$, we obtain the spectral problem:

$$
\begin{aligned}
&((\omega^2-\omega_0^2)(\omega^2-\omega_1^2)(\mathbf{E}-\hat{\mathbf{k}}\hat{\mathbf{k}})\\
&\qquad\qquad +((\omega^2-\omega_0^2)(\omega^2-\omega_1^2)-k^2\kappa(\omega^2-\omega_*^2)/I_1)\hat{\mathbf{k}}\hat{\mathbf{k}})\cdot\boldsymbol{\Theta}_1=\mathbf{0}.\\
&I_0(\omega_0^2-\omega^2)\boldsymbol{\Theta}_0=-i\mathbf{n}\,\mathbf{k}\cdot\boldsymbol{\Theta}_1 N
\end{aligned}
$$

Here $\omega_0^2 > \omega_*^2 \overset{\mathrm{def}}{=} \omega_0^2 - N^2/(\kappa I_0) \geqslant 0$ since $U \geqslant 0$.

There exist two regimes of "independent oscillators":

(1) $\omega = \omega_0, \boldsymbol{\theta}_1 = \mathbf{0}, \boldsymbol{\theta}_0 = \boldsymbol{\Theta}_0 e^{i\omega_0 t}$, where $\nabla\boldsymbol{\Theta}_0 \cdot \mathbf{n} = \mathbf{0}$, and
(2) $\omega = \omega_1, \boldsymbol{\theta}_0 = \mathbf{0}, \boldsymbol{\theta}_1 = \boldsymbol{\Theta}_1 e^{i\omega_1 t}$, where $\nabla \cdot \boldsymbol{\Theta}_1 = \mathbf{0}$. Shear waves in such a material do not propagate, the last regimes corresponds to the degenerate transverse wave.

For the longitudinal wave $\boldsymbol{\Theta}_1 = \Theta_1\hat{\mathbf{k}}, \quad \boldsymbol{\Theta}_0 = -iNk\Theta_1\mathbf{n}, \quad c_p^2 = \kappa/I_1$, and the dispersion relation is

$$
(c_p k)^2 = \frac{(\omega^2-\omega_0^2)(\omega^2-\omega_1^2)}{\omega^2-\omega_*^2}. \tag{43}
$$

The graph of the dispersion relation is presented in Fig. 3, since it is the same as for the transverse wave in the isotropic case.

The same dispersion relation is true for the isotropic nonlinear elastic Cosserat reduced medium in the vicinity of the nonlinear isotropic prestressed state [7]. Effective elastic constants depend on the first and second derivatives of the nonlinear strain energy with respect to the nonlinear strain tensors in the prestressed state. Changing the pressure or tension in such a material, we may partially control the band gap.

Linear elastic reduced Cosserat continuum with axisymmetric coupling between volumetric and vortex deformations is also a single negative acoustic metamaterial (in corresponding domains of frequencies) with respect to all the waves, with exception of waves propagating orthogonal to the axis of symmetry, for certain domain of parameters [10]. The medium with isotropic elastic tensors and anisotropic tensor of inertia has more band gaps [11].

### 6.3 Birotational Isotropic Material as an Example of the Single Negative Acoustic Metamaterial with $N_{10} = 0$

Consider the medium whose body point contains two infinitesimal rigid bodies (two subparticles) with spherical inertia tensors, and their centres of mass are fixed. Denote the densities of tensors of inertia $I_0\mathbf{E}$, $I_1\mathbf{E}$. Subparticles are attached by elastic spiral springs to the continuum of centres of mass of body points. Denote vectors of infinitesimal turn of subparticles $\boldsymbol{\theta}_0, \boldsymbol{\theta}_1$. Elastic interaction between subparticles is determined by the elastic constant $C_{10}$.

Let the densities of kinetic ($K$) and elastic ($U$) energies equal

$$K = \frac{1}{2}(I_0\dot{\boldsymbol{\theta}}_0^2 + I_1\dot{\boldsymbol{\theta}}_1^2), \tag{44}$$

$$U = \frac{1}{2}\nabla\boldsymbol{\theta}_1 \cdot\cdot (\lambda\mathbf{E}\mathbf{E} + 2\mu(\mathbf{i}_m\mathbf{i}_n)^S(\mathbf{i}_m\mathbf{i}_n)^S + 2\alpha(\mathbf{i}_m\mathbf{i}_n)^A(\mathbf{i}_n\mathbf{i}_m)^A) \cdot\cdot \nabla\boldsymbol{\theta}_1^\top + \frac{1}{2}c_1\boldsymbol{\theta}_1^2 + \frac{1}{2}c_0\boldsymbol{\theta}_0^2 + c_{10}\boldsymbol{\theta}_1\cdot\boldsymbol{\theta}_0, \tag{45}$$

$U \geqslant 0$ at $c_0\, c_1 > c_{10}^2$. Dynamic Eq. (23) look as follows:

$$I_0\ddot{\boldsymbol{\theta}}_0 + c_0\boldsymbol{\theta}_0 + c_{10}\boldsymbol{\theta}_1 = \mathbf{0}, \tag{46}$$

$$I_1\ddot{\boldsymbol{\theta}}_1 + c_1\boldsymbol{\theta}_1 + c_{10}\boldsymbol{\theta}_0 = \nabla\cdot(\lambda\mathbf{E}\nabla\cdot\boldsymbol{\theta}_1 + 2\mu\nabla\boldsymbol{\theta}_1^S + 2\alpha\nabla\boldsymbol{\theta}_1^A). \tag{47}$$

We look for the plane wave solution $\boldsymbol{\theta}_0 = \mathbf{Q}_0 e^{i(\omega t+\mathbf{k}\cdot\mathbf{r})}$, $\boldsymbol{\theta}_1 = \mathbf{Q}_1 e^{i(\omega t+\mathbf{k}\cdot\mathbf{r})}$. After standard calculations we obtain that the spectral problem looks as

$$\mathbf{Q}_0 = C_{00}\mathbf{Q}_1/(A_{00}(\omega_0^2 - \omega^2)), \tag{48}$$

$$(A_{11}(\omega_1^2 - \omega^2) - \frac{c_{10}^2}{A_{00}(\omega_0^2 - \omega^2)})\mathbf{E} + k^2((\lambda + 2\mu)\hat{\mathbf{k}}\hat{\mathbf{k}} + (\mu + \alpha)(\mathbf{E} - \hat{\mathbf{k}}\hat{\mathbf{k}})) \cdot \mathbf{Q}_1 = \mathbf{0}. \tag{49}$$

The dispersion relations both for longitudinal and transversal wave have the form

$$c^2k^2 = \omega^2 - \omega_1^2 + \frac{c_{10}^2}{A_{00}A_{11}(\omega_0^2 - \omega^2)}, \tag{50}$$

For the longitudinal wave $\mathbf{Q}_1 = Q_1\hat{\mathbf{k}}$, $c^2 = (\lambda + 2\mu)/A_{11}$, and for the transversal wave $\mathbf{Q}_1\cdot\hat{\mathbf{k}} = 0$, $c^2 = (\mu + \alpha)/A_{11}$.

## 7 Conclusion

We have shown that if a linear elastic continuum with holonomic ideal constraints is a reduced medium, i.e. its elastic energy does not depend on the gradient of certain generalised co-ordinates, under certain conditions for the elastic and inertial constants this continuum will have (a) band gap(s), where it is a single negative acoustic metamaterial, and in some cases the continuum has a decreasing part of dispersion curve, where it is a double negative acoustic metamaterial. The special vectorial generalised co-ordinate, whose gradient does not influence the strain energy, corresponds to the "distributed dynamic absorber", attached to the "bearing continuum" described by another vectorial generalised co-ordinate. At the frequencies close to the partial frequency of the generalised co-ordinate it changes essentially the dynamics of the system. The band gap (or band gaps) exist in all non-degenerate cases. It is shown that if there is a strong coupling between the special co-ordinate and the gradient of the bearing co-ordinate, as well as in the case when the partial frequency of the special co-ordinate ("dynamic absorber" $\omega_0$) is less than the partial frequency of the bearing co-ordinate $\omega_1$, the transversal wave has a decreasing part of dispersion curve. For the isotropic material with $\omega_0 > \omega_1$ this interval increases as the elastic modulus responsible for the coupling, increases. This work does not consider the case when we have finite velocities, for example, as it is in reduced gyrocontinua.

**Acknowledgements** This work was supported by the Russian Foundation for Basic Research (grant 17-01-00230), by Spanish Government Agency Ministerio de Economía y Competitividad (project No. FIS2014-54539-P) and by Andalusian Government (Junta de Andalucía), support for research group FQM-253.

## References

1. Bigoni, D., Guenneau, S., Movchan, A.B., Brun, M.: Elastic metamaterials with inertial locally resonant structures: application to lensing and localization. Phys. Rev. B **87**(17), 174303 (2013)
2. Boutin, C.: Acoustics of porous media with inner resonators. J. Acoust. Soc. Am. **134**(6), 4717–4729 (2013)
3. Craster, R.V., Guenneau, S. (eds.): Acoustic Metamaterials: Negative Refraction, Imaging, Lensing and Cloaking (vol. 166). Springer (2012)
4. Cummer, S.A., Christensen, J., Alú, A.: Controlling sound with acoustic metamaterials. Nat. Rev. Mater. **1**(3), 16001 (2016)
5. D'Alessandro, L., Zega, V., Ardito, R., Corigliano, A.: 3D auxetic single material periodic structure with ultra-wide tunable bandgap. Nat. Sci. Rep. **8**(1), 2262 (2018)
6. Deymier, P.A. (ed.): Acoustic Metamaterials and Phononic Crystals, vol. 173. Springer (2013)
7. Grekova, E.F. (2012). Nonlinear isotropic elastic reduced Cosserat continuum as a possible model for geomedium and geomaterials. Spherical prestressed state in the semilinear material. J. Seism. **16**(4), 695–707
8. Grekova, E.F. (2014). On one class of theoretically constructed isotropic single negative continuous acoustic metamaterials. In Proceedings of the International Conference Days on Diffraction 2014, IEEE Transactions
9. Grekova, E.F.: One class of single negative acoustic metamaterials. In: Doklady Physics, vol. 60(5), pp. 232–235. Pleiades Publishing (2015)
10. Grekova, E.F.: Plane waves in the linear elastic reduced Cosserat medium with a finite axially symmetric coupling between volumetric and rotational strains. Math. Mech. Solids **21**(1), 73–93 (2016)
11. Grekova, E.F.: Waves in elastic reduced Cosserat medium with anisotropy in the term coupling rotational and translational strains or in the dynamic term. In: Advances in Mechanics of Microstructured Media and Structures, pp. 143–156. Springer, Cham (2018)
12. Grekova, E.F.: Harmonic waves in the simplest reduced Kelvin's and gyrostatic media under an external body follower torque. In: Days on Diffraction (DD 2018), pp. 138–144. IEEE Transactions (2018)
13. Grekova, E.F., Kulesh, M.A., Herman, G.C.: Waves in linear elastic media with microrotations, part 2: Isotropic reduced Cosserat model. Bull. Seism. Soc. Am. **99**(2B), 1423-1428 (2009)

14. Kilchevskiy, N.A., Kilchinskaya, G.A., Tkachenko, N.E.: Analytical Mechanics of Continual Systems. Naukova Dumka, Kiev (1979). In Russian
15. Madeo, A., Neff, P., Ghiba, I.D., Placidi, L., Rosi, G.: Wave propagation in relaxed micromorphic continua: modeling metamaterials with frequency band-gaps. Contin. Mech. Thermodyn. **27**(4–5), 551–570 (2015)
16. Miniaci, M., Krushynska, A., Movchan, A.B., Bosia, F., Pugno, N.M.: Spider web-inspired acoustic metamaterials. Appl. Phys. Lett. **109**(7), 071905 (2016)
17. Noll, W.: A mathematical theory of the mechanical behavior of continuous media. Arch. Rat. Mech. Anal. **2**(1), 197–226 (1958)
18. Norris, A.N., Shuvalov, A.L.: Elastic cloaking theory. Wave Motion **48**(6), 525–538 (2011)
19. Schwartz, L.M., Johnson, D.L., Feng, S.: Vibrational modes in granular materials. Phys. Rev. Lett. **52**(10), 831 (1984)
20. Vasiliev, A.A., Miroshnichenko, A.E., Dmitriev, S.V.: Multi-field modeling of a Cosserat lattice: models, wave filtering, and boundary effects. Eur. J. Mech.-A/Solids **46**, 96–105 (2014)
21. Veselago, V.G.: The electrodynamics of substances with simultaneously negative values of $\varepsilon$ and $\mu$. Sov. Phys. Uspekhi **10**(4), 509 (1968)

# Stability Theory of Solitary Loops Propagating Along Euler’s Elastica

**Andrej Il’ichev**

**Abstract** The problem of dynamic stability of twist free solitary wave solutions of the equations describing oscillations of an inextensible elastic rod (Euler’s elastica) is treated. The governing equations describe sufficiently large displacements, though we are restricted to small strains. We show that under the condition of well-posedness of the initial value problem (in some specific sense) the family of solitary wave solutions is nonlinearly stable for two-dimensional perturbations not coming out from the plane of principal bending. The framework of the analysis is largely based on the spectral properties of the “linearized Hamiltonian” $\mathscr{H}$. We show that for planar perturbations $\mathscr{H}$ is positively semidefinite subject to a certain constraint, which implies the orbital stability. We consider also the case of perturbing the solitary wave by three-dimensional spatial perturbations. As a result of linearization about the solitary wave solution, we obtain an inhomogeneous scalar equation. This equation leads to a generalized eigenvalue problem. To establish the instability, we must verify the existence of an unstable eigenvalue (an eigenvalue with a positive real part). The corresponding proof of the instability is done using a local construction of the Evans function depending only on the spectral parameter. This function is analytic in the right half of the complex plane and has at least one zero on the positive real axis coinciding with an unstable eigenvalue of the generalized spectral problem.

## 1 Introduction

The dynamical equations of the theory of elastic rods were formulated in the works [1, 2] (see, also [3]). The forms of bending waves in inextensible thin rods were for the first time, apparently, described by Euler (see [4]). The dynamics of the flexure of a flat rod was discussed in [5], where the traveling waves were classified and it was also noted that the system of dynamical equations can be reduced to a single

---

A. Il’ichev (✉)
Steklov Mathematical Institute of Russian Academy of Sciences, Gubkina Str. 8,
Moscow, Russia
e-mail: ilichev@mi.ras.ru

H. Altenbach et al. (eds.), *Dynamical Processes in Generalized Continua and Structures*, Advanced Structured Materials 103,
https://doi.org/10.1007/978-3-030-11665-1_15

partial differential equation and an algebraic equation representing the inextensibility condition. This observation raised the supposition that the system of equations describing the dynamics of a flat inextensible rod is completely integrable. But the numerical results obtained in [6] suggest that the system is nonintegrable because the solitary waves of a flat inextensible rod interact inelastically, i.e., are not solitons in the strict sense. Solutions of the type of traveling waves in a linearly extensible and unshearable (thin) flat rod were obtained in a closed form in [7]. In [8], the authors described inextensible rods with torsion and obtained expressions for spatial (three-dimensional) traveling waves in the presence of a torsional moment. The dynamics of the flexure of a flat inextensible rod was discussed in [9] with neglect of the rotational part of the kinetic energy, which is small compared with the total energy of the rod. The orbital stability of the solitary wave solutions in the form of a loop under planar perturbations was proved. In [10], the stability analysis was generalized to the case without such a neglect. Methods used for the proof of such a stability can be found in [11] (see also references therein). In the case of deviations of the rod from the principal plane of flexure, the instability of solitary waves under spacial perturbations (departures from the principal plane of flexure) was established in [12, 13], (see, also [14]). In [15], the authors considered the question of the existence of solitary waves in a general model taking the effects of shear and contraction/extension into account.

Here we treat both the cases of planar as well as three dimensional perturbations. For planar perturbations we investigate nonlinear (Lyapunov stability). This investigation is based on the Hamiltonian formulation of the system of equations in question. We prove the orbital Lyapunov stability in this case. We use the smallness of the rotational part of the kinetic energy compared with the total energy of the rod. We therefore consider the terms corresponding to the rotational kinetic energy in the linearized equation to have the second order of smallness, and we consequently neglect them. The stability is due to the fact that we are able construct the Lyapunov function (functional) in this case. The Hessian $\mathscr{H}$ has empty negative spectrum, only one null eigenfunction (due to the translational invariance) and positive spectrum bounded away from zero. The stability occurs due to the fact that the Lyapunov functional has its local minimum on some linear space. The dynamics of the spacial (not planar) rod is described by taking the torsion into account. In this case we obtain the instability results using the properties of the Evans function. Equation for the unstable eigenfunction has the same form as the corresponding equation in [16], but the potential $p_0$ in this equation differs from the potential in [16], which leads to a nontrivial analysis and a difference between the Evans functions in the two cases (see [12]). The authors of [16] generalized the results in [17] to the case of Boussinesq-type equations where two modes decaying at infinity are present in the solutions of the corresponding generalized spectral problem. The ideas of Evans [18] in parabolic problems were developed in [19–21].

The present paper organized as follows. In Sect. 2 we treat the stability of the solitary loop under the planar perturbations. Section 3 is devoted to the proof of spectral (linear) instability of the loop under three dimensional perturbations coming out of the plane of principal bending. In Sect. 4 we give our conclusions and discussion.

# 2 Nonlinear Stability of the Loop About Plane Perturbations

## 2.1 *General Translationally Invariant Hamiltonian Systems: Stability of Solitary Waves*

### 2.1.1 Translationally Invariant Hamiltonian Systems

Let $X$ be a functional space of an infinite dimensional hamiltonian system

$$\frac{d\mathbf{u}}{dt} = J\frac{\delta E}{\delta \mathbf{u}}\big(\mathbf{u}(t)\big), \quad \mathbf{u} \in M, \tag{1}$$

where $E$ is a functional ("energy"), $J$ is a skew-symmetric operator:

$$\langle J\mathbf{u}, \mathbf{v}\rangle = -\langle \mathbf{u}, J\mathbf{v}\rangle, \quad \mathbf{u}, \mathbf{v} \in D(J),$$

$\langle\cdot,\cdot\rangle$ the scalar product in $L^2(\mathbb{R}) \times L^2(\mathbb{R}) \times \cdots \times L^2(\mathbb{R})$, which is the product of spaces of square integrable functions on the real axis $\mathbb{R}$, $M$ is some closed submanifold in $X$, $\delta/\delta\mathbf{u}$ denotes the conditional variational derivative with respect to $\mathbf{u} \in X$, $\mathbf{u} = \mathbf{u}(t, x)$, $x \in \mathbb{R}$ under the condition $\mathbf{u} \in M$.

Let $E\colon X \to \mathbb{R}$ be the $C^2$ functional, which is defined on the whole space $X$, and let $T(\omega)\colon X \to X$ be the one parametric group of translations

$$T(\omega)\mathbf{w}(\cdot, x) = \mathbf{w}(\cdot, x + \omega) = \exp\big(\omega\,\partial_x\big)\mathbf{w}(\cdot, x).$$

Assume, that $E$ is invariant under the action of $T$, i.e.

$$E\big(T(\omega)\mathbf{u}\big) = E(\mathbf{u}). \tag{2}$$

Differentiating (2) with respect to $\omega$ and putting $\omega$ to zero we get

$$\langle E'(\mathbf{u}), \frac{d}{d\omega}T(0)\mathbf{u})\rangle = 0, \quad \frac{d}{d\omega}T(0) = \partial_x,$$

where prime denotes the variational derivative.

Assume further, that there exists the bounded operator $B\colon X \to X^*$ ($*$ denotes the conjugation), such that $JB = dT(0)/d\omega$. Define the functional $Q\colon X \to \mathbb{R}$ by the equality

$$Q(\mathbf{u}) = \frac{1}{2}\langle B\mathbf{u}, \mathbf{u}\rangle.$$

It is easily seen, that $Q(\mathbf{u})$ is also invariant under the action of the grout $T$:

$$Q\big(T(\omega)\mathbf{u}\big) = Q(\mathbf{u}), \quad \omega \in \mathbb{R},\ \mathbf{u} \in X.$$

Indeed

$$\frac{d}{d\omega}Q\big(T(\omega)\mathbf{u}\big) = \big\langle Q'\big(T(\omega)\mathbf{u}\big), \frac{d}{d\omega}T(0)T(\omega)\mathbf{u}\big\rangle = \big\langle BT(\omega)\mathbf{u}, JBT(\omega)\mathbf{u}\big\rangle = 0.$$

Note, that the functionals $E$ and $Q$ are formally conserved under the flow of (1). Indeed

$$\frac{dE}{dt} = \left\langle E'(\mathbf{u}), \frac{d\mathbf{u}}{dt}\right\rangle = \langle E'(\mathbf{u}), JE'(\mathbf{u})\rangle = 0,$$

and it follows that

$$\frac{dQ}{dt} = \left\langle Q'(\mathbf{u}), \frac{d\mathbf{u}}{dt}\right\rangle = \langle B\mathbf{u}, JE'(\mathbf{u})\rangle =$$

$$= -\langle JB\mathbf{u}, E'(\mathbf{u})\rangle = -\left\langle \frac{d}{d\omega}T(0)\mathbf{u}, E'(\mathbf{u})\right\rangle = 0.$$

### 2.1.2 Basic Assumptions

Let us denote by $\phi_c = \phi_c(x - ct)$, where $c$ is a constant wave velocity, a solution of Eq. (1) of solitary wave type.

**Definition 1** We call the Cauchy problem for Eq. (1) well posed, if for arbitrary $\mathbf{w}_0 \in X$ near $\phi_c$ in $X$, $||\mathbf{w}_0 - \phi_c|| < \gamma$, there exist $T = T(\gamma) > 0$ and the vector function $\mathbf{w}(t) \in C([0, T), X)$ (continuous in $t$ with values in $X$, $|| \cdot ||$ denotes the norm in $X$), $\mathbf{w}(0) = \mathbf{w}_0$ such that for all $t$, $0 \le t \le T$, and $E(\mathbf{w}) = E(\mathbf{w}_0)$, $Q(\mathbf{w}) = Q(\mathbf{w}_0)$.

Further we consider that the following assumptions are valid.

**Assumption 1** The solution of the Cauchy problem exists in the above sense.

**Assumption 2** There exist $c_1 < c_2$ *and a smooth mapping* $c \to \phi_c$ of the interval $(c_1, c_2)$ in $X$, such that for all $c \in (c_1, c_2)$

(a) $R(\phi_c) = E'(\phi_c) + c\,Q'(\phi_c) = 0$;
(b) $dT(0)/d\omega \cdot \phi_c \neq 0$.

Next define the operator from $X$ to $X^*$:

$$\mathscr{H} = E''(\phi_c) + c\,Q''(\phi_c).$$

It is proved in [11] that $\mathscr{H}\colon X \to X^*$ is self-adjoint and also that the translational invariance in $x$ implies the existence of the zero eigenvalue of this operator with the associated eigenvector

$$\frac{d}{d\omega}T(0)\phi_c = \partial_x\phi_c.$$

**Assumption 3** There is no negative spectrum of $\mathscr{H}$, its kernel is spanned on $\frac{d}{d\omega}T(0)\phi_c$ and the positive spectrum of $\mathscr{H}$ is bounded away from zero.

### 2.1.3 Stability of Solitary Waves

Solitary wave which is close to a given solitary wave has, nevertheless, slightly different velocity, and, hence, the distance between the both solitary waves will increase with time. Therefore, under dynamic stability of a solitary wave we understand the orbital stability or the stability in form.

**Definition 2** The orbit $\{T(-ct)\phi_c, t \in \mathbb{R}\}$ is stable, if for $\varepsilon > 0$ there exists $\delta > 0$, such that if $||\mathbf{u}_0 - \phi_c|| < \delta$ and $\mathbf{u}(t)$ on some semi-interval $[0, t_0)$ with $\mathbf{u}(0) = \mathbf{u}_0$, then $\mathbf{u}(t)$ can be continued to the solution on $0 \le t < \infty$ and

$$\sup_{0 \le t < \infty} \inf_{\omega \in \mathbb{R}} ||\mathbf{u}(t) - T(\omega)\phi_c|| < \varepsilon.$$

Otherwise, the orbit is called unstable.

The neighborhood $U_\varepsilon$ of the solitary wave orbit is defined by the following way:

$$U_\varepsilon = \{\mathbf{w} \in X, \inf_{\omega \in \mathbb{R}} ||\mathbf{w}(\cdot, t) - T(\omega)\phi_c|| < \varepsilon\}.$$

There exist $\varepsilon > 0$ and the smooth mapping such that $\omega \colon U_\varepsilon \to \mathbb{R}$ such that for all $\mathbf{w} \in U_\varepsilon$

$$\langle T\big(\omega(\mathbf{w})\big)\mathbf{w}, \partial_\zeta \phi_c \rangle = 0, \quad \zeta = x - ct. \tag{3}$$

This fact for general case of translationally invariant hamiltonian systems was proved in [11] by the use of the implicit function theorem. It means that for $\mathbf{w} \in U_\varepsilon$ there exists the optimal shift, which gives the minimum to the distance between the solitary wave and $\mathbf{w}$.

Let $L$ be the linear space tangent to $M$ in $\phi_c$ for $c \in (c_1, c_2)$. Then, the following Theorem follows from the Assumption 3 [11].

**Theorem 1**

$$\langle \mathscr{H}\mathbf{y}, \mathbf{y} \rangle \ge c_0 \langle \mathbf{y}, \mathbf{y} \rangle, \quad \mathbf{y} \in L_1, \quad L_1 = L \cap \langle \mathbf{y}, \partial_\zeta \phi_c \rangle = 0. \tag{4}$$

In the case to be considered here the inequality (4) can imply the inequality

$$\langle \mathscr{H}\mathbf{y}, \mathbf{y} \rangle \ge c\, ||\mathbf{y}||^2, \quad \mathbf{y} \in L_1.$$

We assume further, that there exists one more continuous in $X$ conserving functional under the flow (1) denoted by $N$. Let $R(\mathbf{u}) = E(\mathbf{u}) + cQ(\mathbf{u})) - N(\mathbf{u})$. Then the following theorem is valid [9].

**Theorem 2** *The solitary wave* $\phi_c$ *is stable if*
*(i) Assumptions 1, 2 is valid;*
*(ii)* $R(\mathbf{w}) - R(\phi_c)) \geq c\,||T\big(\omega(\mathbf{w})\big)\mathbf{w} - \phi_c||^2$ *with* $\omega(\mathbf{w})$ *from (3) and* $\mathbf{w} \in U_\varepsilon \cap M$.

## 2.2 Formulation, Solitary Waves, Symmetries and Stability

Consider nonlinear planar bending oscillation of a thin inextensible shear-free elastic rod (Euler's elastica) of infinite length under the action of the tension force and in the undisturbed state coinciding with the $x_1$-axis of the Cartesian coordinate system. The total energy of the rod consists of kinetic and bending energies (the torsion energy is absent because only plane motions are considered in the principal plane od bending $x_1x_2$). Corresponding linear densities kinetic $K$ and potential $W$ energies are given by expressions

$$K = \frac{1}{2}\rho S x^i_t x_{it}, \quad W = \frac{1}{2} I E_0 x^i_{\xi\xi} x_{i\xi\xi},$$

where $x_i$, $i = 1, 2$ are the coordinates of points of the neutral curve of the rod (elastica), $\rho$ is the density, $S$ is the area of the cross section of the rod, $\rho I$ is the moment of inertia of the cross section about a line orthogonal to the principal plane of bending $x_1x_2$, $E_0$ is the Young module, and $\xi$ denotes the arc-length of the elastica. The summation is assumed under the repeating indices. The form of the elastica are given by the equation $x^i = x^i(t, \xi)$. For thin rods, the rotational part of the kinetic energy $K_r = \frac{1}{2}\rho I x^i_{t\xi} x_{it\xi}$ is small compared to the kinetic energy $K$ and bending energy $W$ and is of order $S/R^2$, where $R$ is the curvature radius of the elastica [9] and we neglect it here.

The equations of motion can be obtained by taking the variational derivative of the lagrangian $\Lambda$,

$$\Lambda = \frac{1}{2}\int\limits_{t_0}^{t}\int\limits_{-\infty}^{\infty} (\rho S x^i_t x_{it} - I E x^i_{\xi\xi} x_{i\xi\xi})\, d\xi\, dt$$

under the condition of the inextensibility : $x_{i\xi} x^i_\xi = 1$. These equations are given by

$$\rho S x^i_{tt} = (P x_{i\xi})_\xi - I E x_{i\xi\xi\xi\xi}, \quad x_{i\xi} x^i_\xi = 1, \tag{5}$$

where $P(t, \xi) = p(t, \xi) + p_\infty$ is the Lagrange multiplier, corresponding to physical value of the extension force, $p \to 0$ for $\xi \to \pm\infty$. Making in (5) the scaling transformations

$$p \to p_\infty p, \quad \xi \to \sqrt{IE/p_\infty}\,\xi, \quad t \to \sqrt{\rho S I E/p^2_\infty}\, t$$

and preserving the former notations, we get

$$\begin{aligned} &\tau^i_{tt} = (p\tau^i)_{\xi\xi} + \tau^i_{\xi\xi} - \tau^i_{\xi\xi\xi\xi}, \\ &\tau^i\tau_i = 1, \\ &\tau_1 \to 1, \quad \tau_{2,3} \to 0, \quad \xi \to \pm\infty. \end{aligned} \tag{6}$$

where $\tau_i = x^i_\xi$.

System of Eq. (6) is written in Hamiltonian form

$$\tau^i_t = \frac{\partial}{\partial\xi}\frac{\delta E}{\delta v_i}, \quad v^i_t = \frac{\partial}{\partial\xi}\frac{\delta E}{\delta \tau_i}, \quad \tau^i\tau_i = 1, \tag{7}$$

where

$$E = \int\limits_{-\infty}^{\infty} \left[(v_i v^i + \tau_{i\xi}\tau^i_\xi + \rho(\tau^i\tau_i - 1)\right] d\xi.$$

Along with Hamiltonian $E$ the following two formally conserved quantities take place:

$$Q = \int\limits_{-\infty}^{\infty} (\tau^i - \tau^i_\infty) v_i \, d\xi, \quad N = \int\limits_{-\infty}^{\infty} (\tau^1 - 1)\, d\xi, \quad \tau^1_\infty = 1, \quad \tau^{2,3}_\infty = 0.$$

Denote further $\phi_c = \{\tau^0_1 - 1, \tau^0_2, v^0_1, v^0_2\}^T$ $(v^0_1 = -c(\tau^0_1 - 1),\ v^0_2 = -c\tau^0_2)$, and $\mathbf{w}(t) = \{\tau_1 - 1, \tau_2, v_1, v_2\}^\top$ for vector functions, and also $X = H^1(\mathbb{R}) \times H^1(\mathbb{R}) \times L^2(\mathbb{R}) \times L^2(\mathbb{R})$ for the Hilbert space with the norm $||\cdot||$.

Hence, Eq. (6) has the Hamiltonian form (7),

$$M = \{\tau_1 - 1, \tau_2 : \tau_i\tau^i = 1.\}$$

The functionals $E$, $Q$, and also $N$ are continuous as the functionals from the Hilbert space $X$ to $\mathbb{R}$ (the last one as a consequence of the fact that $\tau_1 - 1 \in L^1(\mathbb{R})$, which follows from the inextensibility condition in (6)).

In this section we present the proof of the following

**Theorem 3** *Let* $\tau_3 \equiv 0$ *and for all* $\mathbf{w}_0 \in X$ *near* $\phi_c$ *in* $X$, $||\mathbf{w}_0 - \phi_c|| < \gamma$, *there exist* $T = T(\gamma) > 0$ *and vector-function* $\mathbf{w}(t) \in C([0,T), X)$ *(continuous with values in* $X$*),* $\mathbf{w}(\cdot, 0) = \mathbf{w}_0 = \{\tau^l_0, 0, v^l_0, 0\}^\top$, $l = 1, 2$, *such, that for all* $t$, $0 \le t \le T$, $\tau^i_0\tau_{0i} = \tau^i\tau_i = 1$ *and* $H(\mathbf{w}) = H(\mathbf{w}_0)$, $Q(\mathbf{w}) = Q(\mathbf{w}_0)$, $N(\mathbf{w}) = N(\mathbf{w}_0)$. *Then for arbitrary* $\varepsilon > 0$ *there exists* $\delta > 0$ *such, that if* $||\mathbf{w}_0 - \phi_c|| < \delta$, *then*

$$\sup_{t>0} \inf_{\omega\in\mathbb{R}} ||\mathbf{w}(t,\cdot) - \phi_c(\cdot + \omega)|| < \varepsilon.$$

The proof of this Theorem is based on the fact, that a family of translations of the solitary wave (orbit) gives the local minimum to the conserved quantity $R(\mathbf{w})$ on the closed submanifold $M \in X$. This, in its turn, follows that "linearized Hamiltonian" $\mathscr{H}(\phi_c) = \delta^2 R(\phi_c)/\delta^2\mathbf{w}$ has exactly one zero eigenvalue and its positive spectrum is bounded away from zero.

### 2.2.1 Solitary Wave Solutions

Solitary wave solutions of (6) are the solutions of traveling wave type tending to zero at infinity. Traveling waves depend on the self-similar combination $\zeta = \xi - ct$ and the equations describing them can be obtained by the integration of (6). These equations have the form

$$\begin{aligned} &-c(\tau^i - \tau^i_\infty) = v^i, \\ &-cv^i = p\tau^i - \tau^i_\infty - \tau^i_{\zeta\zeta}, \quad \tau^i\tau_i = 1. \end{aligned} \tag{8}$$

Multiplying the second equation in (8) by $\tau_i$ and summing by index $i$, we get

$$p = c^2 + (1-c^2)\tau^i_\infty\tau_i - \tau^i_\zeta\tau_{i\zeta}.$$

Further, multiply the same equation by $\tau^i_\zeta$ and sum. In the result we get

$$-\frac{1}{2}\tau^i_\zeta\tau_{i\zeta} - s^2\tau^i_\infty\tau_{i\zeta} = 0, \quad s = \sqrt{1-c^2},$$

and after one time integration

$$-\frac{1}{2}\tau^i_\zeta\tau_{i\zeta} - s^2\tau^i_\infty\tau_i = \Pi. \tag{9}$$

Put further $\Pi = -s^2$. Define the new angle variable $\theta$ as $\tau_1 = \cos\theta$, $\tau_2 = \sin\theta$. In new variables (9) takes the form

$$\theta^2_\zeta = 4s^2\sin^2\theta/2,$$

which can be easily integrated. Finally, we have

$$\begin{aligned} &p = -p^0 = -6(1-c^2)\,\mathrm{sech}^2\sqrt{1-c^2}\zeta, \quad \tau_3 = 0, \\ &\tau_1 = \tau^0_1 = 1 - 2\,\mathrm{sech}^2\sqrt{1-c^2}\zeta, \\ &\tau_2 = \tau^0_2 = -2\,\mathrm{sech}^2\sqrt{1-c^2}\zeta\,\sinh\sqrt{1-c^2}\zeta, \quad \zeta = \xi - ct, \quad 0 \le c < 1. \end{aligned} \tag{10}$$

Classification of various forms of elastic lines was first given Euler, who derived the ordinary differential equation, describing the shape of thin non-tensile rods under

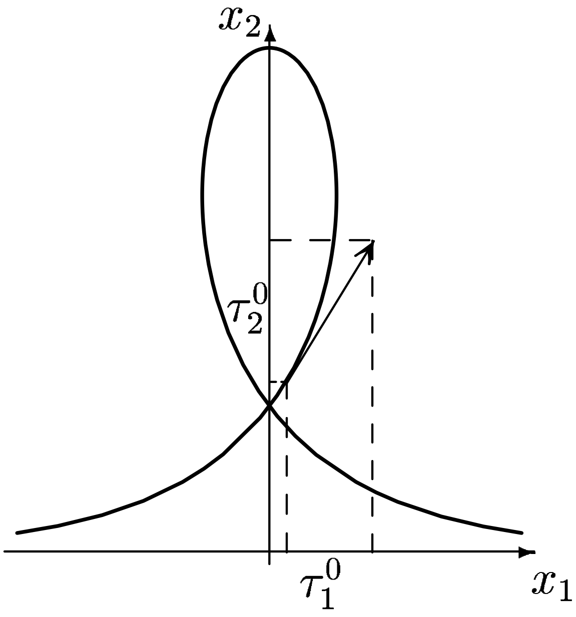

**Fig. 1** Form of solitary wave on the elastica and a tangent vector $\{\tau_1^0, \tau_2^0, 0\}^\top$

by the action of tension force (see, for example, [4]). Elastic curve of the rod of infinite length can have a loop shape, which is the running solitary wave, given by (10) (see Fig. 1).

We note, that system (8) for solitary wave solutions may be also written in the form

$$R'(\phi_c) = \{E(\phi_c) + cQ(\phi_c) - N(\phi_c)\}' = 0. \tag{11}$$

### 2.2.2 Well-Posedness of the Cauchy Problem

We call the Cauchy problem for (6) well posed if Assumption 1 in slightly modified form is valid, namely the Cauchy problem for Eq. (6) is well posed if for arbitrary $\mathbf{w}_0 \in X$ near $\phi_c$ in $X$, $||\mathbf{w}_0 - \phi_c|| < \gamma$, there exist $T = T(\gamma) > 0$ and a vector function $\mathbf{w}(t, \cdot) \in C([0, T), X)$ (continuous with values in $X$), $\mathbf{w}(\cdot, 0) = \mathbf{w}_0 = \{\tau_0^i, v_0^i\}^\top$, $i = 1, 2, 3,$ such, that for all $t$, $0 \leq t \leq T$, $\tau_0^i \tau_{0i} = \tau^i \tau_i = 1$ and $E(\mathbf{w}) = E(\mathbf{w}_0)$, $Q(\mathbf{w}) = Q(\mathbf{w}_0)$, $N(\mathbf{w}) = N(\mathbf{w}_0)$.

### 2.2.3 Symmetry

The functionals $E$, $Q$ and $N$ are invariant under the action of the Lie group of translations

- $T: X \to X$:

$$T(\omega)\mathbf{w}(\cdot,\xi) = \mathbf{w}(\cdot,\xi+\omega)\exp\bigl(\omega\partial_\xi\bigr)\mathbf{w}(\cdot,\xi), \quad \omega \in \mathbb{R}.$$

The vector $\mathbf{k} = \partial_\zeta \phi_c$ is the unique null eigenvector of the operator $\mathscr{H}$. Moreover, for the case in question (3) has the place.

### 2.2.4 Spectral Properties of the Operator $\mathscr{H}$

Let us introduce the following notations: $\mathbf{u} = \{u_1, u_2, u_3, u_4, \}^\top$ is the unknown vector function, $L = \{\mathbf{u} \in X,\ \tau_1^0 u_1 + \tau_2^0 u_2 = 0\}$ is linear closed subspace of $X$, tangent to the submanifold $\hat{M} = \{\mathbf{u} \in X,\ \tau_i \tau^i = 1\}$ at a point $\mathbf{u} = \phi_c$ (see Sect. 2.1.3).

The following inequality takes place $\langle \mathscr{H}\mathbf{u}, \mathbf{u}\rangle \geq 0\ \mathbf{u} \in L$. Indeed, resolving the equality $\tau_i^0 \delta\tau^i = 0$, we get

$$\delta\tau_1 = \tau_2^0, \quad \delta\vartheta, \quad \delta\tau_2 = -\tau_1^0\,\delta\vartheta.$$

The bilinear form $\langle \mathscr{H}\delta\mathbf{w}, \delta\mathbf{w}\rangle$ in $L$ is given by

$$\langle \mathscr{H}\delta\mathbf{w}, \delta\mathbf{w}\rangle = \int_{-\infty}^{\infty} \left[\delta\tau^i\left(-\frac{d^2}{d\xi^2} + 1 - p^0\right)\delta\tau_i + \delta v^i \delta v_i + 2c\delta v^i \delta\tau_i\right] d\xi =$$

$$= \int_{-\infty}^{\infty} \left[\delta\vartheta\left(-\frac{d^2}{d\xi^2} + c^2 + s^2 - 2s^2\mathrm{ch}^{-2} s\xi\right)\delta\vartheta + 2c\tau_2^0\,\delta\vartheta\,\delta v_1 \right.$$
$$\left. -2c\tau_1^0\,\delta\vartheta\,\delta v_2 + \delta v^i \delta v_i\right] d\xi.$$

The eigenvalue problem for the operator $\mathscr{H}$ is formulated as follows

$$\mathscr{R}_2 \chi = \nu\chi, \tag{12}$$

where

$$\mathscr{R}_2 = \begin{pmatrix} \mathscr{H}_1 + c^2 & c\tau_2^0 & -c\tau_1^0 \\ c\tau_2^0 & 1 & 0 \\ -c\tau_1^0 & 0 & 1 \end{pmatrix}, \qquad \chi = \{\chi_1, \chi_2, \chi_3\}^\top,$$
$$\mathscr{H}_1 = -\frac{d^2}{d\zeta^2} + s^2 - 2\,\mathrm{sech}^2 s\,\zeta.$$

The eigenvalue problem (12) can be rewritten in components:

$$\chi_2 = \frac{c\tau_2^0}{\nu - 1}\,\chi_1, \quad \chi_3 = -\frac{c\tau_1^0}{\nu - 1}, \quad \mathscr{H}_1\chi_1 = \left(\nu - \frac{c^2\nu}{\nu - 1}\right)\chi_1,$$

and, consequently, it is reduced to the Sturm-Liouville eigenvalue problem for the component $\chi_1$. From Sturm-Liouville theory it is known, that the operator $\mathscr{H}_1$ has the unique null eigenvalue (with the associated eigenfunction $\partial_\xi\tau_1^0/\tau_2^0$, corresponding to $\partial_\xi\phi_c$), and the other spectrum is positive and is bounded away from zero.

From the expression for the zero eigenvalue

$$\nu - \frac{c^2\nu}{\nu - 1} = 0,$$

one has $\nu_0 = 0$, $\nu_+ = 1 + c^2 > 0$. Essential spectrum $\mathscr{H}$ satisfies the condition

$$\nu - \frac{c^2\nu}{\nu - 1} > s^2,$$

from which it follows that

$$\nu > 1 - c$$

and, consequently the spectrum is bounded away from zero for the fixed velocity $c \in [\,0, 1)$.

It follows then (see Theorem 1 in Sect. 2.1.3), that if $\mathbf{u} \in L$ and $\langle \mathbf{u}, \partial_\zeta\phi_c\rangle = 0$, then

$$\langle \mathscr{H}\mathbf{u}, \mathbf{u}\rangle \geq \alpha_0\langle \mathbf{u}, \mathbf{u}\rangle. \tag{13}$$

Besides, if $\mathbf{u} \in \hat{L}$ and $\langle \mathbf{u}, \partial_\zeta\phi_c\rangle = 0$, then

$$\langle \mathscr{H}\mathbf{u}, \mathbf{u}\rangle \geq \alpha_1||\mathbf{u}||^2. \tag{14}$$

in fact, multiplying both sides of inequality (13) on $1 - \varepsilon$, where $\varepsilon$ is a sufficiently small constant, we get

$$\begin{aligned}\langle \mathscr{H}\mathbf{u}, \mathbf{u}\rangle \geq \varepsilon \int_{-\infty}^{\infty} &\left[(\partial_\xi u_1)^2 + (\partial_\xi u_2)^2 + P^0(u_1^2 + u_2^2) + u_4^2 + u_5^2 + \right.\\ &\left. + 2c\,(u_1u_4 + u_2u_5)\right] d\xi + (1-\varepsilon)\alpha_0\langle \mathbf{u}, \mathbf{u}\rangle \geq \\ &\geq \int_{-\infty}^{\infty} \left[\beta_1(u_1^2 + u_2^2) + \beta_2(u_4^2 + u_5^2) + \varepsilon(\partial_\xi u_1^2 + \partial_\xi u_2^2)\right] \mathrm{d}\xi, \quad P^0 = -p^0 + 1,\end{aligned}$$

where $\beta_1 = (1-\varepsilon)\alpha_0 + \varepsilon(1 - 6s^2 - c)$ and $\beta_2 = (1-\varepsilon)\alpha_0 - \varepsilon c$. In order to get the estimate (14), choose $\alpha_1 = \min(\beta_1, \beta_2, \varepsilon)$.

### 2.2.5 Stability

Let $\mathbf{w}(t,\cdot)$ be the solution of Cauchy problem (6) on some semi-interval $[\,0, T)$. Then the orbit is considered to be stable according Definition 2 of Sect. 2.1.3.

According Theorem 2 the orbit of the solitary wave in question is stable if

the Cauchy problem for (6) is well posed (in the sense of Definition 1);
$R(\mathbf{w}) - R(\phi_c) \geq \alpha ||T\big(\omega(\mathbf{w})\big)\mathbf{w} - \phi_c||^2$ for $\mathbf{w} \in U_\varepsilon \cap M$, ($\alpha$ is some positive constant, $\omega(\mathbf{w})$ is from (3)).

So, it remains to prove that for $\mathbf{w} \in U_\varepsilon \cap M$ the equality is valid

$$R(\mathbf{w}) - R(\phi_c) \geq \alpha ||T\big(\omega(\mathbf{w})\big)\mathbf{w} - \phi_c||^2.$$

Let $\mathbf{w} \in U_\varepsilon \cap M$. Make the decomposition

$$\rho = T\big(\omega(\mathbf{w})\big)\mathbf{w} - \phi_c = \mathbf{u}^0 + \mathbf{u},$$

where $\rho = \{\rho_1, \rho_2, , \rho_3, \rho_4, \}^\top$, $\mathbf{u}_0 = \{u_1^0, u_2^0, 0\}^T$ $\mathbf{u} \in L$. Next, note that

$$2(\tau_1^0\rho_1 + \tau_2^0\rho_2) = -a, \tag{15}$$

where $a = \rho_1^2 + \rho_2^2$. Equality (15) follows from the inclusion $T\big(\omega(\mathbf{w})\big)\mathbf{w} \in M$. From (15) it follows that $\tau_1^0 u_1^0 + \tau_2^0 u_2^0 = -a/2$. Resolving the last equality with respect to $u_1^0$ and $u_2^0$ we get

$$u_1^0 = -\frac{a}{2}\tau_1^0, \quad u_2^0 = -\frac{a}{2}\tau_2^0. \tag{16}$$

For $\mathbf{w} \in U_\varepsilon \cap M$ according to (11) one has

$$R(\mathbf{w}) - R(\phi_c) = \frac{1}{2}\langle \mathscr{H}\rho, \rho\rangle + o(||\rho||^2).$$

Next, we note that

$$\langle \mathbf{u}, \partial_\zeta \phi_c\rangle \;=\; \langle T\big(\omega(\mathbf{w})\big) - \phi_c - \mathbf{u}^0, \partial_\zeta \phi_c\rangle \;= 0$$

as the consequence of the equalities $\langle \phi_c, \partial_\zeta \phi_c\rangle \;= 0$, $\langle \mathbf{u}^0, \partial_\zeta \phi_c\rangle \;= 0$. The last equality follows from (16). Consequently, $\mathbf{u}$ belongs to the positive subspace $\mathscr{H}$ $\langle \mathscr{H}\mathbf{u}, \mathbf{u}\rangle \geq \alpha_1 ||\mathbf{u}||^2$. Finally,

$$||\mathbf{u}|| = ||\rho - \mathbf{u}^0|| \geq ||\rho|| - ||\mathbf{u}^0|| = ||\rho|| - O(||\rho||^2),$$

and for small enough $\rho$

$$R(\mathbf{w}) - R(\phi_c) \geq \frac{\alpha_1}{2}||\rho||^2 = \alpha||\rho||^2.$$

## 3 Spectral Instability of the Loop About Three Dimensional Perturbations

### *3.1 Formulation, Basic Equations*

#### 3.1.1 Basic Equations

In this section we choose the Cartesian coordinate system $\mathbf{x}=(x, y, z)$. As before, we consider a spatial curve $\mathscr{G}(t)$ (elastica), which is the centerline of a prismatic, dynamically symmetric, inextensible rod. We assume that this curve initially coincides with the $z$-axis. The position of the curve can vary with time, i.e., $\mathbf{x} = \mathbf{x}(\xi, t)$. At each point of the curve, we define a director basis $(\mathbf{d}_1, \mathbf{d}_2, \mathbf{d}_3)$, where $\mathbf{d}_3 = \partial\mathbf{x}/\partial\xi$ and $\mathbf{d}_1, \mathbf{d}_2$ are unit vectors in the plane normal to $\mathbf{d}_3$. The triple $(\mathbf{d}_1, \mathbf{d}_2, \mathbf{d}_3)$ forms a right-hand orthonormal basis at each point of $\mathscr{G}(t)$. The Euler angles $\theta$, $\psi$ and $\phi$ in the rod motion depend on $\xi$ and $t$; $\theta$ is the angle between the $z$-axis and the tangent vector $\mathbf{d}_3$, $\psi$ measures the deviation of $\mathscr{G}(t)$ from the principal bending plane $(x, z)$, and $\phi$ is the angle of torsion (see Fig. 1 in [8]). The tangent vector $\mathbf{d}_3(s, t)$ has the components $\tau_1$, $\tau_2$, and $\tau_3$:

$$\tau_1 = \cos\theta, \quad \tau_2 = \cos\psi\ \sin\theta, \quad \tau_3 = \sin\psi\ \sin\theta.$$

The expressions for $\mathbf{d}_1$ and $\mathbf{d}_2$ in terms of the angles $\theta$, $\psi$ and $\phi$ are given in [8]. Together with the trapped basis $\{\mathbf{d}_i\}$, $i = 1, 2, 3$, we introduce the orthonormal basis $\{\tilde{\mathbf{d}}_i\}$, which is obtained by a clockwise rotation of the pair $(\mathbf{d}_1, \mathbf{d}_2)$ about $\mathbf{d}_3$ through the torsion angle $\phi$, i. e.,

$$\begin{aligned} \tilde{\mathbf{d}}_1 &= (\cos\phi)\,\mathbf{d}_1 - (\sin\phi)\,\mathbf{d}_2, \\ \tilde{\mathbf{d}}_2 &= (\sin\phi)\,\mathbf{d}_1 + (\cos\phi)\,\mathbf{d}_2, \\ \tilde{\mathbf{d}}_3 &= \mathbf{d}_3. \end{aligned}$$

In the Kirchhoff rod dynamics model, the total force $\mathbf{F} = \mathbf{F}(\xi, t)$ and the total moment $\mathbf{M} = \mathbf{M}(\xi, t)$ can be expressed in terms of the director basis $\mathbf{d}_i$: $\mathbf{F} = \sum_{i=1}^{3} f_i\mathbf{d}_i$, $\mathbf{M} = \sum_{i=1}^{3} M_i\mathbf{d}_i$. The constitutive relation of linear elasticity theory up to terms of the order $O(S/R^2)$ ( recall that $S$ is the square of the rod cross section and $R$ is the radius of curvature of $\mathscr{G}(t)$) is [3, 8]

$$\mathbf{M} = E_0 I\kappa_1\mathbf{d}_1 + EI\kappa_2\mathbf{d}_2 + \mu J\kappa_3\mathbf{d}_3, \tag{17}$$

where $\mu$ is the shear modulus, and $I$ is the moment of inertia of the cross section as before. The elastic parameter $J$ is given by formula (2.24) in [8], and is equal to $2I$ for rods with a circular cross section. The values $\kappa_i$, $i = 1, 2, 3$, are the components of the curvature vector

$$\boldsymbol{\kappa} = \kappa_1 \mathbf{d}_1 + \kappa_2 \mathbf{d}_2 + \kappa_3 \mathbf{d}_3.$$

The conservation of linear and angular momentum together with constitutive relation (17) lead to the force and moment equations [3, 8]

$$\begin{aligned} &\mathbf{F}' = \rho S \ddot{\mathbf{x}}, \\ &\mathbf{M}' + \mathbf{x}' \times \mathbf{F} = \rho I \big(\mathbf{d}_1 \times \ddot{\mathbf{d}}_1 + \mathbf{d}_2 \times \ddot{\mathbf{d}}_2\big), \end{aligned} \tag{18}$$

where the prime denotes differentiation with respect to the arc-length $\xi$, the dot denotes differentiation with respect to $t$, and $\rho$ is the rod mass density.

We next apply the scaling transformations

$$s \to \nu s, \quad \mathbf{x} \to \nu \mathbf{x}, \quad t \to \beta t, \quad \mathbf{F} \to \frac{\nu^2}{\beta^2} \mathbf{F},$$

where $\nu$ is the characteristic wave length and $\beta = \nu^2 \sqrt{\rho S / EI}$. This scaling implies the replacements $\mathbf{d}_i \to \mathbf{d}_i, \boldsymbol{\kappa} \to \boldsymbol{\kappa}/\nu, M \to EI\nu^{-1}M$. In the new dimensionless variables, Eqs. (17) and (18) become

$$\begin{aligned} &\mathbf{F}'' = \ddot{\mathbf{d}}_3, \\ &\mathbf{M}' + \mathbf{d}_3 \times \mathbf{F} = \varepsilon \big(\mathbf{d}_1 \times \ddot{\mathbf{d}}_1 + \mathbf{d}_2 \times \ddot{\mathbf{d}}_2\big), \\ &M_1 = \kappa_1; \quad M_2 = \kappa_2, \quad M_3 = \Omega \kappa_3, \end{aligned} \tag{19}$$

where $\Omega = \mu J / EI$, $\varepsilon = I/(\nu^2 S) \sim S/R^2$ is a small quantity (as before). In the basis $\{\mathbf{d}_i\}$, $i = 1, 2, 3$, $\kappa_i$ are given by [8]:

$$\begin{aligned} \kappa_1 &= \partial_\xi \theta \sin\phi - \partial_\xi \psi \sin\theta \cos\phi, \\ \kappa_2 &= \partial_\xi \theta \cos\phi - \partial_\xi \psi \sin\theta \sin\phi, \\ \kappa_3 &= \partial_\xi \psi \cos\theta + \partial_\xi \phi. \end{aligned}$$

Projecting the first equation in (19) on the fixed Cartesian basis and the second equation on the vector basis $\tilde{\mathbf{d}}_i$, $i = 1, 2, 3$, we obtain six equations for $\theta$, $\psi$, $\phi$, $F^x$, $F^y$, and $F^z$:

$$\begin{aligned} &\partial^2_{\xi\xi} F^x = \partial^2_{tt} (\cos\psi \, \cos\theta), \\ &\partial^2_{\xi\xi} F^y = \partial^2_{tt} (\sin\psi \, \sin\theta), \\ &\partial^2_{\xi\xi} F^z = \partial^2_{tt} (\cos\theta), \\ &\partial^2_{\xi\xi} \psi \sin\theta + 2 \partial_\xi \psi \partial_\xi \theta \cos\theta - \Omega (\partial_\xi \psi \cos\theta + \partial_\xi \phi) \partial_\xi \theta - F^x \sin\psi + F^y \cos\psi = \end{aligned}$$

$$
\begin{aligned}
&= \varepsilon\big(\partial^2_{tt}\psi \sin\theta - 2\partial_t\theta\,\partial_t\phi\big),\\
&\partial^2_{\xi\xi}\theta - (\partial_\xi\psi)^2 \sin\theta\cos\theta + \Omega(\partial_\xi\psi\cos\theta + \partial_\xi\phi)\partial_\xi\psi\sin\theta + (F^x\cos\psi +\\
&+ F^y\sin\psi)\cos\theta - F^z\sin\theta = \varepsilon\big(\partial^2_{tt}\theta + (\partial_t\psi)^2\sin\theta\cos\theta + 2\partial_t\psi\,\partial_t\phi\sin\theta\big),\\
&\Omega\,\partial_\xi(\partial_\xi\psi\cos\theta + \partial_\xi\phi) = 2\varepsilon\partial_t(\partial_t\psi\cos\theta + \partial_t\phi). \qquad (20)
\end{aligned}
$$

### 3.1.2 Solitary Wave Solutions

The planar dynamics (pure flexure) of the rod is described by the system of equations that follow from (20) by setting $\psi = \phi = 0$:

$$
\begin{aligned}
\partial^2_{tt}\big(\cos\theta\big) &= \partial^2_{\xi\xi}(T\cos\theta - G\sin\theta),\\
\partial^2_{tt}\big(\sin\theta\big) &= \partial^2_{\xi\xi}(T\sin\theta + G\cos\theta),\\
\varepsilon\partial^2_{tt}\theta - \partial^2_{\xi\xi}\theta &= G, \qquad (21)
\end{aligned}
$$

where $T$ is the tension, $G$ is the shear force,

$$\mathbf{F} = F^x\mathbf{i} + F^z\mathbf{k} = T\mathbf{d}_3 + G\mathbf{n},$$

$\mathbf{d}_3$ and $\mathbf{n}(=\mathbf{d}_1)$ are the respective tangent and normal vectors,

$$\mathbf{d}_3 = \mathbf{i}\cos\theta + \mathbf{k}\sin\theta, \quad \mathbf{n} = -\mathbf{i}\sin\theta + \mathbf{k}\cos\theta.$$

We assume that $T(\xi = \infty, t) = T_\infty = p_\infty = \text{const}$.

System (21) describes the planar dynamics of a torsion-free rod. It has a solitary wave solution [9, 10], which is a traveling wave with the constant speed $c$

$$\tau^s_1 = \tau^0_1 + O(\varepsilon),\ \ \tau^s_2 = \tau^0_2 + O(\varepsilon),\ \ T^s = T^0 + O(\varepsilon),\ \ T^0 = (T_\infty - c^2)\tau^0_1 - c^2,$$

where

$$
\begin{aligned}
&\tau^0_1 = 1 - 2\,\mathrm{sech}^2\sqrt{T_\infty - c^2}\,\zeta,\\
&\tau^0_2 = \mp 2\,\mathrm{sech}^2\sqrt{T_\infty - c^2}\,\zeta\,\sinh\sqrt{T_\infty - c^2}\,\zeta, \quad \zeta = \xi - ct, \quad 0 \le c < T_\infty. \qquad (22)
\end{aligned}
$$

Expressions (22) are in full correspondence with (10).

We note that the tension at infinity $T_\infty$ can be set equal to unity by the transformations $t \to t/T_\infty$, $s \to s/\sqrt{T_\infty}$. We introduce the new coordinates $(x_1, x_2)$ and the curve $\mathscr{K}$ such that along $\mathscr{K}$ (see Sect. 2.2),

$$\frac{dx_1}{d\zeta} = \tau^0_1, \quad \frac{dx_2}{d\zeta} = \tau^0_2.$$

The form of $\mathscr{K}$ (the form of the soliton of elevation to the lowest order in $\varepsilon$) is shown in Fig. 1.

## *3.2 Linearization and Stability Analysis*

### 3.2.1 Linearization

We consider Euler angles of the forms

$$\theta = \theta^s, \quad \psi = \psi^s + \delta\psi, \quad \phi = \phi^s + \delta\phi,$$

where $(\theta^s, \psi^s, \phi^s)$ are the Euler angles corresponding to the solitary wave solution and $(\delta\psi, \delta\phi)$ are infinitesimal perturbations. The perturbation of the third component of the tangent vector then becomes

$$\delta\tau_3 = \delta\psi \; \sin\theta^s. \tag{23}$$

We assume that

$$\{\varepsilon\delta\psi, \varepsilon\delta\phi\} \sim \{(\delta\psi)^2, (\delta\phi)^2\} \tag{24}$$

because $\varepsilon$ is considered to be small.

We linearize Eq. (20) about the solitary wave solution (taking (24) in account) and assume that the twisting moment $M_3$ in the perturbed state is absent (no-twist perturbations):

$$\begin{aligned}
&\partial^2_{ss}\delta F^y = \partial^2_{tt}(\delta\psi \; \sin\theta^s),\\
&\partial^2_{ss}\delta\psi \, \sin\theta^s + 2\partial_s\delta\psi\,\partial_s\theta^s \cos\theta^s - F^{xs}\delta\psi + \delta F^y = 0,\\
&\Omega\,\partial_s(\partial_s\delta\psi \cos\theta^s + \partial_s\delta\phi) = 0.
\end{aligned} \tag{25}$$

From (25), using (23) we obtain

$$\partial_{tt}\delta\tau_3 = -\partial_{ss}(p^0\delta\tau_3) + \partial_{ss}\delta\tau_3 - \partial^4_s\delta\tau_3, \tag{26}$$

where (see (10)).

$$-p^0 = T^0 - (\partial_\zeta\tau^0_1)^2 - (\partial_\zeta\tau^0_2)^2 - 1 = -6(1-c^2)\,\mathrm{sech}^2\sqrt{1-c^2}\zeta.$$

### 3.2.2 Instability of the Solitary Wave

We seek the growing solution of Eq. (26) in the form

$$\delta\tau_3 = \mathrm{e}^{\lambda t} w(\lambda, \zeta), \quad \zeta = \xi - ct, \quad 0 \le c < 1,$$

where $w$ decays exponentially as $\zeta \to \pm\infty$ and $\operatorname{Re}\lambda > 0$. It is easy to understand that the function $w(\lambda, \zeta)$ must satisfy an ordinary differential equation with coefficients depending on $c$ and $\lambda$

$$\left(\lambda - c\frac{d}{d\zeta}\right)^2 w = \frac{d^2}{d\zeta^2}w - \frac{d^4}{d\zeta^4}w - \frac{d^2}{d\zeta^2}\big(p^0 w\big). \tag{27}$$

Equation (27) can be written in the matrix form

$$\mathbf{y}' = \mathscr{M}(\lambda, \zeta)\mathbf{y}, \tag{28}$$

$$\mathbf{y} = \{y_1, y_2, y_3, y_4\}^T, \quad y_1 = w, \quad y_2 = w', \quad y_3 = w'', \quad y_4 = w''',$$

where the prime denotes now differentiation with respect $\zeta$ and

$$\mathscr{M}(\lambda, \zeta) = \begin{pmatrix} 0 & 1 & 0 & 0 \\ 0 & 0 & 1 & 0 \\ 0 & 0 & 0 & 1 \\ -\lambda^2 + p^{0''} & 2\lambda c + 2p^{0'} & 1 - c^2 + p^0 & 0 \end{pmatrix}.$$

The equation conjugate to (27) is written as

$$\left(\lambda + c\frac{d}{d\zeta}\right)^2 w^* = \frac{d^2}{d\zeta^2}w^* - \frac{d^4}{d\zeta^4}w^* - p^0\frac{d^2}{d\zeta^2}w^* \tag{29}$$

or

$$\mathbf{z}' = -\mathbf{z}\mathscr{M}(\lambda, \zeta), \tag{30}$$

$$\mathbf{z} = \{z_1, z_2, z_3, z_4\}, \;\; z_4 = w^*, \;\; z_3 = -w^{*'}, \;\; z_2 = w^{*''} - (1 - c^2 + p^0)w^*,$$
$$z_1 = -w^{*'''} + (1 - c^2 + p^0)w^{*'} - (2\lambda c + p^{0'})w^*.$$

Because $\mathbf{y}(\lambda, \zeta)$ and $\mathbf{z}(\lambda, \zeta)$ respectively satisfy (28) and (30),

$$\partial_\zeta\big(\mathbf{z}(\lambda, \zeta) \cdot \mathbf{y}(\lambda, \zeta)\big) = 0,$$

where the dot denotes the scalar product of two vectors.

### 3.2.3 Local Analysis

We set $\mathscr{M}_\infty(\lambda) = \lim\limits_{\zeta\to\pm\infty} \mathscr{M}(\lambda, \zeta)$ and let $\mu_\alpha(\lambda)$ $(\alpha = 1, 2, 3, 4)$ be the eigenvalues of the matrix $\mathscr{M}_\infty(\lambda)$, and $\mathbf{r}_\alpha(\lambda)$ ans $\mathbf{l}_\alpha(\lambda)$ be the right and left eigenvectors of $\mathscr{M}_\infty(\lambda)$. The matrix $\mathscr{M}_\infty(\lambda)$ has the same form as the corresponding matrix in [16]:

$$\mathscr{M}_\infty(\lambda) = \begin{pmatrix} 0 & 1 & 0 & 0 \\ 0 & 0 & 1 & 0 \\ 0 & 0 & 0 & 1 \\ -\lambda^2 & 2\lambda c & 1-c^2 & 0 \end{pmatrix}.$$

The characteristic equation $\det\,[\mathscr{M}_\infty(\lambda) - \mu\mathscr{E}] = 0$, where $\mathscr{E}$ is the unit matrix, has the form

$$\mu^4 - (1 - c^2)\mu^2 - 2\mu c\lambda + \lambda^2 = 0. \tag{31}$$

The asymptotic behavior of solutions of (26) is obviously determined by these eigenvalues.

The following was shown in [16]

- If $|c| < 1$ and $\lambda$ is not on the imaginary axis, then (31) has two roots in the right complex half-plane and two in the left complex half-plane. For $\lambda$ in the right half-plane, we let $\mu_1$ and $\mu_3$ denote the two roots in the left half-plane.
- The functions $\mu_1(\lambda)$ and $\mu_3(\lambda)$ ave branch points for $\lambda$ in the right half-plane, and they are analytic in a neighborhood of the origin:

$$\mu_1(\lambda) = -\sqrt{1-c^2} + \frac{c\lambda}{1-c^2} + \frac{1+2c^2}{2(1-c^2)^{5/2}}\lambda^2 + O(\lambda^3),$$
$$\mu_3(\lambda) = -\frac{\lambda}{1-c} + O(\lambda^3); \tag{32}$$

- The solutions $\mathbf{y}_k$ and $\mathbf{z}_k$, $k = 1, 3$, of (28) and (30) satisfying

$$\lim_{\zeta\to\infty} \mathrm{e}^{-\mu_k(\lambda)^3}\mathbf{y}_k(\lambda,\zeta) = \mathbf{r}_k(\lambda),$$
$$\lim_{\zeta\to-\infty} \mathrm{e}^{\mu_k(\lambda)^3}\mathbf{z}_k(\lambda,\zeta) = \mathbf{l}_k(\lambda), \quad k = 1, 3, \tag{33}$$

  at infinity are analytic in $\lambda$ in a neighborhood of the origin.

Let $Y_k$ be the first component and $Z_k$ be the last component of the vectors $\mathbf{y}_k$ and $\mathbf{z}_k$, $k = 1, 3$, respectively satisfying (28) and (30). From (32) and (33), we have

$$Y_1 = \mathrm{e}^{-\sqrt{1-c^2}\zeta}\left(1+\frac{c\zeta}{1-c^2}\,\lambda+\left[\frac{c^2\zeta^2}{2(1-c^2)^2}+\frac{1+2c^2}{2(1-c^2)^{5/2}}\,\zeta\right]\lambda^2\right)+O(\lambda^3),$$

$$Y_3 = 1 - \frac{\zeta}{1-c}\,\lambda + \frac{1}{2}\frac{\zeta^2}{(1-c)^2}\,\lambda^2 + O(\lambda^3) \tag{34}$$

as $\zeta \to \infty$ and

$$Z_1 = \mathrm{e}^{\sqrt{1-c^2}\zeta}\left(1 - \frac{c\zeta}{1-c^2}\,\lambda + \left[\frac{c^2\zeta^2}{2(1-c^2)^2} - \frac{1+2c^2}{2(1-c^2)^{5/2}}\,\zeta\right]\lambda^2\right) + O(\lambda^3),$$

$$Z_3 = 1 + \frac{\zeta}{1-c}\,\lambda + \frac{1}{2}\frac{\zeta^2}{(1-c)^2}\,\lambda^2 + O(\lambda^3) \tag{35}$$

as $\zeta \to -\infty$.

We seek solutions of (27) and (29) for $\lambda$ in a neighborhood of the origin in the form of the expansions

$$Y_k(\lambda) = Y_{k0} + \lambda Y_{k1} + \frac{1}{2}\lambda^2 Y_{k2} + O(\lambda^3),$$
$$Z_k(\lambda) = Z_{k0} + \lambda Z_{k1} + \frac{1}{2}\lambda^2 Z_{k2} + O(\lambda^3), \quad k = 1, 3,$$

The coefficients of these equations satisfy certain equations [16] that can be solved analytically.

### 3.2.4 External Systems

We consider the vectors $\mathbf{y}^\wedge(\lambda,\zeta)$ and $\mathbf{z}^\wedge(\lambda,\zeta)$ with the components

$$y^\wedge_{\alpha\wedge\beta} = y_{\mathbf{1}\alpha}y_{\mathbf{3}\beta} - y_{\mathbf{1}\beta}y_{\mathbf{3}\alpha},$$
$$z^\wedge_{\alpha\wedge\beta} = z_{\mathbf{1}\alpha}z_{\mathbf{3}\beta} - z_{\mathbf{1}\beta}z_{\mathbf{3}\alpha}, \alpha < \beta, \alpha, \beta = 1, 2, 3, 4,$$

where $y_{\mathbf{k}\alpha}$, and $z_{\mathbf{k}\alpha}$ are the components of the respective vectors $\mathbf{y}_k$ and $\mathbf{z}_k$. We set a correspondence between $\alpha \wedge \beta$ and the numbers as follows: $1\wedge 2 \to 1$, $1 \wedge 3 \to 2$, $1 \wedge 4 \to 3$, $2 \wedge 3 \to 4$, $2 \wedge 4 \to 5$, and $3 \wedge 4 \to 6$. The vectors $\mathbf{y}^\wedge(\lambda,\zeta)$, $\mathbf{z}^\wedge(\lambda,\zeta)$ satisfy the linear systems

$$\mathbf{y}^{\wedge'} = \mathscr{M}^\wedge(\lambda,\zeta)\mathbf{y}^\wedge, \quad \mathbf{z}^{\wedge'} = -\mathbf{z}^\wedge\mathscr{M}^\wedge(\lambda,\zeta), \tag{36}$$

where

$$\mathscr{M}^\wedge(\lambda,\zeta) = \begin{pmatrix} 0 & 1 & 0 & 0 & 0 & 0 \\ 0 & 0 & 1 & 1 & 0 & 0 \\ 2\lambda c + 2p^{0'} & 1 - c^2 + p^0 & 0 & 0 & 1 & 0 \\ 0 & 0 & 0 & 0 & 1 & 0 \\ \lambda^2 - p^{0''} & 0 & 0 & 1 - c^2 + p^0 & 0 & 1 \\ 0 & \lambda^2 - p^{0''} & 0 & -2\lambda c - 2p^{0'} & 0 & 0 \end{pmatrix},$$

with the asymptotic matrixIt is easy to verify that the matrix

$$\mathscr{M}_\infty^\wedge(\lambda) = \mathscr{M}^\wedge(\lambda, \pm\infty) = \begin{pmatrix} 0 & 1 & 0 & 0 & 0 & 0 \\ 0 & 0 & 1 & 1 & 0 & 0 \\ 2\lambda c & 1-c^2 & 0 & 0 & 1 & 0 \\ 0 & 0 & 0 & 0 & 1 & 0 \\ \lambda^2 & 0 & 0 & 1-c^2 & 0 & 1 \\ 0 & \lambda^2 & 0 & -2\lambda c & 0 & 0 \end{pmatrix}.$$

It is easy to verify that the matrix $\mathscr{M}_\infty^\wedge(\lambda)$ has the eigenvalues

$$\mu_\alpha(\lambda) + \mu_\beta(\lambda), \quad 1 \le \alpha, \beta \le 4, \quad \alpha < \beta.$$

### 3.2.5 Evans Function

For $\lambda$ in the right complex half-plane, the matrix $\mathscr{M}_\infty(\lambda)$ has two eigenvalues in the left half-plane. The matrix $\mathscr{M}_\infty^\wedge(\lambda)$ therefore has a simple (hence analytic) leftmost eigenvalue with the least real part $\mu^\wedge(\lambda) = \mu_3(\lambda) + \mu_1(\lambda)$ for $\lambda$ in the right half-plane. By an exact direct analogy with (33), there are solutions of (36) such that

$$\lim_{\zeta\to\infty} \mathrm{e}^{-\mu^\wedge(\lambda)^3} \mathbf{y}^\wedge(\lambda, \zeta) = \mathbf{r}^\wedge(\lambda),$$
$$\lim_{\zeta\to-\infty} \mathrm{e}^{\mu^\wedge(\lambda)^3} \mathbf{z}^\wedge(\lambda, \zeta) = \mathbf{l}^\wedge(\lambda),$$

where $\mathbf{r}^\wedge(\lambda)$ and $\mathbf{l}^\wedge(\lambda)$ are the eigenvectors associated with $\mu^\wedge(\lambda)$. It can be shown that $\mathbf{y}^\wedge(\lambda, \zeta)$ $\mathbf{z}^\wedge(\lambda, \zeta)$ are analytic functions of $\lambda$ for $\lambda$ in the right half of the complex plane [16].

We define the nonnormalized Evans function by

$$\hat{D}(\lambda) = \mathbf{z}^\wedge \cdot \mathbf{y}^\wedge = \det \begin{pmatrix} \mathbf{z}_1(\lambda,\zeta)\cdot\mathbf{y}_1(\lambda,\zeta), & \mathbf{z}_1(\lambda,\zeta)\cdot\mathbf{y}_3(\lambda,\zeta) \\ \mathbf{z}_3(\lambda,\zeta)\cdot\mathbf{y}_1(\lambda,\zeta), & \mathbf{z}_3(\lambda,\zeta)\cdot\mathbf{y}_3(\lambda,\zeta) \end{pmatrix}. \tag{37}$$

The last equality in (37) holds in the neighborhood $U_\lambda(0)$ of the origin where the functions $\mathbf{y}_k(\lambda, \zeta)$ and $\mathbf{z}_k(\lambda, \zeta)$, $k = 1, 3$ are analytic.

For $\operatorname{Re}\lambda > 0$ the function $\hat{D}(\lambda)$ is zero if and only if there is a solution of (27) decaying exponentially as $\zeta \to \pm\infty$ [16, 20].

The normalized Evans function $D(\lambda)$ has the form

$$D(\lambda) = \frac{\hat{D}(\lambda)}{\mathbf{l}^\wedge(\lambda)\cdot\mathbf{r}^\wedge(\lambda)}.$$

For $\lambda \in U_\lambda(0)$, we have

$$\mathbf{l}^{\wedge} \cdot \mathbf{r}^{\wedge} = \det \begin{pmatrix} \mathbf{l}_1(\lambda) \cdot \mathbf{r}_1(\lambda) & \mathbf{l}_1(\lambda) \cdot \mathbf{r}_3(\lambda) \\ \mathbf{l}_3(\lambda) \cdot \mathbf{r}_1(\lambda) & \mathbf{l}_3(\lambda) \cdot \mathbf{r}_3(\lambda) \end{pmatrix} = -4(1-c^2)^{3/2}\lambda + O(\lambda^2).$$

It was proved in [16] (also see [17]) that $D(\lambda) \to 1$ as $|\lambda| \to \infty$.

The following theorem can be proved using the expressions for the coefficients $Y_{k0}$, $Y_{k1}$, $Y_{k2}$, $Z_{k0}$, $Z_{k1}$ and $Z_{k2}$ and conditions (34) and (35) [12].

**Theorem 4** *The Evans function $D(\lambda)$, constructed for the function $w(\lambda, \zeta)$ in* (27)*, is analytic in a neighborhood of the origin and is expanded there in a convergent Taylor series of the form*

$$D(\lambda) = \frac{1-2c^2}{4(1-c^2)^3}\lambda^2 + \sum_{n=3}^{\infty} e_n(c)\lambda^n. \tag{38}$$

For $c^2 < 1/2$ the first coefficient in expansion (38) is negative. It hence follows that in a sufficiently small neighborhood of the origin, the Evans function $D(\lambda)$ is negative on the real axis (because $D(\lambda)$ is real for real $\lambda$). Comparing the behavior of the analytic Evans function in the vicinity of the origin and at infinity indicates that this function must vanish in a finite domain on the real axis. This zero coincides with the unstable eigenvalue of generalized spectral problem (27).

## 4 Conclusion and Discussion

We have discussed questions of the dynamical stability of the Kirchhoff-Clebsch theory of elastic rods. We treat the rod as thin and inextensible. At each instant $t$, the arc-length $\xi$ of the centerline curve $\mathscr{G}(t)$ (elastica) is regarded as a spatial coordinate. We consider both stability to planar perturbations (lying in the plane of principal bending) as well as to perturbations coming out of the plane of principal bending.

The rod dynamics is fully determined by the evolution of the three Euler angles $\theta$, $\psi$, and $\phi$. The rod is considered dynamically symmetric. The rod motion is planar if $\psi = \phi = 0$ and $\mathscr{G}(t)$ is in the plane curve belonging to the pane containing the principal axis of inertia of the cross section (principal plane of bending)). If $\psi \neq 0$, then the curve $\mathscr{G}(t)$ cannot be embedded in a single plane, and the motion of the rod is three-dimensional. We note that in the general case, a nonzero $\psi$ implies torsion in the rod, i.e., $\phi \neq 0$, and a three-dimensional rod motion occurs in the presence of nonzero torsion. The energy of torsion can be neglected only in the case of small twist-free deviations ($M_3 = 0$) from the principal plane of flexure (cf., e.g., [12]). The equations giving the rod dynamics in the general case have forms (17) and (18).

For the planar perturbations we investigate nonlinear (Lyapunov stability). This investigation is based on the Hamiltonian formulation (1) of the system of equation in question. This is due to the fact that the plane motion is twist free and the torsion for it equals to zero. We prove the orbital Lyapunov stability (see Definition 2). The stability is due to the fact that we are able construct the Lyapunov function (functional) in this case. The Hessian $\mathscr{H}$ has empty negative spectrum, only one null eigenfunction (due to the translational invariance) and positive spectrum bounded away from zero. The stability occurs due to the fact that the Lyapunov functional has its local minimum on the linear space $L$ tangent to the closed submanifold $M$ where solutions of the basic equations (6) live intersected with the kernel of $\mathscr{H}$.

Unlike the case of plane perturbations the elastica is unstable about three dimensional perturbations. As it is pointed above the torsion in this case can not be neglected and we need to treat the full system (19). Equations (19) describe the balance of the bending energy, the energy of torsion, the kinetic energy of a point of the elastica, and the kinetic energy of the rotation of the rod cross section. The terms corresponding to the rotational energy of the cross section are collected in the right-hand side of the second equation in (19). Using a natural scaling transformation, we showed that the contribution of the rotational kinetic energy to the total energy is much less than the contribution of the kinetic energy of a point of the elastica (as in the two dimensional case). Therefore, in linearized equations (25), we can neglect the perturbations of the corresponding terms, assuming that they are of the second order of smallness. We considered a particular form of perturbations for which a torsional moment is absent. Linearized equations (25) turned out to be equivalent to the single Eq. (26).

Instability results for (26) were previously obtained in [12] using the properties of the Evans function for the solitary wave solution, solutions of basic equations (6) $\big($or (21)$\big)$ of the type of a planar solitary wave in a loop form. Equation (26) (and spectral problem (27) as a consequence) appear as a result of linearizing much simpler equations for the rod dynamics [12]. These results were schematically reproduced here in Sect. 3.2.2.

The Evans function $D(\lambda)$ was constructed as an analytic function in the right half of the complex plane of the spectral parameter, where it vanishes at points of the discrete spectrum of generalized spectral problem (27). The Evans function is real on the real axis and tends to unity as $|\lambda| \to \infty$. Our instability results followed from comparing the behavior of the Evans function in the neighborhood of the origin (where the function is analytic) with its asymptotic behavior at infinity. Direct calculations using the Matematica package allowed obtaining an analytic expression for the first coefficient of the Taylor expansion of the Evans function around the origin in the complex $\lambda$-plane [12], which is negative for speeds $c^2 < 1/2$. Consequently, for small positive values of $\lambda$, the function $D(\lambda) < 0$. It hence follows immediately that the Evans function vanishes on the positive half-axis, i.e., there exists at least one unstable eigenvalue. This in turn means that solitary waves moving not very rapidly in an inextensible rod are unstable under spatial (non-planar) perturbations of the wave form.

The question about stability of the loop solitary wave for $c \in [1/\sqrt{2}, 1)$ remains open, but there is no doubt that the momentum of the traveling solitary wave for the indicated range of speeds stabilizes it. The analogy with another problem serves as the justification for this assertion. Linearized equation (26) turns out to be absolutely identical to the corresponding linear equation in the problem posed in [22] (also see [14]). That problem relates to wave propagation in one composite-material model representing the idealized case of an elastic matrix with elastic rods with a significant flexural rigidity continuously distributed in it. In such a composite, there exist two families of solitary waves. Written for convenience in dimensionless variables, one family is orbitally (nonlinearly) stable for $c^2 > 1/2$. In these variables, the equations linearized about the solitary wave of this family reduce to a single equation having exactly the same form as (26) with $p_0$ given by formulas (10) and (27). This result, as already mentioned, most likely means that linearized problem (26) with $p_0$ determined by (27) does not have unstable eigenvalues for $c^2 > 1/2$.

We performed an experiment with a long fishing line. We took a sufficiently thick line (although its thickness was small compared with the curvature radius of the evolving elastica) to model an elastic rod with a large value of Young's module. Static ($c = 0$) solitary wave (10) or (27) could be easily produced. It was clearly unstable under spatial perturbations. The experiment showed that the unstable solitary wave under the influence of a twist-free perturbation evolved into a three-dimensional structure with localized torsion ($\phi$ rapidly decaying at infinity).

One of the basic questions in the theory of the stability of flows and states is the form of a stable secondary structure forming from an unstable state. The complete class of solitary wave solutions was obtained in [8]. Among them, solutions are found with a nonzero constant twist moment $M_3$. They correspond to helical structures with $\phi \to \infty$ as $\xi \to \pm\infty$. We note that helical structures are near the threshold of instability of a twisted straight rod and their stability was investigated in several papers; see, e.g., [23–25]. Solitary wave (10) of pure flexure is the only twist-free solitary wave solution.

## References

1. Kirchhoff, G.: Vorlezungen über mathematische Physic. Mechanik. Vorl. **28**. Leipzig: D. G. Teubner (1876)
2. Clebsch, A.: Theorie der Elasticität Fester Körper. Leipzig: B. G. Teubner (1862)
3. Dill, E.H.: Kirchoff's theory of rods. Arch. Hist. Exact Sci. **44**, 1–23 (1992)
4. Love, A.E.H.: A Treatise on the Mathematical Theory of Elasticity. Cambridge University Press, Cambridge (1927)
5. Coleman, B.D., Dill, E.H.: Flexure waves in elastic rods. J. Acoust. Soc. Am. **91**, 2663–2673 (1992)
6. Coleman, B.D., Xu, J.M.: On the interaction of solitary waves of flexure in elastic rods. Acta Mech. **110**, 173–182 (1995)
7. Coleman, B.D., Dill, E.H., Swigon, D.: On the dynamics of flexure and stretch in the theory of elastic rods. Arch. Ration. Mech. Anal. **129**, 147–174 (1995)
8. Coleman, B., Dill, E.H., Lembo, M, Lu, Z. Tobias, I.: On the dynamics of rods in the theory of Kirchoff and Clebsch. Arch. Ration. Mech. Anal. **121**, 339–359 (1993)
9. Beliaev, A., Il'ichev, A.: Conditional stability of solitary waves propagating in elastic rods. Phys. D. **90**, 107–118 (1996)
10. Dichmann, D.J., Maddocks, J.H., Pego, R.L.: Hamiltonian dynamics of an elastica and the stability of solitary waves. Arch. Ration. Mech. Anal. **135**, 347–396 (1996)
11. Grillakis, M., Shatah, J., Strauss, W.: Stability theory of solitary waves in the presence of symmetry. I. J. Funct. Anal. **74**, 160–197 (1987)

12. Il'ichev, A.: Instability of solitary waves on Euler's elastica. Z. Angew. Math. Phys. **57**, 547–566 (2006)
13. Il'ichev, A.T., Tomashpolskii, V. Ja.: Instability of solitons under flexure and twist of an elastic rod. Theoret. Math. Phys. **172**, 1206–1216 (2012)
14. Il'ichev, A.T.: Stability of Localized Waves in Nonlinearly Elastic Rods. Fizmatlit, Moscow (2009) [in Russian]
15. Antman, S.S., Liu, T.-P.: Travelling waves in hyperelastic rods. Quart. Appl. Math. **39**, 377–399 (1979)
16. Alexander, J.C., Sachs, R.: Linear instability of solitary waves of a Boussinesq-type equation: a computer assisted computation. Nonlinear World **2**, 471–507 (1995)
17. Pego, R.L., Weinstein, M.I.: Eigenvalues, and instabilities of solitary waves. Phil. Trans. R. Soc. Lond. A **340**, 47–94 (1992)
18. Evans, J.V.: Nerve axon equations, III: stability of the nerve impulse. Indiana Univ. Math. J. **22**, 577–594 (1972)
19. Jones, C.K.R.T.: Stability of the travelling wave solution of the FitzHugh-Nagumo system. Trans. Am. Math. Soc. **286**, 431–469 (1984)
20. Alexander, J.C., Gardner, R., Jones, C.K.R.T.: A topological invariant arising in the stability analysis of travelling waves. J. Reine Angew. Math. **410**, 167–212 (1990)
21. Kapitula, T.: The Evans function and generalized Melnikov integrals. SIAM J. Math. Anal. **30**, 273–297 (1998)
22. Il'ichev, A.: Stability of solitary waves in nonlinear composite media. Phys. D. **150**, 261–277 (2001)
23. Goriely, A., Tabor, A.M.: New amplitude equations for thin elastic rod. Phys. Rev. Lett. **77**, 3537–3540
24. Lafortune, S., Lega, J.: Instability of local deformations of an elastic rod. Phys. D. **182**, 103–124 (2003)
25. Lafortune, S., Lega, J.: Spectral stability of local deformations of an elastic rod: Hamiltonian formalizm. SIAM J. Math. Anal. **36**, 1726–1741

# Numerical Modelling of Two-Phase Piezocomposites with Interface Mechanical Anisotropic Effects

**G. Iovane and A. V. Nasedkin**

**Abstract** The present paper considers the homogenization problems for two-phase piezocomposite materials with random inclusions and with taking into account the mechanical imperfect interface boundaries. The accepted constitutive equations on the interface correspond to the Gurtin–Murdoch model for surface stresses and give a significant effect only for nanosized inclusions. To find the effective material properties, an integrated approach was used, based on the effective moduli method, on the modelling of representative volume element and on the finite element method. A set of boundary value problems was presented, which allow one to determine a complete collection of effective stiffness moduli, piezomoduli, and dielectric permittivities for a piezocomposite of arbitrary anisotropy class. The numerical realization was carried out in the ANSYS finite element package, which was used for representative volume modelling and for computation of the effective properties for piezocomposite material. The representative volume consisted of a regular mesh of cubic piezoelectric finite elements with the material properties of two phases. The interphase boundaries were covered with anisotropic elastic membrane elements that simulated surface stresses. As an example, the homogenization problem for one ceramomatrix piezocomposite with nanosized inclusions was solved numerically. It was noted that the interface stresses can essentially increase the effective stiffness moduli. However, the mechanical interface had a small influence on the effective piezomoduli and on the dielectric permittivities.

**Keywords** Piezoelectricity · Nanomechanics · Surface Effect · Interface · Piezocomposite · Effective Modulus

---

G. Iovane
Department of Computer Science, University of Salerno, 84084 Fisciano, SA, Italy
e-mail: giovane@unisa.it

A. V. Nasedkin (✉)
Institute of Mathematics, Mechanics and Computer Science, Southern Federal University, Milchakova Street 8a, Rostov-on-Don 344090, Russia
e-mail: nasedkin@math.sfedu.ru

H. Altenbach et al. (eds.), *Dynamical Processes in Generalized Continua and Structures*, Advanced Structured Materials 103,
https://doi.org/10.1007/978-3-030-11665-1_16

# 1 Introduction

Piezocomposite materials and, in particular, two-phase piezoceramic materials with nanosized pores or inclusions are being actively developed in the recent years [27–29]. New nanostructured piezoelectric composite materials have a range of important advantages, such as the possibilities of controllable variation of the functional characteristics within a wide range, the ultra-low mechanical quality factor, etc. Furthermore, the modelling of composite micro- and nanomaterials has the specific features [5, 7, 15, 30, 31]. It is known that some nanomaterials have unconventional physical properties that considerably differ from the characteristics of usual macrosized bodies. Thus, the experimental fact is the increasing of the stiffness with reducing the sizes of nanoobjects. One of the factors that are responsible for this behavior can be surface or interface effects. As research of the recent years shows, for the bodies of submicro- and nanosizes the surface stresses are important and influence the deformation of the bodies. In connection to this, the actual problem can be an extension of this approach to the nanostructured piezoelectric composite materials. Theoretical and numerical investigations of piezoelectric nanosized materials with surface effects and imperfect interface models were also presented in [4, 9, 11–13, 20, 21, 26], etc. Homogenization problems for nanoisized piezoelectric composites were considered in [3, 10, 32–34], etc.

In present investigation the models of two-phase piezoelectric composite materials developed in the framework of classic continuum approaches of solid mechanics and methods of composite mechanics. These models were used to construct more complicated models of the nanosized piezocomposites that were take into account the surface or interphase mechanical boundary conditions with anisotropic surface properties.

We use an integrated approach to the determination of the effective moduli of nanostructured piezoelecrtric composites with stochastically distributed nanosized inclusions. In order to take into account nanoscale level at the borders between two material phases, the Gurtin–Murdoch model of surface stresses are used [5, 7, 14, 15, 30]. ANSYS finite element package was used to simulate representative volumes and to calculate the effective moduli. This approach is based on the theory of effective moduli of composite mechanics, modelling of representative volumes and the finite element method [24, 25]. Here, the contact boundaries between two material phases were covered by the surface membrane elements in order to take the surface stresses into account. The next step consisted in solving the static problems for representative volume with the boundary conditions which were conventional for effective moduli method. Further, the averaged stresses and electric fluxes were calculated, both on the volume finite elements and on the surface finite elements for mechanical stresses. Finally, the effective moduli were calculated by using the estimated average characteristics.

## 2 Homogenization Problem by Effective Moduli Method

Let $\Omega = \Omega^{(1)} \cup \Omega^{(2)}$ be a representative volume occupied by a two-phase medium, composed of piezoelectric matrix (phase 1) and nanosized piezoelectric or elastic inclusions (phase 2); $\Omega^{(j)}$ is the volume or the set of volumes occupied by the material of the phase with number $j$; $\Gamma = \partial\Omega$ is the external boundary of representative volume $\Omega$; $\Gamma^s = \partial\Omega^{(1)} \cap \partial\Omega^{(2)}$ is the aggregate of interface surfaces of materials with different phases; **n** is the vector of external unit normal to $\Gamma$ or to the boundary, outward with respect to the volume $\Omega^{(1)}$; $\mathbf{x} = \{x_1, x_2, x_3\}$ is the vector of the special coordinates; $\mathbf{u} = \mathbf{u}(\mathbf{x})$ is the vector-function of mechanical displacements; $\varphi = \varphi(\mathbf{x})$ is the function of electric potential.

Then, for finding the effective moduli of such composite we can solve in $\Omega$ the static piezoelectric homogenization problems, presented here in a nonstandard vector-matrix form convenient for applying the finite element method

$$\mathbf{L}^*(\nabla) \cdot \mathbf{T} = 0, \quad \nabla \cdot \mathbf{D} = 0\,, \tag{1}$$

$$\mathbf{T} = \mathbf{c} \cdot \mathbf{S} - \mathbf{e}^* \cdot \mathbf{E}, \quad \mathbf{D} = \mathbf{e} \cdot \mathbf{S} + \boldsymbol{\kappa} \cdot \mathbf{E}\,, \tag{2}$$

$$\mathbf{S} = \mathbf{L}(\nabla) \cdot \mathbf{u}, \quad \mathbf{E} = -\nabla\varphi\,, \tag{3}$$

$$\mathbf{L}^*(\nabla) = \begin{bmatrix} \partial_1 & 0 & 0 & 0 & \partial_3 & \partial_2 \\ 0 & \partial_2 & 0 & \partial_3 & 0 & \partial_1 \\ 0 & 0 & \partial_3 & \partial_2 & \partial_1 & 0 \end{bmatrix}, \quad \nabla = \begin{Bmatrix} \partial_1 \\ \partial_2 \\ \partial_3 \end{Bmatrix}, \tag{4}$$

$$\mathbf{L}^*(\mathbf{n}) \cdot [\mathbf{T}] = \mathbf{L}^*(\nabla^s) \cdot \mathbf{T}^s, \quad \mathbf{n} \cdot [\mathbf{D}] = 0, \quad [\mathbf{u}] = 0, \quad [\varphi] = 0, \quad \mathbf{x} \in \Gamma^s\,, \tag{5}$$

$$\mathbf{T}^s = \mathbf{c}^s \cdot \mathbf{S}^s, \quad \mathbf{S}^s = \mathbf{L}(\nabla^s) \cdot \mathbf{u}^s, \quad \mathbf{u}^s = \mathbf{A} \cdot \mathbf{u}, \quad \mathbf{A} = \mathbf{I} - \mathbf{n}\mathbf{n}^*\,, \tag{6}$$

$$\mathbf{u} = \mathbf{L}^*(\mathbf{x}) \cdot \mathbf{S}_0, \quad \mathbf{x} \in \Gamma\,, \tag{7}$$

where $\mathbf{L}^*(\mathbf{a})$ is the matrix operator dependent on the components of the vector **a**; $\mathbf{T} = \{\sigma_{11}, \sigma_{22}, \sigma_{33}, \sigma_{23}, \sigma_{13}, \sigma_{12}\}$ is the array of the stresses $\sigma_{ij}$; $\mathbf{S} = \{\varepsilon_{11}, \varepsilon_{22}, \varepsilon_{33}, 2\varepsilon_{23}, 2\varepsilon_{13}, 2\varepsilon_{12}\}$ is the array of the strains $\varepsilon_{ij}$; **D** and **E** are the electric flux density vector called also the electric displacement vector and the electric field vector, correspondingly; $\mathbf{c}_{\alpha\beta} = \mathbf{c}^E_{\alpha\beta}$ is the $6 \times 6$ matrix of elastic stiffness moduli $c_{\alpha\beta}$; **e** is the $3 \times 6$ matrix of piezoelectric moduli $c_{i\beta}$; $\boldsymbol{\kappa} = \boldsymbol{\kappa}^S = \boldsymbol{\varepsilon}^S$ is the $3 \times 3$ matrix of dielectric permittivity moduli $\kappa_{ij}$; $\mathbf{S}_0$ is the six-dimensional array of the constant components $S_{0\beta}$; $\mathbf{E}_0$ is the constant vector; superscript "*" denotes the transposition operation, and $(\ldots) \cdot (\ldots)$ is the scalar product operation. Here, $\alpha, \beta = 1, \ldots, 6$; $i, j = 1, 2, 3$; $\mathbf{T} = \mathbf{T}^{(j)}$, $\mathbf{c} = \mathbf{c}^{(j)}$, etc. for $\mathbf{x} \in \Omega^{(j)}$.

In Eqs. (5), (6) in accordance with the Gurtin–Murdoch model we assume that on nanosized interphase boundaries $\Gamma^s$ only the surface mechanical stresses $\sigma^s_{ij}$ are exist. Here, $[\mathbf{T}] = \mathbf{T}^{(1)} - \mathbf{T}^{(2)}$ is the jump stresses on the interphase boundary;

equality $\mathbf{n}\cdot[\mathbf{D}]=0$ means the continuity of the value $D_n$ on the transition across the interface, etc.; $\nabla^s=\nabla-\mathbf{n}(\partial/\partial r)$ is the surface gradient operator, where $r$ is the coordinate, measured by the normal to $\Gamma^s$; $\mathbf{T}^s=\{\sigma_{11}^s,\sigma_{22}^s,\sigma_{33}^s,\sigma_{23}^s,\sigma_{13}^s,\sigma_{12}^s\}$ is the array of surface stresses $\sigma_{ij}^s$; $\mathbf{S}^s=\{\varepsilon_{11}^s,\varepsilon_{22}^s,\varepsilon_{33}^s,2\varepsilon_{23}^s,2\varepsilon_{13}^s,2\varepsilon_{12}^s\}$ is the array of surface strains $\varepsilon_{ij}^s$; $\mathbf{c}^s$ is the matrix of surface elastic moduli $6\times 6$; $\mathbf{I}$ is the $3\times 3$ identity matrix.

By using (7), we can select such boundary conditions that enable us to obtain obvious expressions for the effective moduli $c_{\alpha\beta}^{\mathrm{eff}}$, $e_{i\beta}^{\mathrm{eff}}$, $\kappa_{ij}^{\mathrm{eff}}$. Thus, under the assumption of the general form anisotropy for piezoelectric composite, the effective material moduli can be determined, if we solve nine static piezoelectric boundary problems (1)–(7) with various values of $\mathbf{S}_0$ and $\mathbf{E}_0$, having set in (7) only one of the components $S_{0\zeta}$ or $E_{0k}$ ($\zeta=1,\ldots,6$; $k=1,2,3$) not equal to zero.

In particular, if in (7) we accept (problems I–VI, $\beta=1,\ldots,6$)

$$S_{0\zeta}=S_0\delta_{\beta\zeta},\quad \mathbf{E}_0=0\,, \tag{8}$$

then from the solution (1)–(7), (8) we find

$$c_{\alpha\beta}^{\mathrm{eff}}=\langle T_\alpha\rangle_{\Omega\Gamma}/S_0,\quad e_{i\beta}^{\mathrm{eff}}=\langle D_i\rangle_{\Omega}/S_0\,. \tag{9}$$

Similarly, if in (7) we assume (problems VII–IX, $j=1,2,3$)

$$\mathbf{S}_0=0,\quad E_{0k}=E_0\delta_{jk}\,, \tag{10}$$

then from (1)–(7), (8) we obtain

$$e_{j\alpha}^{\mathrm{eff}}=-\langle T_\alpha\rangle_{\Omega\Gamma}/E_0,\quad \kappa_{ij}^{\mathrm{eff}}=\langle D_i\rangle_{\Omega}/E_0\,. \tag{11}$$

Here, in (9), (11) $\alpha=1,\ldots,6$; $i=1,2,3$; the angle brackets $\langle(\ldots)\rangle_{\Omega\Gamma}$ denote the averaged by the volume $\Omega$ bulk and interface integral values, and the angle brackets $\langle(\ldots)\rangle_{\Omega}$ denote the averaged only by the volume bulk integral values

$$\langle(\ldots)\rangle_{\Omega\Gamma}=\frac{1}{|\Omega|}\Big(\int_{\Omega}(\ldots)\,d\Omega+\int_{\Gamma^s}(\ldots)^s\,d\Gamma\Big),\ \ \langle(\ldots)\rangle_{\Omega}=\frac{1}{|\Omega|}\Big(\int_{\Omega}(\ldots)\,d\Omega\Big). \tag{12}$$

Note that the boundary value problems (1)–(7) with (8) or (10) differ from the usual piezoelectric problems by the presence of the interface boundary conditions (5), (6) for nanosized structures which are typical for the Gurtin–Murdoch model of surface stresses [2, 16]. In addition, as we can see from (9), (11), (12), to determine the effective moduli from the solution of the homogenization problems, it is necessary to use not only the volume integrals, but also the interface surface integrals.

## 3 Finite Element Modelling in ANSYS Package. Case of Ceramomatrix Composite

For solving the piezoelectric problem (1)–(7) with (8) or (10) we can pass to their weak statement, use the finite element approximation, and in the result we get the finite element system

$$\mathbf{K}_{uu} \cdot \mathbf{U} + \mathbf{K}_{u\varphi} \cdot \boldsymbol{\Phi} = \mathbf{F}_u \, , \tag{13}$$

$$-\mathbf{K}^*_{u\varphi} \cdot \mathbf{U} + \mathbf{K}_{\varphi\varphi} \cdot \boldsymbol{\Phi} = \mathbf{F}_\varphi \, , \tag{14}$$

where $\mathbf{U}$ is the vector of nodal displacement, $\boldsymbol{\Phi}$ is the vector of nodal electric potential, the vectors $\mathbf{F}_u$, $\mathbf{F}_\varphi$ are obtained from the boundary conditions (7), and the finite element matrices are given by the formulas

$$\mathbf{K}_{uu} = \mathbf{K}_{\Omega uu} + \mathbf{K}_{\Gamma uu} \, , \tag{15}$$

$$\mathbf{K}_{\Omega uu} = \int\limits_{\Omega_h} \mathbf{B}^*_u \cdot \mathbf{c} \cdot \mathbf{B}_u \, d\Omega, \quad \mathbf{K}_{\Gamma uu} = \int\limits_{\Gamma^s_h} \mathbf{B}^{s*}_u \cdot \mathbf{c}^s \cdot \mathbf{B}^s_u \, d\,\Gamma \, , \tag{16}$$

$$\mathbf{K}_{u\varphi} = \int\limits_{\Omega_h} \mathbf{B}^*_u \cdot \mathbf{e}^* \cdot \mathbf{B}_\varphi \, d\Omega, \quad \mathbf{K}_{\varphi\varphi} = \int\limits_{\Omega_h} \mathbf{B}^*_\varphi \cdot \boldsymbol{\kappa} \cdot \mathbf{B}_\varphi \, d\,\Omega \, , \tag{17}$$

$$\mathbf{B}_u = \mathbf{L}^*(\nabla) \cdot \mathbf{N}^*_u, \quad \mathbf{B}^s_u = \mathbf{L}^*(\nabla^s) \cdot \mathbf{A} \cdot \mathbf{N}^*_u, \quad \mathbf{B}_\varphi = \nabla \mathbf{N}^*_\varphi \, . \tag{18}$$

Here, $\Omega_h$ is the volume of finite element mesh; $\Gamma^s_h$ is the finite element approximation of the interface boundary $\Gamma_h$; $\mathbf{N}^*_u$, $\mathbf{N}^*_\varphi$ are the matrix and the row vectors of approximating finite element basis functions ($\mathbf{u} \approx \mathbf{u}_h = \mathbf{N}^*_u \cdot \mathbf{U}$; $\varphi \approx \varphi_h = \mathbf{N}^*_\varphi \cdot \boldsymbol{\Phi}$).

In (16)–(18) the matrices $\mathbf{K}_{\Omega uu}$, $\mathbf{K}_{u\varphi}$ and $\mathbf{K}_{\varphi\varphi}$ are the standard finite element matrices of piezoelectric analysis for solid bodies. The matrix $\mathbf{K}_{\Omega uu}$ defines by the surface stresses. This matrix is analogous to the stiffness matrix for surface or interphase elastic membranes. Hence, for realization the finite element piezoelectric analysis for the bodies with mechanical surface or interphase effects it is necessary to have surface or interphase structural membrane elements along with ordinary solid piezoelectric finite elements.

The system (13), (14) with (15)–(18) was formed and solved in the finite element package ANSYS. The representative volume element (RVE) $\Omega$ was chosen in the shape of a cube with the side $L$, which was evenly divided into smaller geometrically identical cubes. These cubes were eight node hexahedral finite elements SOLID5 with capability of piezoelectric analysis. As a result, the volume $\Omega$ was included $n_\Omega = n^3$ brick finite elements, where $n$ is the number of elements along one of the axis. For the simulation of a two-phase composite, the finite elements were endowed with material properties of one of the phases. Initially, all elements had the properties of the first phase. Farther, based on the required input percentage of the material of the second phase $p_a$, for the randomly selected $n_p = \mathrm{NINT}(n_\Omega p_a/100)$ finite elements, their material properties were modified to the properties of the second phase. Here, NINT is the function to nearest integer in ANSYS APDL programming language. The resulting percentage of inclusions $p = 100n_p/n_\Omega$ can negligible small differ from the input value $p_a$.

Next, the interphase boundaries of the elements with different material properties were automatically covered by four-node shell elements SHELL181 with the option of membrane stresses, which simulated the interface stresses (5), (6) on the boundaries $\Gamma^s$. A detailed description of this algorithm was given in [22]. Farther, it was necessary to provide an anisotropy type for the shell elements SHELL181 which would be conformable with the hexagonal anisotropy of the brick finite elements SOLID5. For a hexagonal system of anisotropy on the interface, supplementary procedure was implemented for the shell elements SHELL181, located perpendicular to the isotropy plane $0x_1x_2$, by permutation of the stiffness moduli in rows and in columns corresponding to the axes $x_2$ and $x_3$. As a result, all interface boundaries became coated by the membrane finite elements which simulated the interface effect of surface stresses.

Figure 1 shows an examples of the representative volumes generated by the simple random algorithm for $n = 20$ with $p = 10\%$, $p = 50\%$ and $p = 90\%$.

Figure 2 illustrates the surface interface elements for different inner structures, corresponding to RVE shown in Fig. 1. The shell elements located perpendicular to the plane $0x_1x_2$ are shown in crimson color, and the shell elements located parallel to the plane $0x_1x_2$ are shown in blue. The varicolored shell elements were endowed here with different anisotropic material properties, conformable to the structures of the surface stiffness moduli $\mathbf{c}^s$ from (5).

At the next stage, for the generated representative volume element, we solve static problems (1)–(7) with (8) or (10), and after that in ANSYS postprocessor we calculate the averaged stresses and electric fluxes by both volume and surface elements. Lastly, using formulae (8), (10) and the obtained averaged stresses and electric fluxes, we determine the effective moduli of the piezocomposite, taking into account the interface stresses.

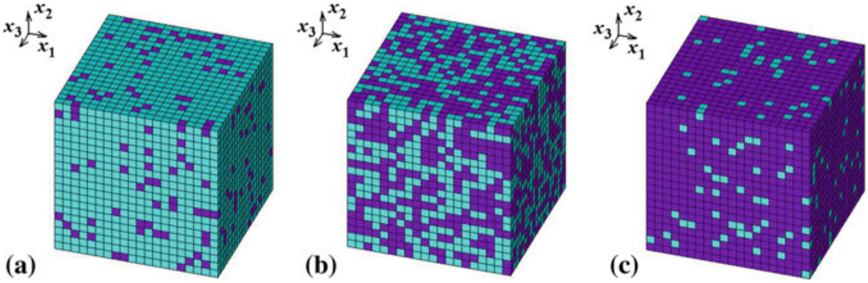

**Fig. 1** Examples of RVE with different percents of inclusions: **a** 10%, **b** 50%, **c** 90%

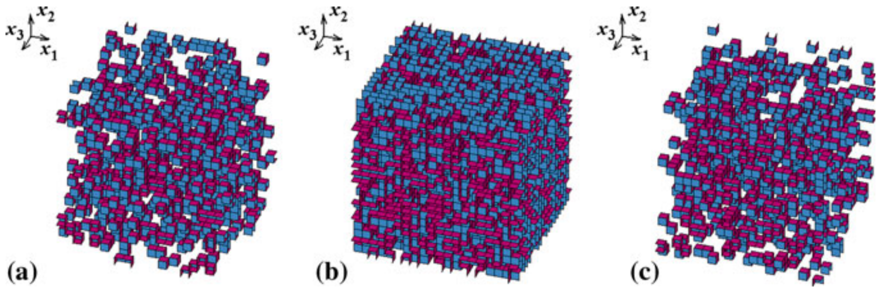

**Fig. 2** Examples of a interface boundaries for RVE with different percents of inclusions: **a** 10%, **b** 50%, **c** 90%

# 4 Numerical Examples

As an example, in this section we consider PZT-4/$Al_2O_3$ piezoceramic/monocrystal composite material. We determine the effective moduli of polycrystalline piezoceramic in two stages. At the first stage, we calculate the effective moduli for material of inclusions. At the second stage, we consider a piezocomposite with isotropic inclusions as a two-phase composite. Here we use the models of representative volume elements with random distributed inclusions, described in the previous sections.

In accordance with [1], after the first stage we obtain the averaged moduli of $\alpha$-corundum as an isotropic elastic material: $E^{(2)} = 40.26 \cdot 10^{10}$ (N/m$^2$); $\nu^{(2)} = 0.23$; $c_{11}^{(2)} = 46.88 \cdot 10^{10}$ (N/m$^2$); $c_{12}^{(2)} = 14.22 \cdot 10^{10}$ (N/m$^2$); $\kappa^{(2)} = 10\varepsilon_0$; $\varepsilon_0 = 8.85 \cdot 10^{-12}$ (F/m). In the calculations, we will consider this material as a piezoelectric material with negligible piezomoduli. For dense piezoceramic PZT-4 we assume the following material constants: $c_{11}^{(1)} = 13.9 \cdot 10^{10}$ (N/m$^2$); $c_{12}^{(1)} = 7.78 \cdot 10^{10}$ (N/m$^2$); $c_{13}^{(1)} = 7.43 \cdot 10^{10}$ (N/m$^2$); $c_{33}^{(1)} = 11.5 \cdot 10^{10}$ (N/m$^2$); $c_{44}^{(1)} = 2.56 \cdot 10^{10}$ (N/m$^2$); $e_{31}^{(1)} = -5.2$ (C/m$^2$); $e_{33}^{(1)} = 15.1$ (C/m$^2$); $e_{15}^{(1)} = 12.7$ (C/m$^2$); $\kappa_{11}^{(1)} = 730\varepsilon_0$; $\kappa_{33}^{(1)} = 635\varepsilon_0$.

Note that in order to determine in ANSYS a shell element with membrane option, it is necessary to define the elastic stiffness moduli $c_{\alpha\beta}^{m}$ and the thickness $h^m$. As it was indicated in [22], we can use the membrane element ANSYS as the interface element, simulated the surface conditions (5), (6), if we pose $c_{\alpha\beta}^{s} = h^m c_{\alpha\beta}^{m}$.

Consequently, here the products of the stiffness moduli $c_{\alpha\beta}^{m}$ of the membrane element by its thickness $h^m$ are the important values, but not the values of the stiffnesses $c_{\alpha\beta}^{m}$ and of the thickness $h^m$ separately. In continuation of the approaches described in [22], in this investigation we define the representative volume in dimensionless way where the finite element side was equal to one. Therefore, the space dimensioning parameter was equal to the minimal size of the inclusion element $a$. As there is not enough reliable data on the values of the surface stiffness moduli for interface between different elastic piezoelectric materials, then in accordance with the data for another materials, we assume that in the case of nanostructured ceramomatrix piezocomposite the surface stiffness moduli were connected to the volume moduli of piezoceramics and of inclusions by the formula $c^s_{\alpha\beta} = l_d|c^{(1)}_{\alpha\beta} - c^{(2)}_{\alpha\beta}|$, where $l_d = 10^{-10}$ (m). Let us also accept that $h^m = a$, $c^m_{\alpha\beta} = k^s|c^{(1)}_{\alpha\beta} - c^{(2)}_{\alpha\beta}|$, where $k^s$ is the dimensionless factor. Then, $c^s_{\alpha\beta} = h^m c^m_{\alpha\beta} = k^s a|c^{(1)}_{\alpha\beta} - c^{(2)}_{\alpha\beta}| = (k^s a/l_d)c^s_{\alpha\beta}$, i.e. $a = l_d/k^s$, and thus the coefficient $k^s$ is inversely proportional to the minimal size of the inclusions $a$. Further in computational experiments with constant surface moduli $c^s_{\alpha\beta}$ the coefficient $k^s$ and the inclusion percentage $p$ were varied. As it can be seen, the growth of factor $k^s$ corresponds to the decrease of the minimal inclusion size $a$, and for $k^s > 1$ the value $a$ becomes smaller as compared with parameter $l_d = 10^{-10}$(m).

For the analysis of the influence of the inclusion percentage and surface stress on the effective moduli, we have carried out the computer calculations of the effective moduli for a fixed number of the elements $n = 20$ along the axes of RVE, but for various percentage of inclusions $p$ and various but not very large values of the factor $k^s$. The numerical results are presented in Figs. 3, 4 and 5. Here and after $r(\ldots)$ denotes the relative values of the effective modulus, with respect to the corresponding values of the modulus for zero percentage of inclusions. For example, $r(c_{33}) = c^{\text{eff}}_{33}/c_{33}$, where $c^{\text{eff}}_{33}$ is the effective stiffness modulus for the nanostructured ceramomatrix piezocomposite, which takes the surface stress into account, $c_{33}$ is the corresponding

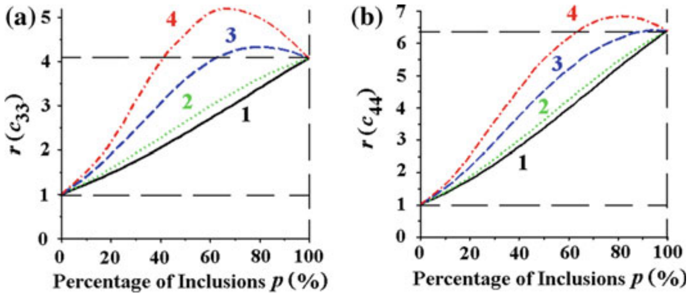

**Fig. 3** Dependencies of the relative effective moduli $c^{\text{eff}}_{33}$ (**a**) and $c^{\text{eff}}_{44}$ (**b**) versus inclusion percentage

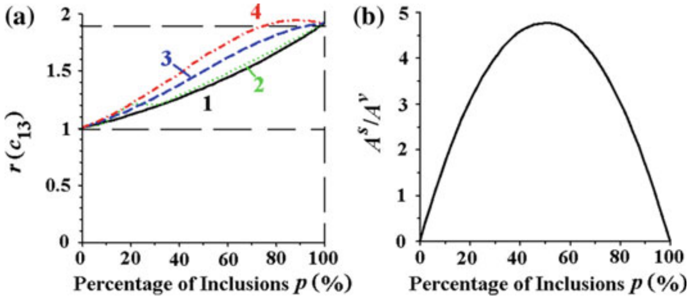

**Fig. 4** Dependencies of the relative effective modulus $c^{\text{eff}}_{13}$ (**a**) and area of interface $A^p$ (**b**) versus inclusion percentage

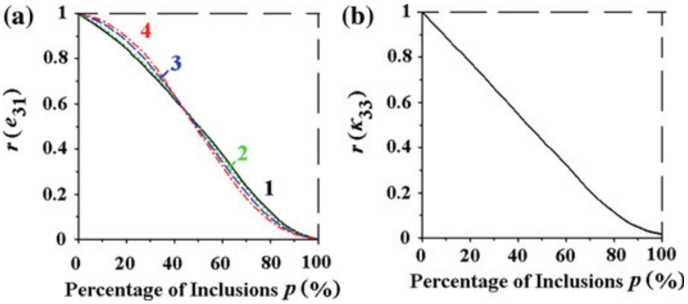

**Fig. 5** Dependencies of the relative effective piezomodulus $e_{31}^{\text{eff}}$ (**a**) and dielectric permittivity $\kappa_{33}^{\text{eff}}$ (**b**) versus inclusion percentage

value of the stiffness modulus for an ordinary dense material of piezoceramic and so on. The curves 1 correspond to the case $k^s = 0$, when there are no surface effects, the curves 2 correspond to the case $k^s = 0.1$, the curves 3 correspond to the case $k^s = 0.5$, and the curves 4 correspond to the case $k^s = 1$.

As Figs. 3 and 4 demonstrate, for relatively small values of the factor $k^s$ (curves 1 and 2) the interface effects do not affect the material moduli. However, for any percentage of inclusions the interface stresses are larger than the effective stiffnesses of the composite material. Moreover, there are cases when the composite material with interfaces can have greater stiffness than the more rigid material in the composite. This situation takes place when $k^s = 1$ for the stiffness modulus $c_{33}^{\text{eff}}$ if $p > 45\%$, for the stiffness modulus $c_{44}^{\text{eff}}$ if $p > 66\%$, and for the modulus $c_{13}^{\text{eff}}$ if $p > 75\%$, (see curves 4 which are located higher that the dashed lines in the Figs. 3 and 4a).

Note that the percentage of tougher inclusions and the interface stresses have the same influence on the effective stiffness: a simple increase of the percentage of tougher inclusions leads to a increase in the stiffness moduli, as well as the interface stresses increase the stiffness. Therefore, these two effects lead to an increase in the total stiffness of the piezocomposite. But with very small and with very large percentages of inclusions, the integral area of the interphase is small (Fig. 4b), and therefore the effective stiffness moduli of the composite become close to the corresponding stiffness moduli of the main material or inclusions.

Meanwhile, the uncoupled surface stresses have much less effect on the effective piezomoduli $e_{i\beta}^{\text{eff}}$ and almost do not influence on the dielectric permittivities $\kappa_{ii}^{\text{eff}}$. Thus. Figure 5 illustrates the dependencies of the most different relative effective transverse piezomodulus $e_{31}^{\text{eff}}$ (Fig. 5a) and dielectric permittivity $\kappa_{33}^{\text{eff}}$ (Fig. 5b) versus percentage of inclusions $p$.

Note that the influence of the surfaces stresses is significant mostly for the relative values of the transverse piezomodulus $r(e_{31}^{\text{eff}})$, and the curves for other piezomoduli and dielectric permittivities for different factors $k^s$ $(0 \le k^s \le 1)$ almost coincide and look like one curve (see, for example, Fig. 5b).

It is obvious that the effective value of piezomoduli and dielectric permittivities should change more appreciably, if instead of uncoupled mechanical interface stresses we take into account fully or partially coupled interface electromechanical effects using the models [9, 21].

## 5 Conclusion

In the paper, the homogenization model was described for a two-phase ceramomatrix piezocomposite with uncoupled surface stresses at the interphase boundaries, which reflected the nanoscale effects for nanostructured composites. This model was applied for the determination of the effective moduli of a piezoceramic–corundum composite with mechanical interphase boundary conditions. The solutions of the homogenization problems were obtained by using the finite element method in ANSYS package for a regular cubic representative volume element with hexahedral finite elements and stochastic distribution of inclusions. In order to take into account the interface effects, shell finite elements with membrane option were added to the finite model on the interphase boundaries. For the considered composite with softer skeleton matrix and stiffer inclusions, it was noted that the effective moduli were dependent on the percentage of inclusions and their sizes. These dependencies are similar to the known dependencies for nanoporous elastic composites [5–8, 17, 22].

Further investigations can be connected with the analysis of the influence of the connectivity and inner structure of the representative volume element on the effective moduli of piezocomposite materials with nanosized inclusions. Such analysis can be realized similarly to the one presented in [18, 19, 23–25] for the two-phase composites without interface effects. Other actual problem consists in the design of shell electromechanical coupled finite elements, which can be used to take into account the surface interface effects in more details for the homogenization of nanostructured piezocomposites.

**Acknowledgements** This work for second author was supported by the Russian Science Foundation (grant number 15-19-10008-P).

## References

1. Bobrov, S.V., Nasedkin, A.V., Rybjanets, A.N.: Finite element modeling of effective moduli of porous and polycrystalline composite piezoceramics. In: Topping, B.H.V., Montero, G., Montenegro, R. (eds.) Proceedings of VIII International Conference on Computational Structures Technology, Civil-Comp Press, Stirlingshire, UK, Paper 107 (2006)
2. Chatzigeorgiou, G., Javili, A., Steinmann, P.: Multiscale modelling for composites with energetic interfaces at the micro-or nanoscale. Math. Mech. Solids **20**, 1130–1145 (2015)
3. Chen, T.: Exact size-dependent connections between effective moduli of fibrous piezoelectric nanocomposites with interface effects. Acta Mech. **196**, 205–217 (2008)
4. Dai, S., Gharbi, M., Sharma, P., Park, H.S.: Surface piezoelectricity: size effects in nanostructures and the emergence of piezoelectricity in non-piezoelectric materials. J. Appl. Phys. **110**, 104305-1–104305-7 (2011)

5. Duan, H.L., Wang, J., Karihaloo, B.L.: Theory of elasticity at the nanoscale. In: Advances in Applied Mechanics, vol. 42, pp. 1–68. Elsevier (2008)
6. Duan, H.L., Wang, J., Karihaloo, B.L., Huang, Z.P.: Nanoporous materials can be made stiffer than non-porous counterparts by surface modification. Acta Mater. **54**, 2983–2990 (2006)
7. Eremeyev, V.A.: On effective properties of materials at the nano- and microscales considering surface effects. Acta Mech. **227**, 29–42 (2016)
8. Eremeyev, V., Morozov, N.: The effective stiffness of a nanoporous rod. Dokl. Phys. **55**(6), 279–282 (2010)
9. Eremeyev, V.A., Nasedkin, A.V.: Mathematical models and finite element approaches for nanosized piezoelectric bodies with uncoulped and coupled surface effects. In: Sumbatyan, M.A. (ed.) Wave Dynamics and Composite Mechanics for Microstructured Materials and Metamaterials. Advanced Structured Materials, vol. 59, pp. 1–18. Springer, Singapore (2017)
10. Gu, S.-T., He, Q.C., Pensée, V.: Homogenization of fibrous piezoelectric composites with general imperfect interfaces under anti-plane mechanical and in-plane electrical loadings. Mech. Mater. **88**, 12–29 (2015)
11. Gu, S.-T., Liu, J.-T., He, Q.-C.: Piezoelectric composites: imperfect interface models, weak formulations and benchmark problems. Comp. Mater. Sci. **94**, 182–190 (2014)
12. Gu, S.-T., Liu, J.-T., He, Q.-C.: The strong and weak forms of a general imperfect interface model for linear coupled multifield phenomena. Int. J. Eng. Sci. **85**, 31–46 (2014)
13. Gu, S.-T., Qin, L.: Variational principles and size-dependent bounds for piezoelectric inhomogeneous materials with piezoelectric coherent imperfect interfaces. Int. J. Eng. Sci. **78**, 89–102 (2014)
14. Gurtin, M.E., Murdoch, A.I.: A continuum theory of elastic material surfaces. Arch. Rat. Mech. Anal. **57**(4), 291–323 (1975)
15. Hamilton, J.C., Wolfer, W.G.: Theories of surface elasticity for nanoscale objects. Surf. Sci. **603**, 1284–1291 (2009)
16. Javili, A., McBride, A., Mergheima, J., Steinmann, P., Schmidt, U.: Micro-to-macro transitions for continua with surface structure at the microscale. Int. J. Solids Struct. **50**, 2561–2572 (2013)
17. Jeong, J., Cho, M., Choi, J.: Effective mechanical properties of micro/nano-scale porous materials considering surface effects. Interact. Multiscale Mech. **4**(2), 107–122 (2011)
18. Kudimova, A.B., Nadolin, D.K., Nasedkin, A.V., Nasedkina, A.A., Oganesyan, P.A., Soloviev, A.N.: Models of porous piezocomposites with 3–3 connectivity type in ACELAN finite element package. Mater. Phys. Mech. **37**(1), 16–24 (2018)
19. Kudimova, A.B., Nadolin, D.K., Nasedkin, A.V., Oganesyan, P.A., Soloviev, A.N.: Finite element homogenization models of bulk mixed piezocomposites with granular elastic inclusions in ACELAN package. Mater. Phys. Mech. **37**(1), 25–33 (2018)
20. Nanthakumar, S.S., Lahmer, T., Zhuang, X., Park, H.S.: Topology optimization of piezoelectric nanostructures. J. Mech. Phys. Solids **94**, 316–335 (2016)
21. Nasedkin, A.V., Eremeyev, V.A.: Harmonic vibrations of nanosized piezoelectric bodies with surface effects. ZAMM **94**(10), 878–892 (2014)
22. Nasedkin, A.V., Kornievsky, A.S.: Finite element modeling and computer design of anisotropic elastic porous composites with surface stresses. In: Sumbatyan, M.A. (ed.) Wave Dynamics and Composite Mechanics for Microstructured Materials and Metamaterials. Advanced Structured Materials, vol. 59, pp. 107–122. Springer, Singapore (2017)
23. Nasedkin, A.V., Nasedkina, A.A., Remizov, V.V.: Finite element modeling of porous thermoelastic composites with account for their microstructure. Vycisl. meh. splos. sred—Comput. Contin. Mech. **7**(1), 100–109 (2014)
24. Nasedkin, A.V., Shevtsova, M.S.: Improved finite element approaches for modeling of porous piezocomposite materials with different connectivity. In: Parinov, I.A. (ed.) Ferroelectrics and Superconductors: Properties and Applications, pp. 231–254. Nova Science Publishers, NY (2011)
25. Nasedkin, A.V., Shevtsova, M.S.: Multiscale computer simulation of piezoelectric devices with elements from porous piezoceramics In: Parinov, I.A., Chang, S.-H. (eds.) Physics and Mechanics of New Materials and Their Applications, pp. 185–202. Nova Science Publishers, NY (2013)

26. Park, H.S., Devel, M., Wang, Z.: A new multiscale formulation for the electromechanical behavior of nanomaterials. Comput. Methods Appl. Mech. Eng. **200**, 2447–2457 (2011)
27. Ringgaard, E., Lautzenhiser, F., Bierregaard, L.M., Zawada, T., Molz, E.: Development of porous piezoceramics for medical and sensor applications. Materials **8**(12), 8877–8889 (2015)
28. Rybyanets, A.N., Rybyanets, A.A.: Ceramic piezocomposites: modeling, technology, and characterization. IEEE Trans. Ultrason. Ferroelectr. Freq. Control **58**, 1757–1773 (2011)
29. Topolov, V.Y., Bowen, C.R.: Electromechanical Properties in Composites Based on Ferroelectrics. Springer, London (2009)
30. Wang, J., Huang, Z., Duan, H., Yu, S., Feng, X., Wang, G., Zhang, W., Wang, T.: Surface stress effect in mechanics of nanostructured materials. Acta Mech. Solida Sin. **24**(1), 52–82 (2011)
31. Wang, K.F., Wang, B.L., Kitamura, T.: A review on the application of modified continuum models in modeling and simulation of nanostructures. Acta Mech. Sin. **32**(1), 83–100 (2016)
32. Wang, Z., Zhu, J., Jin, X.Y., Chen, W.Q., Zhang, Ch.: Effective moduli of ellipsoidal particle reinforced piezoelectric composites with imperfect interfaces. J. Mech. Phys. Solids **65**, 138–156 (2014)
33. Xiao, J.H., Xu, Y.L., Zhang, F.C.: Size-dependent effective electroelastic moduli of piezoelectric nanocomposites with interface effect. Acta Mech. **222**(1–2), 59–67 (2011)
34. Xiao, J.H., Xu, Y.L., Zhang, F.C.: Evaluation of effective electroelastic properties of piezoelectric coated nano-inclusion composites with interface effect under antiplane shear. Int. J. Eng. Sci. **69**, 61–68 (2013)

# Surface Waves in Dissipative Poroviscoelastic Layered Half Space: Boundary Element Analyses

**F. Dell'Isola, L. A. Igumnov, S. Yu. Litvinchuk, A. A. Ipatov, A. N. Petrov and I. A. Modin**

**Abstract** Wave propagation in a poroelastic layer located on a poroelastic half-space is studied. A fully saturated poroelastic medium is described using Biot's mathematical model with four base functions—pore pressure and skeleton displacements. Viscoelastic behavior of porous medium due to viscoelastic properties of the skeleton is considered. The standard viscoelastic solid model is used. The boundary-value problem of the three-dimensional dynamic poroelasticity is written in terms of Laplace transforms. Direct approach of the boundary integral equation (BIE) method is employed. The boundary-element approach is based on the mixed boundary-element discretization of surface with generalized quadrangular elements. Time-step scheme for numerical inversion of the Laplace transforms is used obtain the solution of boundary value problem. To verify the boundary-element model, poroelastic solutions are compared with elastic ones.

**Keywords** Boundary element method · Biot's model · Poroviscoelasticity · Half space

## 1 Introduction

Currently, mathematical modeling is one of the main tools to analyze and optimize oil and gas fields development, to solve the problems of seismic construction and bioengineering [1–7]. The model of poroelastic medium, allowing to describe fluid filtration in pores in together with a full-scale mechanical model of the stress-strain state of medium is usually used to describe the "solid"–"fluid" system.

Modern forms of these models were introduced by Biot [8]. Biot's model correctly describes processes of elastic porous medium deformation and fluid flow in that medium. It is assumed that the space containing poroelastic medium is filled with a

---

F. Dell'Isola · L. A. Igumnov (✉) · S. Yu. Litvinchuk · A. A. Ipatov · A. N. Petrov · I. A. Modin
Research Institute for Mechanics, National Research Lobachevsky State University of Nizhni Novgorod, Nizhni Novgorod, Russia
e-mail: igumnov@mech.unn.ru

H. Altenbach et al. (eds.), *Dynamical Processes in Generalized Continua and Structures*, Advanced Structured Materials 103,
https://doi.org/10.1007/978-3-030-11665-1_17

two-phase material, and one phase corresponds to the elastic skeleton, and the another one to the fluid in pores. Both phases are present at each point of the physical space, and the phase distribution in space is described by macroscopic quantities such as porosity.

Biot's model allows us to solve a number of particular problems, among which the problems of wave propagation in homogeneous and layered poroelastic half-spaces are of particular interest [9–17]. However, the increasing complexity of computational schemes for boundary value problems requires the involvement of advanced methods such as boundary elements method (BEM). Possessing high accuracy and rigor of the approach, BEM is the most suitable method for considering nonstationary processes in semi-infinite bodies, since it ensures automatic fulfillment of the conditions for solution behavior at infinity. Despite the noted advantages of BEM, the possibility of modeling the poroelastic dynamics is mainly determined by the presence of the corresponding boundary integral equations (BIE) and fundamental solutions. Fundamental solutions and BIE of the dynamic theory of poroelasticity were obtained in [18–21]; in [22–25] different variants of boundary element schemes for the solution of problems in porodynamics are presented and results of numerical experiments are provided. Results of boundary element modeling of dynamics of poroelastic halfspaces are presented in [26–30].

The principal difference of poroelastic formulation from elastic and viscoelastic is that it allows to take into account the influence exerted by the fluid moving in pores on the behavior of the medium as a whole. Historically, on the basis of Biot's theory, the existence of two longitudinal waves—fast and slow in porous medium was predicted. The slow longitudinal wave is caused by the movement of fluid particles of the pores relative to the porous skeleton and is peculiar only to porous media. In addition, the frictional interaction of viscous fluid and a skeleton leads to a significant dissipation of energy in the medium, which demonstrates viscoelastic behavior [31, 32]. The viscoelastic behavior of poroelastic medium can also be due to the viscoelastic properties of the skeleton [33–35]. Some results of simulation of wave processes in poroelastic solids with the use of BIE, BEM and various models of viscoelastic behavior of the skeleton are presented in [36–38].

The paper presents the modeling of wave propagation in homogeneous and inhomogeneous poroviscoelastic in semi-infinite bodies using time-step BEM scheme. A poroviscoelastic layer on a semi-elastic halfspace is considered as an implementation of the inhomogeneity model.

## 2 Problem Formulation

Basic poroelastic material is a two-phase material consisting of an elastic skeleton and compressible fluid or gas filler. Porous material of a volume $V$ can be constructed as follows:

$$V = V^f + V^s \tag{1}$$

where $V$ is the total volume, $V^f$ is the summary pore volume and $V^s$ is the volume of the skeleton. It is assumed that filler can openly seep through the pores and all closed pores are assumed as a part of the skeleton. Then a correspondence principle is applied to the skeleton, so we extend poroelastic formulation to poroviscoelasticity.

Considering a boundary-value problem for Biot's model of fully saturated poroelastic continuum in Laplace domain in terms of four unknowns (displacements $\bar{u}_i$ and pore pressure $\bar{p}$) the set of differential equations take the following form [30]:

$$\begin{gathered} G\bar{u}_{i,jj} + \left(K + \frac{G}{3}\right)\bar{u}_{j,ij} - (\psi - \beta)\bar{p}_{,i} - s^2(\rho - \beta\rho_f)\bar{u}_i = -\bar{F}_i, \\ \frac{\beta}{s\rho_f}\bar{p}_{,ii} - \frac{\phi^2 s}{R}\bar{p} - (\psi - \beta)s\bar{u}_{i,i} = -\bar{a}, \quad x \in \Omega, \end{gathered} \tag{2}$$

Boundary conditions:

$$\begin{aligned} \bar{u}(x,s) &= f(x,s), \quad x \in \Gamma^u, \quad \bar{u} = (\bar{u}_1, \bar{u}_2, \bar{u}_3, \bar{p}), \\ \bar{t}(x,s) &= g(x,s), \quad x \in \Gamma^\sigma, \quad \bar{t} = \left(\bar{t}_1, \bar{t}_2, \bar{t}_3, \bar{q}\right), \end{aligned}$$

where $\Gamma^u$ and $\Gamma^\sigma$ denotes boundaries for boundary conditions of 1st and 2nd kind respectively, $G,\ K$ are elastic moduli, $\phi = V^f/V$ is porosity, $\bar{F}_i,\ \bar{a}$ are bulk body forces.

$$\beta = \frac{\kappa\rho_f\phi^2 s}{\phi^2 + s\kappa(\rho_a + \phi\rho_f)}, \psi = 1 - \frac{K}{K_s} \text{and } R = \frac{\phi^2 K_f K_s^2}{K_f(K_s - K) + \phi K_s(K_s - K_f)}$$

are constants reflecting interaction between skeleton and filler, $\kappa$ is permeability. Further, $\rho = \rho_s(1 - \phi) + \phi\rho_f$ is a bulk density, $\rho_s,\ \rho_a,\ \rho_f$ are solid, apparent mass density and filler density respectively, $K_s$, $K_f$ are elastic bulk moduli of the skeleton and filler respectively. Apparent mass density $\rho_a = C\phi\rho_f$ was introduced by Biot to describe dynamic interaction between fluid and skeleton. $C$ is a factor depending on the pores geometry and excitation frequency.

The governing equation system (2) in matrix form can be written as follows:

$$B\bar{u} = F, \quad \bar{u}^{\mathrm{T}} = (\bar{u}_i, p), i = 1, 3$$

$$\mathrm{B} = \begin{bmatrix} G\nabla^2 + \left(K + \frac{1}{3}G\right)\partial_i\partial_j - s^2(\rho - \beta\rho_f) & -(\psi - \beta)\partial_i \\ -s(\psi - \beta)\partial_j & \frac{\beta}{s\rho_f}\nabla^2 - \frac{\phi^2 s}{R} \end{bmatrix}.$$

Boundary conditions are:

$$u(x,s) = f(x,s) \text{ on } \Gamma^u, t_n(x,s) = g(x,s) \text{ on } \Gamma^\sigma.$$

In present paper we consider piecewise homogeneous solid $\Omega$ in Euclidian space $R^3$ with coordinate system $Ox_1x_2x_3$. Solid $\Omega$ is enclosed with boundary denotes as $\Gamma$, boundaries of $\Omega_k$ ($k = 1, \dots, K$) are denoted as $\Gamma_k$. Each part $\Omega_k$ is assumed to be isotropic. Material parameters of each $\Omega_k$ are denotes by upper index « k » So, governing equations for each part $\Omega_k$ in matrix form take a following form:

$$B^k \bar{u}^k = 0, \quad \bar{u}^k = (\bar{u}_i^k, p^k),\ i = 1, 3$$

$$\begin{bmatrix} G^k \nabla^2 + \left(K^k + \frac{1}{3} G^k\right) \partial_i \partial_j - s^2 (\rho^k - \beta^k \rho_f^k) & -(\psi^k - \beta^k) \partial_i \\ -s(\psi^k - \beta^k) \partial_j & \frac{\beta^k}{s \rho_f^k} \nabla^2 - \frac{\phi^{k2} s}{R^2} \end{bmatrix}$$

where $\bar{u}^k(x, s)$—generalized displacements vector at point $x = (x_1, x_2, x_3)$. Assumed that $u^k(x, t)$ fulfill zero initial condition:

$$u^k(x,\ 0) = u^k(x,\ 0) = 0$$

Following boundary conditions are employed for each $\Omega_k$:

$$\begin{gathered} u_l^k(x, t) = f_l^k(x, t),\ x \in \Gamma^u \cap \Gamma_k, \quad l = \overline{1, 3}; \\ t_l^k(x, t) = g_l^k(x, t), \quad x \in \Gamma^\sigma \cap \Gamma_k; \\ u_l^k(x, t) = u_l^m(x, t),\ t_l^k(x, t) = -t_l^m(x, t),\ x \in \mathit{\Gamma}'_{km}\,. \end{gathered}$$

Here, $\Gamma^u$ and $\Gamma^\sigma$ are parts of boundary $\Gamma$ of body $\Omega$, along which displacements and surface tractions, respectively, are assigned; $\mathit{\Gamma}'_{ks}$ is the contact boundary of parts $\Omega_k$ and $\Omega_s$. Functions $f_l^k(x, t)$ and $g_l^k(x, t)$ are assigned functions of the coordinates and time.

Poroviscoelastic solution is obtained from poroelastic solution by means of the elastic-viscoelastic correspondence principle, applied to skeleton's moduli $K$ and $G$ in Laplace domain. Forms of functions $\bar{K}(s)$ and $\bar{G}(s)$ depend on chosen viscoelastic model.

In present paper, standard linear solid model is employed:

$$\begin{aligned} \bar{K}(s) &= K^\infty \cdot \left[ (\chi - 1) \frac{s}{s + \eta} + 1 \right], \\ \bar{G}(s) &= G^\infty \cdot \left[ (\chi - 1) \frac{s}{s + \eta} + 1 \right] \end{aligned}$$

The equilibrium and instantaneous values of the relaxation function associated with material modules are connected as follows:

$$\chi = K^0 / K^\infty = G^0 / G^\infty$$

Equilibrium and instantaneous values are denoted by «$\infty$» and «0» respectively.

## 3 Boundary-Element Approach

Boundary-value problem can be reduced to the BIE system as follows [26–30]:

$$\frac{1-\alpha_\Omega}{2}\upsilon_i(\mathbf{x},s)+\int\limits_\Gamma \Big(T_{ij}(\mathbf{x},\mathbf{y},s)\upsilon_i(\mathbf{y},s)-T^0_{ik}(\mathbf{x},\mathbf{y},s)\upsilon_i(\mathbf{x},s)-U_{ij}(\mathbf{x},\mathbf{y},s)t_i(\mathbf{y},s)\Big)d\Gamma=0,$$

where $\mathbf{x},\mathbf{y}\in\Gamma$ $U_{ij}$, $T_{ij}$ are fundamental and singular solutions, $T^0_{ij}$ contains the isolated singularities, $\mathbf{x}\in\Gamma$ is an arbitrary point. Coefficient $\alpha_\Omega$ equals to 1 in case of finite domain and $-1$ in case of infinite domain.

Boundary surface of our homogeneous solid is discretized by quadrangular and triangular elements and triangular elements are assumed as singular quadrangular elements. The Cartesian coordinates of an arbitrary point of the element are expressed through the coordinates of the nodal points of this element, using shape functions of the local coordinates. Shape functions are quadratic polynomials of interpolation. We use reference elements: square $\xi=(\xi_1,\xi_2)\in[-1,\ 1]^2$ and triangle $0\le\xi_1+\xi_2\le 1$, $\xi_1\ge 0, \xi_2\ge 0$, and each boundary element is mapped to a reference one by the following formula:

$$y_i(\xi)=\sum_{l=1}^{8}N^l(\xi)y_i^{\beta(k,l)},\qquad i=1,\ 2,\ 3,$$

where $l$ is local node number in element $k$, $\beta(k,l)$ is global node number, $N^l(\xi)$ are shape functions. Goldshteyn's displacement-stress mixed model is performed. To discretize the boundary surface eight-node biquadratic quadrilateral elements are used, generalized displacements and tractions are approximated by linear and constant shape functions, respectively.

Subsequent application of collocation method leads to the system of linear equations. As with the collocation nodes we take the approximation nodes of boundary functions. Gaussian quadrature are used to calculate integrals on regular elements. However, if an element contains a singularity, algorithm of singularity avoiding or order reducing is applied. When singularity is excluded we use an adaptive integration algorithm. An appropriate order of Gaussian quadrature is chosen from primarily known necessary precision, if it is impossible, the element is subdivided to smaller elements recursively.

Solving the system of linear equations leads to the solution of the initial boundary-value problem in Laplace domain.

## 4 Laplace Transform Inversion

Consider a method based on the theorem of the integration of the original—the stepped method of numerical inversion of Laplace transform. Consider the following integral:

$$y(t) = \int_0^t f(\tau) d\tau. \tag{3}$$

Integral (3) gives rise to Cauchy problem for an ordinary differential equation:

$$\frac{d}{dt} x(t) = s x(t) + C, x(0) = 0.$$

Integral (3) is substituted for by a quadrature sum, weighting factors of which are determined using Laplace representation $\overline{f}$ and the linear multi-step method [39]. Further derivation is based on the results of those works. The traditional stepped method of integrating the original consists in that integral (3) is calculated using the following relation:

$$y(0) = 0, \quad y(n\Delta t) = \sum_{k=1}^{n} \omega_k(\Delta t), \quad n = 1, \ldots N,$$
$$\omega_n(\Delta t) = \frac{R^{-n}}{2\pi} \int_0^{2\pi} \bar{f}\left(\frac{\gamma(Re^{i\varphi})}{\Delta t}\right) e^{-in\varphi} d\varphi$$

where $\Delta t$ is time step; $\gamma(z) = 3/2 - 2z + z^2/2.$; $n$ is number of a time step, $n = 0, N$; $R$ is parameter of the method.

The traditional method uses a constant-step trapezoid method for integrating. Consider the following formula of constructing $\omega_n$ based on a variable step:

$$\omega_n(\Delta t) = \frac{R^{-n}}{2\pi} \sum_{k=0}^{L-1} \left[ \bar{f}\left(\frac{\gamma(Re^{in\varphi_k})}{\Delta t}\right) e^{-in\varphi_k} + \bar{f}\left(\frac{\gamma(Re^{in\varphi_{k+1}})}{\Delta t}\right) e^{-in\varphi_k+1} \right] \frac{(\varphi_{k+1} - \varphi_k)}{2}.$$

## 5 Numerical Example

The problem of the Heaviside-type load $H(t)$ acting on the surface of a poroelastic layer located on a poroelastic halfspace is considered (Fig. 1). Two variants of geometry problem are considered—with a layer thickness of 5 and 10 m. A vertical load $t_3 = -1000$ N/m$^2 \cdot H(t)$ is specified on a surface area of 1 m$^2$, the rest of the surface is traction-free and permeable. At the boundary between the layer and halfspace, the flow, the force, displacements and pore pressure are assumed to be unknown

**Fig. 1** Layered half space under vertical load

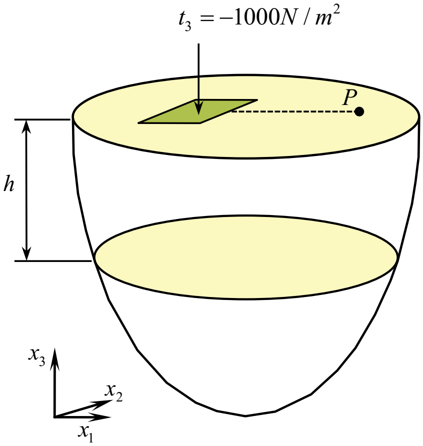

functions. The parameters of the poroelastic soil and the rock are given in Table 1. Moduli characterizing the elastic behavior of the porous material in accordance with the drained and undrained models are also given in Table 1. Dynamic responses of vertical displacements $u_3$ at the point $P$, located at a distance of 10 m from the area of load application are shown in Figs. 2, 3, 4, 5, 6, 7, 8, 9 and 10.

**Table 1** Poroelastic constants for various materials

| Parameter | Poroelastic | | Elastic drained | | Elastic undrained | |
|---|---|---|---|---|---|---|
| | Rock | Soil | Rock | Soil | Rock | Soil |
| Bulk modulus $K$ [N/m$^2$] | $8 \cdot 10^9$ | $2.1 \cdot 10^8$ | $8 \cdot 10^9$ | $2.1 \cdot 10^8$ | $1.57 \cdot 10^{10}$ | $4.83 \cdot 10^9$ |
| Shear modulus $G$ [N/m$^2$] | $6 \cdot 10^9$ | $9.8 \cdot 10^9$ | $6 \cdot 10^9$ | $9.8 \cdot 10^9$ | $6 \cdot 10^9$ | $9.8 \cdot 10^9$ |
| Density $\rho$ [kg/m$^3$] | 2458 | 1884 | 2458 | 1884 | 2458 | 1884 |
| Solid bulk modulus $K_s$ [N/m$^2$] | $3.6 \cdot 10^{10}$ | $1.1 \cdot 10^{10}$ | – | | – | |
| Fluid bulk modulus $K_f$ [N/m$^2$] | $3.3 \cdot 10^9$ | $3.3 \cdot 10^9$ | – | | – | |
| Fluid density $\rho_f$ [kg/m$^3$] | 1000 | 1000 | – | | – | |
| Porosity $\varphi[-]$ | 0.19 | 0.48 | – | | – | |
| Permeability $\kappa$ [m$^4$/(N · s)] | $1.9 \cdot 10^{-10}$ | $3.55 \cdot 10^{-9}$ | – | | – | |

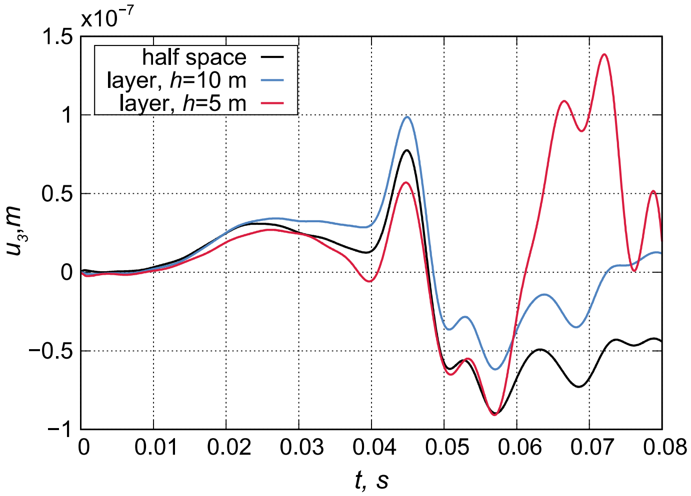

**Fig. 2** Displacement at point $P$ versus time: different depth of the layer

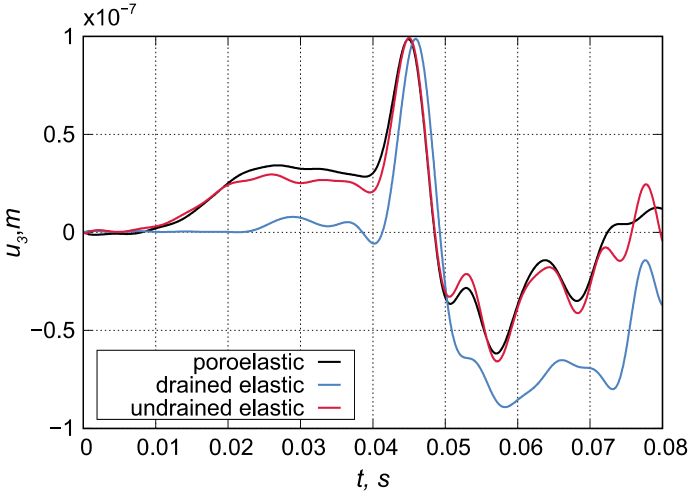

**Fig. 3** Vertical displacement at point $P$ versus time. Comparison of poroelastic and elastic solutions of the soil and rock for layer of 5 m depth

Figure 2 presents the comparison of vertical displacements, calculated for the layer with thicknesses of 5 m и 10 m and labeled $u_3^{5\,\mathrm{m}}$ and $u_3^{10\,\mathrm{m}}$, respectively. Figure 2 also represents solutions for displacements $\left(u_3^{hs}\right)$, calculated for the same values of the halfspace material parameters, which describe layer material. It can be seen that until the appearance of the fast longitudinal wave ($t \approx 0.01$ s) all three curves are almost graphically indistinguishable, however, quantitative differences are observed further. In the moment of Rayleigh wave ($t \approx 0.047$ s) appearance and up to the moment $t \approx$

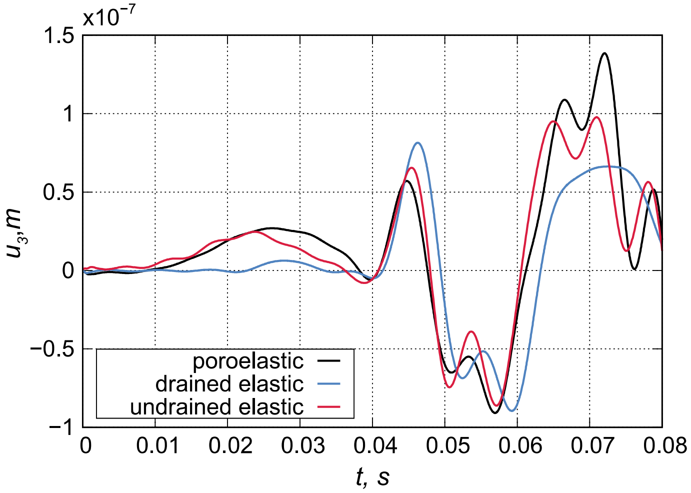

**Fig. 4** Vertical displacement at point *P* versus time. Comparison poroelastic and elastic solutions of the soil and rock for layer of 10 m depth

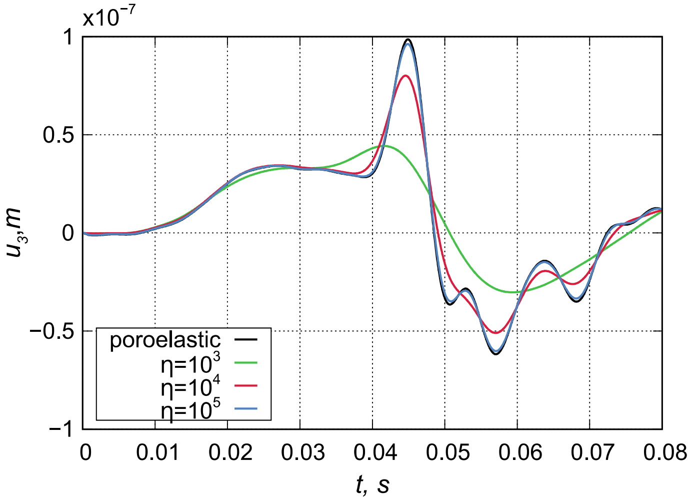

**Fig. 5** Vertical displacement at point *P* versus time. Poroviscoelastic dynamic analysis of the soil and rock for layer of 10 m depth

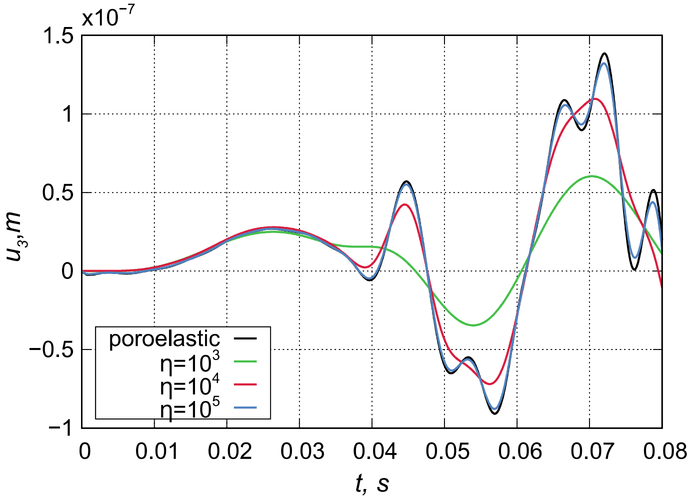

**Fig. 6** Vertical displacement at point *P* versus time. Poroviscoelastic dynamic analysis of the soil and rock for layer of 5 m depth

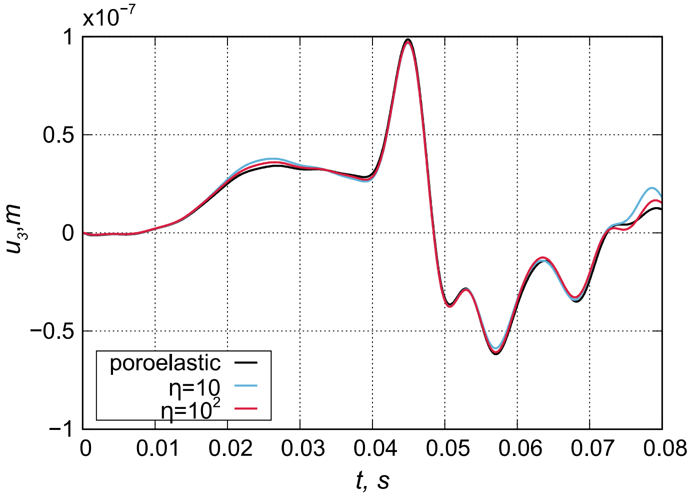

**Fig. 7** Vertical displacement at point *P* versus time. Poroviscoelastic dynamic analysis of the rock for layer of 10 m depth

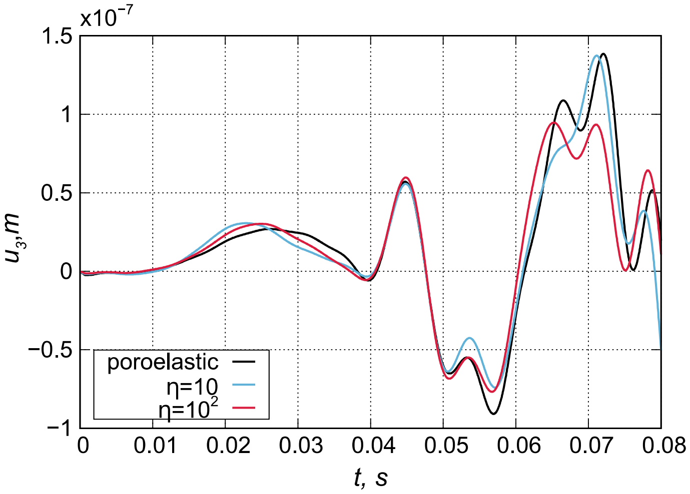

**Fig. 8** Vertical displacement at point *P* versus time. Poroviscoelastic dynamic analysis of the rock for layer of 5 m depth

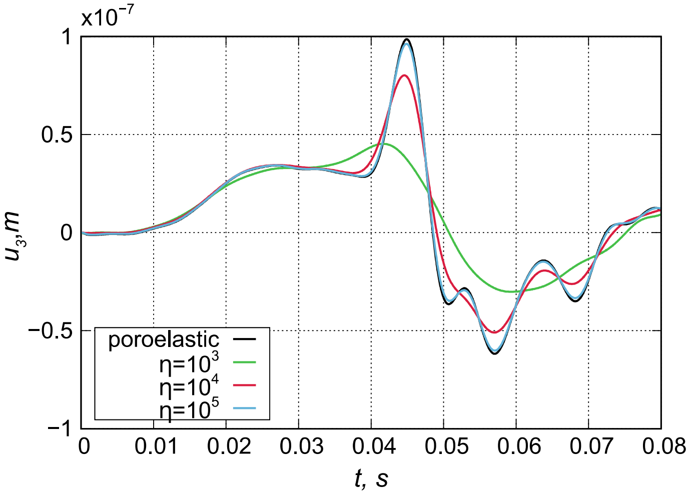

**Fig. 9** Vertical displacement at point *P* versus time. Poroviscoelastic dynamic analysis of the soil for layer of 10 m depth

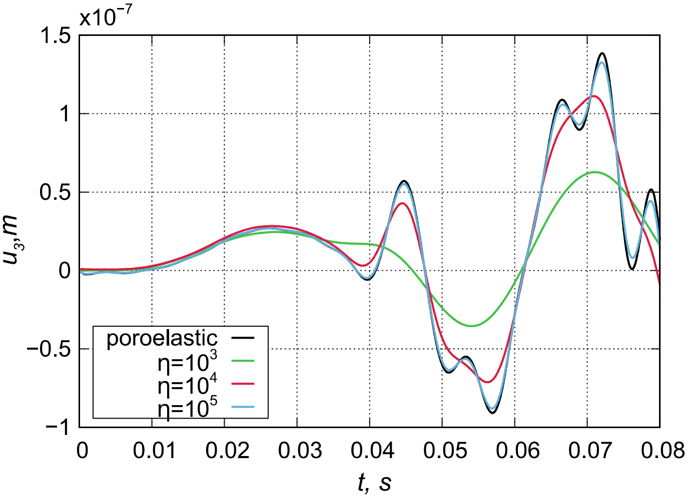

**Fig. 10** Vertical displacement at point $P$ versus time. Poroviscoelastic dynamic analysis of the soil for layer of 5 m depth

0.057 s the displacement behavior is described by the relation $u_3^{5\,\mathrm{m}} \leq u_3^{hs} \leq u_3^{10\,\mathrm{m}}$. The time moment $t \approx 0.057$ s is marked by an increase in displacements $u_3^{5\,\mathrm{m}}$ and $u_3^{10\,\mathrm{m}}$, and the displacements $u_3^{5\,\mathrm{m}}$ increase much more rapidly and exceed $u_3^{10\,\mathrm{m}}$ and $u_3^{hs}$ by amplitude. The observed effect is explained by the influence of longitudinal waves reflected from the halfspace and is less noticeable in the case of a larger layer thickness due to the considerable wave dispersion in porous medium.

Figures 3 and 4 show the comparison of displacements $u_3^{5\,\mathrm{m}}$ and $u_3^{10\,\mathrm{m}}$ ith the displacements calculated using elastic models, respectively. In both cases, the solution obtained from the undrained material model is the best approximation to the poroelastic solution, but the differences are also observed here due to the influence of the waves reflected from the halfspace. Figure 4 shows that the amplitude of the Rayleigh wave of the poroelastic solution is smaller than the corresponding amplitudes of the elastic solutions.

In order to obtain poroviscoelastic solutions standard linear solid model is employed. Parameter $\eta$ characterize viscosity, and parameter $\chi = K^0/K^\infty = G^0/G^\infty$ characterize dependence between equilibrium and instantaneous values of material modules. In further computations parameter $\chi = 4$.

Figures 5, 6, 7, 8, 9 and 10 demonstrate the influence of viscoelastic properties of the skeleton on the dynamic response of vertical displacements. Figures 5 and 6 represent the vertical displacements on the surface of a viscoelastic layer located on a poroelastic halfspace. With increase of the parameter $\eta$, it is seen that viscoelastic solution approaches poroelastic solution, but decrease of $\eta$ leads to reduce of displacement amplitude. The influence of dissipative effects on the surface displacements of the five-meter layer is especially noticeably at $\eta = 10^3$ when the amplitude of the Rayleigh wave displacement does not exceed the amplitude of the longitudinal wave displacements (Fig. 6).

Figures 7 and 8 represent vertical displacements on the surface of poroelastic layer located on a porous viscoelastic halfspace. It can be observed that the dissipative effects associated with viscoelastic behavior of the halfspace have minor effect on the dynamic responses of displacements on the surface of both the 5 and 10 m layers.

Figures 9 and 10 show vertical displacements on the surface of a viscoelastic layer located on the poroelastic halfspace. In this case, the displacement curves almost coincide with the displacement curves presented in Figs. 5 and 6, and the corresponding comments can be repeated. Taking into account the comments made regarding the results in Figs. 7 and 8, we can say that the dynamic responses of the surface displacements of the layer are mainly affected by the viscoelastic properties of the layer.

## 6 Conclusion

The Biot's mathematical model of poroelastic material is given in the present paper. The systems of equations of the theory of dynamic poroelasticity and the formulation of boundary value problems in Laplace transforms are formulated. The technique of numerical inversion of the Laplace transform based on step method is presented. The boundary-element solutions for a problem involving a vertical load acting on the surface of a poroelastic layer located on a poroelastic halfspace are presented. The effect of the viscoelastic properties of the skeleton of porous material on vertical displacements on the surface layer is studied. It is noted, that the form of wave patterns is mainly influenced by dissipative effects caused by the viscoelastic behavior of the layer.

**Acknowledgements** This work was supported by a grant from the Government of the Russian Federation (contract No. 14.Y26.31.0031).

## References

1. Chapelle, D., Gerbeau, J.-F., Sainte-Marie, J., Vignon-Clementel, I.E.: A poroelastic model valid in large strains with applications to perfusion in cardiac modeling. Comput. Mech. **46**, 91–101 (2010). https://doi.org/10.1007/s00466-009-0452-x
2. Phillips, P.J., Wheeler, M.F.: A coupling of mixed and continuous Galerkin finite element methods for poroelasticity. I. The continuous in time case. Comput. Geosci. **11**, 131–144 (2007). https://doi.org/10.1007/s10596-007-9045-y
3. Phillips, P.J., Wheeler, M.F.: A coupling of mixed and continuous Galerkin finite element methods for poroelasticity. II. The discrete-in-time case. Comput. Geosci. **11**, 145–158 (2007). https://doi.org/10.1007/s10596-007-9044-z

4. Phillips, P.J., Wheeler, M.F.: A coupling of mixed and discontinuous Galerkin finite element methods for poroelasticity. Comput. Geosci. **12**, 417–435 (2008). https://doi.org/10.1007/s10596-008-9082-1
5. Causin, P., Guidoboni, G., Harris, A., Prada, D., Sacco, R., Terragni, S.: A poroelastic model for the perfusion of the lamina cribrosa in the optic nerve head. Math. Biosci. **257**, 33–41 (2014). https://doi.org/10.1016/j.mbs.2014.08.002
6. Sobhaniaragh, B., Mansur, W.J., Peters, F.C.: Three-dimensional investigation of multiple stage hydraulic fracturing in unconventional reservoirs. J. Petrol. Sci. Eng. **146**, 1063–1078 (2016)
7. Nazarova, L.A., Nazarov, L.A.: Evolution of stresses and permeability of fractured-and-porous rock mass around a production well. J. Min. Sci. **52**(3), 424–431 (2016)
8. Biot, M.A.: General theory of three dimensional consolidation. J. Appl. Phys. **12**, 155–164 (1941). https://doi.org/10.1063/1.1712886
9. Jin, B., Liu, H.: Horizontal vibrations of a disk on a poroelastic half-space. Soil Dyn. Earthq. Eng. J. **19**(4), 269–275 (2000)
10. Jin, B., Liu, H.: Rocking vibrations of rigid disk on saturated poroelastic medium. Soil Dyn. Earthq. Eng. J. **19**(7), 469–472 (2000)
11. Jin, B., Liu, H.: Vertical dynamic response of a disk on a saturated poroelastic halfspace. Soil Dyn. Earthq. Eng. J. **18**(6), 437–443 (1999)
12. Gazetas, G., Petrakis, E.: Offshore caissons on porous saturated soil. In: Parkash, S. (ed.), Proceedings of International Conference on Recent Advances in Geotechnical Earthquake Engineering and Soil Dynamics, pp. 381–386. University of Missouri-Rolla, Rolla (1981)
13. Degrande, G., De Roeck, G., Van Den Broeck, P.: Wave propagation in layered dry, saturated and unsaturated poroelastic media. Int. J. Solids Struct. **35**(34–35), 4753–4778 (1998)
14. Paul, S.: On the displacements produced in a porous elastic half-space by an impulsive line load (non-dissipative case). Pure Appl. Geophys. **114**(4), 605–614 (1976)
15. Paul, S.: On the disturbance produced in a semi-infinite poroelastic medium by a surface load. Pure Appl. Geophys. **114**(4), 615–627 (1976)
16. Philippacopoulos, A.J.: Axisymmetric vibrations of disk resting on saturated layered half-space. J. Eng. Mech. **115**(10), 2301–2322 (1989)
17. Philippacopoulos, A.J.: Buried point source in a poroelastic half-space. J. Eng. Mech. **123**(8), 860–869 (1997)
18. Schanz, M.: Poroelastodynamics: linear models, analytical solutions, and numerical methods. Appl. Mech. Rev. **62**, 030803 (2009). https://doi.org/10.1115/1.3090831
19. Gatmiri, B., Kamalian, M.: On the fundamental solution of dynamic poroelastic boundary integral equations in time domain. Int. J. Geomech. **2**(4), 381–398 (2002)
20. Gatmiri, B., Nguyen, K.V.: Time 2D fundamental solution for saturated porous media with incompressible fluid. Commun. Numer. Methods Eng. **21**(3), 119–132 (2005)
21. Seyerafian, S., Gatmiri B., Nourzad, A.: Green functions for a continuously nonhomogeneous saturated media. Int. J. Comput. Methods Eng. Sci. (CMES) **15(2),** 115–125 (2006)
22. Gatmiri, B., Eslami, H.: Scattering of harmonic waves by a circular cavity in a porous medium: complex functions theory approach. Int. J. Geomech. **7**(5), 371–381 (2007)
23. Theodorakopoulos, D.D., Beskosa, D.E.: Application of Biot's poroelasticity to some soil dynamics problems in civil engineering. Soil Dyn. Earthq. Eng. **26**, 666–679 (2006)
24. Dominguez, J.: Boundary elements in dynamics. Computational Mechanics Publications, Southampton (1993)
25. Albers, B., Savidis, S., Tasan, H.E., Von Estroff, O., Gehlken, M.: BEM and FEM results of displacements in a poroelastic column. Int. J. Appl. Math. Comput. Sci. **22**(4), 883–896 (2012)
26. Igumnov, L.A., Petrov, A.N., Vorobtsov, I.V.: Analysis of 3D poroelastodynamics using BEM based on modified time-step scheme. IOP Conf. Ser.: Earth Environ. Sci. **87**(8), 082022 (2017)
27. Igumnov, L., Ipatov, A., Belov, A., Petrov, A.: A combined application of boundary-element and Runge-Kutta methods in three-dimensional elasticity and poroelasticity. EPJ Web Conf. **94**, 04026 (2015)
28. Igumnov, L.A., Litvinchuk, S.Y., Petrov, A.N., Belov, A.A.: Boundary-element modeling of 3-D poroelastic half-space dynamics. Adv. Mater. Res. **1040**, 881–885 (2014)

29. Dineva, P., Datcheva, M., Schanz, T.: BIEM for seismic wave propagation in fluid saturated multilayered media. In: Proceedings of the 6th European Conference on Numerical Methods in Geotechnical Engineering—Numerical Methods in Geotechnical Engineering. (2006)
30. Schanz, M., Antes, H.: Waves in poroelastic half space: boundary element analyses. In: Ehlers, W., Bluhm, J. (eds.) Porous Media. Springer, Berlin, Heidelberg (2002)
31. Mow, V.C., Lai, W.M.: Recent developments in synovial joint biomechanics. SIAM Rev. **22**, 275 (1980)
32. Mow, V.C., Roth, V., Armstrong, C.G.: Biomechanics of joint cartilage. In: Frankel, V.H., Nordin, M.A. (eds.) Basic biomechanics of the skeletal system, p. 61. Lea and Febiger, Philadelphia (1980)
33. Ehlers, W., Markert, B.: On the viscoelastic behaviour of fluid-saturated porous materials. Granul. Matter. **2**(3), 153–161 (2000)
34. Mak, A.F.: The apparent viscoelastic behaviour of articular cartilage—the contribution from the intrinsic matrix viscoelasticity and interstitial fluid flows. J. Biomech. Eng. **108**, 123–130 (1986)
35. Banks, H.T., Bekele-Maxwell, K., Bociu, L., Noorman, M., Guidoboni, G.: Sensitivity analysis in poro-elastic and poro-visco-elastic models with respect to boundary data. Q. Appl. Math. **75**(4), 697–735 (2017)
36. Ipatov, A.A., Igumnov, L.A., Belov, A.A.: Boundary element method in three dimensional transient poroviscoelastic problems. Springer Proc. Phys. **193**, 331–346 (2017)
37. Igumnov, L.A., Litvinchuk, SYu., Belov, A.A., Ipatov, A.A.: Boundary element formulation for numerical surface wave modelling in poroviscoelastistity. Key Eng. Mater. **685**, 172–176 (2016)
38. Wuttke, F., Dineva, P., Fontara, I.-K.: Influence of poroelasticity on the 3D seismic response of complex geological media. J. Theor. Appl. Mech. **47**(2), 34–60 (2017)
39. Igumnov, L.A., Petrov, A.N.: Dynamics of partially saturated poroelastic solids by boundary-element method. PNRPU Mech. Bull. **47**(3), 47–61 (2016)

# Weakly-Nonlinear Solution of Coupled Boussinesq Equations and Radiating Solitary Waves

**K. R. Khusnutdinova and M. R. Tranter**

**Abstract** Weakly-nonlinear waves in a layered waveguide with an imperfect interface (soft bonding between the layers) can be modelled using coupled Boussinesq equations. We assume that the materials of the layers have close mechanical properties, in which case the system can support radiating solitary waves. We construct a weakly-nonlinear d'Alembert-type solution of this system, considering the problem in the class of periodic functions on an interval of finite length. The solution is constructed using a novel multiple-scales procedure involving fast characteristic variables and two slow time variables. Asymptotic validity of the solution is carefully examined numerically. We also discuss the limiting case of an infinite interval for localised initial conditions. The solution is applied to study interactions of radiating solitary waves.

**Keywords** Coupled Boussinesq equations · Coupled Ostrovsky equations · Multiple-scales expansions · Averaging · Radiating solitary waves

## 1 Introduction

Low-frequency wave propagation in solids is relevant to a large number of modern applications (see, for example, [1–7] and references therein). Long longitudinal bulk strain solitary waves in elastic waveguides can be modelled using Boussinesq-type equations [1, 2, 8] (see also [5, 9–12]). The stability of bulk strain solitons makes them an attractive candidate for the introscopy of layered structures, in particular delamination, in addition to the existing methods [13–17].

The dynamical behaviour of layered structures depends both on the properties of the bulk material in the layers, and on the type of the bonding between the layers. If the materials of the layers have similar properties and the bonding between the layers

---

K. R. Khusnutdinova (✉) · M. R. Tranter
Department of Mathematical Sciences, Loughborough University,
Loughborough LE11 3TU, UK
e-mail: K.Khusnutdinova@lboro.ac.uk

H. Altenbach et al. (eds.), *Dynamical Processes in Generalized Continua and Structures*, Advanced Structured Materials 103,
https://doi.org/10.1007/978-3-030-11665-1_18

is sufficiently soft (“imperfect interface”), then the bulk strain soliton is replaced with a *radiating solitary wave*, a solitary wave with a co-propagating oscillatory tail [14, 18, 19].

Long nonlinear longitudinal bulk strain waves in a bi-layer with a sufficiently soft bonding can be modelled with a system of coupled regularised Boussinesq (cRB) equations [18] (given below in non-dimensional and scaled form):

$$u_{tt} - u_{xx} = \epsilon \left[ \frac{1}{2} \left(u^2\right)_{xx} + u_{ttxx} - \delta \left(u - w\right) \right], \tag{1}$$

$$w_{tt} - c^2 w_{xx} = \epsilon \left[ \frac{\alpha}{2} \left(w^2\right)_{xx} + \beta w_{ttxx} + \gamma \left(u - w\right) \right], \tag{2}$$

where $\alpha$, $\beta$, $\delta$, $\gamma$ are coefficients depending on the mechanical and geometrical properties of a waveguide, $\epsilon$ is a small amplitude parameter, and $c$ is the ratio of the characteristic linear wave speeds in the layers. We assume that the materials of the layers have close mechanical properties, and therefore $c^2 - 1 = \mathcal{O}(\varepsilon)$.

We consider the initial-value (Cauchy) problem, and the initial conditions are written as

$$u(x, 0) = F_1(x), \quad u_t(x, 0) = V_1(x), \tag{3}$$

$$w(x, 0) = F_2(x), \quad w_t(x, 0) = V_2(x). \tag{4}$$

The dispersion relation is given by the bi-quadratic equation [18]:

$$\begin{aligned} &\omega^4 \left(1 + \epsilon\beta k^2\right) \left(1 + \epsilon k^2\right) \\ &- \omega^2 \left[ \left(1 + \epsilon\beta k^2\right) \left(\epsilon\delta + k^2\right) + \left(1 + \epsilon k^2\right) \left(\gamma\epsilon + c^2 k^2\right) \right] + \epsilon \left(\gamma + \delta c^2\right) k^2 + c^2 k^4 = 0, \end{aligned} \tag{5}$$

where $k$ is the wave number, and $\omega$ is the wave frequency. The two roots of this equation give two modes: acoustic and optical. The acoustic mode has the dispersion relation $\omega = \omega_a(k)$ satisfying the two asymptotic approximations

$$\omega_a^2(k) = \frac{\gamma + \delta c^2}{\gamma + \delta} k^2 + \mathcal{O}(k^4) \quad \text{as} \quad k \to 0 \quad \text{and} \quad \omega_a^2(k) = \frac{c^2}{\epsilon\beta} + \mathcal{O}(k^{-2}) \quad \text{as} \quad k \to \infty. \tag{6}$$

The optical mode has the dispersion relation $\omega = \omega_o(k)$ satisfying the two asymptotic approximations

$$\omega_o^2(k) = \epsilon(\delta + \gamma) + \mathcal{O}(k^2) \quad \text{as} \quad k \to 0 \quad \text{and} \quad \omega_o^2(k) = \frac{1}{\epsilon} + \mathcal{O}(k^{-2}) \quad \text{as} \quad k \to \infty. \tag{7}$$

Pure propagating solitary waves are not supported by the coupled system and are replaced with long-living radiating solitary waves [18, 19].

In this paper we revisit the weakly-nonlinear solution of the Cauchy problem for the coupled Boussinesq-type equations constructed in [20] with the view of extending the applicability of the solution to initial conditions with non-zero mass. We use the novel multiple-scales procedure recently developed in [21].

The paper is organised as follows. In Sect. 2 we construct a weakly-nonlinear solution of the problem using asymptotic multiple-scales expansions for the deviations from the oscillating mean values (similarly to [21, 22]), using fast characteristic variables and two slow time variables [21]. The validity of the constructed solution is examined in Sect. 3, where we compare it with direct numerical simulations of the Cauchy problem. We use both the constructed weakly-nonlinear solution and direct numerical simulations to study the interaction of two radiating solitary waves in Sect. 4 and conclude in Sect. 5. Numerical methods used in these studies are described in Appendix A.

## 2 Weakly Nonlinear D'Alembert-Type Solution

Following our earlier work [21, 22], we consider the equation system (1)–(2) on the periodic domain $x \in [-L, L]$ and adjust the asymptotic expansions to the coupled system of Boussinesq-type equations. Firstly, we integrate (1)–(2) in $x$ over the period $2L$ to obtain an evolution equation of the form

$$\frac{\mathrm{d}^2}{\mathrm{d}t^2}\int_{-L}^{L} u(x,t)\,\mathrm{d}x + \epsilon\delta \int_{-L}^{L} (u(x,t) - w(x,t))\,dx = 0, \tag{8}$$

$$\frac{\mathrm{d}^2}{\mathrm{d}t^2}\int_{-L}^{L} w(x,t)\,\mathrm{d}x - \epsilon\gamma \int_{-L}^{L} (u(x,t) - w(x,t))\,dx = 0. \tag{9}$$

Denoting the mean value of $u$ and $w$ as

$$\overline{u}(t) := \frac{1}{2L}\int_{-L}^{L} u(x,t)\,\mathrm{d}x, \quad \overline{w}(t) := \frac{1}{2L}\int_{-L}^{L} w(x,t)\,\mathrm{d}x, \tag{10}$$

we solve this system to describe the evolution of the mean values:

$$\overline{u} = d_1 + \delta d_2 \cos\omega t + d_3 t + \delta d_4 \sin\omega t, \tag{11}$$

$$\overline{w} = d_1 - \gamma d_2 \cos\omega t + d_3 t - \gamma d_4 \sin\omega t. \tag{12}$$

Taking the mean value of the initial conditions (3), (4) we obtain

$$d_1 = \frac{\gamma\bar{F}_1 + \delta\bar{F}_2}{\delta+\gamma}, \quad d_2 = \frac{\bar{F}_1 - \bar{F}_2}{\delta+\gamma}, \quad d_3 = \frac{\gamma\bar{V}_1 + \delta\bar{V}_2}{\omega\,(\delta+\gamma)}, \quad d_4 = \frac{\bar{V}_1 - \bar{V}_2}{\omega\,(\delta+\gamma)}, \tag{13}$$

where we used the notation $\omega = \sqrt{\epsilon\,(\delta+\gamma)}$ (not to be confused with the wave frequency, which is not used any more) and

$$\bar{F}_i = \frac{1}{2L}\int_{-L}^{L} F_i(x)\,\mathrm{d}x, \quad \bar{V}_i = \frac{1}{2L}\int_{-L}^{L} V_i(x)\,\mathrm{d}x, \quad i = 1, 2. \tag{14}$$

To avoid linear growth in the mean value we require that $d_3 = 0$, corresponding to

$$\gamma \bar{V}_1 = -\delta \bar{V}_2. \tag{15}$$

In the following we consider initial conditions that satisfy the stricter condition $d_3 = d_4 = 0$, that is

$$\frac{1}{2L}\int_{-L}^{L} V_i\,\mathrm{d}x = 0, \quad i = 1, 2. \tag{16}$$

The latter condition appears naturally in many physical applications, and we impose it here in order to simplify our derivations.

The calculated mean values are subtracted from $u$ and $w$ to obtain an equation with zero mean value. We take $\tilde{u} = u - \overline{u}$ and $\tilde{w} = w - \overline{w}$ to obtain the modified evolution problem for the deviations from the mean values:

$$\tilde{u}_{tt} - \tilde{u}_{xx} = \epsilon\left[\frac{1}{2}\left(\tilde{u}^2\right)_{xx} + (d_1 + \delta d_2 \cos\omega t)\,\tilde{u}_{xx} + \tilde{u}_{ttxx} - \delta\left(\tilde{u} - \tilde{w}\right)\right], \tag{17}$$

$$\tilde{w}_{tt} - c^2\tilde{w}_{xx} = \epsilon\left[\frac{\alpha}{2}\left(\tilde{w}^2\right)_{xx} + \alpha\left(d_1 - \gamma d_2 \cos\omega t\right)\tilde{w}_{xx} + \beta\tilde{w}_{ttxx} + \gamma\left(\tilde{u} - \tilde{w}\right)\right]. \tag{18}$$

The initial conditions take the form

$$\tilde{u}(x,0) = \tilde{F}_1(x) = F_1(x) - \bar{F}_1, \quad \tilde{u}_t(x,0) = \tilde{V}_1(x) = V_1(x), \tag{19}$$

$$\tilde{w}(x,0) = \tilde{F}_2(x) = F_2(x) - \bar{F}_2, \quad \tilde{w}_t(x,0) = \tilde{V}_2(x) = V_2(x), \tag{20}$$

and, by construction, have zero mean value.

In this paper we will consider the case when the phase speeds are close, characterised by $c^2 - 1 = O(\epsilon)$. In this case the waves are resonant and an initial solitary wave solution in both layers will evolve into a *radiating solitary wave*, that is a solitary wave with a co-propagating one-sided oscillatory tail [18]. Therefore we rearrange (18) so that the same characteristic variable can be used in both equations, obtaining

$$\tilde{u}_{tt} - \tilde{u}_{xx} = \epsilon\left[\frac{1}{2}\left(\tilde{u}^2\right)_{xx} + (d_1 + \delta d_2 \cos\omega t)\,\tilde{u}_{xx} + \beta\tilde{u}_{ttxx} - \delta\left(\tilde{u} - \tilde{w}\right)\right], \tag{21}$$

$$\tilde{w}_{tt} - \tilde{w}_{xx} = \epsilon\left[\frac{\alpha}{2}\left(\tilde{w}^2\right)_{xx} + \alpha\left(d_1 - \gamma d_2 \cos\omega t + \frac{c^2 - 1}{\epsilon}\right)\tilde{w}_{xx} + \beta\tilde{w}_{ttxx} + \gamma\left(\tilde{u} - \tilde{w}\right)\right], \tag{22}$$

where we note that $(c^2 - 1)/\epsilon = O(1)$. We look for a weakly-nonlinear solution of the form

$$\begin{aligned}\tilde{u}(x,t) =& f_1^-(\xi_-,\tau,T) + f_1^+(\xi_+,\tau,T) + \sqrt{\epsilon}P_1(\xi_-,\xi_+,\tau,T) + \epsilon Q_1(\xi_-,\xi_+,\tau,T)\\ &+ \epsilon^{\frac{3}{2}}R_1(\xi_-,\xi_+,\tau,T) + \epsilon^2 S_1(\xi_-,\xi_+,\tau,T) + O\left(\epsilon^{\frac{5}{2}}\right), \qquad (23)\\ \tilde{w}(x,t) =& f_2^-(\xi_-,\tau,T) + f_2^+(\xi_+,\tau,T) + \sqrt{\epsilon}P_2(\xi_-,\xi_+,\tau,T) + \epsilon Q_2(\xi_-,\xi_+,\tau,T)\\ &+ \epsilon^{\frac{3}{2}}R_2(\xi_-,\xi_+,\tau,T) + \epsilon^2 S_2(\xi_-,\xi_+,\tau,T) + O\left(\epsilon^{\frac{5}{2}}\right), \qquad (24)\end{aligned}$$

where we introduce fast characteristic variables and two slow time variables [21]

$$\xi_\pm = x \pm t, \quad \tau = \sqrt{\epsilon}t, \quad T = \epsilon t.$$

We aim to construct the d'Alembert-type solution on the periodic domain, similarly to [21]. Therefore we substitute (23) and (24) into (21) and (22) then collect terms at powers of $\sqrt{\epsilon}$ to determine expressions for all functions in the expansion.

Here, $u$ and $w$ are $2L$-periodic functions in $x$, therefore we require that $f_{1,2}^-$ and $f_{1,2}^+$ are periodic in $\xi_-$ and $\xi_+$ respectively, and that all terms in the asymptotic expansions are products of the functions $f_{1,2}^\pm$ and their derivatives. Therefore all functions are periodic in $\xi_-$, $\xi_+$ at fixed $\xi_+$, $\xi_-$. Also, as the functions $f_{1,2}^\pm$ have zero mean i.e.

$$\frac{1}{2L}\int_{-L}^{L} f_{1,2}^\pm \, \mathrm{d}\xi_\pm = 0, \qquad (25)$$

then all functions in the expansion have zero mean.

We now collect terms at increasing powers of $\sqrt{\epsilon}$. The equation is satisfied at leading order so we move on to $O\left(\sqrt{\epsilon}\right)$. For the equation in $u$ we have

$$-4P_{1\xi_-\xi_+} - 2f^-_{1\xi_-\tau} + 2f^+_{1\xi_+\tau} = 0. \qquad (26)$$

To obtain equations for $f_1^\pm$ we average (26) with respect to the fast spatial variable $x$ at constant $\xi_-$ and $\xi_+$ (see [20, 21]). Let us first consider the averaging of $P_1$. At constant $\xi_-$ we have

$$\frac{1}{2L}\int_{-L}^{L} P_{1\xi_-\xi_+}\,\mathrm{d}x = \frac{1}{4L}\int_{-2L-\xi_-}^{2L-\xi_-} P_{1\xi_-\xi_+}\,\mathrm{d}\xi_+ = \frac{1}{4L}\left[P_{1\xi_-}\right]_{-2L-\xi_-}^{2L-\xi_-} = 0, \qquad (27)$$

and similarly for averaging at constant $\xi_+$. Therefore under the averaging we have $P_{1\xi_-\xi_+} = 0$. Applying the averaging to (26) we have two equations:

$$f^-_{1\xi_-\tau} = 0 \quad \text{and} \quad f^+_{1\xi_+\tau} = 0, \qquad (28)$$

which implies that

$$f_1^- = \tilde{f}_1^-(\xi_-,T) + B^-(\tau,T) \quad \text{and} \quad f_1^+ = \tilde{f}_1^+(\xi_+,T) + B^+(\tau,T). \qquad (29)$$

As we have zero mean of all functions in the expansion, we have $B^{\pm} = 0$. Similarly for the equation in $w$,

$$-4P_{2\xi_-\xi_+} - 2f^-_{2\xi_-\tau} + 2f^+_{2\xi_+\tau} = 0, \tag{30}$$

which after averaging at constant $\xi_-$ or $\xi_+$ and applying the same reasoning as for $f_1^{\pm}$, we obtain

$$f_2^- = \tilde{f}_2^-(\xi_-, T) \quad \text{and} \quad f_2^+ = \tilde{f}_2^+(\xi_+, T). \tag{31}$$

Substituting (29) into (26) gives

$$P_{1\xi_-\xi_+} = 0 \quad \Rightarrow \quad P_1 = g_1^-(\xi_-, \tau, T) + g_1^+(\xi_+, \tau, T). \tag{32}$$

Similarly substituting (31) into (30) gives

$$P_{2\xi_-\xi_+} = 0 \quad \Rightarrow \quad P_2 = g_2^-(\xi_-, \tau, T) + g_2^+(\xi_+, \tau, T). \tag{33}$$

We omit the tildes on $f^{\pm}_{1,2}$ in subsequent steps. The initial condition for $f^{\pm}_{1,2}$ is found by substituting (23) into (19) and (24) into (20) and comparing terms at $O(1)$ to obtain d'Alembert-type formulae for $f^{\pm}_{1,2}$ of the form

$$\begin{cases} f_1^- + f_1^+\Big|_{T=0} = \tilde{F}_1(x), \\ -f^-_{1\xi_-} + f^+_{1\xi_+}\Big|_{T=0} = \tilde{V}_1(x), \end{cases} \quad \Rightarrow \quad f_1^{\pm}|_{T=0} = \frac{1}{2}\left(\tilde{F}_1(x \pm t) \pm \int_{-L}^{x \pm t} \tilde{V}_1(\sigma)\, \mathrm{d}\sigma\right), \tag{34}$$

and

$$\begin{cases} f_2^- + f_2^+\Big|_{T=0} = \tilde{F}_2(x), \\ -f^-_{2\xi_-} + f^+_{2\xi_+}\Big|_{T=0} = \tilde{V}_2(x), \end{cases} \quad \Rightarrow \quad f_2^{\pm}|_{T=0} = \frac{1}{2}\left(\tilde{F}_2(x \pm t) \pm \int_{-L}^{x \pm t} \tilde{V}_2(\sigma)\, \mathrm{d}\sigma\right). \tag{35}$$

We now move on to the terms at $O(\epsilon)$, using the results from the previous order. For the equation governing $u$ we obtain

$$\begin{aligned} -4Q_{1\xi_-\xi_+} = {} & 2g^-_{1\xi_-\tau} + \left(2f^-_{1T} + f_1^- f^-_{1\xi_-} + d_1 f^-_{1\xi_-} + f^-_{1\xi_-\xi_-\xi_-}\right)_{\xi_-} - \delta\left(f_1^- - f_2^-\right) \\ & - 2g^+_{1\xi_+\tau} + \left(-2f^+_{1T} + f_1^+ f^+_{1\xi_+} + d_1 f^+_{1\xi_+} + f^+_{1\xi_+\xi_+\xi_+}\right)_{\xi_+} - \delta\left(f_1^+ - f_2^+\right) \\ & + d_2\delta\cos(\tilde{\omega}t)\left(f^-_{1\xi_-\xi_-} + f^+_{1\xi_+\xi_+}\right) + f^-_{1\xi_-\xi_-} f_1^+ + 2f^-_{1\xi_-} f^+_{1\xi_+} + f_1^- f^+_{1\xi_+\xi_+}, \end{aligned} \tag{36}$$

where we have introduced the notation $\tilde{\omega} = \sqrt{\delta + \gamma}$. Similarly for the equation governing $w$,

$$
\begin{aligned}
-4Q_{2\xi_-\xi_+} = {} & 2g^-_{2\xi_-\tau} + \left(2f^-_{2T} + \alpha f^-_2 f^-_{2\xi_-} + \alpha d_1 f^-_{2\xi_-} + \beta f^-_{2\xi_-\xi_-\xi_-}\right)_{\xi_-} + \gamma\left(f^-_1 - f^-_2\right) \\
& - 2g^+_{2\xi_+\tau} + \left(-2f^+_{2T} + \alpha f^+_2 f^+_{2\xi_+} + \alpha d_1 f^+_{2\xi_+} + \beta f^+_{2\xi_+\xi_+\xi_+}\right)_{\xi_+} + \gamma\left(f^+_1 - f^+_2\right) \\
& + \left(\frac{c^2-1}{\epsilon} - \alpha d_2 \gamma \cos\left(\tilde{\omega} t\right)\right)\left(f^-_{2\xi_-\xi_-} + f^+_{2\xi_+\xi_+}\right) \\
& + \alpha\left(f^-_{2\xi_-\xi_-} f^+_2 + 2 f^-_{2\xi_-} f^+_{2\xi_+} + f^-_2 f^+_{2\xi_+\xi_+}\right). \qquad (37)
\end{aligned}
$$

Averaging (36) and (37) at constant $\xi_-$ or constant $\xi_+$ gives the system of equations

$$
\begin{aligned}
\pm 2g^\pm_{1\xi_\pm\tau} &= d_2\delta\cos\left(\tilde{\omega} t\right) f^\pm_{1\xi_\pm\xi_\pm} + A^\pm_1\left(\xi_\pm, T\right), \qquad (38) \\
\pm 2g^\pm_{2\xi_\pm\tau} &= -\alpha d_2\gamma\cos\left(\tilde{\omega} t\right) f^\pm_{2\xi_\pm\xi_\pm} + A^\pm_2\left(\xi_\pm, T\right), \qquad (39)
\end{aligned}
$$

where

$$
A^\pm_1 = \left(\mp 2f^\pm_{1T} + f^\pm_1 f^\pm_{1\xi_\pm} + d_1 f^\pm_{1\xi_\pm} + f^\pm_{1\xi_\pm\xi_\pm\xi_\pm}\right)_{\xi_\pm} - \delta\left(f^\pm_1 - f^\pm_2\right), \qquad (40)
$$

and

$$
A^\pm_2 = \left(\mp 2f^\pm_{2T} + \alpha f^\pm_2 f^\pm_{2\xi_\pm} + \left(\alpha d_1 + \frac{c^2-1}{\epsilon}\right) f^\pm_{2\xi_\pm} + \beta f^\pm_{2\xi_\pm\xi_\pm\xi_\pm}\right)_{\xi_\pm} + \gamma\left(f^\pm_1 - f^\pm_2\right). \qquad (41)
$$

To avoid secular terms we require that $A_1 = 0$ and $A_2 = 0$. Therefore we get a system of coupled Ostrovsky equations for $f^\pm_{1,2}$, of the form

$$
\begin{aligned}
&\left(\mp 2f^\pm_{1T} + f^\pm_1 f^\pm_{1\xi_\pm} + d_1 f^\pm_{1\xi_\pm} + f^\pm_{1\xi_\pm\xi_\pm\xi_\pm}\right)_{\xi_\pm} = \delta\left(f^\pm_1 - f^\pm_2\right), \\
&\left(\mp 2f^\pm_{2T} + \alpha f^\pm_2 f^\pm_{2\xi_\pm} + \left(\alpha d_1 + \frac{c^2-1}{\epsilon}\right) f^\pm_{2\xi_\pm} + \beta f^\pm_{2\xi_\pm\xi_\pm\xi_\pm}\right)_{\xi_\pm} = \gamma\left(f^\pm_2 - f^\pm_1\right). \qquad (42)
\end{aligned}
$$

Integrating (38) and (39) with these conditions applied we can find an equation for $g^\pm_{1,2}$ of the form

$$
g^\pm_1 = \pm\frac{d_2\delta}{2\tilde{\omega}}\sin\left(\tilde{\omega}\tau\right) f^\pm_{1\xi_\pm} + G^\pm_1\left(\xi_\pm, T\right) = \pm\theta_1 f^\pm_{1\xi_\pm} + G^\pm_1\left(\xi_\pm, T\right), \qquad (43)
$$

and

$$
g^\pm_2 = \mp\frac{\alpha d_2\gamma}{2\tilde{\omega}}\sin\left(\tilde{\omega}\tau\right) f^\pm_{2\xi_\pm} + G^\pm_2\left(\xi_\pm, T\right) = \mp\theta_2 f^\pm_{2\xi_\pm} + G^\pm_2\left(\xi_\pm, T\right), \qquad (44)
$$

where $G^\pm_1$ and $G^\pm_2$ are functions to be found and we introduce

$$\theta_1 = \frac{d_2\delta}{2\tilde{\omega}} \sin(\tilde{\omega}\tau), \quad \theta_2 = \frac{\alpha d_2 \gamma}{2\tilde{\omega}} \sin(\tilde{\omega}\tau), \tag{45}$$

for convenience. Substituting (42) and (43) into (36) and integrating gives

$$Q_1 = h_1^-(\xi_-, \tau, T) + h_1^+(\xi_+, \tau, T) + h_{1c}(\xi_-, \xi_+, T), \tag{46}$$

where

$$h_{1c} = -\frac{1}{4}\left( f_{1\xi_-} \int_{-L}^{\xi_+} f_1^+(s)\ \mathrm{d}s + 2f_1^- f_1^+ + f_{1\xi_+}^+ \int_{-L}^{\xi_-} f_1^-(s)\ \mathrm{d}s \right). \tag{47}$$

Similarly substituting (42) and (44) into (37) and integrating gives

$$Q_2 = h_2^-(\xi_-, \tau, T) + h_2^+(\xi_+, \tau, T) + h_{2c}(\xi_-, \xi_+, T), \tag{48}$$

where

$$h_{2c} = -\frac{\alpha}{4}\left( f_{2\xi_-} \int_{-L}^{\xi_+} f_2^+(s)\ \mathrm{d}s + 2f_2^- f_2^+ + f_{2\xi_+}^+ \int_{-L}^{\xi_-} f_2^-(s)\ \mathrm{d}s \right). \tag{49}$$

The initial condition for $G_{1,2}^{\pm}$ is found by substituting (23) and (24) into (19) and (20) respectively, and comparing terms at $O\left(\sqrt{\epsilon}\right)$, taking account of the results found in (43) and (44). Therefore we obtain

$$\begin{cases} \theta_1 f_{1\xi_-}^- + \theta_1 f_{1\xi_+}^+ + G_1^- + G_1^+ \Big|_{T=0} = 0, \\ -\theta_1 f_{1\xi_-\xi_-}^- + \theta_1 f_{1\xi_+\xi_+}^+ - G_{1\xi_-}^- + G_{1\xi_+}^+ \Big|_{T=0} = 0, \end{cases} \quad \Rightarrow \quad G_1^{\pm} = 0, \tag{50}$$

as we see from (45) that $\theta_1|_{T=0} = 0$. Similarly we have

$$\begin{cases} \theta_2 f_{2\xi_-}^- + \theta_2 f_{2\xi_+}^+ + G_2^- + G_2^+ \Big|_{T=0} = 0, \\ -\theta_2 f_{2\xi_-\xi_-}^- + \theta_2 f_{2\xi_+\xi_+}^+ - G_{2\xi_-}^- + G_{2\xi_+}^+ \Big|_{T=0} = 0, \end{cases} \quad \Rightarrow \quad G_2^{\pm} = 0. \tag{51}$$

We now consider terms at $O\left(\epsilon^{3/2}\right)$. Substituting the results obtained at previous orders of $\epsilon$ into the weakly-nonlinear expansion (23) and (24), then substituting this into (21) and (22) and gathering terms at $O\left(\epsilon^{3/2}\right)$ gives

$$\begin{aligned} -4R_{1\xi_-\xi_+} = {} & 2h_{1\xi_-\tau}^- - 2h_{1\xi_+\tau} + \left(2g_{1T}^- + \left(f_1^- g_1^-\right)_{\xi_-} + d_1 g_{1\xi_-}^- + g_{1\xi_-\xi_-\xi_-}^-\right)_{\xi_-} - \delta\left(g_1^- - g_2^-\right) \\ & - g_{1\tau\tau}^- - g_{1\tau\tau}^+ + \left(-2g_{1T}^+ + \left(f_1^+ g_1^+\right)_{\xi_+} + d_1 g_{1\xi_+}^+ + g_{1\xi_+\xi_+\xi_+}^+\right)_{\xi_+} - \delta\left(g_1^+ - g_2^+\right) \\ & + d_2\delta\cos(\tilde{\omega}\tau)\left(g_{1\xi_-\xi_-}^- + g_{1\xi_+\xi_+}^+\right) + g_{1\xi_-\xi_-}^- f_1^+ + 2g_{1\xi_-}^- f_{1\xi_+}^+ + g_1^- f_{1\xi_+\xi_+}^+ \\ & + g_{1\xi_+\xi_+}^+ f_1^- + 2g_{1\xi_+}^+ f_{1\xi_-}^- + g_1^+ f_{1\xi_-\xi_-}^-, \end{aligned} \tag{52}$$

and

$$\begin{aligned}
-4R_{2\xi_-\xi_+} = {} & 2h^-_{2\xi_-\tau} + \left(2g^-_{2T} + \alpha\left(f_2^- g_2^-\right)_{\xi_-} + \alpha d_1 g^-_{2\xi_-} + \beta g^-_{2\xi_-\xi_-\xi_-}\right)_{\xi_-} + \gamma\left(g_1^- - g_2^-\right) \\
& - 2h^+_{2\xi_+\tau} + \left(-2g^+_{2T} + \alpha\left(f_2^+ g_2^+\right)_{\xi_+} + \alpha d_1 g^+_{2\xi_+} + \beta g^+_{2\xi_+\xi_+\xi_+}\right)_{\xi_+} + \gamma\left(g_1^+ - g_2^+\right) \\
& + \left(\frac{c^2-1}{\epsilon} - \alpha d_2 \gamma \cos\left(\tilde{\omega}\tau\right)\right)\left(g^-_{2\xi_-\xi_-} + g^+_{2\xi_+\xi_+}\right) - g^-_{2\tau\tau} - g^+_{2\tau\tau} \\
& + \alpha\left[g^-_{2\xi_-\xi_-} f_2^+ + 2g^-_{2\xi_-} f^+_{2\xi_+} + g_2^- f^+_{2\xi_+\xi_+} + g^+_{2\xi_+\xi_+} f_2^- + 2g^+_{2\xi_+} f^-_{2\xi_-} + g_2^+ f^-_{2\xi_-\xi_-}\right].
\end{aligned} \tag{53}$$

Substituting (43) into (52) and averaging at constant $\xi_-$ or constant $\xi_+$ gives

$$\begin{aligned}
\pm 2h^\pm_{1\xi_\pm\tau} = {} & \pm\theta_1\left(\mp 2f^\pm_{1T} + f_1^\pm f^\pm_{1\xi_\pm} + d_1 f^\pm_{1\xi_\pm} + f_{1\xi_\pm\xi_\pm\xi_\pm}\right)_{\xi_\pm\xi_\pm} \mp \delta\left(\theta_1 f_1^\pm + \theta_2 f_2^\pm\right)_{\xi_\pm} \\
& + \left(\mp 2G^\pm_{1T} + \left(f_1^\pm G_1^\pm\right)_{\xi_\pm} + d_1 G^\pm_{1\xi_\pm} + G_{1\xi_\pm\xi_\pm\xi_\pm}\right)_{\xi_\pm} - \delta\left(G_1^\pm - G_2^\pm\right) \\
& \pm \theta_1 \tilde{\omega}^2 f^\pm_{1\xi_\pm} \pm d_2 \delta \cos\left(\tilde{\omega}\tau\right)\theta_1 f^\pm_{1\xi_\pm\xi_\pm\xi_\pm}.
\end{aligned} \tag{54}$$

If we differentiate the equation for $f_1$ in (42) with respect to the appropriate characteristic variable, we can eliminate some terms in the first line in (54) to obtain an expression for $h^\pm_{1\xi_\pm\tau}$ of the form

$$2h^\pm_{1\xi_\pm\tau} = \theta_1\tilde{\omega}^2 f^\pm_{1\xi_\pm} - \delta\left(\theta_1 + \theta_2\right) f^\pm_{2\xi_\pm} + \theta_1 d_2 \delta \cos\left(\tilde{\omega}\tau\right) f^\pm_{1\xi_\pm\xi_\pm\xi_\pm} + \tilde{G}_1^\pm\left(\xi_\pm, T\right), \tag{55}$$

where

$$\tilde{G}_1^\pm\left(\xi_\pm, T\right) = \left(\mp 2G^\pm_{1T} + \left(f_1^\pm G_1^\pm\right)_{\xi_\pm} + d_1 G^\pm_{1\xi_\pm} + G^\pm_{1\xi_\pm\xi_\pm\xi_\pm}\right)_{\xi_\pm} - \delta\left(G_1^\pm - G_2^\pm\right). \tag{56}$$

To avoid secular terms again we require that $\tilde{G}_1^\pm = 0$ and therefore we have an equation for $G_1^\pm$ of the form

$$\left(\mp 2G^\pm_{1T} + \left(f_1^\pm G_1^\pm\right)_{\xi_\pm} + d_1 G^\pm_{1\xi_\pm} + G^\pm_{1\xi_\pm\xi_\pm\xi_\pm}\right)_{\xi_\pm} = \delta\left(G_1^\pm - G_2^\pm\right). \tag{57}$$

Integrating (55) we obtain

$$h_1^\pm = -\frac{\delta d_2}{4}\cos\left(\omega t\right) f_1^\pm + \frac{\delta d_2\left(\delta + \alpha\gamma\right)}{4\tilde{\omega}^2}\cos\left(\omega t\right) f_2^\pm - \frac{\delta^2 d_2^2}{8\tilde{\omega}^2}\cos^2\left(\omega t\right) f^\pm_{1\xi_\pm\xi_\pm} + \phi_1^\pm\left(\xi_\pm, T\right), \tag{58}$$

where the function $\phi_1^\pm$ is to be found. Averaging (53) at constant $\xi_-$ or $\xi_+$, and using (44) and (42) as was done above, we get an expression for $h_2$ of the form

$$2h^{\pm}_{2\xi_{\pm}\tau} = -\theta_2\tilde{\omega}^2 f^{\pm}_{2\xi_{\pm}} + \gamma\left(\theta_1 + \theta_2\right) f^{\pm}_{1\xi_{\pm}} + \theta_2 d_2 \gamma \cos\left(\tilde{\omega}\tau\right) f^{\pm}_{2\xi_{\pm}\xi_{\pm}\xi_{\pm}} + \tilde{G}^{\pm}_2\left(\xi_{\pm}, T\right), \tag{59}$$

where

$$\begin{aligned}\tilde{G}^{\pm}_2\left(\xi_{\pm}, T\right) = &\left(\mp 2G^{\pm}_{2T} + \alpha\left(f^{\pm}_2 G^{\pm}_2\right)_{\xi_{\pm}} + \alpha d_1 G^{\pm}_{2\xi_{\pm}} + \frac{c^2-1}{\epsilon} G^{\pm}_{2\xi_{\pm}} + \beta G^{\pm}_{2\xi_{\pm}\xi_{\pm}\xi_{\pm}}\right)_{\xi_{\pm}} \\ &+ \gamma\left(G^{\pm}_1 - G^{\pm}_2\right).\end{aligned} \tag{60}$$

As before we require that $\tilde{G}^{\pm}_2 = 0$ and therefore we have an equation for $G^{\pm}_2$ of the form

$$\left(\mp 2G^{\pm}_{2T} + \alpha\left(f^{\pm}_2 G^{\pm}_2\right)_{\xi_{\pm}} + \left(\alpha d_1 + \frac{c^2-1}{\epsilon}\right) G^{\pm}_{2\xi_{\pm}} + \beta G^{\pm}_{2\xi_{\pm}\xi_{\pm}\xi_{\pm}}\right)_{\xi_{\pm}} = \gamma\left(G^{\pm}_2 - G^{\pm}_1\right). \tag{61}$$

Taking into account the initial condition in (50), (51), and the form of (57) and (61) we see that $G^{\pm}_{1,2} \equiv 0$. Integrating (59) gives

$$h^{\pm}_2 = \frac{\alpha\gamma d_2}{4}\cos\left(\omega t\right) f^{\pm}_2 - \frac{\gamma d_2\left(\delta + \alpha\gamma\right)}{4\tilde{\omega}^2}\cos\left(\omega t\right) f^{\pm}_1 - \frac{\alpha^2\gamma^2 d_2^2}{8\tilde{\omega}^2}\cos^2\left(\omega t\right) f^{\pm}_{2\xi_{\pm}\xi_{\pm}} + \phi^{\pm}_2\left(\xi_{\pm}, T\right), \tag{62}$$

where again we need to find the function $\phi^{\pm}_2$. Substituting (58) into (52) and integrating with respect to the appropriate characteristic variables gives

$$R_1 = \psi^{-}_1\left(\xi_-, \tau, T\right) + \psi^{+}_1\left(\xi_+, \tau, T\right) + \psi_{1c}\left(\xi_-, \xi_+, T\right), \tag{63}$$

where

$$\psi_{1c} = -\frac{\theta_1}{4}\left[-f^{-}_{1\xi_-\xi_-}\int_{-L}^{\xi_+} f^{+}_1(s)\ \mathrm{d}s - f^{-}_{1\xi_-} f^{+}_1 + f^{-}_1 f^{+}_{1\xi_+} + f^{+}_{1\xi_+\xi_+}\int_{-L}^{\xi_-} f^{-}_1(s)\ \mathrm{d}s\right]. \tag{64}$$

In a similar way we find an expression for $R_2$ by substituting (62) into (53) and integrating with respect to the appropriate characteristic variables to obtain

$$R_2 = \psi^{-}_2\left(\xi_-, \tau, T\right) + \psi^{+}_2\left(\xi_+, \tau, T\right) + \psi_{2c}\left(\xi_-, \xi_+, T\right), \tag{65}$$

where

$$\psi_{2c} = -\frac{\alpha\theta_2}{4}\left[f^{-}_{2\xi_-\xi_-}\int_{-L}^{\xi_+} f^{+}_2(s)\ \mathrm{d}s + f^{-}_{2\xi_-} f^{+}_2 - f^{-}_2 f^{+}_{2\xi_+} - f^{+}_{2\xi_+\xi_+}\int_{-L}^{\xi_-} f^{-}_2(s)\ \mathrm{d}s\right]. \tag{66}$$

The initial condition for the function $\phi^{\pm}_1$ is found by again substituting (23) into (19) and comparing terms at $O\left(\epsilon\right)$, taking account of (58). Therefore we obtain for $\phi^{\pm}_1$

$$\begin{cases} h_1^- + h_1^+ + h_{1c}\big|_{T=0} = 0, \\ f_{1T}^- + f_{1T}^+ + g_{1\tau}^- + g_{1\tau}^+ - h_{1\xi_-}^- + h_{1\xi_+}^+ - h_{1c\xi_-} + h_{1c\xi_+}\Big|_{T=0} = 0, \end{cases}$$

$$\Rightarrow \quad \phi_1^\pm = \frac{1}{2}\left(J_1 \mp \int_{-L}^{\xi_\pm} K_1(s)\ \mathrm{d}s\right), \tag{67}$$

where

$$J_1 = \frac{\delta d_2}{4}\left(f_1^- + f_1^+\right) - \frac{\delta d_2(\delta + \alpha\gamma)}{4\tilde{\omega}^2}\left(f_2^- + f_2^+\right) + \frac{\delta^2 d_2^2}{8\tilde{\omega}^2}\left(f_{1\xi_-\xi_-}^- + f_{1\xi_+\xi_+}^+\right) - 2h_{1c},$$
$$K_1 = f_{1T}^- + f_{1T}^+ + g_{1\tau}^- + g_{1\tau}^+. \tag{68}$$

Similarly for $\phi_2^\pm$ we find the initial condition by substituting (24) into (20) and comparing terms at $O(\epsilon)$, using (62). This gives

$$\begin{cases} h_2^- + h_2^+ + h_{2c}\big|_{T=0} = 0, \\ f_{2T}^- + f_{2T}^+ + g_{2\tau}^- + g_{2\tau}^+ - h_{2\xi_-}^- + h_{2\xi_+}^+ - h_{2c\xi_-} + h_{2c\xi_+}\Big|_{T=0} = 0, \end{cases}$$

$$\Rightarrow \quad \phi_2^\pm = \frac{1}{2}\left(J_2 \mp \int_{-L}^{\xi_\pm} K_2(s)\ \mathrm{d}s\right), \tag{69}$$

where

$$J_2 = -\frac{\alpha\gamma d_2}{4}\left(f_2^- + f_2^+\right) + \frac{\gamma d_2(\delta + \alpha\gamma)}{4\tilde{\omega}^2}\left(f_1^- + f_1^+\right) + \frac{\alpha^2\gamma^2 d_2^2}{8\tilde{\omega}^2}\left(f_{2\xi_-\xi_-}^- + f_{2\xi_+\xi_+}^+\right) - 2h_{2c},$$
$$K_2 = f_{2T}^- + f_{2T}^+ + g_{2\tau}^- + g_{2\tau}^+. \tag{70}$$

To find an equation governing $\phi_{1,2}^\pm$ we need to retain terms at $O\left(\epsilon^2\right)$ in the original expansion. All coupling terms in the expansion are gathered in one function for convenience as we do not require them to determine $\phi_{1,2}^\pm$. Gathering terms at $O\left(\epsilon^2\right)$ we have

$$\begin{aligned} -4S_{1\xi_-\xi_+} = {} & -f_{1TT}^- - f_{1TT}^+ - 2g_{1\tau T}^- - 2g_{1\tau T}^+ - h_{1\tau\tau}^- - h_{1\tau\tau}^+ + 2h_{1\xi_- T}^- - 2h_{1\xi_+ T}^+ \\ & + 2\psi_{1\xi_-\tau}^- - 2\psi_{1\xi_+\tau}^+ + \left(f_1^- h_1^-\right)_{\xi_-\xi_-} + \left(f_1^+ h_1^+\right)_{\xi_+\xi_+} + \frac{1}{2}\left({g_1^-}^2\right)_{\xi_-\xi_-} + \frac{1}{2}\left({g_1^+}^2\right)_{\xi_+\xi_+} \\ & + d_1 h_{1\xi_-\xi_-}^- + d_1 h_{1\xi_+\xi_+}^+ + d_2\delta\cos(\tilde{\omega}\tau)\left(h_{1\xi_-\xi_-}^- + h_{1\xi_+\xi_+}^+\right) + h_{1\xi_-\xi_-\xi_-\xi_-}^- \\ & + h_{1\xi_+\xi_+\xi_+\xi_+}^+ - 2g_{1\xi_-\xi_-\xi_-\tau}^- + 2g_{1\xi_+\xi_+\xi_+\tau}^+ - 2f_{1\xi_-\xi_-\xi_- T}^- + 2f_{1\xi_+\xi_+\xi_+ T}^+ \\ & - \delta\left(h_1^- - h_2^- + h_1^+ - h_2^+\right) - 4\mu_{1c}, \end{aligned} \tag{71}$$

where $\mu_{1c}$ is the coupling terms at this order, and

$$\begin{aligned}
-4S_{2\xi_-\xi_+} = &-f^-_{2TT} - f^+_{2TT} - 2g^-_{2\tau T} - 2g^+_{2\tau T} - h^-_{2\tau\tau} - h^+_{2\tau\tau} + 2h^-_{2\xi_- T} - 2h^+_{2\xi_+ T} + 2\psi^-_{2\xi_-\tau} \\
&- 2\psi^+_{2\xi_+\tau} + \alpha\left(f^-_2 h^-_2\right)_{\xi_-\xi_-} + \alpha\left(f^+_2 h^+_2\right)_{\xi_+\xi_+} + \frac{\alpha}{2}\left({g^-_2}^2\right)_{\xi_-\xi_-} + \frac{\alpha}{2}\left({g^+_2}^2\right)_{\xi_+\xi_+} \\
&+ \alpha d_1 h^-_{2\xi_-\xi_-} + \alpha d_1 h^+_{2\xi_+\xi_+} - \alpha d_2 \gamma \cos\left(\tilde{\omega}\tau\right)\left(h^-_{2\xi_-\xi_-} + h^+_{2\xi_+\xi_+}\right) + \beta h^-_{2\xi_-\xi_-\xi_-\xi_-} \\
&+ \beta h^+_{2\xi_+\xi_+\xi_+\xi_+} - 2\beta g^-_{2\xi_-\xi_-\xi_-\tau} + 2\beta g^+_{2\xi_+\xi_+\xi_+\tau} - 2\beta f^-_{2\xi_-\xi_-\xi_- T} + 2\beta f^+_{2\xi_+\xi_+\xi_+ T} \\
&+ \gamma\left(h^-_1 - h^-_2 + h^+_1 - h^+_2\right) - 4\mu_{2c},
\end{aligned} \tag{72}$$

where again $\mu_{2c}$ is the coupling terms at this order of the expansion. Following the steps from previous orders, we average (71) and (72) at constant $\xi_-$ or constant $\xi_+$ and rearrange to obtain

$$\pm 2\psi_{1\xi_\pm\tau} = H^\pm_1\left(\xi_\pm, \tau, T\right) + \hat{H}^\pm_1\left(\xi_\pm, T\right), \tag{73}$$

and

$$\pm 2\psi_{2\xi_\pm\tau} = H^\pm_2\left(\xi_\pm, \tau, T\right) + \hat{H}^\pm_2\left(\xi_\pm, T\right), \tag{74}$$

where the functions $H^\pm_{1,2}$, $\hat{H}^\pm_{1,2}$ can be found from (71) and (72). The equation for $\phi^\pm_{1,2}$ is captured by the function $\hat{H}^\pm_{1,2}$ and this must be zero to avoid secular terms in the same way as at previous orders. Therefore we look for terms in (71), (72), that depend only on $\xi_\pm$ and $T$. Following this approach we obtain the equations

$$\begin{aligned}
&\left(\mp 2\phi^\pm_{1T} + \left(f^\pm_1 \phi^\pm_1\right)_{\xi_\pm} + d_1 \phi^\pm_{1\xi_\pm} + \phi^\pm_{1\xi_\pm\xi_\pm\xi_\pm}\right)_{\xi_\pm} = \delta\left(\phi^\pm_1 - \phi^\pm_2\right) + f^\pm_{1TT} \mp 2f^\pm_{1\xi_\pm\xi_\pm\xi_\pm T} \\
&+ \frac{\tilde{\omega}^2\tilde{\theta}^2_1}{2} f^\pm_{1\xi_\pm\xi_\pm} - \frac{\tilde{\theta}^2_1}{2}\left(\delta + \alpha\gamma\right) f^\pm_{2\xi_\pm\xi_\pm} - \frac{\tilde{\theta}^2_1}{2}\left({f^\pm_{1\xi_\pm}}^2\right)_{\xi_\pm\xi_\pm},
\end{aligned} \tag{75}$$

and

$$\begin{aligned}
&\left(\mp 2\phi^\pm_{2T} + \alpha\left(f^\pm_2 \phi^\pm_2\right)_{\xi_\pm} + \alpha d_1 \phi^\pm_{2\xi_\pm} + \frac{c^2 - 1}{\epsilon}\phi^\pm_{2\xi_\pm} + \beta\phi^\pm_{2\xi_\pm\xi_\pm\xi_\pm}\right)_{\xi_\pm} = \gamma\left(\phi^\pm_2 - \phi^\pm_1\right) \\
&+ f^\pm_{2TT} \mp 2\beta f^\pm_{2\xi_\pm\xi_\pm\xi_\pm T} + \frac{\tilde{\omega}^2\tilde{\theta}^2_2}{2} f^\pm_{2\xi_\pm\xi_\pm} + \frac{\tilde{\theta}^2_2}{2\alpha}\left(\delta + \alpha\gamma\right) f^\pm_{1\xi_\pm\xi_\pm} - \frac{\alpha\tilde{\theta}^2_2}{2}\left({f^\pm_{2\xi_\pm}}^2\right)_{\xi_\pm\xi_\pm},
\end{aligned} \tag{76}$$

where we have the modified coefficient

$$\tilde{\theta}_1 = \frac{\theta_1}{\sin\left(\tilde{\omega}\tau\right)} = \frac{d_2\delta}{2\tilde{\omega}}, \quad \tilde{\theta}_2 = \frac{\theta_2}{\sin\left(\tilde{\omega}\tau\right)} = \frac{\alpha d_2\gamma}{2\tilde{\omega}}. \tag{77}$$

We have now defined all functions up to and including $O\left(\epsilon\right)$ and so stop our derivation, however the procedure could be continued to any order.

## 3 Validity of the Weakly-Nonlinear Solution

In this section we perform a careful error analysis to test the validity of the constructed solution by numerically solving the equation system (1)–(2) and comparing to the constructed solution (23) and (24) with an increasing number of terms included. To obtain this constructed solution we also need to numerically solve (29), (31) for the leading order solution and (75), (76) for the solution with terms up to and including $O(\epsilon)$. Therefore, we use two types of numerical methods: one for the coupled Boussinesq equations and another for the coupled Ostrovsky equations (see Appendix A).

We compare the solution of the coupled Boussinesq equations (1)–(2) (which we shall refer to as the "exact solution") to the constructed weakly-nonlinear solution for $u$ and $w$ based on (23) and (24) with an increasing number of terms included. The parameters used for the calculations in this section are $\alpha = \beta = c = 1 + \epsilon/2$ and $\delta = \gamma = 1$. We calculate the solution in the domain $x \in [-40, 40]$ and for $t \in [0, T]$ where $T = 1/\epsilon$. The initial conditions are taken to be

$$F_1(x) = A_1 \mathrm{sech}^2\left(\frac{x}{\Lambda_1}\right) + d, \quad F_2(x) = A_2 \mathrm{sech}^2\left(\frac{x}{\Lambda_2}\right),$$
$$V_1(x) = 2\frac{A_1}{\Lambda 1} \mathrm{sech}^2\left(\frac{x}{\Lambda_1}\right), \quad V_2(x) = 2c\frac{A_2}{\Lambda_2} \mathrm{sech}^2\left(\frac{x}{\Lambda_2}\right), \tag{78}$$

where $d$ is a constant and we have $A_1 = 6k_1^2,\ \Lambda_1 = \sqrt{2}/k_1,\ k_1 = 1/\sqrt{6},\ A_2 = 6ck_2^2/\alpha,\ \Lambda_2 = \sqrt{2c\beta}/k_2,\ k_2 = \sqrt{\alpha/6c}$. Here we have only added a pedestal to the initial condition for $u$ in the view of the translation symmetry of the system. In all cases considered here we have $\alpha = c$ and therefore $k_1 = k_2 = k = 1/\sqrt{6}$.

The comparison between the exact and weakly-nonlinear solutions at various orders of $\epsilon$ is shown in Figs. 1 and 2. We can see from the enhanced image that the leading order solution (red, dashed line) is improved with the addition of the $O\left(\sqrt{\epsilon}\right)$ terms (black, dash-dotted line), correcting for a phase shift. The inclusion of $O(\epsilon)$ (green, dotted line) terms adjusts the amplitude and we can see that this lies directly on top of the exact solution (blue, solid line). This is consistent for both values of $\gamma$ and $\delta$, and for both equations. We note that the larger value of $\gamma$ and $\delta$ can show a slightly increased error, however this is not as clear as the previous case for the Boussinesq-Klein-Gordon equation in [21].

To understand the behaviour of the errors we denote the direct numerical solution to the system (1)–(2) as $u_{\mathrm{num}}$, the weakly-nonlinear solution (23), (24), with only the leading order terms included as $u_1$, with terms up to and including $O\left(\sqrt{\epsilon}\right)$ terms as $u_2$ and with terms up to and including $O(\epsilon)$ as $u_3$. We consider the maximum absolute error over $x$, defined as

$$e_i = \max_{-L \le x \le L} \left| u_{\mathrm{num}}(x, t) - u_i(x, t) \right|, \quad i = 1, 2, 3. \tag{79}$$

This error is calculated at every time step and, to smooth the oscillations in the errors we average the $e_i$ values in the final third of the calculation, denoting this value as $\hat{e}_i$. We then use a least-squares power fit to determine how the maximum absolute error varies with the small parameter $\epsilon$. Therefore we write the errors in the form

$$\exp\left[\hat{e}_i\right] = C_i \epsilon^{\alpha_i}, \tag{80}$$

and take the logarithm of both sides to form the error plot (the exponential factor is included so that we have $\hat{e}_i$ as the plotting variable). The values of $C_i$ and $\alpha_i$ are found using the MATLAB function *polyfit*.

The corresponding errors for the cases considered in Figs. 1 and 2 are plotted in Figs. 3 and 4, that is for $\gamma = 0.1$, $\gamma = 0.5$ and $d = 7$. We can see that there is an excellent correlation for each of the curves and that the errors improve with

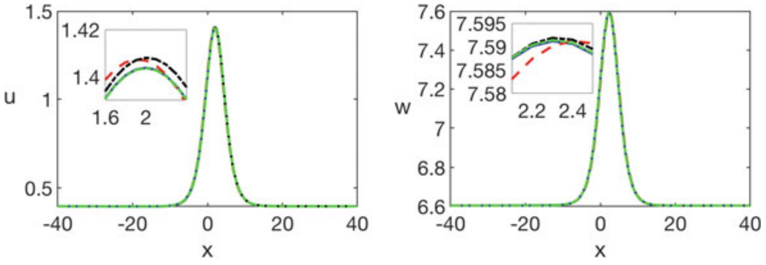

(a) $\gamma = 0.1$, $d = 7$ for $u$. (b) $\gamma = 0.1$, $d = 7$ for $w$.

**Fig. 1** A comparison of the direct numerical simulation (solid, blue) and the weakly-nonlinear solution including leading order (dashed, red), $O\left(\sqrt{\epsilon}\right)$ (dash-dot, black) and $O(\epsilon)$ (dotted, green) corrections, at $t = 1/\epsilon$, for **(a)** $u$ and **(b)** $w$. Parameters are $L = 40$, $N = 800$, $k = 1/\sqrt{6}$, $\alpha = \beta = c = 1 + \epsilon/2$, $\gamma = 0.1$, $\epsilon = 0.0025$, $\Delta t = 0.01$ and $\Delta T = \epsilon \Delta t$. The solution agrees well to leading order, and this agreement is improved with the addition of higher-order corrections

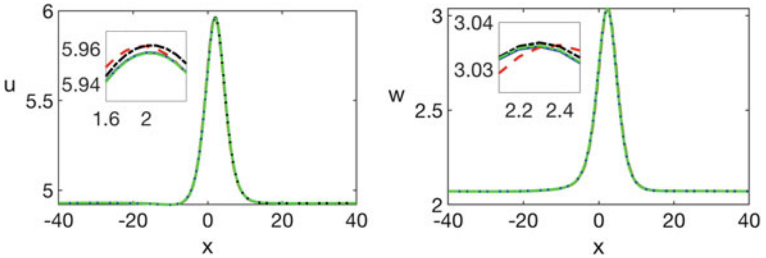

(a) $\gamma = 0.5$, $d = 7$ for $u$. (b) $\gamma = 0.5$, $d = 7$ for $w$.

**Fig. 2** A comparison of the direct numerical simulation (solid, blue) and the weakly-nonlinear solution including leading order (dashed, red), $O\left(\sqrt{\epsilon}\right)$ (dash-dot, black) and $O(\epsilon)$ (dotted, green) corrections, at $t = 1/\epsilon$, for **(a)** $u$ and **(b)** $w$. Parameters are $L = 40$, $N = 800$, $k = 1/\sqrt{6}$, $\alpha = \beta = c = 1 + \epsilon/2$, $\gamma = 0.5$, $\epsilon = 0.0025$, $\Delta t = 0.01$ and $\Delta T = \epsilon \Delta t$. The solution agrees well to leading order and this agreement is improved with the addition of higher-order corrections

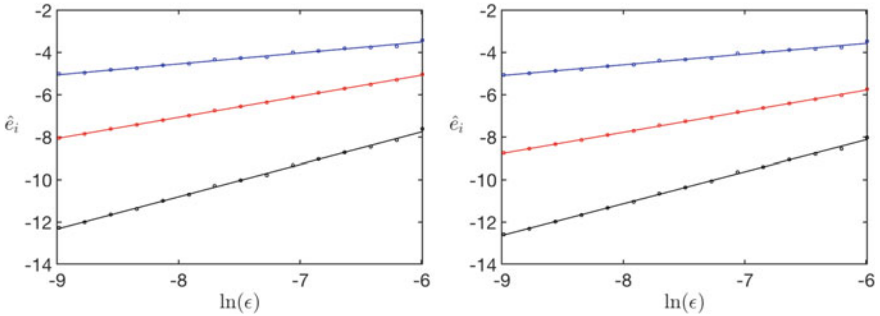

(a) $\gamma = 0.1$, $d = 7$ for $u$. (b) $\gamma = 0.1$, $d = 7$ for $w$.

**Fig. 3** A comparison of error curves for varying values of $\epsilon$, at $t = 1/\epsilon$, for the weakly-nonlinear solution including leading order (upper, blue), $O\left(\sqrt{\epsilon}\right)$ (middle, red) and $O(\epsilon)$ (lower, black) corrections, for **(a)** $u$ and **(b)** $w$. Parameters are $L = 40$, $N = 800$, $k = 1/\sqrt{6}$, $\alpha = \beta = c = 1 + \epsilon/2$, $\gamma = 0.1$, $\Delta t = 0.01$ and $\Delta T = \epsilon\Delta t$. The inclusion of more terms in the expansion increases the accuracy

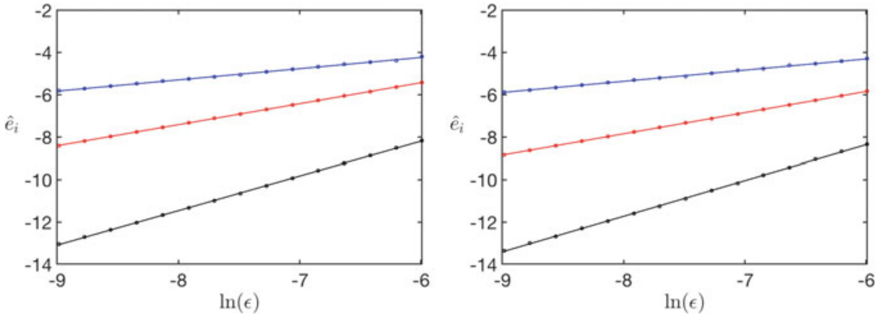

(a) $\gamma = 0.5$, $d = 7$ for $u$. (b) $\gamma = 0.5$, $d = 7$ for $w$.

**Fig. 4** A comparison of error curves for varying values of $\epsilon$, at $t = 1/\epsilon$, for the weakly-nonlinear solution including leading order (upper, blue), $O\left(\sqrt{\epsilon}\right)$ (middle, red) and $O(\epsilon)$ (lower, black) corrections, for **(a)** $u$ and **(b)** $w$. Parameters are $L = 40$, $N = 800$, $k = 1/\sqrt{6}$, $\alpha = \beta = c = 1 + \epsilon/2$, $\gamma = 0.5$, $\Delta t = 0.01$ and $\Delta T = \epsilon\Delta t$. The inclusion of more terms in the expansion increases the accuracy

the addition of more terms in the expansion. In the case of $\gamma = 0.1$ the slope of the error curves is 0.52, 1.00, 1.52 for $u$ and 0.50, 1.00 and 1.50 for $w$, for the inclusion of leading order, $O\left(\sqrt{\epsilon}\right)$ and $O(\epsilon)$ terms in the expansion respectively, in close agreement with the theoretical values. When $\gamma = 0.5$ the slope of the curves is approximately 0.50, 1.00 and 1.63 for $u$ and 0.53, 1.00 and 1.68 for $w$, showing that as $\gamma$ increases the slope of the error curve for the approximation including $O(\epsilon)$ terms increases.

## 4 Radiating Solitary Waves

In this section we study the interaction of two radiating solitary waves, using both the direct numerical simulations and the weakly-nonlinear solution. Firstly we consider the case of a single radiating solitary wave and show that we have a good agreement between the direct numerical simulation and the weakly-nonlinear solution, then we use both methods to reliably study the complicated case of two interacting radiating solitary waves.

In order to better resolve the tail of a radiating solitary wave, we scale the variables as $u = 12\tilde{u}$, $w = 12\tilde{w}$, so that we obtain (omitting tildes)

$$u_{tt} - u_{xx} = \epsilon \left[ 6 \left( u^2 \right)_{xx} + u_{ttxx} - \delta (u - w) \right], \tag{81}$$

$$w_{tt} - c^2 w_{xx} = \epsilon \left[ 6\alpha \left( w^2 \right)_{xx} + \beta w_{ttxx} + \gamma (u - w) \right]. \tag{82}$$

The weakly-nonlinear solution can be easily scaled as well so we obtain, for $f_{1,2}^{\pm}$,

$$\begin{aligned} &\left( \mp 2 f_{1T}^{\pm} + 12 f_1^{\pm} f_{1\xi_\pm}^{\pm} + d_1 f_{1\xi_\pm}^{\pm} + f_{1\xi_\pm\xi_\pm\xi_\pm}^{\pm} \right)_{\xi_\pm} = \delta \left( f_1^{\pm} - f_2^{\pm} \right), \\ &\left( \mp 2 f_{2T}^{\pm} + 12\alpha f_2^{\pm} f_{2\xi_\pm}^{\pm} + \left( \alpha d_1 + \frac{c^2 - 1}{\epsilon} \right) f_{2\xi_\pm}^{\pm} + \beta f_{2\xi_\pm\xi_\pm\xi_\pm}^{\pm} \right)_{\xi_\pm} = \gamma \left( f_2^{\pm} - f_1^{\pm} \right). \end{aligned} \tag{83}$$

Similarly for the function $g_{1,2}^{\pm}$ we have

$$g_1^{\pm} = \pm \frac{6 d_2 \delta}{\tilde{\omega}} \sin (\tilde{\omega} \tau) f_{1\xi_\pm}^{\pm}, \tag{84}$$

and

$$g_2^{\pm} = \mp \frac{6\alpha d_2 \gamma}{\tilde{\omega}} \sin (\tilde{\omega} \tau) f_{2\xi_\pm}^{\pm}. \tag{85}$$

In this section we only use the weakly-nonlinear solution up to and including $O\left(\sqrt{\epsilon}\right)$ terms so we do not consider the effect of the scaling on the higher-order terms. We will show that even this approximation produces good qualitative and reasonable quantitative results, even in very long runs.

To show the agreement between the direct numerical simulations and the weakly-nonlinear solution for a radiating solitary wave, we take the initial condition to be the solitary wave solution of the uncoupled Boussinesq equation for $u$ and $w$, as presented in (78). Therefore we have $f_{1,2}^{+} = 0$. The parameters in the equation are $\alpha = \beta = c = 1 + \epsilon/2, \gamma = 1$ and $\epsilon = 0.01$. The domain size is taken to be $L = 1000$ and therefore we have $N = 20000$, and the time step is $\Delta t = 0.01$ as before. We take the phase shift in the initial conditions to be $x_0 = 800$ and the result of the computation at $t = 1400$ is presented in Fig. 5. We can see that the radiating solitary wave is formed in both equations and that the agreement between the direct numerical simulations

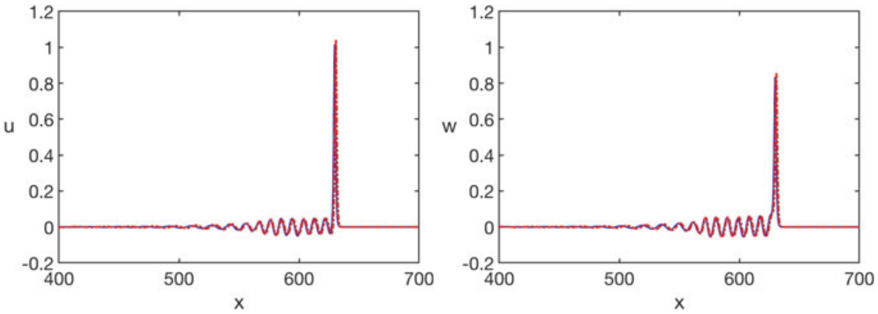

(a) Solution for $u$. (b) Solution for $w$.

**Fig. 5** A comparison of the numerical solution (solid, blue) at $t = 1400$ and the weakly-nonlinear solution including $O\left(\sqrt{\epsilon}\right)$ terms (dash-dot, red), for **(a)** $u$ and **(b)** $w$. Parameters are $L = 1000$, $N = 20000$, $k = 1/\sqrt{6}$, $\alpha = \beta = c = 1 + \epsilon/2$, $\gamma = 1$, $\epsilon = 0.01$, $\Delta t = 0.01$ and $\Delta T = \epsilon\Delta t$

(blue, solid line) and weakly-nonlinear solution (red, dashed line) is good, with a small phase shift between the two solutions and a small discrepancy in the amplitude.

We now consider the case when two radiating solitary waves interact. To obtain an appropriate initial condition we use the two-soliton solution for the KdV equation as the initial condition for the coupled Boussinesq equations and choose the second initial condition in the appropriate form so that there is no left-propagating wave, as was done in [23]. Explicitly we take

$$\begin{aligned} u(x,0) &= \frac{(k_1-k_2)^2 + \sqrt{C}\left(k_1^2\cosh\left(k_2x+x_1\right)+k_2^2\cosh\left(k_1x+x_0\right)\right)}{2\left[\cosh\left(\left(k_1x-k_2x+x_0-x_1\right)/2\right)+\sqrt{C}\cosh\left(\left(k_1x+k_2x+x_0+x_1\right)/2\right)\right]^2}, \\ u_t(x,0) &= -\frac{\mathrm{d}}{\mathrm{d}x}u(x,0), \end{aligned} \tag{86}$$

where $C = \left[(k_1-k_2)\,/\,(k_1+k_2)\right]^2$ and we take the same initial condition for $w$. In what follows, to ensure the radiating solitary waves have enough time to interact, we use a large domain and a long time for the calculation. Therefore we take $L = 5000$ and $N = 100000$ for the calculation, and the parameters are $\alpha = \beta = c = 1 + \epsilon/2$, $\gamma = 1$, $\epsilon = 0.01$. To ensure that the initial solitons are well separated and have sufficiently different amplitudes, we take $k_1 = 1$, $k_2 = 2$, $x_0 = -50$ and $x_1 = 50$. The results of the calculation at various times are presented in Fig. 6.

We can see that the weakly-nonlinear solution (red, dashed line) agrees very well with the results of direct numerical simulations (blue, solid line), even in such a complicated interaction problem, and the two approaches verify each other. There is only a small phase shift, which becomes more noticeable at larger times. At $t = 800$ the larger soliton has begun to travel through the tail of the smaller soliton and the amplitude has begun to reduce as it travels through the tail. At $t = 5800$, the two solitons now lie on top of each other (in direct numerical simulations; the weakly-nonlinear solution has a small phase shift). We can see that the amplitude is reduced in contrast to the initial condition, and the tail now shows the presence of two

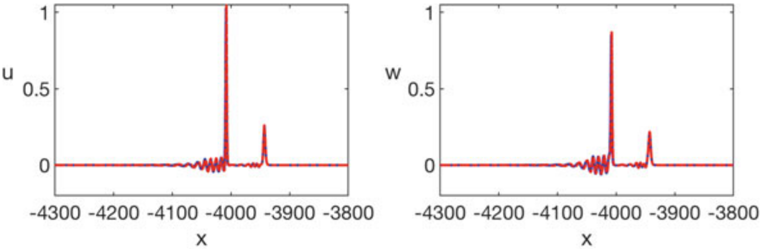

(a) Solution for $u$ at $t = 800$. (b) Solution for $w$ at $t = 800$.

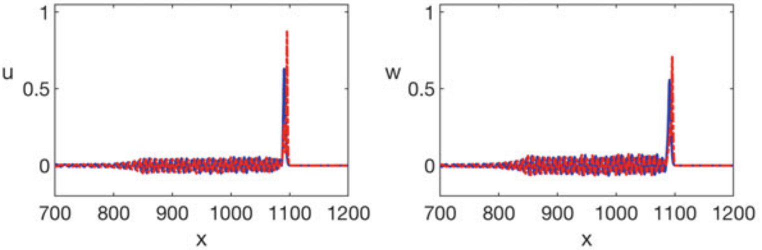

(c) Solution for $u$ at $t = 5800$. (d) Solution for $w$ at $t = 5800$.

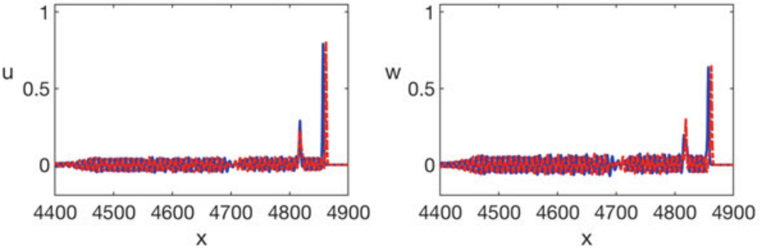

(e) Solution for $u$ at $t = 9500$. (f) Solution for $w$ at $t = 9500$.

**Fig. 6** A comparison of the direct numerical solution (solid, blue) and the weakly-nonlinear solution including $O\left(\sqrt{\epsilon}\right)$ terms (dashed, red) at various times for **(a)**, **(c)**, **(e)** $u$ and **(b)**, **(d)**, **(f)** $w$. Parameters are $L = 5000$, $N = 100000$, $k_1 = 1$, $k_2 = 2$, $x_0 = -50$, $x_1 = 50$, $\alpha = \beta = c = 1 + \epsilon/2$, $\gamma = 1$, $\epsilon = 0.01$, $\Delta t = 0.01$ and $\Delta T = \epsilon \Delta t$. The difference between the amplitudes of the non-stationary solitons during and after the interaction is cased by a small phase shift between the exact and weakly-nonlinear solutions

frequencies. At $t = 9500$, the larger radiating solitary wave has overtaken the smaller wave, and we again have two distinct radiating solitary waves with tails, although with a significantly reduced amplitude. Furthermore, we can see the formation of a wave packet behind the smaller soliton which was generated by the interaction of the solitons. The disagreement between the amplitudes of the smaller soliton after the interaction is again a consequence of a small phase shift, since the amplitude of the smaller soliton keeps oscillating between $u$ and $w$ as the wave tries to settle after the interaction. This has been verified by comparing the maximum of the amplitude of the smaller soliton in the two approaches in a small interval around the fixed moment of time (over the period of oscillations). The difference is of order $O(\epsilon)$, in agreement with the accuracy of the approximation used in this section.

## 5 Conclusions

In this paper we generalised the results of our recent study [21], where we developed a new asymptotic procedure for the construction of the d'Alembert-type solution of the Cauchy problem for a Boussinesq-Klein-Gordon equation with the Ostrovsky term. We have shown that the developed approach can be extended to construct a similar solution for a system of coupled Boussinesq equations (1), (2), describing long longitudinal strain waves in a bi-layer with an imperfect interface [18]. We examined the accuracy of the constructed solution numerically, and we used both the direct numerical simulations for the coupled Boussinesq equations, and our constructed semi-analytical solution in order to study the complicated process of the interaction of two radiating solitary waves. The two approaches showed excellent agreement, even in very long runs. The constructed solution can find useful applications in the studies of the scattering of radiating solitary waves by delamination [16] and other extended inhomogeneities.

**Acknowledgements** We thank D. E. Pelinovsky and A. V. Porubov for useful discussions and references. KRK is grateful to the UK QJMAM Fund for Applied Mathematics for the support of her travel to the ESMC2018 in Bologna, Italy where some of these discussions have taken place. MRT is grateful to the UK Institute of Mathematics and its Applications and the London Mathematical Society for supporting travel to the same conference.

## Appendix A: Numerical Methods

In the following methods we use the Discrete Fourier Transform (DFT) to calculate the Fourier transform of numerical data (e.g., [24]). Let us consider a function $u(x,t)$ on a finite domain $x \in [-L, L]$ and we discretise the domain into $N$ equally spaced points, so we have the spacing $\Delta x = 2L/N$. In all calculations we scale the domain from $x \in [-L, L]$ to $\tilde{x} \in [0, 2\pi]$, which can be achieved by applying the transform $\tilde{x} = sx + \pi$, where $s = \pi/L$. Denoting $x_j = -L + j\Delta x$ for $j = 0, \dots, N$, we define the DFT for the function $u(x,t)$ as

$$\hat{u}\left(k,t\right) = \frac{1}{\sqrt{N}} \sum_{j=1}^{N} u\left(x_j, t\right) e^{-ikx_j}, \quad -\frac{N}{2} \le k \le \frac{N}{2} - 1, \tag{A.1}$$

and similarly the IDFT is defined as

$$u\left(x,t\right) = \frac{1}{\sqrt{N}} \sum_{k=-N/2}^{N/2-1} \hat{u}\left(k,t\right) e^{ikx_j}, \quad j = 1, 2, \dots, N, \tag{A.2}$$

where the discretised and scaled wavenumber is now $k \in \mathbb{Z}$. To perform these transforms we implement the FFTW3 algorithm in C [25].

For the coupled Boussinesq equations (1)–(2) we use a pseudospectral method similar to the one presented in [26], where this method was used to solve a single regularised Boussinesq equation in the context of microstructured solids. We introduce the change of variable

$$U = u - \epsilon u_{xx}, \quad W = w - \epsilon\beta w_{xx}, \tag{A.3}$$

so that we have

$$\begin{aligned} U_{tt} &= u_{xx} + \epsilon\left[\frac{1}{2}\left(u^2\right)_{xx} - \delta\,(u - w)\right], \\ W_{tt} &= c^2 w_{xx} + \epsilon\left[\frac{\alpha}{2}\left(w^2\right)_{xx} + \gamma\,(u - w)\right]. \end{aligned} \tag{A.4}$$

Taking the Fourier transform of (A.3) we obtain

$$\hat{u} = \frac{\hat{U}}{1 + \epsilon k^2}, \quad \hat{w} = \frac{\hat{W}}{1 + \epsilon\beta k^2}. \tag{A.5}$$

We take the Fourier transform of (A.4) and substitute (A.5) into this expression to obtain an ODE in $\hat{u}$ and $\hat{w}$, taking the form

$$\begin{aligned} \hat{U}_{tt} &= -\frac{\epsilon\delta + s^2k^2}{1 + \epsilon s^2k^2}\hat{U} - \frac{\epsilon s^2k^2}{2}\mathscr{F}\left\{\mathscr{F}^{-1}\left[\frac{\hat{U}}{1 + \epsilon s^2k^2}\right]^2\right\} + \frac{\epsilon\delta}{1 + \epsilon s^2\beta k^2}\hat{W}^2 = \hat{S}_1\left(\hat{U}, \hat{W}\right), \\ \hat{W}_{tt} &= -\frac{\epsilon\gamma + c^2s^2k^2}{1 + \epsilon\beta s^2k^2}\hat{W} - \frac{\epsilon\alpha s^2k^2}{2}\mathscr{F}\left\{\mathscr{F}^{-1}\left[\frac{\hat{W}}{1 + \epsilon\beta s^2k^2}\right]^2\right\} + \frac{\epsilon\delta}{1 + \epsilon s^2k^2}\hat{U}^2 = \hat{S}_2\left(\hat{U}, \hat{W}\right), \end{aligned} \tag{A.6}$$

where $\mathscr{F}$ denotes the Fourier transform. We solve this system of ODEs using a 4th-order Runge-Kutta method for time stepping, such as the one used in [16]. Let us rewrite the system as

$$\begin{aligned} \hat{U}_t &= \hat{G}, & \hat{W}_t &= \hat{H}, \\ \hat{G}_t &= \hat{S}_1\left(\hat{U}, \hat{W}\right), & \hat{H}_t &= \hat{S}_2\left(\hat{U}, \hat{W}\right), \end{aligned} \tag{A.7}$$

where we defined $\hat{S}_{1,2}$ as the right-hand side of (A.6). We discretise the time domain and functions as $t = t_n$, $\hat{U}(k, t_n) = \hat{U}_n$, $\hat{W}(k, t_n) = \hat{W}_n$, $\hat{G}(k, t_n) = \hat{G}_n$, $\hat{H}(k, t_n) = \hat{H}_n$ for $n = 0, 1, 2, \ldots$, where $t_n = n\Delta t$, and $k$ discretises the Fourier space. Taking the Fourier transform of the initial conditions as defined in (3) and (4), and making use of (A.5), we obtain initial conditions $\hat{U}_0$, $\hat{W}_0$, and $\hat{G}_0$, $\hat{H}_0$ of the form

$$\begin{aligned} \hat{U}_0 &= \left(1 + \epsilon s^2k^2\right)\mathscr{F}\left\{F_1(x)\right\}, & \hat{W}_0 &= \left(1 + \epsilon\beta s^2k^2\right)\mathscr{F}\left\{F_2(x)\right\}, \\ \hat{G}_0 &= \left(1 + \epsilon s^2k^2\right)\mathscr{F}\left\{V_1(x)\right\}, & \hat{H}_0 &= \left(1 + \epsilon\beta s^2k^2\right)\mathscr{F}\left\{V_2(x)\right\}. \end{aligned} \tag{A.8}$$

Now we have initial conditions, we implement a 4th-order Runge-Kutta method, taking the form

$$\hat{U}_{n+1} = \hat{U}_n + \tfrac{1}{6}\left[k_1 + 2k_2 + 2k_3 + k_4\right], \qquad \hat{G}_{n+1} = \hat{G}_n + \tfrac{1}{6}\left[l_1 + 2l_2 + 2l_3 + l_4\right],$$
$$\hat{W}_{n+1} = \hat{W}_n + \tfrac{1}{6}\left[m_1 + 2m_2 + 2m_3 + m_4\right], \; \hat{H}_{n+1} = \hat{H}_n + \tfrac{1}{6}\left[n_1 + 2n_2 + 2n_3 + n_4\right],$$

where

$$\begin{aligned}
k_1 &= \Delta t \hat{G}_n, & l_1 &= \Delta t \hat{S}_1\left(\hat{U}_n, \hat{W}_n\right),\\
m_1 &= \Delta t \hat{H}_n, & n_1 &= \Delta t \hat{S}_2\left(\hat{U}_n, \hat{W}_n\right),\\
k_2 &= \Delta t\left(\hat{G}_n + \tfrac{l_1}{2}\right), & l_2 &= \Delta t \hat{S}_1\left(\hat{U}_n + \tfrac{k_1}{2}, \hat{W}_n + \tfrac{m_1}{2}\right),\\
m_2 &= \Delta t\left(\hat{H}_n + \tfrac{n_1}{2}\right), & n_2 &= \Delta t \hat{S}_2\left(\hat{U}_n + \tfrac{k_1}{2}, \hat{W}_n + \tfrac{m_1}{2}\right),\\
k_3 &= \Delta t\left(\hat{G}_n + \tfrac{l_2}{2}\right), & l_3 &= \Delta t \hat{S}_1\left(\hat{U}_n + \tfrac{k_2}{2}, \hat{W}_n + \tfrac{m_2}{2}\right),\\
m_3 &= \Delta t\left(\hat{H}_n + \tfrac{n_2}{2}\right), & n_3 &= \Delta t \hat{S}_2\left(\hat{U}_n + \tfrac{k_2}{2}, \hat{W}_n + \tfrac{m_2}{2}\right),\\
k_4 &= \Delta t\left(\hat{G}_n + l_3\right), & l_4 &= \Delta t \hat{S}_1\left(\hat{U}_n + k_3, \hat{W}_n + m_3\right),\\
m_4 &= \Delta t\left(\hat{H}_n + n_3\right), & n_4 &= \Delta t \hat{S}_2\left(\hat{U}_n + k_3, \hat{W}_n + m_3\right).
\end{aligned} \tag{A.9}$$

To obtain the solution in the real domain, we transform $\hat{U}$ back to $u$, and similarly $\hat{W}$ back to $w$, through relation (A.5). Explicitly we have

$$u(x,t) = \mathscr{F}^{-1}\left\{\frac{\hat{U}}{1 + \epsilon s^2 k^2}\right\}, \quad w(x,t) = \mathscr{F}^{-1}\left\{\frac{\hat{W}}{1 + \epsilon s^2 \beta k^2}\right\}. \tag{A.10}$$

We now consider the solution to the coupled Ostrovsky equations. The method is similar to that used in [27]. It is presented for the equations (75), (76), as this method can be reduced to solve the system (29), (31). We present the equations for the negative superscript i.e. for $\phi_1^-$ and $\phi_2^-$. We omit the superscript in the subsequent equations. Let us consider the system of coupled Ostrovsky equations defined as

$$\begin{aligned}
\left(\phi_{1t} + \omega_1\phi_{1x} + \alpha_1\left(f_1\phi_1\right)_x + \beta_1\phi_{1xxx}\right)_x &= \delta\left(\phi_1 - \phi_2\right) + H_1\left(f_1(x), f_2(x)\right),\\
\left(\phi_{2t} + \omega_2\phi_{2x} + \alpha_2\left(f_2\phi_2\right)_x + \beta_2\phi_{2xxx}\right)_x &= \gamma\left(\phi_2 - \phi_1\right) + H_2\left(f_1(x), f_2(x)\right),
\end{aligned} \tag{A.11}$$

where $\alpha_1, \alpha_2, \beta_1, \beta_2, \omega_1, \omega_2, \delta$ and $\gamma$ are constants, and the functions $f_1, f_2$ are known. We consider the equation on domains $t \in [0, T]$ and $x \in [-L, L]$. We calculate the nonlinear terms in the real domain and then transform them to the Fourier space. The spatial domain is discretised by $N$ equidistant points with spacing $\Delta x = 2\pi/N$, and we have the DFT and IDFT as defined in (A.1) and (A.2) respectively, with an appropriately similar transform for $w$. The discrete Fourier transform of equations (A.11) with respect to $x$ gives

$$\begin{aligned}
\hat{\phi}_{1t} + \left(isk\omega_1 - is^3k^3\beta_1\right)\hat{\phi}_1 + isk\alpha_1\mathscr{F}\{f_1\phi_1\} &= -\frac{i\delta}{sk}\left(\hat{\phi}_1 - \hat{\phi}_2\right) - \frac{i}{sk}\hat{H}_1,\\
\hat{\phi}_{2t} + \left(isk\omega_2 - is^3k^3\beta_2\right)\hat{\phi}_2 + isk\alpha_2\mathscr{F}\{f_2\phi_2\} &= -\frac{i\gamma}{sk}\left(\hat{\phi}_2 - \hat{\phi}_1\right) - \frac{i}{sk}\hat{H}_2.
\end{aligned} \tag{A.12}$$

This system is solved numerically using a 4th-order Runge-Kutta method for time stepping as for the coupled Boussinesq equations. Assume that the solution at $t$ is given by $\hat{\phi}_{1,j} = \hat{\phi}_1(k, j\kappa)$ and $\hat{\phi}_{2,j} = \hat{\phi}_2(k, j\kappa)$, where $\kappa = \Delta t$. Then the solution at $t = (j+1)\Delta t$ is given by

$$\begin{aligned}
\hat{\phi}_{1,(j+1)\kappa} &= \hat{\phi}_{1,j\kappa} + \frac{1}{6}\left(a_1 + 2b_1 + 2c_1 + d_1\right),\\
\hat{\phi}_{2,(j+1)\kappa} &= \hat{\phi}_{2,j\kappa} + \frac{1}{6}\left(a_2 + 2b_2 + 2c_2 + d_2\right),
\end{aligned} \tag{A.13}$$

where $a_i, b_i, c_i, d_i$ are functions of $k$ at a given moment in time, $t$, and are defined as

$$\begin{aligned}
a_i &= \kappa F_i\left(\hat{\phi}_{1,j}, \hat{\phi}_{2,j}\right), & b_i &= \kappa F_i\left(\hat{\phi}_{1,j} + \tfrac{a_1}{2}, \hat{\phi}_{2,j} + \tfrac{a_2}{2}\right),\\
c_i &= \kappa F_i\left(\hat{\phi}_{1,j} + \tfrac{b_1}{2}, \hat{\phi}_{2,j} + \tfrac{b_2}{2}\right), & d_i &= \kappa F_i\left(\hat{\phi}_{1,j} + c_1, \hat{\phi}_{2,j} + c_2\right),
\end{aligned}$$

for $i = 1, 2$. The functions $F_i$ are found as a rearrangement of (A.12) to contain all non-time derivatives. Explicitly we have

$$\begin{aligned}
F_1\left(\hat{\phi}_{1,j}, \hat{\phi}_{2,j}\right) &= -iks\alpha_1\mathscr{F}\{f_1\phi_1\} + \left(ik^3s^3\beta_1 - isk\omega_1\right)\hat{\phi}_{1,j} - \frac{i\delta}{sk}\left(\hat{\phi}_{1,j} - \hat{\phi}_{2,j}\right) - \frac{i}{sk}\hat{H}_{1,j},\\
F_2\left(\hat{\phi}_{1,j}, \hat{\phi}_{2,j}\right) &= -iks\alpha_2\{f_2\phi_2\} + \left(ik^3s^3\beta_2 - isk\omega\right)\hat{\phi}_{2,j} - \frac{i\gamma}{sk}\left(\hat{\phi}_{2,j} - \hat{\phi}_{1,j}\right) - \frac{i}{sk}\hat{H}_{2,j}.
\end{aligned}$$

To obtain a solution at the next step, the functions $a_i, b_i, c_i, d_i$, for $i = 1, 2$, must be calculated in pairs, that is we calculate $a_1$ followed by $a_2$, then $b_1$ followed by $b_2$, and so on.

## References

1. Samsonov, A.M.: Strain Solitons in Solids and How to Construct Them. Chapman & Hall/CRC, Boca Raton (2001)
2. Porubov, A.V.: Amplification of Nonlinear Strain Waves in Solids. World Scientific, Singapore (2003)
3. Peake, N., Sorokin, S.V.: A nonlinear model of the dynamics of a large elastic plate with heavy fluid loading. Proc. R. Soc. A **462**, 2205–2224 (2006)
4. Indejtsev, D.A., Zhuchkova, M.G., Kouzov, D.P., Sorokin, S.V.: Low-frequency wave propagation in an elastic plate floating on a two-layered fluid. Wave Motion **62**, 98–113 (2016)
5. Peets, T., Tamm, K., Engelbrecht, J.: On the role of nonlinearities in the Boussinesq-type wave equations. Wave Motion **71**, 113–119 (2017)

6. Abiza, Z., Destrade, M., Ogden, R.W.: Large acoustoelastic effect. Wave Motion **49**, 364–374 (2012)
7. Andrianov, I.V., Danishevsky, V.D., Kaplunov, J.D., Markert, B.: Wide frequency higher-order dynamic model for transient waves in a lattice. In: Andrianov, I.V., et al. (ed.) Problems of Nonlinear Mechanics and Physics of Materials. Springer (2019)
8. Ostrovsky, L.A., Sutin, A.M.: Nonlinear elastic waves in rods. PMM **41**, 531–537 (1977)
9. Nariboli, G.A., Sedov, A.: Burgers-Korteweg de Vries equation for viscoelastic rods and plates. J. Math. Anal. Appl. **32**, 661–677 (1970)
10. Dai, H.-H., Fan, X.: Asymptotically approximate model equations for weakly nonlinear long waves in compressible elastic rods and their comparisons with other simplified model equations. Math. Mech. Solids **9**, 61–79 (2004)
11. Erofeev, V.I., Kazhaev, V.V., Semerikova, N.P.: Waves in Rods: Dispersion, Dissipation, Nonlinearity. Fizmatlit, Moscow (2002) (in Russian)
12. Garbuzov, F.E., Khusnutdinova, K.R., Semenova, I.V.: On Boussinesq-type models for long longitudinal waves in elastic rods. arXiv:1810.07684v3 [nlin.PS], 22 Jan 2019 (submitted to Wave Motion)
13. Khusnutdinova, K.R., Samsonov, A.M.: Fission of a longitudinal strain solitary wave in a delaminated bar. Phys. Rev. E **77**, 066603 (2008)
14. Dreiden, G.V., Khusnutdinova, K.R., Samsonov, A.M., Semenova, I.V.: Bulk strain solitary waves in bonded layered polymeric bars with delamination. J. Appl. Phys. **112**, 063516 (2012)
15. Khusnutdinova, K.R., Tranter, M.R.: Modelling of nonlinear wave scattering in a delaminated elastic bar. Proc. R. Soc. A **471**, 20150584 (2015)
16. Khusnutdinova, K.R., Tranter, M.R.: On radiating solitary waves in bi-layers with delamination and coupled Ostrovsky equations. Chaos **27**, 013112 (2017)
17. Belashov, A.V., Beltukov, Y.M., Semenova, I.V.: Pump-probe digital holography for monitoring of long bulk nonlinear strain waves in solid waveguides. Proc. SPIE **10678**, 1067810 (2018)
18. Khusnutdinova, K.R., Samsonov, A.M., Zakharov, A.S.: Nonlinear layered lattice model and generalized solitary waves in imperfectly bonded structures. Phys. Rev. E **79**, 056606 (2009)
19. Grimshaw, R.H.J., Khusnutdinova, K.R., Moore, K.R.: Radiating solitary waves in coupled Boussinesq equations. IMA J. Appl. Math. **82**, 802–820 (2017)
20. Khusnutdinova, K.R., Moore, K.R.: Initial-value problem for coupled Boussinesq equations and a hierarchy of Ostrovsky equations. Wave Motion **48**, 738–752 (2011)
21. Khusnutdinova, K.R., Tranter, M.R.: D'Alembert-type solution of the Cauchy problem for a Boussinesq-Klein-Gordon equation. arXiv:1808.08150v2 [nlin.PS], 22 Jan 2019 (submitted to Stud. Appl. Math.)
22. Khusnutdinova, K.R., Moore, K.R., Pelinovsky, D.E.: Validity of the weakly nonlinear solution of the Cauchy problem for the Boussinesq-type equation. Stud. Appl. Math. **133**, 52–83 (2014)
23. Khusnutdinova, K.R., Moore, K.R.: Weakly non-linear extension of d'Alembert's formula. IMA J. Appl. Math. **77**, 361–381 (2012)
24. Trefethen, L.N.: Spectral Methods in MATLAB. SIAM, Philadelphia (2000)
25. Frigo, M., Johnson, S.G.: The design and implementation of FFTW3. Proc. IEEE **93**, 216–231 (2005)
26. Engelbrecht, J., Salupere, A., Tamm, K.: Waves in microstructured solids and the Boussinesq paradigm. Wave Motion **48**, 717–726 (2011)
27. Alias, A., Grimshaw, R.H.J., Khusnutdinova, K.R.: On strongly interacting internal waves in a rotating ocean and coupled Ostrovsky equations. Chaos **23**, 023121 (2013)

# The Ballistic Heat Equation for a One-Dimensional Harmonic Crystal

**Anton Krivtsov**

**Abstract** The analytical model of unsteady ballistic heat transfer in a one-dimensional harmonic crystal is analyzed. A nonlocal temperature is introduced as a generalization of the kinetic temperature. A closed equation determining unsteady thermal processes in terms of the nonlocal temperature is derived. For an instantaneous heat perturbation a time-reversible equation for the kinetic temperature is derived and solved. This equation can be referred as the ballistic heat conduction equation, it is somewhat similar to the hyperbolic heat conduction equation, but it has important differences. The resulting constitutive law for the heat flux in the considered system is obtained. This law significantly differs from Fourier's law and it predicts a finite velocity of the heat front and independence of the heat flux on the crystal length. The analytical results are confirmed by computer simulations. Further developments of the presented approach are referred.

## 1 Introduction

An understanding of heat transfer at microlevel is essential to obtain link between microscopic and macroscopic description of solids [1–3]. As far as macroscopic scale level is concerned the Fourier law of heat conduction is widely and successfully used to describe heat transfer processes. At microscopic level, however, analytical and numerical investigations have shown substantial deviations from Fourier's law [4–6]. These inadequacies can be on principle addressed by using special laws of particles interactions [7–10] or complex enough structures [11, 12]. Recent experimental data however showed that Fourier's law is indeed violated in low-dimensional [13–15].

---

A. Krivtsov (✉)
Department of Theoretical Mechanics, Peter the Great St. Petersburg
Polytechnic University, St. Petersburg, Russia
e-mail: akrivtsov@bk.ru

A. Krivtsov
Laboratory of Discrete Models in Mechanics, Institute for Problems
in Mechanical Engineering RAS, St. Petersburg, Russia

H. Altenbach et al. (eds.), *Dynamical Processes in Generalized Continua and Structures*, Advanced Structured Materials 103,
https://doi.org/10.1007/978-3-030-11665-1_19

The main reason is that at microlevel the ballistic heat transfer dominates, in contrast to macrolevel, where the diffusive (Fourier) heat conduction prevails. This motivates interest to the simplest lattice models, in particular harmonic one-dimensional crystals (chains), where the anomalies connected with the ballistic heat transfer are most prominent [1, 16, 17]. Problems of this kind previously have been mainly addressed in the context of the steady-state heat conduction [4–6, 17, 18]. The present work focuses on unsteady conduction regimes [12, 19–22].

Here we describe an approach that allows rigorous derivation of macroscopic heat conduction equations and corresponding anomalous heat conduction law for harmonic systems in a one-dimensional, non-quantum case. This approach for the simplest one-dimensional crystal was first presented in [23], below we show these results in more details. The obtained equations differ substantially from the earlier suggested heat transfer equations [24, 25], however they are in excellent agreement with molecular dynamics simulations and previous analytical estimations [20].

## 2 The System

We consider a one-dimensional crystal, described by the following equation of motion:

$$\ddot{u}_i = \omega_e^2(u_{i-1} - 2u_i + u_{i+1}) \tag{1}$$

where $u_i$ is the displacement, $i$ is the number of the particle, $\omega_e \overset{\text{def}}{=} \sqrt{C/m}$ is the elementary frequency, $m$ is the particle mass, $C$ is the stiffness of the interparticle bond, dot is the time derivative. The crystal is infinite: the index $i$ is an arbitrary integer. The initial conditions are

$$u_i|_{t=0} = 0\,, \qquad \dot{u}_i|_{t=0} = \sigma(x)\rho_i\,, \tag{2}$$

where $\rho_i$ are independent random values with zero expectation and unit variance; $\sigma^2(x)$ is variance of the initial velocities, which is a slowly varying function of the spatial coordinate $x = ia$, where $a$ is the lattice constant. These initial conditions correspond to an instantaneous temperature perturbation, which can be induced in crystals, for example, by an ultrashort laser pulse [26, 27]. The displacements as functions of time $u_i = u_i(t)$ can be found as a solution of the Cauchy problem (1)–(2). These functions are random—they depend linearly on the integration constants, which are linear functions of the random values $\rho_i$ (2).

## 3 Nonlocal Temperature

The first analytical solution of a steady heat conduction problem for a harmonic chain was obtained in [18] using a covariance matrix for coordinates and momenta. Then this approach was extended and applied to various harmonic systems [4, 11, 16, 17]. Study of the covariance matrix allowed obtaining analytical expressions for steady [28] and unsteady [29, 30] temperature profiles. Here a somewhat similar approach based on analysis of covariances for velocities [23, 31, 32] is used. Following [33] the *nonlocal temperature* $\theta_{ij}$ is defined as

$$k_B\theta_{ij} \overset{\text{def}}{=} m\langle \dot{u}_i\dot{u}_j\rangle, \tag{3}$$

where $k_B$ is the Boltzmann constant, angle brackets stand for mathematical expectation, $\langle \dot{u}_i\dot{u}_j\rangle$ is the velocity covariance (note that $\langle \dot{u}_i\rangle \equiv \langle \dot{u}_j\rangle \equiv 0$). Then differentiation of (3) with the use of the dynamics equation (1) allows to obtain the following closed differential-difference equation of the fourth order [31]

$$\ddot{\ddot{\theta}}_{ij} - 2(\mathscr{L}_i + \mathscr{L}_j)\ddot{\theta}_{ij} + (\mathscr{L}_i - \mathscr{L}_j)^2\theta_{ij} = 0, \tag{4}$$

where $\mathscr{L}_i$ is the linear difference operator: $\mathscr{L}_i u_i \overset{\text{def}}{=} \omega_e^2(u_{i-1} - 2u_i + u_{i+1})$. Equation (4) is an exact one, it describes processes of two types: fast transition to the local equilibrium [32] and slow heat transfer process [23]. For continuum description of the heat transfer the nonlocal temperature is redefined as

$$(-1)^n\,\theta_n(x) \overset{\text{def}}{=} \theta_{ij}\,, \qquad n \overset{\text{def}}{=} j - i\,, \qquad x = \frac{i+j}{2}a, \tag{5}$$

where $n$ is the covariance index, $x$ is the macroscopic spatial coordinate. If $n = 0$ then $i = j$ and quantity $\theta_n$ coincides with the kinetic temperature $T$:

$$k_B\theta_0(x) = k_BT(x) = m\langle \dot{u}_i^2\rangle, \tag{6}$$

where $i = x/a$. According to its definition, the nonlocal temperature reflects a nonlocal nature of thermal processes in harmonic crystals and can be considered as a generalization of the kinetic temperature.

To obtain the simplified equation for description of the heat transfer only, the following two approximations are used.

1. **Continualization**. The nonlocal temperature $\theta_n(x)$ is a slowly varying function of the spatial coordinate $x$ (on the distances of order of the lattice constant $a$). This allows replacing the finite differences by the spatial derivatives [34]. The approximation is adequate for processes that are sufficiently smooth in space, e.g. for spatial temperature profiles in a form of waves that are much longer then the lattice constant $a$.

2. **Slow process approximation**. This approximation allows to neglect the term with the fourth time-derivative in Eq. (4) resulting in the second order differential equation with respect to time. Alternatively the second order equation can be obtained [23] using the virial approximation [2]: time or spatial derivatives of mathematical expectations are small with respect to quantities that have non-zero values in thermodynamic equilibrium. This approximation is adequate for processes that are not too far from thermodynamic equilibrium. In particular, the virial approximation allows to express covariances of the bond strains in terms of the nonlocal temperature.

Then the following second order differential-difference equation can be obtained from Eq. (4):

$$\ddot{\theta}_n + \tfrac{1}{4}c^2(\theta_{n-1} - 2\theta_n + \theta_{n+1})'' = 0, \tag{7}$$

where $c = \omega_e a$ is the speed of sound. This is a closed equation describing unsteady thermal processes in the crystal in terms of the nonlocal temperature. The processes under consideration should be such that the nonlocal temperature is sufficiently smooth in time and space. Apart from this limitation any unsteady thermal processes in the considered system satisfy equation (7). This equation in its current form appeared for the first time in [33], its derivation can be found in [23] (in different designations) or in [35] (for more complex problem). After solution (analytical or numerical) of Eq. (7) the kinetic temperature can be obtained as $T(t, x) = \theta_n(t, x)|_{n=0}$.

The initial conditions for Eq. (7) corresponding to the original initial conditions (2) are:

$$\theta_n|_{t=0} = T_0(x)\delta_n\,, \qquad \dot{\theta}_n|_{t=0} = 0, \tag{8}$$

where $T_0(x) = \frac{1}{2k_B}m\sigma^2(x)$ is the initial temperature distribution; $\delta_n = 1$ for $n = 0$, otherwise $\delta_n = 0$. The initial conditions (8) are taken after a fast transition process, which results, according to the virial theorem, in a double reduction of the initial kinetic temperature [32]. Note that in contrast with the random initial value problem (1)–(2), the initial value problem (7)–(8) is expressed in terms of mathematical expectations, and therefore it is a deterministic problem.

## 4 The Ballistic Heat Equation

Using an integral Fourier transform in the spatial coordinate $x$ the problem (7)–(8) can be solved analytically. For the Fourier image $\hat{\theta}_n(t, k)$ we obtain

$$\begin{gathered}\ddot{\hat{\theta}}_n = \tfrac{1}{4}c^2k^2(\hat{\theta}_{n-1} - 2\hat{\theta}_n + \hat{\theta}_{n+1}),\\ \hat{\theta}_n|_{t=0} = \hat{T}_0(k)\delta_n\,, \qquad \dot{\hat{\theta}}_n|_{t=0} = 0,\end{gathered} \tag{9}$$

where $k$ is the spatial frequency, $\hat{T}_0(k)$ is the Fourier image of the initial temperature distribution $T_0(x)$. Let us note the similarity between (1)–(2) and (9): initial value problem (9) can be interpreted as a motion of a harmonic chain having an initial shift of the central particle. This kind of problems can be effectively solved in terms of Bessel functions. In particular, Bessel functions were successfully applied to solution of shock-wave problems in harmonic chains [36, 37]. Similarly, the problem (9) has an analytical solution $\hat{\theta}_n(t,k) = \hat{T}_0(k) J_{2n}(ckt)$, where $J_{2n}$ are the Bessel functions of the 1st kind [38]. From the practical point of view the most interesting case is $n = 0$, which gives Fourier image $\hat{T}(t,k)$ of the kinetic temperature distribution:

$$\hat{T}(t,k) = \hat{T}_0(k) J_0(ckt). \tag{10}$$

From (10) it follows that the image $\hat{T}(t,k)$ satisfies the Bessel differential equation

$$\ddot{\hat{T}} + \frac{1}{t}\dot{\hat{T}} = -c^2 k^2 \hat{T}. \tag{11}$$

Fourier inversion of (11) gives a partial differential equation for the temperature field

$$\ddot{T} + \frac{1}{t}\dot{T} = c^2 T'', \tag{12}$$

which can be referred as the ballistic heat equation. The corresponding initial conditions follow from (8):

$$T|_{t=0} = T_0(x)\,, \qquad \dot{T}|_{t=0} = 0. \tag{13}$$

The obtained equation (12) is a particular case of the Darboux differential equation [39]. For description of the heat transfer in the harmonic one-dimensional crystal it was originally derived in [23]. Later it was proved that the same equation describes the ballistic heat transfer if the crystal is supported by an elastic foundation [40]. The ballistic heat equation describes the evolution of the temperature field after an instantaneous thermal perturbation happened at $t = 0$, that is why this equation can be used only with initial conditions (13). The condition $\dot{T}|_{t=0}$ means absence of the heat flux in the initial state. For more complex situation the general equation for nonlocal temperatures (7) should be used.

Fourier inversion of the representation (10) gives an analytical solution of the initial value problem (12)–(13):

$$T(t,x) = \frac{1}{\pi}\int_{-1}^{1} \frac{T_0(x - cts)}{\sqrt{1 - s^2}}\, ds. \tag{14}$$

Similar integral representation without obtaining equation (12) was derived in [41] using heat energy density correlation functions. Substitution $s = \cos\varphi$ gives an alternative integral form

$$T(t,x)=\frac{1}{\pi}\int_0^{\pi}T_0(x+ct\cos\varphi)\,\mathrm{d}\varphi. \tag{15}$$

The physical meaning of this representation is that $ct\cos\varphi$ is the group velocity of Eq. (1), where $\varphi$ is a half of the wave number. Representation (15) can be interpreted as superposition of the classical wave equation solutions for all wave numbers. Further investigations have shown that the similar rule is fulfilled for much more general harmonic systems [42, 43].

Thus, an evolution of the temperature field in a one-dimensional crystal after an instantaneous thermal perturbation is described by partial differential equation (12) with initial conditions (13) or by integral formulas (14)–(15). According to (14) the thermal front propagates with the sound speed $c$ (in contrast to the thermal conductivity based on Fourier's law where an unphysical instantaneous signal propagation is realized). The obtained wave behavior of the heat front is similar to predictions of the wave theories of heat conduction [24, 25]. However, the obtained solution has important differences, which will be shown in the text to follow.

## 5 Heat Flux

For the considered system the heat flux can be represented [5, 6, 44] as

$$q=\tfrac{1}{2}C\langle(u_i-u_{i+1})(\dot{u}_i+\dot{u}_{i+1})\rangle. \tag{16}$$

The heat flux $q$ satisfies the energy balance equation

$$\rho k_B\dot{T}=-q', \tag{17}$$

where $\rho=1/a$ is the density (number of particles per unit volume), $k_B\dot{T}$ stands for the heat energy for the considered system. Joint consideration of Eqs. (12) and (17) gives the constitutive law for the heat flux

$$\dot{q}+\frac{1}{t}q=-k_Bc^2\rho T', \tag{18}$$

which replaces Fourier's law in the considered system. Alternatively, the law (18) can be derived directly, in the same way as the ballistic heat conduction Eq. (12) is derived. Integral representations for the heat flux follows from (14) and (18):

$$q(t,x)=\frac{k_Bc\rho}{\pi}\int_{-1}^{1}\frac{T_0(x-cts)}{\sqrt{1-s^2}}\,sds. \tag{19}$$

The alternative representation corresponding to (15) is

$$q(t,x) = \frac{k_B c\rho}{\pi} \int\limits_0^{\pi} T_0(x + ct\cos\varphi)\cos\varphi \, \mathrm{d}\varphi. \tag{20}$$

## 6 Comparison of Different Equations Describing the Heat Conduction

Let us consider three models of heat conduction: the classic heat equation based on Fourier's law of heat conduction; the hyperbolic heat equation (thermal wave equation) based on the Maxwell-Cattaneo-Vernotte law [24, 25]; the obtained above ballistic heat equation (12). Brief comparison of these models is given in Table 1. The hyperbolic heat equation and Eq. (12) have similar form and somewhat similar behavior (e.g. a finite velocity of the heat front propagation). However, there are significant differences:

1. The main difference is that $\tau$, a material constant, is replaced in (12) by the physical time $t$. Consequently, these equations are close for intermediate tomes $t \approx \tau$, however they are substantially different for small and large times. Moreover, for $t \to 0$, from the first glance, the ballistic equation (12) has singularity. However, same as for the hyperbolic equation, the solution of this equation does not have any time singularity, which can be easily seen from formula (15). For $t \to \infty$ the asymptotics of the hyperbolic and ballistic equations are different: exponential and power decay respectively—see Table 1(b).
2. The ballistic heat equation, as opposite to the hyperbolic and Fourier equations, is not time-invariant—it changes with substitution $t$ by $t + t_0$. This is because it describes reaction of the system on the instantaneous thermal perturbation at

**Table 1** (a) Heat transfer equation, (b) equation connecting heat flux and temperature, (c) decay law for the sinusoidal heat perturbation. Notations: $t$ is time (variable), $\tau$ is the relaxation time (constant), $\beta$ is the thermal diffusivity, $\kappa$ is the thermal conductivity, $c$ is the sound speed, $\rho$ is the density, $k_B$ is the Boltzmann constant, $k$ is the spatial frequency. Approximation (c) for the hyperbolic heat equation is obtained for $c^2 = \beta/\tau$ and large $k$; approximation for $J_0$ is valid for relatively large $t$

| | Fourier heat equation | Hyperbolic heat equation | Ballistic heat equation |
|---|---|---|---|
| (a) | $\dot{T} = \beta T''$ | $\ddot{T} + \frac{1}{\tau}\dot{T} = \frac{\beta}{\tau}T''$ | $\ddot{T} + \frac{1}{t}\dot{T} = c^2 T''$ |
| (b) | $q = -\kappa T'$ | $\dot{q} + \frac{1}{\tau}q = -\frac{\kappa}{\tau}T'$ | $\dot{q} + \frac{1}{t}q = -k_B c^2 \rho T'$ |
| (c) | $e^{-\beta k^2 t}$ | $\approx e^{-\frac{t}{2\tau}}\cos(kct)$ | $J_0(kct) \approx \frac{\cos(kct - \frac{\pi}{4})}{\sqrt{\frac{\pi}{2}kct}}$ |

$t = 0$, the general situation is described by more general Eq. (7), which is time-invariant.

3. The ballistic heat equation is time-reversible: it does not change with substitution $t$ by $-t$. Same fulfils for the original dynamical equation (1) and the general equation for nonlocal temperatures (7). On contrary, the Fourier and hyperbolic heat equations are not time-reversible. The contradiction between time-reversibility of the classical microscopic equations and irreversibility of the corresponding macroscopic continuum equations is one of the opened questions of the modern physics [2, 45]. The obtained reversible macroscopic equation of the ballistic heat conduction may be a step towards solution of this problem. In particular, it will be shown below that this equation describes irreversible processes, such as decay of the sinusoidal heat perturbation—see Fig. 1. Thus reversible equations can produce irreversible solutions, even in a finite domain.

## 7 Sinusoidal Temperature Perturbation

We consider now a sinusoidal temperature perturbation

$$T_0(x) = A_0 \sin kx + B, \tag{21}$$

where $A_0$ and $B$ are temperature constants, $k = 2\pi/\lambda$ is the spatial frequency, $\lambda$ is the wavelength of the perturbation. These initial conditions provide simple and informative testing of thermal transfer in closed systems [12, 23, 46]. This is especially important for the ballistic heat transfer analysis, because in this case any external heat supply can substantially affect the thermal processes [47, 48]. Formulas (14) and (19) give an exact analytical solution for the temperature and heat flux

$$\begin{aligned} T(t,x) &= A_0 J_0(kct) \sin kx + B, \\ q(t,x) &= -k_B c\rho A_0 J_1(kct) \cos kx, \end{aligned} \tag{22}$$

where $J_0$ and $J_1$ are the Bessel functions of the 1st kind. This solution was obtained in [23]. Previously, without obtaining equation (12), an existence of a Bessel function solution for the sinusoidal temperature distribution in the one-dimensional harmonic crystal was mentioned in [20], and solution similar to (22) for the temperature field was obtained in Master-degree thesis [49].

To justify the assumptions in derivation of the analytical solution we compare it with results of molecular dynamics (MD) simulations. Equation (1) is solved by the central differences method, the time step is $0.01\tau_0$, where $\tau_0 = 2\pi/\omega_e$. The initial conditions (21) are set by a random number generator, the wavelength $\lambda$ is equal to the length of the chain containing $10^4$ particles. To provide correspondence with the analytical approach used above, $10^4$ realizations of such chain with an independent random initiation are computed. To optimize the computations all chains are joined at end-points to form a long chain ($10^8$ particles) with periodic boundary conditions.

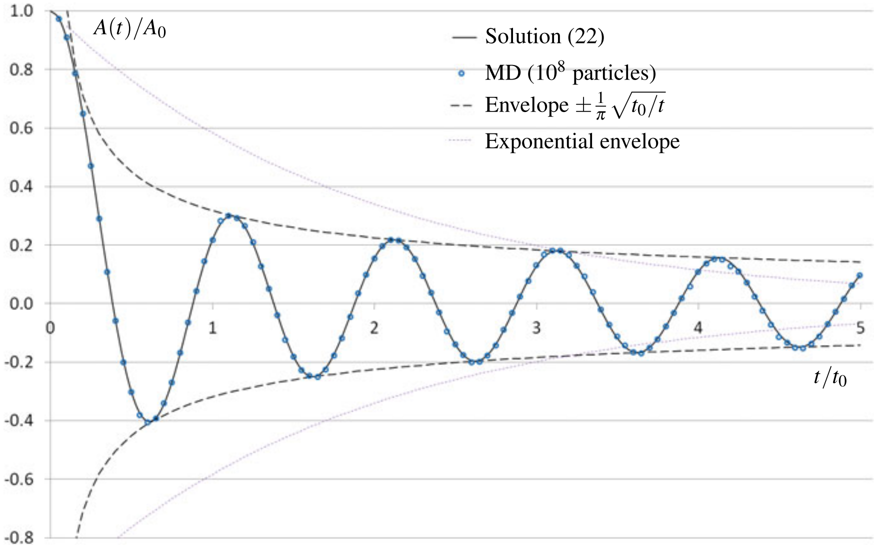

**Fig. 1** Oscillational decay of the thermal perturbation amplitude for 1D harmonic crystal. Comparison of the analytical solution (22) with the MD modeling results ($10^4$ joined chains containing $10^4$ particles each). Dashed lines show the envelope proportional to $1/\sqrt{t}$ and also an exponential envelope inherent to the hyperbolic heat equation

The results of the computations are compared with analytical solution (22) in Fig. 1. The horizontal axis in Fig. 1 represents the dimensionless time $t/t_0$, where $t_0 = \lambda/c$; the vertical axis stands for the oscillation amplitude $A(t)$, which is computed as the first coefficient of a spatial Fourier expansion of the temperature field. According to Fig. 1 there is an excellent agreement between the computational results and the analytical curve.

Due to the Bessel function properties [38], the temperature and heat flux (22) have an oscillational decay, where the oscillation amplitude is asymptotically proportional to $1/\sqrt{t}$. The same asymptotics has been obtained in [20] for one-dimensional harmonic crystals. In Fig. 1 the envelope proportional to $1/\sqrt{t}$ is shown by the dashed lines, perfectly bounding both analytical and computational graphs. The existing theories of heat conduction [24, 25], such as Fourier's, Maxwell-Cattaneo-Vernotte (MCV), dual-phase-lag [50], and spacetime-elasticity [21] yield linear differential equations with constant coefficients, and therefore all of them predict an exponential decay of the sinusoidal perturbation amplitude. In Table 1 a comparison of the analytically obtained decay law for $A(t)/A_0$ with the results based on some other theories is demonstrated, an exponential envelope inherent to the thermal wave model is also shown in Fig. 1. Thus, among the mentioned theories only the current one gives an analytical solution, which agrees with the MD simulations and asymptotic estimations of the oscillation decay for harmonic chains [20].

## 8 Stepwise Temperature Perturbation

Let us consider now a stepwise initial temperature distribution, modeling heat transfer between a hot and a cold body:

$$x < 0: \quad T(x) = T_2\,, \qquad x > 0: \quad T(x) = T_1, \tag{23}$$

where $T_2 > T_1$. In this case the integral representations (14), (19) yield for $|x| \leq ct$ an exact analytical solution

$$\begin{aligned} T(t,x) &= T_1 + \tfrac{\Delta T}{\pi} \arccos \tfrac{x}{ct}, \\ q(t,x) &= \tfrac{k_B c\rho \Delta T}{\pi} \sqrt{1 - \left(\tfrac{x}{ct}\right)^2}, \end{aligned} \tag{24}$$

where $\Delta T = T_2 - T_1$; for $x > ct$ the original temperature distribution remains and the heat flux is zero. According to (24) the heat front propagates with the sound speed $c$ and the heat flux through cross-section $x = 0$ is constant and equal to $\frac{1}{\pi} k_B c\rho \Delta T$. In contrast, use of Fourier's law for the same problem gives the heat flux proportional to $t^{-1/2}$, which is infinite at $t = 0$ (an unphysical consequence of Fourier's law). Thus the heat flux $\frac{1}{\pi} k_B c\rho \Delta T$ is provided by the temperature difference that is realized on the spatial interval $x \in [-ct, ct]$ with increasing length of $2ct$. Consequently, the heat flux depends on the temperature difference rather than on the temperature gradient. This is in qualitative agreement with the known phenomenon of thermal superconductivity: the heat flux through a one-dimensional harmonic crystal placed between two thermal reservoirs does not depend on the length of the crystal [6, 18]. The same value $\frac{1}{\pi} k_B c\rho \Delta T$ was obtained in [51] as a steady-state limit of the heat flux for large $t$.

In Fig. 2 the analytical solution (24) is compared with computer simulations for $T_2 = 2T_1$. The above described computation procedure is used. Figure 2 shows the initial temperature distribution, the analytical solution, and the computation results obtained at $t = t_0/8$ using $10^6$ and $10^8$ particles ($t_0 = L/c$, where $L$ is the chain length; only half of the chain is shown in the figure). Convergence to the analytical solution with the increase of the system size is clearly seen.

Figure 3 shows a part of Fig. 2 corresponding to positive $x$. For symmetry reasons this case can be interpreted as a problem of a half-space heating: the initial temperature for $x > 0$ is $T_1$ and the boundary condition at $x = 0$ is $T = (T_2 + T_1)/2 > T_1$. The advantage of this formulation is that the constant boundary temperature is maintained without any thermostat. This is important since the heat transfer can substantially depend on the thermostat properties [47, 48]. Solutions of the considered problem using four different continuum equations are compared in Fig. 3 with the simulation results. Parameters are chosen in such a way that the total heat quantity transferred through the cross-section $x = 0$ (area under each curve) is equal for all models and the heat front (when it exists) propagates with the sound speed $c$. According to Fig. 3 the computation results almost coincide with the analytical solution of Eq. (12) and significantly differ from the solutions based on the other theories of

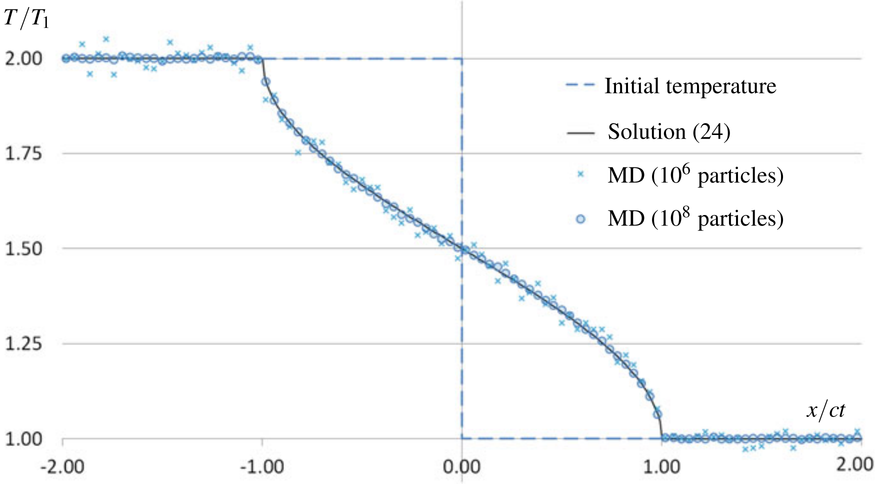

**Fig. 2** Heat transfer between hot (left) and cold (right) areas of 1D harmonic crystal. The analytical solution (24) is compared with the computer simulation (MD): $10^3$ chains containing $10^3$ particles each (cross is an average over 10 particles); $10^4$ chains containing $10^4$ particles (circle is an average over 100 particles)

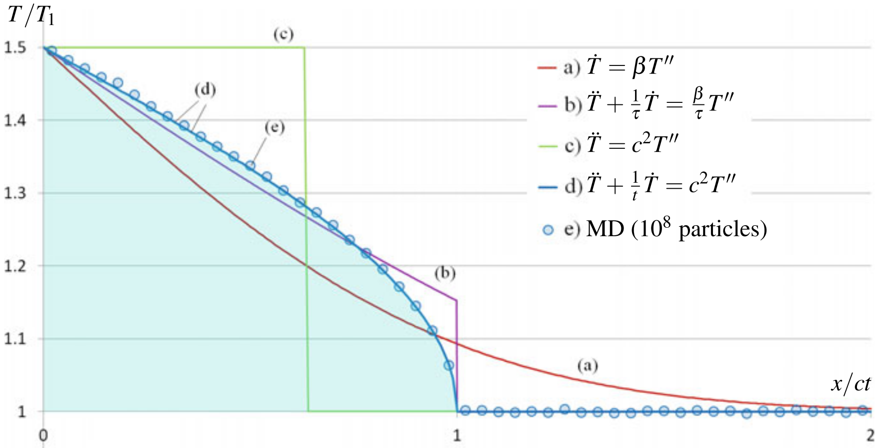

**Fig. 3** Heat propagation for different 1D models: **a** Fourier heat equation, **b** hyperbolic heat equation, **c** wave equation, **d** ballistic heat equation, **e** computer simulation for 1D harmonic crystal ($10^4$ chains containing $10^4$ particles each)

thermal conduction. Indeed, the Fourier heat equation predicts no heat front, the hyperbolic heat equation gives a stepwise front, while the real heat front is described by a smooth curve having a vertical tangent at $x = ct$. Note that the hyperbolic heat equation behaves as the wave equation at small times and as the Fourier heat equation at large times [52]. However, according to the analytical solution (24) and the presented computer simulations, the heat transfer in a one-dimensional harmonic crystal is self-similar, i.e. $T = T(\frac{x}{ct})$, so it demonstrates same behavior for any times.

## 9 Conclusions and Further Research

An approach for description of the ballistic heat transfer in one-dimensional harmonic crystals is described. A notion of nonlocal temperature (a generalization of the kinetic temperature for two separate particles) is used for obtaining a closed system of equations for the thermal transfer description. For the case of an instantaneous heat perturbation this yields to a partial differential equation (12) for the kinetic temperature, which can be referred to as the ballistic heat equation. The resulting macroscopic constitutive law (18) (an alternative of Fourier's law for the considered system) predicts a finite velocity of the heat front and independence of the heat flux on the crystal length. The analytical findings are in excellent agreement with the molecular dynamics simulations and previous analytical estimations.

Further analysis of the ballistic heat equation (12) can be found in [53]. Application of the presented approach for more complex one-dimensional systems is given in [40], where a substrate potential is added, and in [35], where an external heat supply and a viscous environment are considered. Extension of this approach to systems of higher dimensions is presented in [42] for monoatomic and in [43] for polyatomic lattices. The presented approach in frames of the general approach for transition from discrete to continuum thermomechanics is outlined in [54]. The results of the referred investigations are relevant to aspects of nanotechnology that involve heat transfer processes in high purity nanostructures [13, 14, 55, 56].

**Acknowledgements** The author is grateful to O. V. Gendelman, W. G. Hoover, D. A. Indeitsev, M. L. Kachanov, V. A. Kuzkin, S. A. Lurie, N. F. Morozov, and V. F. Zhuravlev for helpful and stimulating discussions; to M. B. Babenkov and D. V. Tsvetkov for additional analysis and computations. This work is supported by the Russian Science Foundation (Grant No. 18-11-00201).

## References

1. Thermal transport in low dimensions: from statistical physics to nanoscale heat transfer. In: Lepri S. (ed.) Lecture Notes in Physics, vol. 921, 418 p. Springer, Switzerland (2016)
2. Hoover, W.G., Hoover, C.G.: Simulation and control of chaotic nonequilibrium systems. In: Advanced Series in Nonlinear Dynamics, vol. 27, 324 p. World Scientific (2015)
3. Charlotte, M., Truskinovsky, L.: Lattice dynamics from a continuum viewpoint. J. Mech. Phys. Solids **60**, 1508–1544 (2012)
4. Bonetto, F., Lebowitz, J.L., Rey-Bellet, L.: Fourier's law: a challenge to theorists. In: Fokas, A., et al. (eds.) Mathematical Physics 2000, pp. 128–150. Imperial College Press, London (2000)
5. Lepri, S., Livi, R., Politi, A.: Thermal conduction in classical low-dimensional lattices. Phys. Rep. **377**, 1–80 (2003)

6. Dhar, A.: Heat transport in low-dimensional systems. Adv. Phys. **57**, 457–537 (2008)
7. Aoki, K., Kusnezov, D.: Bulk properties of anharmonic chains in strong thermal gradients: non-equilibrium $\phi^4$ theory. Phys. Lett. A **265**, 250–256 (2000)
8. Gendelman, O.V., Savin, A.V.: Normal heat conductivity of the one-dimensional lattice with periodic potential. Phys. Rev. Lett. **84**, 2381–2384 (2000)
9. Giardina, C., Livi, R., Politi, A., Vassalli, M.: Finite thermal conductivity in 1D lattices. Phys. Rev. Lett. **84**, 2144–2147 (2000)
10. Gendelman, O.V., Savin, A.V.: Normal heat conductivity in chains capable of dissociation. Europhys. Lett. **106**, 34004 (2014)
11. Bonetto, F., Lebowitz, J.L., Lukkarinen, J.: Fourier's law for a harmonic crystal with self-consistent stochastic reservoirs. J. Stat. Phys. **116**, 783–813 (2004)
12. Le-Zakharov, A.A., Krivtsov, A.M.: Molecular dynamics investigation of heat conduction in crystals with defects. Dokl. Phys. **53**, 261–264 (2008)
13. Chang, C.W., Okawa, D., Garcia, H., Majumdar, A., Zettl, A.: Breakdown of fourier's law in nanotube thermal conductors. Phys. Rev. Lett. **101**, 075903 (2008)
14. Xu, X., Pereira, L.F., Wang, Y., Wu, J., Zhang, K., Zhao, X., Bae, S., Bui, C.T., Xie, R., Thong, J.T., Hong, B.H., Loh, K.P., Donadio, D., Li, B., Ozyilmaz, B.: Length-dependent thermal conductivity in suspended single-layer graphene. Nat. Commun. **5**, 3689 (2014)
15. Hsiao, T.K., Huang, B.W., Chang, H.K., Liou, S.C., Chu, M.W., Lee, S.C., Chang, C.W.: Micron-scale ballistic thermal conduction and suppressed thermal conductivity in heterogeneously interfaced nanowires. Phys. Rev. B **91**, 035406 (2015)
16. Kannan, V., Dhar, A., Lebowitz, J.L.: Nonequilibrium stationary state of a harmonic crystal with alternating masses. Phys. Rev. E **85**, 041118 (2012)
17. Dhar, A., Dandekar, R.: Heat transport and current fluctuations in harmonic crystals. Physica A **418**, 49–64 (2015)
18. Rieder, Z., Lebowitz, J.L., Lieb, E.: Properties of a harmonic crystal in a stationary nonequilibrium state. J. Math. Phys. **8**, 1073–1078 (1967)
19. Rubin, R.J.: Momentum autocorrelation functions and energy transport in harmonic crystals containing isotopic defects. Phys. Rev. **131**, 964–989 (1963)
20. Gendelman, O.V., Shvartsman, R., Madar, B., Savin, A.V.: Nonstationary heat conduction in one-dimensional models with substrate potential. Phys. Rev. E **85**, 011105 (2012)
21. Gusev, A.A., Lurie, S.A.: Wave-relaxation duality of heat propagation in Fermi-Pasta-Ulam chains. Mod. Phys. Lett. B **26**, 1250145 (2012)
22. Guzev, M.A.: The Fourier law for a one-dimensional crystal. Far East. Math. J. (1), 34–39 (2018)
23. Krivtsov, A.M.: Heat transfer in infinite harmonic one-dimensional crystals. Dokl. Phys. **60**, 407–411 (2015)
24. Chandrasekharaiah, D.S.: Hyperbolic thermoelasticity: a review of recent literature. Appl. Mech. Rev **39**, 355–376 (1986)
25. Tzou, D.Y.: Macro- to Microscale Heat Transfer: The Lagging Behavior, 566 p. Wiley (2015)
26. Poletkin, K.V., Gurzadyan, G.G., Shang, J., Kulish, V.: Ultrafast heat transfer on nanoscale in thin gold films. Appl. Phys. B **107**, 137–143 (2012)
27. Indeitsev, D.A., Osipova, E.V.: A two-temperature model of optical excitation of acoustic waves in conductors. Dokl. Phys. **62**(3), 136–140 (2017)
28. Lepri, S., Mejia-Monasterio, C., Politi, A.: A stochastic model of anomalous heat transport: analytical solution of the steady state. J. Phys. A Math. Theor. **42**, 025001, 15 p. (2009)
29. Lepri, S., Mejia-Monasterio, C., Politi, A.: Nonequilibrium dynamics of a stochastic model of anomalous heat transport. J. Phys. A: Math. Theor. **43**, 065002, 22 p. (2010)
30. Delfini, L., Lepri, S., Livi, R., Mejia-Monasterio, C., Politi, A.: Nonequilibrium dynamics of a stochastic model of anomalous heat transport: numerical analysis. J. Phys. A Math. Theor. **43**, 145001, 16 p. (2009)
31. Krivtsov, A.M.: Dynamics of energy characteristics in one-dimensional crystal. In: Procedings of XXXIV Summer School "Advanced Problems in Mechanics", St.-Petersburg, Russia, 2007, pp. 261–273. ISBN 5-98883-009-9

32. Krivtsov, A.M.: Energy oscillations in a one-dimensional crystal. Dokl. Phys. **59**, 427–430 (2014)
33. Krivtsov, A.M.: On unsteady heat conduction in a harmonic crystal (2015). ArXiv:1509.02506
34. Born, M., Huang, K.: Dynamical Theory of Crystal Lattices, 432 p. Clarendon Press, Oxford (1954)
35. Gavrilov, S.N., Krivtsov, A.M., Tsvetkov, D.V.: Heat transfer in a one-dimensional harmonic crystal in a viscous environment subjected to an external heat supply. In: Continuum Mechanics and Thermodynamics (2018)
36. Manvi, R., Duvall, G.E., Lowell, S.C.: Finite amplitude longitudinal waves in lattices. Int. J. Mech. Sci. **11**, 1 (1969)
37. Holian, B.L., Straub, G.K.: Molecular dynamics of shock waves in one-dimensional chains. Phys. Rev. B **18**, 1593 (1978)
38. Abramowitz, M., Stegun, I.A.: Handbook of Mathematical Functions with Formulas, Graphs, and Mathematical Tables, 1046 p. U. S. Government Printing Office (1972)
39. Polyanin, A.D., Nazaikinskii, V.E.: Handbook of Linear Partial Differential Equations for Engineers and Scientists, 2nd edn, 1632 p. CRC Press, Boca Raton-London (2016)
40. Babenkov, M.B., Krivtsov, A.M., Tsvetkov, D.V.: Unsteady heat conduction processes in a harmonic crystal with a substrate potential. In: Proceedings of XXIV ICTAM, 21–26 August 2016, Montreal, Canada, 2440–2441 (2016)
41. Shoby, K., Yoshida, T., Mori, H.: Dynamic properties of one-dimensional harmonic liquids. II, Prog. Theoret. Phys. **66**, 1160–1168 (1981)
42. Kuzkin, V.A., Krivtsov, A.M.: Fast and slow thermal processes in harmonic scalar lattices. J. Phys. Condens. Matter **29**, 505401, 14 p. (2017)
43. Kuzkin, V.A.: Fast and slow thermal processes in harmonic crystals with polyatomic lattice. Arxiv preprint(2018). ArXiv:1808.00504
44. Hoover, W.G.: Molecular dynamics. In: Lecture Notes in Physics, vol. 258, 324 p. Springer-Verlag (1986)
45. Holian, B.L., Hoover, W.G., Posch, H.A.: Resolution of Loschmidt's paradox: the origin of irreversible behavior in reversible atomistic dynamics. Phys. Rev. Lett. **59**, 10–13 (1987)
46. Gendelman, O.V., Savin, A.V.: Nonstationary heat conduction in one-dimensional chains with conserved momentum. Phys. Rev. E **81**, 020103 (2010)
47. Dhar, A.: Heat conduction in the disordered harmonic chain revisited. Phys. Rev. Lett. **86**, 5882–5885 (2001)
48. Hoover, W.G., Hoover, C.G.: Hamiltonian thermostats fail to promote heat flow. Commun. Nonlinear Sci. Numer. Simulat. **18**, 3365–3372 (2013)
49. Kachman, T.: Master-degree thesis under supervision of O. V. Gendelman, 187 p., Technion, Izrael (2011)
50. Tzou, D.Y.: The generalized lagging responce in small scale and high rate heating. Int. J. Mass Transf. **38**, 3231–3240 (1995)
51. Rubin, R.J., Greer, W.L.: Abnormal lattice thermal conductivity of a one-dimensional, harmonic, isotopically disordered crystal. J. Math. Phys. **12**, 1686–1701 (1971)
52. Babenkov, M.B., Ivanova, E.A.: Analysis of the wave propagation processes in heat transfer problems of the hyperbolic type. Contin. Mech. Thermodyn. **26**, 483–502 (2014)
53. Sokolov, A.A., Krivtsov, A.M., Müller, W.H.: Localized heat perturbation in harmonic 1D crystals: solutions for an equation of anomalous heat conduction. Phys. Mesomech. **20**(3), 305–310 (2017)
54. Krivtsov, A.M., Kuzkin, V.A.: Discrete and continuum thermomechanics. In: Encyclopedia of Continuum Mechanics, 16 p (2018)
55. Goldstein, R.V., Morozov, N.F.: Mechanics of deformation and fracture of nanomaterials and nanotechnology. Phys. Mesomech. **10**, 235–246 (2007)
56. Shtukin, L.V., Berinskii, I.E., Indeitsev, D.A., Morozov, N.F., Skubov, D.Y.: Electromechanical models of nanoresonators. Phys. Mesomech. **19**(3), 248–254 (2016)

# Subsurface Stressed State of Functionally Graded Elastic Solids Involved in Dry Axially Symmetric Contacts

**I. I. Kudish, A. S. Vasiliev, S. S. Volkov and S. M. Aizikovich**

**Abstract** In general, the goal of most studies of contact problems of elasticity is to determine the contact stress distributions such as pressure and frictional stress. In many cases this information is sufficient to directly or indirectly evaluate the situations with elevated failure risk. However, there are numerous distinct failure processes which get originated below the contact surface. Among these processes are coating delamination and subsurface originated pitting. To be able to consider such processes one has to know the subsurface stressed state of a solid. Therefore, the motivation of this study is to make a first step in addressing the subsurface stress behavior for functionally graded elastic solids. In this work we consider the behavior of the subsurface stresses in a coated elastic solid which is indented by an axially symmetric punch. The contact is assumed to be frictionless. The goal of the paper is to get detailed information on stress behavior at and near the coating/substrate interface. Usually, this is the region where different failure processes get originated. The expressions for subsurface stresses were derived in terms of certain integrals of pressure. The latter were determined using a semi-analytical and asymptotic methods. The distributions of subsurface stresses were determined numerically and analyzed for various functional dependences of the coating and substrate elastic parameters as well as other problem input parameters. Certain peculiar subsurface stress behavior near coating/substrate interface and contact boundary were observed.

---

I. I. Kudish (✉)
Department of Mathematics, Kettering University, Flint, MI, USA
e-mail: ikudish@kettering.edu

A. S. Vasiliev · S. S. Volkov · S. M. Aizikovich
Research and Education Center “Materials”, Don State Technical University,
Rostov-on-Don, Russia

H. Altenbach et al. (eds.), *Dynamical Processes in Generalized Continua and Structures*, Advanced Structured Materials 103,
https://doi.org/10.1007/978-3-030-11665-1_20

## 1 Introduction

The detailed knowledge of the subsurface stress behavior is critical for understanding fracture and fatigue material properties. The principal stresses and displacements vary within a coating depending on whether the coating elastic parameters are constant or vary with depth (functionally graded materials). Depending on the functional dependence of the Young's modulus it is possible to reduce or increase the concentration of the principal stresses near the coating surface and the interface of the coating and the substrate. Therefore, using the appropriate/optimal selection of elastic properties of the coating substrate it is possible to affect a contact tribological properties and to increase its fatigue life without coating delamination.

Over the years, the behavior of the stresses for functionally graded (FG) elastic coatings was studied in [1–15]. Giannakopoulos and Suresh [1, 2] considered indentation of a FG elastic half-space which was assumed to have a fixed Poisson's ratio and whose Young's modulus vary with depth according to power law or exponential law. Guler and Erdogan [3, 4] considered contact problems for elastic half-plane with FG coating with exponential variation of elastic properties. Problems were reduced to the solution of singular integral equations which were solved numerically using collocation technique. Wang, Ke, Liu and Zhang in [5, 6] applied the linear multilayered model to solve 2-D plane and axisymmetric contact problems for elastic media with FG coating with arbitrary variation of elastic moduli in depth. They use similar collocation technique to solve singular integral equations. This approach was also used to solve contact problems in extended formulation involving friction [7, 8], frictional heating [9, 10], piezoelectric effect [11, 12], etc. Results presented in the current paper based on the asymptotically exact solutions of the dual integral equations of the indentation contact problem [16, 17]. The bilateral asymptotic method [18] is used for that purpose.

Motivation of this research is also related to the study of heavily loaded elastohydrodynamically lubricated contacts made by the authors in previous papers [19–23]. It was shown that FG coatings may significantly alter lubrication film thickness, contact pressure and friction stress distributions. In particular, it was shown that for coatings softer than the substrate the lubrication film thickness and frictional force is higher while for coatings harder than the substrate the lubrication film thickness and frictional force is lower compared to the case of no coating. One of the questions left not addressed is how the elastic properties of coatings and substrates affect subsurface stress distribution. This paper will provide some answer to this question. To simplify the analysis only subsurface stresses for dry contacts will be considered. But it should be noted that the subsurface stresses for lubricated contacts are generally close to the ones for dry contacts. The differences occurring near the inlet and exit zones of heavily loaded lubricated contacts are insignificant for the general understanding of the behavior of subsurface stresses.

## 2 Axisymmetric Problem Formulation

Let us consider an indentation of a rigid spherical punch of radius $R$ into a functionally graded coating of an elastic half-space. The coordinate system $(\rho, \varphi, z)$ is introduced in such a way that the origin is located at the point of the initial contact of the punch with the half-space while the $z$-axis is directed up through the spherical punch center. The polar plane $(\rho, \varphi)$ coincides with the plane $z = 0$. The punch is subjected to a vertical force $P$ along the $z$-axis through its center which causes the punch vertical displacement $\delta_0$.

The shape of the spherical punch is approximated by an axisymmetric paraboloid. The displacement of the punch is described by the relationship

$$w = -\delta_0 + \frac{\rho^2}{2R}, \quad 0 \le \rho \le a. \tag{1}$$

Let the functionally graded coating thickness be $H$ and its elastic parameters depend on the material depth $z$ as follows

$$\{E, \nu\} = \begin{cases} \{E^{(c)}(z),\ \nu^{(c)}(z)\},\ -H \le z \le 0; \\ \{E^{(s)}, \nu^{(s)}\} = \text{const},\ -\infty < z < -H, \end{cases} \tag{2}$$

where $E^{(c)}(z)$ and $\nu^{(c)}(z)$ are arbitrary continuously differentiable or piecewise constant functions. Here and further index $^{(c)}$ corresponds to the parameters associated with the coating while index $^{(s)}$ corresponds to the parameters associated with the substrate. At the interface we have the following conditions of continuity:

$$\{\tau_{\rho z}, \sigma_z, w, u\}\big|_{z=-H-0} = \{\tau_{\rho z}, \sigma_z, w, u\}\big|_{z=-H+0}\,.$$

We will consider the half-space surface outside of the contact region free of stresses. Also, we will assume that there is no friction between the punch and the half-space surface. Then the boundary conditions have the form

$$z = 0:\ \tau_{\rho z} = 0,\ \sigma_z|_{\rho > a} = 0. \tag{3}$$

The solution of this problem is the normal stress $\sigma_z$ at the half-space boundary $z = 0$, i.e.

$$\sigma_z\,|_{z=0} = -p_0(\rho), \quad \rho \le a,$$

where $p_0(\rho)$ is the contact pressure while $a$ is the contact radius.

The linear constitutive equations are:

$$\begin{aligned}
&\sigma_\rho = 2M(z)\frac{\partial u}{\partial \rho} + \Lambda(z)\theta,\ \sigma_\phi = 2M(z)\frac{u}{\rho} + \Lambda(z)\theta,\\
&\sigma_z = 2M(z)\frac{\partial w}{\partial z} + \Lambda(z)\theta,\ \tau_{\rho z} = M(z)\left(\frac{\partial u}{\partial z} + \frac{\partial w}{\partial \rho}\right),\\
&\theta = \frac{\partial u}{\partial \rho} + \frac{u}{\rho} + \frac{\partial w}{\partial z}.
\end{aligned} \tag{4}$$

where $\Lambda = \frac{E\nu}{(1+\nu)(1-2\nu)}$ and $M = \frac{E}{2(1+\nu)}$ are the Lamé elastic parameters.

## 3 Derivation of the Integral Equation

To reduce the formulated problem to an integral equation we will use the Hankel transform

$$\begin{aligned}
w(\rho, z) &= \int_0^\infty W(\gamma, z)J_0(\gamma\rho)\gamma d\gamma,\\
u(\rho, z) &= -\int_0^\infty U(\gamma, z)J_1(\gamma\rho)\gamma d\gamma,\\
p_0(\rho) &= \int_0^\infty P_0(\gamma)J_0(\gamma\rho)\gamma d\gamma.
\end{aligned} \tag{5}$$

Substituting Eq. 5 into Eq. 1 we obtain

$$\int_0^\infty W(\gamma, 0)\gamma J_0(\gamma\rho)d\gamma = -\delta_0 + \rho^2/(2R), \quad \rho \le a \tag{6}$$

Let us introduce the following definitions

$$\left\{W^*, U^*\right\}(\gamma, z) = -\frac{E'(0)}{2}\frac{\{W, U\}(\gamma, z)}{P_0(\gamma)}\gamma, \tag{7}$$

where $E'(0) = E^{(c)}(0)/[1 - \nu^{(c)2}(0)]$ is the effective elastic modulus of the coating material at it upper surface. Taking into account Eq. 7, Eq. 6 can be rewritten in the form

$$\int_0^\infty W^*(\gamma, 0)P_0(\gamma)J_0(\gamma\rho)d\gamma = \frac{E'(0)}{2}\left(\delta_0 - \frac{\rho^2}{2R}\right), \quad \rho \le a, \tag{8}$$

which, in turn, by using the third relationship in Eq. 5 can be rewritten as follows

$$\frac{\rho^2}{2R} + \frac{2}{E'(0)}\int_0^a k(\rho, \xi)p_0(\xi)\xi d\xi = \delta_0, \quad \rho \le a, \tag{9}$$

where $k(\rho, \xi)$ is the kernel of the integral equation determined by the formula

$$k(\rho,\xi)=\int_0^\infty W^*(\gamma,\ 0)J_0(\gamma\rho)J_0(\gamma\xi)d\gamma. \tag{10}$$

In this case for the force $P$ acting on the punch we have

$$P=2\pi\int_0^a p_0(\xi)\xi d\xi \tag{11}$$

Let us introduce the following dimensionless parameters and variables associated with the Hertzian contact of our rigid punch of radius $R$ with an elastic half-space made of the material with the effective elastic modulus $E'(0)$ of the coating surface material. We have

$$\{\rho_c,\xi_c,a_c,\lambda_c\}=\frac{1}{a_{Hc}}\{\rho,\xi,a,H\},\quad p_{0c}=\frac{p_0}{p_{Hc}},\quad \delta_c=\frac{\delta_0}{\delta_{Hc}}, \tag{12}$$

where

$$a_{Hc}=\left[\frac{3PR}{4E'(0)}\right]^{1/3},\ p_{Hc}=\frac{3P}{2\pi a_{Hc}^2},\ \delta_{Hc}=\frac{a_{Hc}^2}{R}, \tag{13}$$

are the radius, maximum Hertzian pressure and punch displacement in such a contact. Then Eqs. 9–11 will take the form

$$\rho_c^2+\frac{8}{\pi}\int_0^{a_c} p_{0c}(a_{Hc}\xi_c)\xi_c k(a_{Hc}\rho_c,a_{Hc}\xi_c)d\xi_c=2\delta_c,\ \ \rho_c\ \le a_c \tag{14}$$

$$k(a_{Hc}\rho_c,a_{Hc}\xi_c)=a_{Hc}\int_0^\infty W^*(\gamma,0)J_0(a_{Hc}\gamma\xi_c)J_0(a_{Hc}\gamma\rho_c)d\gamma \tag{15}$$

$$\int_0^{a_c} p_{0c}(\rho_c)\rho_c d\rho_c=\frac{1}{3} \tag{16}$$

To determine the radius of the contact region it is necessary to use an additional condition following from the continuity of the contact stress at the contact boundary

$$p_{0c}(a_c)=0. \tag{17}$$

## 4 Solution of the Integral Equation

To solve the formulated problem we will employ the bilateral asymptotic method [18, 24]. Let us introduce the following definitions

$$L(\gamma)=W^*(\gamma/H,0),\ \ P_{0c}(\gamma)=\int_0^1 p_{0c}(a_c\zeta)J_0(\gamma\zeta)\zeta d\zeta \tag{18}$$

Function $L(\gamma)$ is determined numerically by solving the initial-value problem for a system of ordinary differential equations with variable coefficients [17]. In case of piecewise constant elastic parameters of the coating the calculation of function $L(\gamma)$ is reduced to solution of a system of linear algebraic equations. Function $L(\gamma)$ possesses the following properties:

$$L(\gamma) = \beta^{-1} + B\gamma + \mathrm{O}(\gamma^2), \gamma \to 0; \quad L(\gamma) = 1 + C\gamma^{-1} + \mathrm{O}(\gamma^{-2}), \gamma \to \infty \tag{19}$$

where $\beta = E'^{(s)}/E'(0)$ and $E'^{(s)} = E^{(s)}/(1 - \nu^{(s)2})$ is the effective elastic modulus of the substrate.

Using definitions Eq. 18 integral equation Eq. 15 can be rewritten as an equivalent dual integral equation

$$\begin{aligned} &\int_0^\infty P_{0c}(\gamma) L\left(\frac{\lambda_c \gamma}{a_c}\right) J_0\left(\frac{\rho_c \gamma}{a_c}\right) d\gamma = \frac{\pi}{8a_c}\left(2\delta_c - \rho_c^2\right), \quad \rho_c \le a_c, \\ &\int_0^\infty P_{0c}(\gamma) J_0\left(\frac{\rho_c \gamma}{a_c}\right) \gamma d\gamma = 0, \quad \rho_c > a_c, \end{aligned} \tag{20}$$

To determine the bilateral asymptotically precise solution we will approximate function $L(\gamma)$ by the following fraction of products of quadratic functions [18]

$$L(\gamma) \approx L_N(\gamma) = \prod_{i=1}^{N} (\gamma^2 + A_i{}^2)/(\gamma^2 + B_i{}^2), \tag{21}$$

where $N$ is a positive integer. The methodology of the calculation of the coefficients $A_i$, $B_i$ is described in [25]. It is worth mentioning that the approximation is constructed in such a way that $L(0) = L_N(0)$. The solution of Eq. 20 has been obtained in [22] for the case of a contact of two elastic solids

$$\begin{aligned} P_{0c}(\gamma) = \beta \Bigg[ &\left(\frac{\delta_c}{2a_c} - \frac{a_c}{2} - \frac{\lambda_c^2}{a_c} E_0\right) \frac{\sin\gamma}{\gamma} - a_c \frac{\gamma\cos\gamma - \sin\gamma}{\gamma^3} + \\ &+ \sum_{i=1}^{N} C_i \frac{\lambda_c \gamma \sin\gamma + a_c A_i \tanh(A_i \lambda_c^{-1} a_c) \cos\gamma}{A_i\left(\gamma^2 + A_i{}^2 \lambda_c^{-2} a_c^2\right)} \Bigg], \quad E_0 = \sum_{i=1}^{N} (A_i^{-2} - B_i^{-2}), \end{aligned} \tag{22}$$

where constants $C_i$ are determined from the solution of the following system of linear algebraic equations

$$\begin{aligned} &\sum_{i=1}^{N} C_i \left[\frac{B_k + A_i \tanh(A_i \lambda_c^{-1} a_c)}{A_i (B_k{}^2 - A_i{}^2)} - \frac{\lambda_c \tanh(A_i \lambda_c^{-1} a_c)}{a_c B_k A_i{}^2}\right] = \\ &\qquad = \frac{1}{B_k \lambda_c}\left[\frac{a_c}{3} - \frac{1}{3\beta a_c^2} + \frac{(B_k a_c + \lambda_c)\lambda_c}{a_c B_k^2}\right] \end{aligned} \tag{23}$$

By inverting function $P_{0c}(\gamma)$ using the Hankel transform we obtain the contact pressure

$$p_{0c}(\rho_c) = \beta\left[\sqrt{a_c^2-\rho_c^2} + \frac{\delta_c - a_c^2 - 2\lambda_c^2 E_0}{2\sqrt{a_c^2-\rho_c^2}} + \right.$$
$$\left. + a_c \sum_{i=1}^{N} C_i \left(\frac{\lambda_c}{A_i\sqrt{a_c^2-\rho_c^2}} - Z\left(\frac{A_i a_c}{\lambda_c}, \frac{\rho_c}{a_c}\right)\right)\right] \tag{24}$$

$$Z\,(A,\rho) = \frac{1}{\cosh(A)}\int_{\rho}^{1}\frac{\sinh(At)dt}{\sqrt{t^2-\rho^2}} \tag{25}$$

To determine the displacement $\delta_c$ we substitute Eq. 24 for $p_{0c}(\rho_c)$ into Eq. 16 and taking into account the substitution Eq. 18 we obtain

$$\delta_c = \frac{a_c^2}{3} + 2\lambda_c^2 E_0 + \frac{2}{3\beta a_c} - 2\lambda_c^2 \sum_{i=1}^{N}\frac{C_i}{A_i^2}\tanh\left(\frac{A_i a_c}{\lambda_c}\right). \tag{26}$$

Equations 22–26 describe the solution of the problem with fixed contact boundary. The contact pressure in this problem has a singularity at $\rho_c = a_c$. Substituting Eq. 24 into Eq. 17 we obtain the equation which determines the radius $a_{0c}$ of the contact region for the problem with a free boundary

$$a_{0c} + 3\lambda_c \sum_{i=1}^{N}\frac{C_i}{A_i}\left[\frac{\lambda_c}{A_i a_{0c}}\tanh\left(\frac{A_i a_{0c}}{\lambda_c}\right) - 1\right] - \frac{1}{\beta a_{0c}^2} = 0 \tag{27}$$

Using Eqs. 27, 22–24 and 26 will take the form

$$P_{0c}(\gamma) = \beta a_{0c} P^*(\gamma),\; P^*(\gamma) = \frac{\sin\gamma - \gamma\cos\gamma}{\gamma^3} +$$
$$+ \sum_{i=1}^{N} C_i \left(\frac{\tanh(A_i\lambda_c^{-1}a_{0c})\cos\ \gamma - A_i\lambda_c^{-1}a_{0c}\gamma^{-1}\sin\gamma}{\gamma^2 + A_i{}^2\lambda_c^{-2}a_{0c}^2}\right) \tag{28}$$

$$\sum_{i=1}^{N} C_i \left(\frac{B_k\tanh(A_i\lambda_c^{-1}a_{0c}) + A_i}{B_k{}^2 - A_i{}^2}\right) = \frac{B_k a_{0c} + \lambda_c}{a_{0c}B_k^2}, \quad k = 1, 2, \ldots, N. \tag{29}$$

$$p_{0c}(\rho_c) = \beta\left[\sqrt{a_{0c}^2-\rho_c^2} - a_{0c}\sum_{i=1}^{N} C_i Z\left(\frac{A_i a_{0c}}{\lambda_c}, \frac{\rho_c}{a_{0c}}\right)\right] \tag{30}$$

$$\delta_c = a_{0c}^2 + 2\lambda_c^2 E_0 - 2\lambda_c a_{0c} \sum_{i=1}^{N} \frac{C_i}{A_i} \tag{31}$$

The obtained formulas are asymptotically precise for $\lambda_c \to 0$ and $\lambda_c \to \infty$ [18]. For intermediate values of $\lambda_c$ the precision of the obtained results obviously depends on the precision of the approximation of function $L(\gamma)$ involved in the transform of the kernel from Eq. 21. It is established in [25] that the errors of approximation in contact pressure $p_{0c}(\rho_c)$ and function $L(\gamma)$ are of the same order of magnitude. In the numerical results presented in this paper the approximation error $\Delta = \sup\limits_{u \geq 0} |L_N(u)/L(u) - 1| \cdot 100\%$ is below 0.2%. That allows to be confident in high precision of the obtained approximate formulas for contact pressure $p_{0c}(\rho_c)$.

## 5 Stressed State of the Coated Half-Space

Using Eqs. 7, 12 and 18 we can rewrite Eq. 5 in the form

$$\{u, w\}(\rho_c, z) = \frac{2p_{Hc}a_c a_{Hc}}{E'(0)} \int_0^\infty \{U^*, -W^*\}\left(\frac{\gamma}{a_c a_{Hc}}, z\right) P_{0c}(\gamma)\{J_1, J_0\}\left(\frac{\gamma \rho_c}{a_{0c}}\right) d\gamma \tag{32}$$

Let us introduce the following dimensionless variables

$$\{\sigma_\rho^c, \sigma_z^c, \sigma_\varphi^c, \tau_{\rho z}^c\} = \frac{\{\sigma_\rho, \sigma_z, \sigma_\varphi, \tau_{\rho z}\}}{p_{Hc}}, \ \{w^c, u^c\} = \frac{\{w, u\}}{\delta_{Hc}}, \ z_0 = \frac{z}{H}. \tag{33}$$

The scaling introduced in Eqs. 12 and 33 is based on the properties of the coating. However, for practical use it is more convenient to use a scaling based on the substrate material properties. It is easy to establish a connection between the same values but scaled differently. Specifically, we have

$$\begin{gathered} \{\sigma_i^s, \tau_{\rho z}^s, p_{0s}\} = \{\sigma_i^c, \tau_{\rho z}^c, p_{0c}\}\,\beta^{-\frac{2}{3}}, \ \{u^s, w^s\} = \{u^c, w^c\}\,\beta^{\frac{2}{3}}, \\ \{a_s, a_{0s}, \lambda_s, \rho_s\} = \{a_c, a_{0c}, \lambda_c, \rho_c\}\,\beta^{\frac{1}{3}} \end{gathered} \tag{34}$$

Using Eqs. 7, 12, 13, 18, 33 and 34 we can rewrite Eqs. 4 and 32 as follows:

$$u^s(\rho_s, z_0) = \frac{4\beta a_{0s}^2}{\pi} I_1(\rho_s, z_0), \quad w^s(\rho_s, z_0) = -\frac{4\beta a_{0s}^2}{\pi} I_3(\rho_s, z_0), \tag{35}$$

$$\begin{gathered} \sigma_\rho^s = 2\beta a_{0s}\left((2M_{0s} + \Lambda_{0s}) I_6 - 2a_{0s} M_{0s} \frac{I_1}{\rho_s} - \frac{a_{0s}}{\lambda_s} \Lambda_{0s} I_4\right), \\ \tau_{\rho z}^s = 2\beta a_{0s} M_{0s}\left(\frac{a_{0s}}{\lambda_s} I_2 + I_5\right), \end{gathered} \tag{36}$$

$$\begin{aligned}\sigma_\varphi^s &= 2\beta a_{0s}\left(2a_{0s}M_{0s}\frac{I_1}{\rho_s} + \Lambda_{0s}\left(I_6 - \frac{a_{0s}}{\lambda_s}I_4\right)\right),\\ \sigma_z^s &= 2\beta a_{0s}\left(\Lambda_{0s}I_6 - (2M_{0s} + \Lambda_{0s})\frac{a_{0s}}{\lambda_s}I_4\right),\end{aligned} \tag{37}$$

where

$$\begin{aligned}I_1(\rho_s, z_0) &= \int_0^\infty U_0\left(\frac{\gamma\lambda_s}{a_{0s}}, z_0\right)P^*(\gamma)J_1\left(\frac{\gamma\rho_s}{a_{0s}}\right)d\gamma,\\ I_2(\rho_s, z_0) &= \int_0^\infty \frac{\partial U_0}{\partial z_0}\left(\frac{\gamma\lambda_s}{a_{0s}}, z_0\right)P^*(\gamma)J_1\left(\frac{\gamma\rho_s}{a_{0s}}\right)d\gamma,\\ I_3(\rho_s, z_0) &= \int_0^\infty W_0\left(\frac{\gamma\lambda_s}{a_{0s}}, z_0\right)P^*(\gamma)J_0\left(\frac{\gamma\rho_s}{a_{0s}}\right)d\gamma,\\ I_4(\rho_s, z_0) &= \int_0^\infty \frac{\partial W_0}{\partial z_0}\left(\frac{\gamma\lambda_s}{a_{0s}}, z_0\right)P^*(\gamma)J_0\left(\frac{\gamma\rho_s}{a_{0s}}\right)d\gamma,\\ I_5(\rho_s, z_0) &= \int_0^\infty W_0\left(\frac{\gamma\lambda_s}{a_{0s}}, z_0\right)P^*(\gamma)J_1\left(\frac{\gamma\rho_s}{a_{0s}}\right)\gamma d\gamma,\\ I_6(\rho_s, z_0) &= \int_0^\infty U_0\left(\frac{\gamma\lambda_s}{a_{0s}}, z_0\right)P^*(\gamma)J_0\left(\frac{\gamma\rho_s}{a_{0s}}\right)\gamma d\gamma\end{aligned} \tag{38}$$

and

$$\begin{aligned}\{U_0, W_0\}\left(\frac{\gamma\lambda_s}{a_{0s}}, z_0\right) &= \{U^*, W^*\}\left(\frac{\gamma\lambda_s}{a_{0s}H}, z_0H\right),\\ \{M_{0s}(z_0), \Lambda_{0s}(z_0)\} &= \frac{\{M(z_0H), \Lambda(z_0H)\}}{E'^{(s)}}\end{aligned} \tag{39}$$

Functions $U_0$, $W_0$ are the solution of the following initial-value problem for a system of ordinary differential equations:

$$\begin{cases}\gamma(M_{0s} + \Lambda_{0s})W_0' + \gamma M_{0s}'W_0 + M_{0s}U_0'' + M_{0s}'U_0' -\\ \qquad\qquad \gamma^2(2M_{0s} + \Lambda_{0s})U_0 = 0;\\ (2M_{0s} + \Lambda_{0s})W_0'' + (2M_{0s}' + \Lambda_{0s}')W_0' - \gamma^2 M_{0s}W_0 -\\ \qquad\qquad \gamma(M_{0s} + \Lambda_{0s})U_0' - \gamma\Lambda_{0s}'U_0 = 0;\end{cases} \tag{40}$$

$$\begin{aligned}&\left((2M_{0s} + \Lambda_{0s})W_0' - \gamma\Lambda_{0s}U_0\right)_{z_0=-1+0} = \left((2M_{0s} + \Lambda_{0s})W_0' - \gamma\Lambda_{0s}U_0\right)_{z_0=-1-0};\\ &\left(M_{0s}\left(U_0' + \gamma W_0\right)\right)\big|_{z_0=-1+0} = \left(M_{0s}\left(U_0' + \gamma W_0\right)\right)\big|_{z_0=-1-0};\\ &U_0(\gamma, z_0)|_{z_0=-1+0} = U_0(\gamma, z_0)|_{z_0=-1-0};\\ &W_0(\gamma, z_0)|_{z_0=-1+0} = W_0(\gamma, z_0)|_{z_0=-1-0};\\ &\left((2M_{0s} + \Lambda_{0s})W_0' - \gamma\Lambda_{0s}U_0\right)_{z_0=0} = \gamma\beta^{-1}/2;\\ &\left(M_{0s}\left(U_0' + \gamma W_0\right)\right)\big|_{z_0=0} = 0\end{aligned} \tag{41}$$

Problem defined by Eqs. 40 and 41 can be solved analytically only for specific cases of variation of elastic properties, for instance, piecewise-homogeneous, exponential or linear. In general, it is solved numerically.

**Table 1** Contact radius $a_{0s}$ as a function of the coating material Poisson's ratio $\nu^{(c)}$ for "soft" and "hard" coatings

| | $E^{(c)}/E^{(s)} = 0.01$ | | | $E^(c)/E^{(s)} = 100$ | |
|---|---|---|---|---|---|
| $\nu^{(c)}$ | 0.33 | 0.499 | −0.4 | 0.33 | 0.499 |
| $a_{0s}$ | 1.96 | 1.33 | 2.02 | 0.73 | 0.71 |

# 6 Numerical Results and Discussion

In the data presented below three cases of "soft" and two cases of "hard" coatings made of a homogeneous material ($E^{(c)}(z) = E^{(c)} = \text{const}$, $\nu^{(c)}(z) = \nu^{(c)} = \text{const}$) are considered. For the cases of "soft" coatings we used the following material elastic parameters $E^{(c)}/E^{(s)} = 0.01$ and the Poisson's ratio $\nu^{(c)} = 0.33$, 0.499 and −0.4. For the cases of "hard" coatings we used the following material elastic parameters $E^{(c)}/E^{(s)} = 100$ and the Poisson's ratio $\nu^{(c)} = 0.33$ and 0.499. In all cases the Poisson's ratio of the substrate material $\nu^{(s)} = 0.33$. The case of $\nu^{(c)} = 0.499$ corresponds to practically incompressible coating material while the case of $\nu^{(c)} = -0.4$ represents an auxetic material. In practice the coatings are usually thin. Therefore, we will consider the case of $\lambda_s = 0.1$. The values of the contact radius for these cases are collected in Table 1.

Let us consider the behavior of the subsurface displacement fields $w$ and $u$ as well as the principal stresses

$$\sigma_{I,III} = \frac{1}{2}\left[\left(\sigma_\rho + \sigma_z\right) \pm \sqrt{D}\right], \quad \sigma_{II} = \sigma_\varphi, \quad D = \left(\sigma_\rho - \sigma_z\right)^2 + 4\tau_{\rho z}^2 \tag{42}$$

and their principal planes orientations:

$$n_{I,III} = \left(\frac{2\tau_{\rho z}}{\sqrt{2D \pm 2(\sigma_\rho - \sigma_z)\sqrt{D}}}, 0, \frac{\sigma_z - \sigma_\rho + \sqrt{D}}{\sqrt{2D \pm 2(\sigma_\rho - \sigma_z)\sqrt{D}}}\right), \quad n_{II} = (0, \pm 1, 0). \tag{43}$$

Here a principal plane is a plane to which the corresponding principal stress is perpendicular. Here and after upper index $^s$ will be omitted in $u^s$, $w^s$, $\sigma_\rho^s$, $\sigma_z^s$, $\sigma_\varphi^s$, $\tau_{\rho z}^s$.

The data confirms an obvious fact that in the cases of "hard" coatings the principal stresses are higher than in the cases of "soft" coatings. In the cases considered below the stresses for the cases of "hard" coatings are over 20 times greater than the same stresses for the cases of "soft" coatings. Moreover, for all cases below the surface the principal stress $\sigma_{III}$ is compressive, i.e. $\sigma_{III} < 0$, while the principal stresses $\sigma_I$ and $\sigma_{II}$ change from compressive to tensile (i.e. they change their signs).

Let us consider in more detail some cases of "soft" coatings. From Fig. 1b it is interesting to notice that for the case of almost incompressible coating material ($\nu^{(c)} = 0.499$) in the vicinity of the contact boundary the vertical displacement field $w$ is noticeably differently curved than for all other cases in which the behavior of $w$ is similar (see Fig. 1a–c). The maximum value of the vertical displacement is observed at the point $\rho_s = 0$ and $z_0 = 0$. The vertical displacements for $\nu^{(c)} = 0.33$ and $\nu^{(c)} = -0.4$ look very similar. Their values in the coating are much higher than in the substrate.

The structure of the radial displacement field $u$ is more complex. These fields for different "soft" coating material Poisson's ratios are presented in Fig. 2. It is clear that the displacement behavior is significantly controlled by the coating material Poisson's ratio. First, let us consider the behavior similarities for different Poisson's ratios. For all considered values of Poisson's ratio the radial displacements change their sign (see Fig. 2). Here and further the dashed curves indicate the positions where the corresponding values are equal to zero. For all three cases of coatings these curves have similar shapes. The level curves in the substrate for all these cases are also similar and resemble inclined ellipses (see Fig. 2). The maximum of the absolute value of the radial displacement is reached at $\rho_s \approx a_{0s}$ and $0 \leq z_0 \leq 0.5$ (see Fig. 2d–f). Now, let us consider the differences in the displacement behavior. For "soft" coatings with $\nu^{(c)} = 0.33$ and $\nu^{(c)} = -0.4$ near the coating surface the displacements are mostly negative (i.e. directed towards the contact center) while sufficiently deep in the substrate they are positive (see Fig. 2a, c, d, and f). The displacement behavior for $\nu^{(c)} = 0.499$ is contrary to that (see Fig. 2b, e). In case of $\nu^{(c)} = 0.33$ near the coating upper surface there exists a small region of positive displacements (see Fig. 2d). In this case the maximum displacement value is reached at $z_0 \approx 0.5$ and $\rho_s \approx a_{0s}$. This region encompasses the region with the lowest negative value of the radial displacement (see Fig. 2a). For the case of $\nu^{(c)} = -0.4$ there is no region with positive radial displacements near coating surface (see Fig. 2f). The level curves of zero displacement are very similar for the cases of $\nu^{(c)} = 0.33$ and $\nu^{(c)} = -0.4$ (see Fig. 2d, f) and very different from the case of $\nu^{(c)} = 0.499$ (see Fig. 2e). For $\nu^{(c)} = 0.499$ the absolute value of $u$ is at least an order of magnitude higher than for the other two cases of $\nu^{(c)} = 0.33$ and $\nu^{(c)} = -0.4$. Also, the magnitudes of the radial and vertical displacements for $\nu^{(c)} = 0.499$ are similar. For $\nu^{(c)} = 0.499$ the value of $u$ is different from zero practically only in the coating right below the contact area.

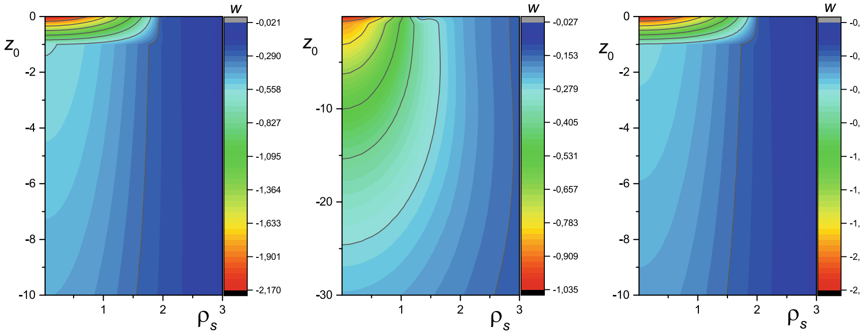

(a) $\nu^{(c)} = 0.33$ (b) $\nu^{(c)} = 0.499$ (c) $\nu^{(c)} = -0.4$

**Fig. 1** Subsurface field of the vertical displacement $w$ for a "soft" coating with **a** $\nu^{(c)} = 0.33$, **b** $\nu^{(c)} = 0.499$, **c** $\nu^{(c)} = -0.4$

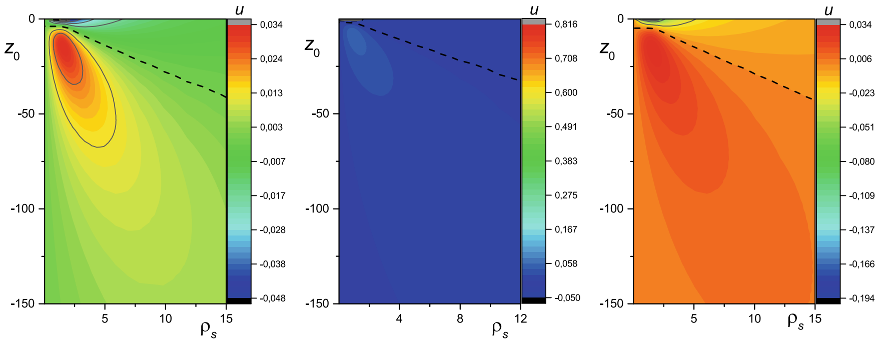

(a) $\nu^{(c)} = 0.33$, small-scale (b) $\nu^{(c)} = 0.499$, small-scale (c) $\nu^{(c)} = -0.4$, small-scale

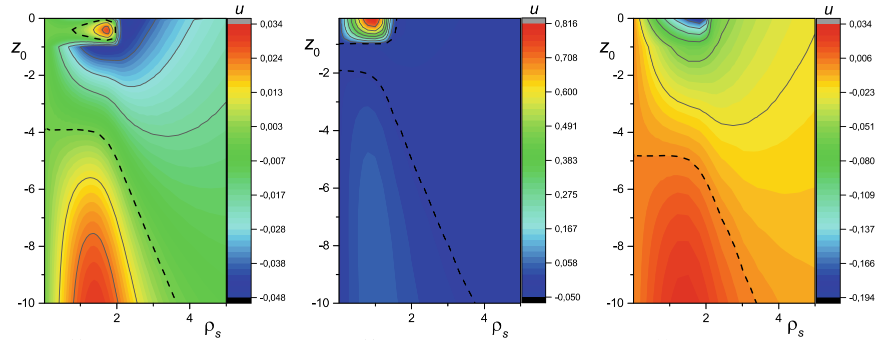

(d) $\nu^{(c)} = 0.33$, large-scale (e) $\nu^{(c)} = 0.499$, large-scale (f) $\nu^{(c)} = -0.4$, large-scale

**Fig. 2** Subsurface field of the radial displacement $u$ for a "soft" coating with **a**, **d** $\nu^{(c)} = 0.33$, **b**, **e** $\nu^{(c)} = 0.499$, **c**, **f** $\nu^{(c)} = -0.4$ in small-scale view (**a**, **b**, **c**) and large-scale view (**d**, **e**, **f**)

However, the most remarkable fact about the fields of $u$ is that $\frac{\partial u(\rho_s,0)}{\partial \rho_s}$ experiences a significant range of variations near the boundary of the contact while within the contact it is small.

Let us consider the behavior of the principal stress fields. As it can be seen from Fig. 3 there is a significant variation of the value of $\sigma_I$ at the coating/substrate interface. In all considered cases the values of $\sigma_I$ are predominantly negative (i.e. compressive). The maximal magnitudes of $\sigma_I$ are reached below the contact center in the substrate near the coating/substrate interface for $\nu^{(c)} = 0.33$ and $\nu^{(c)} = -0.4$ and in the coating for $\nu^{(c)} = 0.499$. The shape of the zero level curves is similar in all three cases. However, for $\nu^{(c)} = 0.33$ and $\nu^{(c)} = 0.499$ the sign change in $\sigma_I$ occurs at a distance from the contact while for the case of $\nu^{(c)} = -0.4$ it occurs at the coating/substrate interface. The fact that the interface may cause a significant stress concentration potentially may cause delamination of the coating in a cyclic loading. For the case of $\nu^{(c)} = 0.499$ the magnitude of $\sigma_I$ is approximately 4 times higher than for the cases of $\nu^{(c)} = 0.33$ and $\nu^{(c)} = -0.4$.

The subsurface fields of the principal stress $\sigma_{II}$ are represented in Fig. 4. Clearly, in the vicinity of the interface, there is a concentration of tensile principal stress

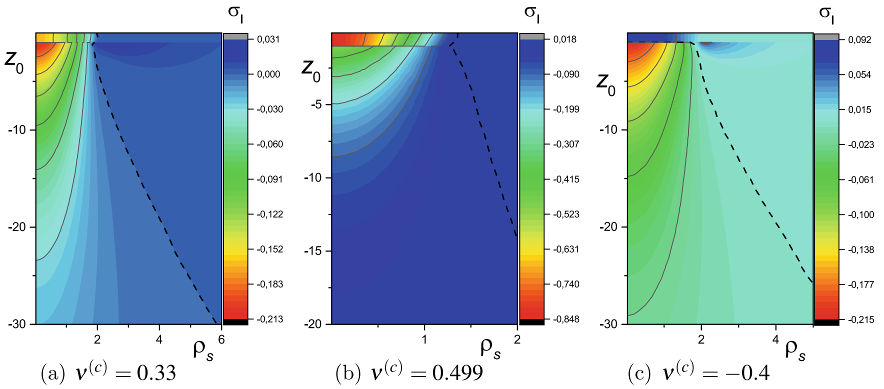

(a) $\nu^{(c)} = 0.33$ (b) $\nu^{(c)} = 0.499$ (c) $\nu^{(c)} = -0.4$

**Fig. 3** Subsurface field of the principal stress $\sigma_I$ for a "soft" coating with **a** $\nu^{(c)} = 0.33$, **b** $\nu^{(c)} = 0.499$, **c** $\nu^{(c)} = -0.4$

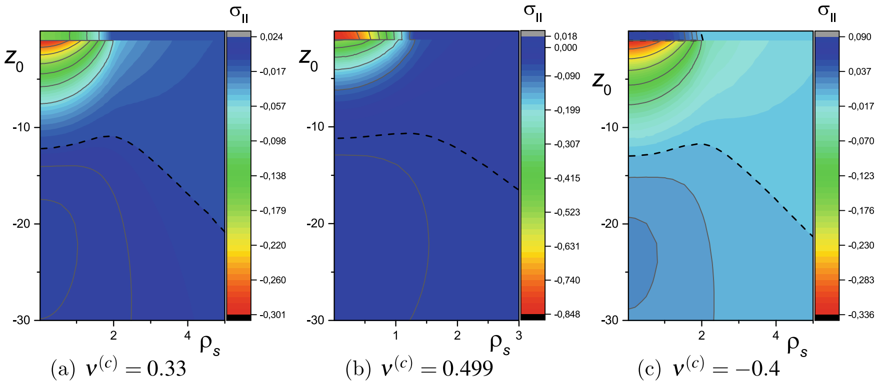

(a) $\nu^{(c)} = 0.33$ (b) $\nu^{(c)} = 0.499$ (c) $\nu^{(c)} = -0.4$

**Fig. 4** Subsurface field of the principal stress $\sigma_{II}$ for a "soft" coating with **a** $\nu^{(c)} = 0.33$, **b** $\nu^{(c)} = 0.499$, **c** $\nu^{(c)} = -0.4$

$\sigma_{II}$ where it experiences a discontinuity. Moreover, for the cases of $\nu^{(c)} = 0.33$ and $\nu^{(c)} = -0.4$ this stress concentration occurs in the substrate part of the material adjacent to the interface while for $\nu^{(c)} = 0.499$ this stress concentration takes place in the coating. In all cases most of the area of stress concentration is within the contact region area. The $\sigma_{II}$ sign change occurs relatively deep at $z_0 \leq -10$. In general, the level curves for all three cases are similar in shape. In the coating, for the case of $\nu^{(c)} = -0.4$ the values of $\sigma_{II}$ are positive. Among the considered cases the maximum compressive value of $\sigma_{II}$ occurs in the case of $\nu^{(c)} = 0.499$ while the maximum tensile value of $\sigma_{II}$ occurs for the case of $\nu^{(c)} = -0.4$.

The fields of the principal stress $\sigma_{III}$ are presented in Fig. 5. The maximum value of $\sigma_{III}$ is reached at $\rho_s = 0$ and $z_0 = 0$. The value of $\sigma_{III}$ decreases rapidly with increase in $\rho_s$ while it decreases slower with $z_0$. In the case of $\nu^{(c)} = 0.499$ there is a sharp change in the value of $\sigma_{III}$ when $z_0$ crosses the coating/substrate interface. For

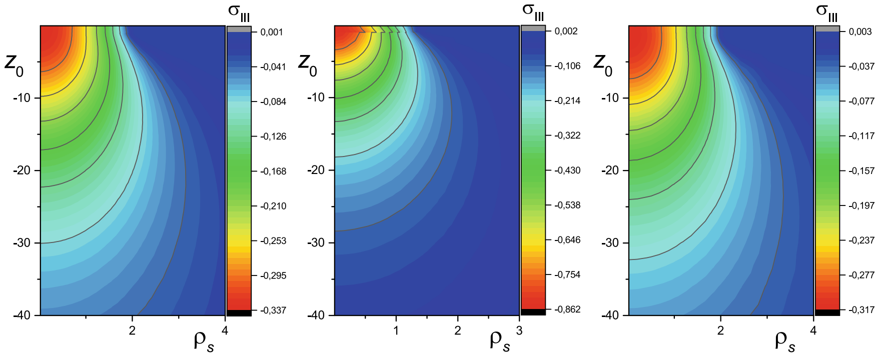

(a) $\nu^{(c)} = 0.33$ (b) $\nu^{(c)} = 0.499$ (c) $\nu^{(c)} = -0.4$

**Fig. 5** Subsurface field of the principal stress $\sigma_{III}$ for a "soft" coating with **a** $\nu^{(c)} = 0.33$, **b** $\nu^{(c)} = 0.499$, **c** $\nu^{(c)} = -0.4$

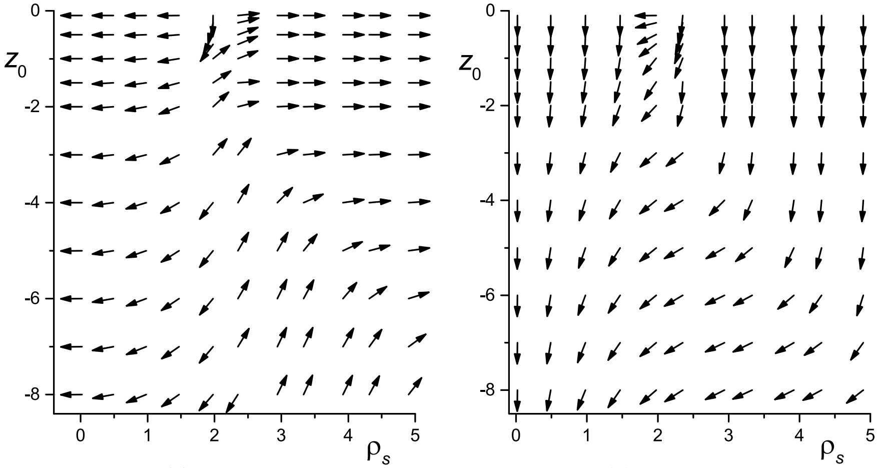

(a) direction of $\sigma_I$ (b) direction of $\sigma_{III}$

**Fig. 6** Direction of the principal stresses $\sigma_I$ and $\sigma_{III}$ for a "soft" coating with $\nu^{(c)} = 0.33$

almost incompressible coating material $\nu^{(c)} = 0.499$ the stress levels are 2–3 times higher than for the cases of $\nu^{(c)} = 0.33$ and $\nu^{(c)} = -0.4$.

Figure 6 depicts the direction fields of the principal stresses $\sigma_I$ and $\sigma_{III}$ for the case of $\nu^{(c)} = 0.33$. Below the contact center and near the coating surface away from the contact the stress $\sigma_I$ is directed practically horizontally. The direction of $\sigma_I$ changes as an observation point gets more and more distant from the contact center and far enough from the contact center the stress $\sigma_I$ is directed practically vertically up. A sharp change of the stress direction is observed near the coating surface in the vicinity of the contact boundary. In this region $\sigma_I$ is directed practically vertically

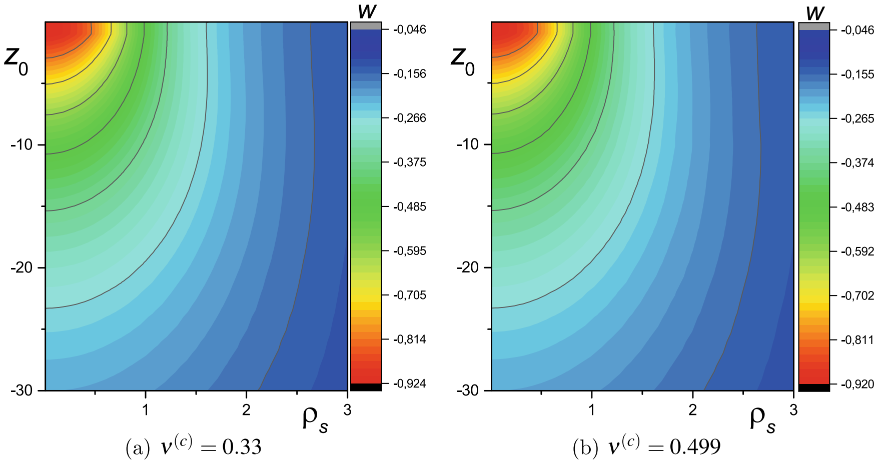

(a) $\nu^{(c)} = 0.33$

(b) $\nu^{(c)} = 0.499$

**Fig. 7** Subsurface field of the vertical displacements $w$ for a "hard" coating with **a** $\nu^{(c)} = 0.33$, **b** $\nu^{(c)} = 0.499$

down. As the sign of the stress $\sigma_I$ changes across the zero-level curve (see Fig. 3a) its direction rapidly changes to the opposite one.

In the absence of the sign change the direction of the principal stress $\sigma_{III}$ varies continuously without any drastic changes. Near the contact center (i.e. at $\rho_s \approx 0$ or $z_0 \approx 0$) the stress $\sigma_{III}$ is directed vertically down. Sufficiently far away from the contact center (i.e. for sufficiently large $\rho_s$ and $z_0$) the stress $\sigma_{III}$ is directed practically horizontally towards the contact center. Similar to the behavior of $\sigma_I$ near the coating surface and near the contact boundary the direction of the stress $\sigma_{III}$ rapidly changes from horizontal to vertical.

Now, let us consider the cases of "hard" coatings. For the cases of "hard" coatings for $\nu^{(c)} = 0.33$ and $\nu^{(c)} = 0.499$ the structures and values of the fields for $w$, $u, \sigma_I,\ \sigma_{II},\ \sigma_{III}$ are very close to each other. The graphs of these fields are given in Figs. 7, 8, 9 and 10, respectively. For the field of $w$ (see Fig. 7) there is a relatively small region (in diameter not greater than the diameter of the contact region) about twenty coating thicknesses deep where most of the displacement takes place. The radial displacement field $u$ is very similar in structure to the one for the "soft" coating with $\nu^{(c)} = -0.4$ (compare Fig. 8a, b with Fig. 2c). The highest values of the radial displacement $u$ are approximately twice higher than the highest values of the magnitude of the negative radial displacements. The magnitude of the radial displacements $u$ is more than an order of magnitude lower than the vertical displacements $w$.

In the cases of "hard" coatings the principal stresses $\sigma_I,\ \sigma_{II},\ \sigma_{III}$ are concentrated practically only in the coating while in the substrate they are close to zero (see Figs. 9 and 10). The principal stress $\sigma_I$ has two regions with negative values. The first is located below the contact up to the depth of $z_0 \approx 0.6$. The second region looks like a rectangle with adjacent to it elliptical region cut by the coating/substrate interface. The maximum magnitude of $\sigma_I$ is reached in the coating below the contact and

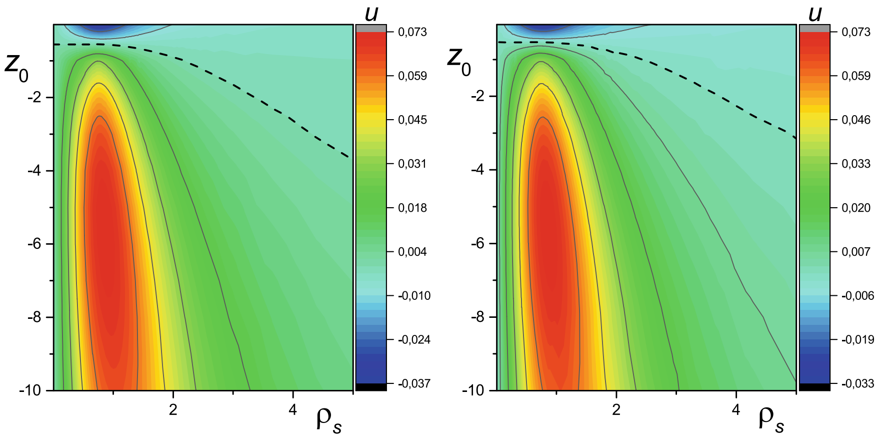

(a) $\nu^{(c)} = 0.33$ (b) $\nu^{(c)} = 0.499$

**Fig. 8** Subsurface field of the radial displacements $u$ for a "hard" coating with **a** $\nu^{(c)} = 0.33$, **b** $\nu^{(c)} = 0.499$

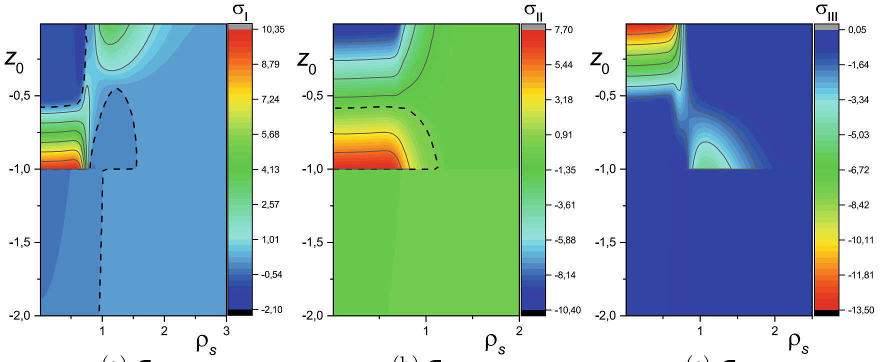

(a) $\sigma_I$ (b) $\sigma_{II}$ (c) $\sigma_{III}$

**Fig. 9** Subsurface fields of the principal stresses $\sigma_I$, $\sigma_{II}$, $\sigma_{III}$ for a "hard" coating with $\nu^{(c)} = 0.33$

close to the coating/substrate interface. There is also a region of the concentration of positive values of the stress $\sigma_I$ which is located near the coating surface not far from the contact boundary.

The principal stress $\sigma_{II}$ is close to zero everywhere except for two distinct regions located below the contact. The maximum positive value of the stress $\sigma_{II}$ is reached at the coating/substrate interface while the maximal negative value of the stress $\sigma_{II}$ is reached at the coating surface. The magnitudes of these values are comparable. The stress $\sigma_{III}$ is concentrated near the coating surface below the contact up to the depth of $z_0 \geq -0.5$ and at some distance from the contact at the coating/substrate interface. Outside of these regions the stress $\sigma_{III}$ is practically equal to zero.

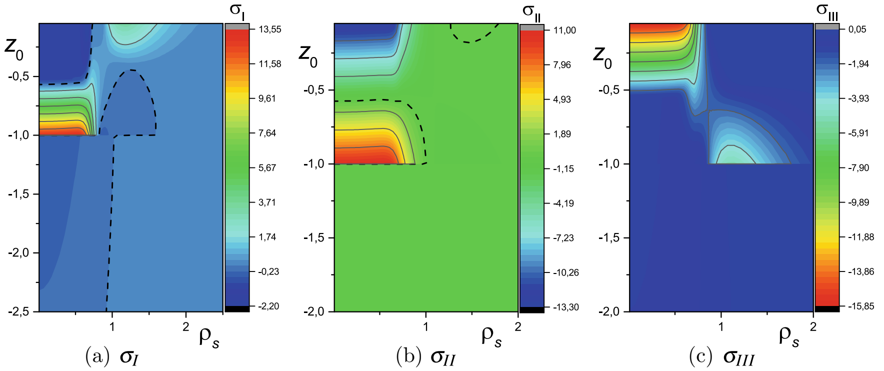

(a) $\sigma_I$ (b) $\sigma_{II}$ (c) $\sigma_{III}$

**Fig. 10** Subsurface fields of the principal stresses $\sigma_I,\ \sigma_{II},\ \sigma_{III}$ for a "hard" coating with $\nu^{(c)} = 0.499$

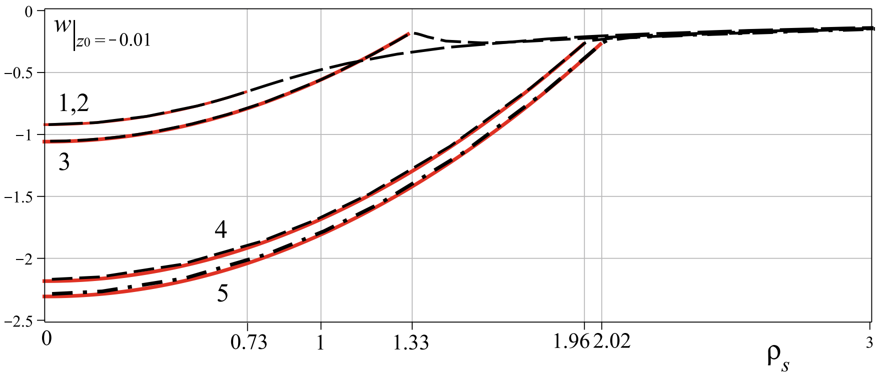

**Fig. 11** Comparison of the punch shape (red lines) with the near coating surface vertical displacement $w(\rho_s, -0.01)$ for "hard" coatings with $\nu^{(c)} = 0.33$ (curve 1) and $\nu^{(c)} = 0.499$ (curve 2) and "soft" coatings with $\nu^{(c)}=0.33$ (curve 4), $\nu^{(c)} = 0.499$ (curve 3), and $\nu^{(c)} = -0.4$ (curve 5)

For all principal stresses it is observed a rapid variation of values in the vicinity of the coating/substrate interface. The latter can serve as a potential source of coating delamination if the solid is involved in cycling loading.

Finally, to show the fact that the numerical solutions are obtained with high precision we present a comparison of the punch shape and the coating vertical displacement $w(\rho_s, -0.01)$ which is very close to its surface. Figure 11 shows that the punch shape and the corresponding near coating surface vertical displacements $w(\rho_s, -0.01)$ are very close. That indirectly demonstrates high precision of the obtained results. Also, for almost incompressible coating material near the contact boundary there is observed a small bump which is not observed for any other Poisson's ratios.

# 7 Conclusions

A semi-analytical solution of an axisymmetric dry contact problem for a parabolic punch indented in a functionally graded material is obtained. The solution includes formulas for contact pressure, contact radius, and subsurface stresses. The solution is realized for the case of a coating and substrate made of different homogeneous materials. The contact frictional stress is neglected. The main focus of the paper is directed toward studying the behavior of the subsurface fields of normal and radial material displacements and subsurface principal stresses. It was observed that the solution is significantly affected by the coating relative "softness/hardness", its thickness, and coating material Poisson's ratio. It is well-known that friction slightly change the distribution of contact normal pressure on the surface. But in some cases it can significantly change the subsurface stresses. The influence of friction on the subsurface stresses and displacements can be studied using similar technique and results obtained earlier for contact with presence of tangential stresses on the surface [26].

**Acknowledgements** The work was supported by the grant of the Government of the Russian Federation (grant no. 14.Z50.31.0046).

# References

1. Giannakopoulos, A.E., Suresh, S.: Indentation of solids with gradients in elastic properties: part I. Point force solution. Int. J. Solids Struct. **34**, 2357–2392 (1997)
2. Giannakopoulos, A.E., Suresh, S.: Indentation of solids with gradients in elastic properties: part II. Axisymetric indenters. Int. J. Solids Struct. **34**, 2392–2428 (1997)
3. Guler, M.A., Erdogan, F.: Contact mechanics of graded coatings. Int. J. Solids Struct. **41**, 3865–3889 (2004)
4. Guler, M.A., Erdogan, F.: The frictional sliding contact problems of rigid parabolic and cylindrical stamps on graded coatings. Int. J. Mech. Sci. **49**, 161–182 (2007)
5. Ke, L.L., Wang, Y.S.: Two-dimensional contact mechanics of functionally graded materials with arbitrary spacial variations of material properties. Int. J. Solids Struct. **43**, 5779–5798 (2006)
6. Liu, T.-J., Wang, Y.-S., Zhang, C.: Axisymmetric frictionless contact of functionally graded materials. Arch. Appl. Mech. **78**, 267–282 (2008)
7. Ke, L.L., Wang, Y.S.: Two-dimensional sliding frictional contact of functionally graded materials. Eur. J. Mech. A-Solids **26**, 171–188 (2007)
8. Alinia, Y., Beheshti, A., Guler, M.A., El-Borgi, S., Polycarpouc, A.A.: Sliding contact analysis of functionally graded coating/substrate system. Mech. Mater. **94**, 142–155 (2016)
9. Liu, J., Ke, L.-L., Wang, Y.-S.: Two-dimensional thermoelastic contact problem of functionally graded materials involving frictional heating. Int. J. Solids Struct. **48**, 2536–2548 (2011)
10. Liu, J., Ke, L.-L., Wang, Y.-S., Yang, J., Alam, F.: Thermoelastic frictional contact of functionally graded materials with arbitrarily varying properties. Int. J. Mech. Sci. **63**, 86–98 (2012)
11. Ma, J., Ke, L.-L., Wang, Y.-S.: Frictionless contact of a functionally graded magneto-electro-elastic layered half-plane under a conducting punch. Int. J. Solids Struct. **51**, 2791–2806 (2014)
12. Su, J., Ke, L.-L., Wang, Y.-S.: Axisymmetric frictionless contact of a functionally graded piezoelectric layered half-space under a conducting punch. Int. J. Solids Struct. **90**, 45–59 (2016)

13. Tokovyy, Y., Ma, C.-C.: An analytical solution to the three-dimensional problem on elastic equilibrium of an exponentially-inhomogeneous layer. J. Mech. **31**(5), 545–555 (2015)
14. Tokovyy, Yu., Ma, C.-C.: Analytical solutions to the axisymmetric elasticity and thermoelasticity problems for an arbitrarily inhomogeneous layer. Int. J. Eng. Sci. **92**, 1–17 (2015)
15. Altenbach, H., Eremeyev, V.A.: Direct approach-based analysis of plates composed of functionally graded materials. Arch. Appl. Mech. **78**, 775–794 (2008)
16. Volkov, S.S., Vasiliev, A.S., Aizikovich, S.M., Seleznev, N.M., Leontieva, A.V.: Stress-strain state of an elastic soft functionally-graded coating subjected to indentation by a spherical punch. PNRPU Mech. Bull. **4**, 20–34 (2016)
17. Vasiliev, A.S., Volkov, S.S., Belov, A.A., Litvinchuk, S. Yu., Aizikovich, S.M.: Indentation of a hard transversely isotropic functionally graded coating by a conical indenter. Int. J. Eng. Sci. **112**, 63–75 (2017)
18. Aizikovich, S.M.: An asymptotic solution of a class of coupled equations. J. Appl. Math. Mech. **54**(5), 719–724 (1990)
19. Kudish, I.I., Volkov, S.S., Vasiliev, A.S., Aizikovich, S.S.: Some criteria for coating effectiveness in heavily loaded line EHL contacts. Part 1. Dry contacts. ASME J. Tribol. **138**, 021504 (2016)
20. Kudish, I.I., Volkov, S.S., Vasiliev, A.S., Aizikovich, S.S.: Some criteria for coating effectiveness in heavily loaded line EHL contacts. Part 2. Lubricated contacts. ASME J. Tribol. **138**, 021505 (2016)
21. Kudish, I.I., Volkov, S.S., Vasiliev, A.S., Aizikovich, S.M.: Effectiveness of coatings with constant, linearly, and exponentially varying elastic parameters in heavily loaded line elastohydrodynamically lubricated contacts. ASME J. Tribol. **139**(2), 021502 (2017)
22. Kudish, I.I., Volkov, S.S., Vasiliev, A.S., Aizikovich, S.M.: Lubricated point heavily loaded contacts of functionally graded materials. Part 1. Dry contacts. Math. Mech. Solids (2017). https://doi.org/10.1177/1081286517704689
23. Kudish, I.I., Volkov, S.S., Vasiliev, A.S., Aizikovich, S.M.: Lubricated point heavily loaded contacts of functionally graded materials. Part 2. Lubricated contacts. Math. Mech. Solids (2017). https://doi.org/10.1177/1081286517704690
24. Vasiliev, A.S., Volkov, S.S., Aizikovich, S.M.: Approximated analytical solution of a problem on indentation of an electro-elastic half-space with inhomogeneous coating by a conductive punch. Dokl. Phys. **63**(1), 18–22 (2018)
25. Aizikovich, S.M., Vasiliev, A.S.: A bilateral asymptotic method of solving the integral equation of the contact problem of the torsion of an elastic half-space inhomogeneous in depth. J. Appl. Math. Mech. **77**(1), 91–97 (2013)
26. Volkov, S.S., Vasiliev, A.S., Aizikovich, S.M., Sadyrin, E.V.: Contact problem on indentation of an elastic half-plane with an inhomogeneous coating by a flat punch in the presence of tangential stresses on a surface. AIP Conf. Proc. **1959**(1), 070037 (2018)

# Mechanistic Model of Generalized Non-antisymmetrical Electrodynamics

**S. A. Lurie, P. A. Belov and Y. O. Solyaev**

**Abstract** In this work, the methods of continuum mechanics are transferred to the four-dimensional continuum, in which the normalized four-dimensional vector-potential of the electromagnetic field is playing the role of 4D-displacement. Classical electrodynamics is presented as a theory of elasticity of 4D-medium with anti-symmetric stress tensor, where Faraday equations are the equations of compatibility, and Ampere equations are the equations of equilibrium. It is shown, that for the considered continuum, the tensor of the fourth rank modules in defining ratios formally allows not only anti-symmetric structure. Uncertain symmetry of electromagnetic "stresses" allows to build a version of the non-anti-symmetric electrodynamics and to predict new effects of the interaction of electromagnetic field with spatially-isotropic material: dynamic, thermal and striction.

**Keywords** 4D-continuum · Transverse isotropy · Electrodynamics · Non-classical effects · Thermo-electro-magneto-elasticity

## 1 Introduction

Significant attempts to introduce equations of electrodynamics as the equations of some continuous medium were carried out repeatedly and, apparently, are related back to Maxwell's works [1–3]. The fundamental works [4–6] are devoted to the development of continual theories of electrodynamics. A four-dimensional space-time canonical formalism was introduced for modeling of the coupoled effects in the deformation of media in [7–9]. In interesting work [10] it is proposed a variant

---

S. A. Lurie (✉) · P. A. Belov
Institute of Applied Mechanics of Russian Academy of Science, Moscow, Russia
e-mail: salurie@mail.ru

S. A. Lurie
Dorodnicyn Computing Centre of FRC CSC RAS, Moscow, Russia

S. A. Lurie · Y. O. Solyaev
Moscow Aviation Institute, Moscow, Russia

H. Altenbach et al. (eds.), *Dynamical Processes in Generalized Continua and Structures*, Advanced Structured Materials 103,
https://doi.org/10.1007/978-3-030-11665-1_21

of the four-dimensional isotropic theory of elasticity, in which the entropy density can be treated as a component of the generalized strain tensor. However, the defining relations of such a theory are not written down.

In [11–15], the methods of continuum mechanics expanded to the space-time 4D-continuum, were used for the construction of variation models, extended thermodynamic for the reversible and non-reversible processes, in which the laws of Duhamel-Neumann's and Maxwell-Cattaneo (non-classical generalization of Fourier's law for heat flow) are direct consequences of the defining relations. In the article [16], the mechanistic model of physical fields was built as a model of mechanics of 4D-continuum with the fields of defects. It is shown, that the equations, obtained by the variational method, describe the whole spectrum of physical interactions and include a complete system of Maxwell's equations of electrodynamics, Einstein's equations for the currents. In [16, 17], it was shown that to obtain consistent model of extended thermodynamics it should be considered the 4D-continuum which is transversely-isotropic with respect to the time coordinate, in which the tensor of interactions, in contrast to the 3D-stresses of continuum mechanics, can not be purely symmetric and should contain anti-symmetric part. In [18, 19] it was further introduced "Landau" dissipation, allowing to obtain a generalization of the law of Maxwell-Cattaneo and to model (scale effects) wave properties in the process of heat conduction.

One of the problems in constructing of mechanistic models of electrodynamics is the anti-symmetry of "power factors" in electrodynamics and, on the contrary, the symmetry of stress tensor in classical continuum mechanics. In [14], it is shown, that the equations of electrodynamics are formally elasticity equations for the generalized 4D-continuum and therefore it is proved the consistency between generally accepted model of classical electrodynamics and the model of mechanics of 4D-continuum with non-symmetric (anti-symmetric) stress tensor. This allowed indirectly to prove the existence of the theory of elasticity with non-symmetric stress tensor, its efficacy in the description of physical processes.

In this article we showed that the electrodynamics model allows not only the existence of anti-symmetric tensor of electromagnetic interactions ("stresses"), but also the existence of symmetric component. In other words, we believe that in common case both the model of electrodynamics (the same as the model of continuum mechanics) have symmetric components in tensors of interactions. This "unification" of models allows one to build a consistent model for the connected dynamic thermo-electro-magneto-elasticity for spatially-isotropic materials.

## 2 Mechanistic Model of Classical Electrodynamics

We construct a model of classical electrodynamics as an option of anti-symmetric theory of elasticity of Minkowski medium and, thus, prove the possibility of Maxwell's idea about the possibility of a correct mechanistic interpretation of the equations of electrodynamics. First let's determine the 4D-vector of "displacements" through the normalized vector-potential of the electromagnetic field:

$$\begin{aligned}&A_i = a_i + ic\varphi N_i = R_i\\&a_i = A_j\delta^*_{ij}, \quad \varphi = -iA_jN_j/c, \qquad a_iN_i = 0\end{aligned} \tag{1}$$

Here $N_i$ is the ort of time, $\delta_{ij}$ is 4D-Kronecker tensor $\delta_{ij}\delta_{ij} = 4$, $\delta^*_{ij} = \delta_{ij} - N_iN_j$ is 3D-Kronecker tensor $\delta^*_{ij}\delta^*_{ij} = 3$, $i = \sqrt{-1}$ is imaginary unit.

Spatial components of the vector-potential $a_i$ have the dimension of length, and the real, time component $\varphi$ has the dimension of time. In accordance with the mechanistic analogy, the magnetic potential $a_i$ is similar to the vector of spatial displacements $r_i$, and the electric potential $\varphi$ is the similar to a local non-uniform time $R$ [11–15]. The normalization coefficient in the definition of the coordinate $x_4$ is selected equal to the speed of light $c$. Continuing mechanistic analogy, we define an analogue of pseudo-tensor of 4D-rotations in continuum mechanics, as follows:

$$\omega_{ij} = -A_{p,q}\ni_{pqij}/2 \tag{2}$$

Here $\ni_{pqij}$is the Tullio Levi-Civita pseudo tensor

Certainly, we can rewrite Eq. (2) in the form:

$$\|\omega_{ij}\| = \left\|\begin{matrix} 0 & -(A_{3,4} - A_{4,3})/2 & (A_{2,4} - A_{4,2})/2 & -(A_{2,3} - A_{3,2})/2 \\ (A_{3,4} - A_{4,3})/2 & 0 & -(A_{1,4} - A_{4,1})/2 & (A_{1,3} - A_{3,1})/2 \\ -(A_{2,4} - A_{4,2})/2 & (A_{1,4} - A_{4,1})/2 & 0 & -(A_{1,2} - A_{2,1})/2 \\ (A_{2,3} - A_{3,2})/2 & -(A_{1,3} - A_{3,1})/2 & (A_{1,2} - A_{2,1})/2 & 0 \end{matrix}\right\|$$

and

$$\begin{aligned}&\omega_{ij}X_iY_j = -(A_{3,4} - A_{4,3})/2, \quad \omega_{ij}X_iZ_j = (A_{2,4} - A_{4,2})/2, \quad \omega_{ij}X_iN_j = -(A_{2,3} - A_{3,2})/2\\&\omega_{ij}Y_iZ_j = -(A_{1,4} - A_{4,1})/2, \quad \omega_{ij}Y_iN_j = (A_{1,3} - A_{3,1})/2\\&\omega_{ij}Z_iN_j = -(A_{1,2} - A_{2,1})/2\end{aligned}$$

Thus, the components of tensor of rotations $\omega_{ij} = -A_{p,q}\ni_{pqij}/2$are recorded through the components of the normalized vector-potential of the electromagnetic field $A_i$ in full compliance with the mechanical analogy. Let's show that the pseudo-tensor of rotations can be recorded via the vector of electric intensity and pseudo-vector of magnetic induction. Indeed, the components of dimensionless vector the electric intensity $E_i$ and dimensionless pseudo-vector of magnetic induction $B_i$ are defined trough the real components of the vector-potential $A_i$ in a conventional manner:

$$\begin{aligned}E_i &= -i\omega_{mn}N_s\ni_{simn}/2 = iA_{p,q}\ni_{pqmn}N_s\ni_{simn}/4 =\\&= i(A_{i,j} - A_{j,i})N_j/2 = (\frac{1}{c}\dot{a}_i + c\phi_{,j}\delta^*_{ij})/2\\B_i &= -\omega_{ik}N_k = A_{p,q}\ni_{pqik}N_k/2 = a_{p,q}\ni_{pqik}N_k/2\end{aligned} \tag{3}$$

We can write Eq. (3) also in the form:

$$\|E_i\| = i\begin{Vmatrix} (A_{1,4} - A_{4,1})/2 \\ (A_{2,4} - A_{4,2})/2 \\ (A_{3,4} - A_{4,3})/2 \\ 0 \end{Vmatrix} \quad \|B_i\| = \begin{Vmatrix} (A_{2,3} - A_{3,2})/2 \\ (A_{3,1} - A_{1,3})/2 \\ (A_{1,2} - A_{2,1})/2 \\ 0 \end{Vmatrix}$$

It follows directly from (3) that the dimensionless vector of electric intensity $E_i$ and the dimensionless pseudo-vector of magnetic induction $B_i$ are the components of antisymmetric 4D-pseudo-tensor.

$$\omega_{ij} = iE_k N_r \text{Э}_{rkij} - B_i N_j + B_j N_i \tag{4}$$

It is not difficult to verify this correspondence between relations (3) and (4) if we use the following known equalities for the generalized Tullio Levi-Civita pseudo tensor

$$\begin{aligned} &\text{Э}_{jipq}\text{Э}_{jimn} = \text{Э}_{jbpq}\text{Э}_{jdmn}\delta_{bd} = \\ &= 4(\delta_{pm}\delta_{qn} - \delta_{pn}\delta_{qm}) - \delta_{dm}(\delta_{pd}\delta_{qn} - \delta_{pn}\delta_{qd}) + \delta_{dn}(\delta_{pd}\delta_{qm} - \delta_{pm}\delta_{qd}) = \\ &= 2(\delta_{pm}\delta_{qn} - \delta_{pn}\delta_{qm}) \end{aligned}$$

Indeed, the operation of convolution of $\omega_{mn}$ with $iN_s\text{Э}_{simn}/2$gives:

$$\begin{aligned} &-i\omega_{mn}N_s\text{Э}_{simn}/2 = \\ &= -i[iE_k N_r \text{Э}_{rkmn} - B_m N_n + B_n N_m]N_s\text{Э}_{simn}/2 = \\ &= E_k N_r N_s \text{Э}_{rkmn}\text{Э}_{simn}/2 = \\ &= E_k N_r N_s [2(\delta_{rs}\delta_{ki} - \delta_{ri}\delta_{ks})]/2 = \\ &= E_k(\delta_{ki} - N_k N_i) = \\ &= E_i \end{aligned}$$

Further, carrying out the convolution of $\omega_{mn}$ with $N_n$ we obtain:

$$\begin{aligned} &\omega_{ij}N_j = [iE_k N_r \text{Э}_{rkij} - B_i N_j + B_j N_i]N_j = \\ &= iE_k N_r N_j \text{Э}_{rkij} - B_i N_j N_j + B_j N_i N_j = \\ &= iE_k N_r N_j \text{Э}_{rkij} - B_i N_j N_j + (B_j N_j)N_i = \\ &= -B_i \end{aligned}$$

Therefore, the antisymmetric 4D-pseudo-tensor $\omega_{ij}$ can be represented in a matrix form

$$\|\omega_{ij}\| = \begin{Vmatrix} 0 & -iE_3 & +iE_2 & -B_1 \\ iE_3 & 0 & -iE_1 & -B_2 \\ -iE_2 & iE_1 & 0 & -B_3 \\ B_1 & B_2 & B_3 & 0 \end{Vmatrix},$$

$$\begin{cases} \omega_{ij}X_iY_j = -iE_3 \\ \omega_{ij}X_iZ_j = iE_2 \\ \omega_{ij}X_iN_j = -B_1 \end{cases} \quad \begin{cases} \\ \omega_{ij}Y_iZ_j = -iE_1 \\ \omega_{ij}Y_iN_j = -B_2 \end{cases} \quad \begin{cases} \\ \\ \omega_{ij}Z_iN_j = -B_3 \end{cases}$$

We have the following lemmas.

**Lemma 1** *4D-vector of electric intensity $E_i$ has only three spatial components, and the time component is equal to zero.*

*Proof*

$$E_iN_i = [-iA_{p,q}\text{Э}_{pqmn}N_s\text{Э}_{simn}/4]N_i = -iA_{p,q}\text{Э}_{pqmn}(N_sN_i\text{Э}_{simn})/4 \equiv 0 \tag{5}$$

**Lemma 2** *4D-pseudo-vector of magnetic induction $B_i$ has only three spatial components.*

*Proof*

$$B_iN_i = [A_{p,q}\text{Э}_{pqik}N_k/2]N_i = A_{p,q}(\text{Э}_{pqik}N_iN_k)/2 \equiv 0 \tag{6}$$

Consider mechanical analogue of compatibility equations:

$$\omega_{ij,j} = -A_{p,qj}\text{Э}_{pqij}/2 \equiv 0 \tag{7}$$

Let's write $\omega_{ij,j}$ via the vector of electric intensity $E_i$ and the dimensionless pseudo-vector of magnetic induction $B_i$ using the definition (2), expansion (4) and Eqs. (5), (6):

$$\omega_{ij,j} = iE_{k,j}N_r\text{Э}_{rkij} - B_{i,j}N_j + B_{j,j}N_i = 0$$

Finally, we expand the vector $\omega_{ij,j} = 0$ on the direction of the time coordinate and orthogonal hyperplane and rewrite Eq. (8) in the following form:

$$\begin{cases} E_{p,q}\text{Э}_{pqin}N_n + iB_{i,k}N_k = 0 \\ B_{i,j}\delta^*_{ij} = 0 \end{cases} \tag{8}$$

As a result, we have proved that the equations of compatibility $\omega_{ij,j} = 0$ can be written in the form of classical three-dimensional equations of Faraday $E_{p,q}\text{Э}_{pqin}N_n + iB_{i,k}N_k = 0$and Gauss equation for the magnetic field $B_{i,j}\delta^*_{ij} = 0$ as a mechanical analogue of equations of compatibility. In what follows we will call the equations of compatibility (7), (8) as 4D-Faraday equations.

Continuing mechanistic analogy, let's define the stress tensor and write the general defining equations (Hooke's law) for formal stress tensor in electrodynamics (electric induction-intensity of magnetic field) by analogy with continuum mechanics. Then we will analyze the structure of the elastic moduli, decipher the entire range of components of the "stress tensor" in the electromagnetic field model and establish the direct analogy with mechanical power factors:

$$\sigma_{ij} = C_{ijnm}A_{n,m} = C_{ijnm}R_{n,m} \tag{9}$$

Equation (9) defines the physical model of the considered space-time continuum. The general expression for the elastic constants of such solids is

We consider the symmetry conditions of the potentiality $C_{ijnm} = C_{nmij}$ and propose that the isotropic elastic body with symmetric stress tensor $t_{ij}$ has place for three-dimension elasticity problem. Then, we receive:

$$\begin{aligned} C_{ijnm} = \\ &= C_1\delta^*_{ij}\delta^*_{nm} + C_2N_iN_j\delta^*_{nm} + C_3\delta^*_{ij}N_nN_m + C_4N_iN_jN_nN_m \\ &\quad + C_5\delta^*_{in}\delta^*_{jm} + C_6N_iN_n\delta^*_{jm} + C_7\delta^*_{in}N_jN_m \\ &\quad + C_8\delta^*_{im}\delta^*_{jn} + C_9N_iN_m\delta^*_{jn} + C_{10}\delta^*_{im}N_jN_n \end{aligned} \tag{10}$$

The tensor of moduli $C_{ijnm}$ for 4D-medium, which is transversely isotropic in the direction of the ort $N_i$ must satisfy the symmetry conditions of the potentiality $C_{ijnm} = C_{nmij}$, which lead to the following relations for the coefficients in tensor of moduli (10):

$$C_3 = C_2, \quad C_{10} = C_9 \tag{11}$$

In addition, the tensor of "stresses" which defines the interactions of the electromagnetic field with the medium, must be anti-symmetric for the classical electrodynamic theory: $\sigma_{ij} + \sigma_{ji} = 0$. This condition leads to the following additional group of relations on the tensor of the elastic moduli (10):

$$\begin{aligned} &C_1 = 0, \;\; C_2 = 0, \;\; C_4 = 0 \\ &(C_5 + C_8) = 0, \;\; (C_6 + C_9) = 0, \quad (C_7 + C_9) = 0 \end{aligned} \tag{12}$$

As a result, taking account (11), (12), the tensor of the moduli becomes:

$$C_{ijnm} = C_8(\delta^*_{im}\delta^*_{jn} - \delta^*_{in}\delta^*_{jm}) \\ + C_9(\delta^*_{jn}N_iN_m + \delta^*_{im}N_jN_n - \delta^*_{jm}N_iN_n - \delta^*_{in}N_jN_m) \tag{13}$$

Using (9), (13) we can write the equilibrium equations:

$$\sigma_{ij,j} + J_i = \\ = C_8(\delta^*_{im}\delta^*_{jn} - \delta^*_{in}\delta^*_{jm})R_{n,mj} + \\ + C_9[(\delta^*_{jn}N_i - \delta^*_{in}N_j)N_m + (\delta^*_{im}N_j - \delta^*_{jm}N_i)N_n)R_{n,mj} + J_i = 0 \tag{14}$$

here $J_i$ is the density of generalized “forces” distributed over the space-time continuum.

As is known, the governing equations of mechanics in displacements are the equilibrium equations of the Lame-Navier, and the governing equations of electrodynamics in the terms of the vector of electric induction $D_i$ and the intensity of magnetic field $H_i$ are the Ampere equations. Let’s show that the generalized Lame-Navier equations (14) can be transformed in such a way that they coincide exactly with the Ampère equations. This will establish a correspondence between the stress on the one hand and the electrical induction $D_i$ and magnetic strength $H_i$ on the other hand.

We believe in the future, that for the model of electrodynamics, the value $J_i$ is vector of 4D-currents. Let’s investigate the conditions under which in this case, the equilibrium equations coincide with the equations of Ampere. First note that the established properties of the tensor of elastic moduli provide identical performance of equality $\sigma_{ij,ij} = 0$. Therefore, the divergence of the equilibrium equations $\sigma_{ij,ij} + J_{i,i} = 0$ leads to equations:

$$J_{i,i} = 0 \tag{15}$$

Equation (15) reflects the property of conservation of 4D-currents similar to the law of conservation of currents in electrodynamics.

The proof of the following lemmas allows us to isolate in the equations of equilibrium such operators over the displacement vector, which can be interpreted as electric intensity $E_i$ and magnetic induction $B_i$. Let’s transform equation (14) so, that it took the standard form of Ampere equations. To do this, let’s first prove the following lemmas.

**Lemma 3** *The equality* $\delta^*_{in}\delta^*_{jm} - \delta^*_{im}\delta^*_{jn} = Э_{ijpc}Э_{nmps}N_cN_s$ *takes place.*

*The proof of lemma follows from the sequence of equalities recorded below:*

$$
\begin{aligned}
&Э_{pabc}Э_{pqks}N_cN_s = \\
&= [\delta_{aq}(\delta_{bk}\delta_{cs} - \delta_{bs}\delta_{ck}) - \delta_{ak}(\delta_{bq}\delta_{cs} - \delta_{bs}\delta_{cq}) + \delta_{as}(\delta_{bq}\delta_{ck} - \delta_{bk}\delta_{cq})]N_cN_s = \\
&= [\delta_{aq}(\delta_{bk} - N_bN_k) - \delta_{ak}(\delta_{bq} - N_bN_q) + \delta_{bq}N_aN_k - \delta_{bk}N_aN_q] = \\
&= [\delta_{aq}(\delta_{bk} - N_bN_k) - \delta_{ak}(\delta_{bq} - N_bN_q) + (\delta_{bq} - N_bN_q)N_aN_k - \\
&= -(\delta_{bk} - N_bN_k)N_aN_q] = \\
&= (\delta_{aq} - N_aN_q)(\delta_{bk} - N_bN_k) - (\delta_{ak} - N_aN_k)(\delta_{bq} - N_bN_q) = \\
&= \delta^*_{aq}\delta^*_{bk} - \delta^*_{ak}\delta^*_{bq}
\end{aligned}
$$

**Lemma 4** *The equality takes place:*

$$
\begin{aligned}
&[(\delta^*_{in}N_j - \delta^*_{jn}N_i)N_m - (\delta^*_{im}N_j - \delta^*_{jm}N_i)N_n] = \\
&= (\delta^*_{ia}N_j - \delta^*_{ja}N_i)N_bЭ_{abpq}Э_{nmpq}/2
\end{aligned}
$$

The proof is established by means of transformations, taking into account delta Kronecker properties and properties of convolutions of Levi-Chivita tensors on two indexes in 4D-space and taking into account the definition $\delta^*_{ij} = \delta_{ij} - N_iN_j$:

$$
\begin{aligned}
&[(\delta^*_{in}N_j - \delta^*_{jn}N_i)N_m - (\delta^*_{im}N_j - \delta^*_{jm}N_i)N_n] = \\
&= (\delta^*_{ia}N_j - \delta^*_{ja}N_i)N_b(\delta_{an}\delta_{bm} - \delta_{am}\delta_{bn}) = \\
&= (\delta^*_{ia}N_j - \delta^*_{ja}N_i)N_bЭ_{abpq}Э_{nmpq}/2
\end{aligned}
$$

Taking into account Lemmas 3 and 4, the equilibrium equations (14) take the form:

$$
\begin{aligned}
\sigma_{ij,j} + J_i = {} & -C_8Э_{ijpc}Э_{nmps}N_cN_sR_{n,mj} - \\
& -C_9(\delta^*_{ia}N_j - \delta^*_{ja}N_i)N_bЭ_{abpq}Э_{nmpq}R_{n,mj}/2 + J_i = 0
\end{aligned}
$$

Let's use the definition (3) and introduce the classic definition of the vector of electric induction $D_i$ and the intensity of magnetic field $H_i$ (as stress analogs):

$$
\begin{cases}
D_i = \varepsilon E_i \\
H_i = B_i/\mu
\end{cases}
\tag{16}
$$

As a result, taking into account (16) we'll receive:

$$\sigma_{ij,j} + J_i = 2\mu C_8 H_{p,q} \text{Э}_{pqic} N_c + \frac{2C_9}{\varepsilon} i(D_{i,j}N_j - D_{j,j}N_i) + J_i = 0 \tag{17}$$

Here $\varepsilon$ is the permittivity constant and, $\mu$ is the permeability constant.

Now let’s suppose that

$$\begin{cases} C_8 = -1/(2\mu) \\ C_9 = \varepsilon/2 \end{cases} \tag{18}$$

Then, with the help of Eq. (18) the equilibrium equations (17) can be represented in the form:

$$-H_{p,q} \text{Э}_{pqic} N_c + i(D_{i,j}N_j - D_{j,j}N_i) + J_i = 0 \tag{19}$$

Finally, we expand 4D-Ampere equations (19) on the direction of the time coordinate and orthogonal hyperplane and rewrite them in the following form:

$$\begin{cases} -H_{p,q} \text{Э}_{pqkc} N_c + iD_{k,j}N_j + J_i\delta^*_{ik} = 0 \\ -iD_{j,j} + J_iN_i = 0 \end{cases} \tag{20}$$

Then we can see that first vector equation (20) is classical 3D-Ampere equation and the second, scalar equation (20), is the Gauss equation for the electric field. In what follows, the Eq. (19) we’ll call 4D-Ampere equation.

In conclusion, let’s give the set of conditions on the elastic moduli in the defining relations (11), (12) and (18) which made it possible to ensure a complete correspondence between the equilibrium equations (14) and the Ampere equations in classical electrodynamics:

$$\begin{cases} C_1 = 0 \\ C_2 = 0 \\ C_3 = 0 \\ C_4 = 0 \end{cases} \quad \begin{cases} C_5 = 1/(2\mu) \\ C_6 = -(\varepsilon/2) \\ C_7 = -(\varepsilon/2) \\ C_8 = -1/(2\mu) \end{cases} \quad \begin{cases} C_9 = (\varepsilon/2) \\ C_{10} = (\varepsilon/2) \end{cases}$$

Tensor of moduli takes the form (anti-symmetric with respect to the first indexes):

$$\begin{aligned} C_{ijnm} &= (\delta^*_{in}\delta^*_{jm} - \delta^*_{im}\delta^*_{jn})/(2\mu) + \\ &+ (\varepsilon/2)(\delta^*_{jn}N_iN_m + \delta^*_{im}N_jN_n - \delta^*_{jm}N_iN_n - \delta^*_{in}N_jN_m) \end{aligned}$$

Hooke’s law equations for electromagnetic field stresses take the form:

$$\sigma_{ij} = C_{ijnm}A_{n,m} = H_p \text{Э}_{ijpc} N_c + i(D_iN_j - D_jN_i) \tag{21}$$

By analogy with the definition (4) of anti-symmetric 4D pseudo-tensor of rotations $\omega_{ij}$ we define the analogues of power factors for classical electromagnetic field that have a sense of stresses in the generalized theory of elasticity for 4D-pseudo-continuum.

Decipher the whole range of components of the "stress tensor" (19). To do this, we use the general relations for the tensor of stresses that were set for dynamic thermo-elasticity recorded for 4D space- time media [6, 9]. Note that in [6, 9] in describing the thermo-mechanical interactions in the space-time of 4D Minkowski continuum, the tensor of stresses $\sigma_{ij}$ was determined, its general structure was listed. It was found that in Minkowski space, the thermomechanical interactions are described by the following tensor of generalized stresses:

$$\sigma_{ij} = \tau_{ij} + p\delta^{*}_{ij}/3 - \tau_{k}\text{Э}_{ijkr}N_{r} + p_{i}N_{j}(iv) + q_{j}N_{i}/(iv) + TN_{i}N_{j}$$

The tensor of stresses $\sigma_{ij}$ was introduced as an expansion to the following real components:

- «3D- tensor-deviator» of stresses $\tau_{ij} = \sigma_{nm}(\delta^{*}_{in}\delta^{*}_{jm}/2 + \delta^{*}_{im}\delta^{*}_{jn}/2 - \delta^{*}_{ij}\delta^{*}_{nm}/3)$,
- «3D-pseudo-vector» of spatial unpaired tangent stresses,
- «3D-vector» of impulses $p_k = \sigma_{nm}\delta^{*}_{nk}N_m/(iv)$,
- «3D-vector» of heat flux $q_k = \sigma_{nm}N_n\delta^{*}_{mk}(iv)$,
- «3D- scalar» of hydrostatic pressure $p = \sigma_{nm}\delta^{*}_{nm}$—amplitude of "3D sphere-tensor" of spatial stresses,
- «3D- scalar» of temperature $T = \sigma_{nm}N_iN_j$.

Here are the analogues of thermomechanical power factors for classical electro-magnetic field:

$$\sigma_{ij} = -H_{p}\text{Э}_{pjic}N_{c} + iD_{i}N_{j} - iD_{j}N_{i}$$

$$\begin{cases} p_{k} = \sigma_{ij}\delta^{*}_{ik}N_{j}/(ic) = D_{k}/c \\ q_{k} = \sigma_{ij}N_{i}\delta^{*}_{jk}(ic) = D_{k}c \end{cases} \quad \begin{cases} p = \sigma_{ij}\delta^{*}_{ij} = 0 \\ T = \sigma_{ij}N_{i}N_{j} = 0 \end{cases} \quad \begin{cases} \tau_{ij} = 0 \\ \tau_{k} = \sigma_{ij}\text{Э}_{ijkq}N_{q} = 2H_{k} \end{cases}$$

From the point of view of classical electrodynamics the interaction with spatially-isotropic material can be carried out only through spatial unpaired tangent stresses by the magnetic field and through impulses and heat flows by the electric field.

Spatial unpairing of tangent stresses (in continuum mechanics) is not observed experimentally, and if it took place, the speed of sound for the transverse waves in the material would have to exceed the theoretical value $v = \sqrt{G/\rho}$. Therefore, the interaction of electromagnetic field with spatially-isotropic material by the magnetic field, from the point of view of classical electrodynamics, seems unlikely.

Interaction of electromagnetic field with spatially-isotropic material by electric field from the point of view of classical electrodynamics is acceptable and implemented through impulses and heat flow. However, even here we can point to the existence of contradictions. In particular, in the medium the heat flow is potential, which follows from the Fourier law of heat conduction, but the electric field can excite only vortex heat fluxes proportional to $D_k$.

On this basis, it should be recognized that the model of classical electrodynamics does not allow to build phenomenological theory of the interaction of electromagnetic field with spatially-isotropic material.

## 3 Mechanistic Model of Nonclassical Electrodynamics

In this section, we'll show that the model of non-classical electrodynamics can be represented as generalized non-anti-symmetric theory of elasticity of 4D-continuum, in which tensor of "stresses" has not only anti-symmetrical components.

Lets again consider the electromagnetic field theory as the four dimension theory of elasticity and first discuss shortly the kinematic model for the generalized variant of the mechanistic model. Accordingly, the normalized vector-potential of the electromagnetic field $A_i$, as a 4D-vector of "displacements", as well as in the previous section, is determined by (1). The real components of the dimensionless vector of electric intensity $E_i$ and ones of dimensionless pseudo-vector of magnetic induction $B_i$ are also expressed in through the real components of the vector-potential $A_i$ by the relations (3). At last, the 4D-Faraday Eq. (7), as a mechanical analogue of the compatibility equations, are satisfied identically. Thus, the kinematic model of the four-dimensional theory of elasticity, which is studied coincides completely with kinematic model that was formulated in the previous section.

The proposed generalization of the mechanistic model of the electrodynamics will concern the constitutive equations and a choice of more general structure of tensor of moduli which is transversally-isotropic in the direction of the time ort.

We try to receive the constitutive equation for the mechanistic four dimension model of the electrodynamics which define the more common tensor of stresses that is not antisymmetric as it was received for the space-time continuum model in the case of classical electrodynamics.

To construct the generalized variant of the space—time continuum model, we should refuse the hypothesis of "pure anti-symmetry of the stress tensor" (9) and assume only that 4D-equations of Ampere (14), (19), (20) and the conservation law of 4D-current (15) are valid. Assuming the existence of the potential energy $C_{ijnm} = C_{nmij}$ and the corresponding Lagrangian, the tensor $C_{ijnm}$ contains eight modules:

$$\begin{aligned} C_{ijnm} &= \\ &= C_1\delta^*_{ij}\delta^*_{nm} + C_2(\delta^*_{nm}N_iN_j + \delta^*_{ij}N_nN_m) + C_4N_iN_jN_nN_m + \\ &+ C_5\delta^*_{in}\delta^*_{jm} + C_6\delta^*_{jm}N_iN_n + C_7\delta^*_{in}N_jN_m + \\ &+ C_8\delta^*_{im}\delta^*_{jn} + C_9(\delta^*_{jn}N_iN_m + \delta^*_{im}N_jN_n) \end{aligned} \tag{22}$$

Let's simmertrizise in (22) the basic tensors on the indices $j, m$:

$$C_{ijnm} = (C_{ijnm} + C_{imnj})/2 + (C_{ijnm} - C_{imnj})/2$$

Then we can show that the moduli included in the tensor $(C_{ijnm} - C_{imnj})/2$ will not appear in the equilibrium equations (equations of Ampere):

$$\begin{aligned}\sigma_{ij,j} + J_i = C_{ijnm}R_{n,mj} + J_i = (C_{ijnm} + C_{imnj})R_{n,mj}/2 \\ + (C_{ijnm} - C_{imnj})R^2_{n,mj}/2 + J_i = 0\end{aligned}$$

Indeed, the first term is the convolution of two tensors that are symmetric over the indices $j, m$ and gives $(C_{ijnm} + C_{imnj})R_{n,mj}/2 = C_{ijnm}R_{n,mj}$, the second term is the convolution of antisymmetric and symmetric over the indices $j, m$ tensors and gives $(C_{ijnm} - C_{imnj})R_{n,mj}/2 \equiv 0$.

Follow to (22) we can write:

$$\begin{aligned}&(C_{ijnm} + C_{imnj})/2 = \\ &= (C_1 + C_8)(\delta^*_{ij}\delta^*_{nm} + \delta^*_{im}\delta^*_{nj})/2+ \\ &+ (C_2 + C_9)(\delta^*_{nm}N_iN_j + \delta^*_{ij}N_nN_m + \delta^*_{nj}N_iN_m + \delta^*_{im}N_nN_j)/2+ \\ &+ C_4N_iN_jN_nN_m + C_5\delta^*_{in}\delta^*_{jm} + C_6\delta^*_{jm}N_iN_n + C_7\delta^*_{in}N_jN_m \\ &(C_{ijnm} - C_{imnj})/2 = \\ &= (C_1 - C_8)(\delta^*_{ij}\delta^*_{nm} - \delta^*_{im}\delta^*_{nj})/2+ \\ &+ (C_2 - C_9)(\delta^*_{nm}N_iN_j + \delta^*_{ij}N_nN_m - \delta^*_{nj}N_iN_m - \delta^*_{im}N_nN_j)/2 \qquad (23)\end{aligned}$$

Both tensors $(C_{ijnm} + C_{imnj})/2$ and $(C_{ijnm} - C_{imnj})/2$ in (23) define the properties of the stress tensor which has now symmetric and antisymmetric components. But only the symmetric tensor $(C_{ijnm} + C_{imnj})/2$ enters into equilibrium equations (Ampere equations).

Let's consider the divergence of the equilibrium equations:

$$\sigma_{ij,ij} + J_{i,i} = 0 \qquad (24)$$

which we can call as the general law of conservation of 4D-current.

Using the first Eq. (23) we rewrite the law of conservation of 4D-current (24) in a form that explicitly includes the differential operator on the value $R^2_{k,k}$:

$$\begin{aligned}&(C_1 + C_5 + C_8)\delta^*_{ij}\delta^*_{nm}R_{n,mji}+ \\ &+ (C_2 + C_7 + C_9)\delta^*_{nm}N_iN_jR_{n,mji}+ \\ &+ (C_2 + C_6 + C_9)\delta^*_{ij}N_nN_mR_{n,mji}+ \\ &+ C_4N_iN_jN_nN_mR_{n,mji} + J_{i,i} =\end{aligned}$$

$$\begin{aligned}
&= [(C_1 + C_5 + C_8)\delta^*_{ij} + (C_2 + C_7 + C_9)N_i N_j]R_{k,kji} + \\
&+ [(C_2 + C_6 + C_9) - (C_1 + C_5 + C_8)]\delta^*_{ij} N_n N_m R_{n,mji} + \\
&+ [C_4 - (C_2 + C_7 + C_9)]N_n N_m N_i N_j R_{n,mji} + J_{i,i} = 0
\end{aligned}$$

Formally, to satisfy last equality it is necessary to require the equality to zero of all four linear combinations of moduli with differential operators of the vector-potential. However, if we assume the necessity for further to introduce some calibration similar to of Lorenz calibration $R_{k,k} = 0$, we can limit ourselves by requirements:

$$\begin{cases} [(C_2 + C_6 + C_9) - (C_1 + C_5 + C_8)] = 0 \\ [C_4 - (C_2 + C_7 + C_9)] = 0 \end{cases}$$

Hence, we can get the following relationships:

$$\begin{cases} (C_2 + C_6 + C_9) = (C_1 + C_5 + C_8) = C_0 \\ C_4 = (C_2 + C_7 + C_9) \end{cases} \Rightarrow \begin{cases} (C_1 + C_8) = C_0 - C_5 \\ (C_2 + C_9) = C_0 - C_6 \\ C_4 = C_0 - C_6 + C_7 \end{cases} \quad (25)$$

Then, the law of conservation of 4D-current takes the form:

$$[C_0(\ldots)_{,ij}\delta^*_{ij} + (C_0 - C_6 + C_7)(\ldots)_{,ij} N_i N_j]R^2_{k,k} + J_{i,i} = 0 \quad (26)$$

Let's consider the equilibrium equations $\sigma_{ij,j} + J_i = 0$. Taking into account (24), Lemmas 3 and 4 leads to the following equations:

$$\begin{aligned}
&\sigma_{ij,j} + J_i = C_0 R_{k,ki} - 2\mu C_5 H_{p,q} \text{Э}_{pqic} N_c - \\
&-(2C_6/\varepsilon) i (D_{i,j} N_j - D_{j,j} N_i) + J_i = 0
\end{aligned} \quad (27)$$

Thus, with use Eqs. (25)–(27) we can set the essential conditions to ensure that, the equilibrium equations (27) would be strictly to the 4D-Ampere equations (19), (20) and the law of conservation 4D-current (15) would be identically satisfied. These are the following conditions:

$$(C_0 R_{k,k})_{,i} = 0, \quad \begin{cases} (C_1 + C_8) = C_0 - 1/(2\mu) \\ (C_2 + C_9) = C_0 + \varepsilon/2 \\ C_4 = C_0 \end{cases} \quad \begin{cases} C_5 = 1/(2\mu) \\ C_6 = -\varepsilon/2 \\ C_7 = -\varepsilon/2 \end{cases} \quad (28)$$

Accordingly to (28), the tensor of modules can be written in the form:

$$\begin{aligned}
&C_{ijnm} = \\
&= C_0(\delta_{ij}\delta_{nm} + \delta_{im}\delta_{nj})/2 + \\
&+ (C_1 - C_8)(\delta^*_{ij}\delta^*_{nm} - \delta^*_{im}\delta^*_{nj})/2 +
\end{aligned}$$

$$\begin{aligned}&+(C_2-C_9)(\delta^*_{nm}N_iN_j+\delta^*_{ij}N_nN_m-\delta^*_{nj}N_iN_m-\delta^*_{im}N_nN_j)/2+\\&+(2\delta^*_{in}\delta^*_{jm}-\delta^*_{ij}\delta^*_{nm}-\delta^*_{im}\delta^*_{nj})/(4\mu)+\\&+(\varepsilon/2)(\delta^*_{nm}N_iN_j+\delta^*_{ij}N_nN_m+\delta^*_{nj}N_iN_m+\\&+\delta^*_{im}N_nN_j-2\delta^*_{jm}N_iN_n-2\delta^*_{in}N_jN_m)/2\end{aligned}\tag{29}$$

The difference between the classical electrodynamics and its non-classical analogue is reduced to the differences in the structure of tensor $C_{ijnm}$ in accordance with (21) and (29). Hooke's law equations for mechanical analogues of "stresses" of the electromagnetic field take the form:

$$\begin{cases}p_k=\varepsilon\dot{a}_k/(2c^2)+(C_0-C_2+C_9+\varepsilon/2)\varphi_{,m}\delta^*_{mk}/2\\q_k=(C_0-C_2+C_9+\varepsilon/2)\dot{a}_k/2+\varepsilon c^2\varphi_{,m}\delta^*_{mk}/2\end{cases}$$

$$\begin{cases}p\;=[2C_0+C_1-C_8-1/(2\mu)]a_{k,k}+(C_0+C_2-C_9+\varepsilon/2)3\dot{\varphi}/2\\T\;=(C_0+C_2-C_9+\varepsilon/2)a_{k,k}/2+C_0^{22}\dot{\varphi}\end{cases}$$

$$\begin{cases}\tau_{pq}=(C_0-C_1+C_8+1/(2\mu))(\delta^*_{mp}\delta^*_{nq}/2+\delta^*_{mq}\delta^*_{np}/2-\delta^*_{mn}\delta^*_{pq}/3)a_{n,m}/2\\\tau_k=[-C_0+C_1-C_8+3/(2\mu)]a_{n,m}Э_{nmkp}N_p/2\end{cases}$$

The resulting structure of the stress tensor for the four dimensions continuum of non-classical electrodynamics can be simplified by analogy with the theory of connected dynamic thermo-elasticity and hyperbolic heat conduction through the introduction of a similar simplifying hypotheses [15, 17]. It was defined "Hooke's law" for the heat flux $q_k$ in the form of a weakened Fourier hypothesis. It lies in the fact that the 3D-vector of the heat flow in the general case is represented by gradient of some 3D-scalar. Then, the heat flux is potential and can not have curls. The analogue of "weakened Fourier hypothesis"—the heat flow is potential, for $q_k=(\varepsilon c^2\varphi/2)_{,m}\delta^*_{mk}$ gives:

$$(C_0-C_2+C_9+\varepsilon/2)=0$$

An analogue of the "hypothesis of the classicism of impulse" for $p_k$ in the four dimensions continuum of non-classical electrodynamics is performed at the same time automatically:

$$p_k=\varepsilon\dot{a}_k/(2c^2)$$

An analogue of the "hypothesis of the symmetry of spatial tangent stresses," for $\tau_k=0$, in the four dimensions continuum of non-classical electrodynamics gives:

$$[-C_0+C_1-C_8+3/(2\mu)]=0$$

From the point of view of non-classical electrodynamics, interaction with spatially-isotropic material can be carried out in a wide range of interactions. In particular, as in classical electrodynamics—through the spatial unpaired tangent stresses by the magnetic field and through impulses and heat flows by the electric field. Additionally, in contrast to the classical electrodynamics—through temperature $T$ and pressure $p$ by means of two linear combinations of the magnetic $a_{n,m}\delta^*_{nm}$ and electric $\dot{\varphi}$ potentials as well as through the analogue of deviator of tangent stresses $\tau_{pq}$ by the non-classical linear differential operator of the magnetic potential.

## 4 Conclusion

On the basis of mechanistic analogue it was implemented the modification of the equations of electrodynamics, leading to the fact that the tensor of "stresses" may not necessarily be purely anti-symmetric. In this case, 4D-equations of Faraday and Ampere and the law of conservation of 4D-current retain their classic form. Uncertain symmetry of electromagnetic "stresses" makes it possible to construct a bilinear form of energy of interaction of electromagnetic field with isotropic material and to predict new effects of their interaction, such as: dynamic, thermal and striction.

It should be noted that this work is purely theoretical, and the existence of non-classical effects in force interactions of the electromagnetic field should be checked experimentally.

**Acknowledgements** The authors are deeply grateful to Professor Dmitriy Indeitsev for professional criticism and extremely useful discussions of our research.

This work was partially supported by the grants RFBR 18-29-10085-mk, 18-01-00553-a, RFBR 18-08-00643-a, MK-1336.2017.8 and funding of IAM RAS program.

## References

1. Maxwell, J.C.: On physical lines of force. Phil. Mag. **90**, 11–23 (1861)
2. Maxwell, J. C.: On Faraday's lines of force. Trans. Camb. Philos. Soc. **10** Part I, 27–65 (1864)
3. Maxwell, J.C.: A dynamical theory of the electromagnetic field. Philos. Trans. R. Soc. Lond. **155**, 459–512 (1865)
4. Eringen, A.C.: A unified continuum theory of electrodynamics of liquid a unified continuum theory of electrodynamics of liquid crystals. Int. J. Eng. Sc. **35**(12/13), 1137–1157 (1997)
5. Maugin, G.A.: Further comments on the equivalence of Abraham's, Minkowski's, and others' electrodynamics. Can. J. Phys. **58**, 1163–1170 (1980)
6. Eringen, A.C., Maugin, G.A.: Electrodynamics of continua, 2. Springer, NY (1990)
7. Maugin G.A.: On the universality of the thermomechanics of forces driving singular sets. Arch. Appl. Mech.**70** 31–45, Springer (2000)
8. Fomethe, A., Maugin, G.A.: Material forces in thermoelastic ferromagnets. Continuum Mech. Thermodyn. **8**, 275–292 (1996)
9. Epstein, M., Maugin, G. A.: Thermoelastic material forces: definition and geometric aspects. C.R. Acad. Sci. Paris II-320, 63–68 (1995)

10. Hernandezjr, W.: Elasticity theory in general Phys. Rev.v. **1**(415), 1013–1018 (1970) (Google Scholar)
11. Lurie, S. A., Belov, P.A.: Mathematical models of continuum mechanics and physical fields, Izd-vo VTs, Moscow, (2000) [in Russian] (Google Scholar)
12. Lurie, S. A., Belov, P.A.: A variational model for nonholonomic media. Mekh. Komp. Mater. Konstr. **7**(2), 266–276 (2001) [J. Comp. Mech. Design (Engl. Transl.)] (Google Scholar)
13. Belov, P.A., Gorshkov, A.G., Lurie, S.A.: Variational model of nonholonomic 4d-media. Mech. Solids **41**(6), 22–35 (2006)
14. Belov, P.A., Lurie, S.A.: Models of deformation of solids and their analogs in field theory. Mech. Solids **43**(3), 128–136 (1998) (Google Scholar)
15. Belov, P.A., Lurie, S.A.: Ideal nonsymmetric 4d-medium as a model of invertible dynamic thermoelasticity. Mech. Solids **47**(5), 580–590 (2012)
16. Belov, P.A., Lurie, S.A.: Theory of 4D-media with stationary dislocations. Mech. Solids **43**(4), 545–557 (2008)
17. Lurie, S.A., Belov, P.A.: Theory of space-time dissipative elasticity and scale effects. Nanoscale Syst. Math. Model. Theory Appl. **2**, 66–178 (2013)
18. Gusev, A., Lurie, S.: Theory of spacetime. Elast. Int. J. Mod. Phys. **26**(05), 50032 (2012)
19. Gusev, A., Lurie, S.: Wave-relaxation duality of heat propagation in fermi-pasta-ulam chains. Mod. Phys. Lett. B **26**(22), 1250145 (2013)

# Kinetic Theory of Dislocation and Mesoscale Formation in Dynamically Deformed Solids

**Yu. I. Meshcheryakov**

**Abstract** The tensor form of dislocation velocity distribution function is introduced. The first and second statistical moments of the distribution function are constructed to coincide with the dynamic variables of continuous theory of dislocation—tensor of dislocation density and tensor of dislocation flow. By using this approach, the problem on mesoscale formation under shock loading is solved. The dynamic mesoparticles are found to be the short-living groups of one-sigh dislocations. Under conditions of dynamic deformation, such a kind of moving mesoparticles generate the velocity pulsations which are experimentally registered as a mesoparticle velocity dispersion. The mesoparticles in form of grains of powder has been discovered in spall zone of target where all-round tension conditions allow to conserve the mesoparticles as separate formations.

**Keywords** Dynamic deformation · Dislocation velocity · Tensor distribution function · Mesoparticle · Velocity dispersion

## 1 Introduction

The problem of description of multiscale dynamic plasticity is a subject of intensive investigations for last fifty years. As the first step, so-called Gilman-Johnston dislocation model was developed as constitutive equation for locking the balance equation of dynamically deformed medium. The main merit of this approach is proof of the fact that direct transition from dislocation dynamic to macroscopic description of dynamic deformation isn't possible as for the adequate description of dynamic deformation the initial dislocation density must be increased by 2–3 order, which isn't corresponds to reality [1]. Besides, there are additional restrictions peculiar to the approach: (i) one-dimensional character model; (ii) the model deals with multiplication and motion of rectilinear dislocations; (iii) stochastic character of dislocation

---

Yu. I. Meshcheryakov (✉)
Institute of Problems of Mechanical Engineering RAS, Saint-Petersburg, Russia
e-mail: ym38@mail.ru

H. Altenbach et al. (eds.), *Dynamical Processes in Generalized Continua and Structures*, Advanced Structured Materials 103,
https://doi.org/10.1007/978-3-030-11665-1_22

motion isn't taken into account. As additional mechanism of plastic deformation the so-called mesoscopic scale has been introduced. It is thought to occupy an intermediate position between atom-dislocation scale and macroscale [2–5]. However, as J. R. Asay noticed, "mesoscale still does not incorporate into shock-wave process" [6].

In the case of dynamic processes in solids, an attempt to introduce multiscale mechanisms of deformation faces three problems: (i) how dynamic mesoparticles are formed; (ii) how to account for the mechanisms of dynamic deformation at the mesoscale; (iii) how to account for the transition from one scale to another. It is clear that deterministic approach to multiscale dynamic deformation is not possible. Firstly, the elementary deformation mechanisms at different scales work in parallel and, secondly, weight and deposit of different mechanisms into total deformation depend on strain rate. The well-known Ashby's formula [7]

$$\Delta\rho \equiv \rho_{ik}^{+} - \rho_{ik}^{-} = -\frac{1}{b} e_{ijl} \frac{\partial \varepsilon_{jk}}{\partial x_l},$$

which links the crystal lattice curvature and dislocation density proves to be applicable only for perfect crystals. Here $\rho_{ik}^{+}$ and $\rho_{ik}^{-}$ are the densities of positive and negative dislocations, $b$ is the Burgers vector, $e_{\mathrm{ijk}}$ is the Levi-Chivita tensor and $\varepsilon_{jk}$ are the deformation tensor components.

The objective of this paper is to develop the dislocation theory which could satisfy the following requirements: (i) to be three-dimensional; (ii) to reflect statistical character of dislocation motion; (iii) to provide the natural transition from dislocation scale to mesoscale.

Solution to above problems is subdivided by two stages.

1. Working out the kinetic theory of continuously distributed dislocations.
2. Elaboration of mesostructure formation as collectivization process of dislocations.

## 2 Kinetic Theory of Continuously Distributed Dislocations

To date the clear understanding of the mechanics of multiscale dynamic deformation is absent. Specifically, it is not revealed the following features of multiscale dynamic deformation;

(a) what dynamic mesoparticle represents as elementary carrier of deformation;
(b) how the forming of mesoparticle occurs in the process of dynamic deformation;
(c) how the statistical nature of motion of elementary carriers of deformation may be taken into account.

The answers may be found by using the kinetic description of dislocation continuum in which dislocation densities and flows are determined as averaged values of velocity distribution function. The kinetic equation for the distribution function must be self-consistently linked with the stress and strain fields through the continuous theory of dislocations. When applied to high-velocity deformation processes in solids, the theory must take into account: (i) inertial properties of elementary carriers of deformation; (ii) dissipative character of dislocation motion; (iii) long-range interaction dislocation with each other; (iv) collective features of dislocations.

Development of kinetic theory of dislocations includes the following steps.

1. Definition of velocity distribution function. Dislocation are considered to be the objects, which in each point in space are characterized by tangent direction to dislocation line and by Burgers-vector; separate segments of the dislocation line may be of different orientations in space and different velocities.
2. Derivation of the kinetic equation for the velocity distribution function. The convective and collision parts of the equation must take into account both the dissipative features of the medium where dislocation move and their mutual long-range interaction.
3. Definition of equilibrium dislocation function.
4. Derivation of the system of moment equations from the kinetic equation. This system must coincide with the well-known equations of the continuous dislocation theory, i.e. the balance equations for the momentum and mass conservation for the medium with dislocations. Different approach based on the statistical dislocation description and the Kirkwood transport equation system has been developed by Zorski [8].

In this study we follow the above sequence in designing the kinetic theory of dislocations. Taking into account the configurational complexity of dislocations, it thought to be appropriate to use the tensor description of the dislocation continuum. Such description is used in continuous dislocation theory where the dislocations density is a second rank tensor. The first index characterizes the tangent direction to the dislocation line and the second one is the direction of the Burgers vector. According to this definition $f_{ik}\left(\vec{r}, \vec{v}, \vec{t}\right)d\vec{r}, d\vec{v}, d\vec{t}$ is a mathematical expectation of the number of dislocation segments of type *ik* in the volume *dr* at the moment from *t* to *t* + *dt* with the velocities in the range from *v* to *v* + *dv*. The zero moment of the distribution function obtained by velocity averaging

$$\rho_{ik}(\vec{r}, t) = \int\limits_{-\infty}^{\infty} f_{ik}(\vec{r}, \vec{v}, t)d\vec{v} \tag{1}$$

yields the dislocation density tensor.

The first statistical moment of the distribution function defines the so-called dislocation velocity tensor or dislocation flow tensor:

$$J_{ij}(\vec{r}, t) = e_{ikl} \int\limits_{-\infty}^{\infty} v_l f_{kj}(\vec{r}, \vec{v}, t)d\vec{v} \tag{2}$$

In such definition, the first and second statistical moments of the distribution function coincide with the dislocation density tensor and dislocation flow tensor introduced in the continuous theory of dislocations. The restrictions on dislocation motion in continuum theory must also be correct for the distribution function. Specifically, from definition of dislocation density

$$\rho_{ik} = -e_{ilm} \frac{\partial w_{mk}}{\partial x_l}$$

it follows:

$$\frac{\partial \rho_{ik}}{\partial x_i} = 0$$

Accordingly, an analogous restriction must be applied to components of the velocity distribution function:

$$\frac{\partial f_{ik}}{\partial x_i} = 0, \tag{3}$$

which means the conservation condition for the Burgers vector along the dislocation line. The average flow of *ik*-dislocations in the direction *p* can be expressed in terms of the dislocation density tensor as

$$J_{ik} = e_{ijp} u_p \rho_{jk}, \tag{4}$$

where $u_p$ is the *p*-component of the average dislocation velocity which can be expressed in terms of the instantaneous velocity *v* and the relative velocity *c*:

$$c_p = v_p - u_p. \tag{5}$$

By analogy with the kinetic theory of gas and fluids, one can introduce the subsequent moments of the distribution function in the form:

$$J_{ij}(\vec{r}, t) = e_{ikl} \int_{-\infty}^{\infty} v_l f_{kj}(\vec{r}, \vec{v}, t) d\vec{v} \tag{6}$$

$$P_{\ln} = e_{ijk} \int_{-\infty}^{\infty} c_l c_k f_{jn} d\vec{v}, \tag{7}$$

$$Q_{mjn} = e_{jkl} e_{ils} \int_{-\infty}^{\infty} c_m c_k c_s f_{\ln} d\vec{v}. \tag{8}$$

Value $mc_k c_l f_{jn}$ characterizes a carrying over the $l$-component of elementary momentum in $k$-direction with dislocation segments of kind $jn$, having the velocities within interval $\vec{v}$ and $\vec{v} + d\vec{v}$. In this case, $\overset{\frown}{P}$ is the analog of stress tensor in the kinetic theory of gas whereas the diagonal elements determine the energy of chaotic motion on the background of flow motion of dislocations with the average velocity $\vec{u}$. Lastly, curl of third statistical moment $Q_{jjn}$ can be identified with the flow of chaotic motion of dislocations.

The common form of kinetic equation can be written in the form:

$$\frac{D\hat{f}}{Dt} = H_c. \tag{9}$$

Kinetic equation for the continuously distributed dislocation must include both the redistribution of dislocations in volume and change of their total number.

The left hand side of this equation represents the convective part of the kinetic equation whereas the right hand side part is the so-called collision part:

$$\frac{D\overset{\frown}{f}}{Dt} = \frac{\partial \overset{\frown}{f}}{\partial t} + \nabla_r \times \left(\vec{v} \times \overset{\frown}{f}\right) + \nabla_v \times \left(\frac{\partial \vec{v}}{\partial t} \times \overset{\frown}{f}\right) = H_c \tag{10}$$

Here $H_c$ is the collision item which takes into account nucleation, annihilation and interaction of dislocations. The components of dislocation acceleration $\frac{\partial \vec{v}}{\partial t}$ can be determined from the equation of dislocation motion:

$$m\frac{\partial \vec{v}}{\partial t} = \vec{F} - B\vec{v}, \tag{11}$$

where $m$ is the "effective" dislocation mass, $\vec{F} = \hat{\sigma}\vec{b}$ is the Peach-Koehler force due to external action onto dislocation and $B$ is the dislocation damping coefficient which takes into account the interaction of moving dislocation with the medium. Then in one-dimensional case the kinetic equation has the form:

$$\frac{\partial \overset{\frown}{f}}{\partial t} + \vec{v}\frac{\partial \overset{\frown}{f}}{\partial \vec{x}} + \left(\frac{\vec{F}}{m} + \frac{B}{m}\vec{v}\right)\frac{\partial \overset{\frown}{f}}{\partial \vec{v}} + \frac{B}{m}\overset{\frown}{f} = H_c. \tag{12}$$

One can see that convective part of the kinetic equation, due to dependence of the acceleration of dislocations on their velocity, differs from that in classical mechanics of fluids and gas where the particles interact with each other only. Both additional terms $\frac{B}{m}v_x$ and $\frac{B}{m}f$ show the dependence of dislocation motion on their dissipative interaction with the medium through the damping coefficient $B$. The collision item includes two components every of which takes into account different kinds of interaction inside the dislocation continuum: $H_c = H_c^1 + H_c^2$. For the case when only a space redistribution of dislocation is taken into account, without change of their density, it is thought to be sufficient to leave the first component only. In the case when processes of nucleation and annihilation of dislocation are also important, both items should be taken into account.

In our theory, the collision part of the kinetic equation $H_c$ is introduced in the Fokker-Plank form:

$$H_c = -\nabla_v \times (D_1 \times \hat{f}) + \frac{1}{2}\nabla_v\nabla_v : (D_2 \times \hat{f}). \tag{13}$$

Here $D_1$ and $D_2$ are the Fokker-Plank diffusion coefficients. $D_1$ is the dynamic friction coefficient and $D_2$ is the coefficient of diffusion in the velocity space.

Now we in position to write the expression for the equilibrium form of distribution function. For that we'll use the Fokker-Plank form of the collision integral. Combination of (11) and (12) yields:

$$\frac{\partial^2}{\partial^2}(D_2 f) - 2\frac{\partial}{\partial f}(D_1 f) - 2\left(\frac{F}{m} - \frac{B}{m}v\right)\frac{\partial f}{\partial v} + 2\frac{B}{m}f = 0. \tag{14}$$

In this analysis, we'll assume that in equilibrium situation the diffusion coefficient doesn't depend on dislocation velocity, which makes it possible to write the equilibrium equation in the form:

$$\frac{\partial^2 f}{\partial v^2} - \frac{2}{D_2}\left(\frac{F}{m} - \frac{B}{m}v\right)\frac{\partial f}{\partial v} + 2\frac{B}{D_2 m}f = 0. \tag{15}$$

If the integration constant is determined from the condition of constancy for dislocation density, the solution to Eq. (15) yields:

$$f_0(x, v) = \left(\frac{B}{D_2 m}\right)^{1/2} \rho(x)\, \exp\left[-\frac{B}{D_2 m}\left(v - \frac{F}{m}\right)^2\right]. \tag{16}$$

The above expression characterizes the equilibrium velocity distribution function for one-dimensional motion of dislocations. The equilibrium distribution corresponds to a mean dislocation velocity $u = \frac{F}{m} = \frac{\sigma b}{m}$ and a velocity dispersion $\langle \Delta v \Delta v \rangle = \frac{D_2 m}{B}$.

### Diffusion Coefficients

The coefficient $D_1 = \frac{\langle \Delta v \Delta v \rangle}{\Delta t}$ calls the dynamic friction coefficient. The value $m\frac{\langle \Delta v \Delta v \rangle}{\Delta t}$ is a friction force directed opposite to mean dislocation velocity $u$. In the case of Fokker-Plank equation, the collision integral $H_c$ includes only the mutual interactions of dislocations. The breaking force due to this interaction is of fluctuative nature. The breaking force due to interaction of dislocations with the medium is taken into account in convective part of the kinetic equation.

It has been shown by Hubburd [9] that the coupling between first and second diffusion coefficients of the Fokker-Plank equation has the form:

$$D_1 = \frac{1}{2}\frac{\partial}{\partial v}\left[\frac{\langle \Delta v \Delta v\rangle}{\Delta t}\right] = \frac{1}{2}\frac{\partial}{\partial v}(D_2). \tag{17}$$

Then the collision integral can be written in a more explicit form:

$$H_c = \frac{\partial^2}{\partial v^2}\left(D_2 \hat{f}\right). \tag{18}$$

Now our goal is to obtain expression for $D_2$. The latter can be obtained with the help of the stress correlation function according to the following:

$$D_2 = \frac{\langle \Delta v \Delta v\rangle}{\Delta t} = \frac{b^2}{m^2}\int\limits_{-\infty}^{\infty} \left\langle \hat{\sigma}(0,0)\hat{\sigma}(v\tau,\tau)\right\rangle dt, \tag{19}$$

where $\langle \sigma\sigma\rangle$ is the stress correlation function.

Derivation of the stress correlation function is based on the use of the continuous dislocation theory developed by Mura [10], Kosevich and Natzic [11]:

$$\rho_0 \frac{\partial^2 U_m}{\partial t^2} = \frac{\partial \sigma_{mn}}{\partial x_{n;}}; \quad \frac{\partial w_{mn}}{\partial t} = \frac{\partial v_m}{\partial x} + J_{mn};$$
$$\sigma_{ik} = \lambda_{iklm} w_{lm}; \quad \rho_{ik} = e_{ikl}\frac{\partial w_{lm}}{\partial x_m}. \tag{20}$$

Here $w_{lm}$—are the components of distortion tensor, $U$ is the displacement, $\rho_0$—is the mass density of medium, $\sigma_{ik}$ are the components of stress tensor and $\lambda_{iklm}$ are the elastic modulus components. Define the Fourier-components of displacement and stress tensor through the integrals:

$$U_k(r,t) = \int\int U_k(\vec{k},\omega) e^{i\vec{k}\vec{r} - i\omega t} d\vec{k} d\omega$$
$$\sigma_{pq}(r,t) = \int\int \sigma_{pq}(\vec{k},\omega) e^{i\vec{k}\vec{r} - i\omega t} d\vec{k} d\omega$$

In common case, the coupling between stress and distortion can be written in the form:

$$\sigma_{pq}(\vec{r},t) = \int\limits_{-\infty}^{t} dt' \int\limits_{-\infty}^{\infty} dr' \, \lambda_{pqmn}(\vec{r} - \vec{r}', t - t') w_{mn}(\vec{r}', t'),$$

or, in Fourier representation:

$$\sigma_{pq}(\vec{k},\omega) = \lambda_{pqmn}(\vec{k},\omega) w_{mn}(\vec{k},\omega).$$

In turn, the Fourier-components of elastic distortion tensor can be written through components of dislocation flow tensor [11]:

$$w_{mn}(\vec{k}, \omega) = \frac{1}{\omega}(\lambda_{ijkl} G_{km} k_l k_n - \delta_{mi}\delta_{nj}) J_{ji}, \tag{21}$$

where $G_{km}$ is the Green-function of dynamic theory of elasticity, $J_{ji}$ is the flow dislocation tensor. Accordingly, the Furrier components of stress tensor equal:

$$\sigma_{pq}(\vec{k}, \omega) = \frac{1}{\omega}\lambda_{pqmn}(\lambda_{ijkl} G_{km} k_l k_n - \delta_{mi}\delta_{nj}) J_{ji}. \tag{22}$$

Let as to write the expression for the stress correlation function $\left\langle \hat{\sigma}(\vec{r}, t)\hat{\sigma}(\vec{r} + \vec{s}, t + \tau) \right\rangle$, which should be understood as mean of product of two stress values in the points $\vec{r}$ and $\vec{r} + \vec{s}$ at the moments of $t$ and $t + \tau$. In Furrier representation the stress correlation function equals:

$$\begin{aligned}&\left\langle \hat{\sigma}(\vec{r}, t)\hat{\sigma} \right\rangle \left\langle \hat{\sigma}(\vec{r}, t)\hat{\sigma}(\vec{r} + \vec{s}, t + \tau) \right\rangle \\ &= \int\int\int\int \left\langle \sigma(\vec{k}', \omega')\sigma(\vec{k}, \omega) \right\rangle \exp\left[ i\vec{k}'\vec{r} + i\vec{k}(\vec{r} + \vec{s}) - i\omega' t - i\omega(\tau + t) \right] d\vec{k}' d\omega' d\vec{k}\, d\omega\end{aligned}$$

In Fourier representation this integral can be written through $\delta$-functions:

$$\left\langle \hat{\sigma}(\vec{k}', \omega')\sigma(\vec{k}, \omega) \right\rangle = \left( \hat{\sigma}\hat{\sigma} \right)_{\vec{k}\omega} \delta(\vec{k} + \vec{k}')\delta(\omega + \omega'), \tag{23}$$

from where

$$\langle \sigma(\vec{r} + \vec{s}, t + \tau) \rangle = \iint (\hat{\sigma}\hat{\sigma})_{\vec{k}\omega} e^{i\vec{k}\vec{r} - i\omega t} d\vec{k} d\omega. \tag{24}$$

Expression (24) can be considered as definition of value $(\vec{\sigma}\vec{\sigma})_{\vec{k}\omega}$, which is the Fourier-amplitude of correlation function. When $s = 0$ and $\tau = 0$ the value $(\vec{\sigma}\vec{\sigma})_{\vec{k}\omega}$ has a meaning of spectral density of mean-square stress fluctuations:

$$\left\langle \hat{\sigma}\hat{\sigma} \right\rangle = \iint \left( \hat{\sigma}\hat{\sigma} \right)_{\vec{k}\omega} d\vec{k} d\omega \tag{25}$$

Using the relationships of dynamic elasticity theory, the expression (25) allows to link the stress correlation function and correlation function of dislocation flow:

$$\left\langle \sigma(\vec{k}', \omega')\sigma(\vec{k}, \omega) \right\rangle = -\frac{\eta\eta}{\omega^2} \left\langle \hat{J}(\vec{k}', \omega')\hat{J}(\vec{k}, \omega) \right\rangle \tag{26}$$

where

$$\eta_{pqij} = \lambda_{pqmn}(\lambda_{ijkl} k_l k_m - \delta_{mj}\delta_{nj}). \tag{27}$$

Introducing the spectral density of means-square density for flow dislocation tensor, by analogy with (24) one obtains:

$$\left(\hat{\sigma}\hat{\sigma}\right)_{\vec{k}\omega} = -\frac{\hat{\eta}\hat{\eta}}{\omega^2}(\hat{J}\hat{J})_{\vec{k}\omega}. \tag{28}$$

The value $\left(\hat{J}\hat{J}\right)_{\vec{k}\omega}$ can be found by using dislocation velocity distribution function. It can be done with a following manner. Components of flow dislocation tensor in point $\vec{r}$ at the moment $t$ are determined as follows:

$$J_{pq}(\vec{r}, t) = e_{pmn} \sum_{j} \rho_{mq} v_n^j \delta(\vec{r} - \vec{r}_j(t)),$$

where $r$ is the position of $j$-dislocation at the moment $t'$, $v_n^j$ is the velocity of $j$-dislocation. In Fourier representation this expression can be written in the form:

$$J(\vec{k}, \omega) = \frac{b^2}{(2\pi)^4} \sum_{j} \vec{v}^j \iint e^{-i\vec{k}\vec{r}_j(t')+i\omega t} dt d\vec{r}.$$

Then for Fourier-amplitude of flow dislocation tensor one obtains:

$$\langle JJ \rangle = \frac{b^4}{(2\pi)^8} \sum_{j} \vec{v}^j \vec{v}^j \iint \iint \left\langle \exp\left[-i\vec{k}'\vec{r}_j(t') - i\vec{k}'\vec{r}_j(t) + i\omega t' + i\omega' t\right]\right\rangle dt dt' d\vec{r} d\vec{r}'$$

In the last expression, the items related to different kinds dislocation are excluded. Let as to express the displacements from position $\vec{r}_j(t)$ to position $\vec{r}_j(t')$ through dislocation velocity $\vec{v}_d$. Taking into account that dislocations of identical kind are not distinguished, one obtains:

$$(JJ) = \frac{b_\theta^2}{(2\pi)^8} \iint \iint \vec{v}^2 f_\theta(\vec{v}) \left\langle \exp\left[-i(\vec{k} + \vec{k}')\vec{r}(t) + i(\omega + \omega')t + i(\omega - \vec{k}\vec{v})\tau\right]\right\rangle d\vec{v} dt d\tau d\vec{r}$$

where $\tau = t - t'$.

Exchange the integral on exponents by $\delta$-functions. Then the expression for correlation function for dislocation flow tensor has the form:

$$\left\langle J(\vec{k}', \omega') J(\vec{k}, \omega)\right\rangle = \frac{b_\theta^2}{(2\pi)^3} \delta(\vec{k} + \vec{k}')\delta(\omega + \omega') \int v^2 f_\theta(\vec{v}) \delta(\omega - \vec{k}\vec{v}) d\vec{v}.$$

Under conditions of $\vec{k} = \vec{k}'$ and $\omega = \omega'$, one obtains the spectral density of mean-square fluctuations for dislocation flow tensor:

$$\left\langle (JJ)_{\vec{k}\omega}\right\rangle = \frac{b_\theta^2}{(2\pi)^3} \int f_\theta(\vec{v}) v^2 \delta(\omega - \vec{k}\vec{v}) d\vec{v}. \tag{29}$$

Then the spectral density of mean-square fluctuations for stress equals:

$$\left(\hat{\sigma}\hat{\sigma}\right)_{\vec{k}\omega} = -\frac{b^2}{\omega^2}(\hat{\eta}\hat{\eta})\int v^2 f_\theta(\vec{v})\delta(\omega - \vec{k}\vec{v})d\vec{v}. \tag{30}$$

Lastly, after summarizing the expressions (22), (24) and (30), one obtains for the diffusion coefficient:

$$D_2 = -\frac{b^4}{(2\pi)^3}\frac{\Delta t}{m^2}\iint \frac{(\eta\eta)}{k^2} f_\theta(\vec{v})d\vec{v}d\vec{k}. \tag{31}$$

Consider the simplest case when motion of dislocations occurs in a single plane and tensor $\left(\hat{\eta}\hat{\eta}\right)$ can simplified up to $\mu^2$. Then the expression (31) reduced to:

$$D_2 = -\frac{b^3}{(2\pi)^3}\frac{\Delta t}{m^2}\mu^2\rho\int\limits_{-\infty}^{\infty}\frac{d\overleftarrow{k}}{k^2}, \tag{32}$$

where $\rho$ is the mean dislocation density according to definition. To avoid the non-physical divergence in the core of dislocation, the cutting procedure on wave vector should be carried out. In this case, as the integration limit, the wave vector $k_0$, may be taken. This wave-vector is determined by the relationship of $k_0 b \approx 1$. Then the diffusion coefficient becomes:

$$D_2 = \frac{1}{(2\pi)^3}\frac{b^4}{\Delta t B^2}\mu^2\rho, \tag{33}$$

Interval $\Delta t$ can be found from equation for dislocation motion (11). Solution to this equation yields the mean dislocation velocity:

$$u_d = \frac{\sigma b}{B}(1 - e^{-\frac{t}{\Delta t}}), \tag{34}$$

where

$$\Delta t = \frac{m}{B} \tag{35}$$

Then the diffusion coefficient takes the form:

$$D_2 = \frac{1}{(2\pi)^3}\frac{b^4}{\Delta t B^2}\mu^2\rho. \tag{36}$$

The velocity dispersion equals:

$$D_{2v} = \langle \Delta v_d \Delta v_d \rangle = \frac{1}{(2\pi)^3} \frac{b^4}{B^2} \mu^2 \rho, \tag{37}$$

which coincides with the expression obtained in [12].

## 3 Transport Equations

During the solution to concrete tasks of dynamic plasticity, the detail description of elementary processes at the microscale with taking into account the velocity distribution is not always necessary. There is a lot of dynamic processes in solids which can be solved at the so-called hydrodynamic scale. The macroscopic equations deal with the averaged characteristics of inner structure in form of the so-called "representative volume". If instead, the moment equations for elementary carriers of deformation (ECD) are obtained by means of averaging the kinetic equation for the elementary carriers of deformation (ECD), one obtains the solution at the hydro-dynamical scale for ECD only. In this case, to link the behavior of ECD with the macroscopical values, such as mean stress and strain one has to use continual theory of dislocations. Just that approach is used in the our paper. At the beginning, the mean densities and mean flow velocities for ECD are found, and after that macroscopic variable can be expressed. The transport equation for dislocations can be obtained from the kinetic equation by using the formal procedure which is commonly used in mechanics of gas and fluids. In accordance with this procedure, the moment equations are obtained by means of multiplying the kinetic equation by reciprocal degree of particle velocity and following integration in velocity space [13].

To obtain the zero statistical moment of kinetic equation the latter must be multiplyed by the zero degree of dislocation velocity, i.e. by unit, and integrate on velocities. During the formal procedures of integration it is necessary to take into account the tensor character of the dislocation velocity distribution function and remember about impossibility to move along the dislocation line. The integration of left (convective) part of kinetic equation yields [14]:

$$\begin{aligned}
&(a) \quad \int \frac{\partial \hat{f}}{\partial t} d\vec{v} = \frac{\partial}{\partial t} \int \hat{f} d\vec{v} = \frac{\partial}{\partial t} \hat{\rho}; \\
&(b) \quad \int \frac{\partial}{\partial \vec{v}} \times \left( \vec{v} \times \hat{f} \right) d\vec{v} = 0; \\
&(c) \quad \int \frac{\partial}{\partial \vec{r}} \times \left( \vec{v} \times \hat{f} \right) d\vec{v} = \frac{\partial}{\partial \vec{r}} \times \int \left( \vec{v} \times \hat{f} \right) d\vec{v} = \frac{\partial}{\partial \vec{r}} \times \hat{J}.
\end{aligned} \tag{38}$$

The second item disappears as the distribution function equal zero on integration limits. For the collision item $H''$ one obtains:

$$(a) \quad \int \alpha \left( \vec{v} \times \hat{f} \right) d\vec{v} = \alpha \hat{J};$$

$$(b) \qquad \int \beta \hat{f}(\vec{v}')d\vec{v}' \int \hat{f}(\vec{v})d\vec{v} = \beta \hat{\rho}\hat{\rho}, \tag{39}$$

so the collision item has the form:

$$H'' = \alpha \hat{J} - \beta \hat{\rho}\hat{\rho}. \tag{40}$$

To obtain the Fokker-Plank part of collision item $H'$, let us multiply the expression (10) by function $\varphi(\vec{v})$ and integrate in the velocity space:

$$\begin{aligned}\int \varphi(\vec{v})\left[-\frac{\partial}{\partial v_\mu}(D_{1\mu} f_{ij}) + \frac{1}{2}\frac{\partial}{\partial v_\mu}\frac{\partial}{\partial v_\nu}(D_{2\nu\mu} f_{ij})\right]d\vec{v} \\ = \int \frac{\partial \varphi}{\partial v_\mu}(D_{1\mu} f_{ij})d\vec{v} - \frac{1}{2}\int \frac{\partial \varphi}{\partial v_\mu}\frac{\partial}{\partial v_\nu}(D_{2\nu\mu} f_{ij})d\vec{v}.\end{aligned}$$

The items in the right hand side of equation equal to zero because of the relationship (17) between diffusion coefficients. This means that long-range interaction between dislocations in Fokker-Plank collision item doesn't influence on macroscopic carrying over the momentum and energy. This carrying over is described by the second part of collision item $H'$. Summarizing (38) and (39) yields the ultimate form of zero moment of kinetic equation:

$$\frac{\partial \hat{\rho}}{\partial t} + \frac{\partial}{\partial \vec{r}} \times \hat{J} = \alpha \hat{J} - \beta \hat{\rho}\hat{\rho}. \tag{41}$$

The Eq. (41) coincides with the analogous equation of continual dislocation theory. If the sources and stops of dislocations are absent, this equation means the Burgers-vector conservation law.

In order to derivate the transport equation corresponding to the second statistical moment of kinetic equation one must multiply the latter by $\vec{v}$ and integrate in velocity space. The first item in left hand side gives:

$$\int \vec{v} \times \frac{\partial \hat{f}}{\partial t}d\vec{v} = \frac{\partial}{\partial t}\int \left(\dot{\vec{v}} \times \hat{f}\right)d\vec{v} - \int \left(\vec{v} \times \hat{f}\right)d\vec{v}. \tag{42}$$

To determine the acceleration of dislocations $\overrightarrow{\dot{v}}$ in the second item, one can use the equation of dislocation motion (11):

$$\int \vec{v} \times \frac{\partial \hat{f}}{\partial t}d\vec{v} = \frac{\partial}{\partial t}\hat{J} - \frac{1}{m}\hat{\sigma} \times \hat{\rho} + \frac{B}{m}\hat{J}. \tag{43}$$

$$\int \vec{v} \times \left(\frac{\partial}{\partial \vec{r}} \times (\vec{v} \times \hat{f})\right)d\vec{v} = -\frac{\partial}{\partial \vec{r}}\hat{P} - \frac{\partial}{\partial \vec{r}}\left[\vec{u}(\vec{u} \times \hat{\rho})\right], \tag{44}$$

where $\hat{P}$ is the kinetic stress tensor and $\vec{u}$ is the mean dislocation velocity. The third item in the left hand side of equation looks as follows:

$$\int \vec{v} \times \left[\frac{\partial}{\partial \vec{v}} \times (\vec{v} \times \hat{f})\right] d\vec{v} = \frac{2}{m}\hat{\sigma} \times \hat{\rho} - \frac{2}{m} B\hat{J}. \tag{45}$$

Collision item of equation after multiplying by $\vec{v}$ and integration in velocity space yields:

$$\alpha \int \vec{v} \times (\vec{v} \times \hat{f})\, d\vec{v} = \alpha(\hat{S} + \vec{u} \times \hat{J}). \tag{46}$$

$$\beta \int \vec{v} \times \hat{f}(\vec{v}) \cdot \int \hat{f}(\vec{v}')d\vec{v}d\vec{v}' = \beta \hat{J}\hat{\rho}, \tag{47}$$

where

$$\hat{S} = \int \vec{c} \times (\vec{c} \times \hat{f}) d\vec{v} \tag{48}$$

and $\vec{c} = \vec{v} - \vec{u}$ is the relative velocity of dislocations. Summarizing the right and left parts one obtains for the first moment equation:

$$\frac{\partial \hat{J}}{\partial t} = \frac{\partial}{\partial \vec{r}} \cdot \left(\hat{P} + \vec{u}\hat{J}\right) + \frac{1}{m}\left(\hat{\sigma} \times \hat{\rho} - B\hat{J}\right) = \alpha\left(\hat{S} + \vec{u} \times \hat{J}\right) - \beta \hat{J} \cdot \hat{\rho}. \tag{49}$$

In absence of sources and stops of dislocations, the transport equation for momentum looks as follows:

$$\frac{\partial \vec{u}}{\partial t} \times \vec{\rho} - \frac{\partial}{\partial \vec{r}} \cdot \hat{P} - \frac{\partial}{\partial \vec{r}}\left(\vec{u} \cdot (\vec{u} \times \hat{\rho})\right) + \frac{1}{m}\left[\left(\hat{\sigma} \times \hat{\rho}\right) - B\vec{u} \times \hat{\rho}\right] = 0. \tag{50}$$

This equation is the analog of the well-known equation for momentum transport in two-phase medium. In our case, one of phase is the dislocation structure and another phase is the crystalline lattice.

Let us derivate the second moment equation of kinetic equation. For that we must multiply two times by velocity vector and integrate on velocities. As result one obtains:

$$\begin{aligned}
&\left(\frac{\partial}{\partial t} - \frac{B}{m}\right)\left[\hat{S} - \vec{u} \times (\vec{u} \times \hat{\rho})\right] + \frac{2}{m}\left[\vec{u} \times \left(\hat{\sigma} \times \hat{\rho}\right)\right] - \frac{1}{m}\hat{\sigma} \times \left(\vec{u} \times \hat{\rho}\right) \\
&\quad + \frac{\partial}{\partial \vec{r}}\left\{\hat{Q} + \vec{u}\left[\hat{S} + \vec{u} \times \left(\vec{u} \times \hat{\rho}\right)\right] + \hat{P}_1\right\} = \\
&\quad = \alpha\left\{\vec{u} \times \left[\hat{S} + \vec{u} \times \left(\vec{u} \times \hat{\rho}\right)\right] + \hat{T} - 2\vec{u} \cdot \hat{P}\right\} - \beta\left[\hat{S} + \vec{u} \times \left(\vec{u} \times \hat{\rho}\right)\right] \cdot \hat{\rho}.
\end{aligned} \tag{51}$$

Here the definitions for $\hat{Q}$ and $\hat{S}$ are used.

If $\hat{S}$ is the energy of chaotic motion of dislocations in random stress fields, then the sum $\left[\hat{S} + \vec{u} \times \left(\vec{u} \times \hat{\rho}\right)\right]$ can be related to common energy transported by dislocations. Herewith, the second item being multiplying by dislocation mass has a sense directed carrying over the kinetic dislocation energy. As the value $\hat{Q}$ characterizes a carrying over the chaotic energy (analog of heat flow vector in kinetic theory of gas) Eq. (51) reflects the energy balance in the system of moving dislocations. Interaction with crystalline lattice is described by the item $\frac{B}{m}\left[\hat{S} + \vec{u} \times \left(\vec{u} \times \hat{\rho}\right)\right]$. Action of external forces on dislocation is reflected by the item $\frac{2}{m}\left[\vec{u} \times \left(\hat{\sigma} \times \hat{\rho}\right)\right] - \frac{1}{m}\hat{\sigma} \times \left(\vec{u} \times \hat{\rho}\right)$.

Obtained above system for transport equations for dislocations in crystalline lattice describes the deformation process at the scale level of elementary carriers of deformation. When determined, the characteristics of dislocation motion can be used for determination of macroscopical variables through the continuum theory of dislocation. However, the equation system (50)–(51) remains non-locked till an additional relationship between kinetic tensor $\hat{P}$ and density of dislocations (analog of equation of state in mechanics of fluid and gas) is absent. As a locking equation, the relationship describing the long-range interaction of dislocations can be used:

$$P = -D^2 \oint\limits_{x_1} \frac{\rho(s,t)}{x-s} ds \tag{52}$$

In developed approach, the accent lies in two aspects: (i) kind of rheological coupling between dislocation and medium and (ii) kind of relationship between dislocation themselves. Both kinds of coupling reflect the microscopical features of material.

In the end of this paragraph, let us to write the one-dimensional version of energy carrying over in the case of absence of sources and stops of dislocations:

$$(\frac{\partial}{\partial t} - \frac{B}{m})(S + u^2\rho) + \frac{1}{m}\sigma b u \rho + \frac{\partial}{\partial x}\left[Q + u\left(S + u^2\rho\right) + P_1\right] = 0$$

or

$$\frac{\partial}{\partial t}\left(S + u^2\rho\right) + \frac{1}{m}\sigma b \rho u - \frac{B}{m}\left(S + u^2\rho\right) + \frac{\partial}{\partial x}\left[Q + u(S + u^2\rho) + P_1\right] = 0 \tag{53}$$

Item $\left(S + u^2\rho\right)$ is the total energy of dislocation motion. Here $S$ is the energy of chaotic motion of dislocation and $u^2\rho$ is the energy of translational motion of dislocations with the mean velocity $u$. Thus, Eq. (53) claims that the common energy balance includes the following parts: (i) expenditure on energy of external forces, (ii) ductile breaking in medium where dislocations move, (iii) energy of interaction of dislocations with each other and (iv) heat transportation. In the presence of sources and stops of dislocations, the right hand side of balance equation characterizes the expenditure of external forces on activation of sources and stopping.

## 4 Mesostructure Formation: Theory and Experiment

Obtained in Sect. 3 transport equations for dislocation structure can be applied for building the new approach to solution the real tasks of dynamic plasticity. This approach is based on joint solution to transport equations for moving dislocations. The equations include: (i) interaction of dislocation with the medium through rheological equation for moving dislocations and (ii) interaction dislocations with each other through the equation of state. The equations of continuity and momentum carrying over in one-dimensional case look as follows:

$$\begin{aligned}&\frac{\partial \rho}{\partial t}+\frac{\partial}{\partial x}(\rho u)=0;\\&\rho\frac{\partial u}{\partial t}+\rho u\frac{\partial u}{\partial x}+\frac{\partial P}{\partial x}-\frac{2}{m}(\sigma b-Bu)=0.\end{aligned}\tag{54}$$

Here $\rho$ is the dislocation density, $u$ is the mean velocity of dislocations, $\sigma$ is the external stress, $b$ is the Burgers-vector, $P$ is the stress due to interaction of dislocations with each other and $B$ is the damping coefficient. The Eq. (54) are obtained from the kinetic equation for tensor velocity distribution function, so one-dimensional case corresponds to behavior of one-sign dislocations. In this situation equation system (54) describes the process of grouping of one-sing dislocations, which means that one deals with the formation of mesostructure.

In the second equation kinetic stress tensor $P$, in accordance with the character of interaction of dislocations in elastic medium, can be written in the form of Coashi-integral

$$P=-D^2\oint\limits_{x_1}\frac{\rho(s,t)}{x-s}ds.\tag{55}$$

For the step-like loading of medium, the boundaries conditions take the form:

(1) $v(x,0)=0$
(2) $\rho(x,0)=\rho_0$
(3) $\sigma(0,t)=\sigma(t)$

In the present work, for the solution to this task the modified Picard's method has been used [14]. The solution concerns the step-like loading of A95 aluminum, as fit-parameter, the damping coefficient $B$ is used. The typical space profiles of dislocation density for different values of damping parameter are provided in Figs. 1 and 2. The figures allow to see the kinetics of forming the mesoparticle as results of collectivization of one-sign dislocations. Simulation shows that space profiles for dislocation density are non-monotonous. In Fig. 1 a series of relative dislocation density for damping coefficient value of $B=10^{-5}$ ns for different moments is presented. The moment $t=45$ ns corresponds to beginning the mesoparticle forming when density of dislocation till didn't reach the maximum value. To the moment of $t=60$ ns the relative dislocation density reaches maximum value of $\frac{\rho}{\rho_0}=1,4$. Then

**Fig. 1** Space profiles of one-sign dislocations for $B = 10^{-5}$ ns at time moments: 1—45 ns, 2—60 ns, 3—90 n, 4—120 ns, 5—150 ns

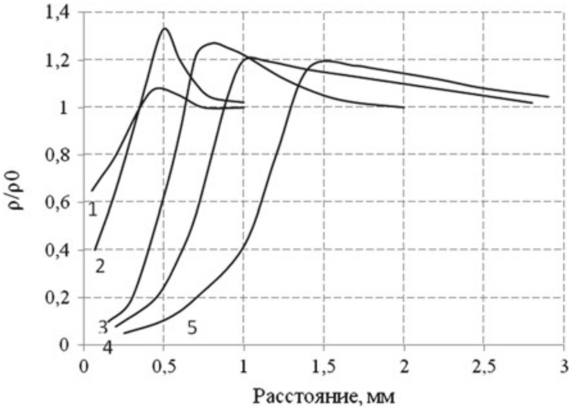

**Fig. 2** Space profiles of one-sign dislocations for B $= 3 \times 10^{-4}$ ns at time moments: 1—45 ns, 2—60 ns, 3—90 n, 4—120 ns, 5—150 ns

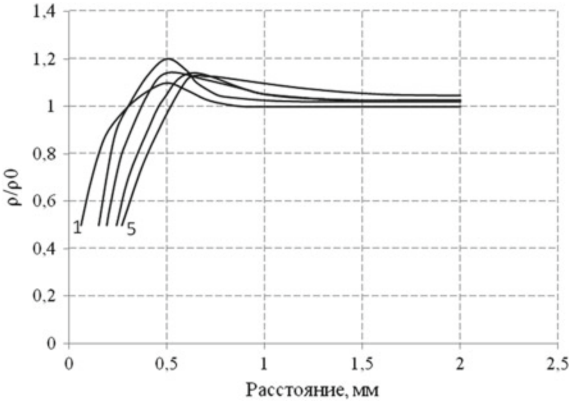

the structure begins to gradually "wash-away" so to the moment of $t = 150$ ns dislocations turn out be uniformly distributed in medium. The life-time of mesoparticle equals 100–150 ns.

The increase of damping coefficient to $B = 3 \times 10^{-4}$ ns leads to stopping of mesoparticle which is localized near the load surface of specimen.

The short-time grouping of one-sign dislocations and following "wash-away" can be considered as pulsations of dislocation density. Simultaneously, the pulsations of velocity occur. In dynamic experiments the pulsation are fixed in the form of the particle velocity distribution the quantitative characteristic of which is the velocity dispersion [15].

It follows from above simulation, that dynamic mesostructure and mesoparticles themselves are the characteristics of the *process* but not a characteristics of the *state* of material as it takes place in quasistatic situation. Existence of dynamic mesostructure is possible only within time intervals during the loading pulse. Outside the loading pulse the conditions for dynamic mesoparticle existence disappear as mesostructure comes to equilibrium state. In this state, the difference between velocities of neighbor mesoparticles disappear and thereby the boundaries between

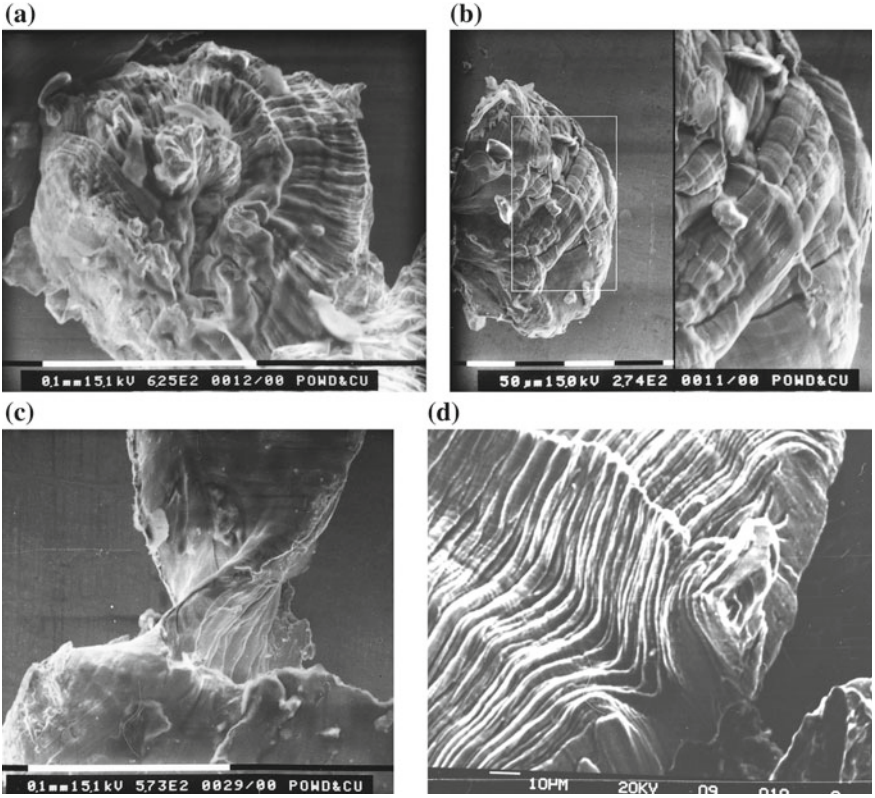

**Fig. 3** Mesoparticles in spall zone of shock-deformed copper

neighbor mesoparticles disappear as well. The only possibility for the visualization of mesostructure is creating the conditions at which the mesoparticles are instantly removing one from another so the equalization of their velocities has not time. This situation is realized within the spall zone of shock deformed material where for a very short time the all-round tension stress is initiated.

During spallation, the spall surfaces of target are quickly removed from each other so the structure of material inside the spall zone is conserved. Accordingly, the boundaries between mesoparticle which separate the volumes of medium with different velocities are also conserved. Under conditions of high-velocity tension, the separation of mesoparticles from each other happens whereas the mesoparticle themselves transform into grains of powder. The typical relict meso-structure is presented in Fig. 3a–d. Every mesoparticle contains a series of shear bands of 5–10 μm in width. The shear bands provide a homogenization of inner structure of mesoparticle, the motion of medium during such a kind of homogenization is characterized by the velocity distribution in the form of particle velocity dispersion. Just that velocity distribution is fixed with the velocity interference technique [15].

## 5 Conclusions

The theory of dynamic deformation based on the kinetics of elementary carriers of deformation is developed. The theory combines both principles of the physical kinetics for the continuously distributed dislocations and continual dislocation theory. For that a concept of tensor dislocation velocity distribution function, the so-called tensor field of deformed medium, is introduced.

The kinetic equation for the dislocation velocity distribution function includes both long-range interaction of dislocations with each other and interaction with the medium where they move. By using this theory it is shown that mesoparticle as elementary carrier of deformation under conditions of high-velocity deforming is short-living accumulation of one-sign dislocations the life-time of which is the order of 100–150 нс. In the process of stochastic motion of mesoparticle, the pulsations of mass velocity are generated which in experiment are fixed in the form of the particle velocity distribution at the mesoscale.

The dynamic mesoparticle have been discovered inside the spall zone of dynamically loaded copper targets.

## References

1. Johnson, J.N., Jones, O.E., Michaels, T.E.: Dislocation dynamics and single-crystal constitutive relation: shock-wave propagation and precursor decay. J. Appl. Phys. **41**(6), 2230–2239 (1970)
2. Vladimirov, V.I., Ivanov, V.N., Priemskii, N.M.: Mesoscopical level of deformation. In: Zhurkov, S.I. (ed.) Physics of Strength and Plasticity, pp. 69–80. M. Nauka (1986)
3. Panin, V.E., Egorushkin, V.E., Panin, A.V.: Physical mesomechanics of deformed solid as multiscale system. Phys. Mesomech. **9**(3), 9–22 (2006)
4. Makarov, P.V.: About hierarchical nature of deformation and fracture of solids. Phys. Mesomech. **7**(4), 25–34 (2004)
5. Rybin, V.V.: Large plastic deformations, 224 pp. M. Metallurgy (1986)
6. Asay, J.R., Chhabildas, L.: Paradigms and challenges in shock wave research. In: Horie, Y.-Y., Davison, L., Thadhani, N.N. (eds.) High-Pressure Shock Compression of Solids VI, pp. 58–119. Springer (2002)
7. Eshby, M.F.: The deformation of plastically non-homogeneous material. Philos. Mag. **21**, 399–422 (1970)
8. Zorski, H.: Statistical theory of dislocations. Int. J. Solids Struct. **4**, 959–974 (1968)
9. Hubburd, J.: The friction and diffusion coefficients of the Fokker-Plank equation. Proc. R. Soc. Lond. **A-260**, 114–126 (1960)
10. Mura, T.: Continuous distribution of moving dislocations. Philos. Mag. **8**, 843–853 (1963)
11. Kosevich, A.M., Natzic, V.D.: Breaking of dislocation in a medium with dispersion of elastic modules. Fizika Tverdogo Tela **4**, 1250–1259 (1966)
12. Alekseev, A.A., Strunin, B.M.: Viscous breaking of dislocations in random stress fields. In: Dislocation Dynamics, pp. 132–137. Naukova Dumka, Kiev (1975)
13. Landau, L.D., Lifshitz, E.M.: Theoretical physics. In: Hydrodynamics, vol. 6, 733 pp. M. Nauka (1988)
14. Meshcheryakov, Yu.I., Prokuratova, E.I.: Kinetic theory of continuously distributed dislocations. Int. J. Solids Struct. **32**, 1711–1726 (1995)
15. Meshcheryakov, Yu.I., Divakov, A.K.: Kinetics of microstructure and strain-rate dependence of materials. Dymat J. **1**, 271–287 (1994)

# Interrelation of Heat Propagation and Angular Velocity in Micropolar Media

**Anna S. Morozova, Elena N. Vilchevskaya, Wolfgang H. Müller and Nikolay M. Bessonov**

**Abstract** This paper is concerned with a materials model within the framework of an extended theory of micropolar media. The extension affects the balance for the tensor field of micro-inertia which, in contrast to the common theory, will now contain a production term. As a consequence the tensor of the moment of inertia becomes an independent field varying in space and time and obeys its own partial differential equation: an extended balance of micro-inertia. The production becomes important if the micropolar material undergoes structural changes. In the present case we consider on the mesoscale an assemblage of statistically uniformly distributed particles of arbitrary shape, which we treat macroscopically as an isotropic linear-thermoelastic continuum. The structural change is then due to a space-dependent transient increase of the temperature field, which leads to an inhomogeneous time-varying expansion of an equivalent thermo-elastic medium. On the continuum scale this will lead to a changing moment of inertia field. For this situation a possible form of the production term on the continuum level can be motivated from mesoscopic considerations and then be evaluated numerically together with the extended balance of micro-inertia. In addition, the temporal and spatial change of the macroscopic inertia field influences rotational motion. By solving the balance of spin numerically the angular velocity evolving in space and time will be determined. The impact of viscosity in the expression of the couple stress will be investigated and different

---

A. S. Morozova (✉) · E. N. Vilchevskaya
Peter the Great Saint-Petersburg Polytechnic University, Politekhnicheskaja 29,
195251 St. Petersburg, Russia
e-mail: aveeanka@gmail.com

E. N. Vilchevskaya
e-mail: vilchevska@gmail.com

E. N. Vilchevskaya · N. M. Bessonov
Institute for Problems in Mechanical Engineering of the Russian Academy of Sciences,
Bol’shoy pr. 61, V.O., 199178 St. Petersburg, Russia

W. H. Müller
Continuum Mechanics and Constitutive Theory, Institute of Mechanics,
Technische Universität Berlin, Einsteinufer 5, 10587 Berlin, Germany
e-mail: wolfgang.h.mueller@tu-berlin.de

H. Altenbach et al. (eds.), *Dynamical Processes in Generalized Continua and Structures*, Advanced Structured Materials 103,
https://doi.org/10.1007/978-3-030-11665-1_23

choices of boundary conditions will be proposed when solving the coupled thermo-mechanical problem.

## 1 Introduction

In today's materials science Generalized Continuum Theories (GCTs) gain increasing importance. They are needed if one wishes to capture the mechanical behavior of high performance materials possessing an inner structure and/or internal degrees of freedom. The applications involve small as well as large structures and they concern solids as well as liquids. There are many concrete examples in light-weight aerospace and automotive technology. They range from liquid crystal displays to micromechanical and microelectronical gadgets.

One particular form of GCTs is referred to a micropolar theory. It emphasizes the aspect of inner rotational degrees of freedom of a material, see [2] for a modern reference. It is particularly suitable for modeling polycrystalline and composite matter, granular and powder-like materials, and it can even be applied to porous media and foams.

Continuum mechanics of solids is traditionally formulated in the Lagrangian way, a.k.a. material description. Here the concept of an indestructible "material particle" prevails, identifiable by its reference position. Hence a bijective mapping for describing the particle's path through three-dimensional space in time uniquely can be used. Note that this requires the neighboring material particles to remain "close" to each other during the motion. Furthermore note that a material particle in the continuum sense is composed of myriads of atoms or molecules, so that statistical fluctuations play no role in a macroscopic continuum. Furthermore there is no exchange of the atoms and molecules between material particles: The mass of a material particle, represented by the mass density, is conserved.

Traditionally this concept is also used in micropolar theory, see for example [5–7]. One may say that the corresponding material particle consists of a statistically significant number of subunits on a mesoscopic scale, for confusion often also called "particles." Now, if the Lagrangian idea of a material particle is followed, the material particles must stay together during the motion and there should be no exchange of subunits between them. Also note that within the material description of a micropolar continuum, each material point is phenomenologically equivalent to a rigid body, and its moment of inertia, the so-called micro-inertia, is a plain constant [7].

However, this is not always true. As a counterexample consider a granular medium being milled. This effects the material particle, because its subunits will be crushed. They will change their mass and their moment of inertia and, what is more, during the milling process there might even be an exchange of crushed subunits between neighboring material particles, which are then no longer material in the original sense. Consequently, on the macroscopic, i.e., on the continuum scale the moments of inertia will change as well. It is for that reason that the authors of [9] have departed from the idea of following the Lagrangian way and turn to the spatial perspective instead. Originally the spatial point of view stems from fluid mechanics. It does not impose strict constraints on the motion of mass-conserved material particles. Rather it embraces the idea of an open system, allowing a priori for exchange of mass, momentum, energy, moment of inertia, etc., between the cells of a Eulerian grid. As a matter of fact the materials considered within the framework of micropolar theory are no longer strictly related to the solid or to the fluid state. They are somewhere in-between, so-to-speak.

Moreover, the authors in [9] proposed a kinetic equation for the microinertia (the field of the local inertia tensor), which in contrast to former theories contains a production term. For a better understanding of this new concept they also presented an underlying mesoscopic theory. Their idea is to connect information on a mesoscale by taking the intrinsic microstructure within a spatial grid cell into account with the macroscopic world, i.e., with the balances of micropolar continua in combination with suitable constitutive equations. These new ideas including the transition from the mesomechanical to the continuum scale have been illustrated by several examples in previous papers, see [9, 11–13, 13, 17]. In particular they considered (a) a homogeneous mix of pressurized hollow spherical particles undergoing a uniform change of external pressure so that their diameter and moment of inertia changes; (b) Particles of type (a) but initially inhomogeneously distributed in an isothermal atmosphere subjected to a barometric pressure distribution falling down and thereby transporting a flux of into new observational points; (c) Changes of anisotropy due to reorientation of initially randomly oriented ellipsoidal particles; (d) Fragmentation of particles in a crusher, analytically as well as numerically; (e) Hollow spherical particles rotating in an heterogeneous transient temperature field with a vanishing couple-stress tensor (dust) when subjected to constant or harmonically oscillating volume moment couples; (f) Interaction of ellipsoidal particles with electric fields leading to their extension and further anisotropy on the continuum scale. What has been missing so far were examples that show the impact of a changing moment of inertia onto rotational motion in combination with a non-vanishing couple-stress tensor.

In this paper the foundations of the extended continuum approach to micropolar media will be presented first and a few remarks regarding the underlying mesoscopic interpretation will be made. In particular, the necessity for a kinetic equation describing the temporal development of the field for the moment of inertia will be explained and motivated. Second, the change of the state of rotation of a isotropic thermoelastic continuum (a spherical material particle so to speak) will be studied, which shall represent the behavior of a homogeneous mix of particles of arbitrary shape on the mesoscale. The continuum particle will undergo a nonuniform change of external temperature affecting its moment of inertia. Note that within the classical framework of micropolar theory a change of temperature would not influence rotation. Within the to-be-presented theory, however, changes in temperature will influence the inertia tensor and hence couple to rotational speed. Additional attention will be paid to the influence of the viscous part in the couple stress tensor. It will be shown that it can have a considerable effect on the internal rotational state of matter. As far as the volume couple moments are concerned use will again be made of the mesoscopic dipole model formulated before in [11] inspired by previous work of Zhilin and Kolpakov [19]. Finally note that the solution of Initial-Boundary-Value-Problems (IBVP) in micropolar theory involves also the use of non-classical boundary conditions. In the present case this concerns the behavior of the angular velocity at the boundary. Therefore different choices for the boundary conditions will be proposed when solving the heat conduction in combination with the spin equation.

## 2 Governing Equations

We shall now briefly present some essential basic relations of micropolar continuum theory in spatial description for the next sections. The following thermodynamical fields are required to be determined in micropolar theory of thermo-elasticity: the scalar field of mass density, $\rho(\boldsymbol{x}, t)$; the symmetric, second rank, and positive definite specific moment of inertia tensor field, $\boldsymbol{J}(\boldsymbol{x}, t)$; the vector field of linear velocity, $\boldsymbol{v}(\boldsymbol{x}, t)$; the angular velocity field, $\boldsymbol{\omega}(\boldsymbol{x}, t)$, and the temperature field, $T(\boldsymbol{x}, t)$, in all points, $\boldsymbol{x}$, and at all times, $t$, within a region of space, $\mathcal{B}$, which can be either a material volume, *i.e.*, it consists of the same matter at all times, or be a region through which matter is flowing.

These fields have to be determined from balance equations complemented by suitable constitutive relations. In regular points the balances for a micropolar medium without coupling between translational and rotational kinetic energies read as follows:

- balance of mass:

$$\frac{\delta \rho}{\delta t} + \rho \nabla \cdot \boldsymbol{v} = 0, \tag{1}$$

- balance of momentum:

$$\rho \frac{\delta \boldsymbol{v}}{\delta t} = \nabla \cdot \boldsymbol{\sigma} + \rho \boldsymbol{f}, \tag{2}$$

- balance of spin:

$$\rho \boldsymbol{J} \cdot \frac{\delta \boldsymbol{\omega}}{\delta t} = -\boldsymbol{\omega} \times \boldsymbol{J} \cdot \boldsymbol{\omega} + \nabla \cdot \boldsymbol{\mu} + \boldsymbol{\sigma}_{\times} + \rho \boldsymbol{m}. \tag{3}$$

We denote by

$$\frac{\delta(\cdot)}{\delta t} = \frac{\mathrm{d}(\cdot)}{\mathrm{d}t} + (\boldsymbol{v} - \boldsymbol{w}) \cdot \nabla(\cdot) \tag{4}$$

the substantial derivative of a field quantity. $\mathrm{d}(\cdot)/\mathrm{d}t$ is the total derivative and $\boldsymbol{w}$ the mapping velocity of the observational point (see [8]). Moreover, $\boldsymbol{\sigma}$ is the non-symmetric Cauchy stress tensor, $\boldsymbol{f}$ is the specific body force, $\boldsymbol{\mu}$ is the couple stress tensor, $(\boldsymbol{a} \otimes \boldsymbol{b})_{\times} = \boldsymbol{a} \times \boldsymbol{b}$ is the Gibbsian cross, and $\boldsymbol{m}$ are specific volume couples.

For heat transfer, the dynamic Eqs. (2) and (3) are supplemented with the heat conduction equation after [18]:

$$\rho\, c_v \frac{\delta T}{\delta t} = \boldsymbol{\sigma}_{\mathrm{d}} : (\nabla \otimes \boldsymbol{v} + \mathbf{I} \times \boldsymbol{\omega}) + \boldsymbol{\mu}_{\mathrm{d}} : \nabla \otimes \boldsymbol{\omega} + \rho q - \nabla \cdot \boldsymbol{h}\,. \tag{5}$$

Here $T$ is the absolute temperature, $c_v$ is the specific heat capacity at constant volume, double convolution means $(\boldsymbol{a} \otimes \boldsymbol{b}) : (\boldsymbol{c} \otimes \boldsymbol{d}) = (\boldsymbol{a} \cdot \boldsymbol{c})(\boldsymbol{b} \cdot \boldsymbol{d})$, $q$ is the heat source per unit mass, $\boldsymbol{h}$ is the heat flux, and $\boldsymbol{\sigma}_{\mathrm{d}}$ and $\boldsymbol{\mu}_{\mathrm{d}}$ are the inelastic (dissipative) parts of the stress tensor and couple stress tensor:

$$\boldsymbol{\sigma} = \boldsymbol{\sigma}_{\mathrm{e}} + \boldsymbol{\sigma}_{\mathrm{d}}, \quad \boldsymbol{\mu} = \boldsymbol{\mu}_{\mathrm{e}} + \boldsymbol{\mu}_{\mathrm{d}}, \tag{6}$$

where $\boldsymbol{\sigma}_{\mathrm{e}}$ and $\boldsymbol{\mu}_{\mathrm{e}}$ are the elastic (velocity independent) parts of the stress tensor and couple stress tensor.

Traditionally, in generalized theories, each material point (particle) of a micropolar continuum is phenomenologically equivalent to a rigid body. Hence, its moments of inertia do not change, see for example [4, 7, 10, 16]. Even if a micromorphic structure is considered, following [3, 5, 7], many papers use an additional balance law for the conservation of inertia (e.g., see [1, 14]).

$$\frac{\delta \boldsymbol{J}}{\delta t} = \boldsymbol{\omega} \times \boldsymbol{J} - \boldsymbol{J} \times \boldsymbol{\omega}\,. \tag{7}$$

Here the terms on the right hand side characterize the change of the moment of inertia tensor due to rigid body rotation.

A different approach was suggested in [9], where a constant elementary volume $V$ was treated as a micropolar particle as is customary in the spatial description. The tensor of inertia of the elementary volume is obtained as a result of averaging of the tensors of inertia particles, of which a representative volume consists. It was shown that in this case the inertia tensor of the volume may change due to the inertia flux or internal structural transformations such as consolidation or defragmentation of particles. Then the specific density of the tensor of inertia on the macrolevel has to be treated as an independent structural field variable rather then parameter. As a result the equation of the inertia conservation (7) should be extended by including an additional production term, $\boldsymbol{\chi}$ on the right hand side. On the continuum level this term must be considered as a new constitutive quantity. It can depend on many physical quantities: temperature, pressure, flow rate, etc., and its form is defined by the process under consideration.

In this paper, we are going to consider a change of the moment of inertia initiated by a temporal and spatial increase of temperature that, in turn, allows us to interrelate the heat propagation in the media with a change of angular velocity.

## 3 Problem Statement

The general problem is as follows. We consider a medium consisting of spherical thermoelastic continuum particles homogeneously distributed over a rectangular region: $x \in [0, L],\ y \in [-L_y, L_y],\ z \in [-L_z, L_z]$. Then, on a continuum level, the homogenized tensor of inertia is isotropic $\boldsymbol{J} = J\mathbf{I}$. Initially the temperature of the media is also homogeneous and equal to $T_0$. However, the temperature of the medium changes within time due to homogeneous heating of the right plate side, while the left side is kept at the initial temperature $T[x = 0, y, z, t] = T_0$.

Due to the increasing temperature field, the particles will expand, which, in turn, leads to an increasing moment of inertia. In order to find the corresponding production term we consider the free thermal expansion of the spherical particle. In this case the production term also has to be isotropic $\boldsymbol{\chi} = \chi\mathbf{I}$.

Under the assumption that the temperature is instantaneously assumed by the particle the dependence of the inertia moment on temperature field is:

$$J(x, t) = J_0\left[1 + \alpha(T(x, t) - T_0)\right]^2, \tag{8}$$

with $J_0$ being the initial moment of inertia, and $\alpha$ being the linear coefficient of thermal expansion. The production can now be found as:

$$\chi = \frac{\partial J}{\partial t} = 2J_0\alpha\left(1 + \alpha(T - T_0)\right)\frac{\partial T}{\partial t}. \tag{9}$$

For simplicity we suppose that the macro-particles have only rotational degrees of freedom and their translational velocities are equal to zero. Then, for an unconstrained medium in absence of body forces the moment balance equation is automatically fulfilled.

Regarding the balance of angular momentum (3) we assume that the elastic part of the couple stress tensor equals to zero, and write the following constitutive equation for its dissipative part according to Zhilin [18]:

$$\boldsymbol{\mu}_{\mathrm{d}} = -\beta(\nabla \times \boldsymbol{\omega}) \times \mathbf{I}, \tag{10}$$

where $\beta$ has the meaning of a frictional coefficient.

In order to keep the problem one-dimensional we also assume that:

$$\boldsymbol{\omega}(x, t) = \omega(x, t)\boldsymbol{e}_z, \quad \boldsymbol{m}(x, t) = m(x, t)\boldsymbol{e}_z. \tag{11}$$

Then Eq. (3) turns into a scalar one:

$$J\rho\frac{\partial \omega}{\partial t} = \beta\frac{\partial^2\omega}{\partial x^2} + \rho m. \tag{12}$$

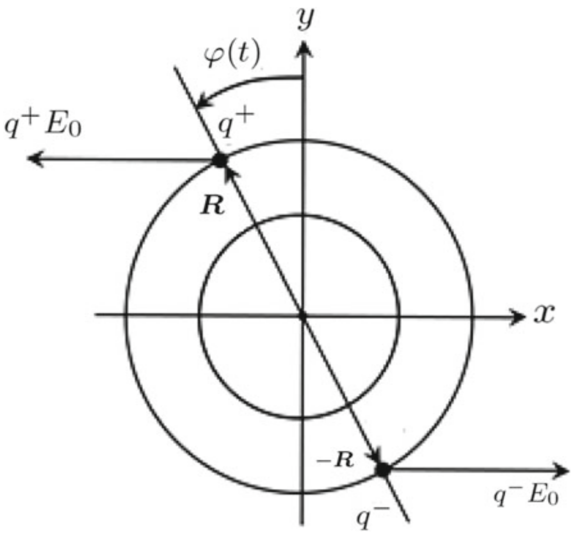

**Fig. 1** A simple model for inducing angular rotation

Now we have to formulate a constitutive equation for the volume couple density. Two different cases will be considered. The simplest one where the density is assumed to be constant, $m(x,t) = m_0$, allows an easy comparison between the to-be-obtained solution and the classical one. It will demonstrate the difference between the two approaches. However, it is not obvious how the constant specific volume couples can be realized and a time-dependent constant specific volume couples also will be considered. Following ideas presented in [19] we imagine the particle to be electrically polarized dipoles with zero net charge, $q^+ = -q^- = q$, as indicated in Fig. 1. Now we apply a constant external electric field, $\boldsymbol{E}_0$, in negative $x$-direction. The total Coulomb force, and therefore (after homogenization) the body force (in $x$-direction) will then vanish. However, the moment couple acting on the sphere will not. Rather it points in z-direction and is given by:

$$\boldsymbol{M} = \left(q^+ - q^-\right) \boldsymbol{R} \times \boldsymbol{E}_0 = 2qRE_0 \cos\varphi(t) \boldsymbol{e}_z \neq \boldsymbol{0}. \tag{13}$$

$q$ being the magnitude of the dipole charge, and $R$ being the particle radius. Hence in this model the volume moment couple density is time-dependent as follows:

$$\boldsymbol{m} = m_0 \cos\left(\int\limits_{\tilde{t}=0}^{\tilde{t}=t} \omega\left(\tilde{t}\right) \mathrm{d}\tilde{t}\right) \boldsymbol{e}_z\ , \quad m_0 = 2\frac{q}{m_\mathrm{p}} R E_0 \tag{14}$$

for $\varphi(0) = 0$ and $m_\mathrm{p}$ being the mass of one particle.

Thus the development of temperature, the moment of inertia and angular velocity can be obtained as a result of solution of a coupled system of partial differential equations:

$$\begin{aligned}
&\frac{\partial \bar{T}}{\partial \bar{t}} = \delta \left( \frac{\partial \bar{\omega}}{\partial \bar{x}} \right)^2 + \frac{\partial^2 \bar{T}}{\partial \bar{x}^2}, \\
&\frac{\partial \bar{J}}{\partial \bar{t}} = 2\bar{\alpha}[1 + \bar{\alpha}(\bar{T} - 1)] \frac{\partial \bar{T}}{\partial \bar{t}}, \\
&\bar{J} \frac{\partial \bar{\omega}}{\partial \bar{t}} = \eta \frac{\partial^2 \bar{\omega}}{\partial \bar{x}^2} + \bar{m}, \\
&\bar{\alpha} = \alpha T_{\text{ini}}, \quad \delta = \frac{\beta m_0}{\kappa T_{\text{ini}} J_0}, \quad \eta = \frac{\beta c_v}{\kappa J_0}, \quad \bar{m} = \omega_0 \frac{L^2}{D}, \\
&\omega_0 = \sqrt{\frac{m_0}{J_0}}, \quad D = \frac{\kappa}{\rho c_v}.
\end{aligned} \tag{15}$$

Here the Fourier law was assumed, $\boldsymbol{h} = -\kappa \nabla T$, with $\kappa$ being the thermal conductivity. The bar on symbols refers to dimensionless quantities, namely:

$$\bar{x} = \frac{x}{L}, \quad \bar{t} = \frac{D}{L^2} t, \quad \bar{T} = \frac{T}{T_0}, \quad \bar{J} = \frac{J}{J_0}, \quad \bar{\omega} = \frac{\omega}{\omega_0}. \tag{16}$$

The initial conditions are:

$$\bar{T}(\bar{x}, \bar{t} = 0) = 1, \quad \bar{J}(\bar{x}, \bar{t} = 0) = 1, \quad \bar{\omega}(\bar{x}, \bar{t} = 0) = 0. \tag{17}$$

Furthermore we are going to consider different types of boundary conditions:

$$\begin{aligned}
&\bar{T}(\bar{x} = 0, \bar{t}) = 1, \quad \bar{T}(\bar{x} = 1, \bar{t}) = \frac{T_L}{T_0} \quad \text{or} \quad \left. \frac{\partial \bar{T}}{\partial \bar{x}} \right|_{\bar{x}=1} = -\frac{hL}{T_0 \kappa}, \\
&\bar{\omega}(\bar{x} = 0, \bar{t}) = \bar{\omega}(\bar{x} = 1, \bar{t}) = 0 \quad \text{or} \quad \left. \frac{\partial \bar{\omega}}{\partial \bar{x}} \right|_{\bar{x}=0;1} = 0,
\end{aligned} \tag{18}$$

where $h$ is the heat flux at the boundary. The first conditions in the second line of Eq. (18) are equivalent to "no slip" (or "strict adhesion," [6], or velocity controlled) boundary conditions for the angular velocity, while the second ones correspond to an absent couple stress on the boundary, which we may also refer to as "force controlled" boundary condition. It is also worth mentioning that the angular velocity related boundary conditions are necessary only if the viscosity is taken into the account. Note that the proper choice of boundary conditions for the angular velocity is a complex issue. This was recently investigated in [15], where many references to the pertinent literature can be found.

In the next section, this system of the differential equations is solved numerically based on the finite difference method.

## 4 Results and Discussion

We start with a simple case without viscosity: $\beta = 0$, $\bar{m} = 100$, $\bar{T}(\bar{x} = 1, \bar{t}) = 2$. Figure 2 shows the developments of temperature and angular velocity at three dimensionless times, $\bar{t} = 0.005$ (green), $\bar{t} = 0.01$ (blue), and $\bar{t} = 0.03$ (red). Note that the obtained profile of angular velocity is nonlinear in contrast to the classical approach without structural change when the angular velocity does not change over the sample length. The nonlinear behavior reflects the fact that distribution of inertia moment over the sample mimics the temperature profile and as a result it follows from Eq. (15) that the angular acceleration varies for particles with different temperature.

The analogue to Fig. 2 for the heat flux boundary condition is shown in Fig. 3 ($q = 10$). In contrast to the previous case the temperature at the right side of the plate grows and, correspondingly, the moment of inertia goes up. This in turn leads to a decrease of the angular velocity. When compared to the temperature governed boundary condition, the decrease is slower at the first stage of the heating process but then becomes more prominent.

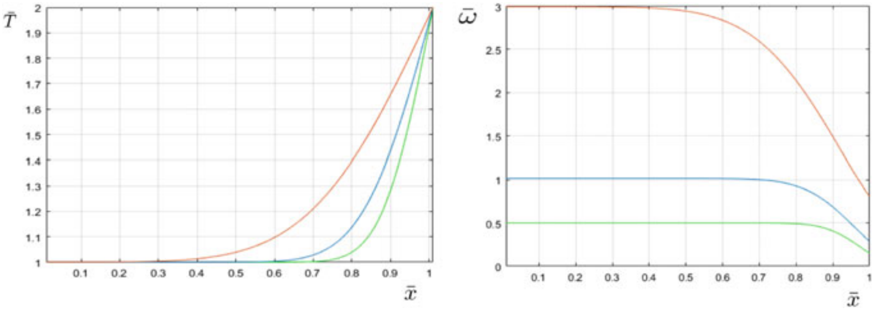

**Fig. 2** Temperature and angular velocity distribution over the sample at different moments of time (for prescribed temperatures at the boundaries)

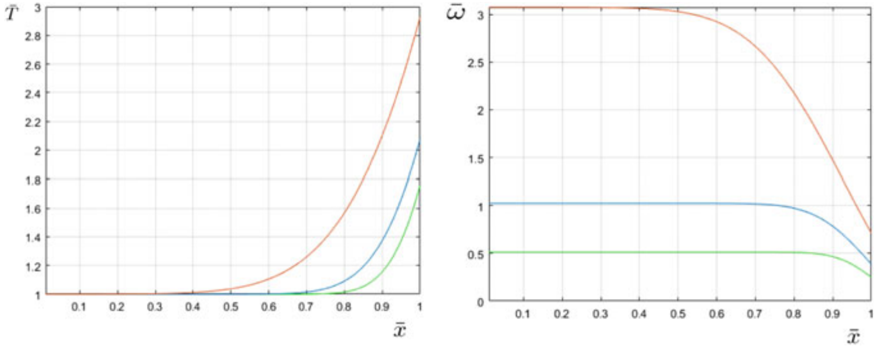

**Fig. 3** Temperature and angular velocity distribution over the sample (for a prescribed heat flux at the right boundary)

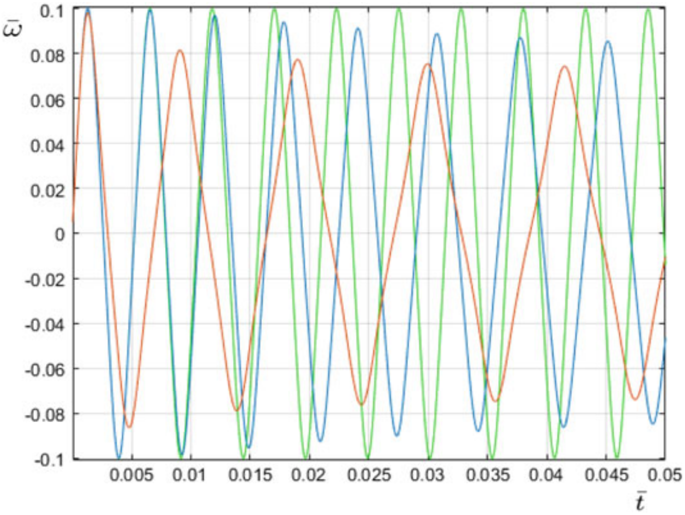

**Fig. 4** Angular velocity at different locations

We shall now consider the periodic specific volume couple

$$\bar{\boldsymbol{m}} = 100 \cos\left( \int_{\tilde{t}=0}^{\tilde{t}=t} \omega\left(\tilde{t}\right) \mathrm{d}\tilde{t} \right) \boldsymbol{e}_z . \tag{19}$$

The numerical solution of the IBVP (15) yields the angular velocities as functions of time shown in Fig. 4 when using the same initial and boundary conditions as for the plots of Fig. 2. Three different positions are examined, namely $\bar{x} = 0.1$ (green), $\bar{x} = 0.7$ (blue), and $\bar{x} = 0.9$ (red). The temperature change influences the amplitudes and the frequencies of the oscillations noticeably. The green curve corresponds to the angular velocity of particles with the initial moment of inertia. Within the classical approach without structural change all particles would possess that angular velocity, however, in our approach the amplitude and frequency of oscillation decrease with increasing temperature.

So far viscous effects were not taken into account. In order to do so, we put $\eta = 1$, $\delta = 1$ and first focus on the velocity controlled boundary condition. The other parameters, initial and boundary conditions are the same as used for plots in Fig. 3. The temperature and angular velocity profiles are shown in Fig. 5. The viscous friction leads to additional temperature increase, particularly noticeable at the left side of the sample, and to a non-symmetric curve for the angular velocity.

As it can be seen in Fig. 6 for the case of a periodic specific volume couple the presence of viscosity causes the angular velocity oscillation to die out. Analogously to the situation depicted in Fig. 4 three different positions were considered, namely,

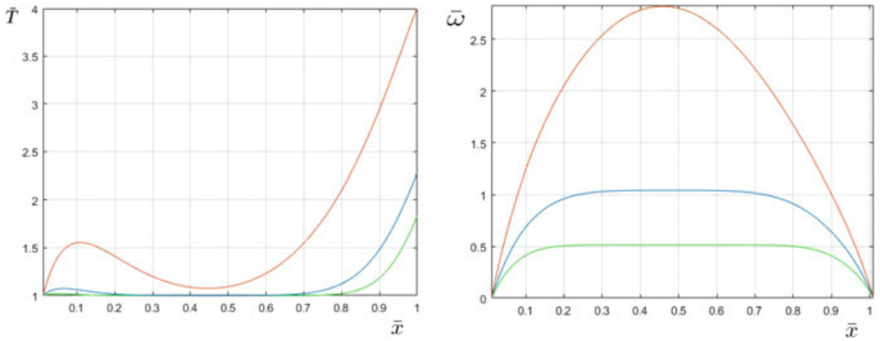

**Fig. 5** Temperature and angular velocity distribution over the sample (strict adhesion boundary condition)

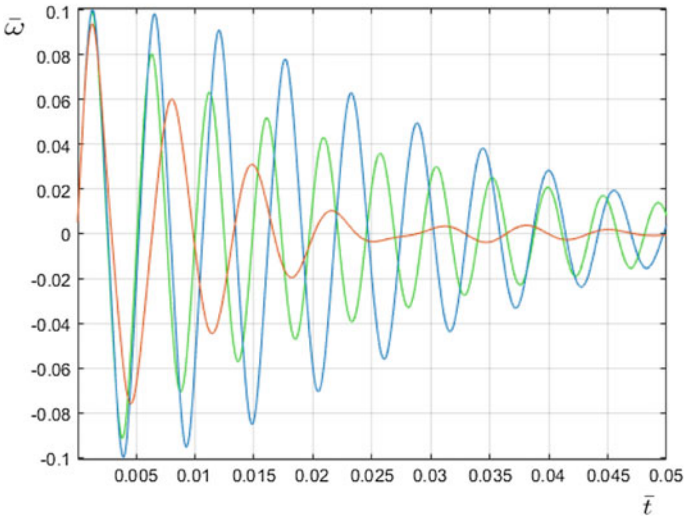

**Fig. 6** Angular velocity at different locations

$\bar{x} = 0.1$ (green), $\bar{x} = 1/3$ (blue), and $\bar{x} = 0.9$ (red). As could be expected the material points at a higher temperature rotate slower and with a lower frequency due to their increasing inertia.

A comparison of the temperature and angular velocities distributions with and without viscous effects at $\bar{t} = 0.03$ is shown in Fig. 7. The blue curves correspond to the case without viscosity. They are the same as in Fig. 3. The red curves were obtained for the viscous case with a force-controlled boundary condition. As to be expected the temperature change in viscous media is more pronounced than in non-viscous ones, which leads to a more significant decrease of the angular velocity.

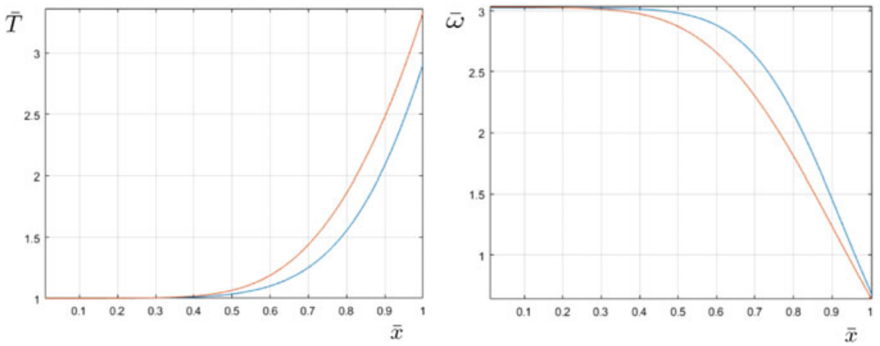

**Fig. 7** Angular velocity and temperature profiles with and without viscosity

## 5 Conclusions and Outlook

This paper was devoted to a detailed numerical study of a model material within the framework of micropolar theory. Attention has been drawn to the following issues:

- The fundamental balance equations for the fields of micropolar media were discussed and presented.
- The reasons for extending the balance of micro-inertia by a production term were explained: The tensor of micro-inertia can no longer be treated as a constant if the micropolar medium undergoes structural change.
- An ensemble of stochastically arranged micro-particles of arbitrary shape was considered on the mesoscale. On the macroscale their behavior was replaced by an equivalent isotropic continuum. The change of its moment of inertia when subjected to a change in temperature was then calculated based on linear thermo-elasticity. This information was used to propose a constitutive relation for the production of micro-inertia for the continuum particle.
- The coupled partial differential equations following from the balance of micro-inertia, the spin balance, and the heat conduction equation were solved numerically by using the finite difference method. A one-dimensional situation was considered where the equivalent (one-dimensional) micropolar medium was subjected to different boundary conditions. A linear viscous constitutive relation was proposed for the viscous part of the couple stress tensor. The specific volume couple vector was either assumed to be a constant or a harmonic function based on a micro-dipole model. The influence of various types of boundary conditions was studied: prescription of temperatures or of the heat flux as well as velocity or force control for the angular velocity at the boundaries. The impact of couple stress viscosity on the damping behavior of the rotational motion was investigated.

The stage is now set for studying three-dimensional problems of micropolar media undergoing structural change on the mesoscale. A possible example are fluid flow problems involving liquid crystals where the structural state of the fluid matter is actively controlled by applying electromagnetic fields from the outside.

**Acknowledgements** Support of this work by a grant from Russian Science foundation by RSF grant no. 18-19-00160 is gratefully acknowledged.

## References

1. Chen, K.: Microcontinuum balance equations revisited: the mesoscopic approach. J. Non-Equilib. Thermodyn. **32**, 435–458 (2007)
2. Eremeyev, V.A., Lebedev, L.P., Altenbach, H.: Foundations of Micropolar Mechanics. Springer, Heidelberg, New York, Dordrecht, London (2012)
3. Eringen, A.: Continuum Physics, vol. IV. Academic Press, New York (1976)
4. Eringen, A.: A unified continuum theory of electrodynamics of liquid crystals. Int. J. Eng. Sci. **35**(12/13), 1137–1157 (1997)
5. Eringen, A.: Microcontinuum Field Theory I. Foundations and Solids. Springer, New York (1999)
6. Eringen, A.C.: Microcontinuum Field Theories-II Fluent Media. Springer, New York (2001)
7. Eringen, A.C., Kafadar, C.B.: Polar field theories. In: Continuum Physics IV. Academic Press, London (1976)
8. Ivanova, E., Vilchevskaya, E., Müller, W.H.: Time derivatives in material and spatial description—what are the differences and why do they concern us? In: Naumenko, K., Aßmus, M. (eds.) Advanced Methods of Mechanics for Materials and Structures, pp. 3–28. Springer (2016)
9. Ivanova, E.A., Vilchevskaya, E.N.: Micropolar continuum in spatial description. Contin. Mech. Thermodyn. **28**(6), 1759–1780 (2016)
10. Mindlin, R.: Micro-structure in linear elasticity. Arch. Rat. Mech. Anal. **16**(1), 51–78 (1964)
11. Müller, W.H., Vilchevskaya, E.N.: Micropolar media with structural transformations-theory illustated by an example problem. Mater. Phys. Mech. **32**(3), 243–252 (2017)
12. Müller, W.H., Vilchevskaya, E.N.: Micropolar theory with production of rotational inertia: A rational mechanics approach. In: Altenbach, H., Pouget, J., Rousseau, M., Collet, B., Michelitsch, T. (eds.) Generalized Models and Non-classical Approaches in Complex Materials 1, pp. 195–229. Springer, Cham (2018)
13. Müller, W.H., Vilchevskaya, E.N., Weiss, W.: A meso-mechanics approach to micropolar theory: a farewell to material description. Phys. Mesomech. **20**(3), 13–24 (2017)
14. Oevel, W., Schröter, J.: Balance equation for micromorphic materials. J. Stat. Phys. **25**(4), 645–662 (1981)
15. Rickert, W., Vilchevskaya, E.N., Müller, W.H.: A note on Couette flow of micropolar fluids according to Eringen's theory. In: Mathematics and Mechanics of Complex Systems (2018)
16. Truesdell, C., Toupin, R.A.: The Classical Field Theories. Springer, Heidelberg (1960)
17. Vilchevskaya, E.N., Müller, W.H.: Some remarks on recent developments in micropolar continuum theory. In: Proceedings of 5th International Conference on Topics Problems of Continuum Mechanics, Armenia, Journal of Physics: Conference Series. IOPScience (2018)
18. Zhilin, P.A.: Рациональная механика сплошных сред (Rational Continuum Mechanics, in Russian) Санкт-Петербург Издательство Политехнического университета, St. Petersburg (2012)
19. Zhilin, P.A., Kolpakov, Y.E.: A micro-polar theory for piezoelectric materials. In: Lecture at XXXIII Summer School—Conference Advanced Problems in Mechanics, pp. 250–261 (2005). http://teormeh.spbstu.ru/Zhilin_New/pdf/Zhilin_Kolpakov2_eng.pdf

# The BIE Method in the Problem of Wave Propagation Through an Infinite Doubly-Periodic Array of Elliptic Obstacles

**M. Yu. Remizov**

**Abstract** In the present paper the author study the propagation of a plane wave through a doubly-periodic infinite array of identical obstacles of elliptic shape. The symmetry of the geometry allows us to reduce the problem to a certain single layer, where a special form of the Green's function leads to a basic boundary integral equation (BIE) for this diffraction problem. The BIE is studied in the one-mode frequency range. Then the author construct an appropriate numerical method, to solve this integral equation, which allows us to evaluate the wave properties of the periodic structure including the reflection and transmission coefficients versus frequency parameter.

## 1 Introduction

Recently, many works have been devoted to the study of metamaterials as the media containing gratings of periodic geometry [1–7]. New properties with impressive mechanical, electromagnetic and acoustical applications have been found in such materials, due to their specific periodic internal structure. The discovered phenomena, such as negative refraction, selective filtration, cloaking, etc., result in numerous applications of the metamaterials in various branches of science and engineering. The most impressive contribution was made in the research of electromagnetic wave processes in such materials. Currently, the problems of acoustic and elastic wave propagation in metamaterials are also being studied very actively, since the phenomena found in the field of electromagnetism pay important role also in mechanical aspect.

Typically, the theoretical studies of the subject discussed above are being performed by applying the Finite Element Method, the Boundary Element Method, or some other direct numerical techniques. In recent years, the experimental base

---

M. Yu. Remizov (✉)
Institute of Mathematics, Mechanics and Computer Science,
Southern Federal University, Milchakova Street 8a, Rostov-on-Don 344090, Russia
e-mail: remizov72@mail.ru

H. Altenbach et al. (eds.), *Dynamical Processes in Generalized Continua and Structures*, Advanced Structured Materials 103,
https://doi.org/10.1007/978-3-030-11665-1_24

devoted to the subject under discussion has also begun to develop rapidly. Natural experiments on the propagation of elastic waves are carried out mainly in the high-frequency ultrasonic range using the advanced modern facilities of ultrasonic analysis. There are also semi-analytical approaches with possible application for infinite or semi-infinite periodic structures. Usually, such methods are based on some asymptotic considerations (low or high-frequency regime), being efficient in the far zone of the wave field only [8–13]. The papers [9–12] provide explicit analytical formulas for reflection and transmission coefficients in the low-frequency range for scalar acoustic or electromagnetic waves penetrating through doubly and triple-periodic arrays of arbitrary-shaped apertures and volumetric obstacles. The 2-D problems on wave propagation through a periodic array of screens in elastic solids for a single-periodic system of cracks have been considered in [11, 12], and for the doubly-periodic geometry – in [10, 13].

The so-called "acoustic metamaterials" possess the property typical for acoustic filters – a cutoff of the propagating wave over certain frequency intervals. This phenomenon for the elastic triple-periodic structures was recently discovered experimentally, see [14]. Some fundamental properties of the acoustic metamaterials are discussed, among many other publications, in [15–19]. The papers [20, 21] provide explicit analytical formulas for scattering parameters in the low-frequency range, in the case of the 3-D problem on elastic wave propagation through doubly and triple-periodic arrays of apertures.

## 2 Mathematical Formulation of the Problem

To study the filtering properties of metamaterials, let us consider the normal incidence of a plane wave $p^{inc} = e^{ikx_1}$ propagating through a doubly periodic system of identical cylindrical obstacles, infinite in $x_3$ direction and located in an unbounded medium. Here $k$ is the wave number, and $i = \sqrt{-1}$ is the imaginary unit. By the symmetry of the problem, the solutions at each section $x_3 = \text{const}$ is the same. Therefore, the problem can be reduced to the two-dimensional form presented in Fig. 1.

According to the linear theory, the total wave field is represented as the sum of the incident and reflected waves: $p = p^{inc} + p^{sc}$, where $p^{sc}$ is the scattered component. The time-dependant factor $e^{-i\omega t}$ is hidden. In frames of the accepted hypotheses, the wave field is described by the Helmholtz equation:

$$\Delta p + k^2 p = 0. \tag{1}$$

To complete the mathematical formulation, one should add to Eq. (1) some boundary conditions. If the boundary of the obstacles is acoustically rigid, then the homogeneous Neumann boundary condition should be satisfied over the obstacles: $v_n|_l = 0$, where $v$ is the velocity vector, $n$ is the outwards normal vector to the boundary and $l$ is the boundary contour.

**Fig. 1** Propagation of the incident wave through a periodic array of elliptic obstacles

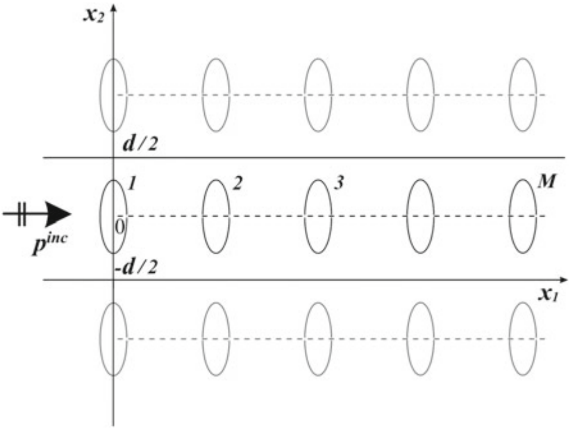

Using the expression for the velocity vector: $v = (1/i\rho\omega)\ \partial p/\partial n$, this boundary condition can be rewritten in terms of pressure, as follows:

$$\left.\frac{\partial p}{\partial n}\right|_l = 0 \quad \sim \quad \left.\frac{\partial p^{sc}}{\partial n}\right|_l = -\left.\frac{\partial p^{inc}}{\partial n}\right|_l . \tag{2}$$

According to [22], in the case of a doubly-periodic array of obstacles, infinite along axis $x_2$, the reduction of the problem to a single layer is possible only if the boundary contour is symmetric along coordinate $x_2$, i.e. if the cross-section of each obstacle is symmetric with respect to axis $x_1$. Note that the cross-sections of different obstacles inside the selected horizontal layer may differ from each other. Let $M$ designate the number of vertical rows of obstacles in the array, therefore $l = \sum_{j=1}^{M} l_j$.

## 3 Derivation of the Basic Integral Equation

Let us assume again that all boundary contours are acoustically hard. Then it is known that the BIE method reduces the diffraction problem to the Fredholm integral equation of the second kind over the boundary of the obstacles:

$$\frac{1}{2}p(x) - \int_l \left[ p(y)\frac{\partial \Phi(y;x)}{\partial n_y}\right] dl_y = e^{ikx_1}, \quad x \in l, \tag{3}$$

where $x = (x_1, x_2)$, $y = (y_1, y_2)$ and the Green's function $\Phi(y;x)$ in the two-dimensional case is expressed in terms of the Hankel function:

$$\Phi(y,x) = \frac{i}{4}H_0^{(1)}(k|x-y|) \rightarrow \frac{\partial \Phi(y,x)}{\partial n_y} = -\frac{ik}{4}H_1^{(1)}(kr)\frac{(r,n_y)}{r}, \tag{4}$$

where $r = |x - y|$ is the distance between two points on the contour of integration.

In such a setting, the integration is carried out along the boundary of each obstacle in the doubly-periodic array under consideration. This can be reduced to integration over the obstacles located inside a single layer, compare with [22].

For this aim let us construct a specific Green's function, which satisfies the following conditions of periodicity:

$$p(y_1, 0) = p(y_1, d), \qquad \frac{\partial p}{\partial y_2}(y_1, 0) = \frac{\partial p}{\partial y_2}(y_1, d) \tag{5}$$

where $d$ is the thickness of one horizontal layer (which is the period of the grating along the vertical direction). According to [8], the Green's function is expressed in the following form:

$$\Phi(y, x) = \frac{i e^{ik|y_1 - x_1|}}{2kd} + \sum_{n=1}^{+\infty} \frac{e^{-\beta_n |y_1 - x_1|} \cos[(2\pi n/d)(y_2 - x_2)]}{\beta_n d}, \tag{6}$$

where the indicated assumption $k < 2\pi/d$ (i.e. $\lambda = 2\pi/k > d$) ensures that the coefficients $\beta_n = \sqrt{(2\pi n/d)^2 - k^2}$ are always positive. Then the kernel of the integral equation (3) is represented by the sum

$$\frac{\partial \Phi(y, x)}{\partial n_y} = n_1^y \frac{\partial \Phi(y, x)}{\partial y_1} + n_2^y \frac{\partial \Phi(y, x)}{\partial y_2}, \tag{7}$$

$$n_1^y \frac{\partial \Phi(y, x)}{\partial y_1} = -n_1^y \, \frac{\operatorname{sign}(y_1 - x_1)}{d} \left( \frac{e^{ik|y_1 - x_1|}}{2} + S_1 \right), \tag{8}$$

$$n_2^y \frac{\partial \Phi(y, x)}{\partial y_2} = -n_2^y \, \frac{2\pi}{d^2} S_2, \tag{9}$$

$$S_1 = \sum_{n=1}^{+\infty} e^{-\beta_n |y_1 - x_1|} \cos[(2\pi n/d)(y_2 - x_2)], \tag{10}$$

$$S_2 = \sum_{n=1}^{+\infty} \frac{n \, e^{-\beta_n |y_1 - x_1|}}{\beta_n} \sin[(2\pi n/d)(y_2 - x_2)]. \tag{11}$$

For efficient treatment of infinite sums $S_1$, $S_2$ in (10), (11), let us extract the behavior of the terms of these series as $n \to \infty$ in explicit form, by taking into account that $\beta_n \sim 2\pi n/d, \; n \to \infty$. Then, omitting some routine mathematical transformations, one obtains the following representation

$$\frac{\partial \Phi(y, x)}{\partial n_y} = \frac{\partial \widehat{\Phi}(y, x)}{\partial n_y} - n_1^y \, \frac{\operatorname{sign}(y_1 - x_1)}{d} \, \widehat{S}_1 - n_2^y \, \frac{2\pi}{d^2} \, \widehat{S}_2, \tag{12}$$

where the two series

$$\widehat{S_1} = \sum_{n=1}^{+\infty} \left(e^{-\beta_n|y_1-x_1|} - e^{-(2\pi n/d)|y_1-x_1|}\right) \cos[(2\pi n/d)(y_2-x_2)], \tag{13}$$

$$\widehat{S_2} = \sum_{n=1}^{+\infty} \left(\frac{ne^{-\beta_n|y_1-x_1|}}{\beta_n} - \frac{de^{-(2\pi n/d)|y_1-x_1|}}{2\pi}\right) \sin[(2\pi n/d)(y_2-x_2)], \tag{14}$$

are rapidly convergent, and the asymptotic (singular) part

$$\begin{gathered}\frac{\partial\widehat{\Phi}(y,x)}{\partial n_y} = \frac{1}{2d}\left\{\left(1-e^{ik|y_1-x_1|}\right)\operatorname{sign}(y_1-x_1)\, n_1^y - \right.\\ \left. - \frac{\sinh[(2\pi/d)(y_1-x_1)]\, n_1^y + \sin[(2\pi/d)(y_2-x_2)]\, n_2^y}{\cosh[(2\pi/d)|y_1-x_1|] - \cos[(2\pi/d)(y_2-x_2)]}\right\}\end{gathered} \tag{15}$$

coincides with the low-frequency approximation developed in [8].

In the case when all obstacles are identical ellipses, the canonical equation of the ellipse is $x_1^2/a^2 + x_2^2/b^2 = 1$, and the equation of the tangent straight line constructed at the point of the ellipse $(x_1^0, x_2^0)$ is written in the form $x_1(x_1^0/a^2) + x_2(x_2^0/b^2) = 1$. The components of the outer unit normal vector at this point are $(x_1^0/a^2, x_2^0/b^2)$. These can easily be written in the polar coordinates $x_1 = r_1\cos\varphi,\ x_2 = r_1\sin\varphi,\ \varphi \in [0, 2\pi]$, where the distance $r_1$ from the origin to the current point at the ellipse is $r_1 = ab\sqrt{a^2\sin^2\varphi + b^2\cos^2\varphi}$. The components of the unit normal vector at this point in the polar coordinates are $\bar{n} = \{b^2\cos\varphi,\ a^2\sin\varphi\}/\sqrt{a^4\sin^2\varphi + b^4\cos^2\varphi}$. In the particular case $a = b$ the ellipse is reduced to a circle, whose radius is denoted as $r_0$.

## 4 Numerical Treatment

The formulas obtained in the previous section make it possible to construct a numerical solution of the described problem. The algorithm applied is based upon the BIE described above, with the use of a collocation technique. According to the approach, the contour of each obstacle is divided to a finite number $n$ of small arcs. It allows to replace the integral in Eq. (3) by a sum of $n$ integrals over the set of the introduced arcs. For the doubly periodic array of obstacles, the integral is replaced by a double sum, where the first summation passes along $M$ contours in the chosen single horizontal layer and the second summation passes over small elementary arcs of each obstacle:

$$\int_l \left[p(y)\frac{\partial\Phi(y;x)}{\partial n_y}\right] dl_y = \sum_{j=1}^{M}\sum_{m=1}^{n}\int_{l_{jm}} \left[p(y)\frac{\partial\Phi(y;x)}{\partial n_y}\right] dl_{jm} \tag{16}$$

The nodes of the computational grid are arranged at the center of each small contour $l_{jm}$. Following the collocation method, both "external" nodes $x$ and "internal" nodes $y$ in Eq. (3) run along the same set of nodes. If all elementary arcs are small, then the integrand is approximately a constant over the small arc, hence in its resulting discrete form the basic BIE is reduced to a system of linear algebraic equations (SLAE), with a matrix of the size $Mn \times Mn$, $(u = 1, \dots, M;\ w = 1, \dots, n)$:

$$\frac{1}{2}p(x^{uw}) - \sum_{j=1}^{M}\sum_{m=1}^{n}\left[p(y^{jm})\frac{\partial \Phi(y^{jm}; x^{uw})}{\partial n_y^{jm}}\right]\Delta l_{jm} = e^{ikx_1}, \quad x^{uw} \in l_{uw}. \tag{17}$$

Note, that when the points of the both variables belong to the same elementary arc, i.e. when $x^{jm} = y^{jm}$, a certain singularity takes place in the kernel of the integral equation. This feature requires accurate calculation in the kernel in this case, when taking integral over the elementary arc. In practice, this means that the integrals over variable $y$ in the singular asymptotic part of the kernel (15) over the small vicinity of the node $x^{uw} \in l_{uw}$ should be carried out precisely. This is attained by a numerical integration. The resulting SLAE (17) can be solved by any suitable numerical technique, for example, by the Gauss elimination method.

Once the boundary values of the unknown wave field are known from the basic BIE, the reflected and the transmitted wave can easily be calculated at arbitrary point in the medium. According to the classical wave theory [23], if the full wave field is a sum of the incident and the scattered ones:

$$p(x) = p^{sc}(x) + p^{inc}(x), \tag{18}$$

then the reflection and the transmission coefficients can be expressed in the left and right far-zones, respectively, in the following form (compare also with [8]):

$$p^{sc}(x) = Re^{-ikx_1}, \qquad p(x) = Te^{ikx_1}, \tag{19}$$

where both the coefficients can be written in the form of relatively simple integrals, as follows:

$$R = -\frac{1}{2d}\int_l p(y)e^{iky_1}n_1(y)dl_y, \qquad T = 1 + \frac{1}{2d}\int_l p(y)e^{-iky_1}n_1(y)dl_y. \tag{20}$$

## 5 Results of the Calculations

When performing the numerical treatment, the basic attention is paid to the physical properties of the doubly-periodic system as an acoustic filter. The author investigates the possibility of using the correct lattice of artificial obstacles of elliptic cross-section, made in the elastic material, to arrange some frequency intervals of locking in the propagation of the plane wave. With so doing, $n = 100$ nodes over the boundary of each obstacle are taken in our numerical experiments, to solve respective SLAE.

By considered elliptical obstacles of varying eccentricity, one can modify the elliptic smooth boundary from the round shape up to a thin screen. This allows us to test the precision of the developed approach, by using the known results published in literature for these limiting cases. In all numerical experiments the elliptic domain is set as the one inscribed inside a circle of radius $r_0$. Numerous calculations show that in practice the case $b = r_0$, $a = r_0/100$ gives the reflection and transmission coefficients coinciding with those known for vertical screens, within two–three right significant digits. The main problem when performing such tests is that to provide a

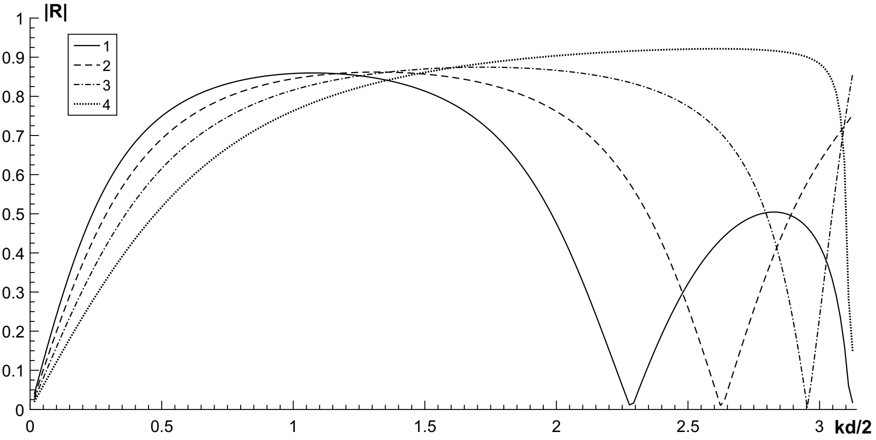

**Fig. 2** Reflection coefficient versus frequency parameter: $M = 1$, $b = r_0$, line 1 – $a = b = r_0$ (circle), line 2 – $a = 0.75r_0$, line 3 – $a = 0.50r_0$, line 4 – $a = 0.25r_0$

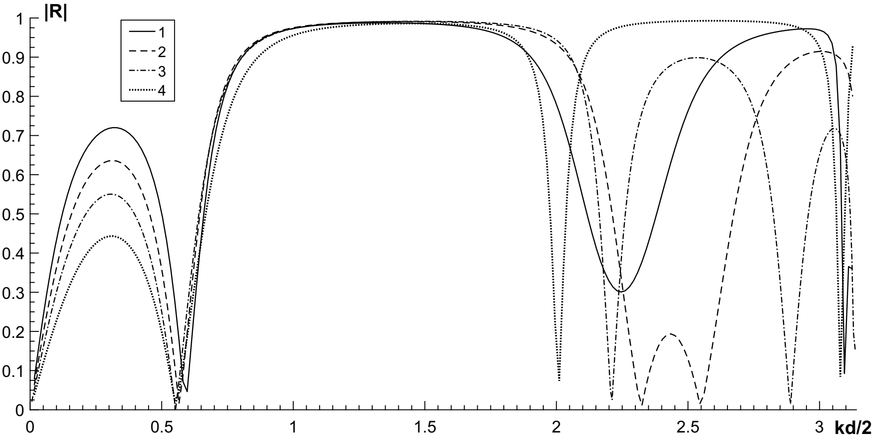

**Fig. 3** Reflection coefficient versus frequency parameter: $M = 2$, $b = r_0$, line 1 – $a = b = r_0$ (circle), line 2 – $a = 0.75r_0$, line 3 – $a = 0.50r_0$, line 4 – $a = 0.25r_0$

significant precision for so elongated obstacles, one should take over each boundary curve more than thousand nodes.

The distance between two adjacent obstacles is assumed to be the same in both the directions, being equal to the layer thickness $d = 0.02\,\mathrm{m}$. The wave speed $c = 6000\,\mathrm{m/s}$ corresponds to the longitudinal wave for a steel material. In such a case the one-mode restriction $k < 2\pi/d$ permits the physical analysis up to the frequency $f = 300\,\mathrm{kHz}$, where $f = \omega/(2\pi)$.

Some examples of the calculations are presented in Figs. 2, 3, 4, 5 and 6, for the elliptic obstacles described by the canonical equation, where $a$, $b$ are semiaxes, and

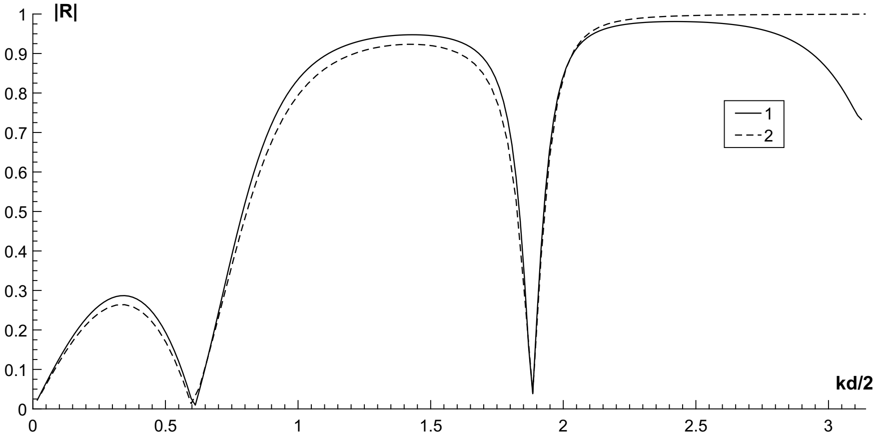

**Fig. 4** Reflection coefficient versus frequency parameter: $M = 2$, $b = r_0$, line 1 – $a = r_0/15$, line 2 – $a = r_0/1000$ (thin screen)

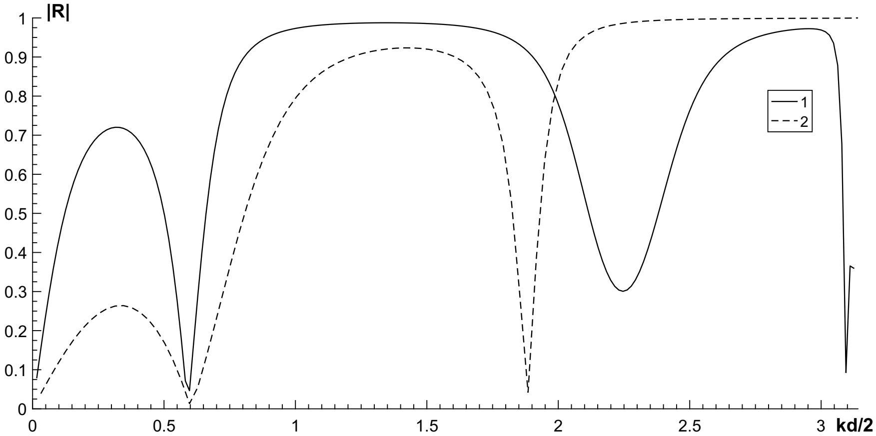

**Fig. 5** Reflection coefficient versus frequency parameter: $M = 2$, $b = r_0$, line 1 – $a = b = r_0$ (circle), line 2 – $a = r_0/1000$ (thin screen)

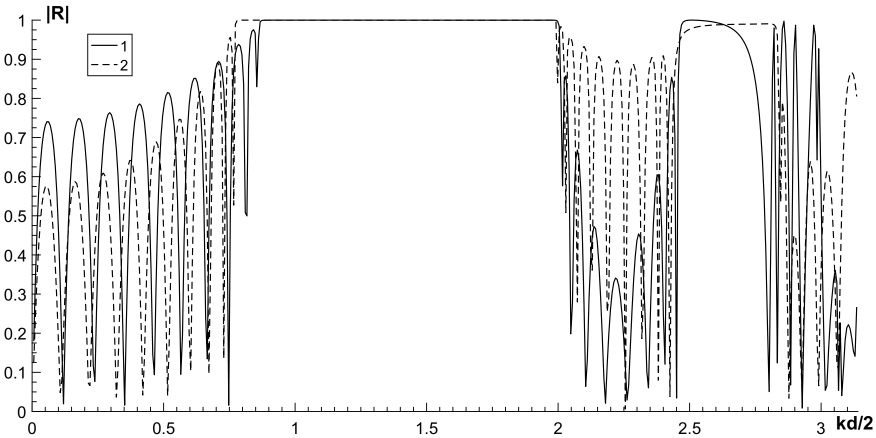

**Fig. 6** Reflection coefficient versus frequency parameter: $M = 10,\ b = r_0$, line 1 – $a = b = r_0$ (circle), line 2 – $a = 0.5r_0$

parameter $r_0 = 0.0075\,\mathrm{m}$. There is also demonstrated the behavior of the reflection coefficient $|R|$ versus frequency parameter $kd/2$ for one, two and ten ($M = 1, 2, 10$) periodic systems of the obstacles.

## 6 Physical Conclusions

The following physical conclusions can be extracted from the undertaken numerical analysis:

1. The behavior of $|R|(kd/2)$ for one periodic system ($M = 1$) in the transition from a circular to elliptic obstacle (Fig. 2) differs rather weakly for low and middle frequencies of the one-mode frequency interval. This is on the contrast to the case of high frequencies, where the narrower shape of the elliptical obstacle leads to an expansion of the locking region and to almost full reflection mode. For the most vertically elongated shape, among four geometries considered in Fig. 2, for the ratio of the ellipse's half-axes $a/b = 0.25$, the possibility of full transmission (when $|R| = 0$) disappears.

2. With increasing number of the vertical arrays ($M = 2$, Fig. 3) and ($M = 10$, Fig. 6) the behavior of the reflection coefficient keeps its qualitative properties. However, the filtering becomes more impressive, since the cut-off over a mid-frequency interval is more uniform, $|R| \approx 1$ in this frequency region, therefore the transmission coefficient $|T|$ is closed to the trivial value.

3. Figure 4 confirms that the elliptic obstacles of small eccentricity may efficiently simulate the thin-screen obstacles. In fact, the behavior of the reflection coefficient over almost full one-mode range for the chosen pair of very narrow obstacles with

$b/a = 15$ and $b/a = 1000$, where the latter is practically a thin screen, even being formally slightly different, but physically are very close to each other. One may use such a grating for a wave filtration both in the central and in the upper parts of the one-mode frequency interval.

4. Figure 5 ($M = 2$) illustrates the difference in the reflection properties between the round obstacles and the thin screens. This figure indicates that the doubly periodic array of round obstacles works well as an acoustic filter at the central part of the one-mode frequency range, while the same doubly-periodic structure of the thin screens is more efficient in this sense over a higher part of the considered frequency interval.

**Acknowledgements** The author expresses his gratitude to Professor M.A. Sumbatyan, Southern Federal University, Russia, for valuable comments. He would also like to notice that this work has been performed in frames of the project 9.5794.2017/8.9 under support of the Russian Ministry for Education and Science.

## References

1. Shenderov, E.L.: Propagation of sound through a screen of arbitrary wave thickness with gaps. Sov. Phys. Acoust. **16**(1), 115–131 (1970)
2. Achenbach, J.D., Li, Z.L.: Reflection and transmission of scalar waves by a periodic array of screens. Wave Motion **8**, 225–234 (1986)
3. Miles, J.W.: On Rayleigh scattering by a grating. Wave Motion **4**, 285–292 (1982)
4. Zarrillo, G., Aguiar, K.: Closed-form low frequency solutions for electromagnetic waves through a frequency selective surface. IEEE Trans. Antennas Propag. **AP-35**, 1406–1417 (1988)
5. Scarpetta, E., Sumbatyan, M.A.: Explicit analytical results for one-mode normal reflection and transmission by a periodic array of screens. J. Math. Anal. Appl. **195**, 736–749 (1995)
6. Scarpetta, E., Sumbatyan, M.A.: On wave propagation in elastic solids with a doubly periodic array of cracks. Wave Motion **25**, 61–72 (1997)
7. Scarpetta, E., Sumbatyan, M.A.: On the oblique wave penetration in elastic solids with a doubly periodic array of cracks. Q. Appl. Math. **58**, 239–250 (2000)
8. Scarpetta, E., Sumbatyan, M.A.: Wave propagation through elastic solids with a periodic array of arbitrarily shaped defects. J. Math. Comput. Model. **37**, 19–28 (2003)
9. Scarpetta, E., Tibullo, V.: Explicit results for scattering parameters in three-dimensional wave propagation through a doubly periodic system of arbitrary openings. Acta Mech. **185**, 1–9 (2006)
10. Scarpetta, E., Tibullo, V.: On the three-dimensionl wave propagation through cascading screens having a periodic system of arbitrary openings. Int. J. Eng. Sci. **46**, 105–111 (2008)
11. Angel, Y.C., Achenbach, J.D.: Harmonic waves in an elastic solid containing a doubly periodic array of cracks. Wave Motion **9**, 377–385 (1987)
12. Scarpetta, E.: In-plane problem for wave propagation through elastic solids with a periodic array of cracks. Acta Mech. **154**, 179–187 (2002)
13. Angel, Y.C., Bolshakov, A.: In-plane waves in an elastic solid containing a cracked slab region. Wave Motion **31**, 297–315 (2000)
14. Mykhaskiv, V.V., Zhbadynskyi, I.Ya., Zhang, Ch.: Dynamic stresses due to time-harmonic elastic wave incidence on doubly periodic array of penny-shaped cracks. J. Math. Sci. **203**, 114–122 (2014)
15. Liu, Z., Zhang, X., Mao, Y., Zhu, Y.Y., Yang, Z., Chan, C.T., Sheng, P.: Locally resonant sonic materials. Science **289**(5485), 1734–1736 (2000)

16. Huang, H.H., Sun, C.T., Huang, G.L.: On the negative effective mass density in acoustic metamaterials. Int. J. Eng. Sci. **47**, 610–617 (2009)
17. Craster, R.V., Guenneau, S.: Acoustic Metamaterials. Springer Series in Materials Science, vol. 166. Springer, Dordrecht (2013)
18. Deymier, P.A.: Acoustic Metamaterials and Phononic Crystals. Springer Series in Solid-State Sciences. Springer, Berlin (2013)
19. Yang, Ch., Achenbach, J.D.: Time domain scattering of elastic waves by a cavity, represented by radiation from equivalent body forces. Int. J. Eng. Sci. **115**, 43–50 (2017)
20. Remizov, M.Yu., Sumbatyan, M.A.: 3-D one-mode penetration of elastic waves through a doubly periodic array of cracks. Math. Mech. Solids **23**(4), 636–650 (2018)
21. Remizov, M.Yu., Sumbatyan, M.A.: On 3D theory of acoustic metamaterials with a triple-periodic system of interior obstacles. Proc. Natl. Acad. Sci. Armen. **70**(4), Mechanics 35–49 (2017)
22. Twersky, V.: Multiple scattering of sound by a periodic line of obstacles. J. Acoust. Soc. Am. **53**, 96–112 (1973)
23. Jones, D.S.: Acoustic and Electromagnetic Waves. Clarendon Press, Oxford (1986)

# Levitation of Small Diamagnetic Particle

**D. Yu. Skubov, A. V. Lukin and I. A. Popov**

**Abstract** The aim of this article consists in the construction of a magneto-electrical scheme, which, due to distribution of a magnetic field, gives the opportunity of obtaining the area of stable equilibrium for small diamagnetic (for example, biological) particle, freely «soaring» in the gravitational field of Earth. At the same time due to small diamagnetic susceptibility of the particle the magnetic field doesn't have essential distortion. This experiment can be considered as a model of a biological object behavior in the weightless conditions or it may give the possibility for investigation of the properties of isolated particles under temperature, magnetic and other physical exposures.

## 1 Introduction

In the works by Martynenko [1, 2] much attention is paid to the possibility of electrostatic, electromagnetic and superconductor levitation, the latter of which opens the opportunity of creating powerful diamagnetic suspensions, the magnetic field of which has already been brought to super high values ~40–50 $T$. The lifting force itself is given by the formula

$$\mathbf{F} = \frac{1}{2}\mu_0(\mu - 1)\int \nabla H^2 d\upsilon, \tag{1}$$

where the integration is carried out over the total volume of a suspended diamagnetic body.

In case of magnetic permeability $\mu < 1$ for diamagnetic materials and in case $\mu = 0$ for superconductivity of the first or the second kind (HTSC-2), the latter of

---

D. Yu. Skubov (✉)
Institute Problems in Mechanical Engineering, V.O, Bolshoj Pr., 61, St. Petersburg 199178, Russia
e-mail: skubov.dsk@yandex.ru

D. Yu. Skubov · A. V. Lukin · I. A. Popov
St. Petersburg Polytechnic University, Polytechnicheskaya Str., 29, St.Petersburg 195251, Russia

H. Altenbach et al. (eds.), *Dynamical Processes in Generalized Continua and Structures*, Advanced Structured Materials 103,
https://doi.org/10.1007/978-3-030-11665-1_25

which is realized at liquid nitrogen temperature, the solid is pushed out from the region with a stronger magnetic field in the direction opposite to the gradient of the square of the induction.

In the present work the levitation of a small diamagnetic particle is considered in a scheme involving the establishment of a large magnetic field gradient with a sufficient area of stable equilibrium position.

The theoretical and experimental possibility of levitation was first shown by Braunbek [3]. The magnetic suspension of ferrite bodies was realized in the thirties of the last century. In 1945, a Moscow scientist VK Arkadiev created a contactless suspension using the phenomenon of superconductivity. He “forced to levitate” a small permanent magnet over the superconducting lead disk.

Diamagnetic materials, originally used for suspension, such as bismuth and graphite, have very weak diamagnetic properties with coefficient of magnetic permeability $\mu$ close to 1. Therefore, till recently, it was possible to hang out only small masses of the order of several tens of milligrams. The appearance of new rare-earth permanent magnets, high-temperature conductivity, substances with better diamagnetic properties allow, in particular, to create heat-shielding coatings for spacecrafts from pyrolytic graphite, whose magnetic susceptibility is several times greater than the one of conventional polycrystalline graphite.

Applying of samarium-cobalt magnets and pyrolytic graphite in Perm University in 1978 made it possible to bring the weight up to 26.7 g [4]. The simplicity of the construction of such a suspension is based on the fact that the displayed magnet is located between the diamagnetic plates and its weight is compensated by an additional stationary permanent magnet. The analysis of stability and the estimation of the maximum mass that can be “hung out” in this way were carried out in [5].

Many substances, such as water, wood, plants, animals, the human body are weak diamagnetics. The invention of powerful magnets, creating an induction of a magnetic field of 16Tl, allow to hang biological objects, for example, mice and frogs, arising a new interest in the diamagnetic suspension [6]. The non-uniform magnetic field created by superconducting magnets opens new possibilities for the control of biological objects, for the synthesis of new materials, and the design of new non-contact devices. The most accessible and complete description of the methods of levitation in electric and magnetic fields is given in a popular scientific paper by Yu. G. Martynenko [2].

Diamagnetic suspension can be used in a system of torque measurement [7] and in electrometer for searching free quarks [8]. A dipmeter with a diamagnetic mass, which register tidal oscillations, seismic waves and microseisms is described in [9]. The necessary damping is provided by the eddy currents induced in the suspended mass during its motion in the magnetic field of the suspension.

Nowadays levitation is actively used in toy products and advertising that allows to maintain the interest in levitation technologies and produce new industrial devices.

## 2 Mathematical Description

In the present work high-gradient magnetic field is provided by using a simple electrical circuit which is represented by a set of micro-coils. In this case, the possibility of levitation for an extremely small (micro or even nano) particle, for example, a biological cell or a molecule, is considered. Essentially, the electromagnetic parameters necessary to realize such a suspension are evaluated.

Numerically-analytical calculation of the magnetic field is carried out in a linear performance. The vector of magnetic induction is given by Bio-Savart law (2) where the integral is taken along the lines of current conductors

$$\vec{B}(\vec{r}) = \frac{\mu_0}{4\pi} \frac{\int_V j_1(\vec{r}_1) \times (\vec{r} - \vec{r}_1)}{|\vec{r} - \vec{r}_1|^3} d\upsilon_1. \tag{2}$$

The vector magnetic potential $\vec{A}$ introduced by relation

$$\vec{B} = \nabla \times \vec{A}, \quad \nabla \cdot \vec{A} = 0. \tag{3}$$

is determined by solving Poisson's equation

$$\Delta \vec{A} = -\mu_0 \vec{j}, \quad \vec{A} = \frac{\mu_0}{4\pi} \frac{\int_V \vec{j}(\vec{r}_1)}{|\vec{r} - \vec{r}_1|} d\upsilon_1. \tag{4}$$

In the case of a single ring, the vector potential is found by calculating the integral

$$\vec{A} = \frac{\mu_0}{4\pi} \frac{\int_S \vec{j} ds}{r}. \tag{5}$$

Here r is the distance from the point of the ring to the point P, where the magnetic potential is determined. If the point P is located at the height $h$ above the plane of the ring with radius $a$, then this distance in cylindrical coordinates $r_p,\ \varphi,\ z$ is given by $r^2 = r_p^2 + a^2 - 2r_p a \cos\varphi + h^2$. After introducing the dimensionless variables $\rho = \frac{r_p}{a},\ \zeta = \frac{z}{a}$ the vector potential takes the form

$$\vec{A} = \vec{e}_\varphi \frac{\mu_0 I}{4\pi} \int_0^{2\pi} \frac{d\varphi}{\sqrt{1 + \rho^2 + \varsigma^2 - 2\rho \cos\varphi}} = \vec{e}_\varphi \frac{\mu_0 I}{4\pi} \int_0^{2\pi} \frac{d\varphi}{\sqrt{(1 + \rho)^2 + \varsigma^2 - 4\rho \cos^2 \frac{\varphi}{2}}} \tag{6}$$

where $I$ signifies the value of the current. In case of a plane ring the vector potential has only a tangential component $A_\varphi$. Substituting into (6) the distance $r$, one can obtain

$$\vec{A} = A_\varphi \vec{e}_\varphi = \vec{e}_\varphi \frac{\mu_0 I}{\pi} \frac{1}{\sqrt{(1+\rho)^2 + \varsigma^2}} K(\kappa). \tag{7}$$

Here the modulus of the elliptic integral of the first kind is given by the expression in terms of dimensionless elliptic coordinates $\kappa^2 = \frac{4\rho}{(1+\rho)^2+\zeta^2}$. The projections of magnetic induction vector in this case are determined by the derivatives of the tangential component of the vector potential:

$$\vec{B} = \nabla \times \vec{A} = \vec{e}_z \left( \frac{\partial A_\varphi}{\partial r} \vec{e}_z + \frac{A_\varphi}{r} \right) - \vec{e}_r \frac{\partial A_\varphi}{\partial z} = \frac{1}{a} \left\{ \vec{e}_z \left( \frac{\partial A_\varphi}{\partial \rho} \vec{e}_z + \frac{A_\varphi}{\rho} \right) - \vec{e}_r \frac{\partial A_\varphi}{\partial \varsigma} \right\}. \tag{8}$$

For calculating of magnetic induction (8) the well-known relations are used $\frac{\partial K}{\partial \kappa} = \frac{1}{\kappa}\left(\frac{E(\kappa)}{1-\kappa^2} - K(\kappa)\right)$, $\frac{\partial E}{\partial \kappa} = \frac{1}{\kappa}(E(\kappa) - K(\kappa))$. For a system of rings with currents, due to the linear statement of the problem, considered in this case, the total vector potential is found as the sum of the potentials of each ring. For example, for a system of two parallel rings with identically directed current, the magnetic potentials in the cylindrical coordinate system with the center located on the vertical axis in the middle between them have the form

$$\vec{A}_i = \vec{e}_\varphi \frac{\mu_0 I}{\pi} \frac{1}{\sqrt{(1+\rho)^2 + \zeta_i^2}} K(\kappa_i),\ \kappa_i^2 = \frac{4\rho}{(1+\rho)^2 + \zeta_i^2},\ i = 1, 2. \tag{9}$$

where $\zeta_1 = \frac{h+z}{a}$, $\zeta_2 = \frac{h-z}{a}$ and $2h$ is the distance between the rings. From (9) we obtain the expressions of components for magnetic induction

$$\begin{aligned} B_{z,i} &= \frac{\mu_0 I}{\pi a} \left\{ -\frac{(1+\rho)}{\left[(1+\rho)^2 + \zeta_i^2\right]^{\frac{3}{2}}} K(\kappa_i) + \frac{\partial K}{\partial \kappa_i} \frac{\left(1 - \rho^2 + \zeta_i^2\right)}{\left[(1+\rho)^2 + \zeta_i^2\right]^4 \rho^{\frac{1}{2}}} \right. \\ &\qquad \left. + \frac{1}{\rho\sqrt{(1+\rho)^2 + \zeta_i^2}} K(\kappa_i) \right\} \\ B_{r,i} &= (-1)^{i-1} \frac{\mu_0 I}{\pi a} \left\{ -\frac{\zeta_i}{\left[(1+\rho)^2 + \zeta_i^2\right]^{\frac{3}{2}}} K(\kappa_i) + \frac{\partial K}{\partial \kappa_i} \frac{2\rho^{\frac{1}{2}} \zeta_i}{\left[(1+\rho)^2 + \zeta_i^2\right]^4 \rho^{\frac{1}{2}}} \right\},\ i = 1, 2 \end{aligned} \tag{10}$$

Small diamagnetic particle with weak negative magnetic susceptibility can't exert a significance influence on external magnetic field and its magnetic energy in this case is given by

$$\mathrm{W} = -\frac{1}{2} \int \vec{J} \cdot \vec{B}_0 d\upsilon, \tag{11}$$

where $\vec{B}_0$ is induction of external magnetic field, $\vec{J} = \chi \vec{H}$—magnetization vector, $\chi = \mu - 1$ – magnetic susceptibility.

Thus, we obtain

$$\mathrm{W} = -\frac{1}{2}\chi\mu_0 H_0^2 V = -\frac{1}{2}\frac{\chi B_0^2 V}{\mu_0}. \tag{12}$$

Here $V$ is the volume of the particle. The total magnetic induction in the considered case in a single cylindrical coordinate system is determined by the vector sum of induction introduced by each of the rings

$$\vec{B} = \sum_i \vec{B}_{oi} = \sum_i \vec{B}_{oi}\vec{e}_r + B_{0zi}\vec{e}_z + B_{0\varphi i}\vec{e}_\varphi. \tag{13}$$

Therefore, the energy of the particle can be presented as the sum:

$$W = -\frac{\chi V}{2\mu_0}\sum B_{0r}^2 + B_{0z}^2 + B_{0\varphi}^2. \tag{14}$$

In the symmetric case for identical parallel rings with equal currents without taking into account gravitation the investigation of stability region of equilibrium is reduced to the problem with only one geometrical dimensionless parameter $\alpha = \frac{h}{a}$. An analytic estimation of stability regions in case of single ring and in case of two rings with parallel equal currents with opposite direction is given in [10]. A numerical-analytic approach, developed in the present work allows to construct regions of stability for a diamagnetic particle in a system of multi-coil rings [11].

For the particle located in the middle of a ring system, it is possible to determine the energy level distribution in a single axisymmetric coordinate system in different cross sections along the vertical between the rings. The graph of magnetic energy distribution for the system of two rings with equal currents in opposite direction for different values of parameter $\alpha$ is shown in Figs. 1, 2 and 3.

These graphs demonstrate that during the reduction of the distance between the rings, energy maximum in the centre gradually decreases, turning to minimum, corresponding to the stable equilibrium position. Moreover, in the regions between the central maximum of the energy and the circumferential maximum, there exists an axisymmetric region of the minimum for the magnetic energy. In this case, it is not difficult to find the values of the parameter α corresponding to the branch points of the equilibriums, and to estimate the region of attraction to them.

In general case of a system of parallel rings with the same radius, a cylindrical coordinate system with the center at the symmetry point is introduced. If the polar coordinates of the center of the ring are denoted as $r_i$, $\beta_i$, $h_i$ and $r_p$, $\psi$, $z$ signify the polar coordinates of a diamagnetic particle, then the position vector of the particle relatively to the center of the ring is given by

$$r^2 = r_f^2 + a^2 - 2r_f a\,\cos\varphi + (z - h_i)^2. \tag{15}$$

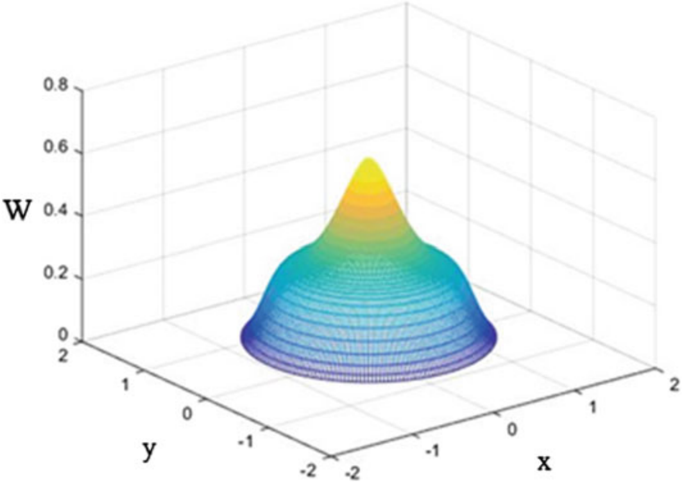

**Fig. 1** Axisymmetric distribution of energy $\alpha = 0.25$

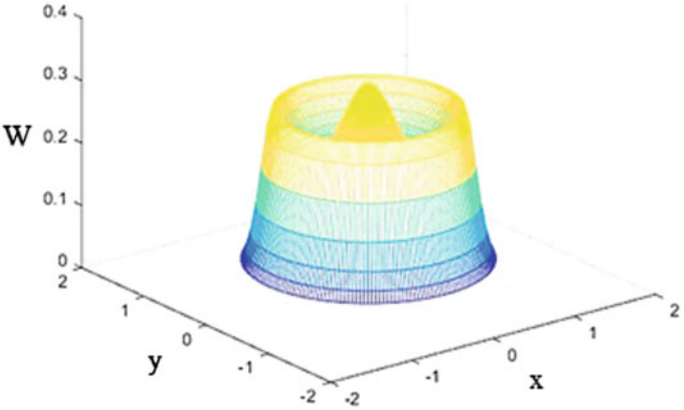

**Fig. 2** Axisymmetric distribution of energy $\alpha = 0.2$

where

$$r_f^2 = r_p^2 + r_i^2 - 2r_p r_i \cos\varphi(\beta_i - \psi). \tag{16}$$

Therefore, after introducing dimensionless coordinates $\rho_f = \frac{r_f}{a}$, $\rho_i = \frac{r_i}{a}$ we obtain the magnetic potential for one of the rings

$$\vec{A}_i = \vec{e}_\varphi \frac{\mu_0 I}{\pi} \frac{1}{\sqrt{\left(1 + \rho_f\right)^2 + (\zeta - \alpha_i)^2}} K(\kappa_i),\ \kappa_i^2 = \frac{4\rho_f}{\left(1 + \rho_f\right)^2 + (\zeta - \alpha_i)^2}, \tag{17}$$

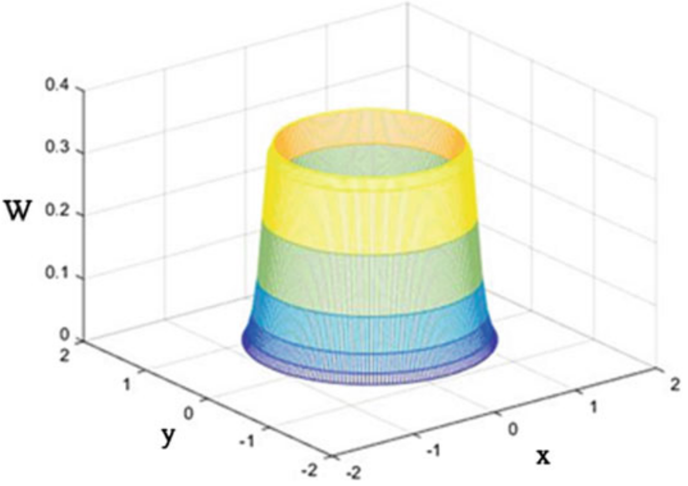

**Fig. 3** Axisymmetric distribution of energy $\alpha = 0.15$

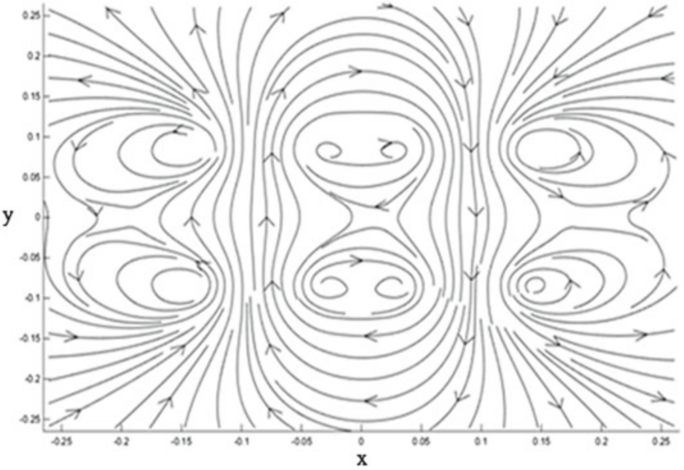

**Fig. 4** Magnetic field lines of four-ring system

where $\kappa_i$ is elliptic module and $\alpha_i = \frac{h_i}{a}$—corresponding dimensionless parameter. The distribution of magnetic field lines for the system consisting of four rings with equal current in the same direction in two of them, located on one vertical, and in the opposite direction in another pair, is depicted in Fig. 4. The region of stable equilibrium position is located in the center of the ring system.

## 3 Conclusion

In conclusion we make the estimation for the currents of the ring system necessary to provide the levitation region for a micro-diamagnetic. Owing to the smallness of the magnetic susceptibility of the diamagnetic, one can neglect the distortion of the external magnetic field and assume that the magnetization is proportional to the external magnetic field with distributed intensity $\vec{H}_0$. In a quasi-homogeneous field, which can be considered constant throughout the whole volume of the body, in the first approximation, ponderomotive forces and angular momentum take the form

$$\vec{F} = \frac{\chi\mu_0}{2}\nabla H_0^2 V, \ \vec{M} = \frac{\chi\mu_0}{2}\vec{r}_c \times \nabla H_0^2 V. \tag{18}$$

where где $\vec{r}_c = \int\limits_V \vec{r} dV$ is the radius vector of the center of mass. Basing on relation given in [11], it is possible to calculate the lifting force acting on a diamagnetic particle of radius $b = 1$ µm

$$F_{0z} = -\frac{3\chi\mu_0}{2a}H^2 V. \tag{19}$$

Taking the radius of the coil $a = 10$ µm, density $\rho_v = 2.2 \cdot 10^2$ КГ/М$^3$, magnetic susceptibility $\chi = \mu - 1 = -0.1$ and using equilibrium condition we obtain

$$H^2 = -\frac{2\rho_v g a}{3\chi\mu_0} = 11.43 \cdot 10^5 \frac{\text{A}^2}{\text{m}^2}. \tag{20}$$

It gives the following estimation for the current of a micro-coil with 100 turns and for the weight of the particle: $I = 2.14 \cdot 10^{-4}$A, $w = 8.8 \cdot 10^{-12}$g.

## References

1. Martynenko, Yu.G.: Motion of solid body in electric and magnetic field—M. Science **368** (1988)
2. Martynenko, Yu.G.: About levitation bodies in force field. Soros Educ. J. **3** (1996)
3. Braubek, W.: Freischwebende Korper im elektrischen und magnetischen Feld. Z. Fur Phisic. **112**, 753–765 (1939)
4. Ponyzovsky, V.M.: Free suspension in a permanent magnet in magnetic field of pyrolitic graphite. PTA **4**, 238–240 (1979)
5. Linkov, R.B.: Diamagnetic suspension of permanent magnet. J. Tech. Phys. **51**(6), 1113–1121 (1981)
6. Simon, M.D., Geim A.K.: Diamagnetic levitation: flying frogs and floating magnets. J. Appl. Ph. **87**(9), 6200–6224 (2001)
7. Braginsky, V.B.: Physical experiment with test body—M. Science 76 (1970)
8. Braginsky, V.B., Osika, V.I.: The ring diamagnetic suspension. PTA **4**, 196–197 (1969)
9. Simon, I., Emsslie, G., Strong, P.F., McConnel, R.K.: Sensitive tiltmeter utilizing a diamagnetic suspension. Rev. Sci. Instr. **39**(11), 1666–1671 (1968)

10. Urman, Yu.G., Bugrova, N.A., Lapin, N.I.: About levitation of diamagnetic bodies in magnetic field. J. Tech. Phys. **80**(9), 945–958
11. Zienkiewicz, O.C., Lyness, J., Owen, D.R.: Three-dimensional magnetic field determination using a scalar potential—a finite element solution. IEEE Trans. Magn. **13**(5), 1649–1656 (1977)

# Applied Theory of Dynamics of Micropolar Elastic Thin Shells and Variation Principles

**Samvel H. Sargsyan**

**Abstract** Micropolar elastic thin shells are complex dynamic systems. To study the dynamic phenomena in these systems, the problem of construction of the applied theory becomes of actual importance. This will enable to adequately describe all the characteristic features of the deformation. To describe the dynamic deformation of micropolar elastic thin shell, starting from the three-dimensional equations of the dynamic theory, a mathematical model based on hypotheses will be constructed in this paper. These hypotheses adequately replace the basic qualitative properties of the asymptotic solution of the three-dimensional boundary value problem in a thin region of the shell. For the constructed applied dynamic theory of micropolar elastic thin shells, D'Alembert-Lagrange and Hamilton variation principles, as well as the general variation principle of Hu-Washizu type are established.

**Keywords** Micropolar · Elastic · Shell · Dynamics · Applied theory · Variation principles

## 1 Introduction

One of the main fields of the development of the moment theory of elasticity is the construction of mathematical models of thin shells and plates based on the three-dimensional theory.

Currently, the construction of the applied theories of micropolar elastic thin shells and plates is most frequently performed with the application of Cosserat surface approach. This approach is developed in papers [1–4] and others. A review of the works related to this issue is demonstrated in paper [5].

In this paper, a different approach is developed, namely, on the basis of assumptions (hypotheses), which adequately replace the basic qualitative properties of the

---

S. H. Sargsyan (✉)
National Academy of Sciences of the Republic of Armenia, Shirak State University,
Gyumri, Armenia
e-mail: s_sargsyan@yahoo.com

H. Altenbach et al. (eds.), *Dynamical Processes in Generalized Continua and Structures*, Advanced Structured Materials 103,
https://doi.org/10.1007/978-3-030-11665-1_26

asymptotic solution of the three-dimensional dynamic problem of the micropolar theory of elasticity in a thin shell region [6–8], the construction of an applied (two-dimensional) theory of the dynamics of micro-polar shells is demonstrated. Variation principles such as d'Alembert-Lagrange, Hamilton, a general variation principle of Hu-Washizu type are established for the mentioned applied dynamic theory of micropolar elastic thin shells.

## 2 Main Equations of Dynamics of the Three-Dimensional Micropolar Theory of Elasticity with Free Fields of Displacements and Rotations

We will consider a shell of thickness 2 h as a three-dimensional micropolar isotropic elastic body, which, under the influence of certain factors, is in a state of motion and is subject to deformation. As a result, each point (we assume the applicability of the concept of "body-point" [9]) will receive a displacement (denoted by the vector $\vec{V}$) and a free rotation (denoted by the vector $\vec{\omega}$).

The basic linear equations of motion of a micropolar elastic medium with free fields of displacement and rotation are given by three groups of relations [10, 11]:

Motion equations

$$\nabla\hat{\sigma} = \rho\frac{\partial^2\vec{V}}{\partial t^2}, \quad \nabla\hat{\mu} + \sigma_x = J\frac{\partial^2\vec{\omega}}{\partial t^2} \tag{1}$$

Geometric relations

$$\hat{\gamma} = \nabla\vec{V} + \hat{I}\times\vec{\omega}, \quad \hat{\chi} = \nabla\vec{\omega} \tag{2}$$

Physical relations of elasticity

$$\begin{gathered}\nabla\hat{\sigma} = \lambda II\cdot\cdot\hat{\gamma}^c + 2\mu\hat{\gamma}^c + 2\alpha\hat{\gamma}^a,\\ \nabla\hat{\mu} = \beta II\cdot\cdot\hat{\chi}^c + 2\gamma\hat{\chi}^c + 2\varepsilon\hat{\chi}^a.\end{gathered} \tag{3}$$

Here $\hat{\sigma}$ is the tensor of stresses, $\hat{\mu}$ is the tensor of moment stresses, $\hat{\gamma}$ is the tensor of deformation, $\hat{\chi}$ is the tensor of bending-torsion, $\lambda, \mu, \alpha, \beta, \gamma, \varepsilon$ are the elastic constants of the micropolar body, $\nabla$ is Hamilton's differential operator, $\hat{I}$ is the unitary tensor, $\hat{\sigma}_x$ is the vector invariant of the tensor of stress $\hat{\sigma}$, $\rho$ is the density, $J$ is the measure of inertia during the rotation of material.

The complete system of relations, given in the invariant form for determination of all characteristics of the motion of an elastic micropolar body, in the studied case will be connected to the coordinate system $\alpha_1, \alpha_2, z$, where $\alpha_1, \alpha_2$ are lines of the main curvatures of the middle surface of the shell ($z = 0$), and the rectilinear axis $z$ is directed along the normal to this surface.

It is necessary to add boundary and initial conditions to the system of Eqs. (1)–(3). It is assumed that on the facial surfaces of the shell stresses and moment stresses are given:

$$\sigma_{3i}|_{z=\pm h} = q_i^{\pm}, \quad \sigma_{33}|_{z=\pm h} = q_3^{\pm}, \quad \mu_{3i}|_{z=\pm h} = m_i^{\pm}, \quad \mu_{33} = m_3^{\pm}. \tag{4}$$

On the surface of the shell edge $\sum = \sum' + \sum''$, stresses and moment stresses are given on $\sum'$, displacements and free rotations-on $\sum''$.

Using the initial conditions in case of $t = t_0$, components of the displacement vector $\vec{V}$ and rotation vector $\vec{\omega}$, as well as components of the linear speed $\frac{\partial \vec{V}}{\partial t}$ and components of the angular speed $\frac{\partial \vec{\omega}}{\partial t}$ are given.

## 3 Hypotheses of the Construction of the Applied Theory of Dynamics of Micropolar Elastic Thin Shells. Displacements and Rotations. Deformations and Bending-Torsions. Stresses and Moment Stresses. Averaged Efforts, Moments and Hypermoments

The main problem of the general theory of thin shells [12] consists in an approximate but adequate reduction of the formulated three-dimensional boundary value problem to a two-dimensional one.

Using the asymptotic method of integration of the three-dimensional boundary-value problem of the moment theory of elasticity with free fields of displacements and rotations in a thin region of the shell (or plate), the problem of reduction is considered in papers [6–8]. Now, bypassing the related mathematical problems, the reduction problem will be solved using some general assumptions (hypotheses), the validity of which is justified in paper [8]. On the other hand, it is necessary to take into account that due to its clarity the method of hypotheses can relatively quickly and simply lead to final results for engineering practice. Thus, our main aim is to construct a general linear theory of micropolar elastic thin shells with free fields of displacements and rotations based on the hypotheses method. We assume that the shell is thin if the dimensionless thickness $\frac{h}{R_0}$ ($R_0$ is the smaller of two main radii of curvature of the middle surface of the shell) can be neglected in relation to unit, i.e.

$$1 + \frac{z}{R_1} \approx 1, \quad 1 + \frac{z}{R_2} \approx 1, \quad -h \le z \le h.$$

The problem of reduction will be solved with the help of some general hypotheses, namely:

**Hypothesis 1** is based on the following assumption: in the process of deformation, initially straight and normal to the middle surface fibers freely rotate in space as a rigid whole at a certain angle, without changing their length and not remaining perpendicular to the deformed middle surface, while in this angular motion free rotations also have their share, for which the linear law of variation along the thickness of the shell will be assumed.

The accepted kinematic hypothesis can be mathematically written as follows: tangential displacements and the normal rotation are distributed along the thickness of the shell according to a linear law

$$V_i = u_i(\alpha_1, \alpha_2, t) + z\psi_i(\alpha_1, \alpha_2, t), \quad i = 1, 2, \quad \omega_3 = \Omega_3(\alpha_1, \alpha_2, t) + z\iota(\alpha_1, \alpha_2, t), \tag{5}$$

and the normal displacement and tangential rotations do not depend on the transverse coordinate $z$, i.e.

$$V_3 = w(\alpha_1, \alpha_2, t), \quad \omega_i = \Omega_i(\alpha_1, \alpha_2, t), \quad \mathrm{i} = 1, 2. \tag{6}$$

It should be noted that from the point of view of displacements the accepted hypothesis (5), (6) coincides with the well-known Tymoshenko kinematic hypothesis in the classical theory of elastic shells [13]. Having this in mind, as a whole we call hypothesis (5), (6) Tymoshenko generalized kinematic hypothesis in the micropolar theory of shells (with free fields of displacements and rotations).

Formulas (5) and (6), with the help of which the components of displacements and free rotations of an arbitrary point of a thin shell are determined through the components of displacements and free rotations of its middle surface, will be put in the base of all relations of the theory of dynamic deformation of a micropolar thin shell, so they should be considered as initial geometric relations in the indicated theory of thin shells.

**Hypothesis 2** is based on the assumption that stress $\sigma_{33}$ plays a secondary role, so that in the generalized Hooke's law (3) this stress will be neglected with respect to the stresses $\sigma_{11}, \sigma_{22}$, and also, in the generalized Hooke's law (3) moment stresses $\mu_{3i} (i = 1, 2)$ will be neglected with respect to the moment stresses $\mu_{i3} (i = 1, 2)$.

**Hypothesis 3** is based on the assumption that in order to determine deformations, bending-torsions, stresses and moment stresses, first, for tangential stresses $\sigma_{31}$,$\sigma_{32}$ and moment normal stress $\mu_{33}$ , we take

$$\sigma_{31} = \overset{0}{\sigma}_{31}(\alpha_1, \alpha_2, t), \; \sigma_{32} = \overset{0}{\sigma}_{32}(\alpha_1, \alpha_2, t), \; \mu_{33} = \overset{0}{\mu}_{33}(\alpha_1, \alpha_2, t). \tag{7}$$

After the calculation of the above mentioned quantities, the values $\sigma_{31}$, $\sigma_{32}$ and $\mu_{33}$ will finally be determined by adding to each expression from (7) a term, determined by the integration of corresponding motion equations from (1) by $z$, in each case requiring a condition that the obtained average over the thickness of the shell integral is equal to zero.

The accepted hypotheses enable us to obtain definite distributions for displacements, rotations, deformations, bending-torsions, force and moment stresses along the thickness of the shell package.

In accordance with the adopted laws of distribution of displacements (5) and free rotations (6), substituting them into formulas (2) and using the assumption of the thinness of the shell, we obtain the following formulas for deformations:

$$\begin{aligned} &\gamma_{ii} = \Gamma_{ii}(\alpha_1, \alpha_2, t) + zK_{ii}(\alpha_1, \alpha_2, t), \quad \gamma_{ij} = \Gamma_{ij}(\alpha_1, \alpha_2, t) + zK_{ij}(\alpha_1, \alpha_2, t), \\ &\gamma_{i3} = \Gamma_{i3}(\alpha_1, \alpha_2, t), \quad \gamma_{3i} = \Gamma_{3i}(\alpha_1, \alpha_2, t), \\ &\chi_{ii} = k_{ii}(\alpha_1, \alpha_2, t), \quad \chi_{ij} = k_{ij}(\alpha_1, \alpha_2, t), \quad \gamma_{33} = 0, \end{aligned} \tag{8}$$

$$\begin{aligned} &\chi_{i3} = k_{i3}(\alpha_1, \alpha_2, t) + zl_{i3}(\alpha_1, \alpha_2, t), \quad \chi_{33} = k_{33}(\alpha_1, \alpha_2, t), \\ &\chi_{3i} = 0, \quad i, j = 1, 2, \quad i \neq j, \end{aligned} \tag{9}$$

where

$$\Gamma_{ii} = \frac{1}{A_i}\frac{\partial u_i}{\partial \alpha_i} + \frac{1}{A_i A_j}\frac{\partial A_i}{\partial \alpha_j}u_j + \frac{w}{R_i}, \quad \Gamma_{ij} = \frac{1}{A_i}\frac{\partial u_j}{\partial \alpha_i} - \frac{1}{A_i A_j}\frac{\partial A_i}{\partial \alpha_j}u_i - (-1)^j \Omega_3, \tag{10}$$

$$K_{ii} = \frac{1}{A_i}\frac{\partial \psi_i}{\partial \alpha_i} + \frac{1}{A_i A_j}\frac{\partial A_i}{\partial \alpha_j}\psi_j, \quad K_{ij} = \frac{1}{A_i}\frac{\partial \psi_j}{\partial \alpha_i} - \frac{1}{A_i A_j}\frac{\partial A_i}{\partial \alpha_j}\psi_i - (-1)^j \iota, \tag{11}$$

$$\Gamma_{i3} = -\vartheta_i + (-1)^j \Omega_j, \quad \Gamma_{3i} = \psi_i - (-1)^j \Omega_j, \quad \vartheta_i = -\frac{1}{A_i}\frac{\partial w}{\partial \alpha_i} + \frac{u_i}{R_i}, \tag{12}$$

$$\begin{aligned} &k_{ii} = \frac{1}{A_i}\frac{\partial \Omega_j}{\partial \alpha_i} + \frac{1}{A_i A_j}\frac{\partial A_i}{\partial \alpha_j}\Omega_j + \frac{\Omega_3}{R_i}, \quad k_{33} = \iota, \\ &k_{ij} = \frac{1}{A_i}\frac{\partial \Omega_j}{\partial \alpha_i} - \frac{1}{A_i A_j}\frac{\partial A_i}{\partial \alpha_j}\Omega_i, \quad k_{i3} = \frac{1}{A_i}\frac{\partial \Omega_3}{\partial \alpha_i} - \frac{\Omega_i}{R_i}, \quad l_{i3} = \frac{1}{A_i}\frac{\partial \iota}{\partial \alpha_i}, \quad i, j = 1, 2, \quad i \neq j. \end{aligned} \tag{13}$$

Here, $\Gamma_{ii}$, $\Gamma_{ij}$ characterize tangential deformations of the shell middle surface, quantities $K_{ii}$, $K_{ij}$ -bending deformation and torsion of the shell middle surface associated with the displacements, $\Gamma_{i3}$, $\Gamma_{3i}-$ the angles of rotation caused by transverse and related shifts, $k_{ii}$, $k_{ij}$, $k_{33}$, $k_{i3}$ -bending deformation and torsion of the shell middle surface associated with the free rotation, $l_{i3}-$ hyper-bendings or hyper-torsions of the shell middle surface.

Formulas (5), (6), (8)–(13) determine the geometric model of the deformed state of micropolar thin shells with free fields of displacements and rotations.

Taking into consideration formulas (8) and (9), which determine the distribution over the thickness of the shell of the components of the deformation and bending-torsion tensors, using hypotheses 2 and 3, on the basis of physical relations of elasticity (3), for the components of tensors of stress and moment stresses (including) $\overset{0}{\sigma}_{3i}(i = 1, 2)$, $\overset{0}{\mu}_{33}$ , we obtain

$$\begin{aligned}
\sigma_{ii} &= \overset{0}{\sigma}_{ii}(\alpha_1, \alpha_2, t) + z\,\overset{1}{\sigma}_{ii}(\alpha_1, \alpha_2, t), \quad (i = 1, 2),\\
\sigma_{ij} &= \overset{0}{\sigma}_{ij}(\alpha_1, \alpha_2, t) + z\overset{1}{\sigma}_{ij}(\alpha_1, \alpha_2, t), \quad (i = 1, 2, \quad i \neq j),
\end{aligned} \tag{14}$$

$$\begin{aligned}
\sigma_{i3} &= (\mu + \alpha)\Gamma_{i3} + (\mu - \alpha)\Gamma_{3i}, \quad (i = 1, 2),\\
\overset{0}{\sigma}_{3i} &= (\mu + \alpha)\Gamma_{3i} + (\mu - \alpha)\Gamma_{i3}, \quad (i = 1, 2),
\end{aligned} \tag{15}$$

$$\begin{aligned}
\mu_{ii} &= \beta k_{mm} + 2\gamma k_{ii}, \quad (i = 1, 2), \quad k_{mm} = k_{11} + k_{22} + k_{33},\\
\mu_{ij} &= (\gamma + \varepsilon)k_{ij} + (\gamma - \varepsilon)k_{ji}, \quad (i, j = 1, 2, \quad i \neq j),
\end{aligned} \tag{16}$$

$$\overset{0}{\mu}_{33} = \beta k_{mm} + 2\gamma k_{33}, \quad \mu_{i3} = \overset{0}{\mu}_{i3}(\alpha_1, \alpha_2, t) + z\overset{1}{\mu}_{i3}(\alpha_1, \alpha_2, t) \quad (i = 1, 2) \tag{17}$$

$$\begin{aligned}
\sigma_{33} &= \overset{0}{\sigma}_{33}(\alpha_1, \alpha_2, t) + z\overset{1}{\sigma}_{33}(\alpha_1, \alpha_2, t),\\
\mu_{3i} &= \overset{0}{\mu}_{3i}(\alpha_1, \alpha_2, t) + z\overset{1}{\mu}_{3i}(\alpha_1, \alpha_2, t) \quad (i = 1, 2).
\end{aligned} \tag{18}$$

Here

$$\begin{aligned}
&\overset{0}{\sigma}_{ii} = \frac{E}{1 - \nu^2}\left(\Gamma_{ii} + \nu\Gamma_{jj}\right), \quad \overset{1}{\sigma}_{ii} = \frac{E}{1 - \nu^2}\left(K_{ii} + \nu K_{jj}\right), (i, j = 1, 2, i \neq j),\\
&\overset{0}{\sigma}_{ij} = (\mu + \alpha)\Gamma_{ij} + (\mu - \alpha)\Gamma_{ji}, \quad \overset{1}{\sigma}_{ij} = (\mu + \alpha)K_{ij} + (\mu - \alpha)K_{ji}, (i, j = 1, 2, i \neq j),
\end{aligned} \tag{19}$$

$$\overset{0}{\mu}_{i3} = (\gamma + \varepsilon)k_{i3}, \quad \overset{1}{\mu}_{i3} = (\gamma + \varepsilon)l_{i3} \quad (i = 1, 2), \tag{20}$$

$$\overset{0}{\sigma}_{33} = \frac{q_3^+ - q_3^-}{2}, \quad \overset{1}{\sigma}_{33} = \frac{q_3^+ + q_3^-}{2h}, \quad \overset{0}{\mu}_{3i} = \frac{m_i^+ - m_i^-}{2}, \quad \overset{1}{\mu}_{3i} = \frac{m_i^+ + m_i^-}{2h} \quad (i = 1, 2). \tag{21}$$

For stresses $\sigma_{3i}(i = 1, 2)$ and moment stress $\mu_{33}$ we finally obtain:

$$\begin{aligned}
\sigma_{3i} = \overset{0}{\sigma}_{3i}(\alpha_1, \alpha_2, t) - z\Bigg\{ &\frac{1}{A_i A_j}\left[\frac{\partial\left(A_j \overset{0}{\sigma}_{ii}\right)}{\partial\alpha_i} + \frac{\partial\left(A_i \overset{0}{\sigma}_{ji}\right)}{\partial\alpha_j}\right] + \frac{1}{A_i A_j}\frac{\partial A_i}{\partial\alpha_j}\overset{0}{\sigma}_{ij} +\\
&+ \frac{\sigma_{i3}}{R_i} - \frac{1}{A_i A_j}\frac{\partial A_j}{\partial\alpha_i}\overset{0}{\sigma}_{jj}\Bigg\} + \left(\frac{h^2}{6} - \frac{z^2}{2}\right)\Bigg\{\frac{1}{A_i A_j}\left[\frac{\partial\left(A_j \overset{1}{\sigma}_{ii}\right)}{\partial\alpha_i} + \frac{\partial\left(A_i \overset{1}{\sigma}_{ji}\right)}{\partial\alpha_j}\right] +\\
&+ \frac{1}{A_i A_j}\frac{\partial A_i}{\partial\alpha_j}\overset{1}{\sigma}_{ij} - \frac{1}{A_i A_j}\frac{\partial A_j}{\partial\alpha_i}\overset{1}{\sigma}_{jj}\Bigg\} \quad (i, j = 1, 2, \quad i \neq j),
\end{aligned} \tag{22}$$

$$\mu_{33} = \overset{0}{\mu}_{33}(\alpha_1, \alpha_2, t) - z\left\{ \frac{1}{A_1A_2}\left[ \frac{\partial\left(A_2\overset{0}{\mu}_{13}\right)}{\partial\alpha_1} + \frac{\partial\left(A_1\overset{0}{\mu}_{23}\right)}{\partial\alpha_2} \right] - \left(\frac{\mu_{11}}{R_1} + \frac{\mu_{22}}{R_2}\right) + \left(\overset{0}{\sigma}_{12} - \overset{0}{\sigma}_{21}\right) \right\} +$$
$$+ \left(\frac{h^2}{6} - \frac{z^2}{2}\right)\left\{ \frac{1}{A_1A_2}\left[ \frac{\partial\left(A_2\overset{1}{\mu}_{13}\right)}{\partial\alpha_1} + \frac{\partial\left(A_1\overset{1}{\mu}_{23}\right)}{\partial\alpha_2} \right] + \left(\overset{1}{\sigma}_{12} - \overset{1}{\sigma}_{21}\right) \right\}. \tag{23}$$

Thus, distribution of stresses and moment stresses along the shell thickness is determined. As a result, on the basis of the accepted hypotheses, the first stage of the problem of reducing the three-dimensional problem to the two-dimensional one for a thin shell is performed.

In order to finally solve this problem and construct a dynamic applied (two-dimensional) theory of micropolar elastic thin shells with free fields of displacements and rotations, instead of stresses and moment stresses we introduce statically equivalent integral characteristics-forces $T_{ii}$, $S_{ij}$, $N_{i3}$, $N_{3i}$, moments $M_{ii}$, $H_{ij}$, $L_{ii}$, $L_{ij}$, $L_{i3}$, $L_{33}$ and hypermoments $\Lambda_{i3}$, which, combined with the condition of the thinness of the shell, are expressed as follows:

$$T_{ii} = \int\limits_{-h}^{h} \sigma_{ii}dz, \quad S_{ij} = \int\limits_{-h}^{h} \sigma_{ij}dz, \quad N_{i3} = \int\limits_{-h}^{h} \sigma_{i3}dz, \quad N_{3i} = \int\limits_{-h}^{h} \sigma_{3i}dz,$$
$$M_{ii} = \int\limits_{-h}^{h} \sigma_{ii}z dz, \quad H_{ij} = \int\limits_{-h}^{h} \sigma_{ij}z dz,$$
$$L_{ii} = \int\limits_{-h}^{h} \mu_{ii}dz, \quad L_{ij} = \int\limits_{-h}^{h} \mu_{ij}dz, \quad L_{33} = \int\limits_{-h}^{h} \mu_{33}dz,$$
$$L_{i3} = \int\limits_{-h}^{h} \mu_{i3}dz, \quad \Lambda_{i3} = \int\limits_{-h}^{h} \mu_{i3}z dz. \tag{24}$$

Here $T_{ii}$ are normal stresses; $S_{ij}$— tangential forces; $N_{i3}$, $N_{3i}$— shearing forces and related forces; $M_{ii}$— bending moments, $H_{ij}$— rotational moments from stresses; $L_{ij}$, $L_{i3}$— bending moments, $L_{ii}$, $L_{33}$— rotational moments from moment stresses; $\Lambda_{i3}$— hypermoments from moment stresses.

## 4 Basic Equations, Boundary and Initial Conditions for the Dynamics of the Applied Theory of Micropolar Elastic Thin Shells with Free Fields of Displacements and Rotations

If we accept the averaged characteristics (24) in the formulas for stresses and moment stresses (14)–(18), we obtain the physical relations of the elasticity of micropolar thin shells:

Physical relations of elasticity

$$\begin{aligned}
&T_{ii} = \frac{2Eh}{1-\nu^2}\left(\Gamma_{ii} + \nu\Gamma_{jj}\right), \quad S_{ij} = 2h\left[(\mu+\alpha)\Gamma_{ij} + (\mu-\alpha)\Gamma_{ji}\right],\\
&M_{ii} = \frac{2Eh^3}{3\left(1-\nu^2\right)}\left(K_{ii} + \nu K_{jj}\right), \quad H_{ij} = \frac{2h^3}{3}\left[(\mu+\alpha)K_{ij} + (\mu-\alpha)K_{ji}\right],\\
&N_{i3} = 2h[(\mu+\alpha)\Gamma_{i3} + (\mu-\alpha)\Gamma_{3i}], \quad N_{3i} = 2h[(\mu+\alpha)\Gamma_{3i} + (\mu-\alpha)\Gamma_{i3}],\\
&L_{ii} = 2h\left[(\beta+2\gamma)k_{ii} + \beta\left(k_{jj} + \iota\right)\right],\\
&L_{ij} = 2h\left[(\gamma+\varepsilon)k_{ij} + (\gamma-\varepsilon)k_{ji}\right], \quad L_{33} = 2h\left[(\beta+2\gamma)k_{33} + \beta(k_{11} + k_{22})\right],\\
&L_{i3} = 2h\frac{4\gamma\varepsilon}{\gamma+\varepsilon}k_{i3}, \quad \Lambda_{i3} = \frac{2h^3}{3}\frac{4\gamma\varepsilon}{\gamma+\varepsilon}l_{i3}, \quad i, j = 1, 2; \quad i \neq j.
\end{aligned} \tag{25}$$

Using the expressions for stresses $\sigma_{31}, \sigma_{32}, \sigma_{33}$ and moment stresses $\mu_{31}, \mu_{32}, \mu_{33}$, satisfying boundary conditions (4) on the facial surfaces of the shell, we consequently obtain the motion equations of micropolar thin shells:

Motion equations

$$\begin{aligned}
&\frac{1}{A_iA_j}\left[\frac{\partial\left(A_jT_{ii}\right)}{\partial\alpha_i} + \frac{\partial\left(A_iS_{ji}\right)}{\partial\alpha_j}\right] + \frac{1}{A_iA_j}\frac{\partial A_i}{\partial\alpha_j}S_{ij} + \frac{N_{i3}}{R_i}\\
&\quad - \frac{1}{A_iA_j}\frac{\partial A_j}{\partial\alpha_i}T_{jj} = -\left(q_i^+ + q_i^-\right) + 2\rho h\frac{\partial^2 u_i}{\partial t^2},\\
&\frac{T_{11}}{R_1} + \frac{T_{22}}{R_2} - \frac{1}{A_1A_2}\left[\frac{\partial(A_2N_{13})}{\partial\alpha_1} + \frac{\partial(A_1N_{23})}{\partial\alpha_2}\right] = \left(q_3^+ + q_3^-\right) - 2\rho h\frac{\partial^2 w}{\partial t^2},\\
&N_{3i} - \left\{\frac{1}{A_iA_j}\left[\frac{\partial(A_jM_{ii})}{\partial\alpha_i} + \frac{\partial(A_iH_{ji})}{\partial\alpha_j}\right] + \frac{1}{A_iA_j}\frac{\partial A_i}{\partial\alpha_j}H_{ij} - \frac{1}{A_iA_j}\frac{\partial A_j}{\partial\alpha_i}M_{jj}\right\}\\
&= h\left(q_i^+ - q_i^-\right) - \rho\frac{2h^3}{3}\frac{\partial^2\psi_i}{\partial t^2}, \quad \frac{1}{A_iA_j}\left[\frac{\partial(A_jL_{ii})}{\partial\alpha_i} + \frac{\partial(A_iL_{ji})}{\partial\alpha_j}\right] + \frac{1}{A_iA_j}\frac{\partial A_i}{\partial\alpha_j}L_{ij} +\\
&\quad + \frac{L_{i3}}{R_i} - \frac{1}{A_iA_j}\frac{\partial A_j}{\partial\alpha_i}L_{jj} + (-1)^j\left(N_{j3} - N_{3j}\right) = -\left(m_i^+ + m_i^-\right) + 2Jh\frac{\partial^2\Omega_i}{\partial t^2},\\
&\frac{L_{11}}{R_1} + \frac{L_{22}}{R_2} - \left\{\frac{1}{A_1A_2}\left[\frac{\partial(A_2L_{13})}{\partial\alpha_1} + \frac{\partial(A_1L_{23})}{\partial\alpha_2}\right] + S_{12} - S_{21}\right\} = \left(m_3^+ + m_3^-\right) - J\frac{\partial^2\Omega_3}{\partial t^2}.
\end{aligned} \tag{26}$$

$$L_{33} - \left\{\frac{1}{A_1A_2}\left[\frac{\partial(A_2\Lambda_{13})}{\partial\alpha_1} + \frac{\partial(A_1\Lambda_{23})}{\partial\alpha_2}\right] + (H_{12} - H_{21})\right\}$$

$$= h\left(m_3^+ - m_3^-\right) - J\frac{2h^3}{3}\frac{\partial^2 \iota}{\partial t^2}.$$

The system of motion equations (26), the physical elasticity relations (25), and the geometric relations (10)–(13) are the basic equations of the applied theory of the dynamics of micropolar elastic thin shells with free fields of displacements and rotations, to which boundary and initial conditions must be added.

The boundary conditions on the boundary contour $\Gamma$ of the region of the middle surface of the shell (for example $\alpha_1 = const$) have the form:

$$\begin{aligned}
&T_{11} = T_{11}^* \text{ or } u_1 = u_1^*,\ S_{12} = S_{12}^* \text{ or } u_2 = u_2^*,\ N_{13} = N_{13}^* \text{ or } w = w^*,\\
&M_{11} = M_{11}^* \text{ or } K_{11} = K_{11}^*,\ H_{12} = H_{12}^* \text{ or } K_{12} = K_{12}^*,\\
&L_{11} = L_{11}^* \text{ or } k_{11} = k_{11}^*,\ L_{12} = L_{12}^* \text{ or } k_{12} = k_{12}^*,\\
&L_{13} = L_{13}^* \text{ or } k_{13} = k_{13}^*,\ \Lambda_{13} = \Lambda_{13}^* \text{ or } l_{13} = l_{13}^*.
\end{aligned} \tag{27}$$

Boundary conditions (27) will be derived with the help of the variation principle.

With the help of the initial conditions, at a point in time $t = t_0$, the values of $u_i, w, \psi_i, \Omega_k, \iota \quad (i = 1, 2; \quad k = 1, 2, 3)$ and their derivatives with respect to $t$ are given as functions of coordinates $\alpha_1, \alpha_2$ .

Thus, a general applied dynamic theory of micropolar elastic thin shells with free fields of displacements and rotations is constructed, which opens great opportunities for solving problems of natural and forced oscillations, as well as other dynamic problems.

## 5 D'Alembert-Lagrange Principle. The Uniqueness of the Solution. Hamilton Principle

### *5.1 D'Alembert-Lagrange Principle. The Law of Conservation of Mechanical Energy. The Uniqueness of the Solution*

To formulate D'Alembert-Lagrange principle in the applied dynamic theory of micropolar elastic thin shells with free fields of displacements and rotations, we will be guided by the hypotheses we have adopted (see Sect. 2) or, what is the same, we will use the obtained formulas of Sect. 2 for displacements and rotations, deformations and bending-torsions.

Performing this, from the equation of D'Alembert-Lagrange principle of the three-dimensional theory [10], we obtain a variation equation of an analogous principle for the applied theory of micropolar elastic thin shells:

$$
\begin{aligned}
&\delta\iint\limits_{(S)} W_0 A_1 A_2 d\alpha_1 d\alpha_2 = \iint\limits_{(S)} \left\{\left[\left(q_1^+ + q_1^-\right) - 2\rho h\frac{\partial^2 u_1}{\partial t^2}\right]\delta u_1 + \left[\left(q_2^+ + q_2^-\right) - 2\rho h\frac{\partial^2 u_2}{\partial t^2}\right]\delta u_2 + \right.\\
&+\left[\left(q_3^+ + q_3^-\right) - 2\rho h\frac{\partial^2 w}{\partial t^2}\right]\delta w + \left[h\left(q_1^+ - q_1^-\right) - \frac{2h^3}{3}\rho\frac{\partial^2 \psi_1}{\partial t^2}\right]\delta\psi_1 + \\
&+\left[h\left(q_2^+ - q_2^-\right) - \frac{2h^3}{3}\rho\frac{\partial^2 \psi_2}{\partial t^2}\right]\delta\psi_2 + \left[\left(m_1^+ + m_1^-\right) - 2Jh\frac{\partial^2 \Omega_1}{\partial t^2}\right]\delta\Omega_1 + \\
&+\left[\left(m_2^+ + m_2^-\right) - 2Jh\frac{\partial^2 \Omega_2}{\partial t^2}\right]\delta\Omega_2 + \left[\left(m_3^+ + m_3^-\right) - 2Jh\frac{\partial^2 \Omega_3}{\partial t^2}\right]\delta\Omega_3 + \\
&+\left.\left[h\left(m_3^+ - m_3^-\right) - \frac{2h^3}{3}J\frac{\partial^2 \iota}{\partial t^2}\right]\delta\iota\right\} A_1 A_2 d\alpha_1 d\alpha_2 + \\
&+\int\limits_{(\Gamma_1')}\left(T_{11}^0\delta u_1 + S_{12}^0\delta u_2 + N_{13}^0\delta w + M_{11}^0\delta\psi_1 + H_{12}^0\delta\psi_2\right.\\
&+\left. L_{11}^0\delta\Omega_1 + L_{12}^0\delta\Omega_2 + L_{13}^0\delta\Omega_3 + \Lambda_{13}^0\delta\iota\right)A_1 d\alpha_1 + \int\limits_{(\Gamma_2')}\left(S_{21}^0\delta u_1 + T_{22}^0\delta u_2 + \right.\\
&+\left. N_{23}^0\delta w + H_{21}^0\delta\psi_1 + M_{22}^0\delta\psi_2 + L_{21}^0\delta\Omega_1 + L_{22}^0\delta\Omega_2 + L_{23}^0\delta\Omega_3 + \Lambda_{23}^0\delta\iota\right)A_2 d\alpha_2. \qquad (28)
\end{aligned}
$$

Here $W_0$ is the surface density of the potential energy of deformation.

$$
\begin{aligned}
W_0 = \frac{1}{2}\Bigg\{ &\frac{2Eh}{1-\nu^2}\left(\Gamma_{11}^2 + 2\nu\Gamma_{12}\Gamma_{21} + \Gamma_{21}^2\right) + \frac{2Eh^3}{3\left(1-\nu^2\right)}\left(K_{11}^2 + 2\nu K_{11}K_{22} + K_{22}^2\right) + \\
&+ 2h\left[(\mu+\alpha)\Gamma_{12}^2 + 2(\mu-\alpha)\Gamma_{12}\Gamma_{21} + (\mu+\alpha)\Gamma_{21}^2\right] + \\
&+ \frac{2h^3}{3}\left[(\mu+\alpha)K_{12}^2 + 2(\mu-\alpha)K_{12}K_{21} + (\mu+\alpha)K_{21}^2\right] + \\
&+ 2h\left[(\beta+2\gamma)\left(k_{11}^2 + k_{22}^2 + \iota^2\right) + 2\beta\left(k_{11}k_{22} + k_{11}\iota + k_{22}\iota\right)\right] + \\
&+ 2h\left[(\gamma+\varepsilon)k_{12}^2 + 2(\gamma-\varepsilon)k_{12}k_{21} + (\gamma+\varepsilon)k_{21}^2\right] + \\
&+ 2h\frac{4\gamma\varepsilon}{\gamma+\varepsilon}\left(k_{13}^2 + k_{23}^2\right) + \frac{2h^3}{3}\frac{4\gamma\varepsilon}{\gamma+\varepsilon}\left(l_{13}^2 + l_{23}^2\right)\Bigg\}. \qquad (29)
\end{aligned}
$$

The equation in variations (28) is considered together with the geometric relations (10)–(13) and with geometric boundary conditions on $\Gamma_1''$ and $\Gamma_2''(\Gamma_i = \Gamma_i' \cup \Gamma_i'',\ \mathrm{i} = 1, 2)$. Equation (28) expresses the principle of possible displacements in the dynamics of micropolar elastic thin shells. From Eq. (28) it follows that the virtual work of external forces and moments, forces and moments of inertia is equal to the variation of the potential energy of deformation. From Eq. (28) differential equations of motion (26) and static boundary conditions on $\Gamma_1'$ and $\Gamma_2'$ can be obtained.

For real displacements and rotations, instead of D'Alembert-Lagrange variation principle (28), we can obtain the law of conservation of mechanical energy in the applied theory of micropolar elastic thin shells:

$$\begin{aligned}
&\tfrac{d}{dt}\left(\iint\limits_{(S)} K_0 A_1 A_2 d\alpha_1 d\alpha_2 + \iint\limits_{(S)} W_0 A_1 A_2 d\alpha_1 d\alpha_2\right) = \\
&= \iint\limits_{(S)} \Big[\left(q_1^+ + q_1^-\right)\tfrac{du_1}{dt} + \left(q_2^+ + q_2^-\right)\tfrac{du_2}{dt} + \left(q_3^+ + q_3^-\right)\tfrac{dw}{dt} + h\left(q_1^+ - q_1^-\right)\tfrac{\partial\psi_1}{\partial t} + \\
&\quad + h\left(q_2^+ - q_2^-\right)\tfrac{\partial\psi_2}{\partial t} + \left(m_1^+ + m_1^-\right)\tfrac{d\Omega_1}{dt} + \left(m_2^+ + m_2^-\right)\tfrac{d\Omega_2}{dt} + \left(m_3^+ + m_3^-\right)\tfrac{d\Omega_3}{dt} + \\
&\quad + h\left(m_3^+ - m_3^-\right)\tfrac{\partial\iota}{\partial t}\Big] A_1 A_2 d\alpha_1 d\alpha_2 + \int\limits_{(\Gamma_1')} (T_{11}^0 \tfrac{\partial u_1}{\partial t} + S_{12}^0 \tfrac{\partial u_2}{\partial t} + N_{13}^0 \tfrac{\partial w}{\partial t} + M_{11}^0 \tfrac{\partial\psi_1}{\partial t} + \\
&\quad + H_{12}^0 \tfrac{\partial\psi_2}{\partial t} + L_{11}^0 \tfrac{\partial\Omega_1}{\partial t} + L_{12}^0 \tfrac{\partial\Omega_2}{\partial t} + L_{13}^0 \tfrac{\partial\Omega_3}{\partial t} + \Lambda_{13}^0 \tfrac{\partial\iota}{\partial t}) A_1 d\alpha_1 + \\
&\quad + \int\limits_{(\Gamma_2')} (S_{21}^0 \tfrac{\partial u_1}{\partial t} + T_{22}^0 \tfrac{\partial u_2}{\partial t} + N_{23}^0 \tfrac{\partial w}{\partial t} + H_{21}^0 \tfrac{\partial\psi_1}{\partial t} + M_{22}^0 \tfrac{\partial\psi_2}{\partial t} + L_{21}^0 \tfrac{\partial\Omega_1}{\partial t} + \\
&\quad + L_{22}^0 \tfrac{\partial\Omega_2}{\partial t} + L_{23}^0 \tfrac{\partial\Omega_3}{\partial t} + \Lambda_{23}^0 \tfrac{\partial\iota}{\partial t}) A_2 d\alpha_2,
\end{aligned} \tag{30}$$

where $K_0$-is surface density of kinetic energy of the shell.

$$\begin{aligned}
K_0 = \frac{1}{2}\Bigg[& 2\rho h\left(\frac{\partial u_1}{\partial t}\right)^2 + 2\rho h\left(\frac{\partial u_2}{\partial t}\right)^2 + 2\rho h\left(\frac{\partial w}{\partial t}\right)^2 + \frac{2\rho h^3}{3}\left(\frac{\partial\psi_1}{\partial t}\right)^2 + \\
&+ \frac{2\rho h^3}{3}\left(\frac{\partial\psi_2}{\partial t}\right)^2 + 2Jh\left(\frac{\partial\Omega_1}{\partial t}\right)^2 + 2Jh\left(\frac{\partial\Omega_2}{\partial t}\right)^2 + \\
&+ 2Jh\left(\frac{\partial\Omega_3}{\partial t}\right)^2 + \frac{2Jh^3}{3}\left(\frac{\partial\iota}{\partial t}\right)^2\Bigg].
\end{aligned} \tag{31}$$

Based on this law, we assert that the increment in time of the kinetic and potential energy of the shell is equal to the increment of work performed by external surface, contour forces and moments.

On the basis of the energy equation (30), we can prove the uniqueness theorem in the applied dynamic theory of micropolar elastic thin shells with free fields of displacements and rotations.

## 5.2 Hamilton's Principle

To construct the variation equation of Hamilton's principle for the applied dynamic theory of micropolar elastic thin shells, similarly with the previous case, we take the equation of Hamilton's principle for the three-dimensional theory [10] as the basis and, in accordance with the applied theory of thin shells, this equation is reducible to the two-dimensional one. As a result, we obtain the following variation equation:

$$
\begin{aligned}
&\int_{t_1}^{t_2}\left[\delta \iint_{(S)} (W_0 - K_0)A_1A_2 d\alpha_1 d\alpha_2\right]dt = \\
&\quad = \int_{t_1}^{t_2}\Bigg\{\iint_{(S)} \big[\big(q_1^+ + q_1^-\big)\delta u_1 + \big(q_2^+ + q_2^-\big)\delta u_2 + \big(q_3^+ + q_3^-\big)\delta w + \\
&\quad + h\big(q_1^+ - q_1^-\big)\delta\psi_1 + h\big(q_2^+ - q_2^-\big)\delta\psi_2 + \big(m_1^+ + m_1^-\big)\delta\Omega_1 + \\
&\quad + \big(m_2^+ + m_2^-\big)\delta\Omega_2 + \big(m_3^+ + m_3^-\big)\delta\Omega_3 + h\big(m_3^+ - m_3^-\big)\delta\iota\big]A_1A_2 d\alpha_1 d\alpha_2\Bigg\}dt + \\
&\quad + \int_{t_1}^{t_2}\Bigg\{\int_{(l_1')}(T_{11}^0\delta u_1 + S_{12}^0\delta u_2 + N_{13}^0\delta w + M_{11}^0\delta\psi_1 + H_{12}^0\delta\psi_2 + \\
&\quad + L_{11}^0\delta\Omega_1 + L_{12}^0\delta\Omega_2 + L_{13}^0\delta\Omega_3 + \Lambda_{13}^0\delta\iota)A_1 d\alpha_1 + \int_{(l_2')}(S_{21}^0\delta u_1 + T_{22}^0\delta u_2 + \\
&\quad + N_{23}^0\delta w + H_{21}^0\delta\psi_1 + M_{22}^0\delta\psi_2 + L_{21}^0\delta\Omega_1 + L_{22}^0\delta\Omega_2 + L_{23}^0\delta\Omega_3 + \Lambda_{23}^0\delta\iota)A_2 d\alpha_2\Bigg\}dt.
\end{aligned}
\tag{32}
$$

The variation equation (32) is the Hamilton's principle of the applied theory of the dynamics of micropolar elastic thin shells with free fields of displacements and rotations.

Euler's equations of Hamilton's variation equation (32) lead to motion equations (29) of the applied dynamic theory of micropolar thin shells and to the static boundary conditions on the contours $l_1'$ and $l_2'$ of the middle surface of the shell.

## 5.3 The General Variation Principle (Hu-Washizu Type)

During the formulation of the general variation principle of the applied dynamic theory of micropolar elastic thin shells with free fields of displacements and rotations, we proceed from the general variation principle of the corresponding three-dimensional theory [10] and, in accordance with the theory of shells, we will bring this equation to a two-dimensional continuum. Using the averaged over the shell thickness concepts (24), as a result the following variation equation will be obtained:

$$
\begin{aligned}
&\int\limits_{t_1}^{t_2} \delta \iint\limits_{(S)} \Bigg\{ (W_0 - K_0) - T_{11}\left[\Gamma_{11} - \left(\frac{1}{A_1}\frac{\partial u_1}{\partial \alpha_1} + \frac{1}{A_1 A_2}\frac{\partial A_1}{\partial \alpha_2}u_2 + \frac{w}{R_1}\right)\right] + \\
&+ T_{22}\left[\Gamma_{22} - \left(\frac{1}{A_2}\frac{\partial u_2}{\partial \alpha_2} + \frac{1}{A_1 A_2}\frac{\partial A_2}{\partial \alpha_1}u_1 + \frac{w}{R_2}\right)\right] - \\
&- S_{12}\left[\Gamma_{12} - \left(\frac{1}{A_1}\frac{\partial u_2}{\partial \alpha_1} - \frac{1}{A_1 A_2}\frac{\partial A_1}{\partial \alpha_2}u_1 - \Omega_3\right)\right] - \\
&- S_{21}\left[\Gamma_{21} - \left(\frac{1}{A_2}\frac{\partial u_1}{\partial \alpha_2} - \frac{1}{A_1 A_2}\frac{\partial A_2}{\partial \alpha_1}u_2 + \Omega_3\right)\right] - \\
&- N_{13}\left[\Gamma_{13} - \left(\frac{1}{A_1}\frac{\partial w}{\partial \alpha_1} - \frac{u_1}{R_1} + \Omega_2\right)\right] + \\
&+ N_{23}\left[\Gamma_{23} - \left(\frac{1}{A_2}\frac{\partial w}{\partial \alpha_2} - \frac{u_2}{R_2} - \Omega_1\right)\right] + N_{31}[\Gamma_{31} - (\psi_1 - \Omega_2)] + \\
&+ N_{32}[\Gamma_{32} - (\psi_2 + \Omega_1)] + M_{11}\left[K_{11} - \left(\frac{1}{A_1}\frac{\partial \psi_1}{\partial \alpha_1} + \frac{1}{A_1 A_2}\frac{\partial A_1}{\partial \alpha_2}\right)\psi_2\right] + \\
&+ M_{22}\left[K_{22} - \left(\frac{1}{A_2}\frac{\partial \psi_2}{\partial \alpha_2} + \frac{1}{A_1 A_2}\frac{\partial A_2}{\partial \alpha_1}\psi_1\right)\right] + \\
&+ H_{12}\left[K_{12} - \left(\frac{1}{A_1}\frac{\partial \psi_2}{\partial \alpha_1} - \frac{1}{A_1 A_2}\frac{\partial A_1}{\partial \alpha_2}\psi_1 - \iota\right)\right] + \\
&+ H_{21}\left[K_{21} - \left(\frac{1}{A_2}\frac{\partial \psi_1}{\partial \alpha_2} - \frac{1}{A_1 A_2}\frac{\partial A_2}{\partial \alpha_1}\psi_2 + \iota\right)\right] + \\
&+ L_{11}\left[k_{11} - \left(\frac{1}{A_1}\frac{\partial \Omega_1}{\partial \alpha_1} + \frac{1}{A_1 A_2}\frac{\partial A_1}{\partial \alpha_2}\Omega_2 + \frac{\Omega_3}{R_1}\right)\right] + \\
&+ L_{22}\left[k_{22} - \left(\frac{1}{A_2}\frac{\partial \Omega_2}{\partial \alpha_2} + \frac{1}{A_1 A_2}\frac{\partial A_2}{\partial \alpha_1}\Omega_1 + \frac{\Omega_3}{R_2}\right)\right] + L_{33}[k_{33} - \iota] + \\
&+ L_{12}\left[k_{12} - \left(\frac{1}{A_1}\frac{\partial \Omega_2}{\partial \alpha_1} - \frac{1}{A_1 A_2}\frac{\partial A_1}{\partial \alpha_2}\Omega_1\right)\right] + \\
&+ L_{21}\left[k_{21} - \left(\frac{1}{A_2}\frac{\partial \Omega_1}{\partial \alpha_2} - \frac{1}{A_1 A_2}\frac{\partial A_2}{\partial \alpha_1}\Omega_2\right)\right] + \\
&+ L_{13}\left[k_{13} - \left(\frac{1}{A_1}\frac{\partial \Omega_3}{\partial \alpha_1} - \frac{\Omega_1}{R_1}\right)\right] + L_{23}\left[k_{23} - \left(\frac{1}{A_2}\frac{\partial \Omega_3}{\partial \alpha_2} - \frac{\Omega_2}{R_2}\right)\right] + \\
&+ \Lambda_{13}\left(l_{13} - \frac{1}{A_1}\frac{\partial \iota}{\partial \alpha_1}\right) + \Lambda_{23}\left(l_{23} - \frac{1}{A_2}\frac{\partial \iota}{\partial \alpha_2}\right)\Bigg\} A_1 A_2 d\alpha_1 d\alpha_2 dt - \\
&- \int\limits_{t_1}^{t_2} \iint\limits_{(S)} \delta\big[(q_1^+ + q_1^-)u_1 + (q_2^+ + q_2^-)u_2 + h(q_1^+ - q_1^-)\psi_1 + h(q_2^+ - q_2^-)\psi_2 + \\
&+ (q_3^+ + q_3^-)w + + (m_2^+ + m_2^-)\Omega_2 + (m_3^+ + m_3^-)\Omega_3 + h(m_3^+ - m_3^-)\iota\big] \\
&A_1 A_2 d\alpha_1 d\alpha_2 dt - \int\limits_{t_1}^{t_2} \Bigg\{ \int\limits_{(\Gamma_1')} \delta\big(S_{21}^* u_1 + T_{22}^* u_2 + N_{23}^* w + H_{21}^* \psi_1 + M_{22}^* \psi_2 + \\
&+ L_{21}^* \Omega_1 + L_{22}^* \Omega_2 + L_{23}^* \Omega_3 + \Lambda_{23}^* \iota\big) A_2 d\alpha_2 + \int\limits_{(\Gamma_1'')} \delta\big[S_{21}(u_1 - u_1^*) + T_{22}(u_2 - u_2^*) + \\
&+ H_{21}(\psi_1 - \psi_1^*) + M_{22}(\psi_2 - \psi_2^*) + N_{23}(w - w^*) + L_{21}(\Omega_1 - \Omega_1^*) + \\
&+ L_{22}(\Omega_2 - \Omega_2^*) + L_{23}(\Omega_3 - \Omega_3^*) \Lambda_{23}(\iota - \iota^*)\big] A_2 d\alpha_2 - \\
&- \int\limits_{(\Gamma_2')} \delta\big(T_{11}^* u_1 + S_{12}^* u_2 + N_{13}^* w + M_{11}^* \psi_1 + H_{12}^* \psi_2 + L_{11}^* \Omega_1 + \\
&+ L_{12}^* \Omega_2 + L_{13}^* \Omega_3 + \Lambda_{13}^* \iota\big) A_1 d\alpha_1 - \int\limits_{(\Gamma_2'')} \delta\big[T_{11}(u_1 - u_1^*) + S_{12}(u_2 - u_2^*) + \\
&+ N_{13}(w - w^*) + M_{11}(\psi_1 - \psi_1^*) H_{12}(\psi_2 - \psi_2^*) + L_{11}(\Omega_1 - \Omega_1^*) + \\
&+ L_{12}(\Omega_2 - \Omega_2^*) + L_{13}(\Omega_3 - \Omega_3^*) + \Lambda_{13}(\iota - \iota^*)\big] A_1 d\alpha_1 \Big\} dt = 0.
\end{aligned}
\tag{33}
$$

Assuming that all the functional arguments $u_i, w, \psi_i, \Omega_k, \iota\,(i = 1, 2;\; k = 1, 2, 3)$, $\Gamma_{ii}$, $K_{ii}$, $\Gamma_{ij}$, $K_{ij}$, $\Gamma_{i3}$, $\Gamma_{3i}$, $k_{ii}$, $k_{33}$, $k_{ij}$, $k_{i3}$, $l_{i3}$, $T_{ii}$, $S_{ij}$, $N_{i3}$, $N_{3i}$, $M_{11}$, $H_{ij}$, $L_{ii}$, $L_{33}$, $L_{ij}$, $L_{i3}$, $\Lambda_{i3}\,(i, j = 1, 2; i \neq j)$ are free, and their variations are arbitrary, after varying the physical relations of elasticity (25), the motion equations (26), the geometric relations (10)–(13) and the boundary conditions (27) will be obtained: static ones on the $l_1', l_2'$ and geometric ones on $l_1'', l_2''$.

The variation principle (33) is rather general, however not an extremal. Equation (33) expresses only the condition of stationarity of a definite functional. This means that among all possible stress-strain states of micropolar elastic thin shells with free fields of displacements and rotations, the genuine is the one, for which the specified functional takes a stationary value.

Various private variation principles can be obtained from the above introduced variation equation (which can be also called Hamilton's generalized variation equation). First, taking some expressions from Euler equations and natural boundary conditions as additional conditions, then eliminating the dependent part of the functional arguments in Eq. (33) with the help of the mentioned conditions, the corresponding particular variation principle will be obtained.

## 6 Conclusion

In the present paper a general applied theory of the dynamics of micropolar elastic thin shells with free fields of displacements and rotations is constructed. The constructed applied dynamic theory of micropolar thin shells makes it also possible to calculate the distribution of stresses and moment stresses along the thickness of the shell. D'Alembert-Lagrange variation equation, the law of conservation of the mechanical energy, Hamilton's variation principle, and the general variation principle of Hu-Washizu type (or Hamilton's generalized variation principle) are established for this theory.

## References

1. Green, A.E., Naghdi, P.M.: The linear elastic cosserat surface and shell theory. Int. J. Solids Struct. **4**, 585–592 (1968)
2. Zhilin, P.A.: Fundamentals of the theory of shells. Applied Mechanics, vol. 167. Publishing House of Polytechnic University (2016). (in Russian)
3. Eremeev, V.A., Zubov, L.M.: Mechanics of elastic shells. M.: Nauka, vol. 280 (2008)
4. Altenbach, H., Eremeyev, V.A.: On the linear theory of micropolar plates: Z angew. Math. Mech. Zamm. **89**(4), 242–256 (2009)
5. Altenbach, H., Eremeyev, V.: Basics of mechanics of micropolar shells. In: CISM International Centre for Mechanical Sciences (Courses and Lectures) Shell-like Structures, vol. 572, pp. 63–112 (2017)
6. Sargsyan, S.H.: Boundary-value problems of asymmetric theory of elasticity for thin plates. J. Appl. Math. Mech. **72**(1), 77–86 (2008)

7. Sargsyan, S.H.: The theory of micropolar thin elastic shells. J. Appl. Math. Mech. **76**(2), 235–249 (2012)
8. Sargsyan, S.H.: Asymptotically confirmed hypotheses method for the construction of micropolar and classical theories of elastic thin shells. Adv. Pure Math. **5**(10), 629–643 (2015)
9. Zhilin, P.A.: Theoretical mechanics. Fundamental Laws of Mechanics, vol. 340. Publishing house St. Petersburg Polytechnical University, St. Petersburg (2003). (in Russian)
10. Nowacкi, W.: Theory of Asymmetric Elasticity, vol. 383. Pergamon Press, Oxford, New York, Toronto, Sydney, Paris, Frankfurt (1986)
11. Palmov, V.A.: Fundamental equations of the theory of asymmetric elasticity. Appl. Math. Mech. **28**(3), 496–505 (1964)
12. Novozhilov, V.V.: The Theory of thin Shells, vol. 370. Sudpromgiz, Leningrad (1958). (in Russian)
13. Pelekh, B.L.: Theory of shells with finite shear stiffness. Naukova Dumka, vol. 248. Publishing House, Kiev (1973). (in Russian)

# Nonlinear Modulation of Surface SH Waves in a Double Layered Elastic Half Space

**Mevlüt Teymur, Halil İbrahim Var and Ekin Deliktas**

**Abstract** The nonlinear shear horizontal (SH) surface waves in an elastic half space coated with two different layers of uniform thickness are examined. The half space and both layers are assumed to be homogeneous, isotropic, incompressible, elastic and having different mechanical properties. In the analysis it is assumed that linear shear velocity of the top layer is slower than velocities of the internal layer and the half space. By employing the method of multiple scales, it is shown that nonlinear modulation of SH waves is governed asymptotically by a nonlinear Schrödinger (NLS) equation. The coefficients of this equation depend on, in a complicated way, on linear and nonlinear material parameters of the layered half space, the thicknesses of the layers and also the wave number of the waves. The effect of the existence of a second layer on the existence of solitary waves has been investigated numerically. Also a comparison between the coefficients of the NLS equation for the double layered half space and that of a single layered half space has been made. It is remarked that the existence of the envelope and dark solitons is affected strongly by the nonlinear material parameter of the top layer.

**Keywords** Surface SH waves · Double layered half space
Nonlinear Schrödinger equation

## 1 Introduction

Linear elastic waves in wave guides made by homogeneous isotropic linear elastic materials are dispersive due to the repeated reflection processes which occur at the boundaries between different media. Dispersive elastic waves have been extensively

---

M. Teymur (✉) · E. Deliktas
Faculty of Science and Letters, Department of Mathematics, İstanbul Technical University,
34469 Maslak, Istanbul, Turkey
e-mail: teymur@itu.edu.tr

H. İ. Var
Faculty of Science and Letters, Department of Mathematics, Marmara University,
Istanbul, Turkey

H. Altenbach et al. (eds.), *Dynamical Processes in Generalized Continua and Structures*, Advanced Structured Materials 103,
https://doi.org/10.1007/978-3-030-11665-1_27

studied because of their important applications in geophysics, nondestructive testing of materials, electronic signal processing devices, etc. (see, e.g. [2, 6, 7] and references there in). In recent years, connected with these applications, the effect of the constitutional nonlinearities on the propagation characteristics of dispersive elastic waves is investigated by employing the asymptotic perturbation methods previously used in the fields of fluid mechanics, lattice dynamics, plasma physics etc., examining the propagation of weakly nonlinear waves (see, e.g. [1, 4, 10, 28]). In these investigations, as a result of balance between nonlinearity and dispersion several different types of nonlinear evolution equations such as Korteweg–de Vries (K–dV), modified K–dV, NLS and Boussinesq (BE), etc. have been derived to describe the propagation of nonlinear elastic waves in media having boundaries causing dispersion such as rods, plates, layered half spaces, etc., asymptotically. Then several aspects of problems, such as nonlinear stability of modulated waves, steady state solutions, the existence of various types of solitary waves, etc. were discussed on the basis of these equations. (see e.g. [3, 8, 13, 14, 20, 21, 23, 25–27]). For an extensive review of most of these works we refer [15–19, 22].

In the present work, the propagation of nonlinear shear horizontal (SH) waves in a half space covered by two homogenous isotropic incompressible elastic layers having different mechanical properties is considered. The corresponding linear problem has been firstly examined by Stoneley and Tillotson [24] since it is a theoretical basis of a method which is developed in order to calculate the thickness of the subcontinental layer. Firstly, [9] calculated the thickness of the subcontinental layer of granite overlying a half space of rock. Stoneley and Tillotson [24] claimed that Jeffrey's study was inadequate, since the existence of a basalt layer under the granite was not regarded, hence they have constituted a two layered half space model on the assumption that the half space, the internal layer and the top layer consist of rock, basalt and granite, respectively. In this analysis it was assumed that between the linear shear velocities of the top layer $c_1$, the internal layer, $c_2$, and the half space, $c_3$, the inequality $c_1 < c_2 < c_3$ is valid. If the phase velocity $c$ of the wave satisfies either the condition $c_1 < c_2 < c < c_3$ or the one $c_1 < c < c_2 < c_3$, it is shown that a surface wave propagates. Under these two conditions, the present work extends this study to the nonlinear propagation of the surface SH waves. The constituent materials are assumed to be generalized neo-Hookean materials having different mechanical properties. In the linear limit, the problem reduces to the problem investigated by Stoneley and Tillotson [24]. Then the propagation of small but finite amplitude waves is considered. By employing a multiple scale perturbation method (see, e.g. [10]), an NLS equation is obtained for the nonlinear modulation of the waves. The coefficients of this equation depend on linear and nonlinear material parameters of the layered half space, the thickness ratio of the layers and also the wave number of the waves. It is also observed that when the thickness of the top layer goes to zero, the coefficients of the NLS equation approach to those of the NLS equation for a single layered half space. Then, since the properties of solutions of the NLS equation strongly depend on the sign of the product of its coefficients, the variation of this product with the wave number is evaluated numerically by giving appropriate values to the material constants and to the thickness ratio of the layers. To observe the effect of nonlinearity on the coefficients, consequently on the solutions of the NLS equation, the linear material constants are held fixed while the nonlinear ones are being changed. From the comparison of the coefficients of the NLS equations for a double layered half space and a single layered half space, it is observed that the propagation is affected considerably by the existence of a second layer. Moreover, for relatively long waves the nonlinear properties of the half space dominate the modulation of the waves.

## 2 Formulation of the Problem

Let $(x_1, x_2, x_3)$ and $(X_1, X_2, X_3)$ be, respectively, the spatial and material coordinates of a point referred to the same rectangular Cartesian system of axes. Consider an elastic half space covered by two different elastic layers each of uniform thickness. In the reference frame $(X_1, X_2, X_3)$, the top layer $(R_1)$, the intermediate layer $(R_2)$ and the half space $(R_3)$ occupy the regions, respectively

$$R_1 = \{(X_1, X_2, X_3) \mid 0 < X_2 < h_1 \quad -\infty < X_1 < \infty, \quad -\infty < X_3 < \infty\} \tag{1}$$

$$R_2 = \{(X_1, X_2, X_3) \mid -h_2 < X_2 < 0 \quad -\infty < X_1 < \infty, \quad -\infty < X_3 < \infty\} \tag{2}$$

$$R_3 = \{(X_1, X_2, X_3) \mid -\infty < X_2 < -h_2 \quad -\infty < X_1 < \infty, \quad -\infty < X_3 < \infty\} \tag{3}$$

where $h_1$ and $h_2$ are positive constants. It is assumed that the free boundary $X_2 = h_1$ is free of traction, the stresses and displacements are continuous at the interfaces $X_2 = 0$ and $X_2 = -h_2$; moreover the displacement in the half space goes to zero as $X_2 \to -\infty$.

Now, we consider a shear horizontal (SH) wave propagating along the $X_1$-axis in this layered half space described by the equations

$$x_1 = X_1, \quad x_2 = X_2, \quad x_3 = X_3 + u^{(r)}(X_1, X_2, t) \quad r = 1, 2, 3 \tag{4}$$

where $t$ is the time, the superscript $r$ refers to the region $R_r$, $u^{(r)}$ is the displacement of a particle in the $X_3$ direction in the region $R_r$. Since $det x_{k,K} = 1$, the deformation field (4) is isochoric and the density $\rho^{(r)}$ in motion remains constant. Then in the absence of body forces, the equations of motion in the reference state are written as

$$T^{(r)}_{K\beta,K} = 0, \quad \beta = 1, 2; \qquad T^{(r)}_{K3,K} = \rho^{(r)} \ddot{u}^{(r)}, \quad r = 1, 2, 3 \tag{5}$$

where $T^{(r)}_{Kl}$ is the first Piola-Kirchoff stress tensor, Latin and Greek indices take the respective ranges (1, 2, 3) and (1, 2), subscripts preceded by a comma indicate partial differentiation with respect to the material coordinates and an over dot represents the partial differentiation with respect to $t$.

The assumption of vanishing tractions on the free surface $X_2 = h_1$ imposes the boundary condition

$$T^{(1)}_{2k} = 0, \quad \text{on} \quad X_2 = h_1, \tag{6}$$

while continuity of stresses and displacements at the interfaces $X_2 = 0$ and $X_2 = -h_2$ is satisfied if

$$T^{(1)}_{2k} = T^{(2)}_{2k}, \quad \text{and} \quad u^{(1)} = u^{(2)} \quad \text{on} \quad X_2 = 0, \tag{7}$$

and

$$T^{(2)}_{2k} = T^{(3)}_{2k}, \quad \text{and} \quad u^{(2)} = u^{(3)} \quad \text{on} \quad X_2 = -h_2, \quad k = 1, 2, 3. \tag{8}$$

In this work, it is assumed that the constituent materials are homogenous, nonlinear, isotropic, incompressible elastic and their strain energy functions are only the functions of the first invariant of Finger deformation tensor $\mathbf{c}^{-1} = [x_{k,K} x_{l,K}]$, i.e. $\Sigma^{(r)} = \Sigma^{(r)}(I^{(r)})$ where $I^{(r)} = tr\mathbf{c}^{-1}$, $r = 1, 2, 3$. Namely, the double layered half space is made of generalized neo-Hooken materials (see, e.g. [11]). For the antiplane motion (4), the first invariants $I^{(r)}$ are found to be

$$I^{(r)} = 3 + \mathcal{K}^{(r)} \qquad \mathcal{K}^{(r)} = \left(\frac{\partial u^{(r)}}{\partial X_1}\right)^2 + \left(\frac{\partial u^{(r)}}{\partial X_2}\right)^2 \quad r = 1, 2, 3 \tag{9}$$

Stress constitutive equations for a generalized neo-Hookean medium can be expressed as (see, e.g. [5])

$$t_{kl} = -p\delta_{kl} + \Phi c^{-1}_{kl} \qquad \text{with} \ \Phi = 2\frac{\partial \Sigma}{\partial I} \tag{10}$$

where $t_{kl}$ is the components of Cauchy stress tensor and $p(X_K, t)$ is a hydrostatic pressure function. Then, by using the relation $T_{Kl} = jX_{K,k}t_{kl}$, where $j = det(x_{k,K}) = 1$, the components of the Piola-Kirchoff stress tensor are written as (see [26] for details)

$$T^{(r)}_{\alpha\beta} = T^{(r)}_{33} = 0\,, \quad T^{(r)}_{\alpha 3} = T^{(r)}_{3\alpha} = \Phi^{(r)} u^{(r)}_{,\alpha} \tag{11}$$

Hence the first two equations in (5) are satisfied identically and therefore the antiplane motion (4) can exist in the double layered elastic half space made of generalized neo-Hooken materials without body forces. Let $X = X_1$, $Y = X_2$, $Z = X_3$, then the third equation in (5) and the boundary conditions of the problem can be written as

$$\frac{\partial}{\partial X}\left(\Phi^{(r)}\frac{\partial u^{(r)}}{\partial X}\right) + \frac{\partial}{\partial Y}\left(\Phi^{(r)}\frac{\partial u^{(r)}}{\partial Y}\right) = \rho^{(r)}\frac{\partial^2 u^{(r)}}{\partial t^2} \quad r = 1, 2, 3 \tag{12}$$

$$\frac{\partial u^{(1)}}{\partial Y} = 0 \quad \text{on the free boundary} \quad Y = h_1 \tag{13}$$

$$u^{(1)} = u^{(2)} \text{ and } \Phi^{(1)}\frac{\partial u^{(1)}}{\partial Y} = \Phi^{(2)}\frac{\partial u^{(2)}}{\partial Y} \text{ on } Y = 0\,(\text{the interface between } R_1 \text{ and } R_2) \tag{14}$$

$$u^{(2)} = u^{(3)} \text{ and } \Phi^{(2)} \frac{\partial u^{(2)}}{\partial Y} = \Phi^{(3)} \frac{\partial u^{(3)}}{\partial Y} \text{ on } Y = -h_2 \text{ (the interface between } R_2 \text{ and } R_3) \tag{15}$$

$$u^{(3)} \to 0 \quad \text{as} \quad Y \to -\infty \text{ (the radiation condition)} \tag{16}$$

## 3 Small but Finite Amplitude Waves

We now examine the propagation of small but finite amplitude surface SH waves. To do this we will employ the method of multiple scales by introducing the following new independent variables

$$x_i = \epsilon^i X, \quad t_i = \epsilon^i t, \quad y = Y, \quad i = 0, 1, 2 \tag{17}$$

in which $\epsilon > 0$ is a small parameter which measures the weakness of the nonlinearity and $(x_1, x_2, t_1, t_2)$ are the slow variables describing the slow variations in the problem whereas $(x_0, t_0, y)$ are fast variables describing the fast variations. Then $u^{(r)}$, $r = 1, 2, 3$, are taken to be functions of these new independent variables and they are expanded in the following asymptotic series in $\epsilon$:

$$u^{(r)} = \sum_{n=1}^{\infty} \epsilon^n u_n^{(r)}(x_0, x_1, x_2, y, t_0, t_1, t_2) \tag{18}$$

Writing the governing equations and boundary conditions in terms of the new independent variables (17) and then employing the expansions (18) in the resulting expressions and collecting the terms of like powers in $\epsilon$ yield a hierarchy of problems from which it is possible to determine $u_n^{(r)}$, successively. Up to third order in $\epsilon$ these are given as below:

$O(\epsilon)$:

$$L(u_1^{(r)}) = \frac{\partial^2 u_1^{(r)}}{\partial t_0^2} - c_r^2 \left( \frac{\partial^2 u_1^{(r)}}{\partial x_0^2} + \frac{\partial^2 u_1^{(r)}}{\partial y^2} \right) = 0 \quad r = 1, 2, 3 \tag{19}$$

$$\frac{\partial u_1^{(1)}}{\partial y} = 0 \quad \text{at} \quad y = h_1 \tag{20}$$

$$u_1^{(1)} = u_1^{(2)} \quad \text{and} \quad \frac{\partial u_1^{(1)}}{\partial y} - \gamma_1 \frac{\partial u_1^{(2)}}{\partial y} = 0 \quad \text{at} \quad y = 0 \tag{21}$$

$$u_1^{(2)} = u_1^{(3)} \quad \text{and} \quad \frac{\partial u_1^{(2)}}{\partial y} - \gamma_2 \frac{\partial u_1^{(3)}}{\partial y} = 0 \quad \text{at} \quad y = -h_2 \tag{22}$$

$$u_1^{(3)} \to 0 \quad \text{as} \quad y \to -\infty \tag{23}$$

$O(\epsilon^2)$:

$$L(u_2^{(r)}) = 2\left(c_r^2 \frac{\partial^2 u_1^{(r)}}{\partial x_0 \partial x_1} - \frac{\partial^2 u_1^{(r)}}{\partial t_0 \partial t_1}\right) \quad r = 1, 2, 3 \tag{24}$$

$$\frac{\partial u_2^{(1)}}{\partial y} = 0 \quad \text{at} \quad y = h_1 \tag{25}$$

$$u_2^{(1)} = u_2^{(2)} \quad \text{and} \quad \frac{\partial u_2^{(1)}}{\partial y} - \gamma_1 \frac{\partial u_2^{(2)}}{\partial y} = 0 \quad \text{at} \quad y = 0 \tag{26}$$

$$u_2^{(2)} = u_2^{(3)} \quad \text{and} \quad \frac{\partial u_2^{(2)}}{\partial y} - \gamma_2 \frac{\partial u_2^{(3)}}{\partial y} = 0 \quad \text{at} \quad y = -h_2 \tag{27}$$

$$u_2^{(3)} \to 0 \quad \text{as} \quad y \to -\infty \tag{28}$$

$O(\epsilon^3)$:

$$\begin{aligned} L(u_3^{(r)}) = {} & 2\left(c_r^2 \frac{\partial^2 u_2^{(r)}}{\partial x_0 \partial x_1} - \frac{\partial^2 u_2^{(r)}}{\partial t_0 \partial t_1}\right) + c_r^2\left(\frac{\partial^2 u_1^{(r)}}{\partial x_1^2} + 2\frac{\partial^2 u_1^{(r)}}{\partial x_0 x_2}\right) - \frac{\partial^2 u_1^{(r)}}{\partial t_1^2} - 2\frac{\partial^2 u_1^{(r)}}{\partial t_0 t_2} \\ & + n_r\left(\frac{\partial}{\partial x_0}\left(\frac{\partial u_1^{(r)}}{\partial x_0}\mathcal{K}_0(u_1^{(r)})\right) + \frac{\partial}{\partial Y}\left(\frac{\partial u_1^{(r)}}{\partial Y}\mathcal{K}_0(u_1^{(r)})\right)\right) \quad r = 1, 2, 3 \end{aligned} \tag{29}$$

$$\frac{\partial u_3^{(1)}}{\partial y} = 0 \quad \text{at} \quad y = h_1 \tag{30}$$

$$\begin{aligned} & u_3^{(1)} = u_3^{(2)} \quad \text{and} \\ & \frac{\partial u_3^{(1)}}{\partial y} - \gamma_1 \frac{\partial u_3^{(2)}}{\partial y} = \gamma_1 \beta_2 \frac{\partial u_1^{(2)}}{\partial y}\mathcal{K}_0(u_1^{(2)}) - \beta_1 \frac{\partial u_1^{(1)}}{\partial y}\mathcal{K}_0(u_1^{(1)}) \quad \text{at} \quad y = 0 \end{aligned} \tag{31}$$

$$\begin{aligned} & u_3^{(2)} = u_3^{(3)} \quad \text{and} \\ & \frac{\partial u_3^{(2)}}{\partial y} - \gamma_2 \frac{\partial u_3^{(3)}}{\partial y} = \gamma_2 \beta_3 \frac{\partial u_1^{(3)}}{\partial y}\mathcal{K}_0(u_1^{(3)}) - \beta_2 \frac{\partial u_1^{(2)}}{\partial y}\mathcal{K}_0(u_1^{(2)}) \quad \text{at} \quad y = -h_2 \end{aligned} \tag{32}$$

$$u_3^{(3)} \to 0 \quad \text{as} \quad y \to -\infty \tag{33}$$

where

$$\mathcal{K}_0(\psi) = \left(\frac{\partial \psi}{\partial x_0}\right)^2 + \left(\frac{\partial \psi}{\partial y}\right)^2 . \tag{34}$$

In the above equations the constants $c_r$, $r = 1, 2, 3$ are the linear shear velocities in the top layer, intermediate layer and half space, respectively, and they are defined as $c_r^2 = \mu^{(r)}/\rho^{(r)}$ where $\mu^{(r)}$ are linear shear modulus given as $\mu^{(r)} = 2d\Sigma^{(r)}(3)/dI$. $n_r$ defined as $n_r = (2/\rho^{(r)})d^2\Sigma^{(r)}(3)/dI^2$ are nonlinear material constants. If $n_r > 0$, the relevant medium is hardening in shear, else it is softening. The constants $\gamma_r$ and $\beta_r$ are defined as $\gamma_r = \mu^{(r+1)}/\mu^{(r)}$, $\beta_r = n_r/c_r^2$. Note that, these perturbation problems, at each step, are linear and first order problem is simply the classic linear wave problem which was first investigated by Stoneley and Tillotson [24]. They showed that between the linear shear velocities of the layers and the half space if the inequalities $c_1 < c_2 < c_3$ hold then when the phase velocity $c$ of the SH wave satisfies the either inequality

$$c_1 < c_2 < c < c_3 \qquad \text{or} \qquad c_1 < c < c_2 < c_3 \tag{35}$$

then SH waves are dispersive. We proceed first by assuming that the first inequality is satisfied by the phase velocity $c$ of the surface SH wave.We also assume that the nonexistence of the long waves in the initial disturbances. Hence by using the separation of variables method and also by employing the radiation conditions (23), the solutions of the Eqs. (19) are found to be

$$u_1^{(1)} = \sum_{l=1}^{\infty} \left\{ A_1^{(l)}(x_1, x_2, t_1, t_2) e^{ilkp_1 y} + B_1^{(l)}(x_1, x_2, t_1, t_2) e^{-ilkp_1 y} \right\} e^{il\theta} + c.c \tag{36}$$

$$u_1^{(2)} = \sum_{l=1}^{\infty} \left\{ C_1^{(l)}(x_1, x_2, t_1, t_2) e^{ilkp_2 y} + D_1^{(l)}(x_1, x_2, t_1, t_2) e^{-ilkp_2 y} \right\} e^{il\theta} + c.c \tag{37}$$

$$u_1^{(3)} = \sum_{l=1}^{\infty} E_1^{(l)}(x_1, x_2, t_1, t_2) e^{lkv_3 y} e^{il\theta} + c.c \tag{38}$$

where

$$\theta = kx_0 - \omega t_0\,, \;\; p_1 = (c^2/c_1^2 - 1)^{1/2}\,, \;\; p_2 = (c^2/c_2^2 - 1)^{1/2}\,, \;\; v_3 = (1 - c^2/c_3^2)^{1/2} \tag{39}$$

and $k$ is the wave number, $\omega$ is the angular frequency, $c = \omega/k$ is the phase velocity, the symbol $''c.c.''$ denotes the complex conjugate of the preceding terms, $A_1^{(l)}$, $B_1^{(l)}$, $C_1^{(l)}$, $D_1^{(l)}$ and $E_1^{(l)}$ are the first order slowly varying amplitude functions of the waves to be determined by using the boundary conditions of the first order perturbation problem. Hence the substitution of first order solutions into the boundary conditions of the first order perturbation problem yields

$$\mathbf{W}_l \, \mathbf{U}_1^{(l)} = \mathbf{0}, \quad l = 1, 2, \ldots, \tag{40}$$

where $\mathbf{W}_l$ is the dispersion matrix defined as

$$\mathbf{W}_l = \begin{pmatrix} iklp_1 e^{ilP_1} & -iklp_1 e^{-ilP_1} & 0 & 0 & 0 \\ iklp_1 & -iklp_1 & -i\gamma_1 klp_2 & i\gamma_1 klp_2 & 0 \\ 1 & 1 & -1 & -1 & 0 \\ 0 & 0 & iklp_2 e^{-ilP_2} & -iklp_2 e^{ilP_2} & -\gamma_2 klv_3 e^{-lV_3} \\ 0 & 0 & e^{-ilP_2} & e^{ilP_2} & -e^{-lV_3} \end{pmatrix} \tag{41}$$

and the vectors $\mathbf{U}_n^{(l)}$ , $n = 1, 2, \ldots,$ are defined as

$$\mathbf{U}_n^{(l)} = (A_n^{(l)}, B_n^{(l)}, C_n^{(l)}, D_n^{(l)}, E_n^{(l)})^T \quad . \tag{42}$$

$\det \mathbf{W}_1 = 0$ gives the dispersion relation of the linear waves

$$p_1 p_2 \tan P_1 + \gamma_2 p_1 v_3 \tan P_1 \tan P_2 - \gamma_1 \gamma_2 p_2 v_3 + \gamma_1 p_2^2 \tan P_2 = 0 \tag{43}$$

where $P_1 = kp_1h_1$, $P_2 = kp_2h_2$, which is first derived by [24]. Note that, when the thickness of the top layer goes to zero, $h_1 = 0$, this dispersion relation reduces to

$$-\gamma_2 p_2 v_3 + p_2^2 \tan P_2 = 0 \tag{44}$$

which is the dispersion relation obtained for the propagation of Love waves in a half space covered by a single layer [12]. In this work, nonlinear self modulation of a group of surface SH-waves centered around a wave number $k$ and corresponding frequency $\omega$ is investigated. Thus the harmonic-resonance phenomena is excluded in the analysis. Then for $l \geq 2$

$$\det \mathbf{W}_l \neq 0 \quad . \tag{45}$$

Hence, considering (45) the solutions of the homogeneous algebraic systems are found to be

$$\mathbf{U}_1^{(1)} = \mathcal{A}_1(x_1, x_2, t_1, t_2)\mathbf{R} \tag{46}$$

$$\mathbf{U}_1^{(l)} \equiv \mathbf{0} \quad \text{for} \quad l \geq 2 \tag{47}$$

where $\mathcal{A}_1$ is a complex function, representing the first order slowly varying amplitude of the self modulation and $\mathbf{R}$ is a column vector satisfying

$$\mathbf{W}_1\mathbf{R} = \mathbf{0}. \tag{48}$$

By using (46) and (47) the first order solutions are written explicitly as

$$u_1^{(1)} = \mathcal{A}_1(R_1 e^{ikp_1y} + R_2 e^{-ikp_1y})e^{i\theta} + c.c \tag{49}$$

$$u_1^{(2)} = \mathcal{A}_1(R_3 e^{ikp_2y} + R_4 e^{-ikp_2y})e^{i\theta} + c.c \tag{50}$$

$$u_1^{(3)} = \mathcal{A}_1 R_5 e^{kv_3y} e^{i\theta} + c.c \tag{51}$$

where $R_m$ , $m = 1, \ldots, 5$ are the components of $\mathbf{R}$, their explicit forms are given in the Appendix A.

To complete the first order solutions $\mathcal{A}_1$ has to be determined. This has been done by examining the higher order perturbation problems. Using the first order solutions in the differential equations of the second order perturbation problem yields

$$L(u_2^{(1)}) = 2iM_{11}^{(1)}(R_1 e^{ikp_1 y} + R_2 e^{-ikp_1 y})e^{i\theta} + c.c \tag{52}$$

$$L(u_2^{(2)}) = 2iM_{11}^{(2)}(R_3 e^{ikp_2 y} + R_4 e^{-ikp_2 y})e^{i\theta} + c.c \tag{53}$$

$$L(u_2^{(3)}) = 2iM_{11}^{(3)} R_5 e^{kv_3 y} e^{i\theta} + c.c \tag{54}$$

where

$$M_{11}^{(\alpha)} = \omega \frac{\partial \mathcal{A}_1}{\partial t_1} + kc_\alpha^2 \frac{\partial \mathcal{A}_1}{\partial x_1}, \quad \alpha = 1, 2, 3 \tag{55}$$

The solutions $u_2^{(r)}$, $r = 1, 2, 3$, of this problem are decomposed as

$$u_2^{(r)} = \bar{u}_2^{(r)} + \tilde{u}_2^{(r)} \tag{56}$$

where $\overline{u}_2^{(r)}$, $r = 1, 2, 3$, are the particular solutions of the nonhomogeneous differential equations while $\widetilde{u}_2^{(r)}$ are the solutions of the corresponding homogeneous equations satisfying the nonhomogeneous boundary conditions derived from the boundary conditions of the second order perturbation problem by considering the decompositions (56). The solutions $\overline{u}_2^{(r)}$ are found by the method of undetermined coefficients. For $\widetilde{u}_2^{(r)}$ the solutions satisfying the radiation condition are written as in the first order problem

$$\widetilde{u}_2^{(1)} = \sum_{l=1}^{\infty} \left\{ A_2^{(l)}(x_1, x_2, t_1, t_2) e^{ilkp_1 y} + B_2^{(l)}(x_1, x_2, t_1, t_2) e^{-ilkp_1 y} \right\} e^{il\theta} + c.c. \tag{57}$$

$$\widetilde{u}_2^{(2)} = \sum_{l=1}^{\infty} \left\{ C_2^{(l)}(x_1, x_2, t_1, t_2) e^{ilkp_2 y} + D_2^{(l)}(x_1, x_2, t_1, t_2) e^{-ilkp_2 y} \right\} e^{il\theta} + c.c. \tag{58}$$

$$\widetilde{u}_2^{(3)} = \sum_{l=1}^{\infty} E_2^{(l)}(x_1, x_2, t_1, t_2) e^{lkv_3 y} e^{il\theta} + c.c. \tag{59}$$

The second order slowly varying amplitudes $\mathbf{U}_2^{(l)} = (A_2^{(l)}, B_2^{(l)}, C_2^{(l)}, D_2^{(l)}, E_2^{(l)})^T$ of the waves are determined by employing the nonhomogeneous boundary conditions. Then the use of $\widetilde{u}_2^{(r)}$ together with the solutions $\overline{u}_2^{(r)}$, $r = 1, 2, 3$, in the boundary conditions of the second order problem yields the following systems of algebraic equations

$$\mathbf{W}_l\, \mathbf{U}_2^{(l)} = \mathbf{b}_2^{(l)} \tag{60}$$

where

$$\mathbf{b}_2^{(1)} = -i \left( \frac{\partial \mathcal{A}_1}{\partial t_1} \frac{\partial \mathbf{W}_1}{\partial \omega} - \frac{\partial \mathcal{A}_1}{\partial x_1} \frac{\partial \mathbf{W}_1}{\partial k} \right) \mathbf{R} \quad \text{and} \quad \mathbf{b}_2^{(l)} \equiv \mathbf{0} \quad \text{for all} \quad l \neq 1 \tag{61}$$

Since it is assumed that $\det \mathbf{W}_l \neq 0$ for $l \geq 2$, for these cases the solutions of (60) are

$$\mathbf{U}_2^{(l)} \equiv \mathbf{0}, \quad l \geq 2 \tag{62}$$

Since $\det \mathbf{W}_1 = 0$ and $\mathbf{b}_2^{(1)} \neq \mathbf{0}$, in order that the Eq. (60) to have a solution for $\mathbf{U}_2^{(1)}$ the compatibility condition

$$\mathbf{L}.\mathbf{b}_2^{(1)} = 0 \tag{63}$$

must be satisfied, where $\mathbf{L}$ is a left vector defined by $\mathbf{L}\mathbf{W_1} = \mathbf{0}$. Then the compatibility condition (63) leads to the result

$$\frac{\partial \mathcal{A}_1}{\partial t_1} + V_g \frac{\partial \mathcal{A}_1}{\partial x_1} = 0 \tag{64}$$

where $V_g = \frac{d\omega}{dk} = -\left(\mathbf{L}\frac{\partial \mathbf{W_1}}{\partial \mathbf{k}}\mathbf{R}\right) / \left(\mathbf{L}\frac{\partial \mathbf{W_1}}{\partial \omega}\mathbf{R}\right)$ is the group velocity of the waves. The Eq. (64) implies that the amplitude $\mathcal{A}_1$ remains constant in a frame of reference moving with the group velocity $V_g$. That is, $\mathcal{A}_1 = \mathcal{A}_1(x_1 - V_g t_1, x_2, t_2)$. Then $\mathbf{U}_2^{(1)}$ is found to be

$$\mathbf{U}_2^{(1)} = \mathcal{A}_2 \mathbf{R} - i \frac{\partial \mathcal{A}_1}{\partial x_1}\left(\frac{\partial \mathbf{R}}{\partial k} + V_g \frac{\partial \mathbf{R}}{\partial \omega}\right) \tag{65}$$

where $\mathcal{A}_2 = \mathcal{A}_2(x_1, x_2, t_1, t_2)$ is a complex function representing the second order slowly varying amplitude of the wave modulation, and it can be determined from higher-order perturbation problems. But, since this work is centered around the small but finite amplitude waves, the aim is here to obtain just the uniformly valid first-order solution. Note that, we assume that $\mathcal{A}_2$ depends on $x_1$ and $t_1$ through the combination $x_1 - V_g t_1$ as $\mathcal{A}_1$, so it is not necessary to evaluate $\mathcal{A}_2$, it is sufficient to determinate $\mathcal{A}_1$ only to obtain the first order solution, and this will be done at the third order perturbation problem. The substitution of the first and second order solutions into the third order equations (29) gives

$$\begin{aligned} L(u_3^{(1)}) = {} & (\mathcal{D}_1 e^{ikp_1 y} + \mathcal{D}_2 y e^{ikp_1 y} + \mathcal{D}_3 e^{-ikp_1 y} + \mathcal{D}_4 y e^{-ikp_1 y} \\ & + \mathcal{D}_5 e^{3ikp_1 y} + \mathcal{D}_6 e^{-3ikp_1 y}) e^{i\theta} + c.c. + \text{ terms in } (e^{\pm 3i\theta}), \end{aligned} \tag{66}$$

$$\begin{aligned} L(u_3^{(2)}) = {} & (\mathcal{D}_7 e^{ikp_2 y} + \mathcal{D}_8 y e^{ikp_2 y} + \mathcal{D}_9 e^{-ikp_2 y} + \mathcal{D}_{10} y e^{-ikp_2 y} \\ & + \mathcal{D}_{11} e^{3ikp_2 y} + \mathcal{D}_{12} e^{-3ikp_2 y}) e^{i\theta} + c.c. + \text{ terms in } (e^{\pm 3i\theta}) \end{aligned} \tag{67}$$

$$L(u_3^{(3)}) = (\mathcal{D}_{13} e^{kv_3 y} + \mathcal{D}_{14} y e^{kv_3 y} + \mathcal{D}_{15} e^{3kv_3 y}) e^{i\theta} + c.c. + \text{ terms in } (e^{\pm 3i\theta}) \tag{68}$$

The explicit forms of the coefficients $\mathcal{D}_i, i = 1, \ldots, 15$ will be given in the Appendix B. The solutions of the third order problem can be sought as in the second order problem. That is we decompose the solutions as

$$u_3^{(r)} = \bar{u}_3^{(r)} + \tilde{u}_3^{(r)}, \quad r = 1, 2, 3 \tag{69}$$

where $\bar{u}_3^{(r)}$, $r = 1, 2, 3$, are the particular solutions found by using the method of undetermined coefficients. $\widetilde{u}_3^{(r)}$, $r = 1, 2, 3$, the solutions of the corresponding homogenous equations satisfying the nonhomogeneous boundary conditions (30)–(33) are written as in the second order problem replacing $\mathbf{U}_2^{(l)}$ by $\mathbf{U}_3^{(l)}$ respectively in (57)–(59). $\mathbf{U}_3^{(l)} = (A_3^{(l)}, B_3^{(l)}, C_3^{(l)}, D_3^{(l)}, E_3^{(l)})^T$ are third order amplitude functions depending on the slow variables $x_1, x_2, t_1, t_2$.

The particular solutions $\bar{u}_3^{(r)}$, $r = 1, 2, 3$, can be expressed as a sum of linearly independent terms of the forms

$$\bar{u}_3^{(r)} = f_r^{(1)}(x_1, x_2, t_1, t_2)e^{i\theta} + f_r^{(3)}(x_1, x_2, t_1, t_2)e^{3i\theta} + c.c. \quad r = 1, 2, 3 \tag{70}$$

where the terms $f_r^{(1)}$, $r = 1, 2, 3$, are related with the self-interaction of the waves while the terms $f_r^{(3)}$, $r = 1, 2, 3$, are representing the third harmonic interaction effects. Since, we are only interested in the self interaction, the explicit form of term $f_r^{(3)}$, $r = 1, 2, 3$, will not be required. Therefore, we only calculate $f_r^{(1)}$, $r = 1, 2, 3$. Hence, these solutions are obtained by the method of undetermined coefficients as

$$f_1^{(1)} = (\varepsilon_1 + \varepsilon_2 y)ye^{ikp_1 y} + (\varepsilon_3 + \varepsilon_4 y)ye^{-ikp_1 y} + \varepsilon_5 e^{3ikp_1 y} + \varepsilon_6 e^{-3ikp_1 y} + c.c \tag{71}$$

$$f_2^{(1)} = (\varepsilon_7 + \varepsilon_8 y)ye^{ikp_2 y} + (\varepsilon_9 + \varepsilon_{10} y)ye^{-ikp_2 y} + \varepsilon_{11} e^{3ikp_2 y} + \varepsilon_{12} e^{-3ikp_2 y} + c.c \tag{72}$$

$$f_3^{(1)} = (\varepsilon_{13} + \varepsilon_{14} y)ye^{kv_3 y} + \varepsilon_{15} e^{3kv_3 y} + c.c \tag{73}$$

Explicit forms of the $\varepsilon_i, i = 1, 2, \ldots, 15$ are given in the Appendix B. Then, the use of these solutions together with $\bar{u}_1^{(r)}$, and $\widetilde{u}_1^{(r)}$, $r = 1, 2, 3$, in the boundary conditions of the third-order problem yields the following systems of algebraic equations to determine $\mathbf{U}_3^{(l)}$'s;

$$\mathbf{W}_l \, \mathbf{U}_3^{(l)} = \mathbf{b}_3^{(l)} \ . \tag{74}$$

where $\mathbf{b}_3^{(1)} \neq \mathbf{0}$, $\mathbf{b}_3^{(3)} \neq \mathbf{0}$ and $\mathbf{b}_3^{(l)} \equiv \mathbf{0}$ for all $l \neq 1, 3$, and $\mathbf{b}_3^{(1)}$ can be written as in the form

$$\mathbf{b}_3^{(1)} = \left[ -i \left( \frac{\partial \mathbf{W}_1}{\partial \omega} \frac{\partial \mathcal{A}_1}{\partial t_2} - \frac{\partial \mathbf{W}_1}{\partial k} \frac{\partial \mathcal{A}_1}{\partial x_2} \right) + \frac{1}{2} \left( \frac{\partial^2 \mathbf{W}_1}{\partial \omega^2} \frac{\partial^2 \mathcal{A}_1}{\partial t_1^2} - 2 \frac{\partial^2 \mathbf{W}_1}{\partial k \partial \omega} \frac{\partial^2 \mathcal{A}_1}{\partial x_1 \partial t_1} + \frac{\partial^2 \mathbf{W}_1}{\partial k^2} \frac{\partial^2 \mathcal{A}_1}{\partial x_1^2} \right) \right] \mathbf{R}$$
$$+ \left( \frac{\partial \mathbf{W}_1}{\partial k} \frac{\partial^2 \mathcal{A}_1}{\partial x_1^2} - \frac{\partial \mathbf{W}_1}{\partial \omega} \frac{\partial^2 \mathcal{A}_1}{\partial x_1 \partial t_1} \right) \left( \frac{\partial \mathbf{R}}{\partial k} + V_g \frac{\partial \mathbf{R}}{\partial \omega} \right) + \mathbf{F} \mid \mathcal{A}_1 \mid^2 \mathcal{A}_1 \ . \tag{75}$$

where $\mathbf{F}$ is a constant vector depending on material parameters and the wave number $k$, their components are given in Appendix B. The explicit form of the vector $\mathbf{b}_3^{(3)}$ is not given, since it is not required for self modulation solution. Since we have assumed that $\det \mathbf{W}_l \neq 0$ for $l \neq 1$ the solutions of (74) are found to be

$$\mathbf{U}_3^{(3)} = \mathbf{W}^{-1} \mathbf{b}_3^{(3)} \quad \text{and} \quad \mathbf{U}_3^{(\mathrm{l})} \equiv 0 \quad \text{for} \quad \mathrm{l} \neq 1, 3$$

Since $\det \mathbf{W}_1 = 0$, in order that (74) has a solution for $\mathbf{U}_3^{(1)}$ the compatibility condition

$$\mathbf{L}.\mathbf{b}_3^{(1)} = 0 \tag{76}$$

must be satisfied. This compatibility condition yields the following nonlinear Schrödinger (NLS) equation

$$i\frac{\partial \mathcal{A}}{\partial \tau} + \Gamma\frac{\partial^2 \mathcal{A}}{\partial \xi^2} + \Delta \mid \mathcal{A} \mid^2 \mathcal{A} = 0.$$

with the following definitions

$$\tau = \omega t_2 \ , \ \ \xi = k\epsilon^{-1}(x_2 - V_g t_2) = k(x_1 - V_g t_1) \ , \ \ \mathcal{A} = k\mathcal{A}_1,$$

$$\Gamma = \frac{k^2}{2\omega}\frac{d^2\omega}{dk^2}, \quad \Delta = \frac{1}{\omega k^2}\Big[-(\mathbf{L}.\mathbf{F})\Big/[\mathbf{L}(\partial \mathbf{W}_1/\partial\omega)\mathbf{R}]\Big].$$

Thus the task is completed, since a solution for $\mathcal{A}$ is derived from NLS equation for a given initial value of the form $\mathcal{A}(\xi, 0) = \mathcal{A}_0(\xi)$ then the first-order solutions $u_1^{(r)}$ can be obtained from (49)–(51).

This analysis is also carried out for the case in which $c_1 < c < c_2 < c_3$ and we obtain dispersion relation as

$$p_1 v_2 \tan P_1 + \gamma_2 p_1 v_3 \tan P_1 \tanh V_2 - \gamma_1\gamma_2 v_2 v_3 - \gamma_1 v_2^2 \tanh V_2 = 0 \tag{77}$$

where $V_2 = k v_2 h_1$. For the nonlinear wave modulation of the waves again an NLS equation is obtained whose coefficients $\Gamma$ and $\Delta$ can be obtained by substituting $p_2 = i v_2$ in previous ones.

## 4 Conclusions

It is known that the sign of the product $\Gamma\Delta$ is important in determining how a given initial data will evolve for long times for the asymptotic wave field governed by the NLS equation. An initial disturbance vanishing as $\mid \xi \mid \to \infty$ tends to become a series of envelope solitary waves if $\Gamma\Delta > 0$, while it evolves into the decaying oscillations if $\Gamma\Delta < 0$. (see, e.g. [1, 4]). The traveling wave solutions of the NLS equation of the form

$$A(\xi, \tau) = \phi(\eta)\mathrm{e}^{\mathrm{i}(\mathrm{K}\xi - \Omega\tau)}, \quad \eta = \xi - \mathrm{V}_0\tau, \quad \mathrm{V}_0 : \text{constant} \tag{78}$$

also depend on sign of $\Gamma\Delta$. For $\Gamma\Delta > 0$, if $\phi \to 0$ and $d\phi/d\eta \to 0$ as $|\eta| \to \infty$, the envelope or bright soliton $\phi$ can be obtained as

$$\phi = \phi_0 sech\left[(\Delta/2\Gamma)^{1/2}\phi_0\eta\right], \tag{79}$$

where $V_0 = 2K\Gamma$, $\Omega = \Gamma K^2 - \Delta\phi_0^2/2$. For $\Gamma\Delta < 0$ and $(\Gamma K^2 - \Omega)/\Delta\phi_0^2 = 1$, if $\phi \to \phi_0$ as $\eta \to -\infty$, the solution for $\phi$ which represents the propagation of a phase jump can be expressed as

$$\phi = \phi_0 \tanh\left[(-\Delta/2\Gamma)^{1/2}\,\phi_0\eta\right], \quad V_0 = 2K\Gamma. \tag{80}$$

Also for $\Gamma\Delta < 0$ dark soliton solutions exist [29]. By taking into account the above review about the effect of the sign of $\Gamma\Delta$ on the properties of the solutions of an NLS equation, the behaviour of the solutions for SH waves propagating in a double layered nonlinear half space is now examined. As the properties of solutions of the NLS equation strongly depend on the sign of the product $\Gamma\Delta$, the variation of it with respect to the nondimensional wave number $K = k(h_1 + h_2)$ has to be found out. In this paper, the evaluation of these coefficients is carried out numerically for the lowest branch of the dispersion relation giving appropriate values to the materials constants. Similar calculations may be performed for any other branch of the dispersion relations.

The coefficient $\Gamma$ depends only on the linear material constants and the ratio $h_2/h_1$, whereas $\Delta$ also depends on nonlinear material properties. Therefore to observe the variation in the $\Gamma\Delta$ with nonlinearity, in the numerical evaluations of $\Gamma\Delta$, the linear material constants are fixed to be $\rho^{(1)} = \rho^{(2)} = \rho^{(3)} = 1$, $\mu_1 = 1$, $\mu_2 = 4$, $\mu_3 = 9$ while the nonlinear ones $\beta_1 = n_1/c_1^2$, $\beta_2 = n_2/c_2^2$ and $\beta_3 = n_3/c_3^2$ are being changed. In Fig. 1 the variation of $\Gamma$ with respect to $K$ for the first branch of the dispersion relations (43) and (77) is plotted for $h_2/h_1 = 1$ and also for $h_1 = 0$ for a single layered half space. Note that for $h_2/h_1 = 1$, $\Gamma$ is zero approximately at $K \approx 2.18$ where the related group velocity curve has a minimum. As mentioned before, if $\beta_r > 0$ the relevant medium exhibits hardening characteristic, while if $\beta_r < 0$ softening characteristic. First we consider the variation of $\Gamma\Delta$ with respect to $K$ for a hardening internal layer and a hardening half space with the nonlinear parameters $\beta_2 = \beta_3 = 2$

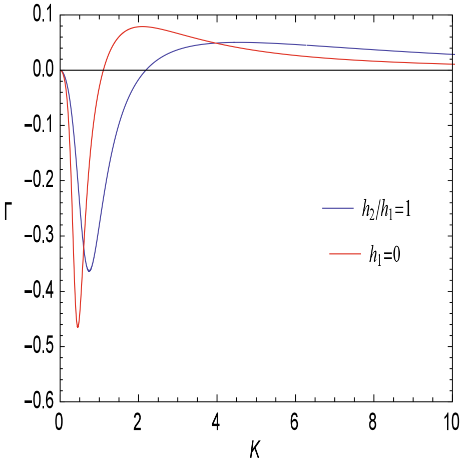

**Fig. 1** $\Gamma$ versus $K$ for $h_1/h_2 = 1$ and $h_1 = 0$

**Fig. 2** $\Gamma\Delta$ versus $K$ for fixed $\beta_3 = 2.0$, $\beta_2 = 2.0$ (hardening half space covered by hardening internal layer) and for $\beta_1 = -1, -2$ (softening top layers), $\beta_1 = 1, 2$ (hardening top layers). The curve for $\beta_3 = 2.0$, $\beta_2 = 2.0$ and $h_1 = 0$ represents the $\Gamma\Delta$ versus $K$ curve for a single layered half space

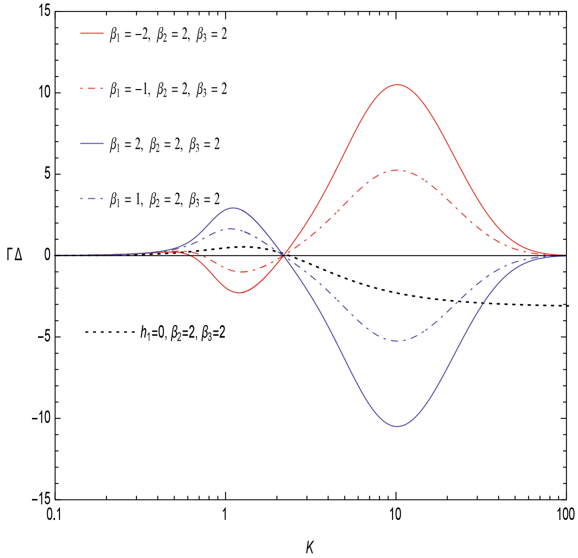

in Fig. 2. To observe the effect of the nonlinearity of the top layer on $\Gamma\Delta$; $\beta_2$ and $\beta_3$ are fixed and the variation of $\Gamma\Delta$ with K is computed for $\beta_1 = -1$, $\beta_1 = -2$ (softening nonlinear layers) and for $\beta_1 = 1$, $\beta_1 = 2$ (hardening nonlinear layers). When $\beta_1 = 1$ and $\beta_1 = 2$ (i.e. a hardening half space covered by two hardening top layers), $\Delta < 0$ for all $K > 0$, therefore the sign of $\Gamma\Delta$ will be positive when $K < 2.18$ since $\Gamma < 0$ then envelope solitary wave solution given by (79) will exist but $\Gamma\Delta$ will be negative for $K > 2.18$ as it is seen in Fig. 2, then only the dark solitons exist for this case. When $\beta_1 = -1$ and $\beta_1 = -2$ (i.e. a hardening half space covered by softening top layer and hardening internal layers) $\Delta < 0$ initially and its sign changes with the variation in the nonlinear material parameter of top layer. In Fig. 2 the second zero of each $\Gamma\Delta$ curve is the zero of $\Gamma$ curve and the first one is the zero of $\Delta$ curve. Since the linear material constants and the ratio $h_2/h_1$ are fixed for all nonlinear models, the second zeros are the same for all $\Gamma\Delta$ curves, the other zeros are changing depending on the nonlinear material parameter of the top layer. For softening half space covered by softening internal layer and different top layer models, variations of $\Gamma\Delta$ with respect to $K$ are given in Fig. 3. It is seen that the curves having same absolute $\beta_r, r = 1, 2, 3$ values are symmetric with respect to $K$ axis. Therefore the behavior of the solutions of the NLS equation is reversed. In Figs. 2 and 3 the variations of $\Gamma\Delta$ with $K$ for a single layered half space (for $h_1 = 0$) are also depicted. From these figures, it can be seen that the wave propagation is affected considerably by the existence of a second (top) layer. As a result of the numerical evaluation of $\Gamma\Delta$ for fixed linear material properties, it is observed that the existence of the envelope solitary waves are affected strongly the nonlinear material parameter of top layer.

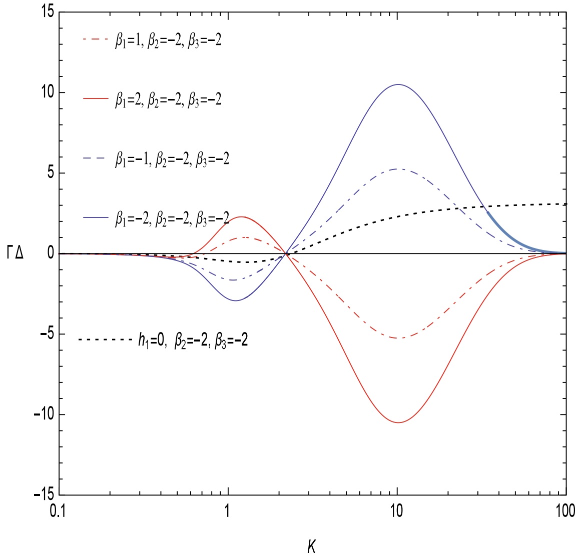

**Fig. 3** $\Gamma\Delta$ versus $K$ for fixed $\beta_3 = -2.0$, $\beta_2 = -2.0$ (softening half space covered by softening internal layer) and for $\beta_1 = -1, -2$ (softening top layers), $\beta_1 = 1, 2$ (hardening top layers). The curve for $\beta_3 = -2.0$, $\beta_2 = -2.0$ and $h_1 = 0$ represents the $\Gamma\Delta$ versus $K$ curve for a single layered half space

# 5 Appendix A

$$R_1 = \frac{1}{2\cos P_1} e^{-(iP_1+V_3)} \left(\cos P_2 + \frac{v_3\gamma_2 \sin P_2}{p_2}\right), \quad R_2 = \overline{R_1} \tag{81}$$

$$R_3 = \frac{1}{2} e^{iP_2 - V3} \left(1 - i\frac{v_3\gamma_2}{p_2}\right), \quad R_4 = \overline{R_3}, \quad R_5 = 1 \tag{82}$$

# 6 Appendix B

$$\begin{aligned}
\mathcal{D}_1 &= 2\Lambda_1 \frac{\partial}{\partial x_1}\mathcal{M}_{11}^{(1)} + R_1\mathcal{N}^{(1)} + 2iR_1\mathcal{M}_{12}^{(1)} - \mathcal{P}_1^- + 2iR_1\mathcal{M}_{21}^{(1)} \\
\mathcal{D}_2 &= -i\frac{2R_1}{p_1 k c_1^2}\left(\omega\frac{\partial}{\partial t_1} + kc_1^2\frac{\partial}{\partial x_1}\right)\mathcal{M}_{11}^{(1)} \\
\mathcal{D}_3 &= 2\Lambda_2 \frac{\partial}{\partial x_1}\mathcal{M}_{11}^{(1)} + R_2\mathcal{N}^{(1)} + 2iR_2\mathcal{M}_{12}^{(1)} - \mathcal{P}_1^+ + 2iR_2\mathcal{M}_{21}^{(1)} \\
\mathcal{D}_4 &= \frac{2iR_2}{p_1 k c_1^2}\left(\omega\frac{\partial}{\partial t_1} + kc_1^2\frac{\partial}{\partial x_1}\right)\mathcal{M}_{11}^{(1)} \\
\mathcal{D}_5 &= \mathcal{Q}_1^-
\end{aligned}$$

$$
\begin{aligned}
\mathcal{D}_6 &= \mathcal{Q}_1^+ \\
\mathcal{D}_7 &= 2\Lambda_3 \frac{\partial}{\partial x_1}\mathcal{M}_{11}^{(2)} + R_3\mathcal{N}^{(2)} + 2iR_3\mathcal{M}_{12}^{(2)} - \mathcal{P}_2^- + 2iR_3\mathcal{M}_{21}^{(2)} \\
\mathcal{D}_8 &= -\frac{2iR_3}{p_2kc_2^2}\left(\omega\frac{\partial}{\partial t_1} + kc_2^2\frac{\partial}{\partial x_1}\right)\mathcal{M}_{11}^{(2)} \\
\mathcal{D}_9 &= 2\Lambda_4 \frac{\partial}{\partial x_1}\mathcal{M}_{11}^{(2)} + R_4\mathcal{N}^{(2)} + 2iR_4\mathcal{M}_{12}^{(2)} - \mathcal{P}_2^+ + 2iR_4\mathcal{M}_{21}^{(2)} \\
\mathcal{D}_{10} &= \frac{2iR_4}{p_2kc_2^2}\left(\omega\frac{\partial}{\partial t_1} + kc_2^2\frac{\partial}{\partial x_1}\right)\mathcal{M}_{11}^{(2)} \\
\mathcal{D}_{11} &= \mathcal{Q}_2^- \\
\mathcal{D}_{12} &= \mathcal{Q}_2^+ \\
\mathcal{D}_{14} &= \frac{2R_5}{v_3kc_3^2}\left(\omega\frac{\partial}{\partial t_1} + kc_3^2\frac{\partial}{\partial x_1}\right)\mathcal{M}_{11}^{(3)} \\
\mathcal{D}_{15} &= n_3k^4(-3 + 2v_3^2 + 9v_3^4)R_5^3|A_1|^2A_1
\end{aligned}
\tag{83}
$$

and

$$
\begin{aligned}
\mathcal{M}_{\beta\gamma}^{(\alpha)} &= \omega\frac{\partial A_\beta}{\partial t_\gamma} + kc_\alpha^2\frac{\partial A_\beta}{\partial x_\gamma} \\
\mathcal{N}^{(\alpha)} &= c_\alpha^2\frac{\partial^2 A_1}{\partial x_1^2} - \frac{\partial^2 A_1}{\partial t_1^2} \\
\Lambda_\alpha &= \left(\frac{\partial R_\alpha}{\partial k} + v_g\frac{\partial R_\alpha}{\partial \omega}\right) \\
\mathcal{P}_1^- &= n_1k^4\left(9p_1^4 + 2p_1^2 + 9\right)R_1|R_1|^2|A_1|^2A_1 \\
\mathcal{P}_1^+ &= n_1k^4\left(9p_1^4 + 2p_1^2 + 9\right)R_2|R_2|^2|A_1|^2A_1 \\
\mathcal{Q}_1^- &= n_1k^4\left(9p_1^4 - 2p_1^2 - 3\right)R_1^3|A_1|^2A_1 \\
\mathcal{Q}_1^+ &= n_1k^4\left(9p_1^4 - 2p_1^2 - 3\right)R_2^3|A_1|^2A_1 \\
\mathcal{P}_2^- &= n_2k^4\left(9p_2^4 + 2p_2^2 + 9\right)R_3^2R_4|A_1|^2A_1 \\
\mathcal{P}_2^+ &= n_2k^4\left(9p_2^4 + 2p_2^2 + 9\right)R_4^2R_3|A_1|^2A_1 \\
\mathcal{Q}_2^- &= n_2k^4\left(9p_2^4 - 2p_2^2 - 3\right)R_3^3|A_1|^2A_1 \\
\mathcal{Q}_2^+ &= n_2k^4\left(9p_2^4 - 2p_2^2 - 3\right)R_4^3|A_1|^2A_1
\end{aligned}
\tag{84}
$$

where $|\phi|$ denotes the modulus of $\phi$.

$$
\begin{aligned}
&\varepsilon_1 = \frac{i\mathcal{D}_1}{2kp_1c_1^2} - \frac{\mathcal{D}_2}{4k^2p_1^2c_1^2}, \quad \varepsilon_2 = \frac{i\mathcal{D}_2}{4kp_1c_1^2}, \quad \varepsilon_3 = -\frac{i\mathcal{D}_3}{2kp_1c_1^2} - \frac{\mathcal{D}_4}{4k^2p_1^2c_1^2} \\
&\varepsilon_4 = -i\frac{\mathcal{D}_4}{4kp_1c_1^2}, \quad \varepsilon_5 = \frac{\mathcal{D}_5}{8k^2p_1^2c_1^2}, \quad \varepsilon_6 = \frac{\mathcal{D}_6}{8k^2p_1^2c_1^2}, \quad \varepsilon_7 = \frac{i\mathcal{D}_7}{2kp_2c_2^2} - \frac{\mathcal{D}_8}{4k^2p_2^2c_2^2}
\end{aligned}
$$

$$\begin{aligned}
\varepsilon_8 &= \frac{i\mathcal{D}_8}{4kp_2c_2^2} \quad \varepsilon_9 = -\frac{i\mathcal{D}_9}{2kp_2c_2^2} - \frac{\mathcal{D}_{10}}{4k^2p_2^2c_2^2}, \quad \varepsilon_{10} = -\frac{i\mathcal{D}_{10}}{4kp_2c_2^2} \\
\varepsilon_{11} &= \frac{\mathcal{D}_{11}}{8k^2p_2^2c_2^2}, \quad \varepsilon_{12} = \frac{\mathcal{D}_{12}}{8k^2p_2^2c_2^2}, \quad \varepsilon_{13} = -\frac{\mathcal{D}_{13}}{2kv_3c_3^2} + \frac{\mathcal{D}_{14}}{4k^2v_3^2c_3^2} \\
\varepsilon_{14} &= -\frac{\mathcal{D}_{14}}{4kv_3c_3^2}, \quad \varepsilon_{15} = -\frac{\mathcal{D}_{15}}{8k^2v_3^2c_3^2}
\end{aligned} \tag{85}$$

$$F_1 = -\beta_1 h_1 \frac{k^4(9p_1^4 + 2p_1^2 + 9)}{8\cos^3 P_1} \left(\frac{\gamma_2 v_3}{p_2} \sin P_2 + \cos P_2\right)^3 \mathrm{e}^{-3\mathrm{V}_3} \tag{86}$$

$$\begin{aligned}
F_2 = \ & \beta_1 \frac{k^3(9p_1^4 + 2p_1^2 + 9)}{8p_1 \cos^3 P_1} \left(\frac{\gamma_2 v_3}{p_2} \sin P_2 + \cos P_2\right)^3 \sin P_1 \mathrm{e}^{-3\mathrm{V}_3} \\
& - \frac{3}{32} \beta_1 \frac{k^3(9p_1^4 - 2p_1^2 - 3)}{p_1 \cos^3 P_1} \left(\frac{\gamma_2 v_3}{p_2} \sin P_2 + \cos P_2\right)^3 \sin 3P_1 \mathrm{e}^{-3\mathrm{V}_3} \\
& + \gamma_1 \beta_2 \frac{k^3(9p_2^4 + 2p_2^2 + 9)}{8p_2} \left(1 + \frac{\gamma_2^2 v_3^2}{p_2^2}\right) \left(\sin P_2 - \frac{\gamma_2 v_3}{p_2} \cos P_2\right) \mathrm{e}^{-3\mathrm{V}_3} \\
& - \gamma_1 \beta_2 \frac{3k^3(9p_2^4 - 2p_2^2 - 3)}{32p_2} \left(1 - \frac{3\gamma_2^2 v_3^2}{p_2^2}\right) \sin 3P_2 \mathrm{e}^{-3\mathrm{V}_3} \\
& + \gamma_1 \beta_2 \frac{3k^3(9p_2^4 - 2p_2^2 - 3)}{32p_2} \left(3 - \frac{\gamma_2^2 v_3^2}{p_2^2}\right) \frac{\gamma_2 v_3}{p_2} \cos 3P_2 \mathrm{e}^{-3\mathrm{V}_3} \\
& - \beta_1 \frac{k^3 p_1}{\cos^3 P_1} \left(\frac{\gamma_2 v_3}{p_2} \sin P_2 + \cos P_2\right)^3 (\sin P_1 \cos^2 P_1 + 3p_1^2 \sin^3 P_1) \mathrm{e}^{-3\mathrm{V}_3} \\
& - \gamma_1 \beta_2 \frac{k^3 p_2}{4} \left\{ (1 + 9p_2^2) \left(1 + \frac{\gamma_2^2 v_3^2}{p_2^2}\right) \left(\sin P_2 - \frac{\gamma_2 v_3}{p_2} \cos P_2\right) + \right. \\
& \left. (1 - 3p_2^2) \left[ \left(1 - \frac{3\gamma_2^2 v_3^2}{p_2^2}\right) \sin 3P_2 - \left(3 - \frac{\gamma_2^2 v_3^2}{p_2^2}\right) \frac{\gamma_2 v_3}{p_2} \cos 3P_2 \right] \right\} \mathrm{e}^{-3\mathrm{V}_3}
\end{aligned} \tag{87}$$

$$\begin{aligned}
F_3 = \ & -\beta_1 \frac{k^2 \left(9p_1^4 - 2p_1^2 - 3\right) \left(\frac{v_3 \gamma_2}{p_2} \sin P_2 + \cos P_2\right)^3}{32p_1^2 \cos^3 P_1} \cos 3P_1 \mathrm{e}^{-3\mathrm{V}_3} \\
& + \beta_2 \frac{k^2 \left(-3 - 2p_2^2 + 9p_2^4\right)}{32p_2^2} \left(1 - \frac{3v_3^2 \gamma_2^2}{p_2^2}\right) \cos 3P_2 \mathrm{e}^{-3\mathrm{V}_3} \\
& + \beta_2 \frac{k^2 \left(9p_2^4 - 2p_2^2 - 3\right)}{32p_2^2} \left(3 - \frac{v_3^2 \gamma_2^2}{p_2^2}\right) \frac{v_3 \gamma_2}{p_2} \sin 3P_2 \mathrm{e}^{-3\mathrm{V}_3}
\end{aligned} \tag{88}$$

$$
\begin{aligned}
F_4 = \;& \beta_2 \frac{k^3\left(9+2p_2^2+9p_2^4\right)}{8p_2}\left(1+\frac{v_3^2\gamma_2^2}{p_2^2}\right)\frac{v_3\gamma_2}{p_2}\mathrm{e}^{-3\mathrm{V}_3} \\
& + \beta_2 \frac{h_2k^4\left(9+2p_2^2+9p_2^4\right)}{8}\left(1+\frac{v_3^2\gamma_2^2}{p_2^2}\right)\mathrm{e}^{-3\mathrm{V}_3} \\
& - \beta_2 \frac{3k^3\left(-3-2p_2^2+9p_2^4\right)}{32p_2}\left(3-\frac{v_3^2\gamma_2^2}{p_2^2}\right)\frac{v_3\gamma_2}{p_2}\mathrm{e}^{-3\mathrm{V}_3} \\
& - \gamma_2\beta_3 \frac{3k^3\left(-3+2v_3^2+9v_3^4\right)}{8v_3}\mathrm{e}^{-3\mathrm{V}_3} + \gamma_2\beta_3\mathrm{k}^3\mathrm{v}_3(1+3\mathrm{v}_3^2)\mathrm{e}^{-3\mathrm{V}_3} \\
& - \gamma_2\beta_2 k^3 v_3(1+3\gamma_2^2 v_3^2)\mathrm{e}^{-3\mathrm{V}_3}
\end{aligned}
\tag{89}
$$

$$
\begin{aligned}
F_5 = \;& -\beta_2 \frac{h_2k^3\left(9+2p_2^2+9p_2^4\right)}{8p_2}\left(1+\frac{v_3^2\gamma_2^2}{p_2^2}\right)\frac{v_3\gamma_2}{p_2}\mathrm{e}^{-3\mathrm{V}_3} \\
& - \beta_2 \frac{k^2\left(-3-2p_2^2+9p_2^4\right)}{32p_2^2}\left(1-\frac{3v_3^2\gamma_2^2}{p_2^2}\right)\mathrm{e}^{-3\mathrm{V}_3} \\
& - \beta_3 \frac{k^2\left(-3+2v_3^2+9v_3^4\right)}{8v_3^2}\mathrm{e}^{-3\mathrm{V}_3}.
\end{aligned}
\tag{90}
$$

# References

1. Ablowitz, M.J., Clarkson, P.A.: Solitons, Nonlinear Evolution Equations and Inverse Scattering. Cambridge University Press, Cambridge (1991)
2. Achenbach, J.D.: Wave Propagation in Elastic Solids. North Holland Publishing Co., Amsterdam (1973)
3. Ahmetolan, S., Teymur, M.: Non-linear modulation of SH waves in a two-layered plate and formation of surface SH waves. Int. J. Non-Linear Mech. **38**(8), 1237–1250 (2003)
4. Dodd, R.K., Eilbeck, J.C., Gibbon, J.D., Morris, H.C.: Solitons and Nonlinear Wave Equations. Academic, London (1982)
5. Eringen, A.C., Suhubi, E.S.: Elastodynamics, vol. I. Academic, New York (1974)
6. Eringen, A.C., Suhubi, E.S.: Elastodynamics, vol. II. Academic, New York (1975)
7. Ewing, W.M., Jardetsky, W.S., Press, F.: Elastic Waves in Layered Media. McGraw-Hill, New York (1957)
8. Fu, Y.B.: On the propagation of nonlinear travelling waves in an incompressible elastic plate. Wave Motion **19**, 271–292 (1996)
9. Jeffrey, H.: On the surface waves of earthquakes. Geophys. Suppl. MNRAS **1**(6), 282–292 (1925)
10. Jeffrey, A., Kawahara, T.: Asymptotic Methods of Nonlinear Wave Theory. Pitman Advanced Publishing Program, Boston (1982)
11. Knowles, J.K.: The finite anti-plane shear field near the tip of a crack for a class of incompressible elastic solids. Int. J. Fract. **13**(5), 611–639 (1977)
12. Love, A.E.H.: A Treatise on the Mathematical Theory of Elasticity, 4th edn. Dover Publications Inc., New York (1944)
13. Maugin, G.A., Hadouaj, H.: Solitary surface transverse waves on an elastic substrate coated with a thin film. Phys. Rev. B **44**(3), 1266–1280 (1991)

14. Maugin, G.A., Hadouaj, H., Malomed, B.A.: Nonlinear coupling between shear horizontal surface solitons and Rayleigh modes on elastic structures. Phys. Rev. B **45**(17), 9688–9694 (1992)
15. Mayer, A.P.: Surface acoustic waves in nonlinear elastic media. Phys. Rep. **256**, 4–5 (1995)
16. Norris, A.: Finite amplitude waves in solids. In: Hamilton, M.F., Blackstock, D.T. (eds.) Nonlinear Acoustics, pp. 263–277. Academic, San Diego (1998)
17. Parker, D.F.: Nonlinear surface acoustic waves and waves on stratified media. In: Jeffrey, A., Engelbrecht, J. (eds.) Nonlinear Waves in Solids, International Centre for Mechanical Sciences, Course and Lectures, vol. 341, pp. 289–347. Springer, New York (1994)
18. Parker, D.F., Maugin, G.A. (eds.): Recent Developments in Surface Acoustic Waves. Springer Series on Wave Phenomena, vol. 7. Springer, Berlin (1988)
19. Porubov, A.V.: Amplification of Nonlinear Strain Waves in Solids. World Scientific, Singapore (2003)
20. Porubov, A.V., Samsonov, A.M.: Long nonlinear strain waves in layered elastic half space. Int. J. Eng. Sci. **30**(6), 861–877 (1995)
21. Pucci, E., Saccomandi, G.: Secondary motions associated with anti-plane shear in nonlinear isotropic elasticity. Q. J. Mech. Appl. Math. **66**(2), 221–239 (2013)
22. Samsonov, A.M.: Nonlinear strain waves in elastic wave guides. In: Jeffrey, A., Engelbrecht, J. (eds.) Nonlinear Waves in Solids, International Centre for Mechanical Sciences, Course and Lectures, vol. 341, pp. 349–382. Springer, New York (1994)
23. Soerensen, M.P., Christiansen, P.L., Lomdahl, P.S.: Solitary waves on nonlinear elastic rods I. J. Acoust. Soc. Am. **24**, 871–879 (1984)
24. Stoneley, R., Tillotson, E.: Effect of a double surface layer on Love waves. Geophys. J. Int. **1**, 521–527 (1928)
25. Teymur, M.: Nonlinear modulation of Love waves in a compressible hyperelastic layered half space. Int. J. Eng. Sci. **26**, 907–927 (1988)
26. Teymur, M.: Small but finite amplitude waves in a two-layered incompressible elastic medium. Int. J. Eng. Sci. **34**, 227–241 (1996)
27. Teymur, M.: Propagation of long extensional nonlinear waves in a hyperelastic layer. In: Inan, E., Kiris, A. (eds.) Springer Proceeding in Physics, vol. 111, pp. 109–233. Springer, Dordrecht (2007)
28. Whitham, G.B.: Linear and Nonlinear Waves. Wiley, New York (1974)
29. Zakharov, V., Shabat, A.: Exact theory of two-dimensional self-focusing and one-dimensional self-modulation of waves in nonlinear media. Sov. Phys. JETP **34**(1), 62–69; translated from Zh. Eksp. Teor. Fiz. (1971), **61**(1), 118–134 (1972) (Russian)

# Wave Dynamics of Deformation and Fracture

**Sanichiro Yoshida**

**Abstract** Deformation and fracture of solids are formulated comprehensively as wave dynamics based on a gauge field theoretical approach. With the application of the least action principle, a set of field equations are derived, which describe the dynamics of deformation that propagates as a wave. The elasticity and plasticity are characterized by the form of the longitudinal force term of the field equations. For elasticity, the longitudinal term represents elastic force proportional to the volume expansion. For plasticity, the longitudinal force term represents the velocity damping force that causes the irreversibility of plastic deformation and the decaying feature in the wave characteristics. The oscillatory feature of plasticity comes from the elastic shear force. The fracture is characterized as the final stage of plastic deformation where the solid totally loses the restoring mechanism. Consequently, the dynamics loses the oscillatory feature and the displacement becomes unidirectional generating material discontinuity. A number of supporting experimental observations are presented.

## 1 Introduction

The conventional approach to deformation and fracture of solids involves the use of stage-dependent theories. Continuum mechanics [1, 2] is predominantly used to describe deformation in the elastic stage based on the linear constitutive relation. Various theories are available for deformation in the plastic stage. They are mostly a phenomenological theory [3–6] based on a certain physical process such as dislocations and thermodynamic processes, or a mathematical theory [7, 8] based on empirically known or numerically modeled nonlinear constitutive relation. There are a number of theories for fracture mechanics as well. These theories usually assume the existence of a crack in the solid and describe the crack propagation considering

---

S. Yoshida (✉)
Department of Chemistry and Physics, Southeastern Louisiana University, SLU 10878,
Hammond, LA 70402, USA
e-mail: syoshida@selul.edu

H. Altenbach et al. (eds.), *Dynamical Processes in Generalized Continua and Structures*, Advanced Structured Materials 103,
https://doi.org/10.1007/978-3-030-11665-1_28

the underlying physics such as the energy balance or using an empirical parameter such as the crack resistance.

These theories are well-established and able to accurately describe the deformation phenomenon in the respective stages. However, they have limitations when applied to some engineering problems. In the field of nondestructive inspections, the evaluation of the transition from one stage to the next is important. Often, mechanical systems fail because at the time of inspection a defect that can cause failure does not exist. It is possible that an aircraft passes the routine inspection for that reason and a crack newly generated after the take off leads to a catastrophic accident. It is desirable that the inspection uses a theory that can describe deformation and fracture comprehensively, and thereby formulate the dynamics of the transitional stage. Another area of application to be mentioned is the strength evaluation of new materials and conventional materials with an unconventional size. New materials do not have empirical constitutive data, and therefore modeling of nonlinear deformation is difficult. It is well known that a microscopic or nanoscopic-scale object of conventional materials shows different phenomenological behaviors than a macroscopic object of the same material. It is desirable to have a universal theory of deformation and fracture that does not rely on phenomenology.

This situation motivates us to develop a comprehensive theory of deformation and fracture. A possible approach to this end is to describe deformation and fracture at a fundamental level of physics. We have been developing the present theory [9, 10] over the last couple of decades with such a concept, conducting a number of experiments [11–16] to support the theoretical development. Using the physical principle known as the symmetry in physics [17], this theory formulates the dynamics of all stages of deformation, including fracture, on the same basis. This approach yields a set of field equations that describe the displacement and velocity fields of solids under deformation. The field equations yield wave equations that describe the oscillatory dynamics of deformation field that propagates through the solid. In this formalism, the nonlinearity of plastic deformation is formulated with a curvilinear coordinate system in conjunction with the introduction of a compensation (gauge) field [18–20]. The irreversibility in the plastic regime is considered as energy dissipative feature of the wave dynamics.

Some authors apply the same concept for different symmetry to describe dislocation dynamics [21–23]. Panin et al. [24–27] introduce a gauge field in association with the $GL(3, R)$ Lie transformation group and derive field equations that represent wave dynamics of plastic deformation. The group reports a number of experimental studies that evidence the wave dynamics of plastic deformation [28–30]. Our approach stems from their work. Noting that after the summation over the group index the $GL(3, R)$ transformation matrix reduces to the deformation gradient tensor, we start from the deformation gradient tensor as the transformation to represents deformation. We request local symmetry in the transformation, and derive the same type of field equations as Panin et al.'s. Through interpretation of various terms of the field equations and experimental observations, we derive the wave equation that describes the elastoplastic behavior of the deformation field [31]. We formulate fracture as the condition where the solid completely loses the elastic mechanism for the oscillatory behavior of the deformation field, and thereby generates discontinuity [31].

The aim of this chapter is to review past work on this topic, interpret various experimental observations based on the wave dynamics, and discuss new findings. In Sect. 2, the gist of the formalism is described. After the qualitative explanation of the formalism, the gauge field is introduced and its physical meaning is discussed. The Lagrangian associated with the gauge term is identified and the field equations are derived. In Sect. 3, experimental observations are presented. These observations are important because various aspects of the theoretical development are based on the interpretation of these experimental observations. Section 4 focuses on the dynamical aspect of the formalism. One of the field equation is interpreted as the equation of motion that governs the dynamics of deformation, and the pertinent term is interpreted as medium force acting on the unit volume. This force can be elastic or energy dissipative. The equation of motion is further transformed into a wave equation, which represents the oscillatory and energy dissipative nature of the deformation field associated with the elastic and energy dissipative medium forces.

## 2 Formalism

### *2.1 The Big Picture*

The present theory is based on two postulates. The first postulate is that a solid under plastic deformation locally obeys the law of linear elasticity. This postulate is justified by the fact that when a plastically deformed specimen is reloaded (after the removal of the initial load) the loading characteristic always shows linearity at the beginning [32]. We call the local entity that obeys the linear elastic law the deformation structural element (DSE) [9, 26]. The second postulate is that all DSEs are logically connected as long as the object is a continuum. This postulate is associated with the concept known as the gauge (compensation) field theory. Figure 1 illustrates the concept of DSE schematically. Figure 1a represents the situation that under the tensile load, the elastic object is stretched vertically in accordance with Hooke's law and compressed horizontally according to Poisson's effect. Figure 1b represents the situation where the same object undergoes plastic deformation. The central part of the object is weaker than the rest due to a defect. Consequently, the same external load as (a) causes the different deformation behavior. The four blocks (DSEs) around the central defect are still linear elastic, and therefore, their deformations respectively obey Hooke's law when described with the local coordinate system. However, at the global level the overall deformation does not obey Hooke's law as the law does not incorporate the local weakness or the rotational behaviors of the DSEs.

In a gauge theory, a gauge (compensation) field is introduced so that at the global level the dynamics obeys the same physical law as the local level. It is also said that the gauge field makes the underlying theory locally symmetric. In the present context, we introduce a gauge field so that at the global level we can apply the law of linear elasticity to a plastically deformed solid. When the deformation exceeds the linear

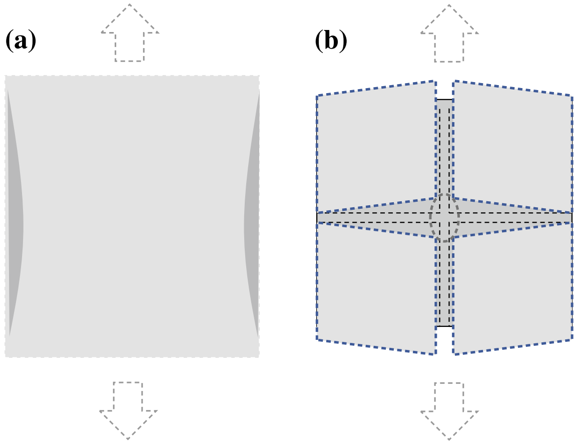

**Fig. 1** **a** Elastic deformation obeying Hooke's law and Poisson's effect; **b** Plastic deformation with local elasticity

elastic limit the specimen does not follow the linear elastic constitutive relation. At the global level, the overall deformation is not proportional to the applied force. On the other hand, at the local level each individual DES obeys the law of linear elasticity. The gauge field compensates this conflict. More specifically, the logic is as follows. We first pretend that we can describe the dynamics of plastic deformation at the global level using the law of linear elasticity. Then we compensate the discrepancy from the true dynamics by taking the dynamics that governs the gauge field into consideration.

As a simple analogy, we can digest the concept by considering the following thought experiment. Suppose we analyze the dynamics of a simple pendulum in a swirling wind pattern. Imagine that we place the pendulum at a location where the wind blows the bob to the left. The bob will swing more to the left than the right from the neutral position. When we repeat the same experiment on the other side of the circular path of the wind pattern, the bob will swing more to the right. It is obvious that the usual equation of motion for a simple pendulum written in the global coordinate system affixed to the ground does not describe this pendulum motion. However, if we somehow add the effect of the wind as an extra potential energy in addition to the gravitational potential energy, we should be able to solve the problem.

In the case of deformation, we can formulate the above logic by the use of the transformation associated with the deformation gradient tensor. The deformation gradient tensor represents an orientation preserving transformation [33]. This is because the law of linear elasticity is orientation preserving. If we apply a tensile load to an elastic object along a certain direction, the resultant stretch is parallel to this axis. The linear elastic law (Hooke's law) is the underlying physical law. If we apply the Poisson's effect, we can argue that the object is compressed in the directions orthogonal to the tensile axis. As long as the medium is linear elastic, there is no stretch or compression in other directions. This fact is justified by the concept of the principal axes. If we use the principal axes to express linear elastic deformation, the elastic matrix is diagonal. When the object undergoes plastic deformation, it is obvious

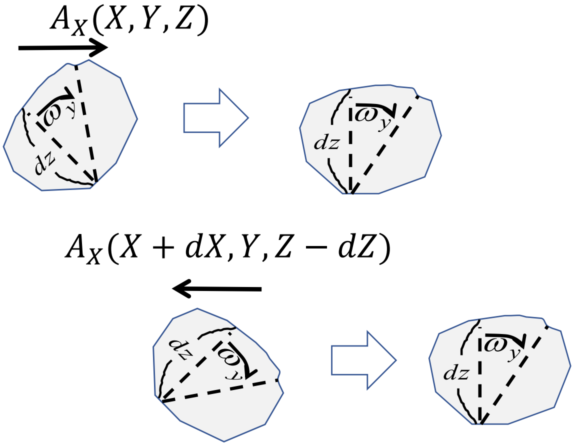

**Fig. 2** Vector potential aligns DESs at global coordinate $(X, Y, Z)$ and $(X + dX, Y, Z - dZ)$ so that they are oriented in the same direction

that we cannot express the deformation with a diagonal matrix because there are no principal axes at the global level. However, in each individual DSE, we should be able to express the local linear elastic deformation using a locally defined diagonal matrix.

Now the question becomes how we can introduce a gauge field in the above situation. The answer is rather straightforward. Since the deformation gradient tensor is an orientation preserving transformation, all we need to do is to align all the DSEs in the same orientation. The gauge field does this aligning operation. Since each DSE has a coordinate system of its own principal axes in a certain direction in the global coordinate system, this aligning operation is a vector quantity with the dimension of displacement. We can identify this displacement vector as the vector potential associated with the gauge field. Figure 2 illustrates the situation schematically.

Once we align all DSEs we can apply the law of linear elasticity at the global level. However, this is not all. We need to somehow take "the compensation part" into consideration. This can be done by applying the Lagrangian formalism to the gauge field in conjunction with the replacement of usual derivatives with the covariant derivatives [34]. The covariant derivative eliminates the geometric factor from the differentiation so that it is physically meaningful. When the coordinate axis is curved, the usual differentiation does not represent the physics underlying the differentiation. Consider a force vector at point $P$ in Fig. 3. This vector represents the normal force exerted by the spherical surface on the point mass to counteract to the centripetal force exerted by the sphere. There is no other external force acting on the point mass. At another point $P'$, a tangential force is acting on a point mass identical to the one at point $P$. Consequently, the total force exerted by the spherical surface has a tangential component. The friction of the spherical surface counteracts to the tangential force and therefore the point mass is still. How can we find the tangential force? The answer is easy. Simply compare the total force exerted by the spherical surface and the normal force at point $P'$. Now imagine that the point mass is initially at point $P$, and is displaced to point $P'$ on the exertion of the tangential force. In

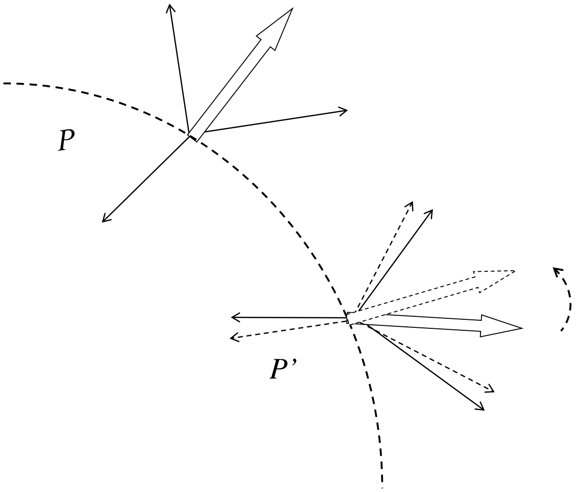

**Fig. 3** Covariant derivatives

this case, we cannot simply compare the two vectors before and after the exertion of the tangential force. It is because the normal force at point $P'$ is different from the normal force at point $P$ on the global coordinate system. They are normal in the local coordinate systems at the respective points. In order for us to evaluate the tangential force using the global coordinate system, it is necessary to remove the change in direction due to the curvature of the surface. The covariant derivative makes this correction.

The necessity of this operation regarding the differentiation in the present case makes total sense if we look at the dynamics in the following way. The governing law is Hooke's law where the elastic force is proportional to the stretch, which is the spatial differentiation of the displacement. When DSEs have different orientations, we cannot define derivatives at the global level because the spatial differentiation proportional to the force for all DSEs have different orientation. So, in order to use the differential operation at the global level, we need to realign the orientation of the differential operation. This can be done by adding a gauge term to the usual derivatives. The resultant derivative is the covariant derivative $D_i$.

$$D_i \equiv \frac{\partial}{\partial x^i} - \Gamma_i \tag{1}$$

Here the subscript $i$ denotes the differentiation with respect to the variable $x^i$. At a given point in a three-dimensional geometry, we need to consider $D_i$ for $i = 1, 2, 3$ separately.

By replacing the usual derivatives with covariant derivatives, we can use the deformation gradient tensor with the global coordinates. We say that we make the elastic force law locally symmetric. Naturally, the guage term $\Gamma_i$ is related to the vector potential. We can easily understand the relation by considering the total differential $D_i\xi_i$.

We can formulate the dynamics of the gauge field by considering the field stress tensor, which represents the interaction of the field to the dynamic system. In this process, we find a quantity that is invariant under the transformation. We can interpret this quantity as the Lagrangian, and by applying the least action principle we can formulate the law of dynamics for the gauge field. This yields a set of field equations similar to Maxwell equations of electrodynamics [35]. If we add Lagrangian of materials, the field equations reduce to the the equation of motion associated with the guage field and that associated with the linear elastic law. The situation is analogous to the electromagnetic field. If we add the material Lagrangian terms, the Lagrangian equation of motion reduce to both Schrödinger equation and Maxwell equations [36].

## 2.2 Deformation Gradient Tensor

Linear elastic deformation is defined as the deformation in which an external load causes a tensile or compressive stress to a solid and the resultant strain is proportional to the stress. The constant of proportionality is referred to as the elastic modulus and it is a material constant. Being connected by a constant, the stress and strain have a linear relationship, hence the deformation is linear. If the external load is removed, the solid regains the initial state with no deformation.

Mathematically, we can express deformation using the deformation gradient tensor. Figure 4 illustrates the concept of deformation gradient tensor. Deformation displaces Point $P$ to point $P'$ and point $Q$ to $Q'$, respectively. The displacement vector $\boldsymbol{\xi}$ depends on the coordinate variables $x$ and $y$. Consequently, the position (line element) vector $\overrightarrow{PQ}$ changes both its magnitude and direction by being transformed to $\overrightarrow{P'Q'}$, i.e., deformation takes place. Although Fig. 4 uses a two-dimensional picture for simplicity, the same concept applies to three-dimensions. Equation (2) shows a compact form of the deformation gradient tensor.

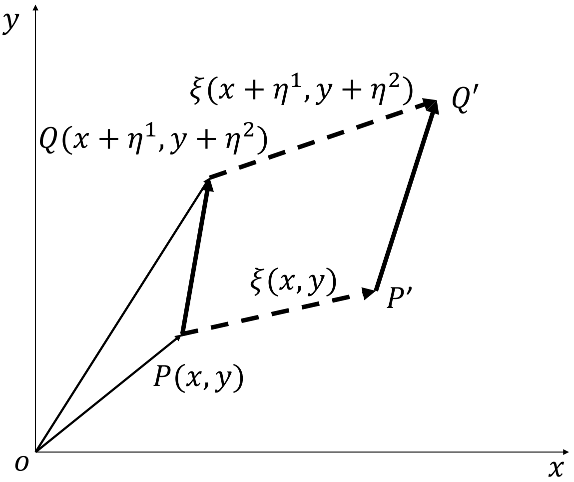

**Fig. 4** Deformation gradient tensor

$$U_{ij} = \delta_{ij} + \frac{\partial \xi_i}{\partial x^j} \tag{2}$$

where $\delta_{ij}$ is the unit matrix and $\xi_i$ is the $i$ component of displacement vector $\boldsymbol{\xi}$. The second term is referred to as the displacement gradient tensor, and often split into the symmetric and asymmetric terms as follows.

$$\frac{\partial \xi_i}{\partial x^j} = \varepsilon_{ij} + \omega_{ij} \tag{3}$$

The symmetric term $\varepsilon_{ij}$ and the asymmetric term $\omega_{ij}$ are known as the strain and rotation tensors. Equations (4) and (5) are explicit forms of the two tensors.

$$\varepsilon_{ij} = \begin{bmatrix} \frac{\partial \xi_x}{\partial x} & \frac{1}{2}\left(\frac{\partial \xi_y}{\partial x} + \frac{\partial \xi_x}{\partial y}\right) & \frac{1}{2}\left(\frac{\partial \xi_x}{\partial z} + \frac{\partial \xi_z}{\partial x}\right) \\ \frac{1}{2}\left(\frac{\partial \xi_y}{\partial x} + \frac{\partial \xi_x}{\partial y}\right) & \frac{\partial \xi_y}{\partial y} & \frac{1}{2}\left(\frac{\partial \xi_z}{\partial y} + \frac{\partial \xi_y}{\partial z}\right) \\ \frac{1}{2}\left(\frac{\partial \xi_x}{\partial z} + \frac{\partial \xi_z}{\partial x}\right) & \frac{1}{2}\left(\frac{\partial \xi_z}{\partial y} + \frac{\partial \xi_y}{\partial z}\right) & \frac{\partial \xi_z}{\partial z} \end{bmatrix} \tag{4}$$

$$\omega_{ij} = \begin{bmatrix} 0 & -\frac{1}{2}\left(\frac{\partial \xi_y}{\partial x} - \frac{\partial \xi_x}{\partial y}\right) & \frac{1}{2}\left(\frac{\partial \xi_x}{\partial z} - \frac{\partial \xi_z}{\partial x}\right) \\ \frac{1}{2}\left(\frac{\partial \xi_y}{\partial x} - \frac{\partial \xi_x}{\partial y}\right) & 0 & -\frac{1}{2}\left(\frac{\partial \xi_z}{\partial y} - \frac{\partial \xi_y}{\partial z}\right) \\ -\frac{1}{2}\left(\frac{\partial \xi_x}{\partial z} - \frac{\partial \xi_z}{\partial x}\right) & \frac{1}{2}\left(\frac{\partial \xi_z}{\partial y} - \frac{\partial \xi_y}{\partial z}\right) & 0 \end{bmatrix} \tag{5}$$

Here the symmetric term represents the strain and the asymmetric term rigid-body rotation. The linear relationship between the stress and strain is conveniently expressed in the following matrix form.

$$\sigma_{ij} = C_{ij}^{kl} \varepsilon_{kl} \tag{6}$$

where $C_{ij}^{kl}$ is called the stiffness tensor. Note that in the law of linear elasticity, only the symmetric term represents deformation.

It is convenient to express the dynamics of deformation as a linear transformation $U$ as follows. Here $U$ transforms the line element vector from the before deformation state $\eta$ to the after deformation state $\eta'$. Figure 5 illustrates the transformation schematically. Notice that the line element changes its length and orientation. The length change is represented by the strain tensor and the orientation change by the rotation tensor.

$$\eta' = U\eta \tag{7}$$

The linearity between the stress and strain breaks when the deformation reaches the linearity limit referred to as the yield point. Beyond this point, the relation between the strain and stress becomes nonlinear at the global level. This can be explained as follows. After the yield point, due to the increased dislocation density, the solid starts to have weak areas. Consequently, at the global level the stress becomes lower than before for the same strain. At the same time, different parts of the specimen have

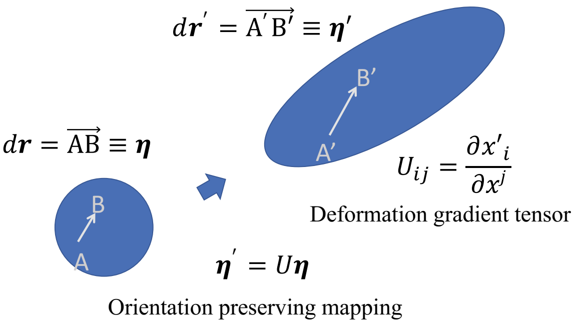

**Fig. 5** Transformation $U$ representing deformation gradient tensor

different elastic modulus because the weakening does not occur uniformly over the entire specimen. This situation makes impossible to describe the global deformation based on the linear elastic model because the elastic modulus is no more a constant for the entire specimen. However, within each area where the elastic modulus is considered to be the same (within the same DSE), the deformation is still linearly elastic. At the boundary of a pair of DSEs represented by mutually different elastic modulus, the two DSEs share the same stress. However, due to the difference in the elastic modulus, the resultant strain is different from each other. Under this condition, it becomes necessary to make $U$ coordinate dependent.

The coordinate dependence of $U$ causes a problem in the description of dynamics at the global level as follows. Consider differential of the line element of the deformed state using Eq. (7). Since $U$ depends on the coordinate, we must consider the differentiation of it as follows.

$$\frac{\partial \eta'}{\partial x^i} = U\frac{\partial \eta}{\partial x^i} + \frac{\partial U}{\partial x^i}\eta \tag{8}$$

Equation (8) indicates that under this condition, the differential of the line element vector does not transform in the same fashion as the line element vector itself (Eq. (7)). There is the additional term that contains the coordinate dependence of the transformation ($\partial U/\partial x_i$). Since the description of linear elastic law involves the differential operation, it is necessary that the differential transforms in the same fashion as the vector. Because of this extra term, we cannot describe linear elastic deformation at the global level. We can solve this problem by replacing the derivatives with the covariant derivative (1) as discussed in the next section.

## 2.3 Gauge Term and Covariant Derivatives

Using covariant derivative (1), we can write the left-hand side of Eq. (8) as follows.

$$D_i'\eta' = D_i'(U\eta) \tag{9}$$

Here subscript $i$ denotes the partial differentiation with respect to $x^i$, and the prime $'$ indicates that the differentiation is performed after the transformation.

Now we force that the differential after the transformation is the same as the transformation of the differential with the following equality.

$$D_i'\eta' = U(D_i\eta) \tag{10}$$

The next step is to find the necessary condition for the above equality. Substitute Eq. (1) into (10).

$$\left(\partial_i'U\right)\eta + U\left(\partial_i'\eta\right) - \Gamma_i'(U\eta) = U(\partial_i\eta) - U(\Gamma_i\eta) \tag{11}$$

Since the usual derivative is invariant under the transformation [9], $\partial_i' = \partial_i$, the second term on the left-hand side and the first term on the right-hand side cancel each other. Viewing $\Gamma_i'U$, $U\Gamma_i$ and $\partial_i$ are operators operating on vector $\eta$, we find the following equality as the necessary condition that $\Gamma$ must obey.

$$\Gamma_i'U = U\Gamma_i + \partial_i U \tag{12}$$

Here, knowing the usual partial differentiation is invariant under transformation $U$, we replace $\partial_i'$ with $\partial_i$ in Eq. (12). Further, by multiplying $U^{-1}$ from the right, we can rewrite Eq. (12) in the form that explicitly describe how $\Gamma$ transforms.

$$\Gamma_i' = U\Gamma_i U^{-1} + \frac{\partial U}{\partial x^i}U^{-1} \tag{13}$$

With transformation (13), the differential $D_i\eta$ transforms in the same fashion as $\eta$.

$$D_i'\eta' = U(D_i\eta) \tag{14}$$

The pair of transformations (7) and (13) is referred to as the gauge transformation that makes the differential of vector transform in the same fashion as the vector itself under $U$.

According to the argument made in Sect. 2.1, the above gauge transformation makes the linear elastic law locally symmetric. If we apply the same rule of differentiation to the displacement vector $\boldsymbol{\xi}$, it becomes clear that the gauge transformation indeed makes the elastic law locally symmetric. Using the covariant derivatives with the gauge term $\Gamma$, express the total differential of the displacement vector, $\boldsymbol{\xi}$.

$$\begin{aligned} D\xi_i &= \left(\frac{\partial \xi_i}{\partial x} - \Gamma_x \xi_i\right) dx + \left(\frac{\partial \xi_i}{\partial y} - \Gamma_y \xi_i\right) dy + \left(\frac{\partial \xi_i}{\partial z} - \Gamma_z \xi_i\right) dz \\ &= \left(\frac{\partial \xi_i}{\partial x} dx + \frac{\partial \xi_i}{\partial y} dy + \frac{\partial \xi_i}{\partial z} dz\right) - \left(\Gamma_x \xi_i dx + \Gamma_y \xi_i dy + \Gamma_z \xi_i dz\right) \\ &\equiv d\xi_i - A_i \end{aligned} \tag{15}$$

Note that the first part of the second line of Eq. (15) is the total differential of the usual derivatives, and hence it represents the change in the length of the line element vector (Fig. 5). The second term on the second line represents the effect due to the gauge field on the $i$ component of the displacement vector. Repeating the same argument for the other components and noting that the first term in the second line of Eq. (15) has the form of a diagonalized strain tensor times vector $(dx, dy, dz)$, we obtain the following expression.

$$\begin{aligned} D\boldsymbol{\xi} &= \begin{pmatrix} \varepsilon_{xx} & \varepsilon_{xy} & \varepsilon_{xz} \\ \varepsilon_{yx} & \varepsilon_{yy} & \varepsilon_{yz} \\ \varepsilon_{zx} & \varepsilon_{zy} & \varepsilon_{zz} \end{pmatrix} \begin{pmatrix} dx \\ dy \\ dz \end{pmatrix} - \begin{pmatrix} 0 & -\omega_z & \omega_y \\ \omega_z & 0 & -\omega_z \\ -\omega_y & \omega_x & 0 \end{pmatrix} \begin{pmatrix} dx \\ dy \\ dz \end{pmatrix} \\ &\equiv d\boldsymbol{\xi} - \boldsymbol{A} \end{aligned} \tag{16}$$

Thus, we can naturally interpret the second term of Eq. (16) as the explicit form of the vector potential. As discussed in Sect. 2.1, vector potential $\boldsymbol{A}$ rotates the DSEs so that with the total differential represents the deformation. In this fashion the gauge field makes the law of linear elastic deformation locally symmetric. The component of vector potential can be expressed as follows.

$$A_i = \omega_j dx^k - \omega_k dx^j; \quad i, j, k = x, y, z \tag{17}$$

Equation (17) explicitly represents the meaning of the vector potential in connection with the material's differential rotation. Note that $A_i$ comes from the gauge term $\Gamma_i$ as part of the spatial covariant derivative $D_i$. It constitutes the spatial part of the gauge field. To complete the role of the gauge field as the compensation field to make the linear elastic dynamics locally symmetric, we need to introduce the temporal component $D_0$ in association with the temporal derivative $\partial/\partial t$. We will discuss the temporal covariant derivative along with the physical meaning of the corresponding potential $A_0$ in the following section in association with the field stress tensor.[1]

---

[1] See Ref. [9] for more detailed explanation about $D_0$.

**Fig. 6** Interaction with gauge field

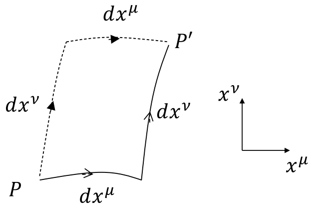

## 2.4 Least Action Principle and Field Equations

With the explicit form of $A_i$ (17) and the quantity known as the field stress tensor, we can discuss the interaction of the gauge field with the deformation. The result of this discussion represents the dynamics of the gauge field. The field stress tensor is defined as the commutation of the covariant derivatives [20].

$$\left[D_\mu, D_\nu\right] \xi_s ds = \left(\partial_\nu A_\mu - \partial_\mu A_\nu\right) + \frac{1}{\xi_s ds}\left[A_\mu, A_\nu\right] \equiv F_{\mu\nu} \tag{18}$$

Here $ds = dx^\nu = dx^\mu$. In the infinitesimal limit, $dx^\nu$ and $dx^\mu$ can be considered to be equal to each other.

Figure 6 illustrates the meaning of $\left[D_\mu, D_\nu\right]$. Here the horizontal and vertical axes are defined as $x_\mu$ and $x_\nu$. Consider differentiation with respect to point $P$ and $P'$ using covariant derivative $D$. There are two pathways to reach point $P'$ from $P$ in conducting this differentiation. The clockwise differentiation means that we apply $D_\nu$ first and then $D_\mu$. The counterclockwise differentiation means the application of the respective covariant derivatives in the reversed order. The commutation in Eq. (18) indicates the difference in the result between the clockwise and counterclockwise differentiation. If the answer is not zero, it means that the gauge field does some work on the physical system. Remember the thought experiment on the simple pendulum discussed as an analogy in Sect. 2.1. Apparently, the swirling wind does work on the pendulum in the direction of the wind. If there is no wind, the clockwise and counterclockwise application of the covariant derivative do not differ from each other.

Now consider how $F_{\mu\nu}$ transforms under $U$. From Eq. (14), we find

$$D'\left(U\eta\right) = U\left(D\eta\right). \tag{19}$$

Rearranging the terms in Eq. (19), we therefore can express the covariant derivative after the transformation as follows.

$$D' = UDU^{-1}. \tag{20}$$

Using expression (20), we can write $F_{\mu\nu}$ after the transformation as follows.

$$\begin{aligned} F'_{\mu\nu} &= \left[D'_\mu, D'_\nu\right] \xi_s ds = \left(D'_\mu D'_\nu - D'_\nu D'_\mu\right) \xi_s ds \\ &= \left(U D_\mu U^{-1} U D_\nu U^{-1} - U D_\nu U^{-1} U D_\mu U^{-1}\right) \xi_s ds \\ &= U \left[D_\mu, D_\nu\right] U^{-1} \xi_s ds = U F_{\mu\nu} U^{-1} \end{aligned} \tag{21}$$

Apparently, $F'_{\mu\nu} \neq F_{\mu\nu}$, indicating that the stress tensor is not invariant under the transformation. However, we find its trace $F'_{\mu\nu} F'^{\mu\nu}$ is invariant from the mathematical identity $tr(AB) = tr(BA)$ holding for general matrices $A$ and $B$.

$$\begin{aligned} tr\left(F'_{\mu\nu} F'^{\mu\nu}\right) &= tr\left(U F_{\mu\nu} U^{-1} U F^{\mu\nu} U^{-1}\right) = tr\left(U F_{\mu\nu} F^{\mu\nu} U^{-1}\right) \\ &= tr\left(U \left[F_{\mu\nu} F^{\mu\nu} U^{-1}\right]\right) = tr\left(\left[F_{\mu\nu} F^{\mu\nu} U^{-1}\right] U\right) \\ &= tr\left(F_{\mu\nu} F^{\mu\nu}\right) \end{aligned} \tag{22}$$

We can interpret this quantity $F_{\mu\nu} F^{\mu\nu}$, which is invariant under the gauge transformation, as the Lagrangian associated with the dynamics of the gauge field.

Before discussing this Lagrangian, it is a good idea to write down $F_{\mu\nu}$ and $F^{\mu\nu}$ explicitly. To this end, the relativistic expression of the time and space components (the four vector) is convenient [20, 35]. So we take some time to review this expression. The physical quantity including the coordinate variables are expressed in the following fashion.

$$x^\mu = (x^0, x^1, x^2, x^3) = (ct, x, y, z) \tag{23}$$

$$x_\mu = (x_0, x_1, x_2, x_3) = (ct, -x, -y, -z) \tag{24}$$

Here the superscript and subscript are defined in accordance with the Einstein's notation of summation. The superscript represents a component of a vector and the subscript a component of a covector. If a pair of superscript and subscript appear next to each other in the form of a product, the product is a inner product.

$$x_\mu x^\mu = \sum_{\mu=0}^{3} = (x^0)^2 - (x^1)^2 - (x^2)^2 - (x^3)^2 = (ct)^2 - (x^2 + y^2 + z^2) \tag{25}$$

In general relativity, Eq. (25) indicates the invariance of the space-time interval [34].

Vector potential $\boldsymbol{A}$ can be written in the same fashion.

$$A^\mu = (A^0, A^1, A^2, A^3) = \left(\frac{\phi^0}{c}, A^x, A^y, A^z\right) \tag{26}$$

$$A_\mu = (A_0, A_1, A_2, A_3) = (A^0, -A^1, -A^2, -A^3) = \left(\frac{\phi^0}{c}, -A^x, -A^y, -A^z\right) \tag{27}$$

The quantity $\phi^0$ in Eqs. (26) and (27) is the scalar potential, which constitutes the time component of the four vector potential $(A^0, A^1, A^2, A^3)$. Its physical meaning will be discussed shortly.

The partial derivatives can also be expressed in the four vector notation as follows.

$$\partial^{\mu} = \left(\frac{\partial}{\partial x^0}, -\frac{\partial}{\partial x^1}, -\frac{\partial}{\partial x^2}, -\frac{\partial}{\partial x^3}\right) = \left(\frac{1}{c}\frac{\partial}{\partial t}, -\frac{\partial}{\partial x}, -\frac{\partial}{\partial y}, -\frac{\partial}{\partial z}\right) \tag{28}$$

$$\partial_{\mu} = \left(\frac{\partial}{\partial x_0}, -\frac{\partial}{\partial x_1}, -\frac{\partial}{\partial x_2}, -\frac{\partial}{\partial x_3}\right) = \left(\frac{1}{c}\frac{\partial}{\partial t}, \frac{\partial}{\partial x}, \frac{\partial}{\partial y}, \frac{\partial}{\partial z}\right) \tag{29}$$

Note that the sign of the spatial components of the derivatives behave opposite to those of the vector components.

With the above four vector notations, the field stress tensor $F^{\mu\nu}$ and $F_{\mu\nu}$ can be expressed compactly as follows.

$$F^{\mu\nu} = \partial^{\mu} A^{\nu} - \partial^{\nu} A^{\mu} = \frac{\partial A^{\nu}}{\partial x^{\mu}} - \frac{\partial A^{\mu}}{\partial x^{\nu}} \tag{30}$$

$$F_{\mu\nu} = \partial_{\mu} A_{\nu} - \partial_{\nu} A_{\mu} = \frac{\partial A_{\nu}}{\partial x_{\mu}} - \frac{\partial A_{\mu}}{\partial x_{\nu}} \tag{31}$$

When $\mu$ and $\nu$ are spatial coordinate variables, Eqs. (26)–(29) yield the following expressions. We use Eq. (17) in going through the rightmost equal sign.

$$F^{ij} = -\frac{\partial A^j}{\partial x^i} + \frac{\partial A^i}{\partial x^j} = -\left(\frac{\partial A^j}{\partial x^i} - \frac{\partial A^i}{\partial x^j}\right) = -\omega^k \tag{32}$$

$$F_{ij} = \frac{\partial(-A^j)}{\partial x^i} - \frac{\partial(-A^i)}{\partial x^j} = -\left(\frac{\partial A^j}{\partial x^i} - \frac{\partial A^i}{\partial x^j}\right) = -\omega^k \tag{33}$$

When the time coordinate variable is involved, we obtain the following expressions.

$$F^{0i} = \frac{\partial A^i}{\partial x^0} + \frac{\partial A^0}{\partial x^i} = \frac{1}{c}\left(\frac{\partial A^i}{\partial t} + \frac{\partial \phi^0}{\partial x^i}\right) = \frac{v^i}{c} \tag{34}$$

$$F_{0j} = \frac{\partial(-A^i)}{\partial x^0} - \frac{\partial A^0}{\partial x^i} = -\frac{1}{c}\left(\frac{\partial A^i}{\partial t} + \frac{\partial \phi^0}{\partial x^i}\right) = -\frac{v^i}{c} \tag{35}$$

Here we use the analogy to electrodynamics in the rightmost expression in Eqs. (34) and (35); $\boldsymbol{v}$ and $\boldsymbol{\omega}$ correspond to the electric and magnetic fields as we will see shortly. More generally, this expression can be put as follows.

$$\boldsymbol{v} = \frac{\partial \boldsymbol{A}}{\partial t} + \nabla\phi \tag{36}$$

The meaning of the first term on the right-hand side of Eq. (36) is straightforward. The temporal derivative of the vector potential is velocity. The second term indicates the physical meaning of the scalar potential as a source of velocity such as the gravitational potential. As far as the wave dynamics is concerned, the scalar potential is not significant.

Using Eqs. (32)–(35), we can express the field stress tensor explicitly.

$$F^{\mu\nu} = \begin{pmatrix} 0 & v^1/c & v^2/c & v^3/c \\ -v^1/c & 0 & -\omega^3 & \omega^2 \\ -v^2/c & \omega^3 & 0 & -\omega^1 \\ -v^3/c & -\omega^2 & \omega^1 & 0 \end{pmatrix} \tag{37}$$

$$F_{\mu\nu} = \begin{pmatrix} 0 & -v^1/c & -v^2/c & -v^3/c \\ v^1/c & 0 & -\omega^3 & \omega^2 \\ v^2/c & \omega^3 & 0 & -\omega^1 \\ v^3/c & -\omega^2 & \omega^1 & 0 \end{pmatrix} \tag{38}$$

The above expression allows us to put the Lagrangian density $F_{\mu\nu}F^{\mu\nu}$ in a physically meaningful form.

$$\begin{aligned} F_{\mu\nu}F^{\mu\nu} &= F_{01}F^{01} + F_{10}F^{10} + F_{02}F^{02} + \cdots + F_{12}F^{12} + F_{21}F^{21} + \cdots \\ &= -2\left\{\left(\frac{v^1}{c}\right)^2 + \left(\frac{v^2}{c}\right)^2 + \left(\frac{v^3}{c}\right)^2\right\} + 2\left\{(\omega^1)^2 + (\omega^2)^2 + (\omega^3)^2\right\} \\ &= -2\left\{\left(\frac{v}{c}\right)^2 - \omega^2\right\} \end{aligned} \tag{39}$$

Equation (39) indicates that if we use the expression of the shear wave velocity for $c$ and divide by 4, $F_{\mu\nu}F^{\mu\nu}$ has the form of the kinetic energy minus potential energy per unit volume. Thus we can identify the Lagrangian density as follows.

$$c = \sqrt{\frac{G}{\rho}} \tag{40}$$

$$\mathscr{L}_{F_{\mu\nu}} = -\frac{G}{4}F_{\mu\nu}F^{\mu\nu} = \frac{1}{2}G\left(\frac{v^2}{c^2} - \omega^2\right) = \frac{\rho}{2}v^2 - \frac{G}{2}\omega^2 \tag{41}$$

In Eq. (41) the subscript $F_{\mu\nu}$ denotes that this Lagrangian density is associated with the field stress tensor, which originates from the temporal and spatial differentiation of the gauge (vector) potential $\boldsymbol{A}$ (Eqs. (32)–(35).) By adding Lagrangian density terms associated with the $\boldsymbol{A}$, we can express the total Lagrangian density due to the gauge field as follows.

$$\mathscr{L}_{tot} = -\frac{G}{4}F_{\mu\nu}F^{\mu\nu} + Gj^{\mu}A_{\mu} = \frac{\rho v^2}{2} - \frac{G\omega^2}{2} + \frac{G}{c}j^0A_0 + Gj^iA_i \tag{42}$$

On the right-hand side of Eq. (42), the terms containing $A_0$ and $A_i$ represent the Lagrangian density associated with the temporal and spatial components of the vector potential, respectively. The quantity $j^0$ and $j^i$ are referred to as the charge and current of symmetry [20]. These are conserved quantity whose physical meanings will be discussed later.

With the total Lagrangian density expression (42), we obtain the following expression for the total variation of action.

$$\delta S = \int dt \int \left( \frac{\partial \mathscr{L}_{tot}}{\partial A_\mu} \delta A_\mu + \frac{\partial \mathscr{L}_{tot}}{\partial (\partial A_\mu / \partial x^i)} \delta \left( \frac{\partial A_\mu}{\partial x^i} \right) + \frac{\partial \mathscr{L}_{tot}}{\partial \dot{A}_\mu} \delta \dot{A}_\mu \right) dx^i \tag{43}$$

Here the second integration is with respect to the spatial coordinates. We can integrate the second and third terms of the integrand by parts with respect to space and time, respectively, and write $\delta S$ as follows.

$$\begin{aligned} \delta S = & \int dt \int \frac{\partial \mathscr{L}_{tot}}{\partial A_\mu} \delta A_\mu dx^i \\ & + \int dt \left[ \frac{\partial \mathscr{L}_{tot}}{\partial (\partial A_\mu / \partial x^i)} \delta A_\mu \right]_{\infty}^{\infty} - \int dt \int dx^i \left( \frac{\partial}{\partial x^i} \frac{\partial \mathscr{L}_{tot}}{\partial (\partial A_\mu / \partial x^i)} \right) \delta A_\mu \\ & + \int dx^i \left[ \frac{\partial \mathscr{L}_{tot}}{\partial \dot{A}_\mu} \delta A_\mu \right]_{t1}^{t2} - \int dt \int dx^i \left( \frac{\partial}{\partial t} \frac{\partial \mathscr{L}_{tot}}{\partial \dot{A}_\mu} \right) \delta A_\mu \end{aligned}$$

Putting the surface integrals zero,

$$\delta S = \int dt \int dx^i \delta A_\mu \left( \frac{\partial \mathscr{L}_{tot}}{\partial A_\mu} - \frac{\partial}{\partial x^i} \left( \frac{\partial \mathscr{L}_{tot}}{\partial (\partial A_\mu / \partial x^i)} \right) - \frac{\partial}{\partial t} \left( \frac{\partial \mathscr{L}_{tot}}{\partial \dot{A}_\mu} \right) \right) \tag{44}$$

Putting the variation $\delta S = 0$, we obtain the Lagrange equation of motion from Eq. (44).

$$\frac{\partial \mathscr{L}_{tot}}{\partial A_\mu} - \frac{\partial}{\partial x^i} \left( \frac{\partial \mathscr{L}_{tot}}{\partial (\partial A_\mu / \partial x^i)} \right) - \frac{\partial}{\partial t} \left( \frac{\partial \mathscr{L}_{tot}}{\partial \dot{A}_\mu} \right) = 0 \tag{45}$$

With the use of Lagrangian density (42), Lagrangian equation of motion (45) yields the following field equations.

$$\nabla \cdot \boldsymbol{v} = -j_0 \tag{46}$$

$$\nabla \times \boldsymbol{v} = \frac{\partial \boldsymbol{\omega}}{\partial t} \tag{47}$$

$$\nabla \times \boldsymbol{\omega} = -\frac{\rho}{G} \frac{\partial \boldsymbol{v}}{\partial t} - \boldsymbol{j} \tag{48}$$

$$\nabla \cdot \boldsymbol{\omega} = 0 \tag{49}$$

Equations (46) and (48) come from Lagrangian equation of motion (45), Eq. (47) is the relation between the translational and rotational displacement ($\nabla \times \boldsymbol{\xi} = \boldsymbol{\omega}$) and Eq. (49) comes from the mathematical identity $\nabla \cdot (\nabla \times \boldsymbol{\omega}) = 0$ (rotational field is divergenceless).

Field equations (46)–(49) are very similar to Maxwell equations. The similarity is not only formulaic. The electromagnetic field and deformation field have similarities in the fundamental level of physics. Among those physical similarities, the wave dynamics is the most important one. It is clear that field equations (47) and (48) yield wave equations. In the following sections, we discuss a number of wave dynamical behaviors of deformation field. Before these discussions, we first review experimental observations. Many of these wave dynamical behaviors of deformation field and their field theoretical explanations have been found from experiments.

## 3 Experimental Observations

We have conducted a number of experiments to characterize the deformation field of thin metal specimens under tensile loads using an optical interferometric technique known as the Electronic Speckle-Pattern Interferometry (ESPI) [37, 38]. In this section we discuss various experimental observations from the viewpoint of wave dynamics.

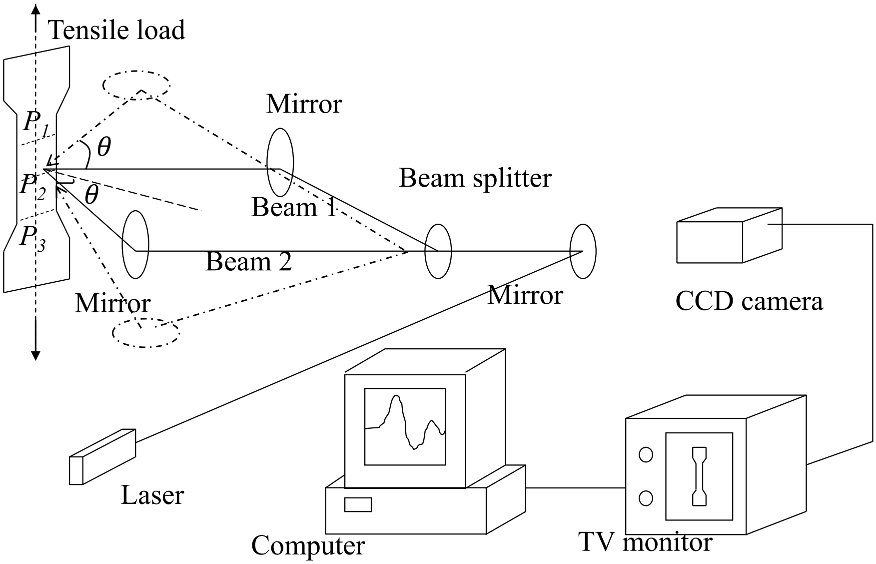

**Fig. 7** Horizontally-sensitive and vertically-sensitive ESPI setups. $P_1$–$P_3$ are reference points where data are evaluated in Fig. 11

## 3.1 Experimental Arrangement

Figure 7 illustrates the arrangement of a typical ESPI experiment. A laser beam is split into interferometric paths (labeled Beam 1 and Beam 2 in the figure) with a beam splitter. Each of these beams is directed to the specimen with a folding mirror after expanded with a beam expander (not shown in the figure) to cover the area of interest. The two beams are recombined on the specimen so that the two optical fields interfere with each other. Because of the surface roughness, the reflection from the specimen is diffusive. Thus, on the image plane of the CCD (Charge Coupled Devise) camera, the reflections from the respective beams form speckle patterns. Since each speckle results from coherent superposition of the laser light associated with the diffusive reflection, it has a definite optical phase. Therefore, when a pair of speckles (one from one interferometric path and the other from the other interferometric path) overlap at a point on the image plane, the two speckles interfere with each other. If the interference is destructive, the intensity of the overlapping point is low, if the interference is constructive the intensity is high. In this fashion, the superposition of the two speckle fields form a map of relative phase difference at all points on the image plane.

When the specimen undergoes deformation due to the load applied by the tensile machine, points on the specimen undergoes displacement. When the displacement at a point on the specimen surface is rightward (in the direction to the folding mirror for Beam 1), the optical phase for this interferometric path decreases. At the same time, the phase for the other interferometric path increases. Consequently, the relative phase difference at the corresponding point on the image plane changes from the

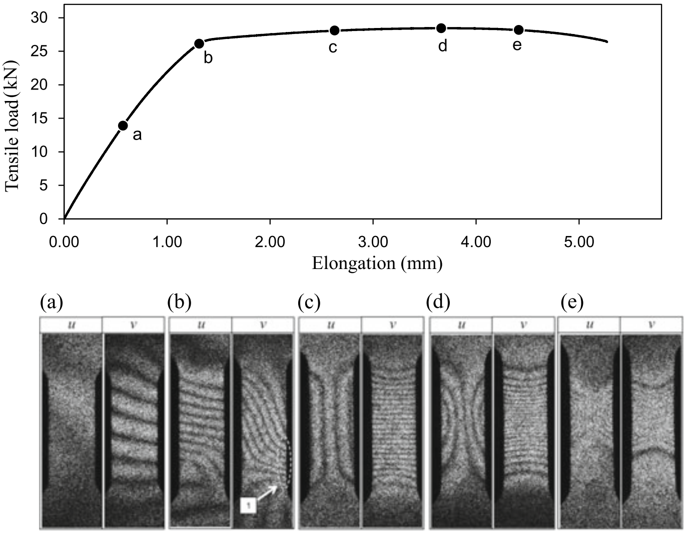

**Fig. 8** Loading curve of aluminum alloy 7075 T6 and fringe patterns corresponding to horizontal (u) and vertical (v) displacement components

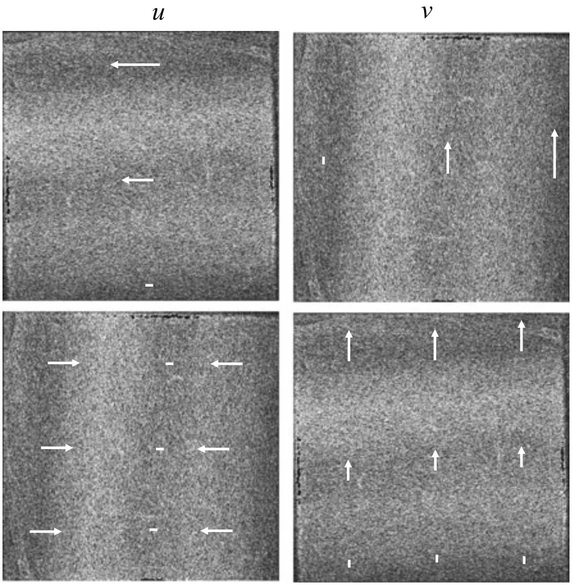

**Fig. 9** Interpretation of fringe patters

value before the deformation. Thus, by subtracting the image data taken before the deformation from the one taken after the deformation, an interference fringe pattern is formed. Here, if the relative phase change due to the deformation is destructive, the corresponding point on the subtracted image appears dark. Those points where the interference is constructive, the image appears bright. The interference fringe pattern is a map of contours of the destructive interference. The lower part of Fig. 8 shows typical interference fringe patterns.

By configuring a similar arrangement of interferometric paths vertically (as shown in Fig. 7 with dashed lines), and taking the same image acquisition and processing procedures as the horizontal case, we can form fringe patterns that represent vertical deformation. Hereafter we call the interferometric arrangement sensitive to horizontal displacement the horizontally-sensitive ESPI configuration, and the one sensitive to vertical displacement the vertically sensitive ESPI configuration.

Figure 8 [39] shows a series of typical fringe patterns observed in a tensile test on a thin plate specimen of an aluminum alloy 7075 T6 along with the loading curve. The dimension of the specimen is 25 mm long, 10 mm wide (the parallel part of the dog-bone shape specimen) and 5 mm thick. The tensile speed is constant at 1.0 mm/min. In the fringe patterns, those labeled "u" are generated with the horizontally sensitive ESPI configuration, and those labeled "v" are by the vertically sensitive configuration. Several points on the loading curve are marked "a" through "e". The fringe patterns formed at these points are identified by the corresponding letter in the parenthesis above the pair of "u" and "v" fringe patterns.

Fringe patterns generated from a horizontally or vertically sensitive ESPI configuration indicates a certain pattern of deformation. Consider a sample fringe image where dark fringes are parallel. Figure 9 illustrates some possibilities. Here the left two images are formed by a horizontally sensitive ESPI configuration (called the $u$ fringe pattern) and the right two images are formed by a vertically sensitive ESPI configuration (the $v$ fringe pattern). It is assumed that a tensile load is applied vertically. Each dark fringe represents a contour of a displacement that corresponds to an integral multiple of unit displacement (see the next paragraph for the definition of the unit displacement). Arrows in the images indicate the constant displacements corresponding to the respective dark fringes. In the upper images, $u$ fringes are horizontally parallel and the $v$ fringes are vertically parallel. On the other hand, the lower images show vertically parallel fringes in the $u$ fringe pattern and horizontally parallel fringes in the $v$ fringe pattern. Since the displacement caused by the tensile load is dominantly vertical, if the deformation is uniform the $v$ fringe pattern is expected to show a gradual increase in the displacement as the lower right image indicates, whereas the $u$ fringe pattern is expected to show a uniform compressive displacement according to the Poisson's effect (the lower left image). If the fringe patterns are like the upper images, the $u$ and $v$ fringe patterns indicate $\partial u/\partial y \neq 0$ and $\partial v/\partial x \neq 0$, respectively. These are when the specimen undergoes rotation or shear deformation. More specific will be discussed under Sect. 4.2.4.

In the case where the two interferometric beams have the same angle of incidence (like Fig. 7), the displacement and the fringes corresponding to integer multiples of unit displacement have a simple relation. Let $\delta$ be the displacement of a speckle pattern in a direction that the ESPI configuration is sensitive. The change in the relative phase difference due to $\delta$ is given by the following equation.

$$\frac{\phi}{2} = 2\pi \frac{\delta \sin\theta}{\lambda} \tag{50}$$

where $\lambda$ is the wavelength of the laser, and $\theta$ is the angle of incidence (Fig. 7). A dark fringe represents the contour of displacement where the change in the relative phase difference $\phi$ is an integral multiple of the period, i.e., $\phi = 2n\pi$ ($n$: integer). By substituting this condition into Eq. (50), we can find the displacement corresponding to $n$th dark fringe as follows.

$$u = \frac{n\lambda}{2\sin\theta} \tag{51}$$

The unit displacement is the minimum displacement represented by a dark fringe. In Eq. (51), the unit displacement corresponds to $u$ with $n = 1$, i.e., $u_0 = \lambda/(2\sin\theta)$. With a typical angle of incident 45°, the unit displacement $u_0$ is $1/\sqrt{2}$ of the wavelength.

Between dark fringes, we can evaluate the relative phase changes by interpolation. Figure 10a illustrates that we can assign the fringe order for a tensile experiment from the stationary grip side. Figure 10b shows the continuous phase map resulting from interpolation. Once we know the relative phase $\phi$ continuously, we can convert it to displacement data using Eq. (50) backward (find $\delta$ from $\phi$).

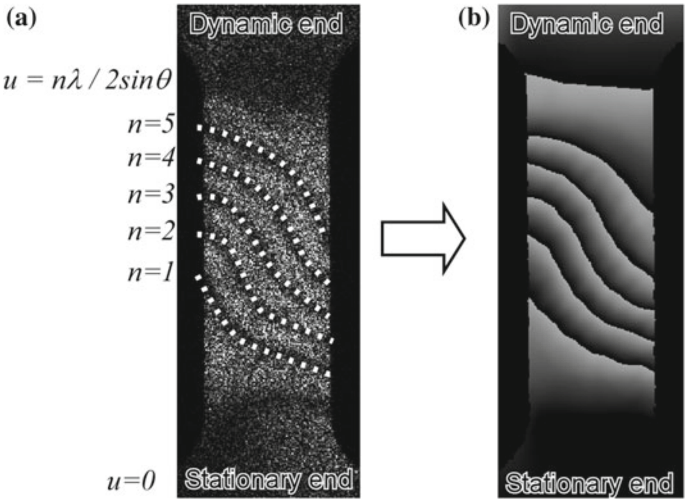

**Fig. 10** Intensity and phase map [39]

## 3.2 *Plastic Deformation Wave*

Figure 11 [40] shows wave characteristics observed in the velocity component perpendicular to the tensile axis. The specimen is an aluminum alloy A6063 plate of 200 mm long, 25 mm wide and 1 mm thick. The grain size is approximately 15 μm. A tensile load is applied at a constant rate of 0.1 mm/min. The horizontally sensitive ESPI configuration shown in Fig. 7 takes interferometric images continuously, and fringe patterns are formed at a constant rate by the image subtraction procedure described above. The relative phase change of the speckles are evaluated on the dark fringes along the vertical central line on which three reference points are set. The phase data are interpolated between dark fringes and converted to continuous data as shown in Fig. 10. With the use of Eq. (51), the phase data are converted into the displacement data occurring between the two time steps used for the image subtraction. Thus, the evaluated data has the dimension of velocity, and called the velocity data hereafter. The three reference points are along the center of the specimen parallel to the tensile axis at the vertical center, and at a upper and lower point approximately the same vertical distance from the central point. These points are marked $P_1$–$P_3$ in Fig. 7 and called "upper" - "lower" in the legend of Fig. 11. Also shown in Fig. 11 is the loading curve. The horizontal axis of this figure indicates the time elapsed from the beginning of the tensile load.

The three plots shown in Fig. 11 show the oscillatory behavior of the velocity component perpendicular to the tensile load. The oscillation rises slightly prior to the yield point observed at approximately 14 min after the tensile loading starts. Among the three reference points, the velocity data at the upper reference point are greater than the other reference points, indicating that the tensile load causes the specimen to undergo a lateral swinging motion in which the upper side of the specimen swings more largely than the lower side. There is a time delay among the three reference points in the first peaks observed slightly before 15 min. The dashed line connecting the peaks of the three reference points indicates the time delay. The fact that the upper reference point is behind the other reference points with the greater amplitude indicates that the specimen undergoes rotation with the rotational center located somewhere lower than the lower reference point. We can view this time delay as the transverse velocity-wave travels upwards along the tensile axis. Interestingly, the time delay disappears at the third peak observed slightly before 20 min. As the time delay decreases, the peak height decays exponentially, as the curved dashed line connecting the peaks indicates. The specimen fractures after the third peak.

We can explain the above observation from the wave dynamics in the following fashion. Every wave carries energy. The present velocity wave carries the mechanical energy as follows. When a point is swinging to a side with velocity $u$, the unit volume has the kinetic energy $\rho u^2/2$, where $\rho$ is the density. When the swinging motion reaches the turning point, the velocity becomes zero. However, at that point the rotational energy is at a maximum because the angle of rotation is at a maximum. This rotational potential energy can be expressed with the shear modulus as $G\omega^2/2$. Thus, as the oscillatory swinging motion continues, the form of the mechanical energy switches between the kinetic and potential energy (per unit volume). When the kinetic energy is at the maximum, the potential energy is zero, and when the potential energy is at the maximum the kinetic energy is zero. Since the vector $\boldsymbol{\omega}$ is out of plane and $\boldsymbol{v}$ is in plane, this energy flow can be considered as analogous to the Poynting vector of the electromagnetic field. Apparently, the electric field vector corresponds to $\boldsymbol{v}$ and the magnetic field vector corresponds to $\boldsymbol{\omega}$.

When the phase delay disappears, we can interpret that the velocity wave stops traveling. From the viewpoint of the energy carried by the velocity wave, this is when the mechanical energy stops being carried. If the external load continues, the specimen does not have a mechanism to consume the energy. This leads to the fracture. From the viewpoint of wave propagation, the zero wave velocity corresponds to zero frequency, or infinite period. The swinging motion cannot change its direction any more, and consequently, the velocity of the point does not change its sign. This makes the point keep being displaced in one direction. Naturally, a discontinuity is generated and the solid fractures. In Fig. 11, this phenomenon is observed after the third peak; all the three reference points keeps going in the positive direction. The specimen fractures immediately after this happens.

### *3.3 Shear Bands*

In many occasions [14, 15, 41, 42], shear bands appear in the fringe images. The band pattern consists of parallel concentrated dark fringes running at approximately 45° to the tensile axis. One specific feature of the fringe pattern representing a shear band is that the $u$ and $v$ fringe patterns overlap each other [41]. This observation can be explained as follows. When a shear bad is formed, dislocations starting from one side of the specimen propagate to the other side. When the dislocations bridge the specimen laterally in this fashion, the banded area where a shear band runs undergoes a concentrated stretch isolated from the rest of the specimen. A previous study [12] indicates that the formation of a shear band is accompanied by acoustic emission. This is consistent with the above explanation that the formation of a shear band is due to the bridging of dislocations. When the dislocations complete their propagation to the other side of the specimen, the material snaps causing acoustic emission. At the same time, the stress is relaxed and the relaxation causes serration [43, 44] in the loading curve.

The shear band observed in a tensile experiment with a constant pulling rate travels along the specimen. Figure 12 [15] shows an example of traveling shear band. The numbers put under the images indicate the frame number when the shear band image above the number is recorded. Note that the numbers are separated by an approximately constant increment and the shear band moves approximately the same distance, indicating that the moving speed of the shear band is constant. Other similar study reveals that the motion of shear bands is at a constant rate proportional to the tensile speed [15]. Another interesting observation is that the shear band appears narrower as it travels [41]. This observation indicates that with the elapse of time, the strain associated with the shear band is more concentrated. We will discuss the shear band later in this chapter in association with a velocity wave in the form of a solitary wave.

Under some condition, the ESPI fringe patterns shows both a plastic deformation wave like the one shown in Fig. 11 and a shear band. Figure 13 shows the oscillatory characteristics of the velocity component perpendicular to the tensile axis and the location of the shear band as a function of the elapse time from the beginning of the tensile loading [40]. The plots marked "Shear-band" indicates the location that the shear band appears on the specimen as a function of time. It is seen that as the

**Fig. 11** Velocity wave and loading curve

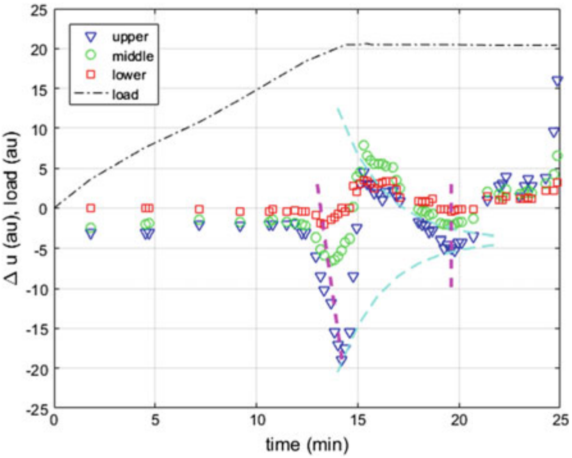

shear band appears intermittently the oscillation of the velocity becomes discontinuous. This observation is consistent with the above observation and explanation that the formation of a shear band accompanies stress relaxation. Each time the stress is relaxed in conjunction with the formation of a shear band, the material recoils breaking the oscillatory behavior of the velocity field. After the stress relaxation, the stress is recovered and it is accompanied by the reappearance of the oscillatory feature of the velocity field. It is interesting to note that even the oscillatory behavior is intermittent the peak of the oscillation decays exponentially as indicated by the solid curve in Fig. 13.

Figure 14 shows the location of shear bands and the loading curve [45]. It is seen that initially the shear band moves across the specimen for the entire vertical span of the specimen back and forth. With the elapse of the time, the slope of the shear band location with the time decreases, indicating that the moving speed of the shear

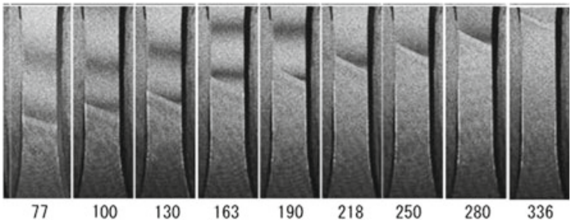

**Fig. 12** Shear band traveling along specimen

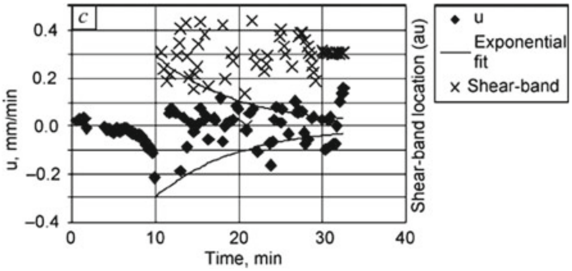

**Fig. 13** Velocity wave, shear band locations and loading curve

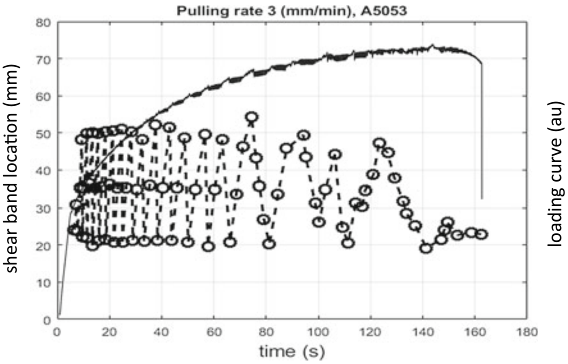

**Fig. 14** Shear band and loading curve

band decreases. Eventually, the shear band stops moving and stays at the location marked 22 mm on the vertical axis. Approximately 10 s after the shear band becomes stationary the specimen fractures as the loading curve indicates. The fracture always occurs at the location where the shear band becomes stationary and the fracture line runs exactly on the stationary shear band [46]. This observation supports the above explanation that the shear band accompanies a concentrated stretch and stress relaxation. The same phenomenon is observed in a number of similar ESPI experiments [14, 41, 42]. The fact that the fracture is accompanied by the stationary shear band is explained later in this chapter in association with the solitary wave representing the shear band and its energy. Like the velocity wave discussed with Fig. 11, when the solitary wave stops traveling the material loses its mechanism to consume the work provided by the external load and stagnated energy causes material discontinuity that leads to the fracture.

## 4 Dynamics of Deformation and Fracture

In Sect. 2, we formulated the nonlinear deformation by requesting the local symmetry in the law of linear elastic deformation. We derived field equations that describe the displacement and velocity field of nonlinear deformation. There we discussed that the dynamics is applicable to plastic deformation but did not clearly discuss the irreversibility of plastic deformation. The field equations have the form that yields wave dynamics of the displacement and velocity field. In Sect. 3, we discussed various wave-like phenomena of deformation observed in experiments. It is time to develop the discussion of the field theoretical description of deformation to the next level using experimental observations. In this section, we first interpret one of the field equations as the equation of motion. This allows us to interpret some quantities resulting from the field theoretical formalism from the viewpoints of dynamics. The irreversibility of plastic deformation is explained as the velocity damping force that the solid exerts. These discussions are followed by the derivation of wave equations from the field equations, and the explanation of various experimental observations as the wave dynamics of deformation. These discussions lead to the comprehensive description of all stages of deformation, including the fracture dynamics, based on the same theoretical foundation.

### 4.1 *Equation of Motion*

We can interpret one of the field equations derived above as the equation of motion that governs the dynamics of solid under deformation [10]. Rearrange field equation (48) as follows.

$$\rho \frac{\partial \boldsymbol{v}}{\partial t} = -G\nabla \times \boldsymbol{\omega} - G\boldsymbol{j} \tag{52}$$

**Fig. 15** **a** Shear elastic force and **b** longitudinal elastic force [10]

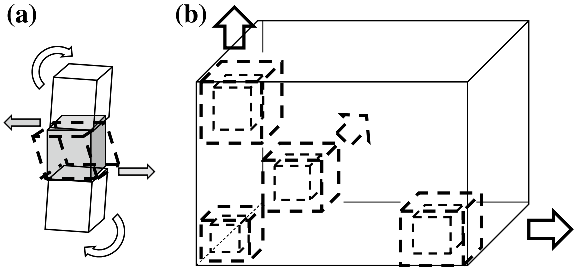

The left-hand-side of Eq. (52) is the mass times acceleration of the unit volume. Hence, we can interpret that the right-hand side of this equation represents the external force acting on the unit volume. Further, from its form of differential rotation times shear modulus, we can interpret the first term as the shear force acting on the unit volume exerted by the neighboring unit volumes as schematically illustrated by Fig. 15a. Here Fig. 15b illustrates the longitudinal elastic force of linear elasticity for contrast. Note that the shear elastic force is proportional to differential rotation whereas the longitudinal elastic force is proportional to the differential volume expansion. Later we will discuss more on this type of longitudinal elastic force.

The second term $G\boldsymbol{j}$ has a deeper physical meaning. Since vector $G\boldsymbol{j}$ is in line with the acceleration $\partial \boldsymbol{v}/\partial t$ with the negative sign, we can view this term as the longitudinal resistant force exerted by the solid. Different stages of deformation can be identified by the form of the longitudinal resistant force, and by expressing this term appropriately, we can describe all the stages including fracture in a comprehensive fashion. In the following section we discuss this term for each dynamics.

### 4.1.1 Plastic Deformation Dynamics

As clear from the above interpretation, the oscillatory feature of plastic deformation is caused by the shear elastic force. We also know that plastic deformation is irreversible, which means that the energy associated with plastic deformation is not recoverable as a form of mechanical energy, or it is dissipative. Equation (52) indicates the other external force on the unit volume is the longitudinal force. It is natural to interpret that this longitudinal force is the source of energy dissipation in plasticity. This interpretation is justified by the following argument.

Take divergence of Eq. (52) and use the mathematical identity $\nabla \cdot (\nabla \times \boldsymbol{\omega}) = 0$. We obtain the following equality.

$$\frac{\partial \nabla \cdot (\rho \boldsymbol{v})}{\partial t} = -G\nabla \cdot \boldsymbol{j} \tag{53}$$

The left-hand side of Eq. (53) is the temporal change of the net momentum of all the particles in the unit volume. Particles flow into the unit volume with certain velocity and flow out from the volume with certain velocity. If the average velocity of the flowing-in particles is greater than that of the flowing-out particles, there is a net loss of the total momentum by the unit volume over the time of the particles' flow. If the flowing-out particles have a greater average velocity, the volume experiences a net momentum gain. $\nabla \cdot \rho \boldsymbol{v}$ represents this net momentum gain or loss. Equation (53) tells such a net momentum gain (loss) in the unit volume over time is equivalent to the differential value of $\boldsymbol{Gj}$ expressed by $\nabla \cdot \boldsymbol{Gj}$. According to Newton's second law, the momentum change per unit time is equal to the net external force. From this argument, we can interpret that the quantity $\boldsymbol{Gj}$ is a field-force like entity where the differential value $\nabla \cdot \boldsymbol{Gj}$ represents the net force on the unit volume. Being a field force, it is a function of the coordinate variables. From the fact that the differential force takes the form of divergence as $\nabla \cdot \boldsymbol{Gj}$, we can further interpret that $\boldsymbol{Gj}$ is a longitudinal force. It is a function of the coordinate variable associated with the axis along which the particles flow.

The longitudinal force $\boldsymbol{Gj}$ can be elastic or inelastic force to change the particle's momentum. It depends on the interaction that particles undergo inside the unit volume. If the interaction is elastic, the corresponding longitudinal force is an elastic force, and if the interaction is inelastic, the longitudinal force is energy dissipative force. It should be noted that the particles flowing out from the unit volume are not the one flowing in to the volume. These particles are not free particles but part of the solid (atoms). When particles move to the unit volume, they feel reaction force from the particles ahead of them. The incoming particles exert force in the direction of their flow and the particles inside the unit volume (the existing particles) push them backward. While this happens, the existing particles come out of the unit volume and appear to be the flowing out particles. When reacting to the incoming particles, the existing particles exert resisting force in accordance with the force law determined by the solid. If the solid is purely elastic, the force law is Hooke's law. The incoming particles lose their momentum and the existing particles gain the momentum. The momentum of the total system is conserved. Since the interaction is elastic, the mechanical energy of the total system is also conserved. If the solid is plastic, the situation is different. Although the existing particles gain their momentum as much as the incoming particles lose, the mechanical energy of the total system is not conserved.

The above dynamics is analogous to the classical problem of collisions between two billiard balls. Consider that a billiard ball (Ball 1) collides with another identical billiard ball (Ball 2) that is stationary, and that the two billiard balls undergo a perfectly elastic collision. The momentum is transferred from Ball 1 to Ball 2. Having the same mass as Ball 1, Ball 2 moves with the Ball1's velocity before the collision. Instead, Ball 1 becomes stationary after the collision. Now consider that the collision is inelastic. Although the momentum of the two-ball system is conserved upon the collision, the energy is not conserved. On the right-hand side of Eq. (53), $\boldsymbol{Gj}$ describes the force law. If the force law represents perfect elasticity, the flowing out particles have the same average velocity as the incoming particles (assumed to be initially stationary). The same interaction keeps occurring as the elastic wave (compression wave) travels through the solid, as a number of billiard balls are arranged and the Ball

**Fig. 16** Velocity damping force

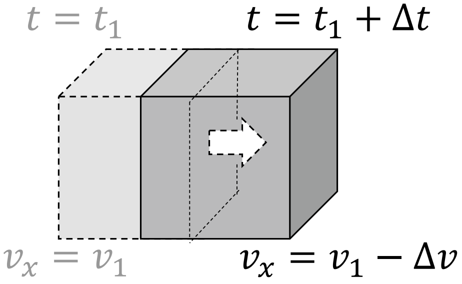

1's collision initiates a number of collisions like a domino-like chain-reaction. The particles keep the initial average velocity. In fact, when $\boldsymbol{Gj}$ represents an elastic force in proportion to the volume expansion (Fig. 15b), Eq. (53) yields to a compression wave equation [10]. If the force law represents inelasticity, the particle velocity decreases as the wave travels. In this case, Eq. (53) yields a decaying wave equation [10].

A possible scenario for the inelastic case is that $\boldsymbol{Gj}$ represents a velocity damping force. The friction that dynamic dislocations undergo is a possible micromechanical mechanism to explain the velocity damping force [47]. Figure 16 illustrates this effect schematically. A group of particles with an average velocity of $v_x$ are flowing in the positive $x$-direction into a unit volume where the medium in that region exerts velocity damping force. As the interaction travels downstream, the flowing-out particles keep losing the average velocity. Hence, $\partial \nabla \cdot (\rho \boldsymbol{v})/\partial t < 0$. This causes the dynamics to lose the mechanical energy with the passage of time, and explains the energy dissipative feature of plasticity. We can interpret that the longitudinal force $\boldsymbol{Gj}$ proportional to the particle velocity represents the velocity-damping mechanism of the solid.

From the gauge theoretical viewpoint, Eq. (53) raises an interesting point. Using Eq. (46) we can put Eq. (53) in the following form.

$$\frac{\partial(\rho j_0)}{\partial t} = -\nabla \cdot (G\boldsymbol{j}) \tag{54}$$

We can view Eq. (54) as an equation of continuity associated with conservation of the quantity $\rho j_0$. Here, $j_0$ is the charge of symmetry, corresponding to the electric charge density in electrodynamics. In Maxwell's electrodynamics theory, the electric charge is a conserved quantity and therefore temporal change in a unit volume must be accounted for by electric current. In the present case, the current of symmetry $\boldsymbol{j}$ corresponds to the electric current. The associated law of conservation is Newton's law in the sense that the momentum is conserved. Also, this argument characterizes the quantity $\rho j_0$ as a charge of symmetry, which is a conserved quantity as the electric charge is [20].

The above velocity damping mechanism allows us to replace the longitudinal force term $\boldsymbol{Gj}$ as follows in the pure plastic dynamics.

$$G\boldsymbol{j} = \boldsymbol{W}_d \rho j_0 \tag{55}$$

$$G\boldsymbol{j} = \boldsymbol{W}_d \rho(\nabla \cdot \boldsymbol{j}) = \rho(\nabla \cdot \boldsymbol{v})\sigma_0 \boldsymbol{v} \tag{56}$$

Here $\boldsymbol{W}_d$ is the drift velocity of the volume moving as a whole in Fig. 16, $\sigma_0$ is the quantity representing the proportionality of $\boldsymbol{W}_d$ with particle velocity $\boldsymbol{v}$, equivalent to the electric conductivity. It represents the above argument that in the pure plastic dynamics, the longitudinal force is not a restoring (elastic) force but energy dissipative resistance force. The solid reacts to the load in the pure plastic dynamics by exerting velocity-damping resistance force, as opposed to exerting elastic resistance force in the elastic dynamics. The conductivity indicates how easily the charge can flow in the particle's velocity field.

With Eq. (56), we can rewrite field Eq. (48) as follows.

$$\nabla \times \boldsymbol{\omega} = -\frac{\rho}{G}\frac{\partial \boldsymbol{v}}{\partial t} - \rho(\nabla \cdot \boldsymbol{v})\sigma_0 \boldsymbol{v} \tag{57}$$

$$= -\frac{\rho}{G}\frac{\partial \boldsymbol{v}}{\partial t} - \sigma_c \boldsymbol{v} \tag{58}$$

Note that in the pure plastic dynamics, the solid still possesses shear elastic force. This is the driving mechanism of the plastic deformation wave. In Eq. (58) $\sigma_c = \rho(\nabla \cdot \boldsymbol{v})\sigma_0$ represents the rate of the velocity damping. Experiments indicate that $\sigma_0$ is a material constant [41, 48]. For a given material, the velocity damping, hence the energy dissipation intensifies with $(\nabla \cdot \boldsymbol{v})$. This indicates that the more the deformation becomes non-uniform, the faster the solid loses its kinetic energy associated with the shear elastic force.

There is another possible scenario to make the equality represented by Eq. (53) as shown in Fig. 15b. In this case, the force acting on the boundaries of the unit volume is proportional to the volume expansion $\nabla \cdot \boldsymbol{\xi}$. Here $\boldsymbol{\xi}$ represents the displacement vector associated with the spatial components of vector potential $\boldsymbol{A}$. As we discuss more in the following section, this force is an elastic force. This form is possible only when the compensation potential $\boldsymbol{A}$ is associated with elastic nonlinear deformation;, i.e., for some reason originally linear-elastic deformation becomes nonlinear, and consequently, different DSEs start to posses their own orientation. This requires $\boldsymbol{A}$ to align all DSEs so that linear elastic law is applicable at the global level. However, the process does not involve energy dissipation, the corresponding force term $G\boldsymbol{j}$ represents the elastic force. In the case the solid enters nonlinear regime due to yield, it is unlikely that $G\boldsymbol{j}$ represents an elastic force. However, as a possibility, this option should be considered. More importantly, as will be discussed in the following section, the material displacement (the displacement irrelevant to the compensation field) exerts this form of longitudinal force. By allowing $G\boldsymbol{j}$ to have this form, we can describe plastic and elastic dynamics in the same form.

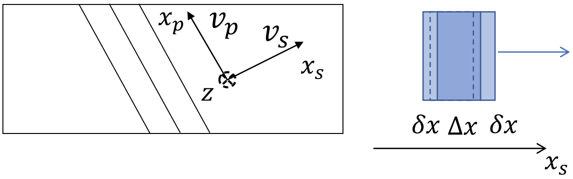

**Fig. 17** Possible mechanism of shear band formation

### 4.1.2 Elastic Deformation Dynamics

In the above discussed plastic deformation dynamics, the longitudinal force term comes to the field equation from the Lagrangian's potential energy term as its dependence on the vector potential. Besides the special case discussed above where the solid exhibits nonlinear elasticity, the elastic longitudinal force does not arise from the gauge field. Rather it comes from the Lagrangian representing the normal (material's not the gauge field's) potential energy term. Thus, most naturally, we can include the longitudinal force term representing the elastic force in the following form.

$$G\boldsymbol{j}_e = (\lambda + 2G)\nabla(\nabla \cdot \boldsymbol{\xi}) \tag{59}$$

Here on the left-hand side $G\boldsymbol{j}_e$ denotes the elastic longitudinal force acting on the unit volume.

### 4.1.3 Shear Band Dynamics

It is widely known that from time to time plastic deformation shows shear bands. In the case of steel, the shear band is known as the Lüders band [49] and normally appears in the post-yield plateau of the stress-strain curve. Our study [50] indicates that the dynamics associated with the shear band formation is formulated through consideration of an order higher term in the Lagrangian of the material energy.

$$\frac{\partial \mathscr{L}}{\partial \phi} - \partial_t\left(\frac{\partial \mathscr{L}}{\partial(\partial_t \phi)}\right) - \partial_x\left(\frac{\partial \mathscr{L}}{\partial(\partial_x \phi)}\right) + \partial_{tt}\left(\frac{\partial \mathscr{L}}{\partial(\partial_{tt} \phi)}\right) + \partial_{xx}\left(\frac{\partial \mathscr{L}}{\partial(\partial_{xx} \phi)}\right) = 0 \tag{60}$$

We have not understood details of this dynamics, but experimentally observed phenomena indicate that it represents a one-dimensional case of the charge $\nabla \cdot \boldsymbol{v}$ [31, 50]. So, here we restrict the discussion in one-dimension.

Figure 17 shows a possible mechanism of the elastic deformation associated with the shear band. The displacement field is characterized by a concentrated stretch running in the direction of maximum shear stress. Here $x_p$ and $x_s$ are coordinate variable parallel and perpendicular to the band.

The Lagrangian that represents the above potential energy can be given as follows.

$$\mathscr{L}_{sb} = \frac{E}{2}\left(\frac{\partial^2 \xi_s}{\partial x_s^2}\right)^2 (\delta x_s \Delta x_s) \tag{61}$$

Considering the term corresponding to the last term on the left-hand side of Eq. (60), we obtain the following force term for the longitudinal force associated with the dynamics of shear band.

$$Gj_{sb} = \frac{\partial^2}{\partial x_{x_s}^2}\left(\frac{\partial \mathscr{L}_{sb}}{\partial(\partial_{x_s}^2 \xi_s)}\right) = E\frac{\partial^4 \xi_s}{\partial x_s^4}(\delta x_s \Delta x_s) \tag{62}$$

Thus we can identify $Gj_{sb}$ as follows.

$$Gj_{sb} = E\frac{\partial^4 \xi_s}{\partial x_s^4}(\delta x_s \Delta x_s) \tag{63}$$

## *4.2 Wave Equations*

### 4.2.1 Plastic Deformation Wave

We can eliminate $\boldsymbol{\omega}$ or $\boldsymbol{v}$ from Eqs. (47) and (48). The resultant equation represents the wave dynamics of $\boldsymbol{v}$ and $\boldsymbol{\omega}$, respectively.

$$\rho\frac{\partial^2 \boldsymbol{v}}{\partial t^2} - G\nabla^2 \boldsymbol{v} + \sigma_c \frac{\partial \boldsymbol{v}}{\partial t} = -G\nabla\left(\nabla \cdot \boldsymbol{v}\right) \tag{64}$$

$$\rho\frac{\partial \boldsymbol{\omega}}{\partial t^2} - G\nabla^2 \boldsymbol{\omega} + \sigma_c \frac{\partial \boldsymbol{\omega}}{\partial t} = 0 \tag{65}$$

Note that the wave equation that governs $\boldsymbol{v}$ (64) has the source term $-G\nabla\left(\nabla \cdot \boldsymbol{v}\right)$. We can view this source term as the gradient of the charge $j_0 = \nabla \cdot \boldsymbol{v}$. When the charge is distributed uniformly, even if $\nabla \cdot \boldsymbol{v} \neq 0$ , its gradient can be considered to be negligible. Under this condition, the right-hand side of Eq. (64) can be approximated by null, and the solution has the following general form.

$$v_p = e^{-\frac{\sigma_c}{2\rho}t}\cos\left\{\left(\frac{G}{\rho}k^2 - \frac{\sigma_c^2}{4\rho^2}\right)^{1/2} t - \boldsymbol{k}\cdot\boldsymbol{r}\right\} \tag{66}$$

Here $\boldsymbol{k}$ is the propagation vector and $\boldsymbol{r} = x\hat{x} + y\hat{y} + z\hat{z}$. Solution (66) is a decaying sinusoidal wave.

Our numerical study [31] indicates that when the right-hand side of Eq. (64) is not negligible, the system becomes unstable and the solution represents an exponentially growing displacement field. We can interpret this situation as the fracture. When the charge $\nabla \cdot \boldsymbol{v}$ becomes nonuniform, the solid fractures. From this viewpoint, we can interpret that the source term $-G\nabla(\nabla\cdot\boldsymbol{v})$ represents the stress concentration. Quite interestingly, when the solid possesses longitudinal elasticity, the system is still stable [31].

Wave equation (65) indicates that the rotation wave also has the same general form as (66). The difference is that in the case of the rotational wave, there is no source term under all conditions. This comes form the fact that there is no rotational charge as field Eq. (48) indicates. The situation is analogous to the electromagnetic field where there is no magnetic monopole.

$$\omega_p = e^{-\frac{\sigma_c}{2\rho}t}\cos\left\{\left(\frac{G}{\rho}k^2 - \frac{\sigma_c^2}{4\rho^2}\right)^{1/2} t - \boldsymbol{k}\cdot\boldsymbol{r}\right\} \tag{67}$$

### 4.2.2 Elasto-Plastic Waves

When elastic and plastic deformation coexist, the wave equation should have source terms representing the elastic and plastic source terms. To formulate this dynamics, first integrate wave equation (64) with respect to time.

$$\rho\frac{\partial^2\boldsymbol{\xi}}{\partial t^2} - G\nabla^2\boldsymbol{\xi} + \sigma_c\frac{\partial\boldsymbol{\xi}}{\partial t} = -G\nabla(\nabla\cdot\boldsymbol{\xi}) \tag{68}$$

Now to include the linear elastic dynamics, we can add the elastic longitudinal force $G\boldsymbol{j}_e$ (59) to the right-hand side of Eq. (68). In doing so, we should note that the displacement vector $\boldsymbol{\xi}$ in Eq. (68) represents the displacement associated with the gauge potential $\boldsymbol{A}$ whereas the displacement vector in expression (59) is the usual displacement arising from the Lagrangian of strain energy. We have not fully understood the relation between these two types of displacement but we know that they are parallel to each other. So here, we absorb the discrepancy from the true displacement associated with the strain energy into the parameter $\lambda$; we can use $\lambda$ different from the normal value for the stage where the deformation is dominantly linear elastic. This treatment is legitimate because under the condition where elastic and plastic deformation is coexist, the value of $\lambda$ is considered to be different from the normal value.

$$\rho\frac{\partial^2\boldsymbol{\xi}}{\partial t^2} - G\nabla^2\boldsymbol{\xi} + \sigma_c\frac{\partial\boldsymbol{\xi}}{\partial t} = -G\nabla(\nabla\cdot\boldsymbol{\xi}) + (\lambda+2G)\nabla(\nabla\cdot\boldsymbol{\xi}) \tag{69}$$

### 4.2.3 Solitary Waves

Experiments indicate that the contours of displacement run parallel to the $x_p$-axis. This allows us to assume the following condition.

$$\frac{\partial \xi_x}{\partial x_p} = \frac{\partial \xi_y}{\partial x_p} = 0 \tag{70}$$

Condition (70) represents the experimental observation that both components of the displacement in the two-dimensional field are independent of variable $x_p$. Under this condition, the $s$-component of the shear restoring force $G\nabla \times \boldsymbol{\omega}$ is null. Also, the fringe pattern generated by the horizontally sensitive and vertically sensitive setup of the same ESPI interferometer show the same pattern [41].

$$(\nabla \times \boldsymbol{\omega})_s = \frac{\partial \omega_p}{\partial z} - \frac{\partial \omega_z}{\partial x_p} = -\frac{\partial}{\partial x_p}\left(\frac{\partial \xi_s}{\partial x_p} - \frac{\partial \xi_p}{\partial x_s}\right) = 0 \tag{71}$$

In Eq. (71), $\partial/\partial z = 0$ because we consider the dynamics in the $x_p - x_s$ plane as a one-dimensional model and $\partial/\partial x_p = 0$ because the displacement components are independent of $x_p$.

With condition $(\nabla \times \boldsymbol{\omega})_s = 0$ shown by Eq. (71) and the longitudinal force expression (63), we can rewrite equation of motion (52) as follows [50].

$$\rho \frac{\partial v_s}{\partial t} + \rho\sigma_0 \frac{\partial v_s}{\partial x_s} v_s + \frac{E\delta x_s \Delta x_s}{c_s} \frac{\partial^3 v_s}{\partial x_s^3} = 0 \tag{72}$$

Equation (72) is known as the Korteweg–de Vries equation, and yields a solitary wave solution in the following form.

$$v_s = A\mathrm{sech}^2\left(b(x_s - c_s t)\right) \tag{73}$$

Here $A$ is the amplitude of the solitary velocity wave in (m/s), $b$ is a shape factor in (1/m) that determines the width of the shear band. The greater the value of $b$, the narrower the shear band. Substitution of solution (73) into wave equation (72) leads to the following conditions.

$$c_s = \frac{\sigma_0 A}{3} \tag{74}$$

$$b = \left(\frac{\sigma_0 A}{3}\right)\sqrt{\frac{\rho}{4E\delta x_s \Delta x_s}} \tag{75}$$

The sign of solitary wave velocity $c_s$ determines the direction of the wave [31]. The physical mechanism that determines the direction of the solitary wave has not been fully understood. However, the following speculation seems reasonable. When the deformation develops to the level where a shear band is formed, dislocations starting from one side of the specimen propagate along the line of maximum shear stress. When they reach the other side of the specimen, the trajectory of the dislocations undergoes a large stretch. This stretch is observed as a shear band, and it travels as a solitary wave. When this stretching event happens, the particles on the respect side of the stretch recoil in mutually opposite directions away from the shear band. This

**Fig. 18** Solitary waves traveling mutually opposite directions

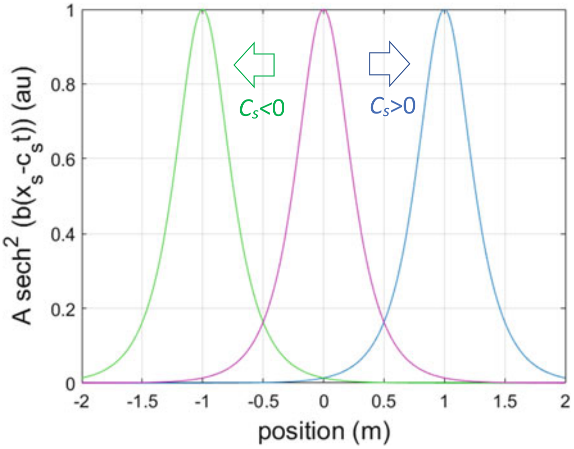

direction determines the sign of the amplitude $A$. If the recoil is in the positive $x_s$ direction, $c_s > 0$, and if it is in the negative $x_s$ direction, $c_s < 0$ (Fig. 18). In principle, a pair of solitary waves traveling opposite directions can be generated from the same large stretching event. However, experiments indicate that from one event, only one solitary wave is generated and travels in a direction. The probability to travel in the positive direction seems to be the same as to travel in the negative direction. It is not clear at this time what determines the direction of the solitary wave.

### 4.2.4 Evolution of Deformation Dynamics

Figure 19 is a close view of fringe patterns (b) and (c) in Fig. 8. The arrows inserted in (b) indicate the horizontal and vertical displacement components. The pair of the fringe patterns show the rotational features in both displacement components. Notice that the $v$ pattern shows that the fringes above the stretched region marked "1" run from the top left to the bottom right. Since these fringes are formed by a tensile deformation, the fringes appearing toward the top of the specimen represent greater upward displacement than the one towards the bottom. So, above the region "1", the upward displacement is greater in going to the right side of the specimen. The situation is opposite below region "1". The fringes run from the top right to the bottom left.[2] In other words, the rotation is counterclockwise above the stretched region[3] and clockwise below the region, indicating $\nabla \times \boldsymbol{\omega} \neq 0$ at this stage. In contrast, Fig. 19c indicate less $\nabla \times \boldsymbol{\omega}$ feature, and instead, shows clearly a rather uniform $\nabla \cdot \boldsymbol{\xi}$ feature ($\partial u/\partial x \neq 0$ and $\partial v/\partial y \neq 0$ and the patterns are uniform over the specimen). The loading curve in Fig. 8 indicates that the stress increase in stage (b) is slightly higher

---

[2] The arrows are drawn longer here to emphasize that the displacement is greater on the left side. The lengths are not to scale as compared with above region "1".

[3] The fringes in the $u$ pattern also indicate counterclockwise rotation.

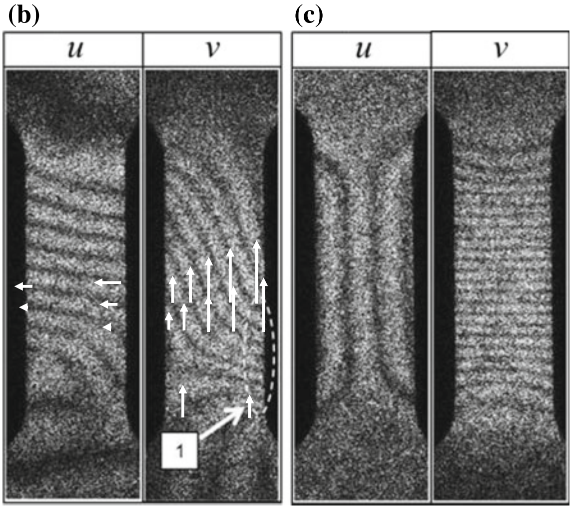

**Fig. 19** Close view of fringes in Fig. 8. Arrows represent components of displacement occurring during time difference of two interferometric images used for subtraction of fringe formations

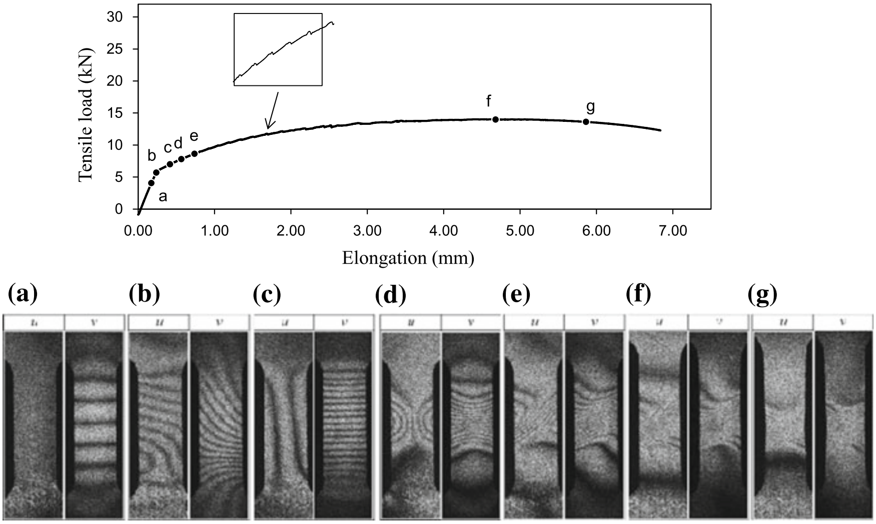

**Fig. 20** Loading curve of aluminum alloy 7075 T7 and fringe patterns corresponding to horizontal (u) and vertical (v) displacement components [39]

than (c). It is possible to interpret that the stress increase in these stages is due to the shear force $G\nabla \times \boldsymbol{\omega}$ and the shear force is greater in (b) than (c).

The change in the fringe pattern in association with the evolution of deformation is also seen in Fig. 20 [39]. This figure shows the fringe patterns at several points on the

**Fig. 21** Comparison of charges $\partial v/\partial y$ between stages (c) and (d)

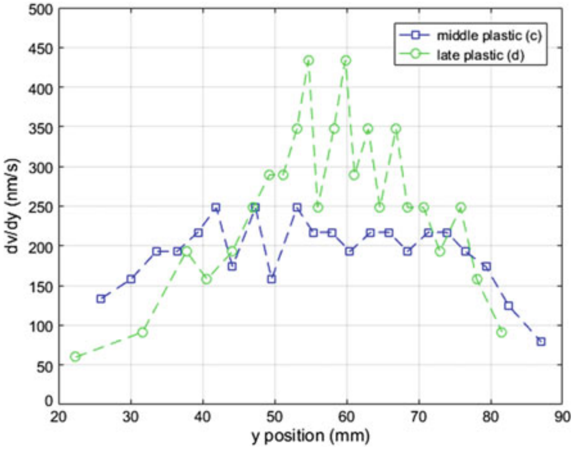

loading characteristics for a specimen of aluminum alloy 7075 T7, and is equivalent to Fig. 8 for aluminum alloy 7075 T6. Here, aluminum alloy 7075 T7 is slightly softer than aluminum alloy 7075 T6 with the same chemical composition[4] At stage (a), the $v$ fringe pattern shows equidistant, straight dark fringes indicating uniform $\nabla \cdot \boldsymbol{\xi}$, and $\boldsymbol{\omega} = 0$, hence $\nabla \times \boldsymbol{\omega} = 0$. This characterizes linear elastic deformation. The loading curve indicates that this stage is well before the yield point.

In stage (b), the fringe pattern indicates the $\nabla \times \boldsymbol{\omega} \neq 0$ feature similar to Fig. 8b. The rotational feature diminishes in going to stage (c), while $\nabla \cdot \boldsymbol{\xi}$ is uniform, as is the case of Fig. 8c. The non-uniformity of $\nabla \cdot \boldsymbol{\xi}$ increases with the evolution of deformation toward the final fracture. The $\partial v/\partial y$ pattern is more concentrated to the middle of the specimen keeping the horizontal symmetry.

Figure 21 plots $\partial v/\partial y$ along the vertical central line for $v$ fringe images at stage (c) and (d). It is seen that the $\partial v/\partial y$ (the one dimensional $\nabla \cdot \boldsymbol{\xi}$) is more concentrated in the middle region in stage (d) than (c).

At stage (e), the symmetry starts to break. The curved feature observed on the left side in the $u$ fringe (highlighted with a dashed circle) indicates that the rotational feature becomes prominent again as the $\nabla \cdot \boldsymbol{\xi}$ pattern becomes more concentrated. At stage (f), the right side of the specimen shows rotational feature in the opposite direction to the one on the left side. At the same time, more concentrated $\nabla \cdot \boldsymbol{\xi}$ pattern appears at the boundary of the mutually opposite rotational features, running diagonally at approximately 45° to the tensile axis. It is natural to interpret that this concentrated $\nabla \cdot \boldsymbol{\xi}$ along the boundary of rotations develops to a shear band. At stage (g), the $u$ and $v$ patterns are very similar to each other, showing the characteristic feature of the fringe pattern of a shear band, i.e., the $u$ and $v$ fringe patterns show the same feature as condition (70) holds (see Sect. 4.2.3).

---

[4] The aluminum alloy 7705 (Al-Zn-Mg-Cu alloy) specimen was first solid-solution treated and hardened by nano-scale precipitates up to the peak hardness (7075 T6). Subsequently, the alloy was over-aged at 400 °C for 30 min to soften the matrix by coarsening the precipitates (7075 T7).

In terms of the wave dynamics, we can discuss the above transition as follows. In the initial stage when the deformation is characterized as linear elasticity (stage (a)), the displacement field does not have the rotational feature. Therefore, $\nabla \times \boldsymbol{\omega} = \nabla(\nabla \cdot \boldsymbol{\xi}) - \nabla^2 \boldsymbol{\xi} = 0$. In addition, the solid does not have velocity damping mechanism. In wave equation (69), the corresponding terms $\nabla^2 \boldsymbol{\xi}$ and $\nabla(\nabla \cdot \boldsymbol{\xi})$ do not appear on the left-hand and right-hand sides of equation, respectively, and $\sigma_c = 0$. The only remaining terms are $\rho \partial^2 \boldsymbol{\xi} / \partial t^2$ and $(\lambda + 2G)\nabla\, (\nabla \cdot \boldsymbol{\xi})$. Consequently, the wave equation takes the following form.

$$\rho \frac{\partial^2 \boldsymbol{\xi}}{\partial t^2} = \nabla(\nabla \cdot \boldsymbol{\xi}) \tag{76}$$

If divergence is applied to both-hand side, Eq. (76) reduces to the well-known equation of compression wave.

$$\rho \frac{\partial^2 (\nabla \cdot \boldsymbol{\xi})}{\partial t^2} = \nabla^2 (\nabla \cdot \boldsymbol{\xi}) \tag{77}$$

When the deformation develops to stage (b), the rotational effect becomes significant. This makes $\nabla \times \boldsymbol{\omega}$ terms appear in the equation. However, since $(\nabla \cdot \boldsymbol{\xi})$ is still uniform, the $\nabla(\nabla \cdot \boldsymbol{\xi})$ is not effective. Only $\nabla^2 \boldsymbol{\xi}$ and $\sigma_c (\partial \boldsymbol{\xi} / \partial t)$ terms appear in the wave equation. This situation yields a sinusoidal decaying wave solution represented by Eq. (66) and Fig. 11.

As the deformation develops further, the shear elastic mechanism represented by $G \nabla^2 \boldsymbol{\xi}$ decreases. The $v$ fringe pattern in this stage is characterized by unequally distanced pseudo-parallel horizontal fringes getting concentrated to the middle of the specimen (stage (c)–(f)). This change is accompanied by the reduction in the positive slope (the slope is proportional to $G$) on the loading curve. The wave solution is still sinusoidal-like but with the reduction in the shear modulus $G$, the wave velocity decreases, and consequently, the oscillation period increase. Eventually, the oscillation period becomes infinite and this generates discontinuity in the solid.

When the displacement field starts to show a concentrated $\partial v / \partial y$ running diagonally across the specimen, the dislocations are ready to bridge the width of the specimen. At this point, the elasticity is not sustained by $G \nabla^2 \boldsymbol{\xi}$ but the longitudinal force (63) associated with the potential energy of shear band. The wave equation takes the form of Eq. (72) yielding the solitary wave solution.

### 4.2.5 Fracture

In the preceding section we discussed various forms of deformation wave. Experiments indicate that when the deformation wave stops traveling the specimen fractures. Waves in general carry energy. As discussed above, the deformation wave carry the strain energy. It is naturally understood that when a deformation wave stops traveling and the external load keeps providing the specimen with energy, the solid material loses the mechanism to transfer energy from one point to another. Consequently, the strain energy stagnates at a certain point and that causes the fracture. Tensile experiments [41] indicate that in some cases the shear band does not appear until the very last stage of deformation when the specimen fractures, and in other cases a dynamics shear band appears in an early stage and fracture occurs when the shear band becomes stationary. Call the first type "Type 1 fracture" and the second type "Type 2 fracture", and consider the fracture mechanism for the respective cases.

Type 1 Fracture

In this case, the decaying sinusoidal wave explains the fracture. When the wave stops traveling, the fracture occurs. The wave velocity is the product of the wavelength and frequency. Normally, the wavelength is determined by the boundary condition such as the way the specimen is clamped. When the wave velocity becomes zero and the boundary condition remains the same, hence the wavelength remains the same, it follows that the frequency approaches zero. Zero frequency means a infinite period, indicating that the displacement does not change the sign. Consequently, the points on the specimen keep moving in the same direction, and this leads to the generation of discontinuity. In a three dimensional picture, this can be expressed as an infinite volume expansion.

Type 2 Fracture

In this case, the solitary wave carries concentrated stress energy. The material resists to the external load via velocity damping force. When the external load keeps providing the specimen with energy and the solitary wave stops moving, the following conditions hold in the energy damping force expression $Gj_p = W_d \rho (\nabla \cdot \boldsymbol{v}))$; $Gj_p \neq 0$ and $W_d = 0$. Since $\rho$ is a finite value, these conditions lead to $(\nabla \cdot \boldsymbol{v}) \rightarrow \infty$, indicating that the particles flow out from a unit volume at the infinite rate. It is also possible to interpret this condition as the infinite rate of volume expansion. Naturally, it causes material discontinuity and the specimen fractures.

## 5 Conclusions

Deformation and fracture of solids have been discussed comprehensively as wave dynamics based on the same theoretical basis. The nonlinearity of deformation in the plastic stage is formulated through the application of the local symmetry principle to the theory of linear elasticity. In this process, the compensation (gauge) field has been introduced and the corresponding Lagrangian has been identified. With the application of the least action principle, a set of field equations have been derived.

From the dynamical point of view, the field equations describe the translational and rotational behaviors of the deformation field. Transverse and longitudinal forces are identified as being represented by certain terms of the field equations. The elasticity and plasticity are characterized by the respective forms of the longitudinal force term. For elasticity, the longitudinal force term represents elastic force proportional to the volume expansion. For plasticity, the longitudinal force term represents a velocity damping force that causes the irreversibility of plastic deformation. These forces are interpreted as the resistance force exerted by the solid in response to the external load. The oscillatory feature of plasticity comes from the elastic shear force.

The fracture has been identified as the final stage of plastic deformation where the solid totally loses the elastic restoring mechanism. Consequently, the dynamics loses the oscillatory feature and the displacement field becomes unidirectional. This causes the solid to generate material discontinuity. A number of experimental observations that support the theoretical development have been presented and interpreted based on the present theory.

**Acknowledgements** The present theoretical development has been made with the help of a number of people. The author owes a debt of gratitude to all of them. In particular, the author is extremely grateful to Academician V. E. Panin for the introduction of his original theory that the present theory stemmed out, and Professor V. E. Egorushkin for his guidance that helped the author to deepen his understanding of the gauge field theory. The author also highly appreciate Professor C. A. Sciammarella for his continuous encouragement and fruitful discussions. It is unfortunate that the space is not enough to mention more people that I would like to express my gratitude.

## References

1. Timoshenko, S.P., Goodier, J.N.: Theory of Elasticity. McGraw-Hill, New York (1951)
2. Landau, L.D., Lifshitz, E.M.: Theory of Elasticity, 3rd edn. Butterworth-Heinemann, Oxford (1986)
3. Orowan, E.: Z. Phys. **89**, 605–613, 614–633, 634–659 (1934)
4. Polanyi, M.: Z. Phys. **89**, 660–664 (1934)
5. Taylor, G.I.: Proc. R. Soc. A **145**, 362–387 (1934)
6. Lublinaer, J.: Plasticity Theory. Courier Dover, New York (2008)
7. Gokhfeld, D.A., Sadakov, O.S.: A unified mathematical model for plasticity and creep under variable repeated loading. In: Zyczkowski, M. (ed.) Creep in Structures, pp. 23–28. Springer, Berlin (1991)
8. Hill, R.: The Mathematical Theory of Plasticity. Oxford University Press, Oxford (1998)
9. Yoshida, S.: Deformation and Fracture of Solid-State Materials - Field Theoretical Approach and Engineering Applications. Springer, New York (2015)
10. Yoshida, S.: Comprehensive description of deformation of solids as wave dynamics. Math. Mech. Comput. Syst. **3** (2015). https://doi.org/10.2140/memocs.2015.3.243
11. Yoshida, S., Muhamad, I., Pardede, M., Widiastuti, R., Siahaan, M.B., Kusnowo, A.: Optical interferometry applied to analyze deformation and fracture of aluminum alloys. Theor. Appl. Fract. Mech. **27**, 85–98 (1997)
12. Yoshida, S.: Optical interferometric study on deformation and fracture based on physical mesomechanics. J. Phys. Meso. Mech. **2**(4), 5–12 (1999) [in English and Russian]
13. Yoshida, S.: Interpretation of mesomechanical behaviors of plastic deformation based on analogy to Maxwell electromagnetic theory. J. Phys. Meso. Mech. **4**(3), 29–34 (2001)
14. Yoshida, S., Ishii, H., Ichinose, K., Gomi, K., Taniuchi, K.: Observation of optical interferometric band structure representing plastic deformation front under cyclic loading. J. Jpn. Appl. Phys. **43**, 5451–5454 (2004)
15. Yoshida, S., Ishii, H., Ichinose, K., Gomi, K., Taniuchi, K.: An optical interferometric band as an indicator of plastic deformation front. J. Appl. Mech. **72**, 792–794 (2005)

16. Yoshida, S., Rourks, R.L., Mita, T., Ichinose, K.: Physical mesomechanical criteria of plastic deformation and fracture. Phys. Mesomech. **12**(5–6), 249–253 (2009)
17. Elliott, J.P., Dawber, P.G.: Symmetry in Physics, vol. 1. Macmillan, London (1984)
18. Chaichian, M., Nelipa, N.F.: Introduction to Gauge Field Theories. Springer, Berlin (1984)
19. Frampton, P.H.: Gauge invariance. Gauge Field Theories. The Benjamin/Cummings Publishing Company, Menlo Park (1987)
20. Aitchson, I.J.R., Hey, A.J.G.: Gauge Theories in Particle Physics. IOP Publishing, Bristol (1989)
21. Egorushkin, V.E.: Gauge dynamic theory of defects in nonuniformly deformed media with a structure, interface behavior. Sov. Phys. J. **33**, 135–149 (1990)
22. Edelen, D.G.B.: A correct, globally defined solution of the screw dislocation problem in the gauge theory of defects. Int. J. Eng. Sci. **34**, 81–86 (1996)
23. Lazar, M.: On the fundamentals of the three-dimensional translation gauge theory of dislocations. Math. Mech. Solids **16**, 253–264 (2011)
24. Panin, V.E., Grinaev, Y.V., Egorushkin, V.E., Buchbinder, I.L., Kulükov, S.N.: Spectrum of excited states and the rotational mechanical field. Sov. Phys. J. **30**, 24–38 (1987)
25. Panin, V.E.: Wave nature of plastic deformation. Sov. Phys. J. **33**, 99–110 (1990)
26. Panin, V.E. (ed.): Physical Mesomechanics and Computer-Aided Design of Materials. Nauka, Novosibirsk (1995) [in Russian]
27. Panin, V.E.: Physical fundamentals of mesomechanics of plastic deformation and fracture of solids. In: Panin, V.E. (ed.) Physical Mesomechanics of Heterogeneous Media and Computer-Aided Design of Materials. Cambridge International Science Publishing, Cambridge (1998)
28. Danilov, V.I., Zuyev, L.B., Mnikh, N.M., Paninand, V.Y., Shershova, L.V.: Phys. Met. Metallogr. **71** (1991)
29. Danilov, V.I., Zuev, L.B., Panin, V.E.: Wave nature of plastic deformation of solids. In: Panin, V.E. (ed.) Physical Mesomechanics and Computer-Aided Design of Materials, vol. 1, p. 241. Nauka, Novosibirsk (1995) [in Russian]
30. Barannikova, S.A., Zuev, L.B., Danilov, V.I.: Kinetics of periodic processes during plastic flow. Phys. Solid State **41**(7), 1112–1114 (1999)
31. Yoshida, S., McGibboney, C.: Fracture of solids based on deformation wave dynamics. In: AIP Conference Proceedings, in press (2018)
32. Sasaki, T., Yoshida, S.: Revealing load hysteresis based on electronic speckle pattern interferometry and physical mesomechanics. Phys. Mesomech. **15**, 47–57 (2012)
33. Marsden, J.E., Hughes, T.J.R.: Mathematical Foundations of Elasticity. Prentice-Hall, Englewood Cliffs (1983)
34. Kenyon, I.R.: Kenyon General Relativity. Oxford University Press, Oxford (1990)
35. Griffiths, D.J.: Introduction to Electrodynamics, 3rd edn. Prentice Hall, Upper Saddle River (1999)
36. Schiff, L.I.: Quantum Mechanics, 3rd edn. International Student Edition, pp. 521–522. McGraw-Hill, Kogakusha, LTD., Tokyo (1968)
37. Sirohi, R.S. (ed.): Speckle Metrology. Marcel Dekker, New York (1993)
38. Sciammarella, C.A., Sciammarella, F.M.: Experimental Mechanics of Solids. Wiley, Hoboken (2012)
39. Sasaki, T., Suzuki, H., Yoshida, S.: Evaluation of dynamic deformation behavior of aluminum alloy by electronic speckle pattern interferometry. In: Jin, H., Sciammarella, C., Furlong, C., Yoshida, S. (eds.) Imaging Methods for Novel Materials and Challenging Applications. Conference Proceedings of the Society for Experimental Mechanics Series, vol. 3. Springer, New York (2013)
40. Yoshida, S., Siahaan, B., Pardede, M.H., Sijabat, N., Simangunsong, H., Simbolon, T., Kusnowo, A.: Phys. Lett. A **251**, 54–60 (1999)
41. Yoshida, S., Widiastuti, S.R., Pardede, M., Hutagalung, S., Marpaung, J.S., Muhardy, A.F., Kusnowo, A.: Direct observation of developed plastic deformation and its application to nondestructive testing. Jpn. J. Appl. Phys. **35**, L854–L857 (1996)

42. Yoshida, S., Sasaki, T.: Field theoretical description of shear bands. In: Beese, A.M., et al. (eds.) Fracture, Fatigue, Failure and Damage Evolution, Proceedings of the SEM 2015 Annual Conference, vol. 8, pp. 141–149 (2016)
43. Yoshida, S., Toyooka, S.: Field theoretical interpretation on dynamics of plastic deformation-Portevin-Le Chatelie effect and propagation of shear band. J. Phys. Condens. Matter **13**, 1–17 (2001)
44. Sasaki, T., Nakamura, T., Yoshida, S.: Observation of grain-size effect in serration of aluminum alloy. In: Jin, H., Sciammarella, C., Yoshida, S., Lamberti, L. (eds.) Advancement of Optical Methods in Experimental Mechanics. Conference Proceedings of the Society for Experimental Mechanics Series, vol. 3. Springer, Cham (2015)
45. Sasaki, T.: Private communication (2014)
46. Yoshida, S., Muhamad, M., Widiastuti, R., Kusnowo, A.: Optical interferometric technique for deformation analysis. Opt. Exp. **2**, 516–530 (1998)
47. Suzuki, T., Takeuchi, S., Yoshinaga, H.: Dislocation Dynamics and Plasticity. Springer, Berlin (1989)
48. Toyooka, S., Widiastuti, R., Qingchuan, Z., Kato, H.: Dynamic observation of localized strain pulsation generated in the plastic deformation process by electronic speckle pattern interferometry. Jpn. J. Appl. Phys. **40**, 310–313 (2001)
49. Lders, W.: Dinglers Polytech. J. **155**, 18–22 (1860)
50. Yoshida, S.: Wave nature in deformation of solids and comprehensive description of deformation dynamics. Proc. Est. Acad. Sci. **64**, 438–448 (2015)